Fall 12-15-2012

Analysis and Characterization of Residual Stresses in Pipe and Vessel Welds

Shaopin Song
ssong@uno.edu

Analysis and Characterization of Residual Stresses in Pipe and Vessel Welds

A Dissertation

Submitted to the Graduate Faculty of the
University of New Orleans
in partial fulfillment of the
requirements for the degree of

Doctor of Philosophy
in
Engineering and Applied Science
Naval Architecture & Marine Engineering

by

Shaopin Song

B.S. Dalian University of Technology, Dalian, China, 2007
M.S. University of New Orleans, New Orleans, LA, 2009

December, 2012

DEDICATION

To my lovely wife and dear parents

ACKNOWLEDGEMENT

First and foremost, I would like to express my sincere gratitude to my advisor, Dr. Pingsha Dong, for his support, enthusiasm, encouragement and patience throughout the period of this research. His guidance as a scientist and mentor is deeply appreciated.

Special thanks are also due to Dr. Jinmiao Zhang who has shared his comprehensive knowledge at various stages of this research, and to Dr. Anna Paradowska who gave me valuable suggestions on this dissertation. Thanks are also extended to the other members of my thesis committee, Dr. Dongming Wei, Dr. Lothar Birk, Dr. Brandon Taravella and Dr. Paul Schilling, for their time and effort in reviewing the manuscript. I would also express my appreciation to Dr. William Vorus who offered me the opportunity to study in the University of New Orleans.

I would like to thank our group, welded structures laboratory, and all faculties and students in school of Naval Architecture and Marine Engineering for their help during this research.

Finally, I would like to thank my family for their unconditional love and support. I can never thank them enough for that. They are the backbone of my world.

Table of Contents

NOMENCLATURE

A_p	plastic zone area, mm^2
A_{pass}	averaged pass area, mm^2
C_p	specific heat, J/(Kg K)
CTE	coefficient of thermal expansion, /K
D	flexural rigidity
d_p	distance from the weld toe to the boundary of plastic zone, mm
E	Young's modulus, GPa
F_w	circumferential shrinkage force, N
I	current
k	conductivity, W/(mm K)
ℓ	weld pool length
L_{surf}	weld pass surface contacted to the surroundings
M_0	bending moment at the weld toe for seam welds, N mm
M_x	axial bending moment, N mm
M_θ	hoop bending moment, N mm
n	number of layers
N_0	normal force at the weld toe for seam welds, N
N_x	axial shear force, N
N_θ	hoop shear force, N
q	heat source strength, q=UI η
Q'	linear heat input, J/mm
$\hat{Q}$	characteristic heat input, J/mm^2
r	mean radius of the pipe
r_w	radius of the averaged pass area, mm
S_y	yield strength, MPa
$S_+^{s.e.}$	surface value of self-equilibrating part where bending is positive (tension)
$S_-^{s.e.}$	surface value of self-equilibrating part where bending is negtive (compression)
t	pipe thickness
t_n	layer thickness, mm
T_0	ambient temperature, ℃
T_m	melting temperature, ℃
ΔT_p	temperature to reach yield magnitude on heating in rigid constraints condition, ℃
U	voltage
v	welding speed, mm/sec
w	deflection in z-direction, mm
w_p	weld zone width, mm
α	thermal diffusivity, mm^2/s
$\sigma(x)$	residual stress, MPa
σ_m	membrane component of the residual stress, MPa
σ_b	bending component of the residual stress , MPa
$\sigma_{s.e.}$	decomposed self-equilibrating component of the residual stress, MPa
$\sigma_{x,b}$	decomposed bending component of the residual stress in the pipe axial direction, MPa
$\sigma_{\theta,m}$	decomposed bending component of the residual stress in pipe hoop direction, MPa

$\sigma_{\theta,b}$ decomposed bending component of the residual stress in pipe hoop direction, MPa

$\sigma_{\theta,m}^{ave}$ decomposed membrane component at the weld centerline of hoop residual stress from FEA, MPa

$\sigma_{\theta,m}^{0}$ decomposed membrane component at the weld toe of hoop residual stress from FEA, MPa

$\sigma_{\theta,b}^{0}$ decomposed bending component at the weld toe of hoop residual stress from FEA, MPa

$\sigma_{x,b}^{0}$ decomposed bending component at the weld toe of axial residual stress from FEA, MPa

λ time, sec

λ_w time for travelling per unit thickness, sec/mm

ρ density, g/mm^3

η welding efficiency

η' factor in linear heat input equation

ABBREVIATIONS

API	American Petroleum Institute
ASME	American Society of Mechanical Engineering
BS	British Standards
CTE	Coefficient of Thermal Expansion
DHD	Deep-Hole Drilling
DMW	Dissimilar Metal Weld
DV	Double V
EPRI	Electric Power Research Institute
FE	Finite Element
FEA	Finite Element Analysis
FFS	Fitness-For-Service
FPSO	Floating Production, Storage and Offloading
HAZ	Heat Affected Zone
IIW	International Institute of Welding
ID	Inner Diameter
JIP	Joint Industry Project
ND	Neutron Diffraction
NeT	European network on neutron techniques standardization for structural integrity
NG	Narrow Groove
NRC	Nuclear Regulatory Commission
OD	Outer Diameter
ONR	Office of Naval Research
PVRC	Pressure Vessel Research Council
PWSCC	Primary Water Stress Corrosion Cracking
RSDP	Residual Stress and Distortion Prediction
SD	Synchrotron X-ray Diffraction
SV	Single V
TG	Task Group
VORSAC	Variation of Residual Stress in Aged Components
WCL	Weld Centerline
WT	Weld Toe
XRD	Laboratory X-ray Diffraction

ABSTRACT

This research sought to establish residual stress distribution characteristics in typical pipe and vessel welds by carrying out a comprehensive parametric study using an advanced sequentially coupled thermo-mechanical finite element procedure. The software package used in this study was ABAQUS 6.9. The parametric study covered vessel and pipe components with a ranging radius to thickness ratio r/t from 2 to 100, for thickness t ranging from 1/4" to 10". Component materials varied from low carbon steel to high alloy steels, such as stainless steel and titanium alloy. Furthermore, a structural mechanics based framework is proposed to generalize through-thickness residual stress distributions (often referred to as profiles) for a broad spectrum of joint geometry and welding conditions. The results of this study have been shown to provide both a significantly improved understanding of important parameters governing residual stresses in pipe and vessel welds, as well as a unified scheme for achieving consistent residual stress prescriptions for supporting fitness-for-service (FFS) assessments of engineering structures. Specific contributions of this investigation may be summarized as follows:

(a) A welding heating input characterization procedure has been developed and validated to relate prescribed temperature thermal modeling procedure to conventional linear input definition. With this development, a large number of parametric analyses can be carried out in a cost-effective manner without relying on the heat flux based weld pool model that can be exhaustively time-consuming.
(b) A set of governing parameters controlling important residual stress distribution characteristics regardless of joint types, materials, and welding procedures have been identified. These are characteristic heat input intensity and radius over thickness ratio (r/t).
(c) A shell theory based residual stress estimation scheme has been developed to interrelate all parametric analysis results for circumferential girth welds, which can also be used to estimate residual stress distributions in both through-thickness and at any distance away from the weld, for cases that are not covered in the parametric study.
(d) In a similar manner, a curve bar theory based residual stress estimation scheme has also been developed for longitudinal seam welds.

These developments can significantly advance current knowledge of the residual stress profiles and will provide valuable feedback for the prescription methods stipulated in the current national and international FFS Codes and Standards such as 2007 API 579 RP/ASME FFS-1 and BS 7910: 2011.

Key Words: Residual Stress, Finite Element Analysis, Girth Welds, Seam Welds, Linear Heat Input, Shell Theory, Curved Bar Theory, Full-Field Stress Distribution, Fitness-for-Service, Fracture Mechanics

1. INTRODUCTION

1.1 Background

Welding has been extensively used as one of the most important mechanical joining processes in engineering industries. In general, welding provides many attractive unique advantages such as: low cost, design flexibility, versatility, enhanced efficiency and productivity, reduced overall weight, improved structural performance, as well as many other advantages. However, welding, by nature, also presents a number of challenging problems to the design, manufacturing and maintenance community. Such challenges are attributed to the complicated nature of the welding process which is associated with multiple engineering fields such as: physics, heat transfer, fluid mechanics, metallurgy, mechanics (mechanics of materials, structural mechanics, theory of plates and shell, elasticity, plasticity, computational mechanics) and finite element analysis. Consequently, some of welding-induced phenomena are sophisticated problems that need to be carefully examined, for example, residual stress distributions.

Welding-induced residual stresses are due to plastic deformation which is produced by highly localized heating and cooling processes under a certain level of restraint condition. Such restraint conditions include parent metal (restricting weld material from free expansion on heating and contraction on cooling), external fixtures, or other attachments to the component being welded. The overall residual stress distribution in a welded component achieves an equilibrium condition. Furthermore, some specific residual stress features can be attributed to factors such as material properties, phase transformation, weld geometry, number of passes, weld pass sequence, welding process, and welding parameter, among others. As such, predicting residual stresses, especially in complex structures, is sometimes an intractable problem owing to the mentioned complex multi-physics nature associated with welding procedure.

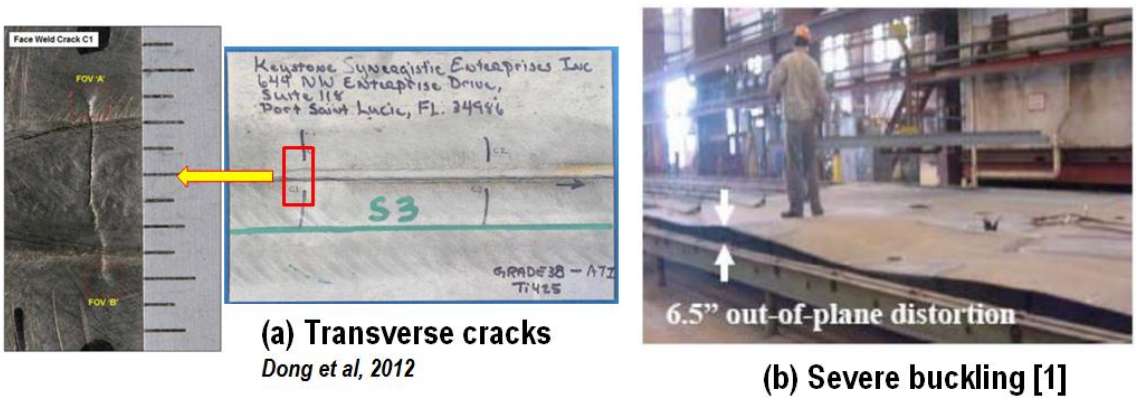

(a) Transverse cracks
Dong et al, 2012

(b) Severe buckling [1]

Figure 1-1 Welding-induced residual stress impact manufacturability: (a) transverse cracks in titanium butt welds, and (b) buckling distortions in light ship structures [1]

Generally speaking, the inevitable welding-induced residual stresses existing in welded structures can significantly impact manufacturability and structural integrity. In terms of manufacturability, a large number of issues could be encountered during assembly processing. For instance, numerous transverse cracks were recently found in titanium butt welds as shown in Figure 1-1 (a), which is primarily owing to the high tensile longitudinal residual stress in a butt welded plate. In Figure 1-1 (b), a wide spread of bucking distortions can be clearly seen in lightweight ship panels. These distortions are mainly caused by a high shrinkage force generated by welding-induced residual stress. In terms of structural integrity, cracks/defects may be initiated or formed by the presence of residual stress which would increase the susceptibility of structures to catastrophic consequences. One of examples is corner cracks in FPSOs (Floating production, storage and offloading) as shown in Figure 1-2 (a), and another one is typical defects in pipe girth welds which are widely used in offshore, nuclear and petrochemical industries as shown in Figure 1-2 (b). In order to ensure structural safety and reliability for the entire service life, these cracks/defects near or in a weld must be evaluated by performing the FFS (fitness-for-service) based assessment procedure. Residual stress fields at defect locations are required for these assessments and need to be accurately obtained [4].

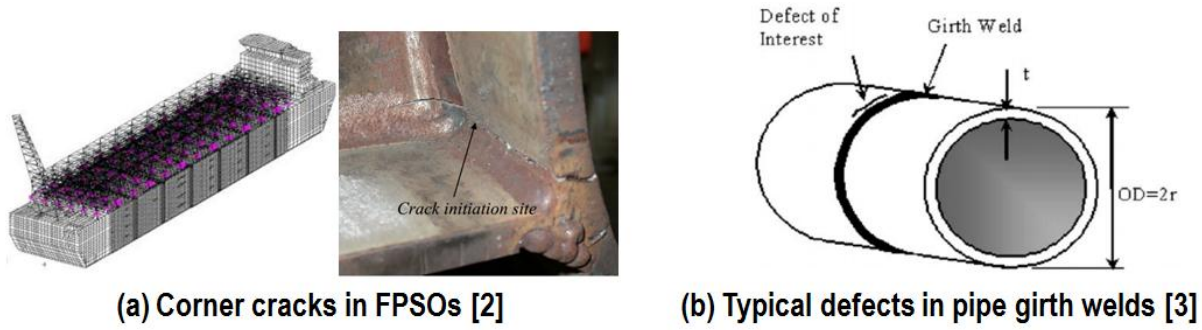

Figure 1-2 Welding-induced residual stress impact structural integrity: (a) corner cracks in FPSO s [2], and (b) typical defects in pipe girth welds [3]

Welding-induced residual stress distributions for typical weldments have been documented in some well-known FFS based structural integrity assessment procedures [5-9], e.g., API 579 RP, BS 7910, R6, SINTAP, FITNET, etc.. These distributions are intended to provide upper bond or conservative residual stress prescriptions based on available experimental measurements and finite element results. However, the above codes and standards [5-9] are only valid for the structure thickness less than 2" (50mm). In today's engineering structures, thickness of many components can easily go up to 4" or 10". Furthermore, only limited joint configurations are considered in [5-9]. For instance, Narrow Groove welds are not addressed in [5-9], but are extensively used today.

Above all, a prescribed through-thickness residual stress profile at a weld location can exhibit a significant variation from one procedure to another [5-9] for a simple pipe girth weld with the same welding conditions, as shown in Figure 1-3 [4]. It should be noted that the API579 used in Figure 1-3 was an earlier version, not the one recently revised in 2007 [5]. Several possible

reasons, as discussed in [3-4,10-12], contribute to these drastically different residual stress distributions. They are summarized as below:

1) As stated before, the residual stress development during the multi-physics welding process is immensely complicated.
2) Various finite element (FE) modeling techniques and assumptions have been attempted and predicted results show a high degree of variability. Such assumptions and modeling techniques include melting/re-melting, material hardening models, boundary conditions, and others, which will be discussed in the following chapters.
3) Different measurement techniques could present a broad range of results owing to resolution, preparation, and specimen cut size for interested locations. Moreover, all measurement techniques are subjected to interpretation which may further introduce discrepancy.
4) Assorted bounding methods have been applied to various sub-sets of FE/measurement residual stress data, covering a wide range of materials and welding parameters, among others.
5) Last but not least, these results lack physical and mechanics based interpretation, which are only based upon limited FE results or measurement data.

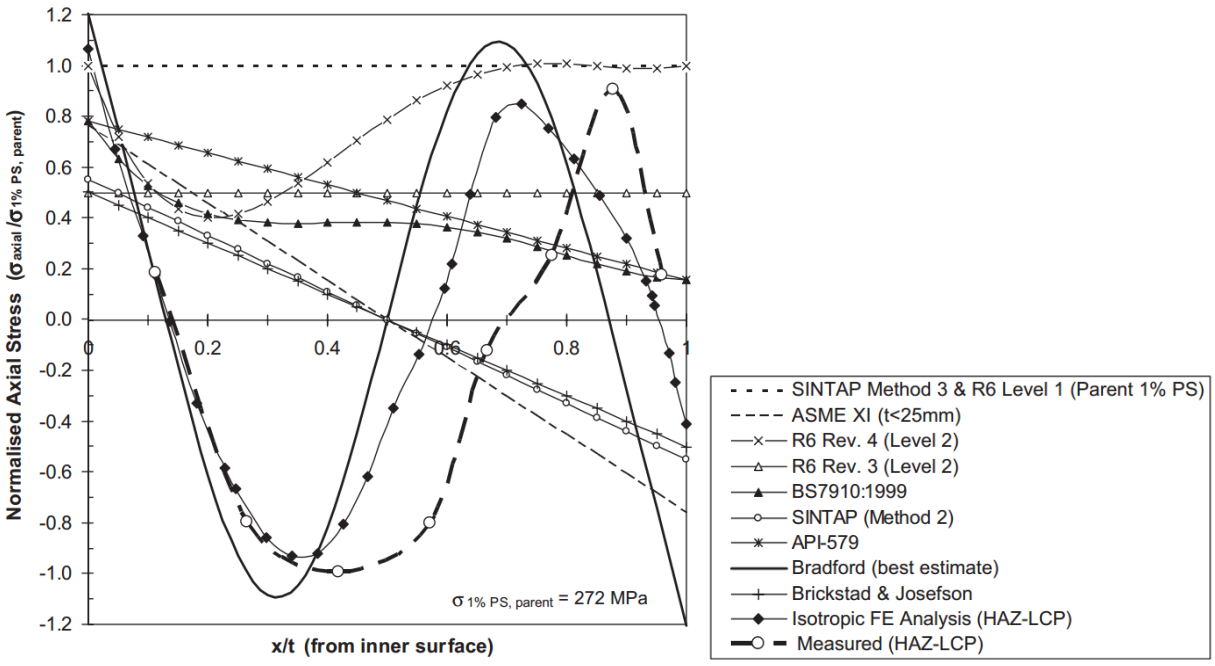

Figure 1-3 Comparison of axial residual stress profiles for pipe girth weld (t=19.6mm, r/t=10.5, E=1.4kJ/mm) using different codes/standards/recommended practices [4]

More interestingly, if the R6 defect assessment procedure [7] is performed based upon above through-thickness residual stress distributions, drastically different results are obtained as shown in Figure 1-4 [4]. As can be seen, the bar chart indicates that the crack is closed for through-thickness residual stress distributions gained from ASME XI and SINTAP for a 5mm deep and

50mm long circumferential external crack, and others show crack is just open or developing at different rates. The fundamental reason for various conclusions is that residual stress profiles are not identical for the same weld based upon [5-9]. It also implies that FFS based defect assessment is highly sensitive to the residual stress distribution. Consequently, accurate prediction of the residual stress profile is needed for FFS assessment, so as to avoid non-conservative or misleading conclusions.

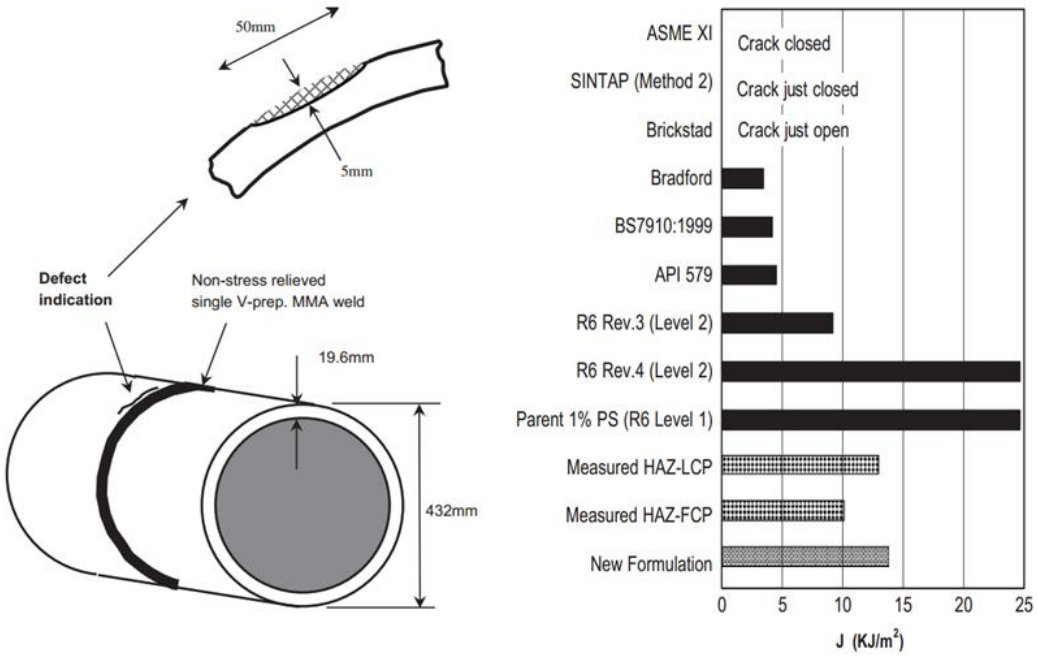

Figure 1-4 R6 estimated J-integral results using the residual stress profiles for a 5mm deep, 50mm long circumferential external crack in a t=19.6mm pipe girth weld using residual stress prescriptions from Figure 1-3 [4]

Furthermore, high surface residual stress can be presented at quite a distance away from a weld, which may have a significant impact on fracture mechanics based structural integrity assessments [5-9]. Therefore, it is of practical importance to have a full-field residual stress distribution. At present, there is a limited number of estimation schemes for providing such residual stress information, as shown in Figure 1-5. Among these, only API 579 RP [5] has the ability to provide residual stress distributions in both directions, axial and hoop, with an overly conservative bonding curve away from weld toe for pipe girth welds. SINTAP and FITNET [8-9] only give an upper bond residual stress distribution in hoop direction, and it varies noticeably compared with the curves obtained from API 579 RP. Some others codes/standards don't even provide this type of information.

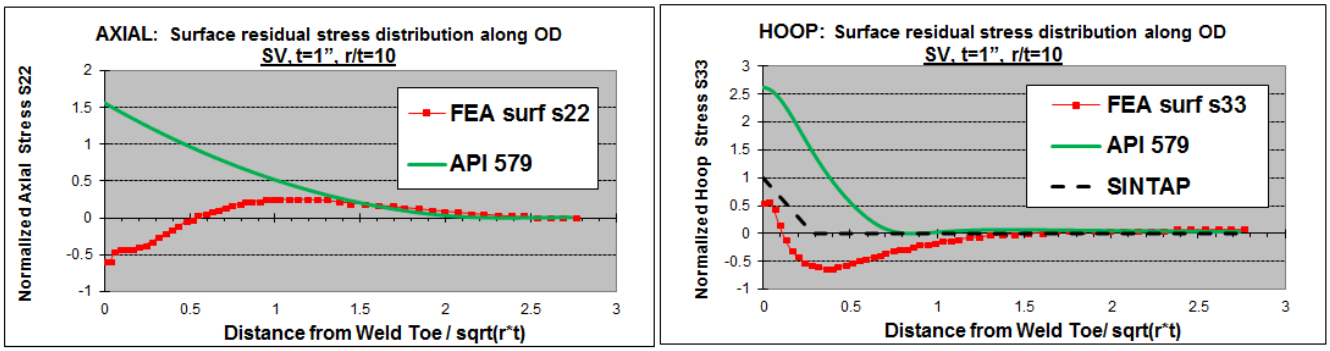

Figure 1-5 Axial and hoop surface residual stress along outer surface for single-V joint preparation with thickness of 1" and r/t=10 (pipe material 2.25CrMo-V)

In summary, current codes and standards [5-9] can only provide residual stress profiles for a limited range of joint geometry and weld configuration, which cannot cover today's needs. For a given joint profile with the same welding condition, drastically different prescribed residual stress distributions can be acquired for the weld location (Figure 1-3) and away from the weld (Figure 1-5), which may result in diverse conclusions if FFS based defect assessment is performed.

1.2 Objectives

The current study is built upon Dong's previous work [12-13] funded by approximately 20 international companies and government agencies for developing residual stress prescriptions for FFS of pressure vessel and piping components. Based upon the above discussions, the objective of this study is to develop an effective and consistent mechanics based scheme for describing full-field residual stress distributions/profiles (not only at weld locations, but also away from the weld) for pipe girth and seam welds (see Figure 1-6 and Figure 1-7, respectively) for future adoption by ASME and API FFS codes. This is to be accomplished by:

1) Performing a large number of parametric analyses covering a broad range of component geometries, joint preparations, materials, and welding procedures.

2) Synthesizing parametric analysis results to identify key parameters that can be effectively used for describing important residual stress features in terms of though-thickness membrane, bending and self-equilibrating components

3) Generalizing results using structural mechanics principles, e.g., shell theory or curved bar theory.

In order to do so, this study adopts the FE modeling procedures developed by Dong et al [3, 10-23], which have been accepted by various industries including shipbuilding, aerospace, nuclear, petrochemical, automobile, and among others. The detailed modeling procedures will be discussed in the Chapter 3.

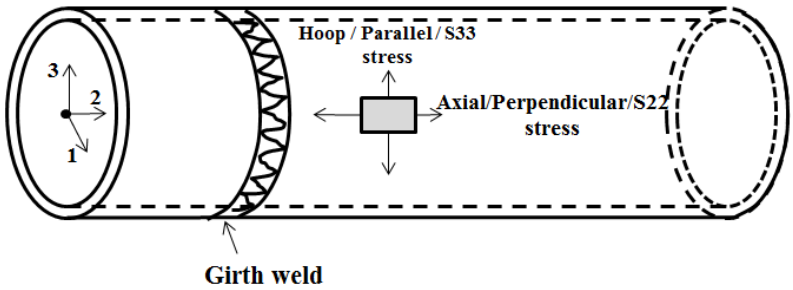

Figure 1-6 Typical pipe girth weld and stress identification

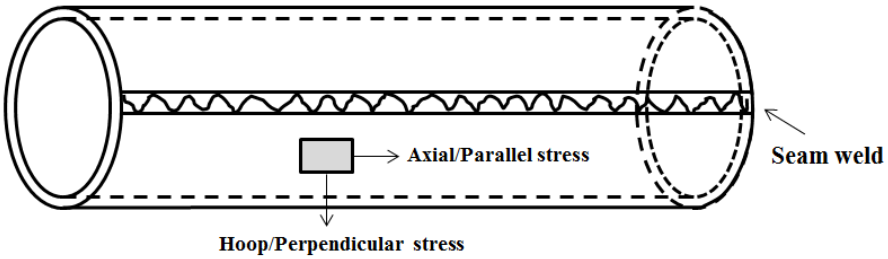

Figure 1-7 Typical pipe seam weld and stress identification

2. LITERATURE REVIEW

Residual stresses are those stresses that remain within in a body at an equilibrium condition in the absence of external forces and restraints. In the literature, various terminologies are referred to residual stresses, such as inherent stresses, secondary stresses, thermal stresses, internal stresses, and locked-in stresses. As summarized in [24], welding-induced residual stresses presented in a welded structure are determined by the following main factors:

1) Material properties of parent and weld materials, including phase transformation, mismatch of thermal expansion coefficients between parent and weld materials, thermal properties, mechanical properties, material composition, etc.
2) Restraints applied during welding, including parent material restricted weld from free expansion on heating and contraction on cooling, external fixtures/clamping, or attachment by tacking to other structures, etc.
3) Joint profile, including weld shape, number of passes, number of layers, welding sequence, etc.
4) Welding procedure, including welding processes (shielded metal arc welding, submerged arc welding, flux cored arc welding, gas tungsten arc welding, electron beam welding, friction stir welding, etc.), welding parameters (voltage, current, welding speed, etc.) and welding conditions.
5) After welding post-weld heat treatment, service loading including thermal and mechanical, in-service repairs, creep, distortion correction, surface treatment including peening and coating.

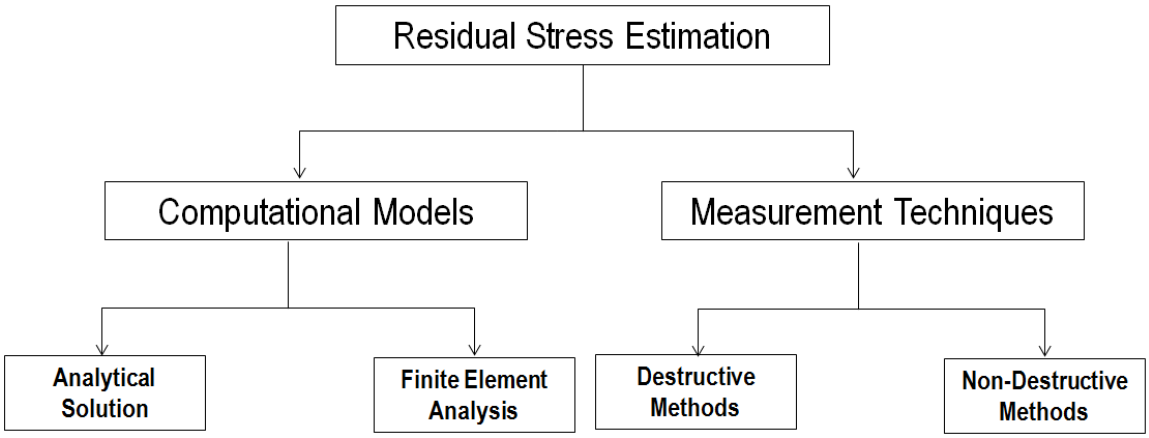

Figure 2-1 Summary of existing method for estimating weld residual stress

In this section, as shown in Figure 2-1, computational models and measurement techniques, which are two major methods for predicting welding residual stress, are historically reviewed. The former concentrates on analytical solutions and finite element analysis, for pipe girth and seam welds, over the years. The latter can be classified into destructive methods and non-destructive methods based upon the degree of damage to a specimen. Also, recent major research programs of weld residual stress analysis are presented.

2.1 Weld Residual Stress Models

A large number of reviews [11, 14, 25-30] summarized the development of weld residual stress models. Most of them [25-30] focused on finite element methods since the late 1970s, which will be elaborated on later. However, the two papers by Dong [11, 14] introduced methods for estimating weld residual stress from an analytical solution in the late 1930s to recent finite element models, which covered the most important history of understanding of fundamental physics and mechanics on residual stress development.

2.1.1 Analytical solution

In 1936, Boulton and Lance Martin [31] were perhaps the first to predict residual stresses in a welded structure by using a plastic analysis. For an edge-welded plate with a dimension of 9ft × 6in × 3/8in, they assumed that a constant longitudinal stress existed. This longitudinal stress was the only residual stress component in the plate. They proved that the weld produced a plastic region, which resulted in the residual stresses after cooling, in both analytical and experimental results.

In 1938, also for an edge-welded plate, Rodgers and Fetcher [32] provided an analytical way to predict the complete history of residual stress distribution as it corresponds to the recorded temperature history during welding. The estimated temperature distribution given by Byerly using constant thermal properties was found in good agreement with the experimental result. Then the residual stress calculation was based upon the determined temperature history. It employed a superposition method to find the final state of the residual stress distribution. The procedure used temperature-dependent mechanical properties, e.g., Young's modulus and coefficient of thermal expansion. Nevertheless, thermal properties were assumed constant over temperature. This method satisfied the equilibrium condition for any time interval. The calculated stress distributions had a good agreement with the residual stresses measured by the relaxation method. They first provided a quantitative insight into the relationship between temperature and residual stress patterns. Two years later in 1940, Rosenthal and Zabrs [33] conducted a similar study.

Based on the solutions provided by Rodgers et al [32] and Rosenthal et al [33], Tall [34] presented a step-by-step computational method for calculating longitudinal residual stress in 1964. He considered two types of welded plate: edge-welded plate and center-welded plate. This method employed the obtained temperature distribution from the existing equations developed by the previous researchers. However, it still used constant thermal material properties. The boundary of the plastic zone was automatically included in the calculations. The method took equilibrium into consideration for all the cooling stages at different time intervals. Tall might be the first researcher to use a digital computer to accurately calculate residual stresses. Four years later in 1968, Masubuchi [35] developed a more mature numerical program to compute the residual stresses based on Tall's [34] method, which was improved by using a line heat source solution with temperature-dependent thermal material properties.

In 1973, Vaidyanathan, Todaro and Finnie [36] might have been the first who intended to provide an approximate analytical solution of longitudinal residual stresses in pipe girth welds. They first used Tall's [34] method to obtain the longitudinal residual stress of a butt welded flat plate. Then, they "wrapped" this flat plate into a circular cylinder. The welded cylinder, now with initial hoop stress, was allowed to deform. Its final radial displacement was determined by the condition that its elastic strain energy would be minimal by using shell theory. It was a brilliant idea for calculating residual stresses in pipe girth welds presented by the authors, and it vividly illuminated the physical relationship between a flat plate and a circular cylinder under a butt weld condition. In addition, this was the first attempt to use classical shell theory to solve residual stress distribution in pipe girth welds. Vaidyanathan et al. [37] extended the solution to a three-pass weld, by taking the superposition temperature from a point heat source model, which used constant material thermal and mechanical properties.

In the 1980s, Umemoto [38-39] deduced an approach to estimate the longitudinal residual stress in pipe girth welds by solving the shell theory based fourth order governing equation. A comparison between residual stresses predicted by this calculation method and experimental data showed a fairly good agreement. The governing equation in this method was similar to the general equation of thin shell theory. However, it involved an approximate axisymmetric temperature distribution on the right side of equation, which made the solution much more complicated. Temperature distribution took different wall thickness effects into consideration, such as thin wall and thick wall. For thin wall, the temperature was assumed the same through the thickness, and for thick wall, the temperature was different at the inner and outer surfaces of the pipe.

These analytical solutions are remarkable and enhance the understanding of the physics and mechanics in the welding process. They often provided reasonable residual stress predictions compared to the experimental data, even though they were either limited to the longitudinal residual stress or constant material properties. However, these methods didn't take heat loss or pipe geometry effects into account, for example, thickness and r/t.

2.1.2 Finite element modeling

With the availability of finite element method and rapid progress in computational techniques, researchers began to employ these powerful tools to compute residual stresses associated with non-linear interactions in material behaviors. Detailed historical reviews of the development of finite element modeling procedure from the early 1970s to 2001 are presented by Markerle [28-29] and Lindgren [25-27]. The former provided a detailed paper list for various categories of welding simulation by finite element method, for instance, modeling of specific welding processes, influence of geometrical parameters, heat transfer and fluid flow in welds, residual stresses and deformations in welds, among others. The latter outlined the historical improvement of the finite element model which consisted three parts. The first part showed increased complex modeling could account for multi-pass welding, repair welding, more realistic heat input, etc. The second part discussed the different material modeling assumptions that contribute to final residual stress state. The third part introduced ways to increase computation efficiency, such as using adaptive meshing, changing element type, downsizing the model, improving finite element techniques, etc.

In the following, finite element modeling procedures are reviewed within the context of pipe girth and seam welds. The earliest published finite element models for predicting weld residual stresses appeared in the early 1970s, such as those given by Ueda and Yamakawa in 1971 [40], Hibbitt and Marcal in 1972 [41]. Ueda and Yamakawa [40] developed a theoretical thermal elastic-plastic analysis based on the finite element method, with the consideration of temperature dependent mechanical material properties (Young's modulus, yield stress, thermal expansion coefficient). Transit and resulting residual stresses could be obtained for both butt-welded plate and fillet weld. Under the support of ONR (Office of Naval Research), a detailed report provided by Hibbitt and Marcal [41] documented a sequentially coupled thermal-mechanical analysis using finite element method. The thermal model, a nonlinear transient finite element solution, was designed to simulate the gas-metal arc welding process, which accounted for different welding parameters. The transient temperature distribution was then used as "a forcing function' for the mechanical analysis to obtain residual stresses. One of the examples in the report used a 2D axisymmetric element type to simulate the welding of a disc. This element type was also used for pipe girth welds [44] some years later. Moreover, it was the first method to consider a large amount of phenomena associated with welding process which include temperature dependent thermal material properties, latent heat, phase transformation, irregular weld geometry, and radiation boundary condition, among others. This numerical approach is a great achievement in the history of welding simulation. Basically, it was the prototype of today's finite element modeling procedure for welding-induced residual stress estimation.

In 1975, based upon the work of Hibbitt and Marcal [41], Nickell and Hibbitt [42] and Friedman [43] further improved the finite element modeling procedure. Still under ONR support, Nickell and Hibbitt [42] discussed element type effects (plane strain, plane stress, generalized plane strain) and problems associated with heat transfer analysis, such as source characterization, latent heat effects, cooling rate, etc. The example used in the paper was an omega seal weld problem. Friedman [43] emphasized applying the analysis technique to gas-tungsten arc welding in a butt-welded plate, other than gas-metal arc welding in [41]. The analysis procedures could be applied to planar or axisymmetric welds.

The above finite element modeling procedures are limited to single pass weld. In the late 1970s, Rybicki et al. [44-45] first developed a model to calculate residual stresses in a multipass girth welded pipe using 2D axisymmetric element type. The finite element model was able to update the geometry by adding each pass sequentially. The temperature field was achieved based on an analytical moving heat source solution. Temperature and residual stress distributions obtained from finite element modeling had a fairly good agreement with the experimental data.

This sequentially coupled thermal-mechanical modeling procedure served as a useful tool to predict residual stresses in pipe girth welds for nuclear power industry. In the early 1980s, quite a number of residual stress analyses [46-50] were performed in order to reduce the risk for stress corrosion cracking in pipe inner surfaces. Methods for mitigating tensile residual stresses in pipe inner surfaces were developed and optimized using this finite element modeling procedure: heat sink welding [46-47] which used water to cool the inner surface during welding with high heat input, backlay welding [48] which added a series of axial welds deposited around pipe outer surface after the completion of normal welding, and induction heating for stress improvement [49-50] which heated the welded region with an induction heating coil fitted around the outside

of the pipe after normal welding. Residual stresses obtained from finite element analysis showed good agreement with the measurement data. These methods could introduce compressive stresses in pipe inner surfaces, and are still used in many industries today. This set of works probably is the first industrial application of using a welding simulation model to solve an engineering problem.

Since the late 1970s, finite element modeling procedure was extensively used as a computational tool (e.g., ADINA system [51]) to examine various issues related to welding-induced residual stresses, such as those given in [52-53] for investigating pipe geometry effects on residual stress distribution. With the increasing need for finite element method in various industries, commercial finite element analysis packages became available to provide a user friendly interface and to improve calculation productivity. As such, these packages were accepted by most researchers who didn't want to struggle with writing the complicated codes.

However, there was some complex thermo-mechanical phenomena associated with the welding process which could not be correctly modeled, such as re-melting and annealing effects. Since the mid-1990s, Dong [11-17] and his co-workers [22, 54] began to significantly improve the numerical simulation tools. From a FFS assessment point of view, one-dimensional bar model is a good example to clearly illustrate how the re-melting and annealing effects influenced the strain development during welding, as shown in Figure 2-2 [11]. By considering a fixed bar subjected to heating and cooling, with elastic perfectly plastic material behavior, the strain or stress history can be obtained analytically. Without loss of generality, it can be assumed that material yield strength decreases from θ_2 to θ_1, and zero from θ_1 to melting temperature θ_m. On cooling, a material point going through melting or re-melting should lose memory and start from a virgin state, shown as the "Correct" line in Figure 2-2. However, plastic strain histories are incorrectly obtained from finite element analysis. The primary reason is due to the continuum and structural mechanics based FE codes do not intend to deal with a material state change (liquid to solid). This effect may also serve as one of the main factors on drastically different residual stress distributions for a simple pipe girth weld, as shown in Figure 1-3. In addition, for multi-pass welds, the effect can have much more severe and alter the finial state of residual stress field to a significant degree.

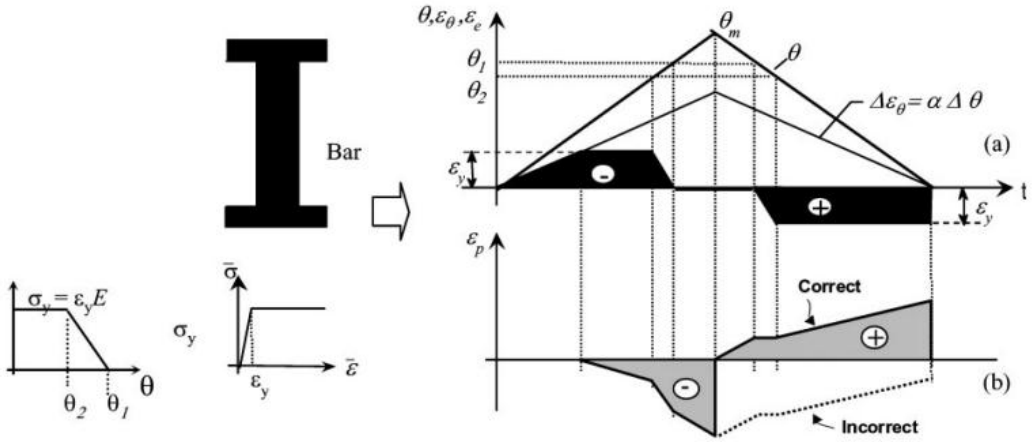

Figure 2-2 Graphic solutions for thermoplastic stress-strain evolution 1D problem [11]

Melting and re-melting effects are of critical importance in residual stress analysis, particularly in using commercial FE codes. A fundamental approach to this issue was to formulate a material constitutive model (UMAT) which was provided by Dong's group [11, 17, 22, 54]. This model has well considered the melting/re-melting effect as well as phase transformation and the material hardening effect. It is the only tool powerful enough to accurately calculate welding-induced residual stresses today, even though this scheme was invented in mid-1990s.

So far, finite element models mentioned above use a 2D axisymmetric element type. This type of element assumes that each weld layer is simultaneously applied to the circumference. In practice, an axisymmetric weld deposition almost never happens as long as the arc-welding process is concerned. However, depending on the weld profile and welding condition, residual stresses of girth welded pipes can show an axisymmetric type which is confirmed by some of the experiments [555-56]. Results obtained from a 2D axisymmetric model tend to reflect an average sense of the residual stress profile in a girth weld, which can capture the characterization of residual stress distribution. Furthermore, a 2D axisymmetric model offers rather high efficiency in model generation and residual stress calculation with nowadays computer capability. Consequently, it is an ideal choice to perform a large number of parametric or sensitivity analyses, as those shown in [4, 12, 23, 52-53, 57]. As such, a 2D axisymmetric model still dominates the published work so far.

However, a 2D axisymmetric model cannot be used as a representation of weld start/stop positions where residual stresses could vary to a significant degree. For a multi-pass weld, this effect could be amplified if travel directions or start/stop positions are varied from weld to weld. Moreover, stress concentration areas like start/stop positions tend to result in cracking and fatigue failure. In order to capture such effect, 3D analysis needs to be carried out.

The first 3D model for residual stress prediction in a full pipe girth weld was provided by Lindgren and Karlsson in 1988 [58]. They used shell element to simulate metal arc welding on a carbon-manganese steel pipe with a thickness of 8.8mm and an outer diameter of 203mm. The temperature and residual stress distributions showed good agreement with measurement data. Furthermore, the case they analyzed illustrated that the residual stress field is close to axisymmetric, except for the start position.

Two years later in 1990, Karlsson and Josefson [59] were the first to use 3D solid element to predict residual stresses in the same pipe conducted in [58] using ADINA system [51]. The results obtained also matched the measurement except at the weld center. Notable residual stress varied at the weld start/stop positions. They suggested that a 2D axisymmetric model could be a better choice if focus was upon average residual stress distribution away from the weld start/stop positions, due to the large amount time consumed in 3D analysis.

The above two 3D models are only accounted for with single-pass pipe girth weld. A 3D multipass pipe girth weld model was first developed by Li in 1995 [60]. Solid element type was chosen to simulate a four-pass narrow gap pipe welding process. Calculated temperature distribution was in good agreement with measurement data. A reasonable agreement was

demonstrated between residual stress distribution obtained from the 3D model and neutron diffraction measurement data.

In 1997, Zhang and Dong [61, 18] developed a 3D composite shell element model to account for multi-pass pipe girth weld. They proposed that a laminated shell composed of sequentially-deposited layers could be used for a multi-pass weld. As such, it improves residual stress calculation efficiency compared with a traditional 3D model [58-60]. Away from start/stop positions, residual stresses obtained from a 3D composite shell model and a 2D axisymmetric model showed good agreement, as well as with measurement data.

With the rapid progress of computational techniques, calculation efficiency has been significantly improved for residual stress analysis on a 3D model. Researchers and investigators are obsessed with developing complex welding simulation processes by taking this advantage. Recently, Maekawa [62-63] developed a fast computational method by separating a model into two parts- a nonlinear part and a linear part. The former represented the welding-induced nonlinear plastic region, and the latter represented the rest region, which was linear elastic. However, there is no clear boundary proposed by this method about how to differentiate plastic and elastic parts.

Even though the finite element modeling procedure for predicting residual stresses tends to be mature, some modeling assumptions and underlying mechanics of welding-induced residual stress are still under discussion and investigation. In order to further investigate the mechanism of residual stresses and support engineering industries, several major research programs for residual stress analysis were conducted in the last few decades, such as PVRC (Pressure Vessel Research Council) project, European VORSAC (Variation of Residual Stress in Aged Components), International Institute of Welding (IIW) X/XV RSDP (residual stress and distortion prediction) round robin, NRC/EPRI (Nuclear Regulatory Commission and Electric Power Research Institute) welding residual stress validation program international round robin, the European network on neutron techniques standardization for structural integrity (NeT), etc. Detailed finite element modeling procedures and findings based upon the availability in the open literature are reviewed in the last part of this section.

2.2 Residual Stress Measurement Techniques

Analytical and finite element methods discussed above can be validated by experimental measurement of residual stress. In [64-70], various residual stress measurement techniques have been developed and reviewed. However, welding-induced residual stress cannot be directly measured. Only the average residual strain can be determined over a sampled gauge volume. As such, all residual stress measurements are subjected to interpretation of residual strain. With that in mind, different measurement techniques, sizes of gauge volume and interpretation schemes may result in various residual stress distributions, such as those shown in Figure 1-3.

Generally speaking, measurement techniques can be classified based upon the degree of damage to a specimen as destructive (semi-destructive) methods and non-destructive methods. The former includes hole drilling (HD), trepanning technique (TT), contour method (CM), slitting technique (ST) and deep hole drilling technique (DHD). Examples for the latter are diffraction

methods, such as laboratory X-ray diffraction (Lab.XR/XRD), synchrotron X-ray diffraction (SXD/SD) and neutron diffraction (ND). Detailed spatial resolution and penetration depth measured from a specimen surface of each technique is given in Figure 2-3 [69].

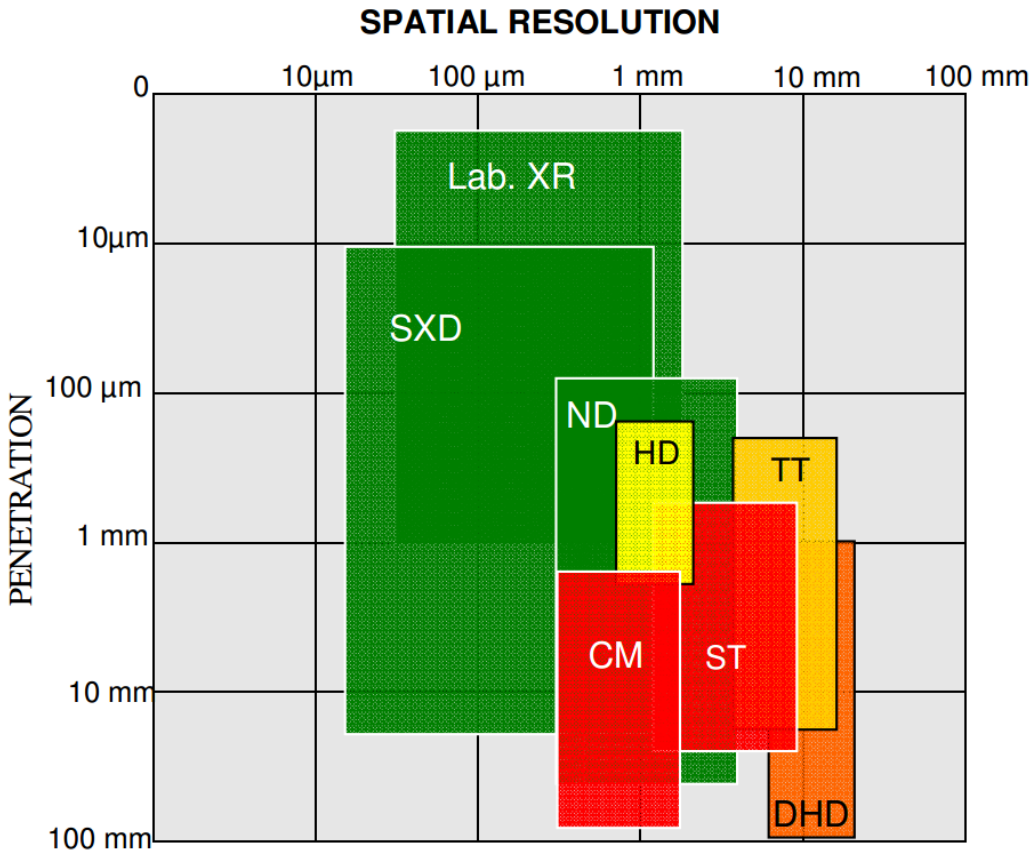

Figure 2-3 Comparison of RS spatial resolution versus penetration for steel components [69]

In the following, four major measurement techniques related to this study are reviewed: deep-hole drilling, laboratory X-ray diffraction, synchrotron X-ray diffraction and neutron diffraction. These techniques are widely used today, and dominate more than 70% of experimentally determined residual stress results in the published literature [65].

2.2.1 Deep-Hole Drilling (DHD)

Through-thickness residual stress distribution is often required for performing fracture mechanics based defect assessments [5-9]. Deep-hole drilling measurement technique, well known as a stress-relaxation technique, is one of the few methods that can obtain sufficiently accurate through-thickness distribution of in-plane residual stresses. It is capable of measuring residual stresses at depth of up to 100mm, as shown in Figure 2-3 [69]. Deep-hole drilling has many advantages, such as portability, reliability and it is applicability to very thick sections of a

complex shaped structure. The main disadvantages are that is destructive, relatively expensive, and the measurements are spotty usually only in the middle of the weld

This type of measurement technique is still in development. Its origin could be traced back to 1934, when Mathar [71] first proposed a pioneering work for modern hole drilling method. He used a slow-speed drill to cut a metal plate and applied an extensometer to record the material deformation which was then converted to surface axial stresses. In the 1960s [72-73], researchers improved this method to determine the geological stresses within the interior of large rocks, other than at the surface. Later in the 1990s, Leggatt [74] further extended the method to measure residual stresses in large metal components, which is the so-called deep-hole drilling technique nowadays. Since then, DHD has been widely used to characterize residual stress distributions in various engineering industries, such as petrochemical and nuclear power [75-79].

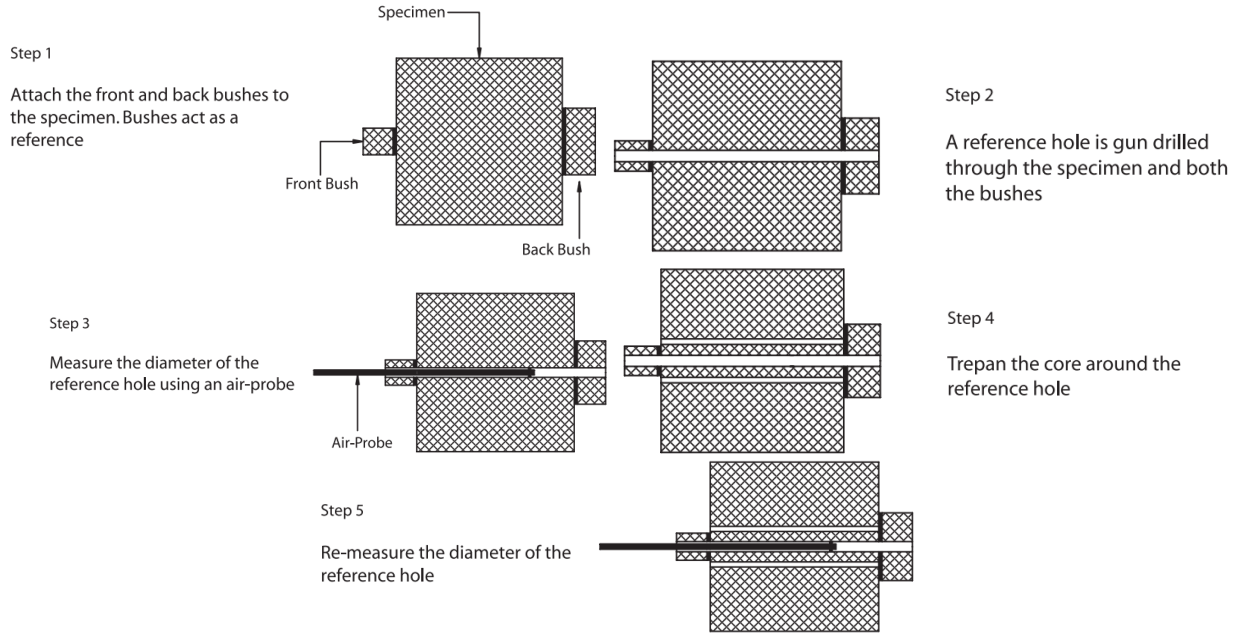

Figure 2-4 Schematic diagram of the deep-hole drilling measurement method [78]

A typical deep-hole drilling method involves five steps, as illustrated in Figure 2-4 [78].

1) Reference bushes with similar material of the specimen are attached to the specimen using an adhesive.
2) A reference hole is gun-drilled though the bushes and specimen. The diameter of a reference hole is from 1.5mm to 3mm [70].
3) Precise measurement of the reference hole diameter is made through the entire thickness of the specimen. Measurements are taken at different depths and angles using a calibrated air-probe system.
4) A core of material is removed by trepanning using an electric-discharge machining (EDM). A typical core diameter is from 5mm to 20mm [69].

5) The diameter of the reference hole is re-measured due to the strain relaxation by the core removal in Step 4.

Changes in the reference hole diameter between Step 3 and Step 5 are used to obtain the original residual stresses along the dilled hole in though-thickness direction. Detailed formulation for converting strain to residual stresses can be found in the literature [74, 78-79]

Recent advances to improve the accuracy of residual stress distribution mainly focus upon: air-probe calibration method [78], residual stress calculation method [78-81], front and back bushes analysis [78], and strain measurement techniques [80-81].

2.2.2 Diffraction Methods

Diffraction techniques are the most important non-destructive technique for determining residual stresses. It includes x-ray diffraction (laboratory or synchrotron) and neutron diffraction. These methods share the same principle, which uses crystalline lattice as an atomic strain gauge as shown in Figure 2-5 [69]. However, methodologies of these methods are different. Neutron diffraction technique is emphasized as below. In 1912, Braggs discovered the relationship between diffraction phenomena and lattice spacing in crystal structure, mathematically described as:

$$n\lambda = 2d_{hkl}\sin\theta \qquad \textbf{(2.1)}$$

Where n is an integer, λ the incident wavelength, d_{hkl} the lattice plane spacing, and θ is the diffraction angle, which is half of the scattering angle 2θ. The condition of Eq. (2.1) is that the diffraction beam has an intensity-maximum.

Applied stress can alter the lattice plane spacing of an isotropic material. Such a change contributes to differences in the diffraction angle θ for stressed and unstressed materials. Based upon Eq. (2.1), elastic strain for determining residual stress is derived from comparing the lattice spacing change between these two stress states, given as:

$$\varepsilon_{hkl} = \frac{d_{hkl} - d_0}{d_0} = -\cot\theta\Delta\theta \qquad \textbf{(2.2)}$$

Where d_0 is the strain-free lattice spacing and $\Delta\theta$ is an angular shift in diffraction angles for intensity-maximum positions. Withers provides various methods to determine d_0 because some factors (material composition, temperature, etc.), other than stress, tend to alter the measured lattice spacing [82]. As discussed in [67], the peak positions of elastic strains obtained from Eq. (2.2) are not sensitive to the plastic component of the strain which only affects peak width. Consequently, residual stresses can be converted directly from the elastic strains using Hook's law.

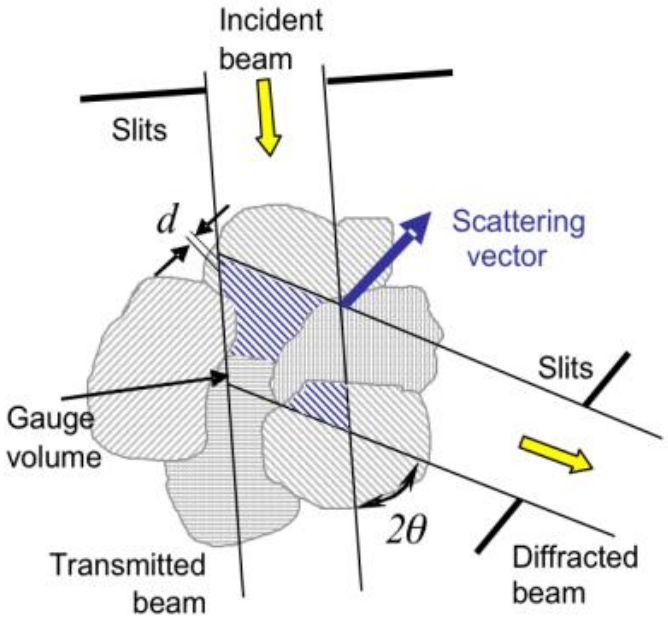

Figure 2-5 Principles of neutron diffraction technique showing Bragg's reflection from the crystal plane "d" [69]

Laboratory x-ray diffraction (XRD)

X-ray is a form of electromagnetic radiation, which was first discovered by Rontgen in 1895. Over a century development, X-ray is now extensively used in both the medical and engineering industries. Portable instruments are available, which can be taken into the field. However, due to its poor level of penetration, laboratory (or conventional, soft) X-ray diffraction is only limited to a depth of 5-50μm from the surface. If combined with destructive layer removal, residual stress distribution can be obtained at greater depth, up to about 1mm, as shown in Figure 2-3 [69]. As such, laboratory X-ray diffraction is not practically useful for determining through-thickness residual stresses in welded components.

Synchrotron x-ray diffraction (SD)

In the 1990s, with the availability of new generation sources, synchrotron (or hard) X-ray is used for probing residual strain in bulk materials [83-84]. Synchrotron x-ray provides a million times more intense beams of high-energy than the one generated by conventional sources, which leads to a higher depth penetration from the specimen surface (see Figure 2-3). Furthermore, owing to such a high intensity of nearly parallel photons, synchrotron offers a better spatial resolution and faster acquisition times (about 60s per point per direction [85]). On the downside, high-energy synchrotron associated with short wave length results in low scattering angles (2 °to 20 °, [68]). As a consequence, it makes it difficult to measure strains along sufficient directions, which usually yields a 2D residual stress result.

Neutron diffraction (ND)

Neutron diffraction (ND) for residual stress measurements has been recognized since 1980 [86-87]. The greatest advantage of neutron diffraction is that it larger penetration depth compared with X-ray diffraction, which can measure up to several cm from the specimen surface, as shown in Figure 2-3. Neutron also offers a sufficient spatial resolution ($0.25mm^3$) to capture high stress gradient, such as a crack tip or HAZ region. Moreover, the scattering angles for neutron diffraction are close to 90 °, which produces complete 3D residual stress results by tiling and rotation the specimen. However, it takes much longer measurement time for one point, for example, 20 min in transverse and normal directions, 60 min in longitudinal directions [85]. An international standard ISO/TS 21432-2005[88] for determining residual stresses using neutron diffraction is being developed in order to achieve reliable residual stress measurement results.

Neutron diffraction is only available in a few facilities, in much the same way as with synchrotron diffraction. One of facilities is located in Bragg institute, ANSTO (Australian Nuclear Science and Technology Organisation**)**, Australia. The Kowari instrument, in full service since 2009, is a strain scanner using neutron diffraction, as shown in Figure 2-6. With it, structural integrity of pressure vessels and residual stresses in welded components can be examined in detail.

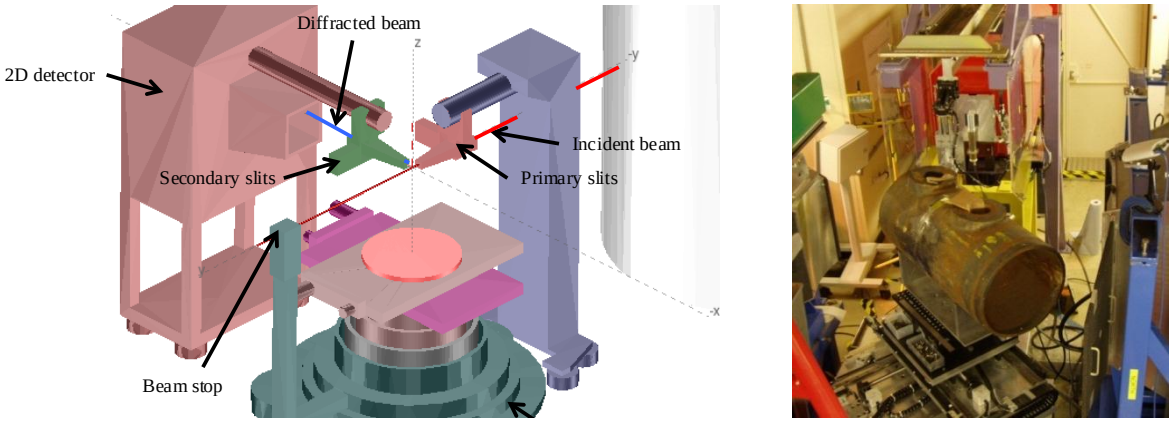

Figure 2-6 Kowari – neutron strain scanner, ANSTO, Australia (courtesy of Dr. Paradowska)

Synchrotron x-ray diffraction and neutron diffraction are widely used for determining residual stress fields in various engineering industries since 2000 [89-97]. With much more mature techniques, these two methods can provide consistent residual stress distributions between each other [85,89,90,93,95] and also comparable measurement data with analytical and finite element results [94,96,97].

In summary, a comparison of the physical characteristics, advantages and disadvantages of discussed measurement techniques are summarized in Table 2-1 based upon the literature review. More details on the application of various measurement methods to welding components can be found in the review paper [69].

Table 2-1 Comparison of residual stress measurement techniques [69]

	Destructive?	Resolution	Max penetration	Advantages	Disadvantages	Equipment
Deep-Hole Drilling (DHD)	YES	Ring diameter (5-20mm)	100mm – Al 100mm – Fe	• Portable • Suitable for thick sections • Biaxial RS measurements	• Relative low resolution • Limited to few locations	Available
Laboratory X-ray Diffraction (XRD)	NO	500μm – 1mm	50μm – Al 20μm – Fe	• Versatile, widely available • Portable • No stress-free sample needed • Biaxial RS measurements	• Surface measurement only • Most of time with destructive layer removal	Available
Synchrotron X-ray Diffraction (SD)	NO	20μm lateral 1mm parallel	100mm – Al 20mm – Fe	• Highest resolution • Improved penetration • Fast 2D strain maps • Biaxial RS measurements	• High cost • Lab based • Stress-free sample required	Specialist/ Strategic government facility
Neutron Diffraction (ND)	NO	500μm – 4mm	100mm – Al 50mm – Fe 8mm – Ti	• Excellent penetration & resolution • Suitable for thick sections • Triaxial RS measurements	• High cost • Lab based • Stress-free sample required	Specialist/ Strategic government facility

2.3 Recent Residual Stress Research Programs

Over the last decade or so, several major research programs for residual stress analysis have been conducted in order to further investigate the mechanism of residual stresses and support engineering industries, such as PVRC (Pressure Vessel Research Council) residual stress JIP (Joint Industry Project), NRC/EPRI (Nuclear Regulatory Commission and Electric Power Research Institute) welding residual stress validation program international Round Robin, European network on neutron techniques standardization for structural integrity (NeT), International Institute of Welding (IIW) X/XV RSDP (residual stress and distortion prediction) round robin, European VORSAC (Variation of Residual Stress in Aged Components), etc. In the following, some of the major findings and issues are addressed, based upon the availability of information in the open literature.

2.3.1 PVRC Residual Stress JIP

The Pressure Vessel Research Council launched a residual stress joint industry project in late 1999, and the projected plan was carried out into late 2000. Two major areas of interest were: to develop a consistent residual stress estimation scheme for various welded components for performing FFS assessment, and to develop a recommended procedure for performing local post-weld heat treatment. The Phase I outcome of this research program [12-13, 21] has been served as a basis for a recent issue of API 579 RP Appendix E [5]. This study is a major part of the Phase II effort and is built upon the Phase I results.

With the improved modeling procedure [11-17], a large number of parametric analyses were performed in PVRC JIP [13]. It was found that even though residual stresses might depend upon material microstructure, joint profile, and welding procedure, the general distribution of residual stress characteristics could be related to a few distinct parameters for performing FFS assessment, e.g., thickness (t), pipe mean radius to thickness ratio (r/t), and linear heat input (Q). As shown in Figure 2-7 [13, 21], thickness and r/t ratio can contribute to the changes in through-thickness residual stress distributions in axial direction (see Figure 1-6 for stress direction

definition used in this study). Two characteristics of axial through-thickness residual stress distribution are summarized as self-equilibrating and bending. The former presents both tension on inner and outer surfaces and compression in the mid-thickness, as shown in Figure 2-7 for the case of t=2", r/t=100. The latter has two types: one is local bending with tension on outer surface and compression on inner surface (t=1" or 2", r/t=10 in Figure 2-7), the other is global bending with tension on inner surface and compression on outer surface accompanied by a counter bending presented away from the weld (t=1/4", r/t=10 in Figure 2-7). Along this line, a mechanics based parametric functional form was proposed to describe the through-thickness residual stress distributions [13, 21], which is adopted by the API 579 RP/ASME FFS-1 Appendix E.

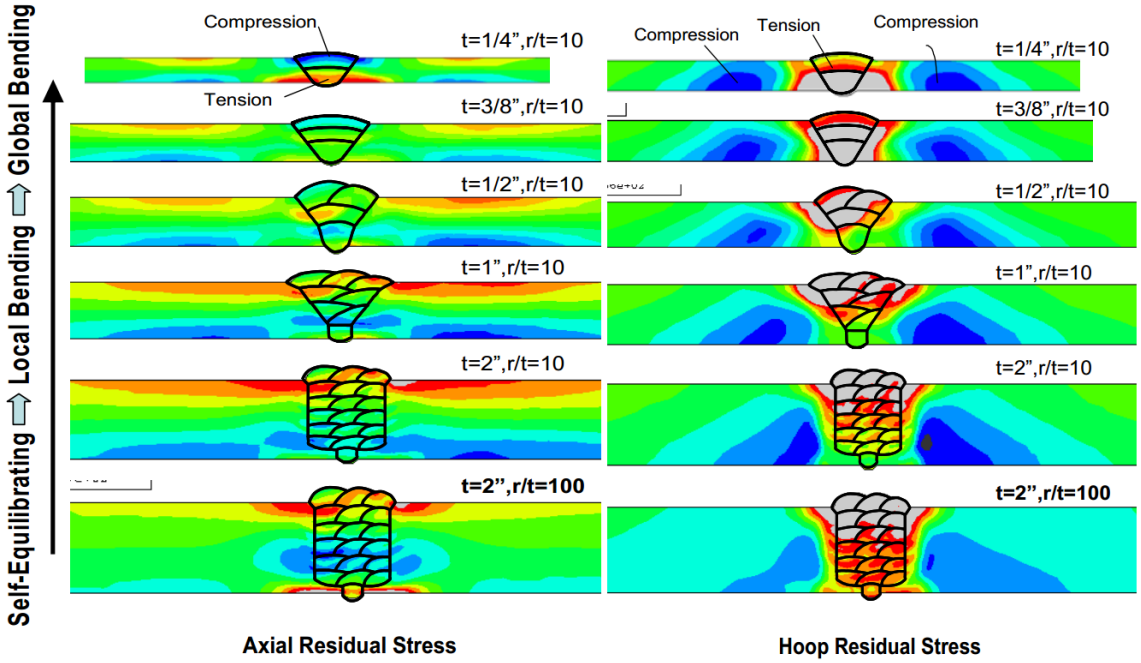

Figure 2-7 Axial and hoop residual stress distributions in pipe girth welds: transition from through-thickness self-equilibrating to local bending and global bending as a function of r/t and t (maintaining the same linear heat input) [13]

Currently, PVRC residual stress JIP phase II is still undergoing. The main objective of Phase II investigation is to provide characteristics of residual stress distributions for thick welded components up to 10" [23], and dissimilar welds used in nuclear power plants [98], among others. In addition, it intends to explore the residual stress relaxation behavior during post-weld heat treatment of welded components [99].

2.3.2 NRC/EPRI Weld Residual Stress Program

Nickel based dissimilar metal welds (DMW) used in pressurized water coolant systems are susceptible to primary water stress corrosion cracking (PWSCC), which leads to reactor cooling system leakage. As discussed before, welding-induced residual stresses are the dominant driving force to initiate and propagate cracks within the DMW due to PWSCC.

Since 2007, the US Nuclear Regulatory Commission (NRC) and the Electric Power Research Institute (EPRI) have been working cooperatively to validate welding residual stress estimations against measurement data for pressurized water reactor cooling systems containing DMW. As described in [102], the NRC/EPRI welding residual stress program consists of four phases, with each phase increasing in complexity from lab size specimens (Phase I) to fabricated prototypic mock-ups (Phase II) and ex-plant components (Phase III & IV). Some of the findings for the first three phases are presented in recent ASME Pressure Vessel and Piping conferences, e.g., Phase I [100-101], Phase II [102-105], and Phase III [106].

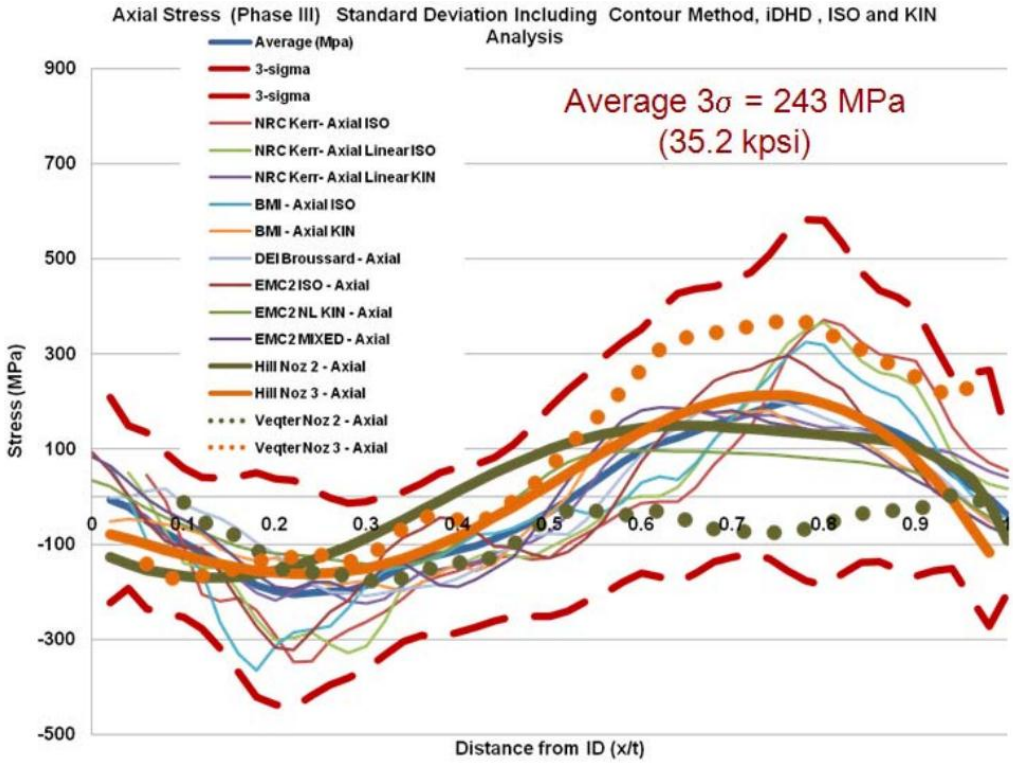

Figure 2-8 Axial stress FEA prediction and measurements at the DMW weld centerline [106]

One of NRC/EPRI weld residual stress program objectives is to validate finite element modeling procedure against measured residual stresses using DHD, ND, XRD, etc. for the purpose of reducing uncertainty in FEA calculations. Such a need can be vividly observed in Figure 2-8 [106] where the results are obtained from various organizations using different modeling assumptions and measurement techniques. Various residual stress distributions could be presented for the same DMW. Similar situations have been noticed as those shown in Figure 1-3. In addition, as shown in Figure 2-8, kinds of material hardening laws (linear/non-linear

kinematic, isotropic and mixed) can yield various residual stress distributions altered in magnitudes. This is primarily due to the fact that multiple heating and cooling cycles associated with multi-bead welding process can have a drastic effect on material hardening behavior, especially for a material with strong hardening, like stainless steel. Recently, investigators prefer to use mixed isotropic/kinematic hardening law which produces the closest residual stress distribution to the measurement data compared with results provided by other hardening laws [103,105,106].

2.3.3 NeT

As introduced in [107], European network on neutron techniques standardization for structural integrity (NeT) was established in 2002 and managed by Joint Research Centre (JRC). 39 organizations participate in this program. One of NeT's main objectives is to employ neutron based measurement techniques for further understanding the underlying mechanism of residual stresses and material degradation. A 3D finite element model is used in NeT program.

NeT Task Group 1 (TG1) focuses on the residual stress analysis of a bead-on-plate specimen with stainless steel 316L. Residual stress distributions from finite element analysis and measurement data from neutron diffraction show a good agreement [108-117]. Detailed information like welding parameters, material properties, temperature distributions and macrographs of cross sections are also documented in [108-117].

The specimen for NeT TG4 is a three-pass bead-in-slot weld, and is also built with stainless steel 316L. Finite element analysis and measurement data are documented in [118-119], along with some other detailed information.

NeT TG5 concentrates on an edge-welded plate with SA508 Grade 3 steel. Considering phase transformation effect, finite element results have a good agreement with neutron measurement data [121].

2.3.4 Others

Introduced by [20], a joint working group on residual stress and distortion prediction (RSDP) was formed by Commission X (fracture avoidance) and Commission XV (fundamentals of weld design) of International Institute of Welding (IIW) in 1996. One of RSDP major activities is to conduct a round-robin investigation on residual stress prediction for girth welds. Phase I results are documented in [20], which addressed the annealing effect, hardening law effect and heating effect owing to large discrepancies of results obtained from various organizations. Some of the improved modeling techniques used in this study are further explained and documented in [11-17].

European VORSAC (Variation of Residual Stress in Aged Components) was carried out during the mid-90s, with an aim of providing a validated finite element modeling procedure for residual

stress relaxation and creep damage on delayed reheat cracking. In addition, it also shed some light on residual stress remedial methods. Detailed information can be found in [122].

The Swedish Radiation Safety Authority, SSM established a research on welding residual stress modeling procedure improvement and validation. It carried out a sensitivity study on material hardening behavior effect and annealing temperature effect. The full report was available in 2009 [123].

3. RESIDUAL STRESS ANALYSIS PROCEDURE

In this chapter, the sequentially coupled nonlinear thermal-mechanical analysis procedure using ABAQUS [124] is first discussed in the context of previously mentioned objectives and issues. A temperature history for a given finite element model is first generated though a transient thermal analysis. Then the temperature history serves as an input to the subsequent mechanical analysis for evaluating residual stress by using a unified material constitutive model (UMAT). This finite element analysis procedure developed by Dong has been validated by various applications [10-23]. Further refinement and validation of this method is then presented based upon measurement data provided by Dr. Paradowska and recent available data in the literature. Some special considerations for this study are addressed in order to capture the characteristics of residual stress distribution and to facilitate the data processing for a large number of parametric analyses which will be carried out in the following chapters.

3.1 Thermal Analysis

In this section, the energy balance based governing equation and boundary conditions used in thermal analysis are first introduced. Then typical temperature dependent material properties are presented corresponding to parameters derived in the governing equation. At last, a linear heat input estimation scheme based on 2D finite element model is proposed to correlate the heat input in the model with the actual heat input from welding fabrication.

3.1.1 Governing Equation

The governing equation of heat flow analysis used in ABAQUS [124] is based upon the energy balance proposed by Green and Naghdi [125]. It basically describes that the heat entering a body is equal to the heat increased in this body. It is mathematically shown as follows:

$$\int_V \rho \dot{U} dV = \int_S q dS + \int_V r dV \qquad \textbf{(3.1)}$$

Where ρ is the material density; $U(\theta)$ is the internal energy per unit mass as a function of temperature θ only; $\dot{U}$ is the material time rate of the internal energy; q is the heat flux per unit area crossing surface S flowing into the body; r is the heat per unit volume supplied externally into the body.

Heat flux scalar q can be further described by a heat flux vector $\tilde{q}$ as:

$$q = -\tilde{q} \cdot \tilde{n} \qquad \textbf{(3.2)}$$

Where $\tilde{n}$ is the unit outward normal to the surface. Combined Eq. (3.2) with the divergence theorem, the middle term in Eq. (3.1) can be rewritten as:

$$\int_S q dS = -\int_S \tilde{q} \cdot \tilde{n} dS = -\int_V \frac{\partial}{\partial \tilde{x}} \tilde{q} dV \quad \textbf{(3.3)}$$

In order to get the solution of Eq. (3.1), it is preferred to be converted to its weak form which can be solved using finite element method. In doing so, an arbitrary variational temperature field δθ is multiplied to Eq. (3.1) of which middle term is replaced by Eq. (3.3):

$$\int_V \rho \dot{U} \delta\theta \cdot dV = -\int_V \delta\theta \cdot \frac{\partial}{\partial \tilde{x}} \tilde{q} dV + \int_V \delta\theta \cdot r dV \quad \textbf{(3.4)}$$

With chain rule, middle term in Eq. (3.4) can be expressed as:

$$-\int_V \delta\theta \cdot \frac{\partial}{\partial \tilde{x}} \tilde{q} dV = \int_V \tilde{q} \cdot \frac{\partial}{\partial \tilde{x}} \delta\theta dV - \int_V \frac{\partial}{\partial \tilde{x}} (\delta\theta \cdot \tilde{q}) dV \quad \textbf{(3.5)}$$

Then Eq. (3.4) is reorganized with Eq. (3.5), resulting in:

$$\int_V \rho \dot{U} \delta\theta \cdot dV - \int_V \tilde{q} \cdot \frac{\partial}{\partial \tilde{x}} \delta\theta dV = -\int_V \frac{\partial}{\partial \tilde{x}} (\delta\theta \cdot \tilde{q}) dV + \int_V \delta\theta \cdot r dV \quad \textbf{(3.6)}$$

Using Eq. (3.3), the heat flux vector term on the left hand side of Eq. (3.6) can be converted back to its scalar term. The weak form of the thermal energy balance equation can then be written as:
:

$$\int_V \rho \dot{U} \delta\theta \cdot dV - \int_V \tilde{q} \cdot \frac{\partial}{\partial \tilde{x}} \delta\theta dV = \int_S \delta\theta \cdot q dS + \int_V \delta\theta \cdot r dV \quad \textbf{(3.7)}$$

Heat conduction is assumed to be governed by the Fourier law as:

$$\tilde{q} = -\tilde{k} \cdot \frac{\partial \theta}{\partial \tilde{x}} \quad \textbf{(3.8)}$$

Where $\tilde{k}$ is the conductivity matrix. By introducing Eq. (3.8) to the weak form of the thermal energy balance Eq. (3.7), it becomes:

$$\int_V \rho \dot{U} \delta\theta \cdot dV + \int_V \frac{\partial \delta\theta}{\partial \tilde{x}} \cdot \tilde{k} \cdot \frac{\partial \theta}{\partial \tilde{x}} dV = \int_S \delta\theta \cdot q dS + \int_V \delta\theta \cdot r dV \quad \textbf{(3.9)}$$

Eq. (3.9) is served as the basis for the finite element method of heat transfer analysis. It is required to discretize the volume geometrically with finite elements and interpolate the temperature as:

$$\theta = N^N \theta^N \tag{3.10}$$

Where N^N are interpolation functions (N=1,2,…); θ^N are nodal temperatures. With the Galerkin approach, the variational field δθ is interpolated by the same functions:

$$\delta\theta = N^N \delta\theta^N \tag{3.11}$$

By using above interpolations, Eq. (3.9) becomes:

$$\delta\theta^N \left\{ \int_V N^N \rho \dot{U} dV + \int_V \frac{\partial N^N}{\partial \tilde{x}} \cdot \tilde{k} \cdot \frac{\partial N^M}{\partial \tilde{x}} dV = \int_S N^N \cdot q dS + \int_V N^N \cdot r dV \right\} \tag{3.12}$$

Since the variational fields $\delta\theta^N$ are independent, this produces the system of equations:

$$\int_V N^N \rho \dot{U} dV + \int_V \frac{\partial N^N}{\partial \tilde{x}} \cdot \tilde{k} \cdot \frac{\partial N^M}{\partial \tilde{x}} dV = \int_S N^N \cdot q dS + \int_V N^N \cdot r dV \tag{3.13}$$

With the constitutive relation, rate change of internal energy can be described as:

$$\dot{U} = \frac{dU}{d\theta} \frac{d\theta}{dt} = C_p \dot{\theta} \tag{3.14}$$

Where C_p is the material specific heat. This results in the matrix form of Eq. (3.13)

$$[C]\{\dot{\theta}\} + [K]\{\theta\} = \{Q\} \tag{3.15}$$

Where heat capacitance matrix [C], conductivity matrix [K] and external flux vector {Q} are given as follows:

$$\begin{aligned} [C] &= \int_V N^N \rho C_p dV \\ [K] &= \int_V \frac{\partial N^N}{\partial \tilde{x}} \cdot \tilde{k} \cdot \frac{\partial N^M}{\partial \tilde{x}} dV \\ [Q] &= \int_S N^N \cdot q dS + \int_V N^N \cdot r dV \end{aligned} \tag{3.16}$$

The above governing equation is based upon heat conduction which is the primary phenomenon in heat flow analysis. The other two heat transfer mechanisms, convection and radiation, are applied as boundary conditions. The convection boundary condition is given as:

$$q = h(\theta - \theta^0) \tag{3.17}$$

Where h is the film coefficient with the unit of W/m^2/°K; θ is the current element material point temperature; θ^0 is the sink temperature. Usually, convection is applied to all of the free surfaces of a FE model except weld area. The film coefficient is determined based on the welding condition. If without specific instructions, typical normal air film coefficient is used in thermal analysis.

Radiation boundary condition is expressed as:

$$q = A(\theta^4 - \theta^{0^4}) \quad \textbf{(3.18)}$$

Where A is the radiation constant (emissivity times the Stefan-Boltzmann constant) with the unit of W/m^2/°K^4. Generally speaking, for welding, radiation dissipates a small amount of heat because it only occurs at high temperature for a short period of time. Therefore, it is ignored in the current study.

As such, the governing equation and boundary conditions of thermal analysis are all presented. However, in order to solve these equations, time-dependent $\dot{\theta}$ in Eq. (3.15) is first solved by a finite difference scheme. ABAQUS uses the backward difference algorithm described as below:

$$\dot{\theta}_{t+\Delta t} = (\theta_{t+\Delta t} - \theta_t)(1/\Delta t) \quad \textbf{(3.19)}$$

Where Δt is the time increment automatically adjusted by ABAQUS, which is based upon a user-defined tolerance on the maximum temperature change allowed in a time increment. Eq. (3.19) is then substituted into Eq. (3.15). The resultant equation combined with boundary conditions Eq. (3.17-18) is now ready to be solved to obtain temperature history.

3.1.2 Thermal Material Property Representation

Based upon the heat conduction matrix in Eq. (3.15), the following thermal material properties are basically required in heat flow analysis:

- Density ρ [kg/m^3]
- Conductivity k [W/m/°C]
- Specific Heat C_p [J/kg/°C]

In the following, the above material properties used FEA are illustrated by 2.25CrMo-V which is a typical low alloy steel used in the pressure vessel and piping industries. 2.25CrMo-V is served as the main material of interest in this study. The density of this material is 7840 kg/m^3 at room temperature 23°C. Usually, material density would decrease a little bit as temperature increases due to metal expansion at high temperature. However, it is assumed that the density remains constant for thermal analysis in the current study. Temperature dependent conductivity and specific heat are shown in Figure 3-1. The raw data of conductivity, k, and thermal diffusivity, α, of 2.25CrMo-V are provided by courtesy of MPC material property data base. Specific heat is calculated from the raw data based upon $C_p = k/\rho/\alpha$.

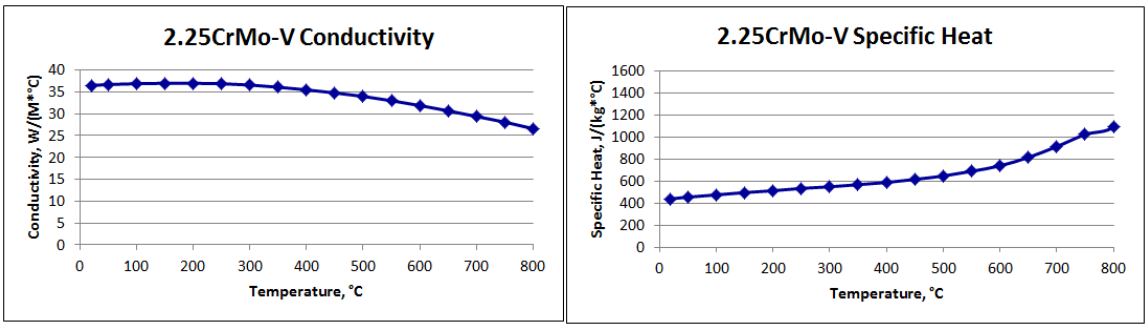

Figure 3-1 Temperature dependent conductivity and specific heat for 2.25CrMo-V

Besides above basic material properties, latent heat is an optional parameter that accounts for the system heat energy that alters during a phase change. However, this parameter is not widely observed in the literature.

3.1.3 Heat Input Characterization and Validation

3.1.3.1 Linear Heat Input Formulation

In order to perform a large number of parametric analyses and facilitate data processing, most analyses in this study are performed using 2D cross-section models (e.g., axisymmetric or generalized plane strain) due to their computational efficiency and simplicity in data reduction process. One major disadvantage of 2D model is that the linkage between heat input modeled and actual input used in welding fabrication is no longer clearly defined. This is because the linear heat input definition used by welding engineers can't be directly used since heat transport process in a 2D model by definition ignores heat loss in the third direction. The widely used linear input definition, referred to as Q'_{actual} here, is given as:

$$Q'_{actual} = \frac{U \cdot I \cdot \eta}{v}, \quad [J/mm] \tag{3.20}$$

where U is arc voltage, I welding current, η welding efficiency and v welding travel speed.

With a simplified 2D cross-section model, the resulting net heat input imported to the model consists of two parts, i.e., Q_1' and Q_2', as described in Eqs. (3.21) and (3.22), respectively:

$$Q_1' = \rho \cdot C_p \cdot \Delta T \cdot A_{pass}, \quad [J/mm] \tag{3.21}$$

$$Q_2' = 2k \cdot \Delta T \cdot \sqrt{\frac{l/v}{\pi\alpha}} \cdot L_{surf}, \quad [J/mm] \tag{3.22}$$

where ρ is material density, C_p specific heat, A_{pass} averaged cross section weld pass area, k conductivity, ℓ total weld pool length in the arc travelling direction, α thermal diffusivity, L_{surf}

weld pass surface contacted to the surroundings, ΔT temperature difference (e.g., temperature change from room temperature to the prescribed weld metal temperature in Eq. (3.21) or temperature difference between weld pass and surroundings in Eq. (3.22)). The prescribed weld metal temperature is set at 10% above the weld melting temperature. For simplicity, the averaged material property values over the available temperature range are used in above equations.

Consistent with the thermodynamics theory, Q_1' in Eq. (3.21) represents the heat content contributed by weld deposit introduced when a weld pass is activated at a prescribed temperature such as 10% above melting in 2D finite element model. Q_2' in Eq. (3.22) is the amount of heat that should be supplied to a FE model for maintaining deposit temperature while the model is subjected to transient heat conduction process into the surrounding plate material for a duration of time or dwell time related to welding travel speed. Dwell time can be estimated through an analytical 1D transient heat conduction solution ℓ/v, where ℓ is an estimated weld pool length and v the welding travel speed. Weld pass cross-section area A_{pass} and weld pool length L_{surf} can be taken directly from weld pass profile descriptions given in welding procedure specifications or weld macrographs.

Weld pool length ℓ in Eq. (3.22) remains to be determined. A simple estimation procedure can be established using a classical moving heat source solution such as Rosenthal's [126], which is illustrated in Figure 3-2. From Eqs. (3.21)-(3.22), total linear heat input is the sum of the two parts and can be described as:

$$Q'_{estimate} = (Q_1' + Q_2') \cdot \eta', \quad [J/mm] \tag{3.23}$$

where η' is a factor for taking account of 3D heat loss not explicitly considered in Eqs. (3.21) and (3.22) and can be determined when correlating the actual linear heat input Q'_{actual}.

3.1.3.2 Estimation of Weld Pool Length Parameter and Validation

The analytical solution given by Rosenthal [126] is expressed as below:

$$T(\xi, y, z) - T_0 = \frac{q}{2\pi k\sqrt{\xi^2 + y^2 + z^2}} e^{-\frac{v}{2\alpha}(\xi + \sqrt{\xi^2 + y^2 + z^2})} \tag{3.24}$$

where a moving coordinate ξ is expressed as $\xi = x - v\lambda$ at a given time λ, T_0 is the ambient temperature and q denotes the heat source strength with the expression of $q = UI\eta$. The weld pool length ℓ along x-axis at the arc travelling direction (including the rear section behind the arc center where $\xi<0$ and front section in front of the arc center where $\xi>0$) is determined by a 3D analytical heat transfer solution with a moving point source q, as shown in Figure 3-2.

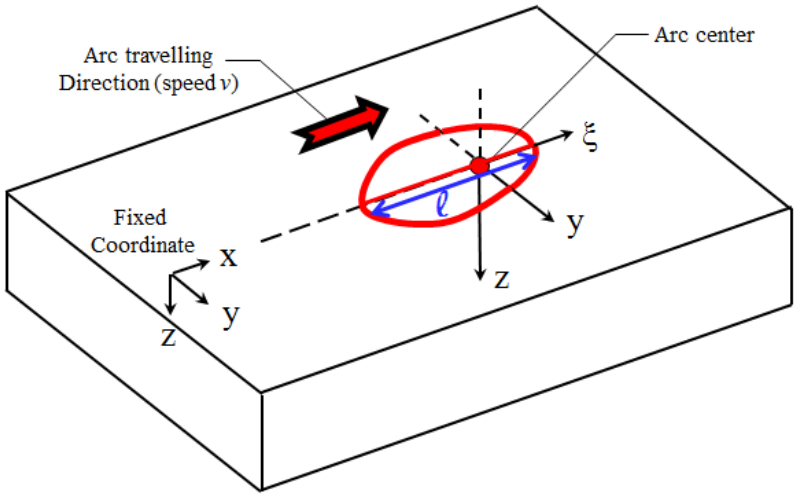

Figure 3-2 Rosenthal's moving heat source model and weld pool length l in the arc travelling direction

The weld pool length parameter *l* can be obtained by setting $y = 0$ and $T = T_m$ (melting temperature), Eq. (3.24) then becomes:

$$T_m - T_0 = \frac{q}{2\pi k|\xi|} e^{-\frac{v}{2\alpha}(\xi+|\xi|)} \qquad \textbf{(3.25a)}$$

The above equation can be re-written into two parts: one is for the rear section of weld pool length ($\xi<0$) and the other one front section of weld pool length ($\xi>0$):

$$\xi < 0, \quad T_m - T_0 = -\frac{q}{2\pi k\xi}$$
$$\xi > 0, \quad T_m - T_0 = \frac{q}{2\pi k\xi} e^{-\frac{v}{\alpha}\xi} \qquad \textbf{(3.25b)}$$

Then, weld pool length ℓ can be estimated using Eq. (3.25.a) or (3.25.b). Thermal conductivity *k* and diffusivity α are taken as averaged value over a temperature range on which these properties are available. It is interesting to note that from Eq. (3.25.b), the rear part of weld pool length behind the arc center remains unchanged regardless of the arc travelling speed *v*, but the front section length gets smaller when the welding speed *v* is increased.

Validation – Case 1

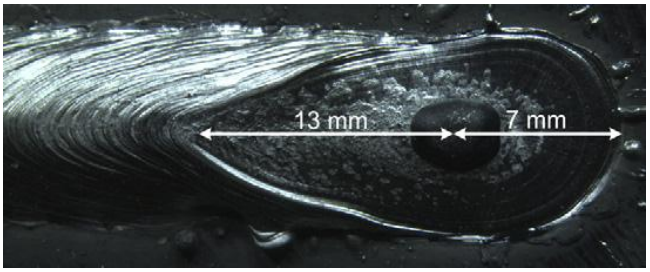

Figure 3-3 Actual weld pool length: front and rear sections from [127]

Validations are conducted against some of the experimental results available in the literature. Fig. 2-9 shows a picture of an actual weld pool length with gas metal arc welding (GMAW) process [127]. It can be clearly seen that the total weld pool length is 20*mm* which has 13*mm* rear section and 7*mm* front section. The corresponding welding parameters shown in Table 3.1 are directly taken from [127]. By substituting these welding parameters into Eq. (3.25), the result is plotted in Figure 3-4. Melting temperature T_m is 1460 ℃, and room temperature T_0 is set as 23 ℃. Fig. 2.10 indicates that the total weld pool length is 19*mm* which includes 17*mm* rear section and 2*mm* front section at about 1437 ℃. The total weld pool length ℓ (including both front and rear parts) is in good agreement between the measured (Figure 3-3) and the estimated values using Eq. (3.25), even though the front and back segments of the weld pool length are not closely matched. Such a discrepancy can be attributed to various simplifications made in Rosenthal's point source solution derived from semi-infinite body conditions, among others. As was previously stated, the purpose of this estimation scheme is to provide a way to calculate total weld pool length ℓ. It will be further demonstrated in a later section that the discrepancy in the estimated rear and front sections of the weld pool length does not affect the accuracy of the estimated total weld pool length to any significant degree in other cases too.

Table 3.1 Welding parameters [127]

Variable	Dimension	Value
Current, I	A	250
Voltage, U	V	30
Arc efficiency, η	–	0.8
Welding speed, V	mm s^{-1}	10
Preheating temperature, T_0	°C	20
Thermal conductivity, λ	W mm^{-1} $°C^{-1}$	0.036
Thermal diffusivity, a	mm^2 s^{-1}	8
Plate thickness, d	mm	18
Distance between subsurface heat sources, δ	mm	0.7
Number of vertical and horizontal heat sources, α	–	8

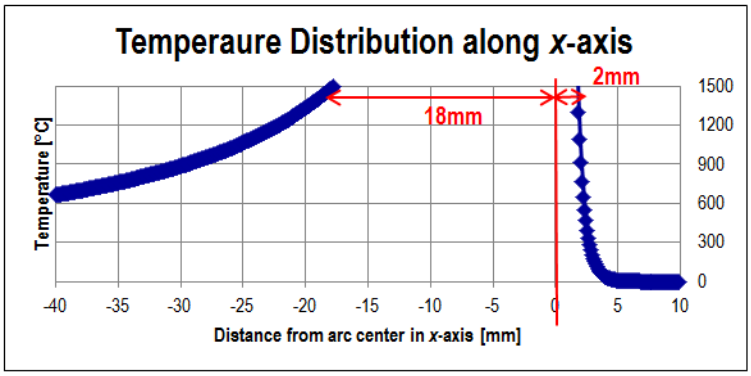

Figure 3-4 Estimated weld pool length using Eq. (3.25)

Validation – Case 2

Wahab and Painter [128] provided a method of measurement for obtaining weld pool size and shape parameters for gas metal arc welding processes. They used a mechanical ejection device to instantaneously empty molten metal from a weld pool by rapidly accelerating and decelerating the test plate being welded. Then they used a non-contact laser profiling device to digitize the exposed weld pool cavity shape. The highest resolution of the laser profiling device is 0.2*mm*. They determined the relationship between welding parameters (current, voltage, welding speed, etc.) and resulting weld pool geometry, as shown in Figure 3-5. The experiments were conducted on same material and welding procedure but with different linear heat inputs. Solid diamond is for linear heat input of 0.5*KJ/mm*, solid square 1*KJ/mm* and hollowed triangle 1.5*KJ/mm*.

As can be seen from Figure 3-5 (a) and (b), the total length of weld pool is increased as current I or voltage U is increased. It is consistent with Eq. (3.25), since ξ is monotonically changed with $q=UI\eta$. Figure 3-5 (c) shows that when the same linear heat input is maintained a faster welding speed will result in a longer weld pool length. It is interesting to interpret Figure 3-5 (c) in another way that when the total heat input q ($UI\eta$) is the same but welding speed is different (as highlighted red square symbols), the total weld pool length is not changed too much. This is mainly because the welding speed does not affect the length of weld pool rear section as is analytically described by Eq. (3.25b), which is the dominant part of the total weld pool length (e.g., shown in Figure 3-4).

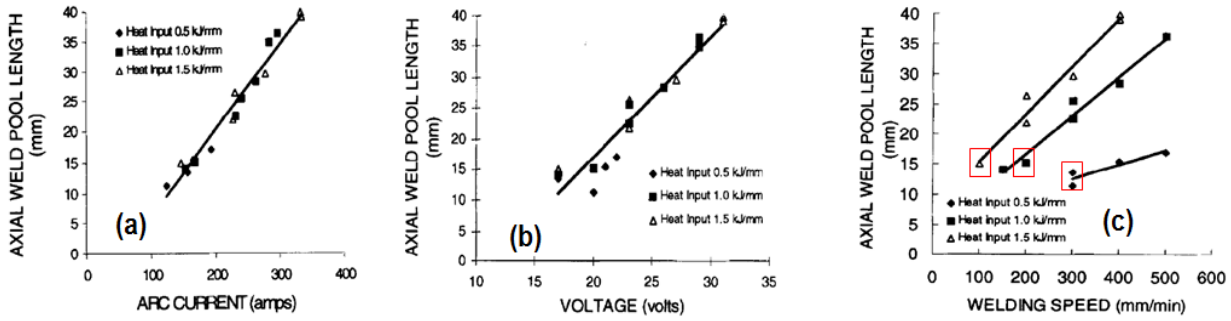

Figure 3-5: Total weld pool length as a function of: (a) arc current, (b) voltage, and (c) welding speed [128]

By extracting the welding parameters, i.e., current, voltage and welding speed of selected data points in Figure 3-5 (a-c) and substituting into Eq. (3.25), the estimated weld pool lengths using Eq. (3.25) are plotted in Figure 3-6 in red against its corresponding measurement data in dark blue. Detailed welding parameters for the cases summarized in Figure 3-6can be found in Table 3.2. Material used in this study is low carbon steel. Overall, the results obtained from Eq. (3.25) and actual measurements show a good agreement.

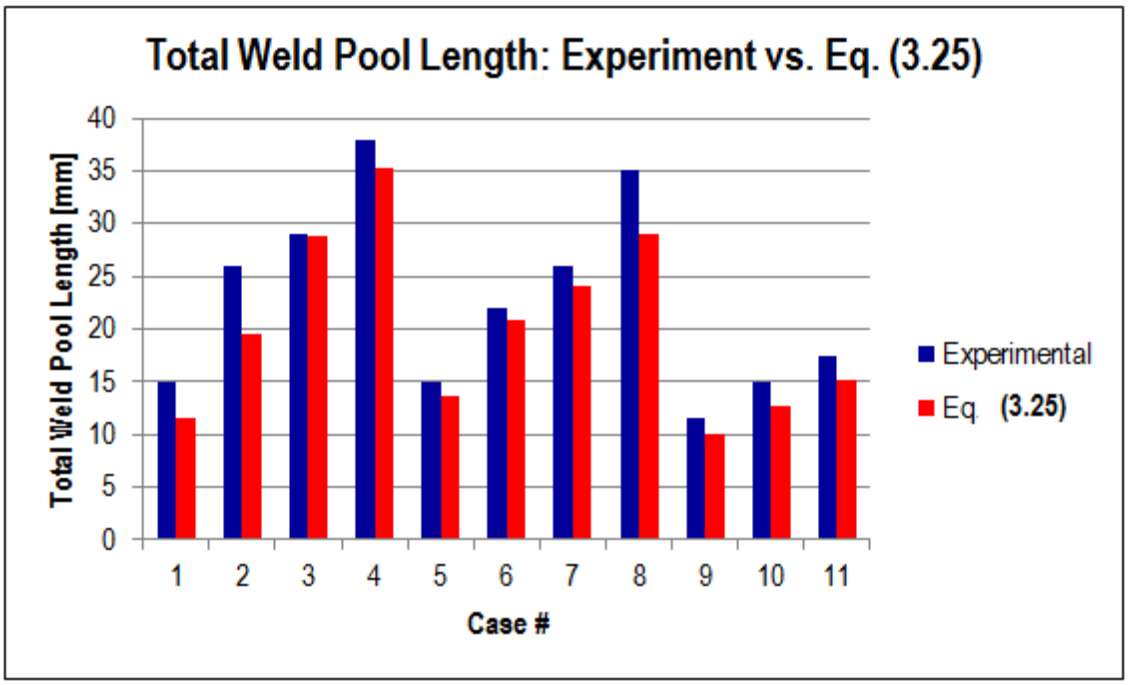

Figure 3-6: Total weld pool length: experimental results versus Eq. (3.25)

Table 3.2 Welding parameters for cases in Figure 3-6

Case #	Voltage	Current	Speed	Heat Input	ℓ	
					Experimental	Eq. (3.25)
1	17	150	100	25.5	15	11.6
2	23.5	215	200	1500	26	19.5
3	26.5	290	300	1500	29	28.8
4	31	330	400	1500	38	35.3
5	20	170	200	17	15	13.7
6	23.5	220	300	1000	24.5	20.8
7	26	260	400	1000	26	24
8	29	290	500	1000	35	29.1
9	20	125	300	500	11.5	10
10	21	160	400	500	15	12.6
11	22	190	500	500	17.5	15.2

3.1.3.3 Validation of Linear Heat Input Estimation in 2D Models

With the validation of pool length ℓ the calculation procedure (Eq. 3.25) discussed in the section above, the adequacy of linear heat input estimation scheme for 2D and axisymmetric residual stress models according to Eq. (3.22) can now be demonstrated, particularly for heat input parameter Q_2'. The validation effort reported in this section covers various cases in residual stress evaluations in which welding procedure details are well documented in the literature [18, 109, 118]. These cases include various welding processes such as manual metal arc, submerged arc, tungsten inert gas, and electron beam welding etc. Base materials vary from stainless steel, titanium alloy, and to carbon steel. The heat loss parameter η' in Eq. (3.23) can then be determined by comparing the actual linear heat input Q'_{actual} obtained in Eq. (3.20) for a given set of welding parameters.

Validation – Case 1

Detailed welding parameters and weld profile for a pipe girth weld were documented by Dong in [18]. Figure 3-7 shows the geometry for a pipe girth weld mock-up. The weld pass profiles are based on the detailed examination of the macrographs of the weld cross section. The inner passes are deposited using manual metal arc (MMA) welding procedure, and the corresponding weld parameters are shown in Table 3.3. The averaged pass area A_{pass} in Eq. (3.21) for each pass is given in Table 3.3. Weld pass perimeter in contact with surrounding material after deposition L_{surf} in Eq. (3.22) can be determined by the total length highlighted in red in Figure 3-7.

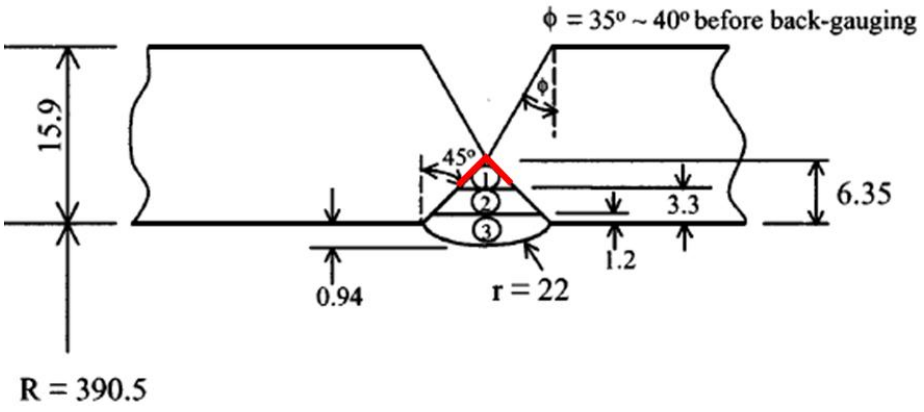

Figure 3-7: Inner MMA weld profile [18] and L_{surf} for the first pass

Table 3.3 Detailed inner MMA welding parameters [18]

Pass	Electrode Diameter (mm)	Voltage (V)	Current (A)	Average Bead Length* (mm)	Average Advance Rate (mm/sec)	Estimate Weld Bead Section Area (mm^2)
1	2.5	22.5	85	146.5	3.25	9.3
2	3.2	23	121	131.0	2.63	17.1
3	4.0	22.4	156	160.0	2.52	21.9

The results are shown in Figure 3-8 where the actual linear heat input of each weld pass is calculated by Eq. (3.20) using the welding parameters shown in Table 3.3. By substituting weld profile information in Figure 3-7 and proper material properties into Eq. (2.23) with η' of 1.0, estimated linear heat input of each weld is plotted as green square showed in Figure 3-8. As we can see, the estimated linear heat input is smaller than the actual one. This makes sense because the 2D based first principle linear heat input estimation does not consider the 3D heat flow effect. Factor η' in Eq. (2.23) takes this issue into account. After some try-and-errors, η' is found to be 1.35 to best correlate the actual heat input with the estimated one, as shown in red triangle in Figure 3-8. With this adjustment, the actual linear heat input and the estimated one using Eq. (2.23) are in a good agreement.

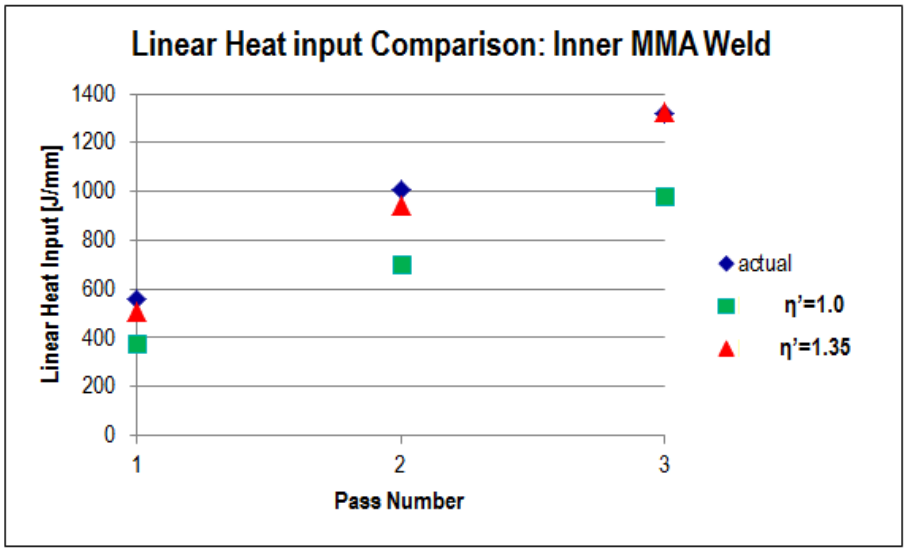

Figure 3-8: Comparison of Estimated Using Eq. (3.23) and Actual Linear Heat Input

The outer welds for this pipe girth weld are documented in the same manner in [18]. Figure 3-9 presents the outer weld profile, and L_{surf} of Pass 1 is marked in red. Table 3.4 shows the welding parameters for the outer welds which are deposited using the submerged arc (SA) welding procedure. Linear heat input for each weld is plotted in Figure 3-10. Icon for each type of heat input calculation maintains the same as the previous one in Figure 3-8 (e.g., blue diamond is for the actual, green square for Eq. (2.23) with η' of 1.0, and red triangle for Eq. (2.23) with η' of 1.35). It can be seen that linear heat inputs calculated by actual welding parameters and Eq. (2.23) with $\eta' = 1.35$ show a good agreement.

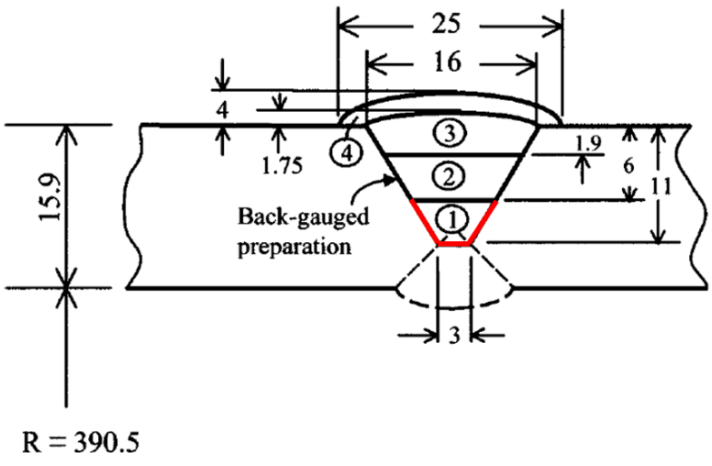

Figure 3-9: Outer passes with submerged arc weld pass profile [18] and L_{surf} for the first pass

Table 3.4 Detailed outer submerged arc welding parameters [18]

Pass	Voltage (V)	Current (A)	Advance Rate (mm/sec)	Estimated Weld Bead Section Area (mm^2)
1	28	300	6.35	29.3
2	30	421	5.93	47
3	30	421	5.93	47
4	30	440	5.93	49.2

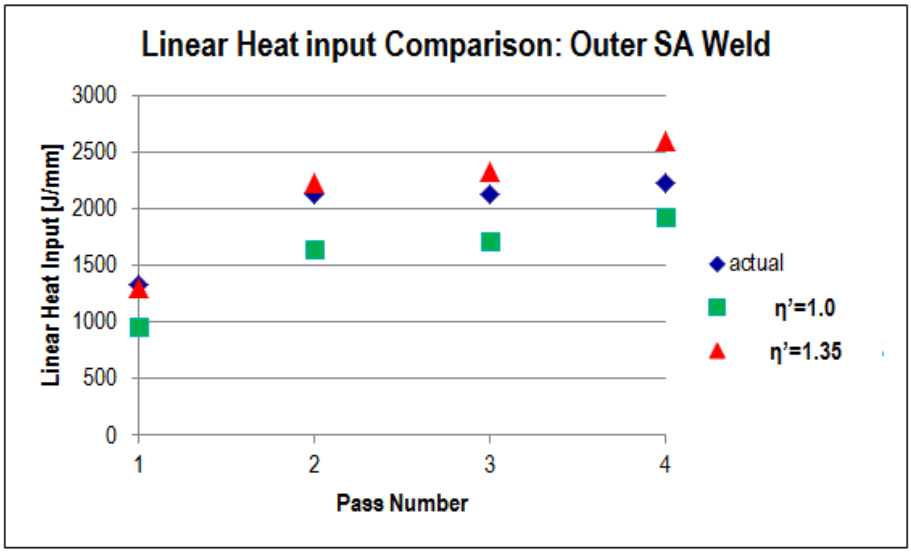

Figure 3-10: Linear heat input comparison for outer SA weld

Validation – Case 2

Two related publications [109, 118] documented the weld profiles and welding parameters for a Task Group 1 (TG1) and TG4, respectively, under the auspices of the European network on Neutron Techniques Standardization for Structural Integrity (NeT). NeT TG1[109] was focused on the residual stress analysis of a bead-on-plate specimen of which the cross section macrograph is shown in Figure 3-11. Red lines represents L_{surf} of this bead. Welding parameters are given in Table 3.5. Specimen for NeT TG4 [118] is a three-pass bead-in-slot weld. Its

corresponding cross section macrograph is shown in Figure 3-12. Again, the edge of the first pass marked in red is its L_{surf}. Table 3.6 lists the welding parameters for each pass. All the specimens were made by using an automated tungsten inert gas (TIG) process. Material used in those investments is 316L stainless steel, and detailed temperature dependent material properties are given in [109, 118].

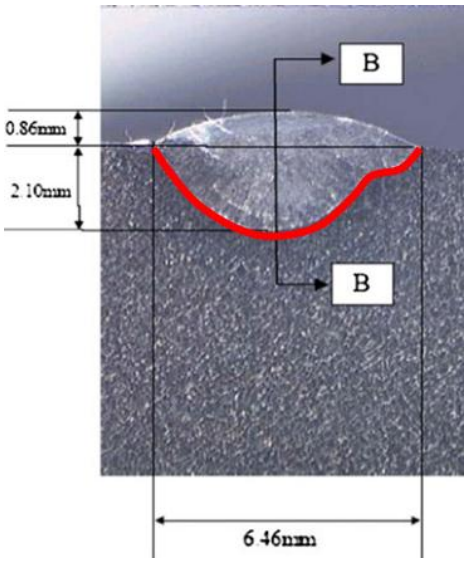

Figure 3-11: Bead-on-plate weld profile NeT TG1 [107] and L_{surf}

Table 3.5 Detailed bead-on-plate welding parameters NeT TG1[107]

Specimen	Heat input (J/mm)	Energy (KJ)	Arc time (s)	Torch traverse length (mm)	Advance rate (mm/s)
A11	633	38	26.4	60	2.27

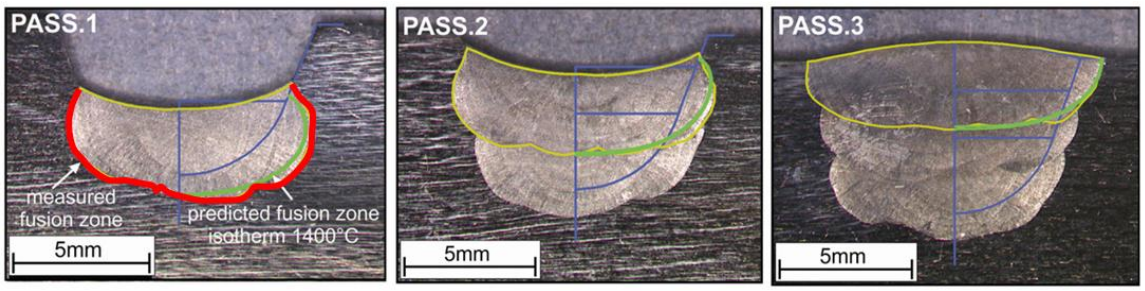

Figure 3-12: Three-pass bead-in-slot weld profile NeT TG4 [118] and L_{surf} for the first pass

Table 3.6 Detailed three-pass bead-in-slot welding parameters NeT TG4 [118]

Defined welding parameters for all passes.					Efficiency [%]	Fusion area
	Welding current [A]	Arc voltage [V]	Travel speed [mm/sec]	Heat input [J/mm]		Measured [mm^2]
PASS 1	220	10	1.27	1732	73	28.81
PASS 2	195	10	1.27	1535	72	29.16
PASS 3	185	10	1.27	1457	71	30.22

Linear heat input calculated for actual using Eq. (3.20) (in blue) and estimated using Eq. (3.23) with η' = 1.35 (in red) for TG1 and TG4 are shown in Figure 3-13 and Figure 3-14, respectively. It can be seen that a good agreement has been achieved between the actual linear heat input and the estimated one.

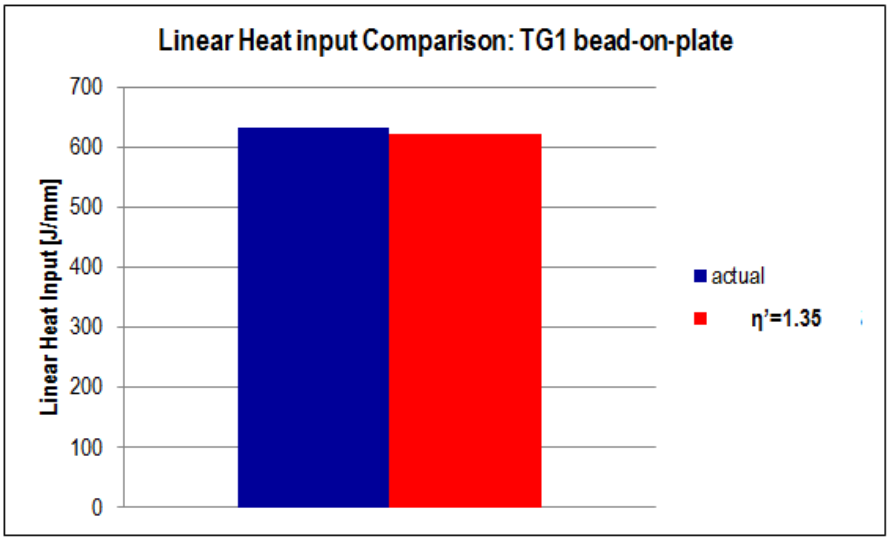

Figure 3-13: Linear heat input comparison for bead-on-plate weld NeT TG1

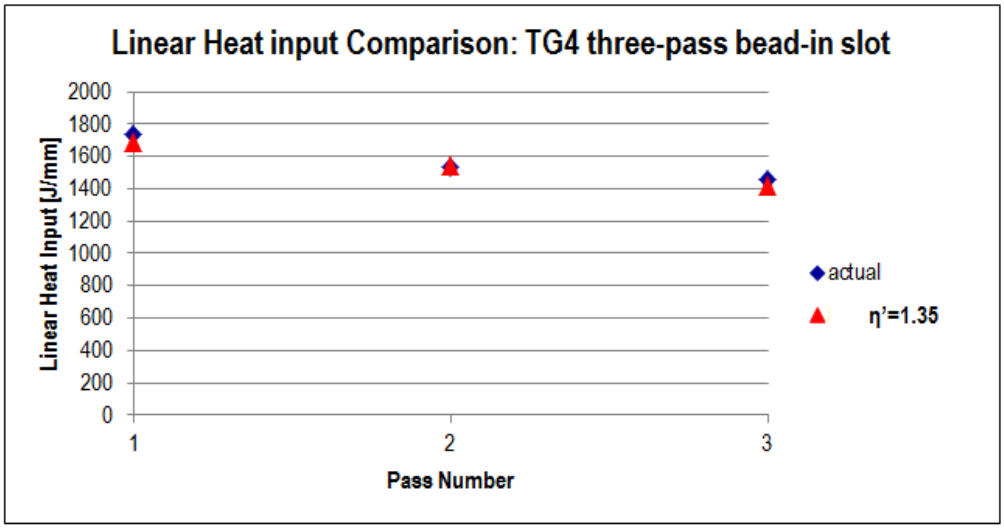

Figure 3-14: Linear heat input comparison for three-pass bead-in-slot weld NeT TG4

Validation – Case 3

Reference [129] documented the welding parameters of an electron beam weld, given by Table 3.7, for a titanium alloy Ti-834 plate of which the weld profile is shown in Figure 3-15. Line marked in red is L_{surf}. Temperature-dependent material properties are available in [129]. Actual linear heat input calculated using Eq. (2.20) (in blue) and estimated using Eq. (2.23) with $\eta' = 1.35$ (in red) is exhibited in Figure 3-16. A good agreement is also obtained for this case.

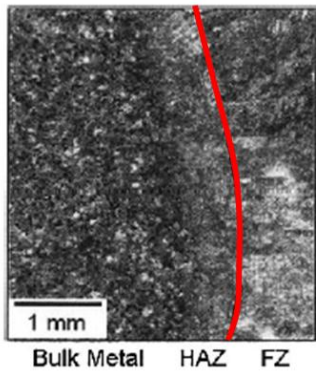

Figure 3-15: Weld profile for the electron beam welding [129] and L_{surf}

Table 2.7 Electron beam welding parameters [129**]**

Accelerating voltage (V)	130 kV
Beam current (I)	40 mA
Welding velocity	50.8 mm s^{-1}
Focal point	~40 mm above surface

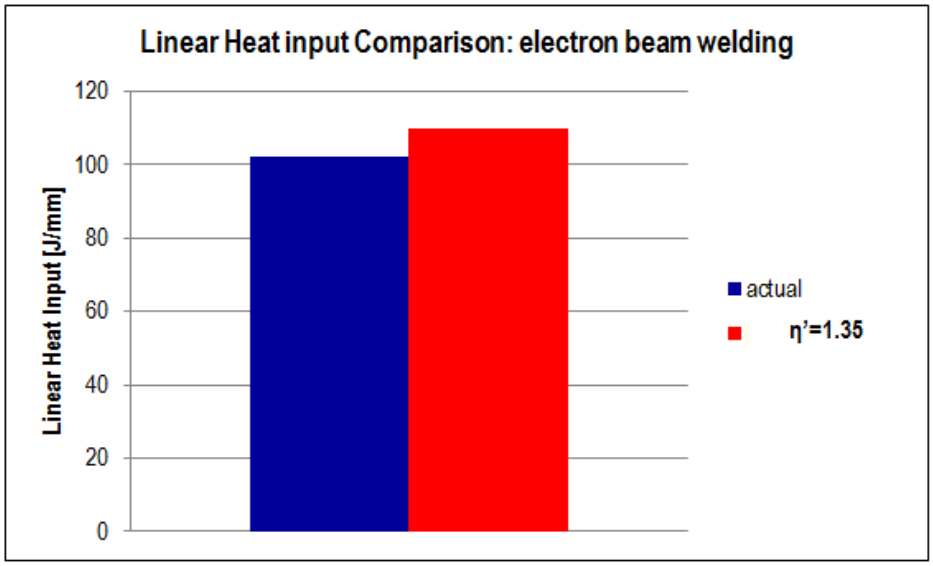

Figure 3-16: Linear heat input comparison for electron beam welding

3.1.3.4 Interim Summary

A new estimation scheme is proposed in this section for the linear heat input calculation in the 2D cross section model. This scheme is derived based on the basic concept of thermodynamics and heat transfer. The major findings can be summarized as follows:

(1) Total weld pool length ℓ estimated using Eq. (2.25) based on Rosenthal's moving heat source model has a good agreement with actual weld pool length.
(2) The first principle based linear heat input estimation using Eq. (3.21-3.23) shows a good agreement with actual linear heat input, if taking account of η' of 1.35.
(3) With known welding parameters, such as arc voltage U, welding current I, welding travel speed v and welding efficiency η, linear heat input used in 2D cross section model is:

$$Q' = \frac{U \cdot I \cdot \eta}{v} \cdot \frac{1}{\eta'}, \quad [J/mm]$$

3.2 Thermomechanical Analysis

Time dependent temperature distributions determined in the thermal analysis are provided as input to mechanical analysis as the driving force for residual stress development. Generally speaking, temperature fields affect mechanical analysis through thermal expansion/contraction which is served as external loads. Mechanical analysis is carried out incrementally with time in order to satisfy the stress equilibrium condition at each time increment. A unified material constitutive model (UMAT) developed by Dong and his co-workers [11-17, 50-51] is first introduced. This constitutive model is implemented in the form of special subroutine which can be interfaced with various commercial FE codes, e.g, ABAQUS. It is the only effective model to calculate welding-induced residual stress. Then temperature dependent material properties used in mechanical analysis are then exhibited. At last, the dominant residual stress development mechanics are identified by using 1-D bar model.

3.2.1 A Unified Material Constitutive Model

Welding induced residual stress is due to plastic deformation which is attributed to nonlinear temperature gradients produced by highly localized rapid heating and cooling. During this process, complex multi-physics and multi-scale mechanics phenomena are occurred. However, some of these phenomena cannot be correctly nor efficiently modeled using current general purpose FE packages. Therefore, a particular tool is needed in order to account for some of the unique features associated with the welding process e.g., material melting/re-melting discussed in Figure 2-2, material phase transformation, among others. For this reason, a unified material constitutive model (UMAT) was invented by Dong and his co-workers in mid-1990s. Until today, UMAT which has been validated for various applications [11-17] is still the only effective model to calculate residual stress.

It is assumed the total strain rate tensors can be written as:

$$\dot{\tilde{\varepsilon}}^{Tot} = \dot{\tilde{\varepsilon}}^{e} + \dot{\tilde{\varepsilon}}^{p} + \dot{\tilde{\varepsilon}}^{\theta} + \dot{\tilde{\varepsilon}}^{A} + \dot{\tilde{\varepsilon}}^{Tr} \qquad \textbf{(3.26)}$$

where $\dot{\tilde{\varepsilon}}^{Tot}$, $\dot{\tilde{\varepsilon}}^{e}$, $\dot{\tilde{\varepsilon}}^{p}$, $\dot{\tilde{\varepsilon}}^{\theta}$, $\dot{\tilde{\varepsilon}}^{A}$, $\dot{\tilde{\varepsilon}}^{Tr}$ represent the total, elastic, plastic, thermal, annealing, and phase transformation strain rate tensors, respectively. Elastic, plastic and thermal strains are easily understood, which are formulated in all of the commercial FE packages dealing with stress calculation. As for welding process, weld material and its surroundings are at melting temperature. It is well known that a material point going through melting or re-melting should lose memory. Therefore annealing strain starts to "anneal" the strain history at a reference annealing temperature θ_A which is a high temperature. Then at a second reference temperature θ_m, usually melting temperature or below, all accumulated elastic and plastic strains are eliminated. As such, material returns to a virgin state for new strains generation. Mathematically, it can be described as:

$$\begin{aligned} &\dot{\tilde{\varepsilon}}^{A} = 0, \quad for \quad \theta < \theta_A \\ &\dot{\tilde{\varepsilon}}^{A} = \left(\frac{\dot{\theta}}{\theta_m - \theta} \right)^{q} \tilde{\varepsilon}, \quad for \quad \theta_A < \theta < \theta_m \end{aligned} \qquad \textbf{(3.27)}$$

where q is a parameter that characterizes the material annealing behavior. Based upon this formulation, the FE model is numerically stable and achieves rapid solution convergence. It is mainly because that this constitutive model eliminates huge strains developed within the weld area. Such huge strains are physically unrealistic and extremely affect solution convergence process. Consequently, annealing or melting/re-melting effects are of critical importance to welding-induce residual stress analysis, particularly in using commercial FE codes. Because continuum and structural mechanics based FE codes are not intended to deal with material state change. In practical, phase transformation temperature is served as annealing start temperature θ_A.

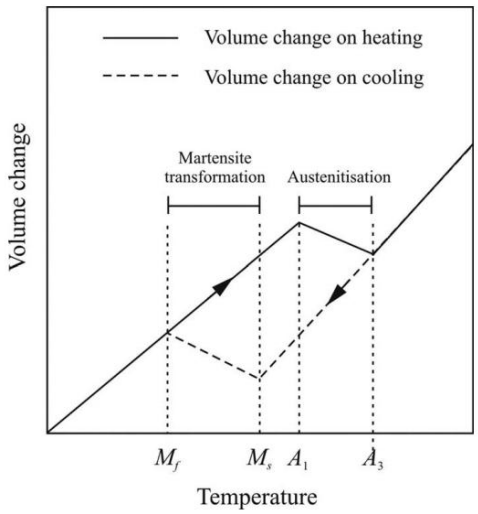

Figure 3-17 Volume change due to austenite and martensite phase transformations [130]

Phase transformation is occurred due to microstructural changes caused by thermal cycles of welding process. Generally for steels, austenitic (face centered cubic) transformation takes place during heating and martensitic (body centered cubic) during cooling. Both phase transformations introduce changes in volume, as shown in Figure 3-17. The volume change would result in altering residual stress state. As far as residual stresses are concerned, the austenitic transformation is much less significant compared with the martensitic transformation. This is primary due to the fact that austenitic transformation happens at a rather high temperature, 900°C, at which the stresses are very small. However, the martensitic transformation can be taken place at the temperature as low as 185°C for some pipe steels, e.g., P91. Therefore, the effect of phase transformation needs to be taken into account, especially for martensitic transformation in low temperature.

In the UMAT, the volume change can be taken into account by the corresponding coefficient of thermal expansion (CTE). Then thermal strain and phase transformation strain based on the calculated CTE are superimposed in an incremental formulation to allow two separate paths for heating and cooling. Without loss of generality, this can achieve the overall effect of volumetric change shown in Figure 3-17.

Detailed annealing and phase transformation effects using UMAT will be illustrated using 1-D bar model later. As presented in Figure 3-18, UMAT has been implemented as a special material subroutine which is readily interfaced with various commercial packages, such as ABAQUS.

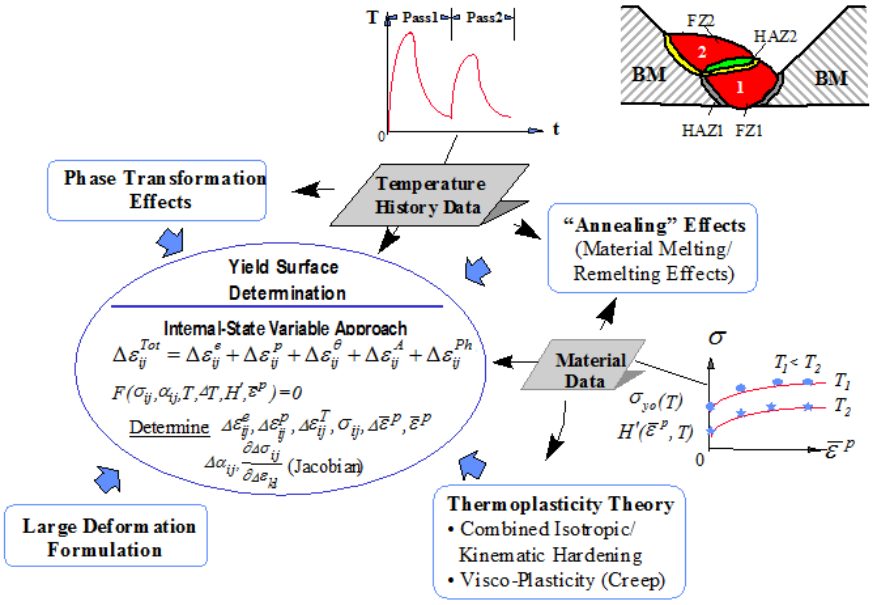

Figure 3-18 Illustration of the unified material constitutive model [13]

3.2.2 Mechanical Material Property Representation

For mechanical analysis, the following temperature dependent material properties are basically required:

- Poisson's ratio, v
- Young's modulus, E [N/mm^2]
- Coefficient of thermal expansion, CTE [1/°C]
- Stress-strain curves

Again, material 2.25CrMo-V is taken as an example to exhibit the corresponding mateiral properties. The raw mateiral data are provided by courtesy of MPC material property database. Possion's ratio is assumed as a constant of 0.3 in the current study. Temperature dependent Young's modulus and coefficient of thermal expansion are plotted in Figure 3-19 (a) and (b), respectively.

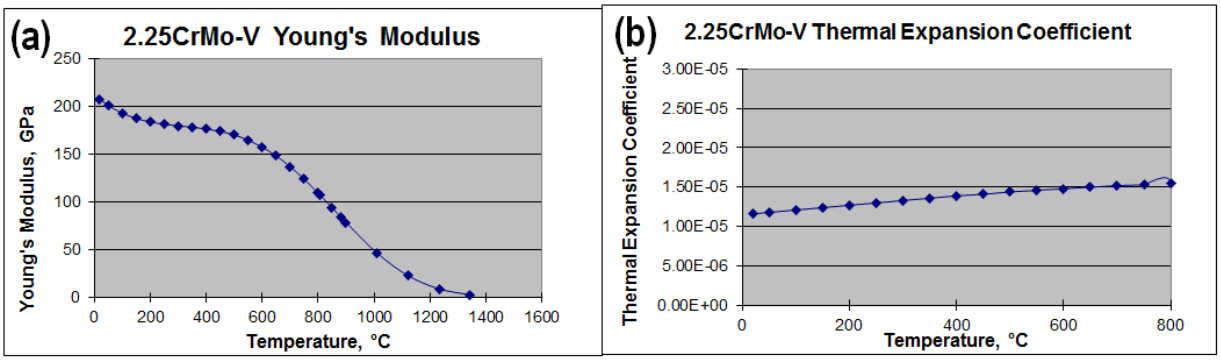

Figure 3-19 Temperature dependent Young's modulus and coefficient of thermal expansion

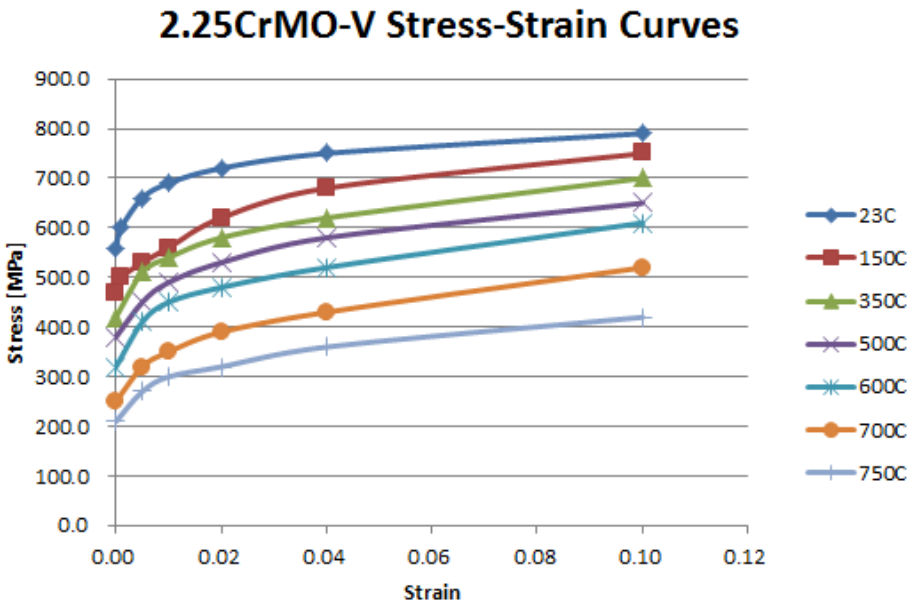

Figure 3-20 Temperature dependent stress-strain curves

The raw stress-strain curves from the MPC database are described in a form of true stress and strain curves at various temperatures. These raw stress-strain curves are needed to be converted to meet ABAQUS material property definition. In doing so, assuming the material reaches yielding at approximately about 0.2% true strain and then shifting the stress-strain curves accordingly, as shown in Figure 3-20. It can be seen that the stress-strain curves are available for a temperature range from room temperature up to 700-800^{o}C. Beyond this temperature range, data are linearly interpolated between the last temperature at which a property value is available and the melting temperature at which is assumed to be 1/100 of its respective values at room temperature. As indicated in the Phase I report [13], any more complex variations within this temperature have been proven to be insignificant as far as final residual stresses are concerned.

In addition to the basic material properties mentioned above, annealing start and end temperatures, austenitic and martensitic transformation temperatures, and melting temperature are required in UMAT. Furthermore, two different curves of thermal expansion coefficients for heating and cooling are needed, other than one curve as shown in Figure 3-19 (b).

3.2.3 1-D Bar Model Illustration

As aforementioned complex phenomena associated with the welding process, it is impossible to reveal in detail about each strain evolution history based upon which residual stress is developed. In order to identify the dominant residual stress development mechanics, multi-physics phenomena have to be simplified without losing helpful information for engineering applications. With this intention, 1-D bar model can be effectively used to highlight some issues clearly. Moreover, the analytical solution for a simple 1-D bar model can be obtained easily for further validation purposes.

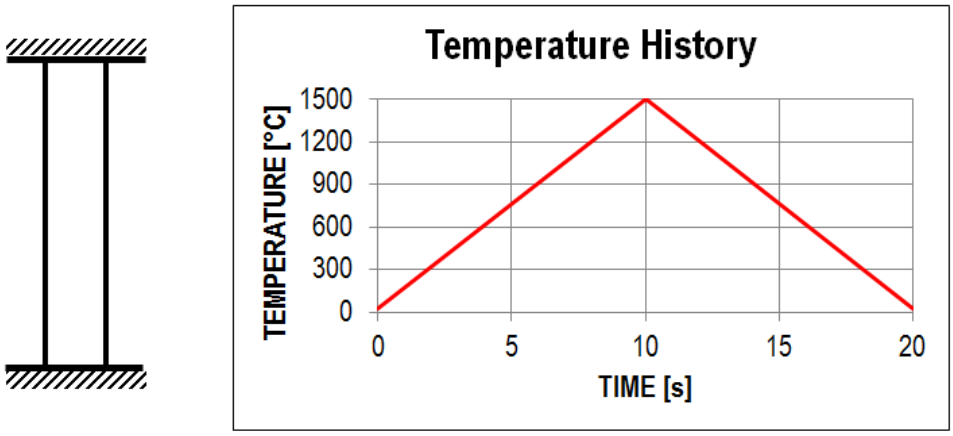

Figure 3-21 Simple 1-D bar model definition

As shown in Figure 3-21, a 1-D bar with two ends fixed is uniformly heated and cooled in a linear manner. The bar experiences one 20s thermal cycle of temperature change from room to melting temperature 1500°C (10s) and back to room temperature 23°C again (10s).

3.2.3.1 Annealing (Melting/Re-Melting) Effects

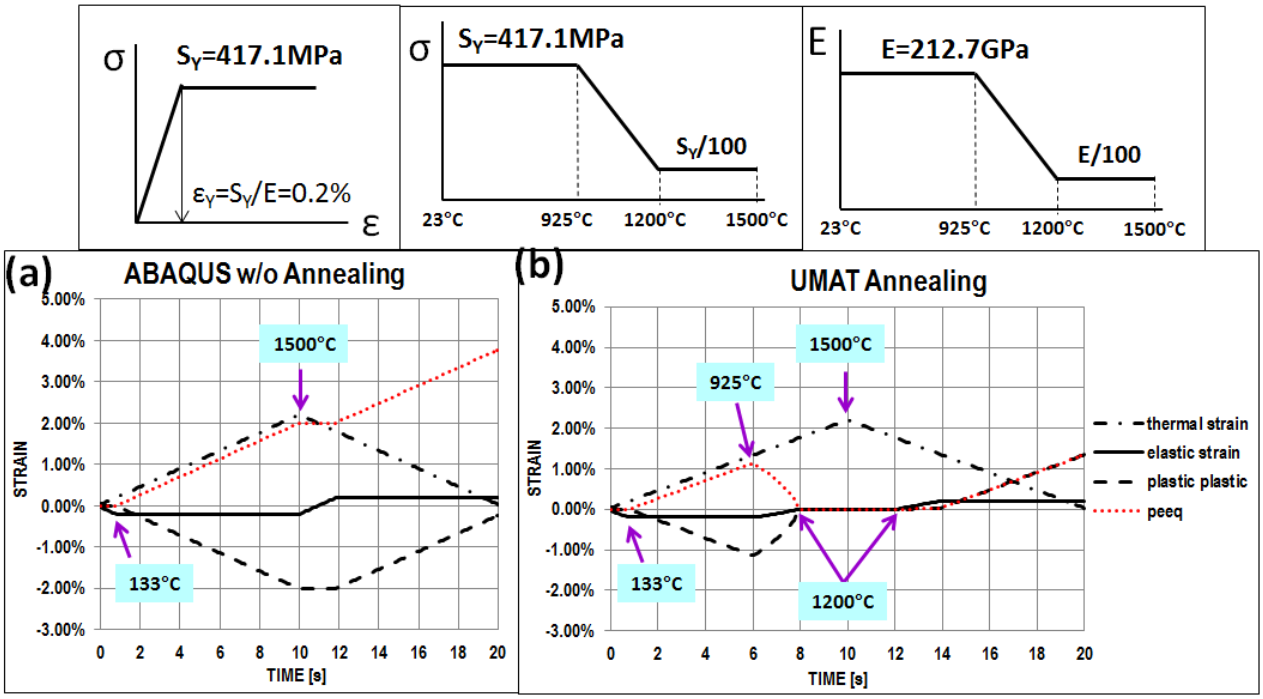

Figure 3-22 Annealing effects (from 925°C to 1200°C) illustration using 1-D bar model with material properties definition: (a) Strain developments using ABAQUS only without annealing, and (b) strain developments using UMAT with annealing

Annealing or melting/re-melting effects are first examined. In order to compare the differences between with and without annealing effects, evolution history of each strain component corresponding to the thermal cycle shown in Figure 3-21 are illustrated in Figure 3-22 (a) and (b), respectively. For demonstration purpose, it is assumed elastic perfectly plastic material behavior and yield strength history dependent on linear temperature. Without loss of generality, it can be further assumed that with temperature increases, yield strength decreases from 925°C, to its 1/100 value at 1200°C and melting at 1500°C. Accordingly, Young's modulus E presents the same manner as yield strength. As such, yield elastic strain ε_y would maintain the same at all time. Coefficient of thermal expansion (CTE) is assumed to be a constant value of 14.71E-6 at various temperatures.

The results of (a) are obtained from ABAQUS only using the material properties described above. Output of (b) are gained from ABAQUS using UMAT subroutine with annealing start temperature 925°C, annealing end temperature 1200°C and melting temperature 1500°C in addition to the same material properties used in (a). By comparison, some observations are summarized as follows:

- Thermal strain ($\varepsilon_\theta = CTE \times \Delta T$) is only dependent on temperature since CTE maintains a constant at all time. Consequently, thermal strains for both cases are identical.
- Elastic strain exhibits compression in heating and tension in cooling. For both cases, elastic strains at the end of cooling are the same as 0.2% which indicates the yield strength. Therefore, residua stress can be normalized by its yield strength magnitude of room temperature.

- For both cases, elastic strains reach to its yield compression at about 133°C during heating. It is can be explained by the equation below:

$$\Delta T_p = \frac{S_y}{CTE \times E} = 133.3°C \quad \textbf{(3.28)}$$

  where ΔT_p is the temperature for a bar to reach yield magnitude on heating in rigid constraint condition. Then it can be deduced that residual stress magnitude reaches yield strength at the end of cooling as long as a temperature difference of $2\Delta T_p$ in heating is met.
- Plastic strain occurs at ΔT_p 133°C and can be obtained by simply subtracting the elastic strain from the thermal strain.
- "peeq" is the equivalent plastic strain which is calculated based upon isotropic Mises plasticity. It always has positive value. In this 1-D bar model, the magnitude of equivalent plastic strain is always equal to plastic strain as long as UMAT is concerned. Generally, this parameter can be used to indicate where plasticity is occurred.
- Since annealing starts at 925°C and ends at 1200°C, it can be seen in (b) that elastic, plastic and equivalent plastic strains decrease from 925°C to zero at 1200°C. Then they maintain as zero to the melting temperature 1500°C. On cooling, elastic strain starts from a virgin state. It begins to generate after 1200°C. When elastic strain reaches to its yield magnitude, plastic and equivalent plastic stains are begin to produce from zero. As such, elastic, plastic and equivalent strains develop properly in UMAT. However in (a), without annealing, these three strains are continually accumulated near melting temperature and after it. Plastic strain develops in the wrong direction same as "incorrect" curve shown Figure 2-2. At the end of cooling, equivalent plastic strain results in a pretty large value which is almost three times compared with the same red dotted curve in (b). These phenomena are unrealistic and can lead a lot issues in finite element analysis, such as more iterations, slow speed, and difficult convergence.

In summary, annealing or melting/re-melting effects are simulated correctly in UMAT. The magnitude of final residual stress is governed by its yield strength at room temperature. Only $2\Delta T_p$ variation in heating or cooling can result in yield magnitude of residual stress. Despite this, the final residual stress states are identical for both 1-D bar models. This is mainly because the material is assumed to be perfectly plastic. If strain hardening had been considered, the residual stress results would be much different. This is especially true for multi-pass weld.

Recently, ABAQUS implements this annealing option into its material property definition. However, it still has at least two imperfections. First, ABAQUS annealing can be only applied at one sudden temperature, not like UMAT which has a transitional temperature range (annealing start and end temperatures). In addition, UMAT can also anneal at one temperature if setting the same annealing start and end temperatures. Second, ABAQUS can only eliminate equivalent plastic strain above a given annealing temperature. It allows the individual components of elastic and plastic strains to be continuously accumulated. In this way, ABAQUS still has a large amount of component strains produced in high temperature, which may result in difficult/slow

solution convergence. Detailed illustration as what have been discussed can be found in Figure 3-23.

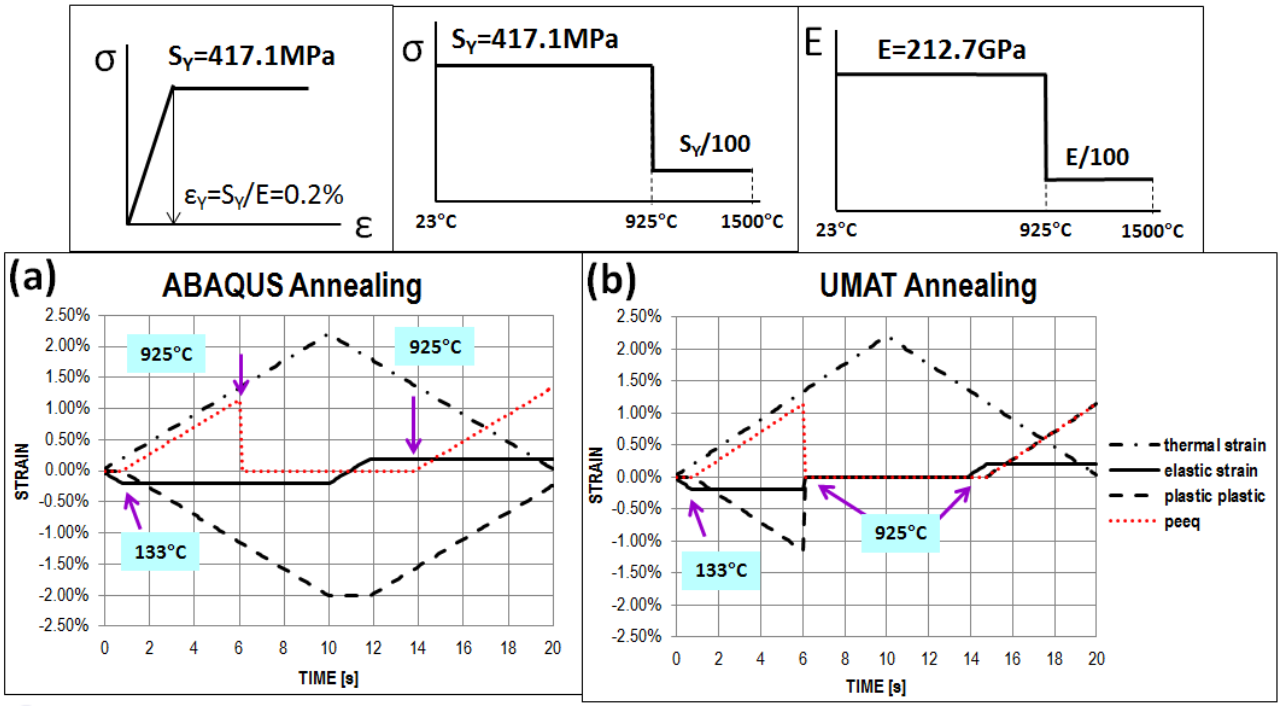

Figure 3-23 Annealing effects (at 925°C) illustration using 1-D bar model with material properties definition: (a) Strain developments using ABAQUS only, and (b) strain developments using UMAT

3.2.3.2 Phase Transformation Effects

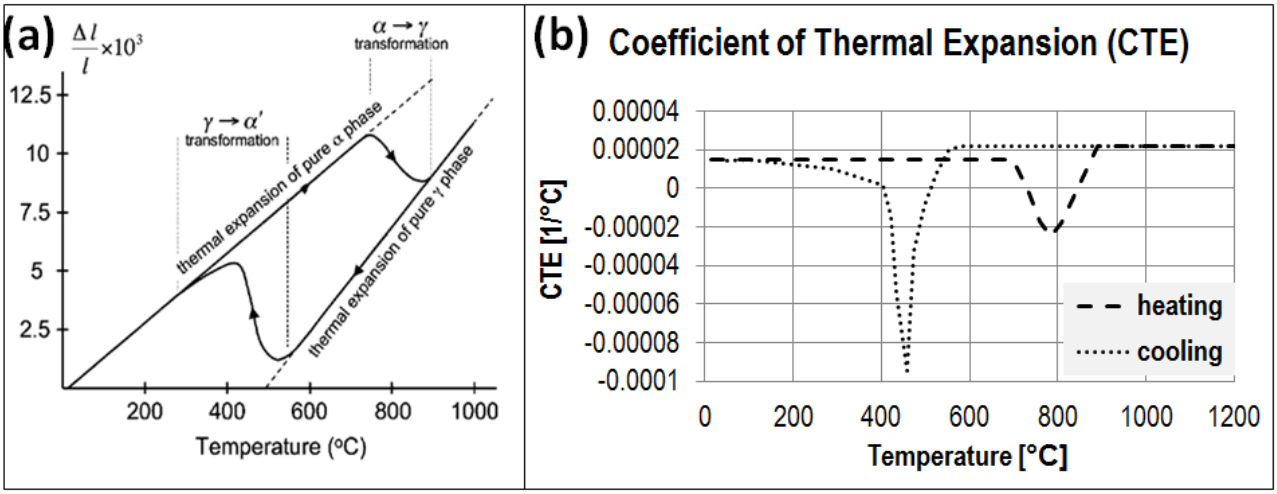

Figure 3-24 (a) Dilatometric diagram of A508 CL3 reactor pressure vessel steel [131], and (b) the corresponding CTE for heating and cooling deduced from (a)

A508 class 3 steel is used as example to demonstrate phase transformation effects. This material is a typical reactor pressure vessel steel which is widely used in nuclear power plants. The volume changes as a function of temperature during heating and cooling can be experimentally determined by using dilatometry. Figure 3-24 (a) presents such an experiment [131]. The upper straight line indicates the expansion of perlite-ferrite/martensite (α phase, body centered cubic), and the lower line is for that of austenite (γ phase, face centered cubic). The data in between of two lines correspond to the co-existence of the parent and product phases, e.g., martensite transferred to austenite (α to γ) around 700°C – 800°C of which phase change is also called austenitic transformation. The corresponding coefficients of thermal expansion for heating and cooling are deduced from (a) shown in Figure 3-24 (b). Since ABAQUS only allows one set of CTE with respect to temperature, the obtained two sets of CTE can be used in the UMAT subroutine to simulate phase transformation effects.

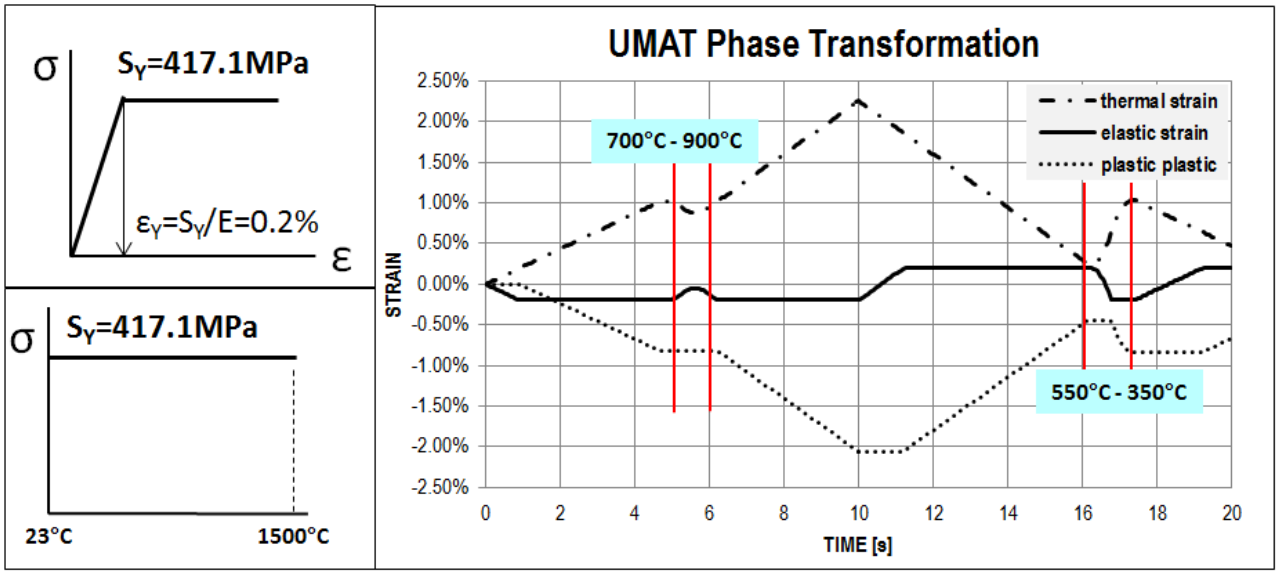

Figure 3-25 Phase transformation effects illustration using 1-D bar model with material properties definition: strain developments using UMAT

For illustration purposes, it is assumed to have elastic perfectly plastic material behavior and a constant yield strength history with respect to the temperature. Accordingly, Young's modulus also keeps constant as a function of the temperature. Annealing effect is not considered in this case. Figure 3-25 exhibits the evolution history of strain components. Thermal strain (ε_θ =CTE×ΔT) vividly represents the variation on coefficients of thermal expansion which are shown in Figure 3-24 (b). The temperature ranges of thermal strain change marked between red lines correspond to that of phase transformation. During heating from 700°C to 900°C, steel is subjected to a contraction which introduces a little bit of tension as shown by elastic strain. During cooling from 550°C to 350°C, a quite bit of expansion is occurred to the material. As shown in elastic strain curve, such a large expansion of volume contributes to the residual stress reaching yield compression.

Although the final state of residual stress for phase transformation is the same as the one obtained by (a) in Figure 3-22, in reality the residual stress distributions would be different if martensitic phase change happens at a low temperature range with a large compression shown in Figure 3-25. Particularly for multi-pass weldment, some locations may be experienced several times of phase transformation due to the heat flow of each pass.

3.2.3.2 Material Hardening Law Effects

It is shown in Figure 2-8 that several discrepancies are exhibited in the residual stress predictions with either linear isotropic or linear kinematic hardening law. Dong demonstrated the effects of different hardening laws on residual stress developments using 1-D bar model [12] presented in Figure 3-26. It can be seen that, kinematic hardening provides the minimum residual stress estimation than isotropic hardening model. However, annealing effects were not taken into account in this demonstration.

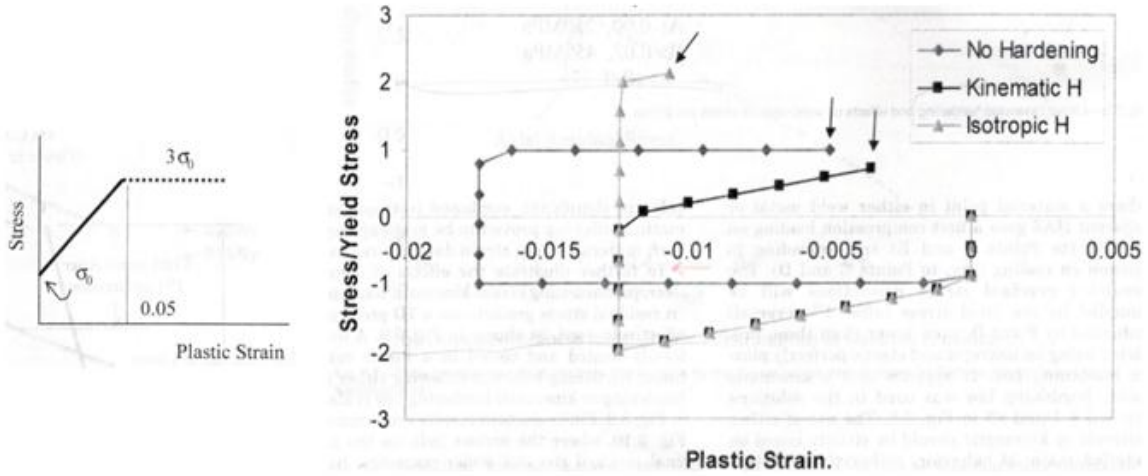

Figure 3-26 Effects of using linear kinematic hardening vs. isotropic hardening laws on residual stress predictions [12]

An attempt is made in this study to further demonstrate the annealing effects on residual stress estimations with difference hardening laws. Duplicated Figure 3-26 results are shown in Figure 3-27(a) without considering annealing. The results with annealing effect are shown in Figure 3-27 (b). It is clear that, when annealing is considered, both plasticity models yield the same results as long as a 1-D bar model is concerned. This is primary due to the fact that strains for both hardening laws start from a virgin state on cooling. Based on this finding, all of the residual stress analyses are performed using isotropic hardening law in this study with annealing effect consideration.

Furthermore, by examining various strain hardening without annealing effect, the material with higher strain hardening produces a larger difference in the predicted residual stress than the materials with medium and lower hardening (Figure 3-28) between the linear isotropic and

kinematic hardening models. With more thermal cycles, the difference would become larger.

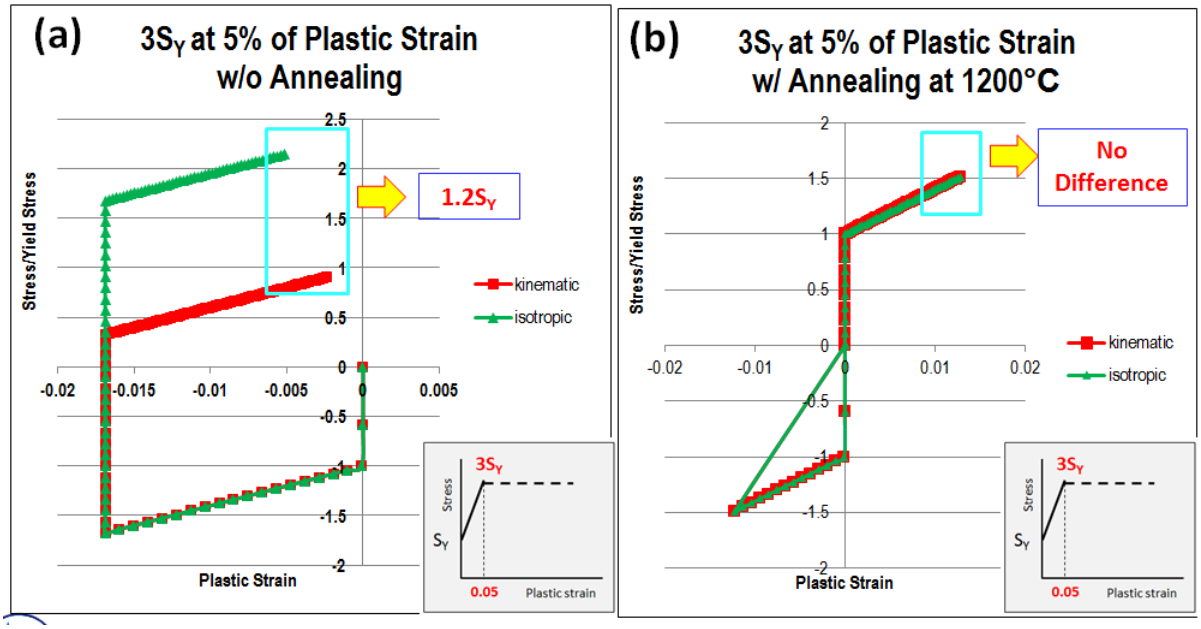

Figure 3-27 Annealing effects on residual stress prediction with different linear hardening laws: (a) without annealing, and (b) with annealing

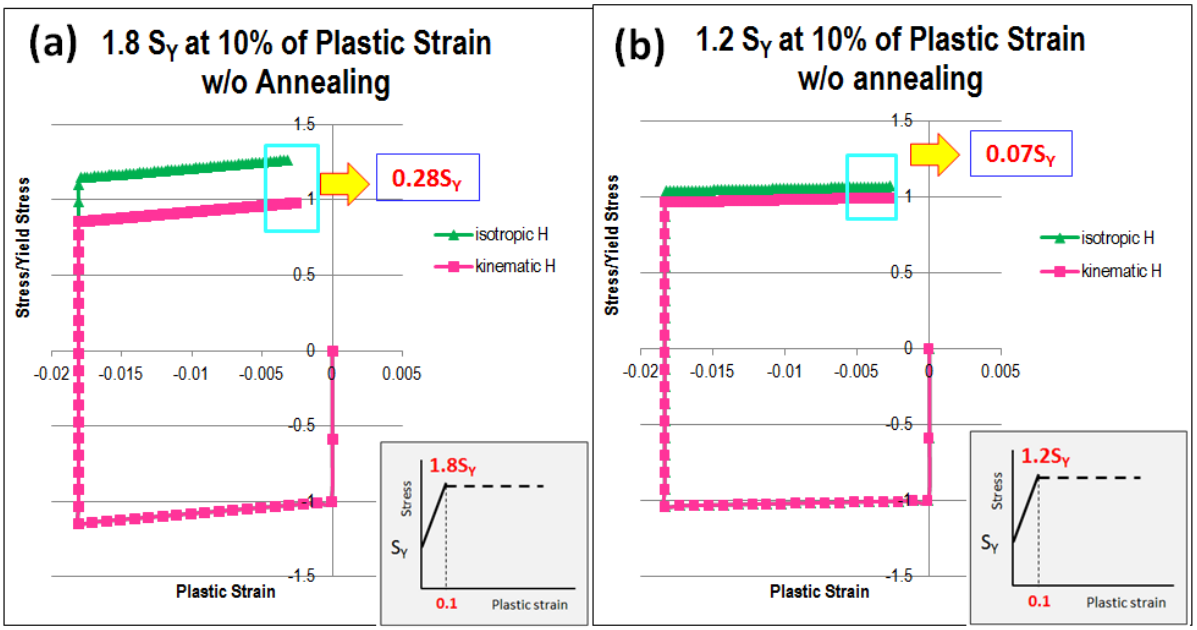

Figure 3-28 Strain hardening effects on residual stress prediction with different linear hardening laws: (a) 1.8 S_Y at 10% of Plastic Strain, and (b) 1.2 S_Y at 10% of Plastic Strain

3.3 Validation of Residual Stress Analysis Procedure

In addition to those validation cases documented in the Phase I report, further validation is performed as a part of Phase II effort by taking advantage of more recently published residual stress measurement data with an emphasis on thick section weldments.

3.3.1 P91 girth weld

Figure 3-29 shows the details of a P91 pipe girth weld geometry and weld cross-section details [133]. The mock-up weld was made with a V preparation and 73 weld passes using a manual metal arc welding processes. Measured residual stress results using both X-ray diffraction and deep-hole drilling (DHD) are documented in [133].

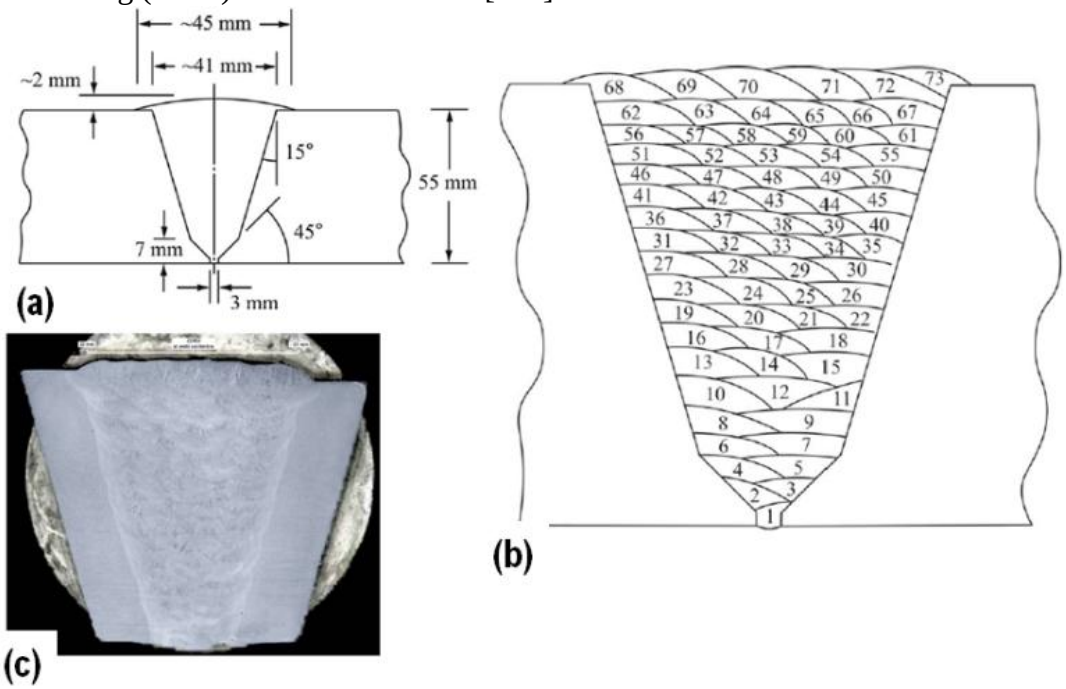

Figure 3-29 Single V girth weld configuration - (a) weld geometry (b) weld pass sequence and (c) macrograph of the weld cross section [133].

An axisymmetric finite element model with 14893 nodes and 14662 quadrilateral linear elements is used, as shown in Figure 3-30. The weld pass profiles are modeled according to descriptions given in Figure 3-29. In performing welding heat flow analysis, heat input for each pass is simulated by assuming a deposition temperature of slightly above melting, i.e., 1650 ℃ in the present study. All temperature-dependent material properties are directly taken from [133] and are re-plotted in Figure 3-31, in which all material properties are normalized by their respective values at ambient temperature 20 ℃. Note that the stress-strain curves for both base material and weld metal were assumed to follow the same hardening behavior, except with their respective yield strengths. At and above melting temperature 1420 ℃, all the material properties are

assumed to be constant except the thermal conductivity which is assumed to be doubled in order to account for the enhanced convection effect by the molten weld pool. Both Poisson ratio and density are assumed to be constant over temperature, i.e., 0.3, and 7770 kg/m^3, respectively [133]. Von Mises yield criterion following isotropic hardening law is used for this case study and all analyses reported here.

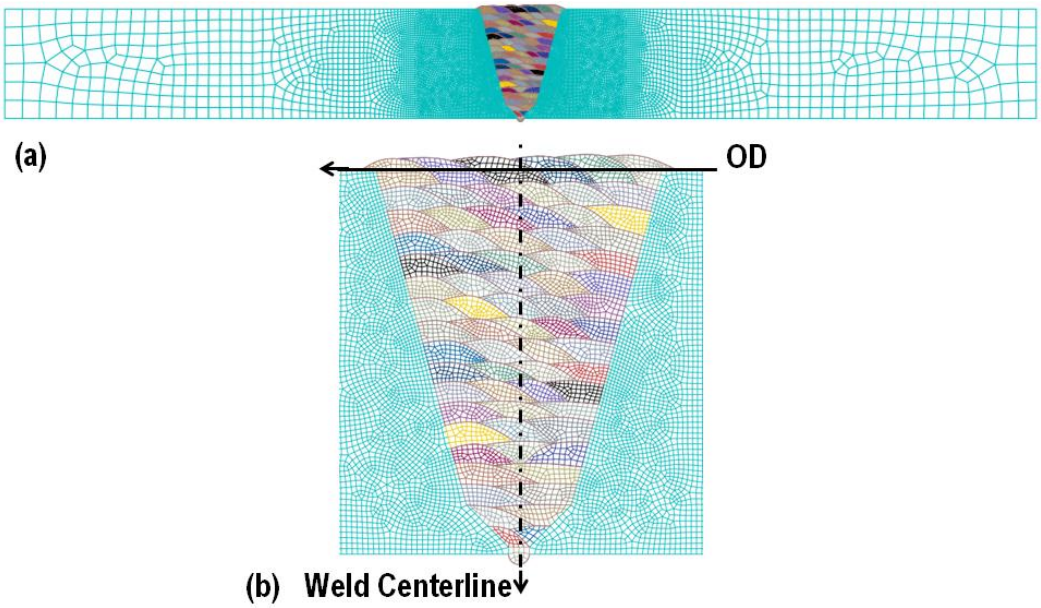

Figure 3-30 Axisymmetric FE model - (a) complete model (b) detailed weld pass profiles with the definition of lines

The effects of solid state phase transformation on residual stresses are taken into consideration in a unified weld material constitutive model [130, 133] due to P91 steel's hardenability. As given in [130], the starting temperature for martensitic transformation is estimated at 375 ℃ and finish temperature at 185 ℃ according to an empirical equation [130]. The Koistinen-Marburger relationship is employed to describe the transformation effect. The strain value of 3.75×10^{-3} is used for the volumetric change associated with a full martensitic transformation [130]. The austenitic transformation temperature is from 820 ℃ to 920 ℃ [130]. The strain due to volumetric change in a full austenitic transformation assumed for P91 is -2.288×10^{-3} [130]. As far as residual stresses are concerned, the austenitic transformation is less significant compared with the martensitic transformation. This is due to the fact that austenitic transformation occurs at a rather high temperature at which the stresses are very small. In the unified weld constitutive model (UMAT), thermal strain and phase transformation strain (data taken from [130]) are superimposed in an incremental formulation to allow two separate paths for heating and cooling. In addition, the plastic strain annealing temperature is set to start at 1200 ℃ and finish at melting temperature of 1420 ℃.

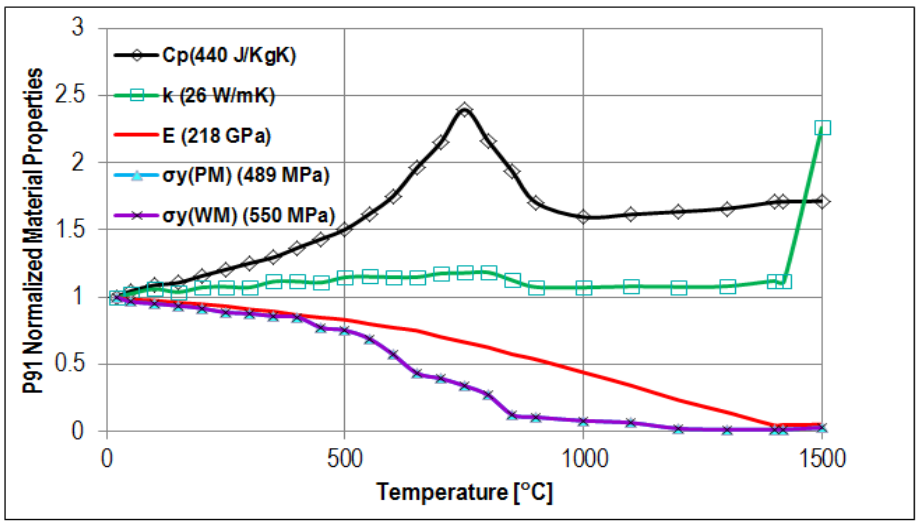

Figure 3-31 Temperature dependent material properties for P91 steel

Two lines of residual stress measurement results on the mock-up weldment (see Figure 3-30b) were reported in [133]: One is along the pipe outer surface using X-Ray diffraction technique with weld cap being removed and the other is along the weld center line in the through-thickness direction using a deep-hole drilling (DHD) technique. Accordingly, the residual stress results from the present finite element simulation are processed and compared with the measured data in Figure 3-32 and Figure 3-33. It can be seen that the modeling results and residual stress measurements show a good agreement. It is interesting to note that on the outer surface of the pipe, there exists a region (10~15mm from weld centerline) of compressive residual stresses in both axial and hoop directions, as shown by both the modeling and measured residual stress results. The size and location of this area approximately correspond to the last weld pass area. This is because in this area, the material has undergone a martensitic phase transformation associated with the volumetric expansion in both weld pass itself and surrounding heat affected zone (HAZ). This last weld pass area is mechanically restrained by the surrounding material, resulting in significant compressive residual stresses. Similar residual stress distributions can also be found in [134].

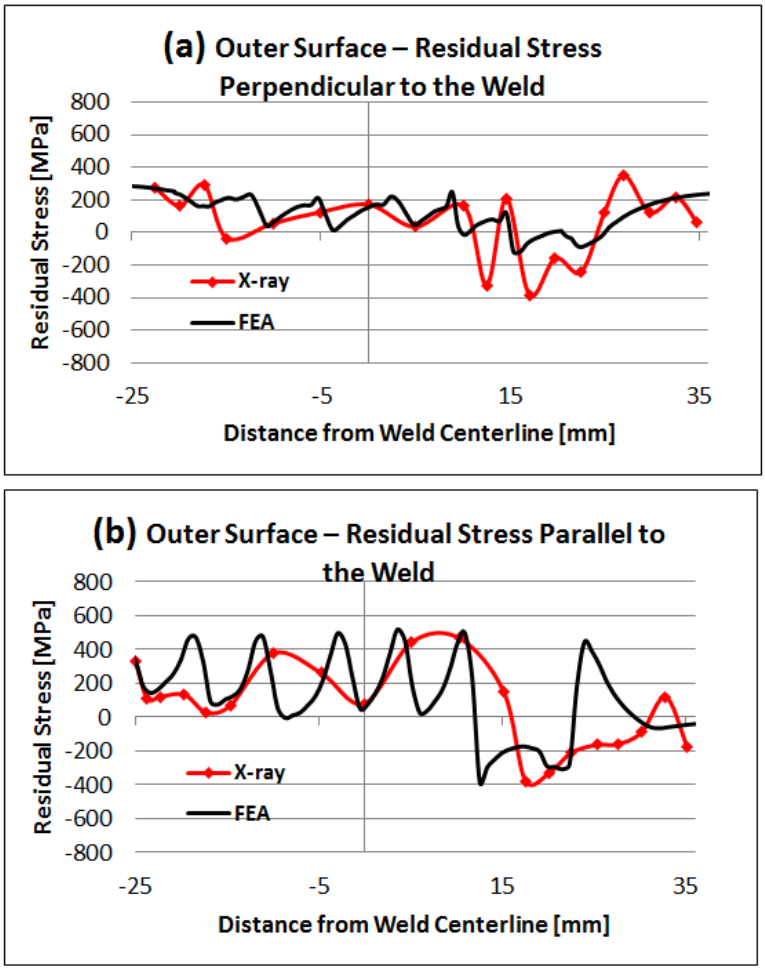

Figure 3-32 FE results versus X-ray diffraction measurement data along the OD (a) axial stresses and (b) hoop stresses

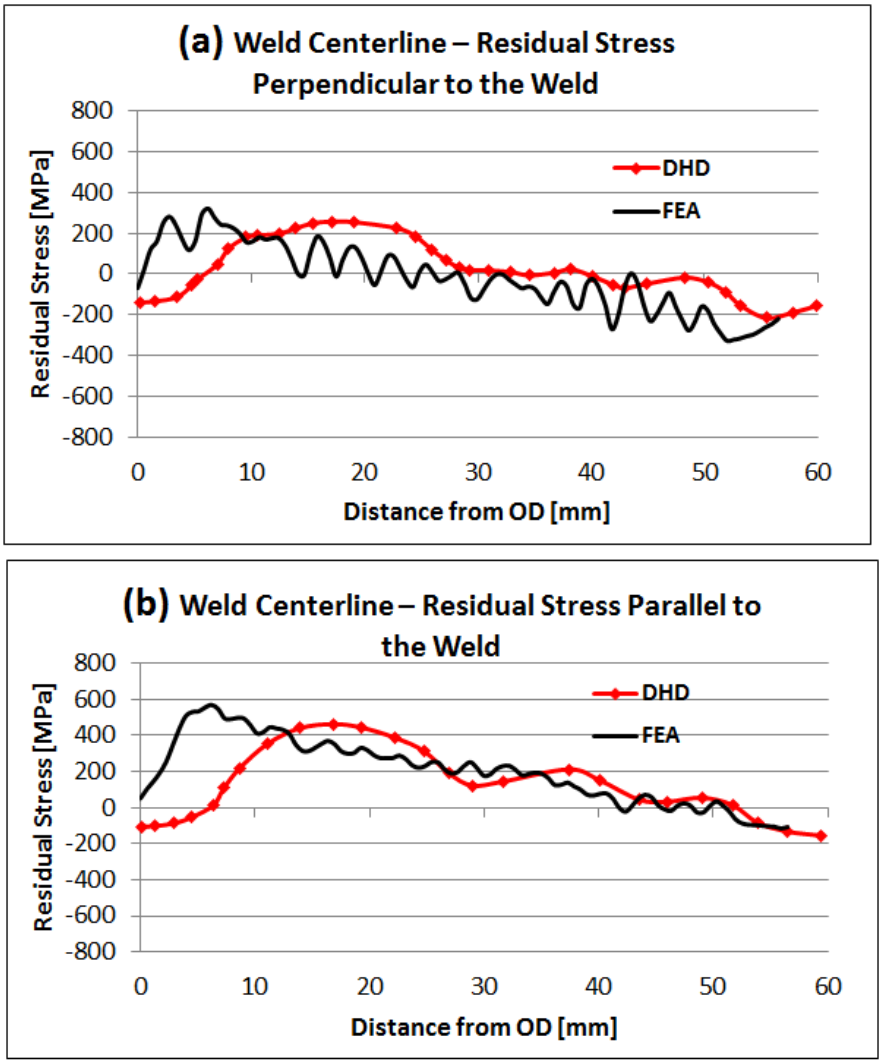

Figure 3-33 FE results versus DHD measurement data along the weld centerline (a) axial stresses and (b) hoop stresses

It is well known that element size is of importance to finite element analysis. In order to make sure the element size used in the previous validation analysis is good enough, which means residual stress distributions do not change much if this element size increases or decreases a little bit, a coarse model is generated. Previous model, Figure 3-30, is referred as the "fine" model here with element size of 0.6mm within the heat affected zone (HAZ). Element size for the new coarse model is twice times larger than the one used in fine model, which is 1.2mm within the HAZ. Detailed mesh comparisons between these two models are exhibited in Figure 3-34. In addition, Table 3.7 shows the comparison of total node and element numbers for the two models. As can be seen, total number of nodes and elements in coarse model are more than twice time less than the ones in fine model.

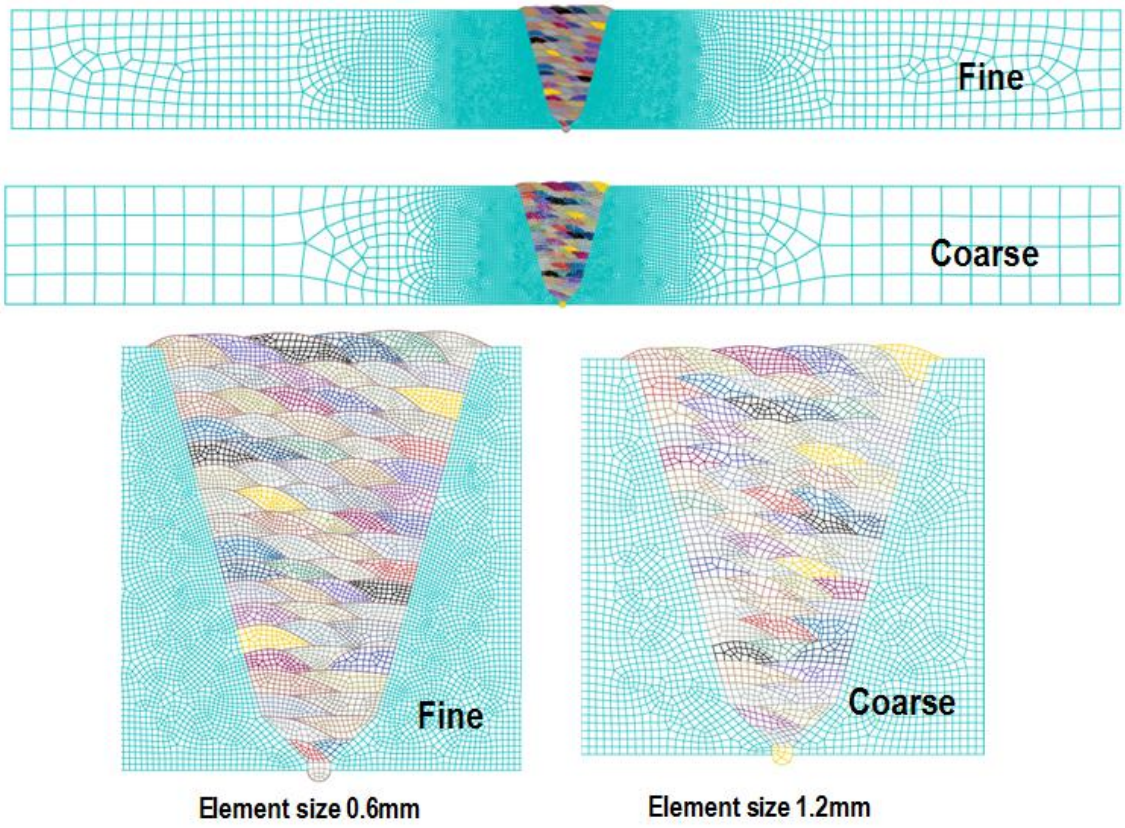

Figure 3-34 Fine and coarse mesh models for P91 girth weld

Table 3.7 Comparison of element sizes, total number of nodes and elements

	Element Size	Nodes #	Element #
Fine Model	0.6mm	14893	14662
Coarse Model	1.2mm	6445	6300

Axial (perpendicular to the weld) and hoop (parallel to the weld) residual stress contour plots for fine and coarse models are expressed in Figure 3-35. It is can be seen that there are no differences between these two models in contour plots. Detailed line plots along weld centerline are shown in Figure 3-36. Results from fine and coarse models are almost matched to each other. Figure 3-35 and Figure 3-36 demonstrate that the element size of fine model used in the previous validation study is good enough. Residual stress distributions do not alter with increasing the element size. In this study, element size within the HAZ are all smaller than 1/50t in order to obtain accurate residual stress profiles.

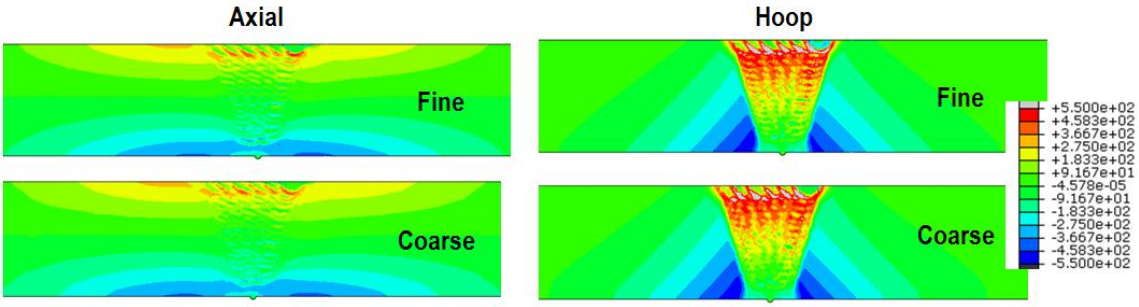

Figure 3-35 Contour plots of axial and hoop residual stresses for fine and coarse models, indicate scale from 550MPa to -550MPa

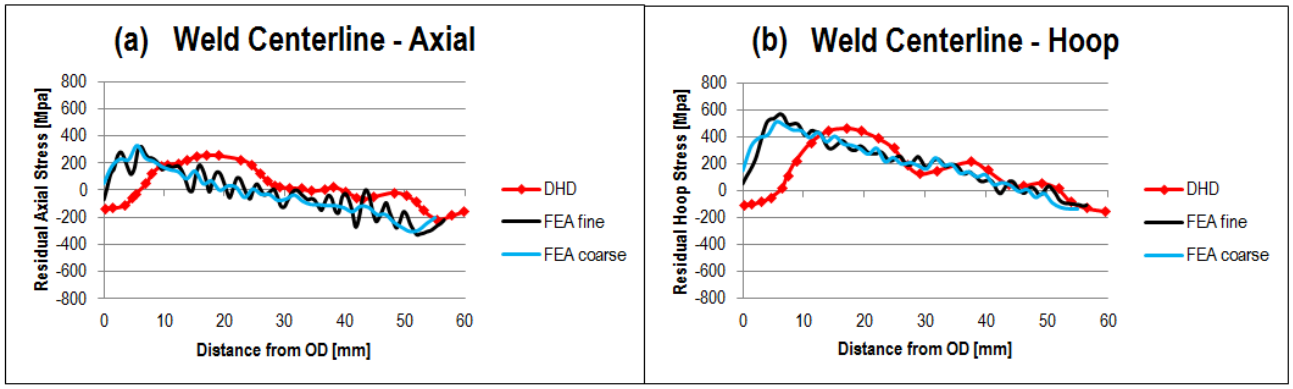

Figure 3-36 FEA results from fine and coarse models versus DHD measurement data along the weld centerline (a) axial stress, and (b) hoop stress

3.3.2 CrMo Steel Nozzle Weld

Figure 3-37 shows the details of nozzle weld geometry and meshing for 75 passes in the weld zone documented in [132]. Two different base materials were used for this validation, one is 10CrMo9-10 (2.25CrMo) and the other one is 13CrMoV9-10 (2.25CrMo-V). Preheating and interpass temperature were 200 ℃. Finite element residual stress predictions using somewhat different analysis procedures along with experimental validations using deep-hole-drilling (DHD) in weld centerline were performed in [132]. With the detailed analysis procedures discussed in the foregoing, a re-analysis of residual stress distribution was carried out in this investigation by following the detailed thermal and thermo-mechanical procedures outlined in the previous sections. An axisymmetric model with 75-pass sequence definition is presented in Figure 3-38. Two material properties (2.25CrMo and 2.25CrMo-V) used in re-analysis are provided by the MPC property database.

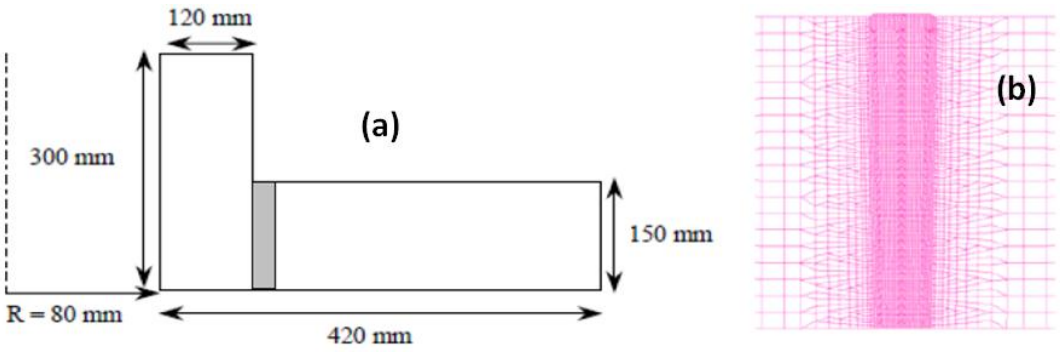

Figure 3-37 Nozzle weld configuration – (a) nozzle dimensions and (b) meshing of the weld zone [132]

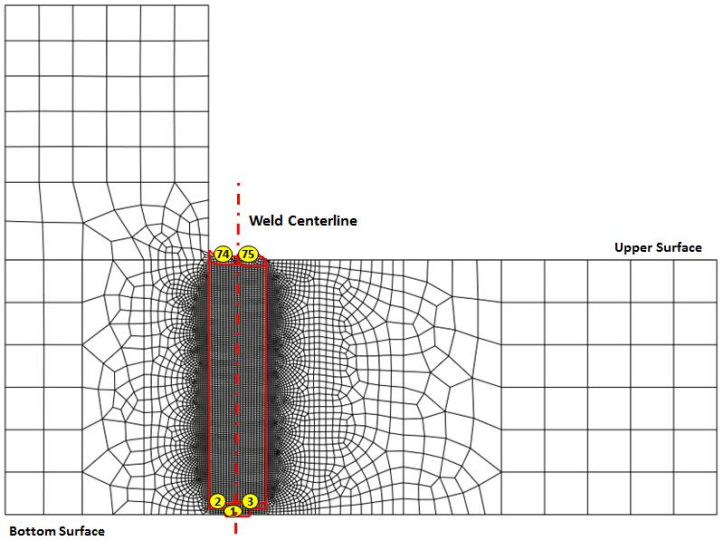

Figure 3-38 Axisymmetric FE model and pass sequence

The University of Bristol carried out the residual stress measurements using DHD technique in the weld centerline for two different base materials mock-ups. The finial residual stress distribution results are compared with the experimental measurements in Figure 3-39 and Figure 3-40 for the material of 10CrMo9-10 (2.25CrMo) and 13CrMoV9-10 (2.25CrMo-V), respectively. Finite element results performed using foregoing analysis procedures are the black lines and measurements data are in dotted red lines. As we can see, the modeling results and residual stress measurements show a good agreement for both materials. The residual stresses perpendicular to the weld, as shown in Figure 3-39 (a) and Figure 3-40 (a), exhibit a local bending type.

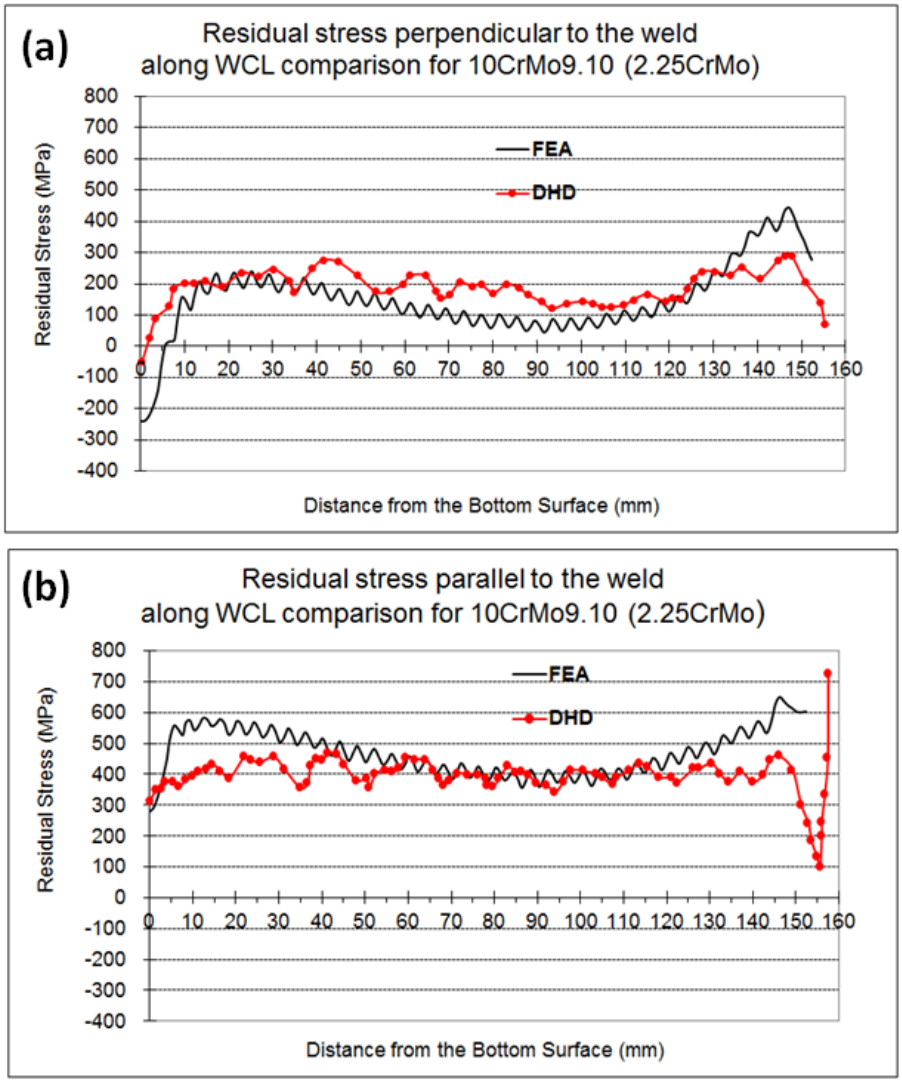

Figure 3-39 FE results versus deep-hole drilling measurements along weld centerline for 10CrMo9.10 (2.25CrMo) (a) residual stress perpendicular to the weld and (b) residual stress parallel to the weld

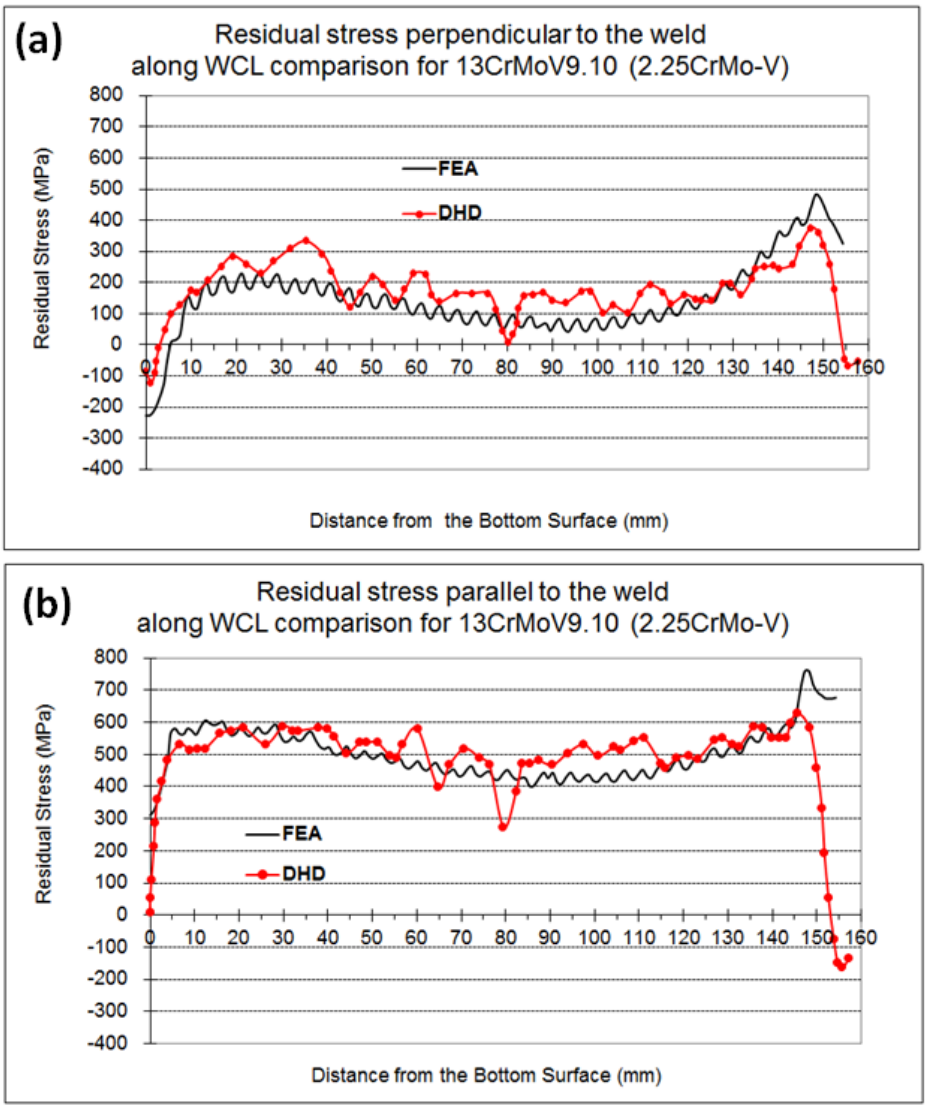

Figure 3-40 FE results versus deep-hole drilling measurements along weld centerline for 13CrMoV9.10 (2.25CrMo-V) (a) residual stress perpendicular to the weld and (b) residual stress parallel to the weld

3.3.3 Ti-6-4 "T" Joint Fillet Weld

Titanium alloy has low density, high strength, good malleability, and corrosion-resistance, such as Ti-6-4. The corresponding temperature dependent material properties are exhibited in Figure 3-41. Both Poisson's ratio and density are assumed to be constant over temperature in FE analysis, i.e., 0.31, and 4420 kg/m^3. Two Ti-6-4 alloy plates of which dimension is 12"×5"×0.25" are perpendicularly welded as a "T" Joint using the same material of weld wire, as shown Figure 3-42. Welding procedure is MIG (metal inert gas) with voltage 29.5V, current 156A, and traveling speed 23" per minute.

Figure 3-43 presents the corresponding 2D cross section FE model. The nominal weld leg is 3/16". However, FE weld beads marked in red are modeled according to the actual weld shape. The left weld pass is first deposited at slightly above melting temperature, 1700°C. The right weld is then deposited after the first pass cools down to room temperature. Forced convection condition is applied for the bottom surface because of anvil, and normal air convection condition for the rest of the surfaces. Annealing start temperature is assumed to be its β transus temperature 950°C, and end temperature is the melting temperature. Element type of thermal analysis is 4-node linear heat transfer, and for mechanical analysis generalized plain strain element.

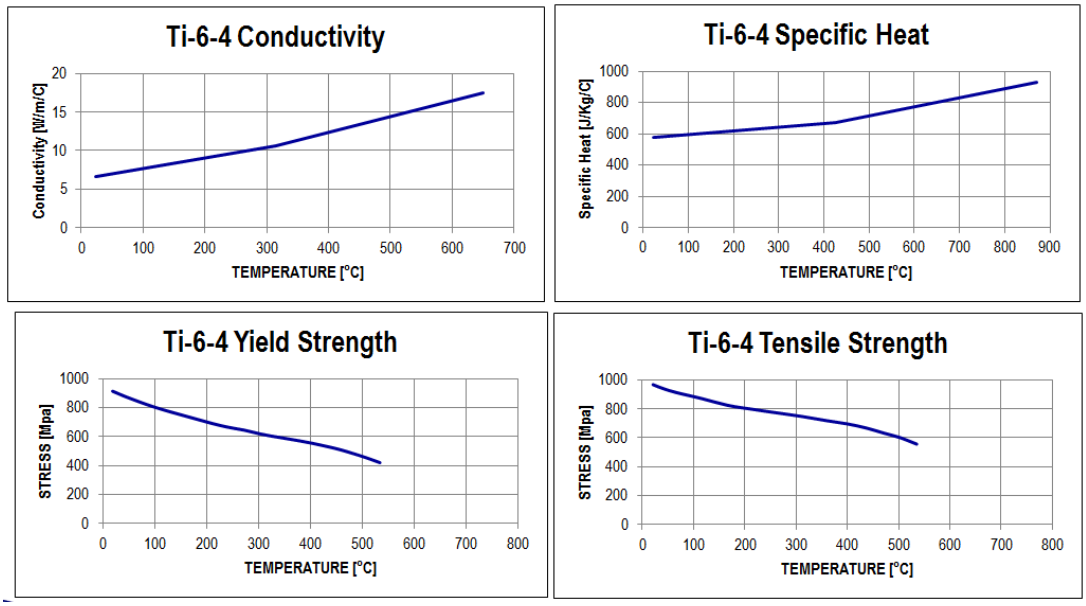

Figure 3-41 Ti-6-4 temperature dependent material properties

Figure 3-42 Ti-6-4 "T" joint fillet weld produced using MIG process

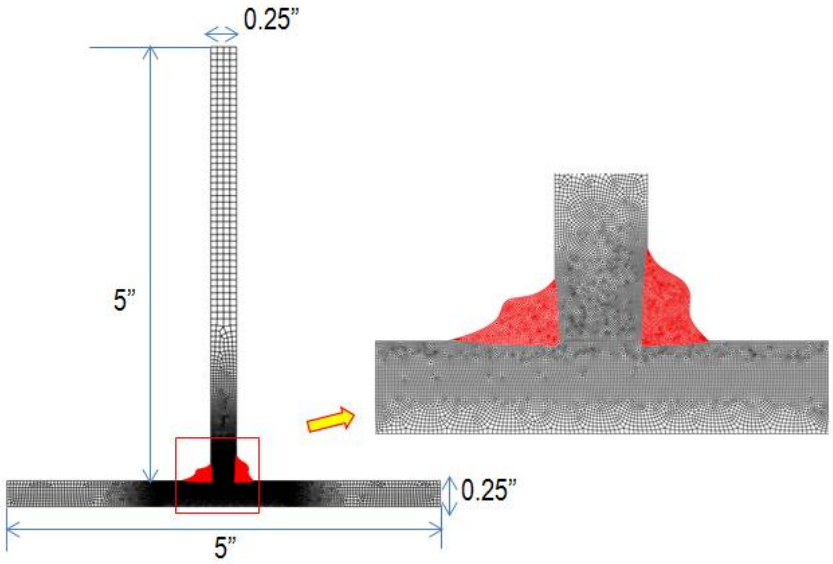

Figure 3-43 2D cross section FE model and geometry dimensions

Residual stress measurement of this “T” joint fillet weld was carried out at ANSTO (Australian Nuclear Science and Technology Organisation**)** by Dr. Paradowska. Neutron diffraction technique was performed at 1.6mm below the upper surface with a gauge volume size $2\times2\times2mm^3$. Finite element results and measurement data are shown in Figure 3-44. It can be seen that a good agreement is achieved between the two results.

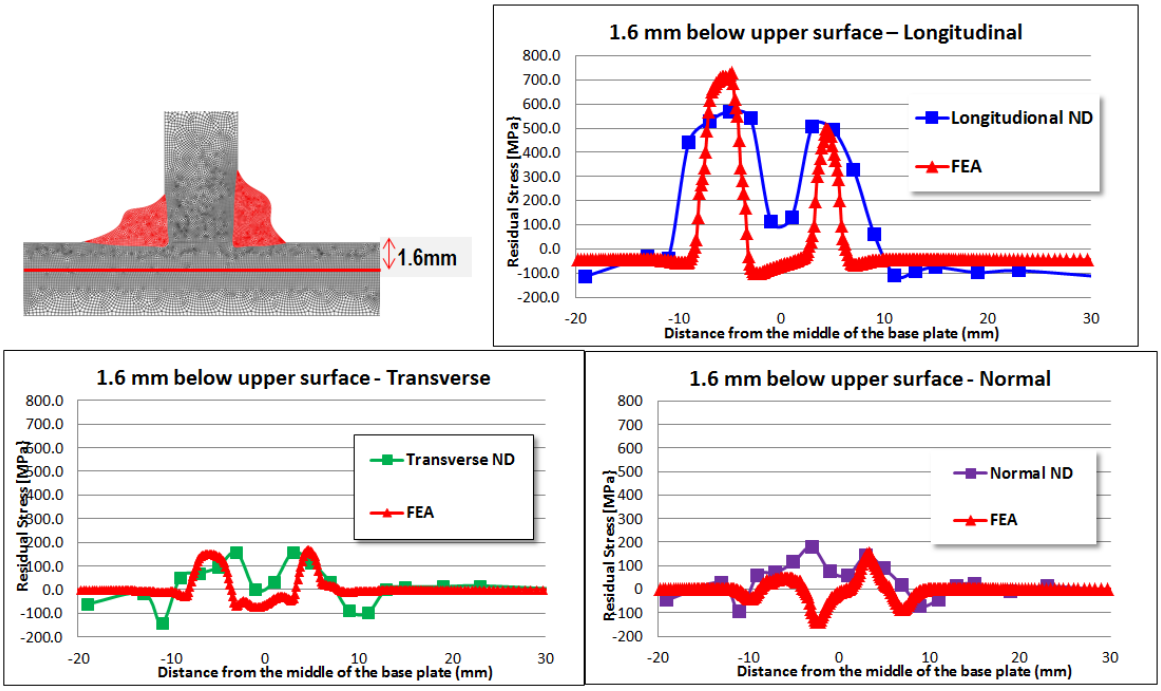

Figure 3-44 FE results versus neutron diffraction (ND) measurement data 1.6mm below upper surface: (a) longitudinal stresses, (b) transverse stresses, and (c) normal stresses

3.3.4 Ti-6-4 Friction Stir Weld

Compared to the above traditional fusion welding, friction stir welding (FSW) is an innovative technique invented by The Welding Institute (TWI) in 1991. It is well known as a solid-state joining process. The welding process is to plunge a rotating tool into a joint, and then traverse along the joint with the rotating tool. Heat is generated by friction and plastic work cause by material flow, which can lead to a pretty high temperature, just below material melting point. It is reported that this temperature can reach to 660°C for aluminum and 1200°C for steel [135]. Forces and torque from FSW machine during welding could be very large, which is required the welding pieces are rigidly clamped. Such a severe restraint condition can reduce welding induced distortion.

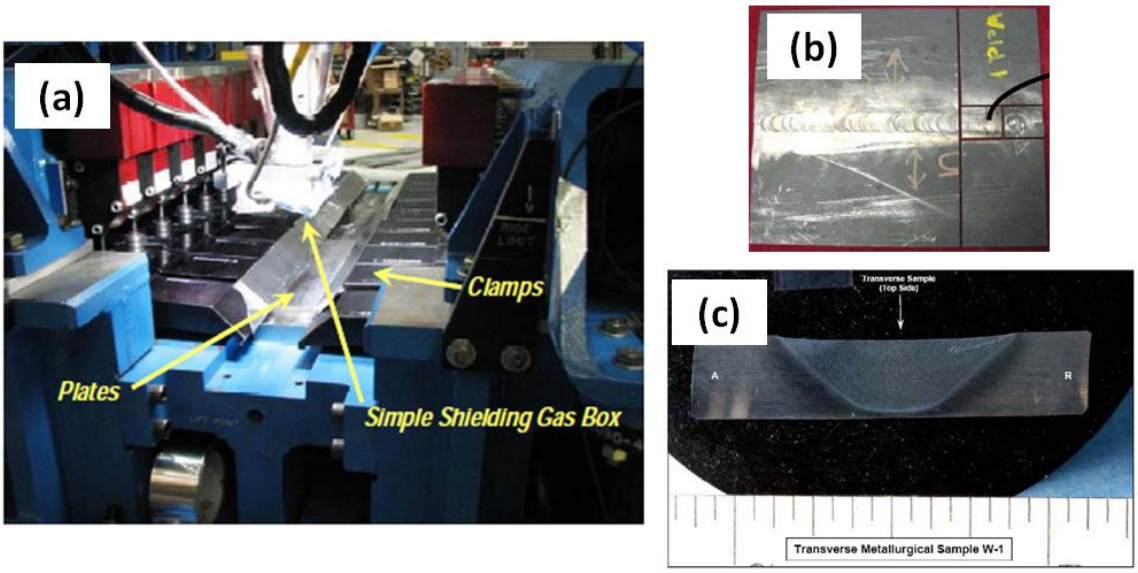

Figure 3-45 (a) Welding condition for Ti-6-4 butt weld, (b) Ti-6-4 butt welded plate made by FSW, and (c) weld cross section macrograph of (b)

Figure 3-45 presents the welding condition for Ti-6-4 butt weld during FSW and the macrograph of a trial plate cross section. The trial butt welded plate dimension is 12”×10”×0.265”. From (a), it can be seen that the plate is subjected to heavy clamping condition. Stir zone and thermomechanically affected zone (TMAZ) are clearly defined in (c). Based on this macrograph, 2D FE model is generated as shown in Figure 3-46. The stir zone profile is measured as the weld area marked in red in FE model. In thermal analysis, the deposit temperature for weld area is 1000°C. Normal air convection condition is used for upper surface and forced convection for bottom surface because of anvil. In mechanical analysis, an annealing temperature range of 900°C – 1000°C is implemented in UMAT. Clamping conditions are enforced on both sides as rigid surfaces. In order to simulate the forging pressure effects provided by shoulder of the tool, a uniformed compressive pressure based on the average plunge force and tool dimensions is instantaneously applied at a few seconds later of the cooling stage and then relieved during the rest of cooling stage. This is mainly because the material at high temperature is too soft to support pressure. Using the tool’s traveling speed and rotating speed during FSW, the time duration over a unit length of weld can be calculated. The compressive pressure is then applied at the end of the calculated time duration. The element type for thermal analysis is 4-node linear

heat transfer element, and the type for mechanical analysis is a generalized plain strain element. Material properties are used according to Figure 3-41.

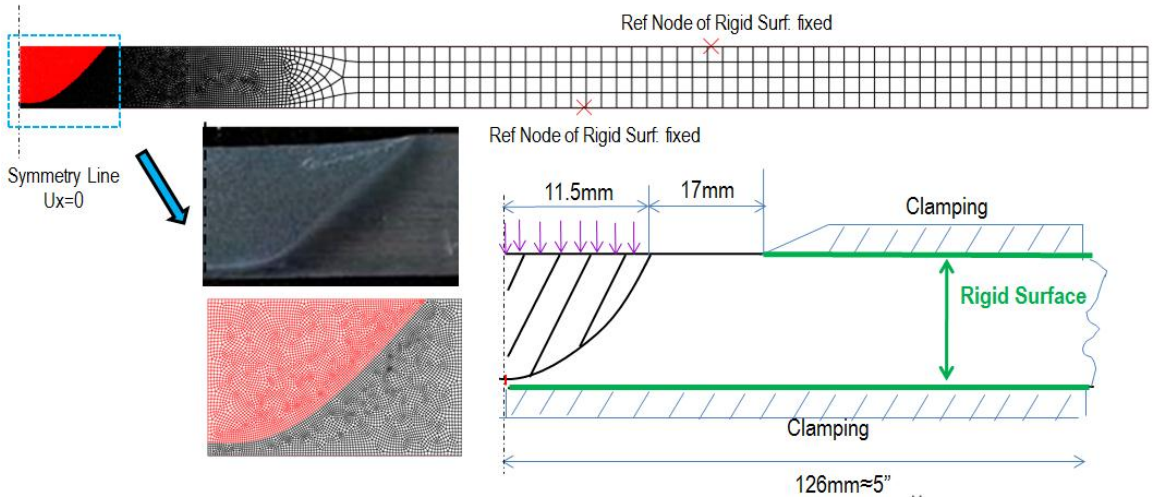

Figure 3-46 2D cross section FE model for FSW butted weld plate and its corresponding weld geometry based on the macrograph in Figure 3-45(c)

Residual stress measurement of this trial FSW plate was performed by Dr. Paradowska. Two major measurement locations were chosen in the middle cross section of the plate: one was 1.6mm below the upper surface using neutron diffraction (ND) on the Engin-X beamline at ISIS, UK with a gauge volume size $2\times2\times2mm^2$, and the other was along the mid-thickness (3.3mm below the upper surface) using ND with the same beam size. The second location was also measured by synchrotron diffraction (SD) on the JEEP beamline at Diamond, UK with a spatial resolution of 20microns×20microns×1.2mm

Accordingly, the residual stress results from the finite element simulation are processed and compared with the measured data in Figure 3-47 and Figure 3-48. The data are presented in terms of normalized residual stress by Ti-6-4 yield strength. It can be seen that the modeling results and residual stress measurements show a good agreement. In addition, SD (in green) and ND (in dark blue) exhibit constant residual stress distributions in Figure 3-48 (a) and (b). It should be noted that Figure 3-47 (a) and Figure 3-48(a) show a spike in the longitudinal residual stress distribution at about 10mm. This sudden change is corresponding to the boundary of plastic zone. Ti-6-4 has rather low conductivity which makes almost no transitional distance between yield and non-yield material. Such a sudden change in residual stress distribution is usually hard to be detected by measurement technique, even though it is measured by high resolution diffraction methods.

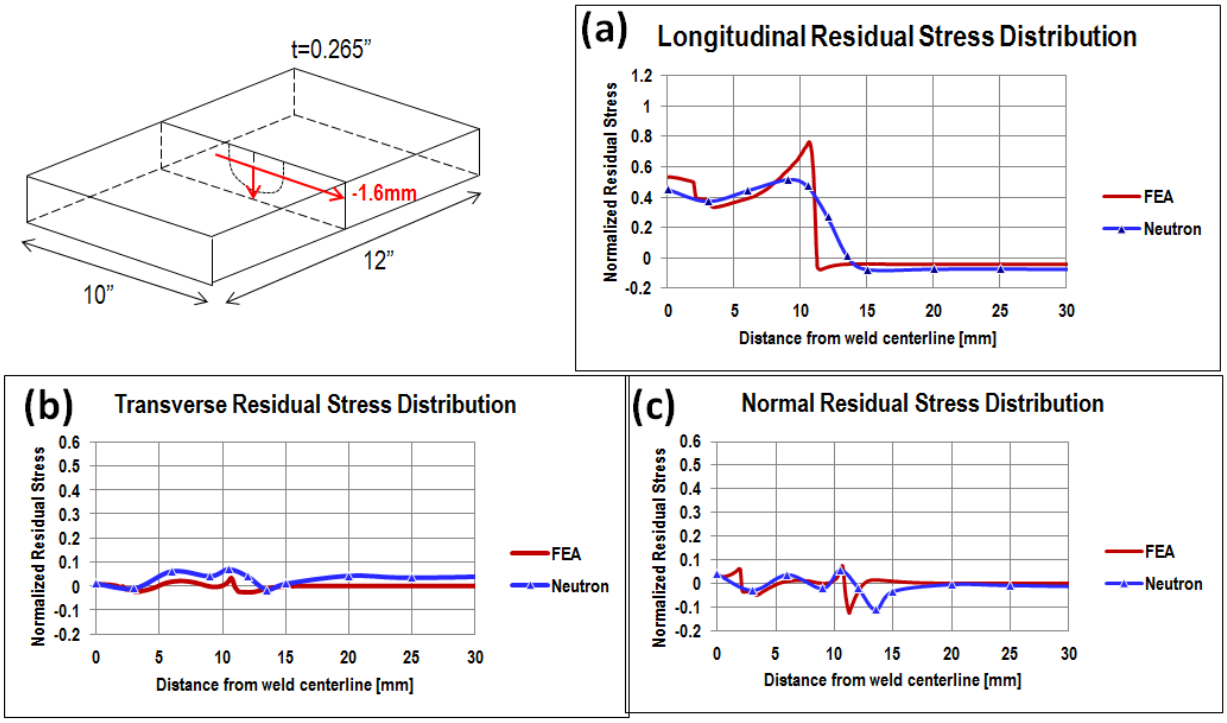

Figure 3-47 FE results versus neutron diffraction measurement data 1.6mm below upper surface: (a) longitudinal stresses, (b) transverse stresses, and (c) normal stresses

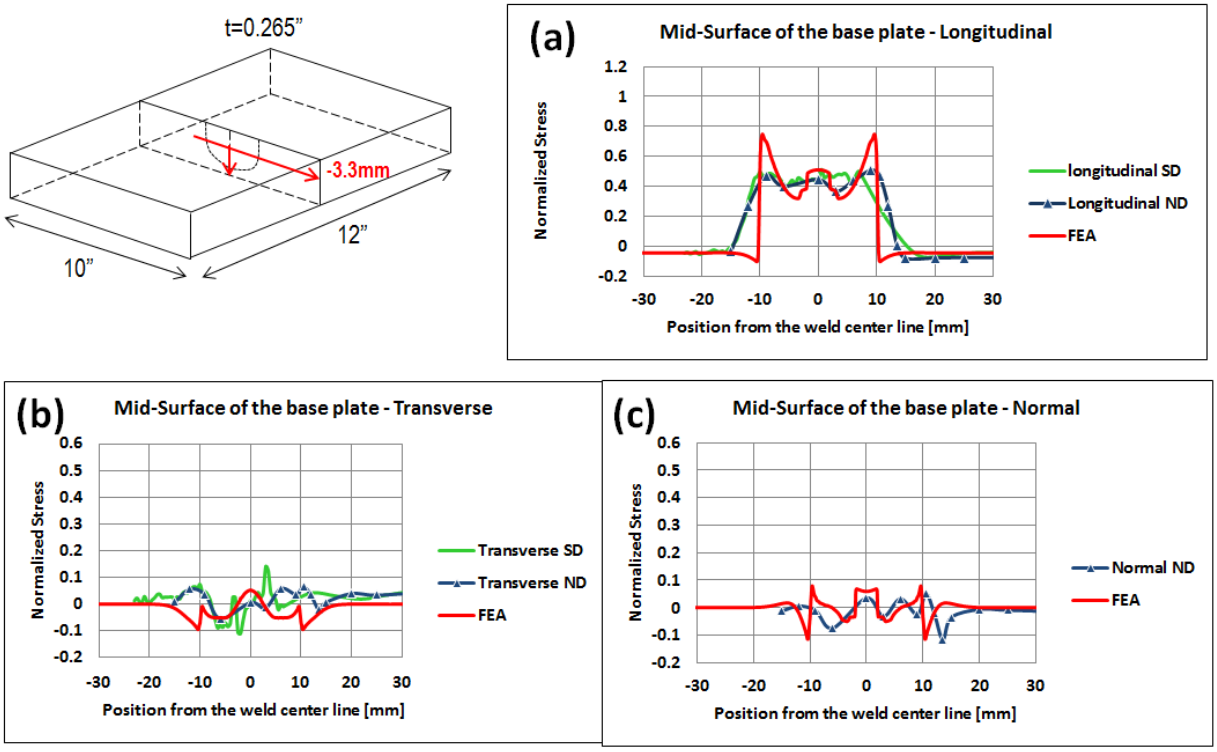

Figure 3-48 FE results versus neutron diffraction(ND) and synchrotron diffraction (SD) measurement data along mid-thickness (3.3 mm below upper surface): (a) longitudinal stresses, (b) transverse stresses, and (c) normal stresses

3.4 Special Considerations in This Study

3.4.1 Stress Decomposition Technique

In order to support fracture mechanics based structural integrity assessment, a through-thickness residual stress decomposition technique is adopted in this study. A given through-thickness residual stress can be decomposed into three fundamental components: membrane, bending and self-equilibrating corresponding to decreasing in length scale [10] based upon the equation below:

$$\sigma_m = \frac{1}{t}\int_0^t \sigma(x)dx$$
$$\sigma_b = \frac{6}{t^2}\int_0^t \sigma(x)\left(\frac{t}{2} - x\right)dx \qquad \textbf{(3.29)}$$
$$\sigma_{s.e.}(x) = \sigma(x) - \sigma_m - \sigma_b\left(1 - \frac{2x}{t}\right)$$

An example of through-thickness residual stress decomposition based upon above equation is shown in Figure 3-49 for a T fillet weld transverse residual stress [10].

The most apparent benefit of the stress decomposition scheme is to separate the contribution of global and local residual stress features to the fracture mechanics based stress intensity factor (K). The contributions from the membrane and bending stresses are global and the contribution from the self-equilibrating part is local. Recalling the two dominant types of residual stress distributions as shown in Figure 2-7, the bending type distribution is governed by σ_b component, while the self-equilibrating type is dominated by $\sigma_{s.e.}$ part. Membrane part is usually negligible in transverse direction, unless final assembly welds or severe restraints are concerned. However, membrane part in longitudinal direction can mostly reach to material yield magnitude owing to severe restraint condition, as shown in Figure 2-7 for hoop residual stress distribution.

In addition, by using the stress decomposition technique, patterns of residual stress distributions can be more easily categorized. This is helpful in analyzing a large number of residual stress cases to identify controlling parameters. Moreover, this technique can facilitate data processing, especially for dealing with a large amount of parametric analyses. Eventually, this will lead to

the fulfillment of current research objective to establish a generalized residual stress estimation scheme for fitness-for-service assessment purpose.

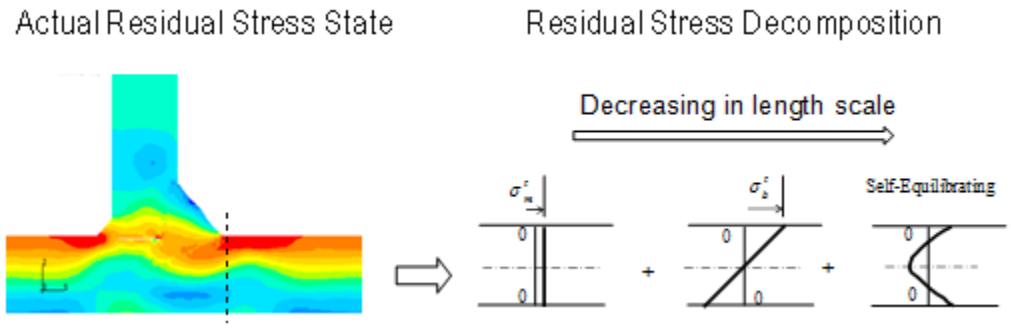

Figure 3-49 Illustration of residual stress decomposition of a through-thickness residual stress distribution with decreasing in length scale [10]

3.4.2 Plastic Zone and Shrinkage Force Method

Welding induced residual stress distributions and distortions are dominated by plastic zone size and shape which can be detected by aforementioned equivalent plastic strain in finite element analysis. As shown in 1-D model illustration in 3.2.3, residual stress magnitude reaches yield strength as long as a temperature difference between temperature in the plastic zone and ambient temperature reaches $2\Delta T_p$, beyond which further temperature increasing seem to have insignificant effects on resulting residual stresses. For a low carbon steel A508 class 3, this temperature differential is only less than 300^{o}C in order to develop yield magnitude residual stresses.

The above observation is important in justifying shrinkage force based approach by imposing shrinkage strain of about yield magnitude [2.8]. The consideration of producing yield magnitude shrinkage force in a proper plastic zone can achieve quite accurate residual stress distributions and distortions compared with the ones obtained from 2D model or even 3D moving heat source model. A comparison study is shown below [13]. Model (b) in Figure 3-50 is a 3D shell model with moving heat source in thermal analysis. The obtained temperature history is applied to mechanical analysis to gain longitudinal residual stress distribution as shown. The resultant plastic zone w_p is employed in model (a), the same FE mode as (b), by imposing a uniformed yield shrinkage strain. Therefore, model (a) bypasses the thermal analysis. By comparison, it can be seen that the two residual stress distributions predicted using the two different methods are in a good agreement. Furthermore, for the distortion prediction shown in Figure 3-51, an excellent agreement is achieved between two models and three experimental measurements.

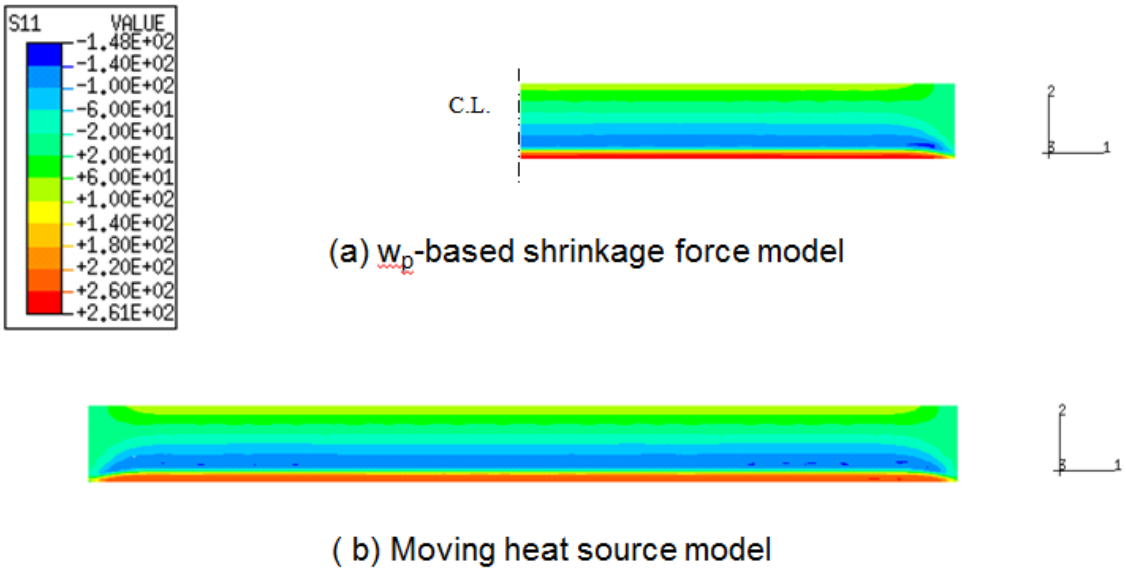

Figure 3-50 Comparison of residual stress distributions using two modeling schemes [13]

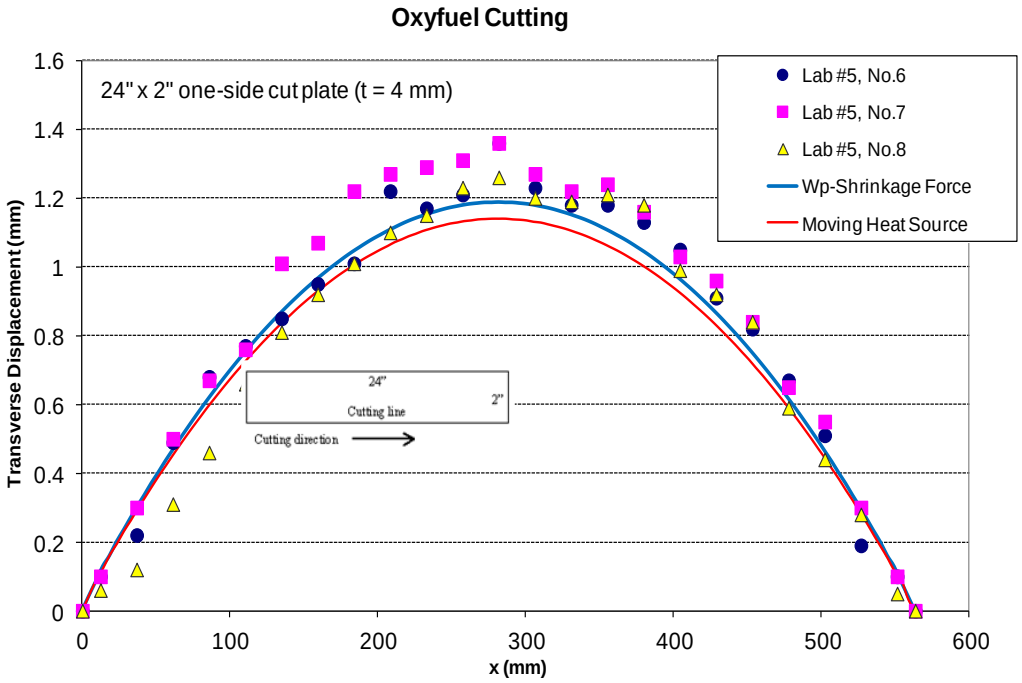

Figure 3-51 Comparison of predicted distortions (two models) with experimental measurements [13]

This method is referred to as a shrinkage force method. As long as plastic zone size and shape can be accurately obtained, key residual stress distribution characteristics can be well captured by imposing yield magnitude shrinkage force. Such a finding is served as a basis for the further study of the residual stress estimation scheme proposed in this investigation.

4. GIRTH WELDS

With the modeling procedure validated in the previous section, a series of parametric residual stress analyses for pipe/vessel girth welds have been performed by varying pass size, welding sequence, radius to wall thickness ratio (r/t), thickness, joint preparation, material, as well as heat input. Owing to the nature of restraints in the radial direction, girth welds represent a unique class of residual stress problems. For this reason, important residual stress distribution features and their governing parameters are better to be thoroughly investigated through a large number of parametric analyses so that simple forms of residual stress profiles can be developed for fitness for service assessment purpose. One effective method for facilitating this process is to introduce a length-scale based residual stress decomposition procedure (as described in Section 3.4.1) with respect to pipe wall thickness in the form of:

$$\sigma_m = \frac{1}{t}\int_0^t \sigma(x)dx$$
$$\sigma_b = \frac{6}{t^2}\int_0^t \sigma(x)\left(\frac{t}{2}-x\right)dx \qquad \textbf{(4.1)}$$
$$\sigma_{s.e.} = \sigma(x) - \sigma_m - \sigma_b\left(1-\frac{2x}{t}\right)$$

in which x is measured from pipe inner surface in the through-thickness direction. With such decomposition procedure, a large number of complex residual stress distributions influenced, e.g. by pass size, r/t, t, and heat input etc. can be effectively compared and contrasted to identify important distribution characteristics in both through thickness and pipe axial direction (perpendicular to the weld).

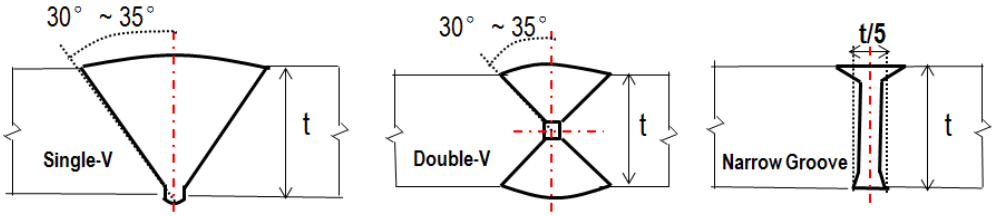

Figure 4-1 Representative joint preparations investigated in this study: Single-V, Double-V, and Narrow Groove

The parametric analyses are focused upon the thick wall vessel/pipe girth welds, of which thickness greater than 1" and all the way to 10" with joint preparations of Single-V, Double-V, and Narrow Groove. Some representative joint preparations considered in this investigation are shown in Figure 4-1 and the corresponding detailed weld profiles are exhibited in Figure 4-2. Please note that only half of the weld profile is shown for Narrow Groove joint preparation because the weld is symmetrical to its centerline. For the purpose of completeness, some of thin wall welds (e.g., thickness of quarter inch and half inch) documented in [13] are also re-analyzed

in this study. Welding sequence for Single-V and Narrow Groove girth welds is from ID to OD, and for Double-V welds inner groove first and then outer groove.

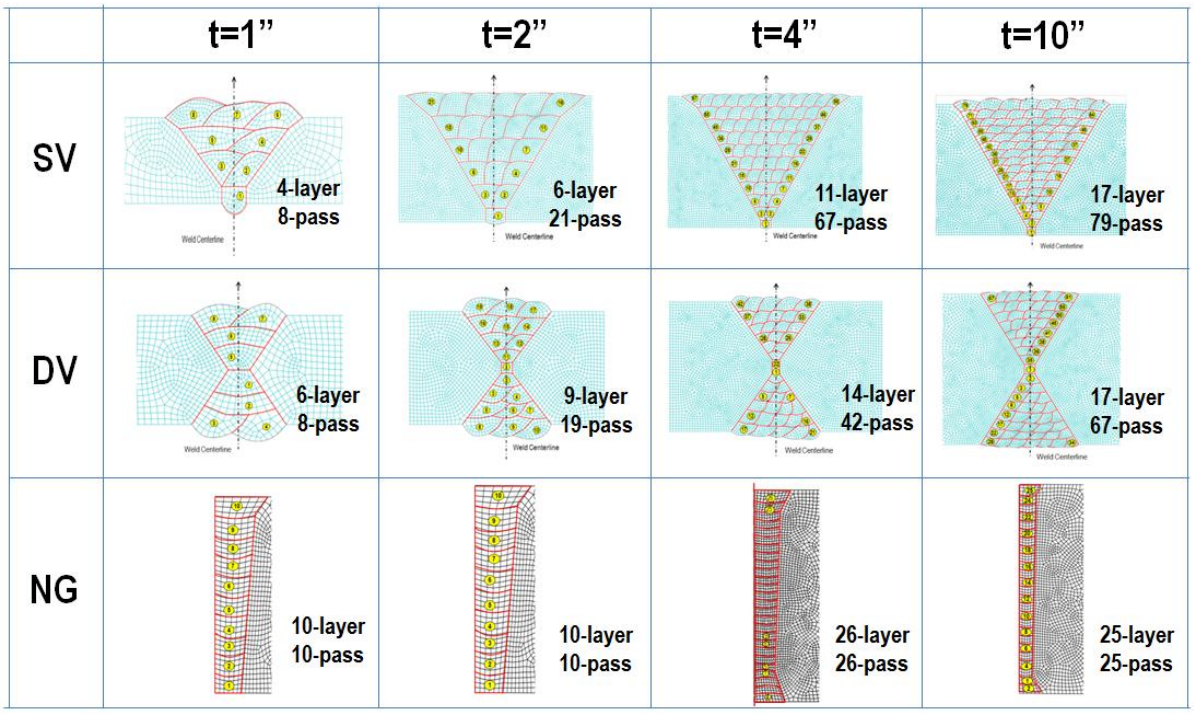

Figure 4-2 Detailed weld profiles investigated in this study with different wall thicknesses: Single-V, Double-V, and Narrow Groove

Material for most of cases reported here is 2.25CrMo-V which has temperature dependent properties shown in Figure 4-3 in which all material properties are normalized with respect to their values at room temperature of 23 ℃.

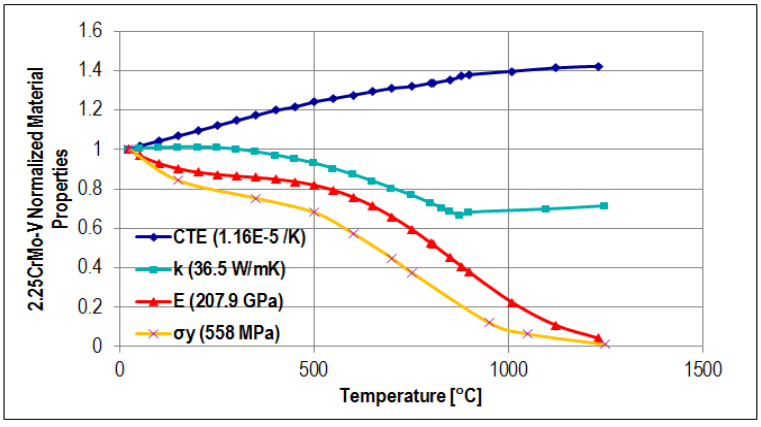

Figure 4-3 Temperature dependent material properties for 2.25CrMo-V steel

For the sake of clarity, Figure 4-4 defines the girth weld location and the associated stress directions used throughout this section.

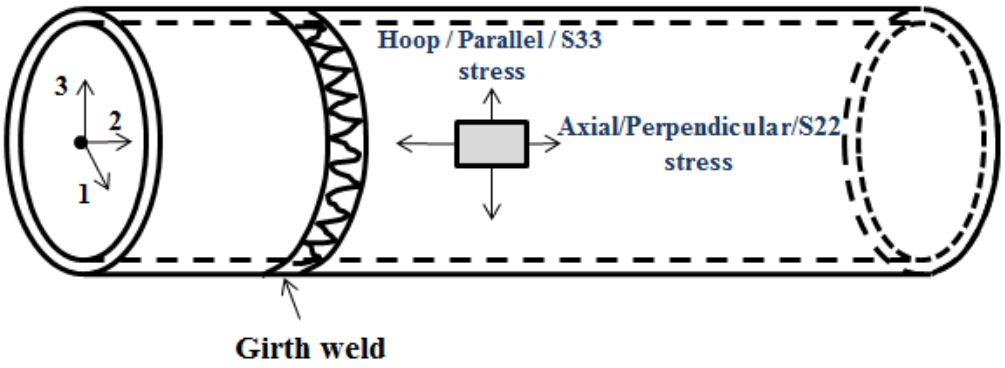

Figure 4-4 Definition of girth weld and stress directions

4.1 Lumped pass effects for thick wall section

When pipe or vessel wall thickness becomes large, such as 4" or up to 10", the number of weld passes involved can be in the order of hundreds. One question for residual stress analysis is: can the actual number of passes be effectively lumped for the purpose of numerical modeling efficiency without losing important residual stress information? If the answer is yes, in addition to its obvious benefit to residual stress modeling, reduced number of weld passes can also result in significant increase of productivity in fabrication of thick pipes/vessels. Because of this consideration, it was suggested at the beginning of the project that lumped pass effect be first examined before performing a large number of parametric analyses.

Narrow groove joint preparation was selected to perform the parametric analyses for the lumped pass effect, owing to its nature of weld profile without introducing additional localized residual stress features. Cases studied are summarized in Table 4-1. As we can see, each thickness of narrow groove girth welds has 5 or 6 models and each model is associated with a difference number of passes. The number of passes varies from the largest number in Model 1 to the smallest one in Model 6. The pipe inner radius to thickness ratio (r/t) is also varied from 2 to 10 for each thickness. The total number of cases performed in Table 3-1 is 69. The pass size is maintained to be the same for each lumped model in order to obtain an idealized residual stress distribution without other effects. It is interesting to note that with this particular weld profile, the characteristics of through-thickness residual stress distributions at the weld centerline and weld toe are very similar. As an example, the cases for thickness of 4" are discussed in detail in the section below.

Table 4-1 Cases analyzed for lumped pass effects

Narrow Groove							
Thickness	r/t	Number of Passes					
		Model 1	Model 2	Model 3	Model 4	Model 5	Model 6
t=1"	2	20	10	8	6	4	2
	5						
	10						
t=2"	2	20	10	8	6	4	2
	5						
	10						
t=4"	2	52	26	13	7	4	2
	5						
	10						
t=10"	2	25	18	10	5	2	\
	5						
	10						

Figure 4-5 shows a 4" thick narrow groove axisymmetric finite element model with 4024 nodes and 3880 quadrilateral linear elements. Symmetric boundary condition is applied at the weld centerline in the stress analysis and rigid body motion is eliminated. The area marked in red is the half weld zone with a width of 11mm. Figure 4-6 shows the detailed information of the weld pass size and welding sequence for each lump model with decreasing pass number from 52 to 2. It can also be seen from Figure 4-6 that the pass size retains almost the same for each lumped model. The welding sequence is from ID to OD.

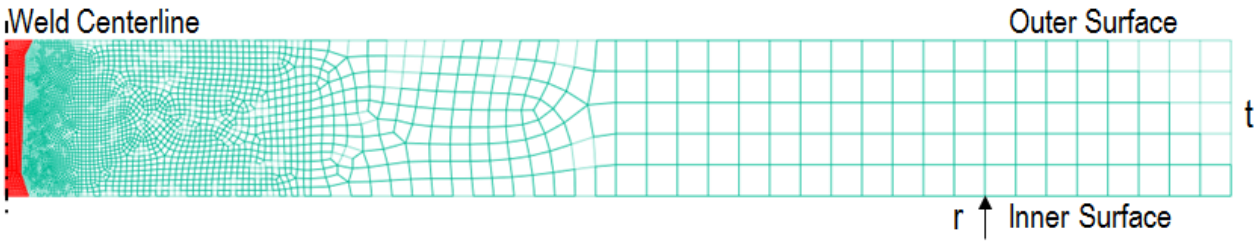

Figure 4-5 Axisymmetric FE model for thickness of 4" narrow groove joint preparation

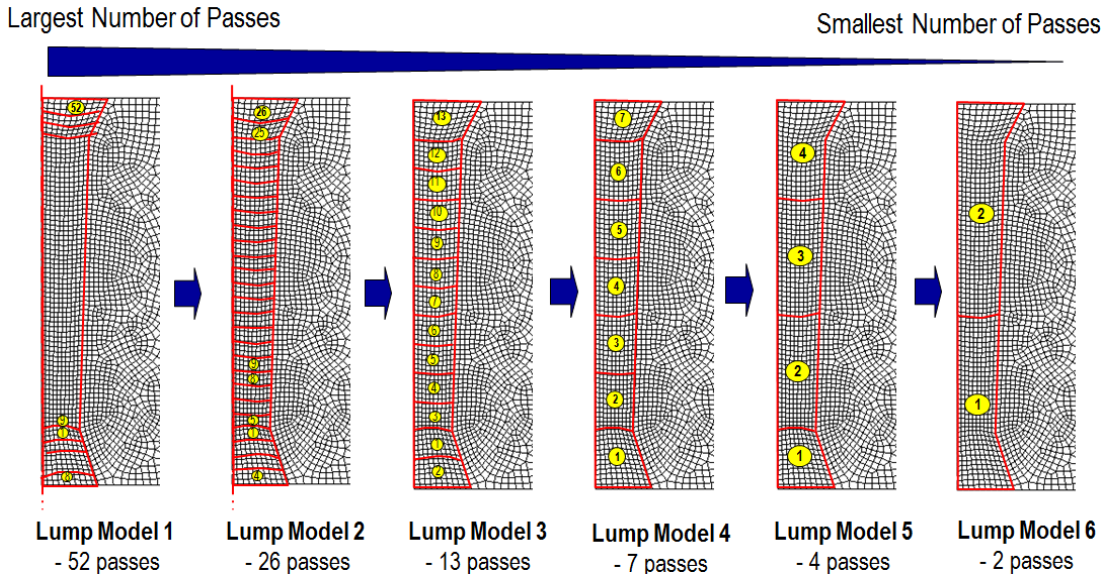

Figure 4-6 Six lumped models with pass number from 52 to 2 for NG 4" thickness welds: detailed pass size and welding sequence

Perpendicular residual stress distributions at the weld centerline (marked in Figure 4-5) are exhibited in Figure 4-7. r/t ratio for these cases is 10. It is can be seen that the overall characteristics of perpendicular residual stress distribution alters significantly with the decrease of the number of passes, especially when the number of passes is smaller than 4 (Lump Model 5 and 6 in Figure 4-6). With the decrease of pass number, the degree of stress oscillation is increased through the thickness. This is primary due to the fact that the larger a weld pass becomes, the more heat input is required. A larger heat input results in a larger area surrounding the weld pass being affected. Despite the difference, the overall perpendicular stress distribution of Lump Model 3 (13-pass) is very similar to the ones of Model 1 and 2 which have 52-pass and 26-pass, respectively. This suggests that 52-pass/26-pass for 4" thickness Narrow Groove joint preparation may not be necessary compared with 13-pass case as far as residual stress is concerned. The result of Lump Model 4 (7-pass) has a similar overall trend, but the stress oscillation is clearly overwhelming. From Figure 4-7, it suggests that there exists a minimum number of passes with which the overall characteristics of residual stress distribution can be well captured.

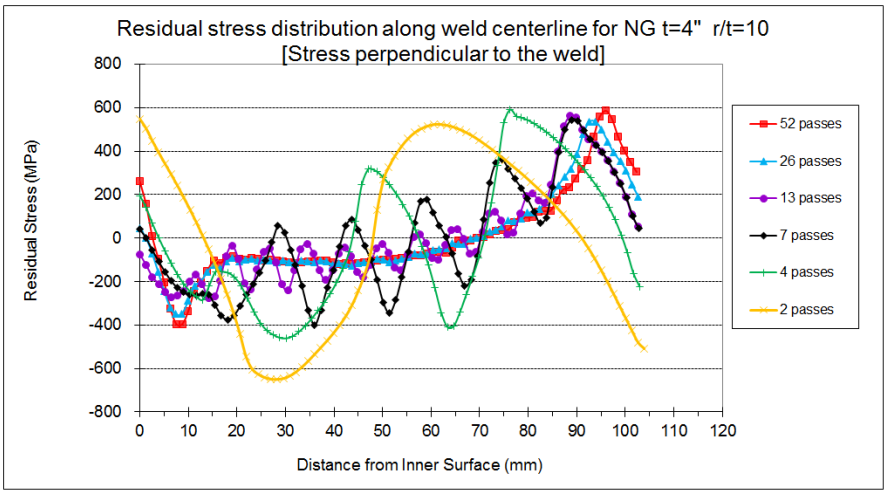

Figure 4-7 Perpendicular residual stress distributions along weld centerline for Narrow Groove joint preparation with thickness of 4" and r/t ratio of 10

Decomposed residual stress results for the above narrow groove weld of 4" thick pipe is shown in Figure 4-8 as a function of both number of passes modeled and r/t ratio. Through-wall perpendicular (axial) and parallel (hoop) residual stress distributions are decomposed into membrane and bending components according to Eq. (3.1). Figure 4-8(a) shows the bending component of the axial residual stresses at the weld centerline (membrane stress is negligible for all cases). Indeed, there is a clear indication of the existence of a minimum number of passes, e.g. about 5-10, beyond which the bending component of the axial residual stress no longer changes in any significant manner. The slight reduction in all residual stress components with more passes than the minimum number of passes suggests that the use of the minimum number of passes will result in a conservative residual stress estimate. Hoop residual stresses in terms of membrane and bending components show an identical behavior (Figure 4-8 b and c). In addition, r/t ratio seems not have any significant effects on the minimum number of passes and can be characterized as a simple shifting in stress magnitude in all cases.

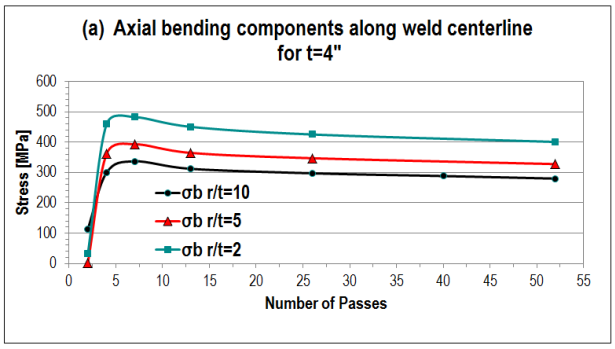

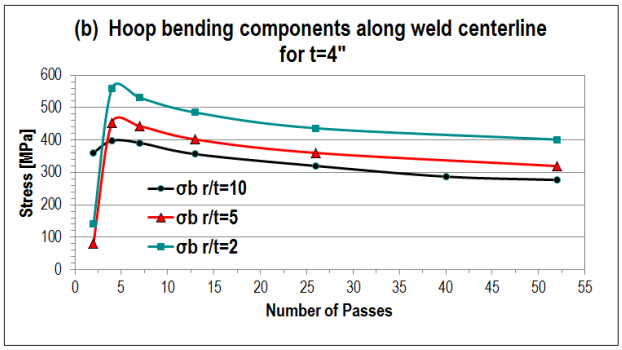

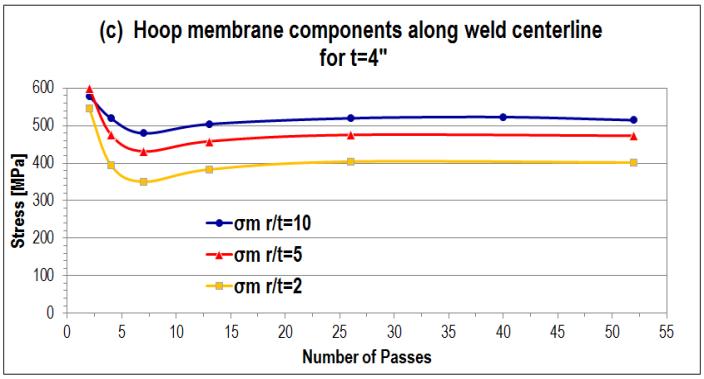

Figure 4-8 Decomposed residual stress components vs. Number of passes modeled for 4" thickness Narrow Groove joint preparation – (a) axial bending residual stresses (b) hoop bending residual stresses and (c) hoop membrane residual stresses

For completeness, the self-equilibrating parts calculated based on Eq. (3.1) are plotted in Figure 4-9 corresponding to residual stress distributions shown in Figure 4-7. Same trends as discussed for Figure 4-7 can be found. Stress distribution of self-equilibrating part alters drastically with the decrease of the number of passes, especially when the number of passes is smaller than 4.

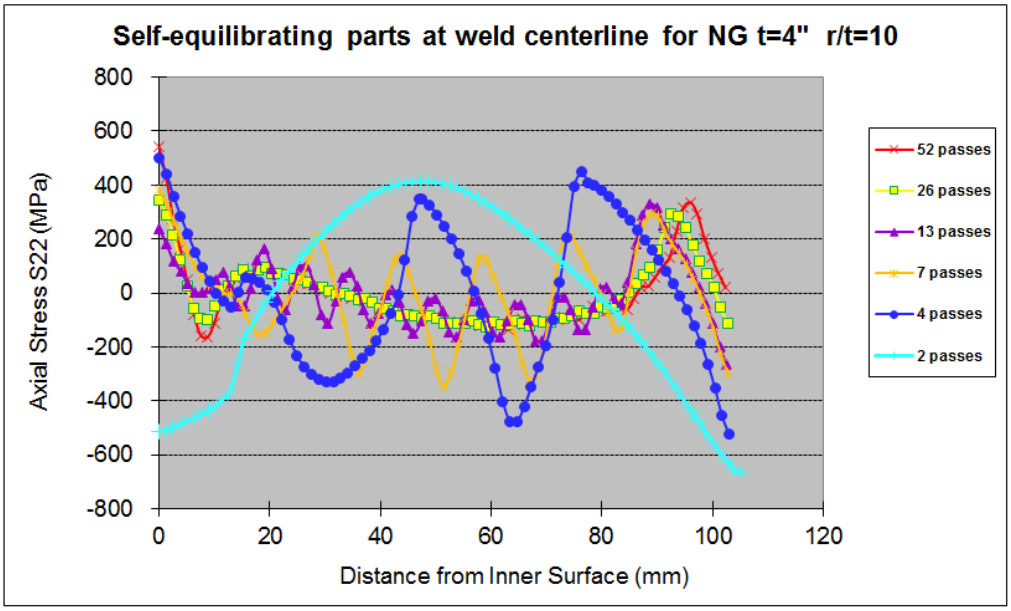

Figure 4-9 Decomposed self-equilibrating parts of perpendicular residual stress distributions along weld centerline for Narrow Groove joint preparation with thickness of 4" and r/t ratio of 10

Other cases shown in Table 3-1 are summarized in the same manner. Detailed pass lumping information for the wall thickness of 1", 2", 10" are represented in Figure 4-10, Figure 4-12, and Figure 4-14 respectively. Decomposed residual stress components with respect to a function of

pass number and r/t ratio are shown in Figure 4-11, Figure 4-13 and Figure 4-15 for wall thickness of 1”, 2” and 10”, respectively. By examining all of the results, it is observed that a minimum number of passes is existent for each wall thickness.

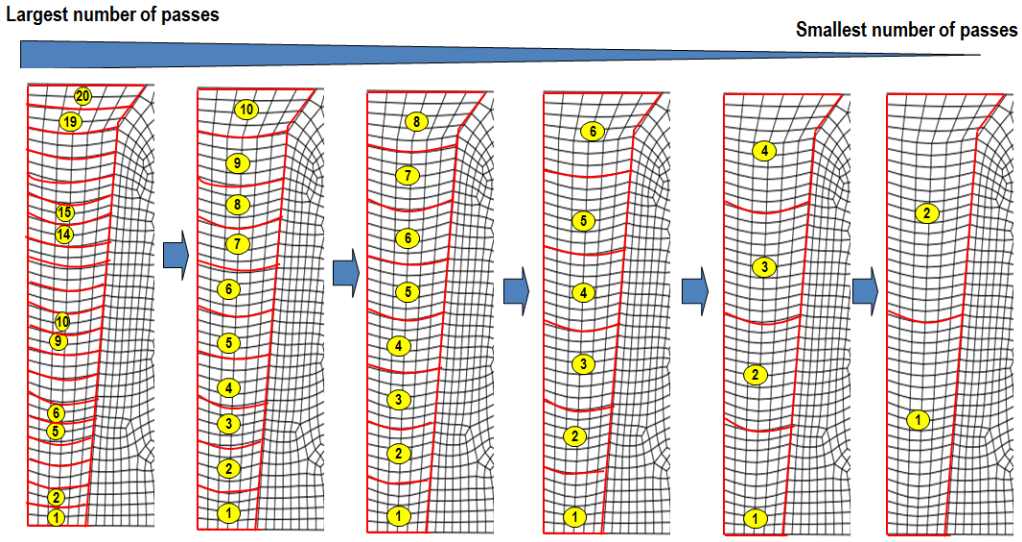

Figure 4-10 Six lumped models with pass number from 20 to 2 for NG 1” thickness welds: detailed pass size and welding sequence

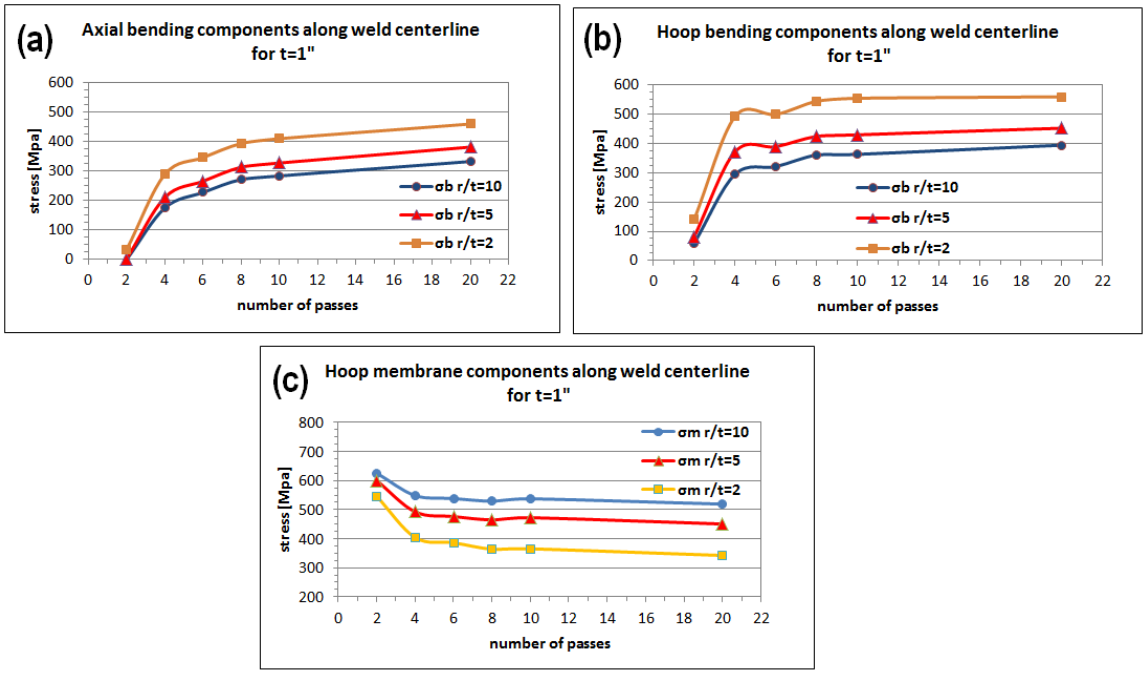

Figure 4-11 Decomposed residual stress components vs. Number of passes modeled for 1" thickness Narrow Groove joint preparation – (a) axial bending residual stresses (b) hoop bending residual stresses and (c) hoop membrane residual stresses

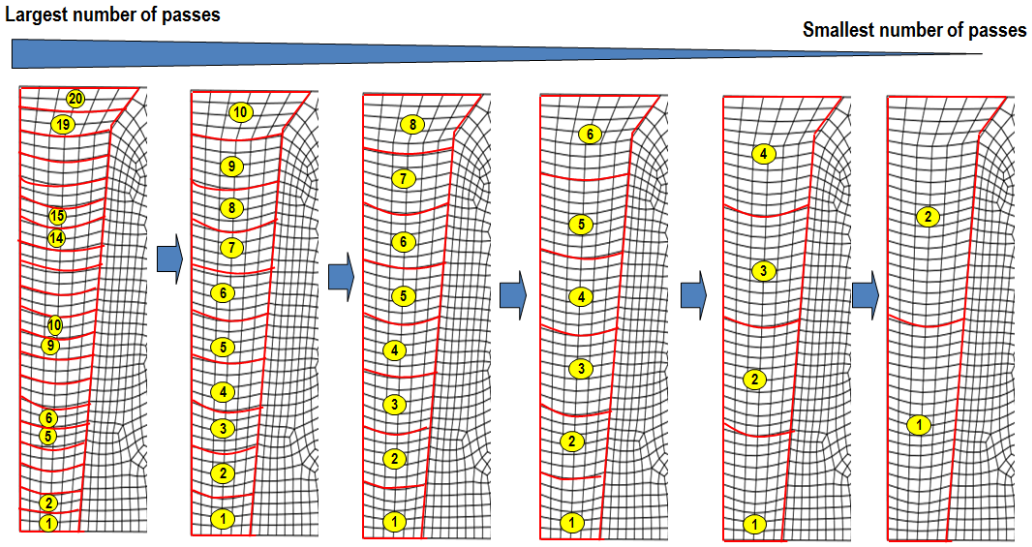

Figure 4-12 Six lumped models with pass number from 20 to 2 for NG 2" thickness welds: detailed pass size and welding sequence

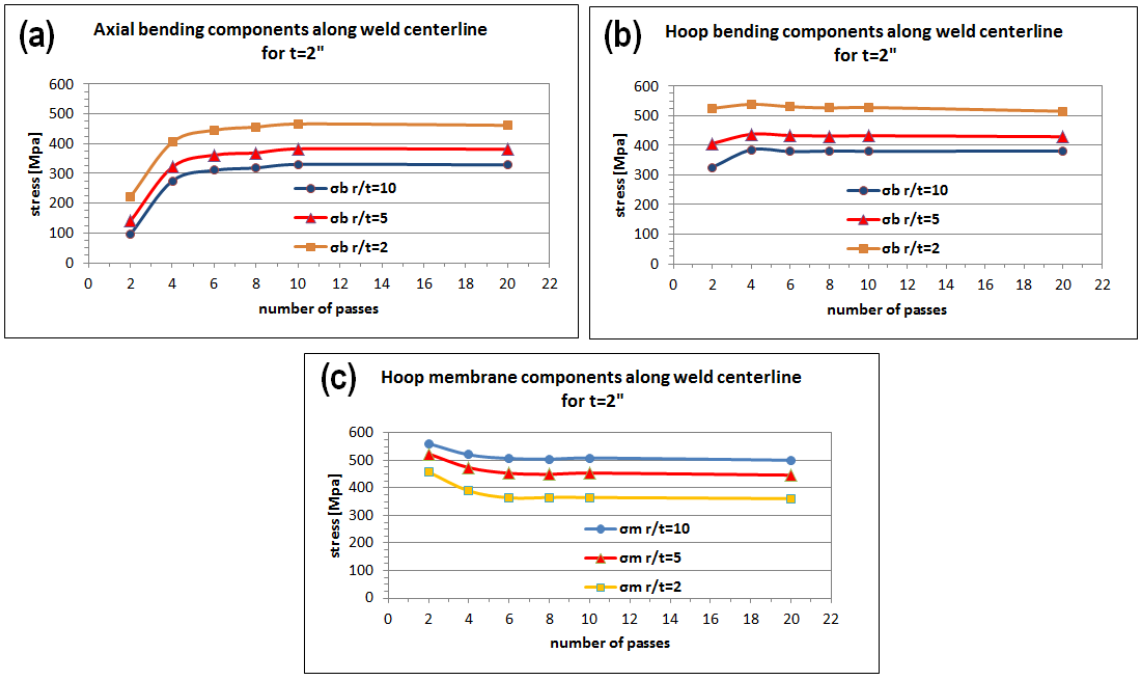

Figure 4-13 Decomposed residual stress components vs. Number of passes modeled for 2" thickness Narrow Groove joint preparation – (a) axial bending residual stresses (b) hoop bending residual stresses and (c) hoop membrane residual stresses

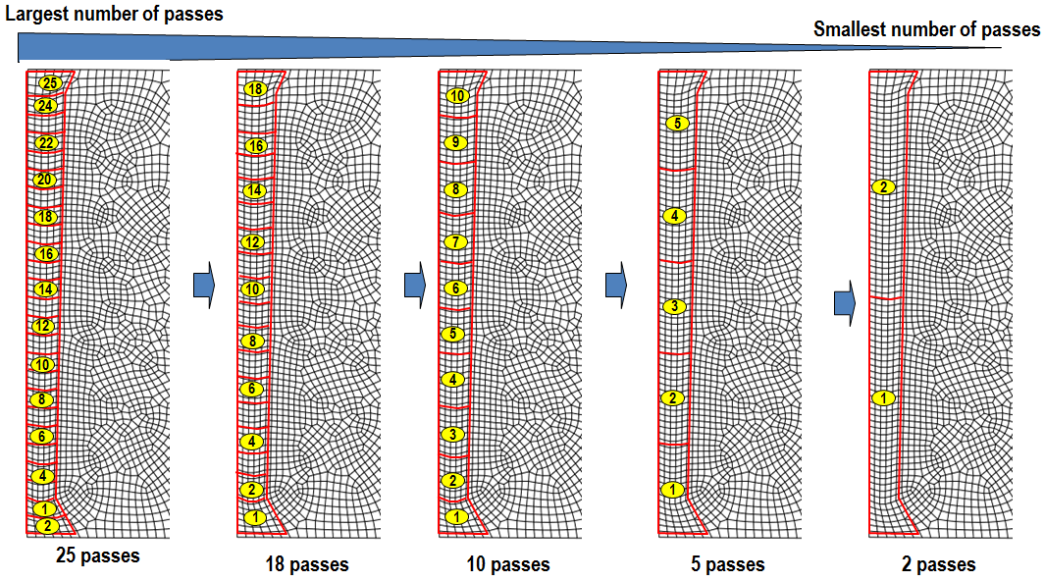

Figure 4-14 Five lumped models with pass number from 25 to 2 for NG 10" thickness welds: detailed pass size and welding sequence

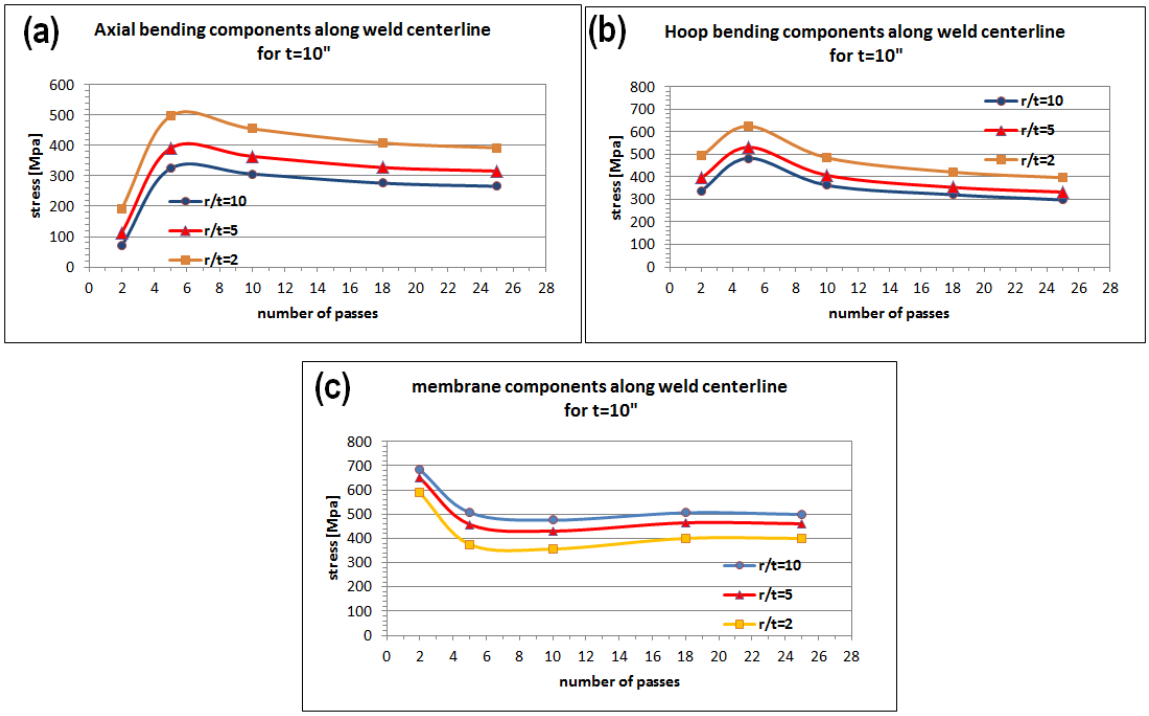

Figure 4-15 Decomposed residual stress components vs. Number of passes modeled for 10" thickness Narrow Groove joint preparation – (a) axial bending residual stresses (b) hoop bending residual stresses and (c) hoop membrane residual stresses

With a further analysis, it is found that instead of the number of weld passes, the number of weld pass layers (a layer may contain more than one pass) is a better parameter for characterizing the through-thickness residual stress distributions such as those shown in Figure 4-8 to Figure 4-12. An approximate minimum number of weld pass layers as a function of wall thickness is shown in Fig. 3.14 based on the results from the present study. Note that the vertical axis should be identified as the number of through-thickness layers which often consists of more than one weld pass. On the basis of this finding, FE models (shown in Figure 4-2) are generated and used with confidence for all of the parametric studies in this investigation.

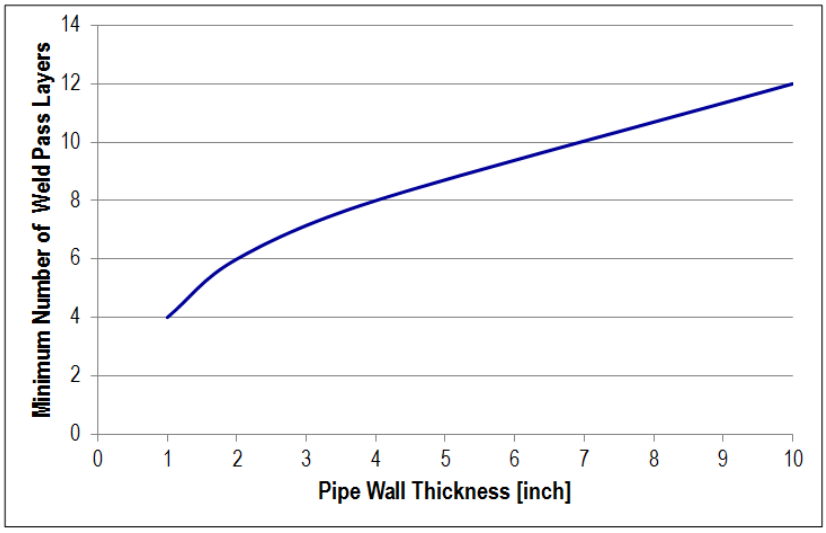

Figure 4-16 Minimum number of weld pass layers versus pipe wall thickness

4.2 r/t ratio effects

For the wall thickness less than 1", as pipe radius to wall thickness ratio (r/t) varies over a wide range, the resulting through-thickness residual stress exhibits some distinct characteristic types of distributions [13, 136-137]. In this section, a large number of parametric analyses are performed for thicker wall pipes ($t \geq 1$") along with varying r/t ratio from 2 to 100. The detailed analysis matrix is shown in Table 4-2. The corresponding weld profiles representing each combination are shown in Figure 4-2. The total number of cases analyzed in this section is 60. The FE models were generated based on the minimum number of layers required for each thickness in Figure 4-16. Welding sequence for Single-V and Narrow Groove welds is from ID to OD, and for Double-V welds the sequence is to weld the inner groove first and then outer groove.

Table 4-2 Analyses matrix for r/t ratio effects

Single-V Double-V Narrow Groove		Wall Thickness			
		t=1”	t=2”	t=4”	t=10”
r/t	r/t=2	X	X	X	X
	r/t=5	X	X	X	X
	r/t=10	X	X	X	X
	r/t=20	X	X	X	X
	r/t=100	X	X	X	X

First, we will discuss the cases of 1” thick Single-V (SV) weld joints. Figure 4-17 exhibits the residual stress contour plots with varying r/t ratio from 2 to 100. The stress on the left hand side is perpendicular to the weld (axial), and on the right hand side parallel to the weld (hoop). The stress scale is from -350MPa to 558MPa for all of the plots in this figure. The blue/dark color indicates compression and red/white tension. As we can see, at r/t=2, the axial residual stress distribution shows a well-defined through-thickness bending mode, with the OD subjected to tension and ID to compression. This is primary due to the fact that pipe is very stiff with a small r/t ratio. Such through-thickness residual stress distribution caused by the welding-induced shrinkage force is referred to as “local bending type”. As r/t ratio increases, the compressive zone in ID reduces its magnitude and moves away from the weld. The axial stress in weld area is more towards a “self-equilibrating” type in through-thickness direction. A larger r/t ratio increases pipe wall flexibility and hence promotes more self-equilibrating component. Hoop residual stresses are highly tensile in the weld area as r/t ratio is increased, and the compressive hoop stress zone at ID shifts away from the weld area with reduced magnitude.

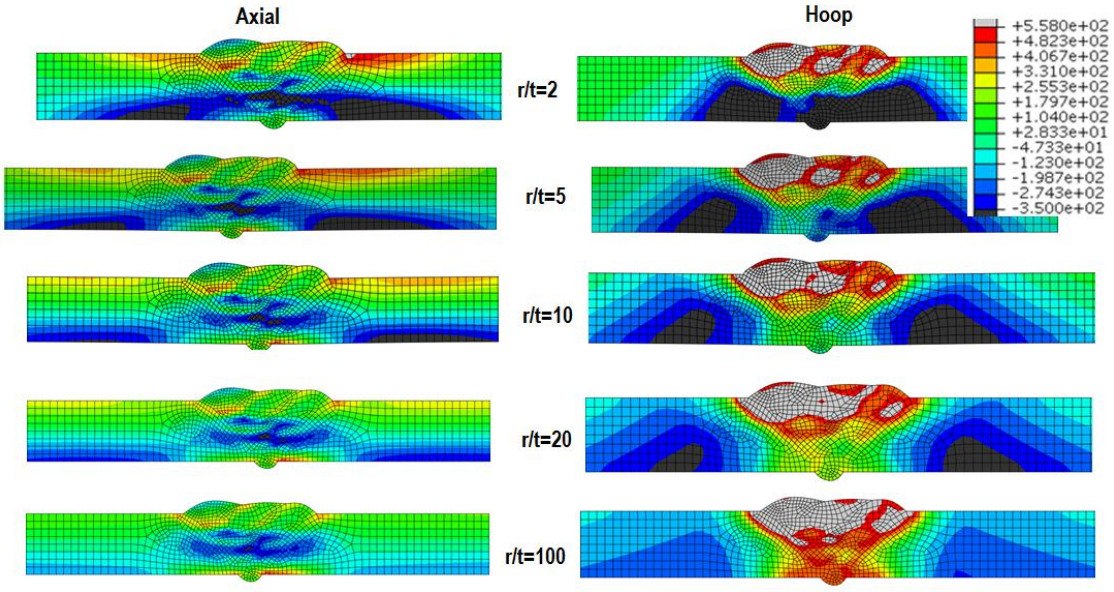

Figure 4-17 Residual stress contour plots for SV girth welds with t=1": r/t ratio effects

Detailed through-thickness residual stress distribution at both weld centerline (WCL) and weld toe (WT) positions are summarized in Figure 4-18and Figure 4-19, respectively. The results are presented in terms of normalized residual stresses by material yield strength and varying r/t ratio from 2 to 100. The horizontal axis is measured from ID and normalized by thickness. Lines for residual stress distribution at weld toe are much smoother than the ones at weld centerline. This is due to the fact that weld toe has less complex local interactions among weld passes than weld centerline. Overall, it is clearly indicated that, with the increase of r/t ratio, lines become flatter and move towards higher value, resulting in reduced bending component and increased membrane component. This is consistent with the observations from the contour plots in Figure 4-17.

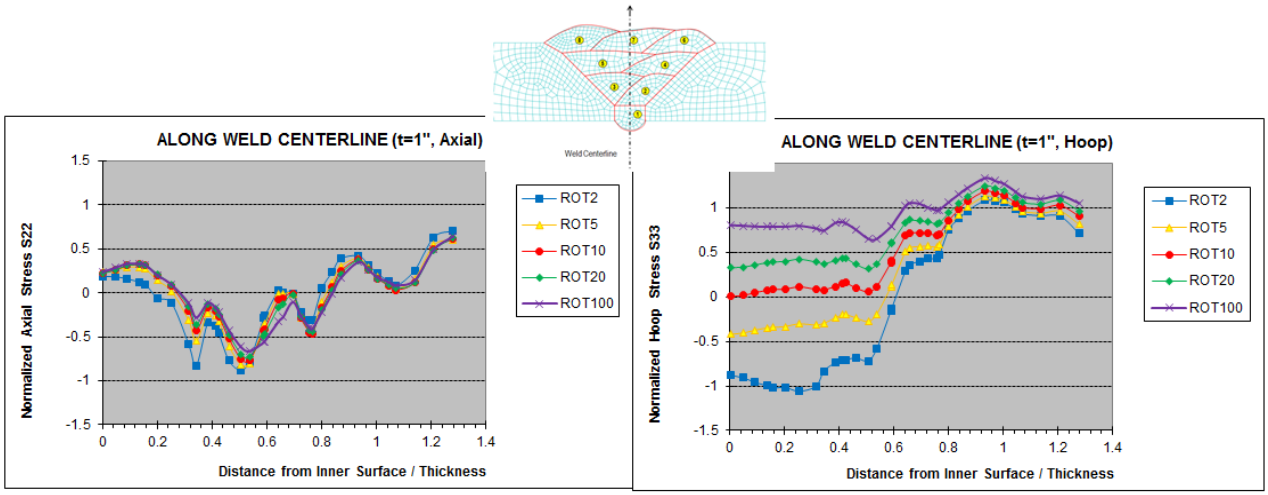

Figure 4-18 Through-thickness residual stress line plots along WCL for SV girth welds with t=1": r/t ratio effects

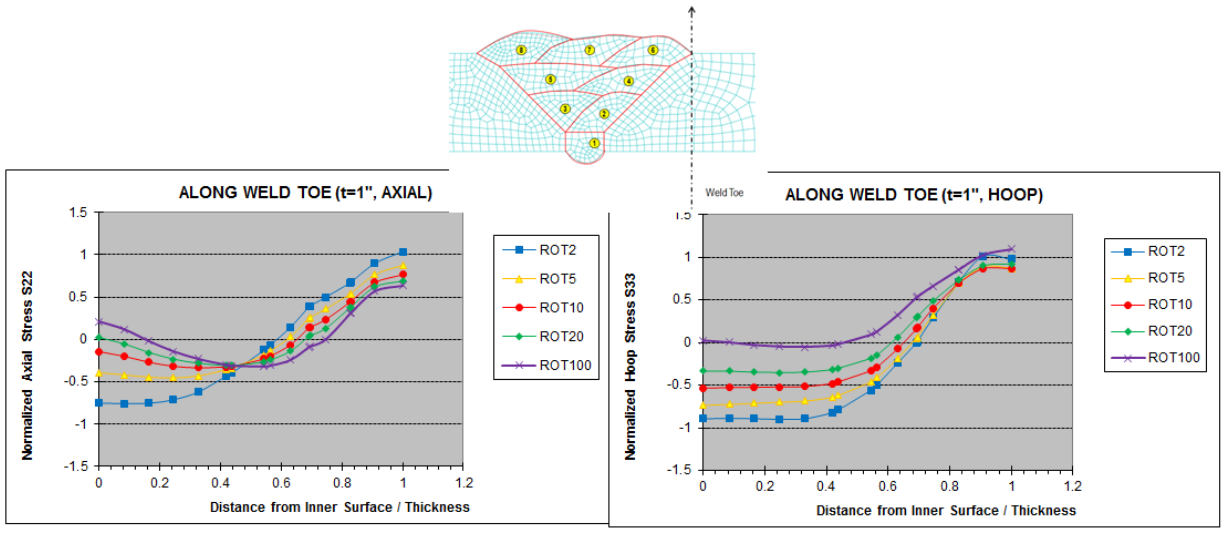

Figure 4-19 Through-thickness residual stress line plots along WT for SV girth welds with t=1": r/t ratio effects

In practice, it is essential to have a full-field residual stress distribution and its corresponding characteristics. Axial and hoop surface residual stress distributions for 1" thickness Single-V girth welds are plotted in Figure 4-20 along ID and OD. The horizontal axis is measured from the edge of the weld pass and normalized by $\sqrt{rt}$ which was found as a characteristic parameter to correlate surface residual stress distribution in axial direction [13]. Again, it can be clearly seen from ID plots that the compressive stress zone reduces its magnitude and moves toward to the weld with increasing r/t ratio. From OD plots, axial residual stress magnitude decreases and hoop stress does not change drastically as r/t ratio increases. It is important to note that a large area of tensile residual stress is present on OD at quite a distance away from the weld for small r/t ratio. This may have an impact on fracture assessment for flaws away from the weld. All residual stresses are reduced to nearly zero after $2.5\sqrt{rt}$ which is served as a characteristic distance beyond which residual stress is vanished [13].

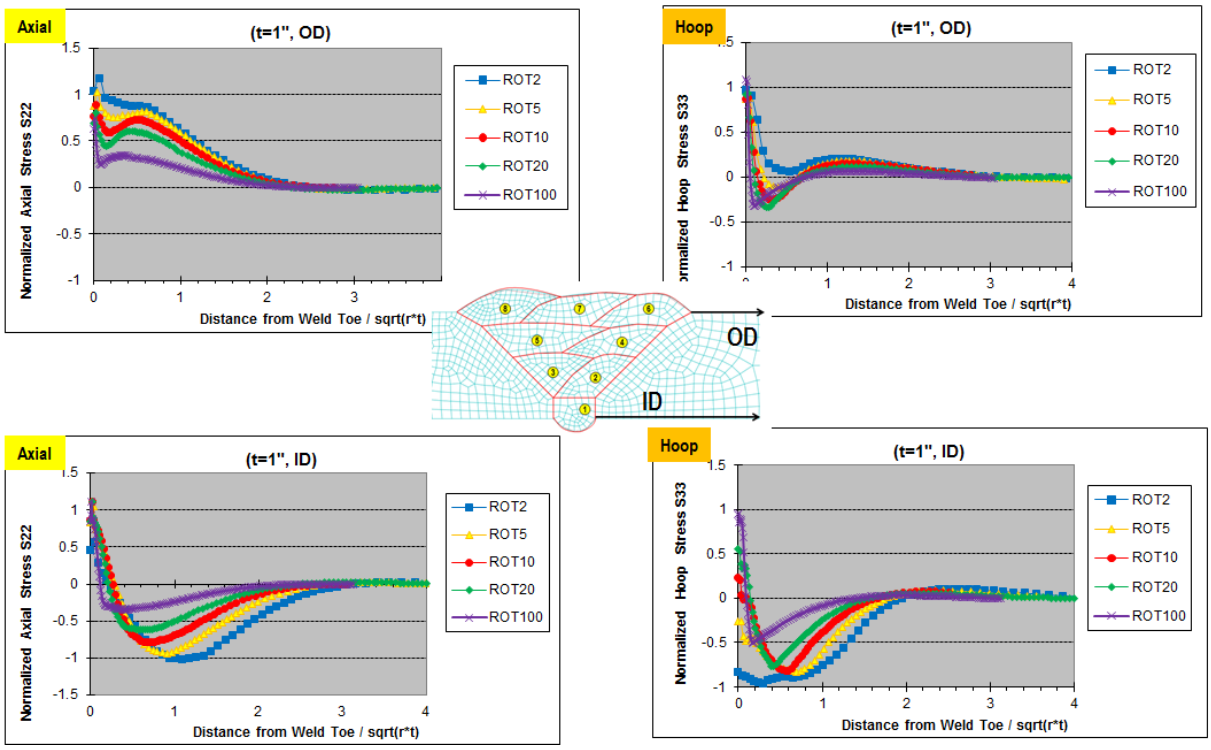

Figure 4-20 Surface residual stress line plots along ID and OD for SV girth welds with t=1": r/t ratio effects

It is of practical interest to establish an overall pipe radial displacement as a function of r/t ratio due to welding-induced shrinkage force. Figure 4-21 exhibits distortion plots for 1" thickness Single-V girth welds with a deformation scale factor of 10. Red line is the original shape and

pipe position before welding, and black line indicates the distortion after welding. It is no surprise to see that the maximum deflection is at the weld area for each r/t ratio. The deflection increases as r/t ratio is increased, which implies a reduced radial restraint and increased shrinkage force within the weld area (highly tensile hoop residual stress at r/t=10, shown in Figure 4-17). This can be clearly seen by detailed radial deflection line plots along ID shown in Figure 4-22. Again, the horizontal axis is measured from the weld pass and normalized by $\sqrt{rt}$. The deflection vanishes after $2.5\sqrt{rt}$, which is consistent with the finding of pipe characteristic length for residual stress in Figure 4-20.

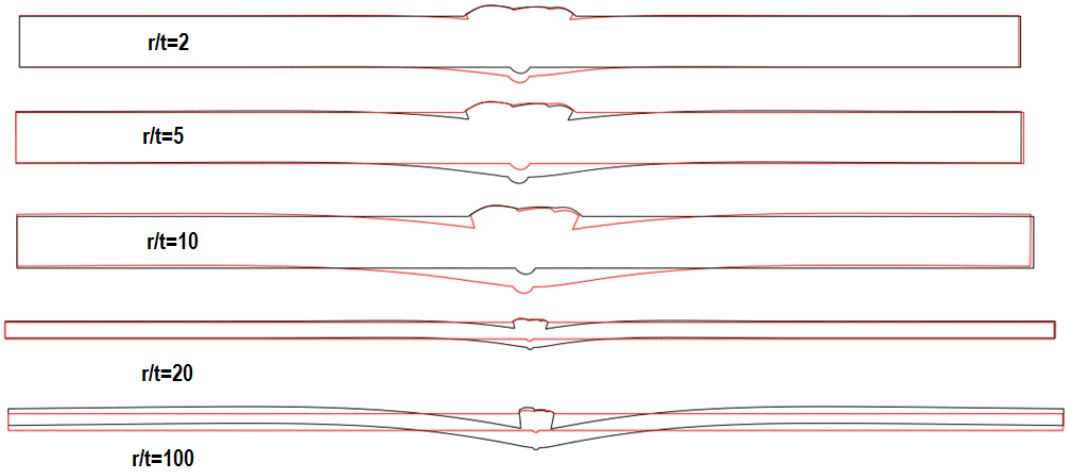

Figure 4-21 Distortion for SV girth welds with t=1": r/t ratio effects

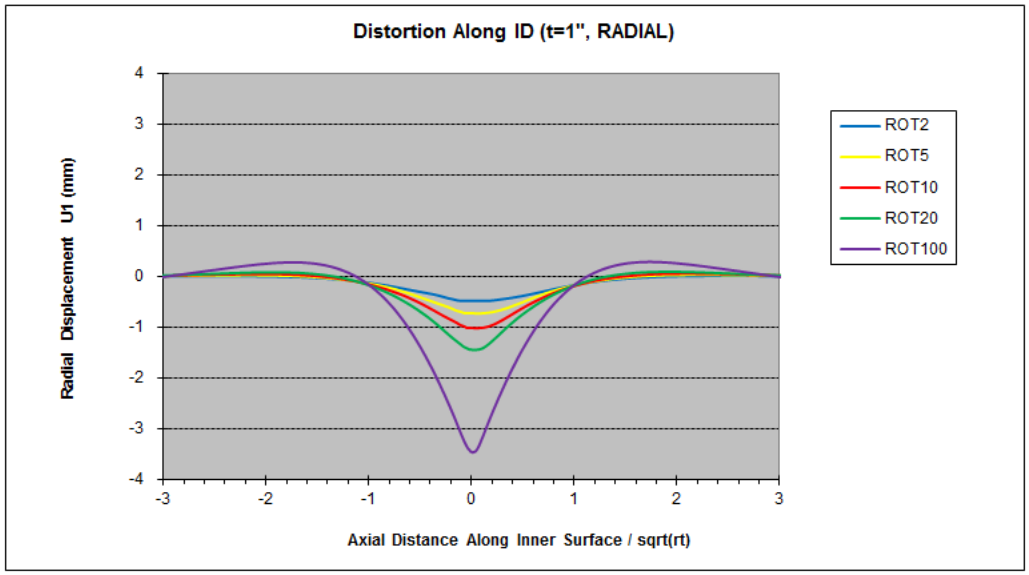

Figure 4-22 Distortion line plots along ID for SV girth welds with t=1": r/t ratio effects

Figure 4-23, Figure 4-24, and Figure 4-25 show residual stress contour plots for Single-V girth welds of 2” thickness, 4” thickness and 10” thickness, respectively. The scale is the same as the one used for 1” thickness Single-V welds shown in Figure 4-17. The overall trends are similar to 1” thickness Single-V welds residual stress distribution. Axial residual stress shows a through-thickness bending type with small r/t ratio, and becomes self-equilibrating type as r/t ratio reaches to 100. Hoop residual stress is highly tensile in the weld area with increasing r/t ratio. Compressive stress zone at ID for both axial and hoop residual stresses moves away from the weld with reduced magnitude as r/t ratio increases.

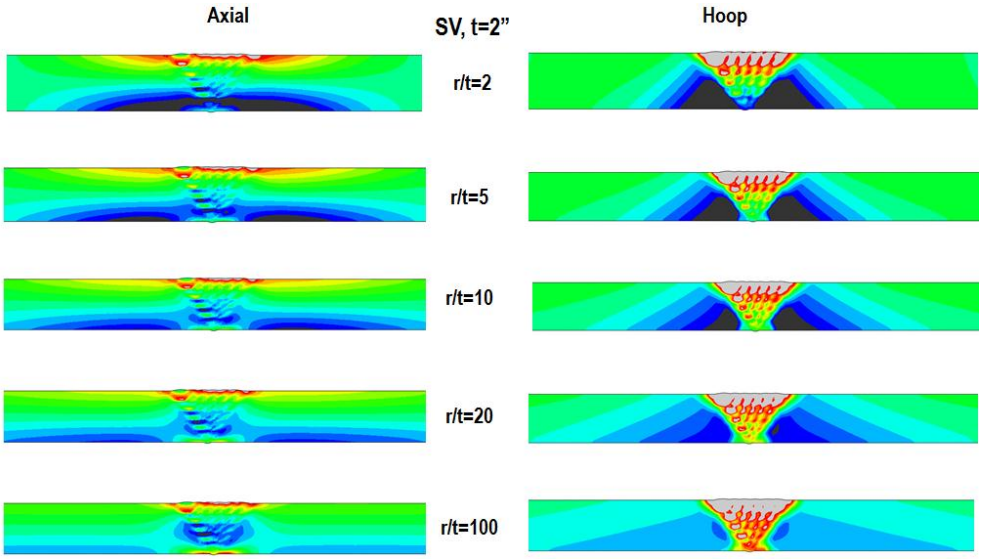

Figure 4-23 Residual stress contour plots for SV girth welds with t=2”: r/t ratio effects

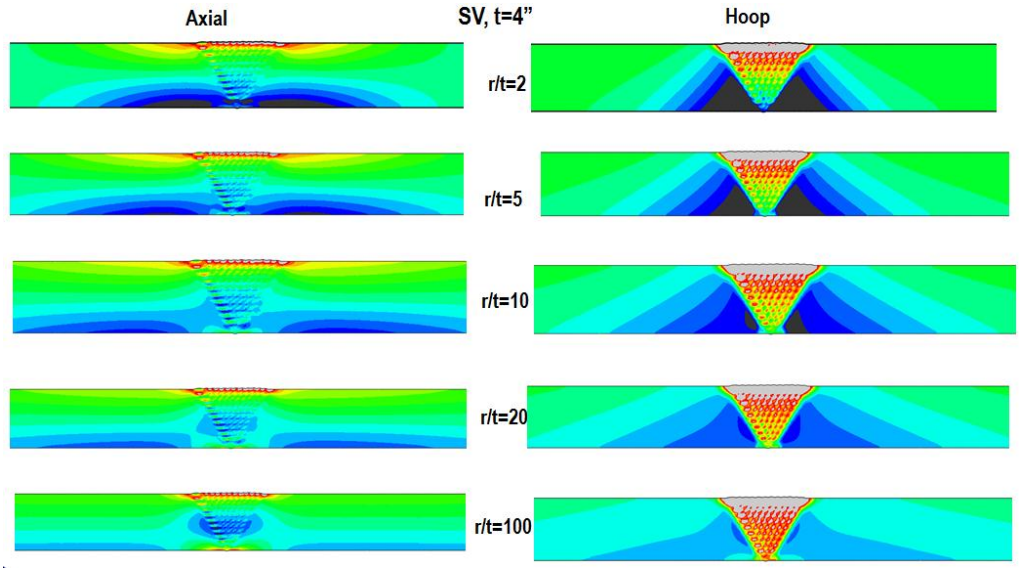

Figure 4-24 Residual stress contour plots for SV girth welds with t=4": r/t ratio effects

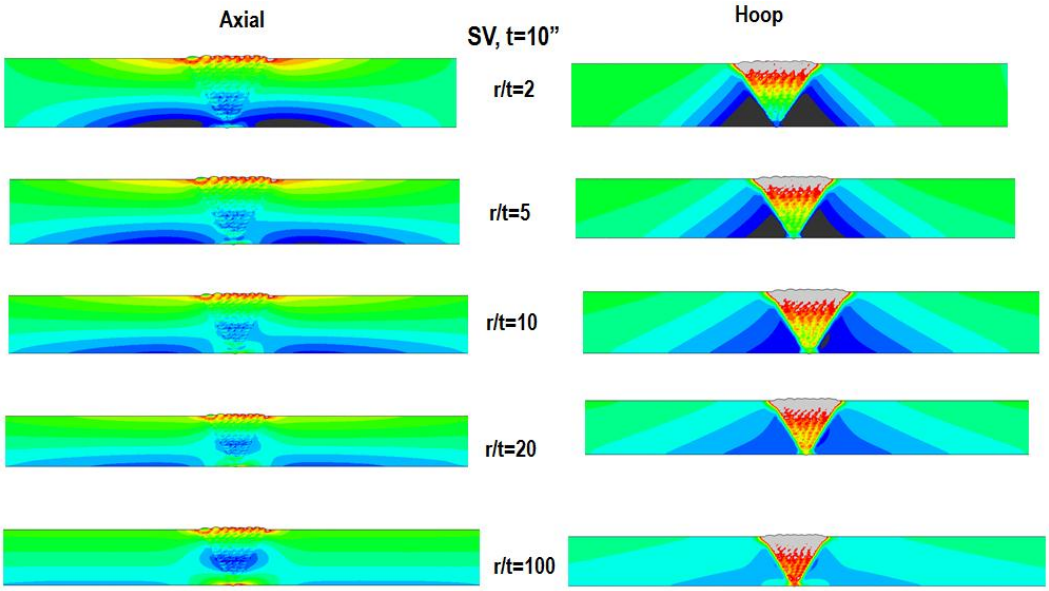

Figure 4-25 Residual stress contour plots for SV girth welds with t=10": r/t ratio effects

Figure 4-26, Figure 4-27, Figure 4-28, and Figure 4-29 represent residual stress contour plots for Narrow Groove (NG) girth welds of t=1",t= 2",t= 4" and t=10", respectively. The scale is the same as before. Please note that due to the nature of Narrow Groove weldment, only half of model is shown here. Again the overall trends are similar to the Single-V girth welds. Detailed examination of joint preparation effects is to be discussed in the later section.

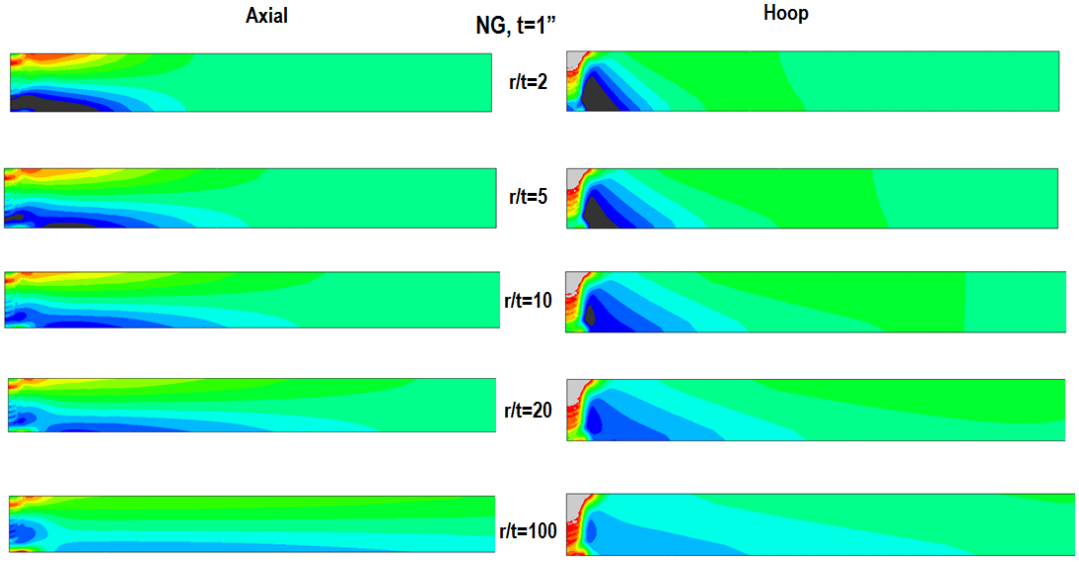

Figure 4-26 Residual stress contour plots for NG girth welds with t=1": r/t ratio effects

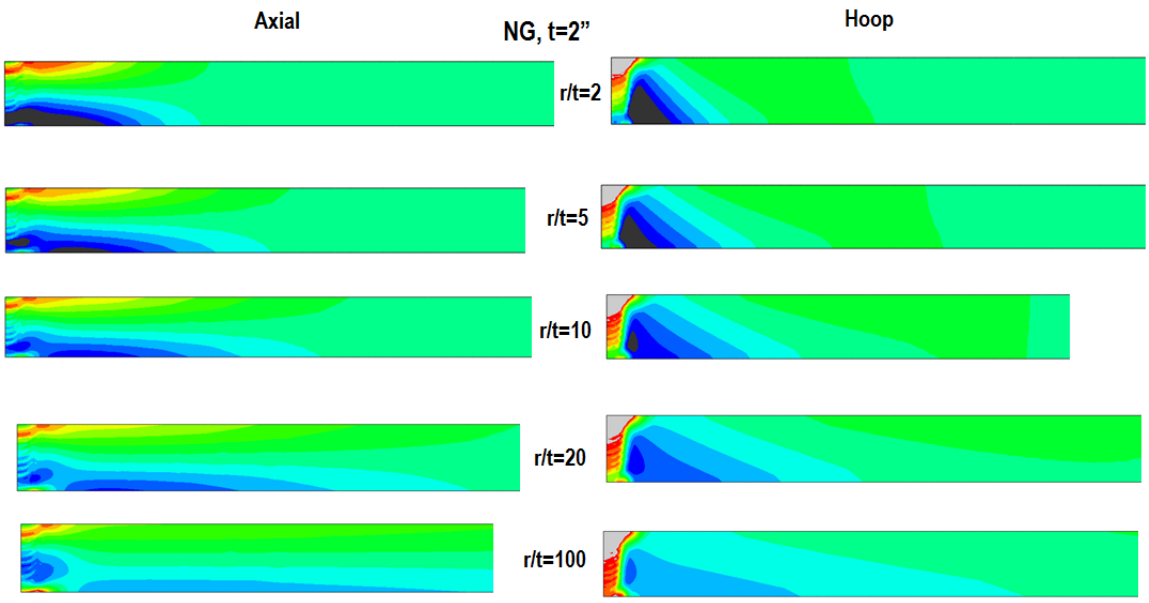

Figure 4-27 Residual stress contour plots for NG girth welds with t=2": r/t ratio effects

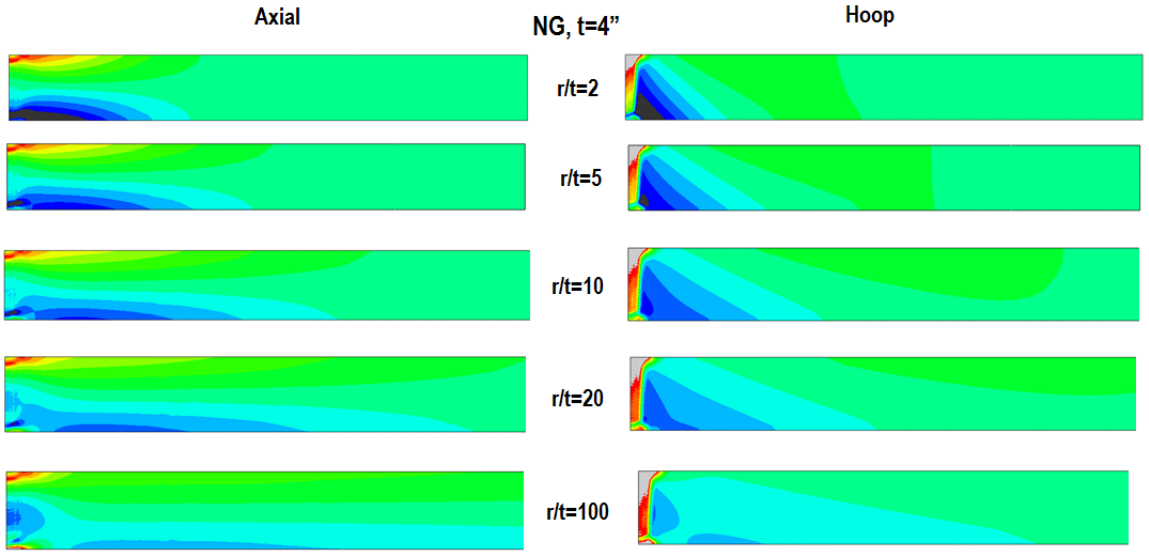

Figure 4-28 Residual stress contour plots for NG girth welds with t=4": r/t ratio effects

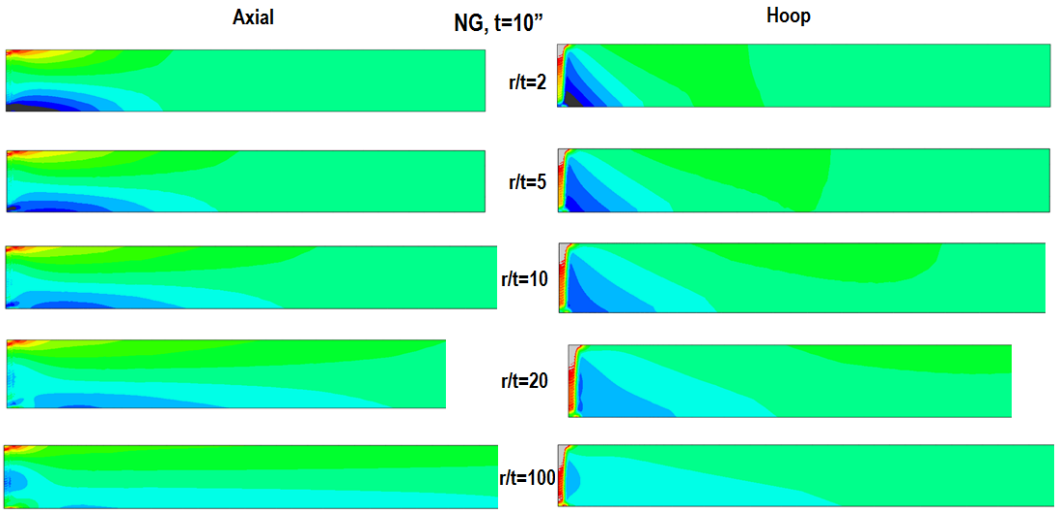

Figure 4-29 Residual stress contour plots for NG girth welds with t=10”: r/t ratio effects

Figure 4-30 shows residual stress contour plots for Double-V (DV) girth welds of t=1”. The inner groove of Double-V weld is deposited first and then outer groove. Through-thickness axial residual stress distribution exhibits a self-equilibrating type within the weld area with high tensile zones at both ID and OD and compressive zone in the mid thickness. This is primary due to the unique joint preparation. Hoop residual stress within the weld area becomes highly tensile with increasing r/t ratio. Compressive zones at ID for both of axial and hoop residual stress move away from the weld and finally vanish as r/t ratio increases.

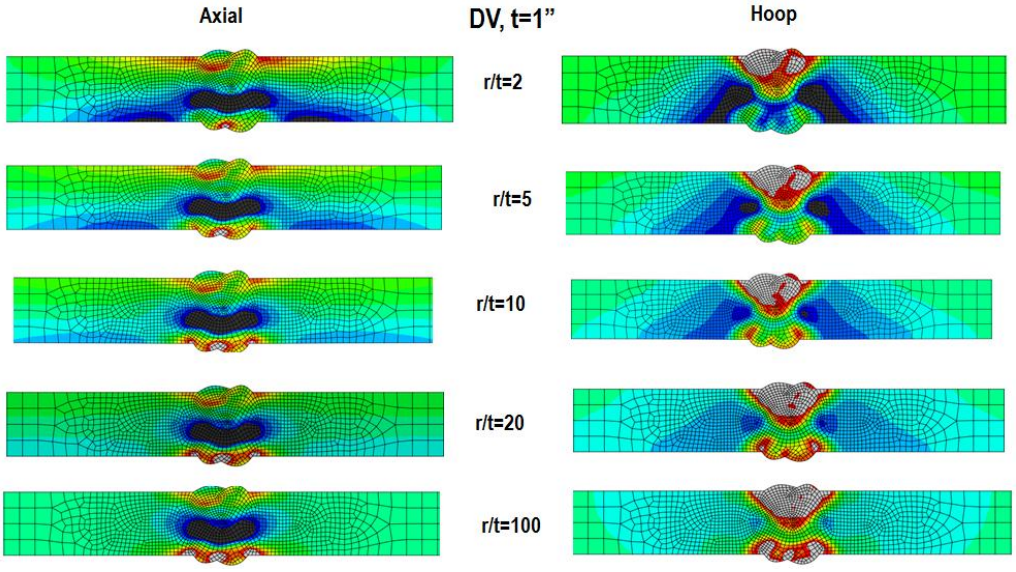

Figure 4-30 Residual stress contour plots for DV girth welds with t=1”: r/t ratio effects

The detailed line plots along weld centerline and weld toe are present in Figure 4-31 and Figure 4-32, respectively. Surface line plots along ID and OD are plotted in Figure 4-33. The results are

summarized in the same manner (e.g., same vertical and horizontal axes). The plots are consistent with the findings discussed before.

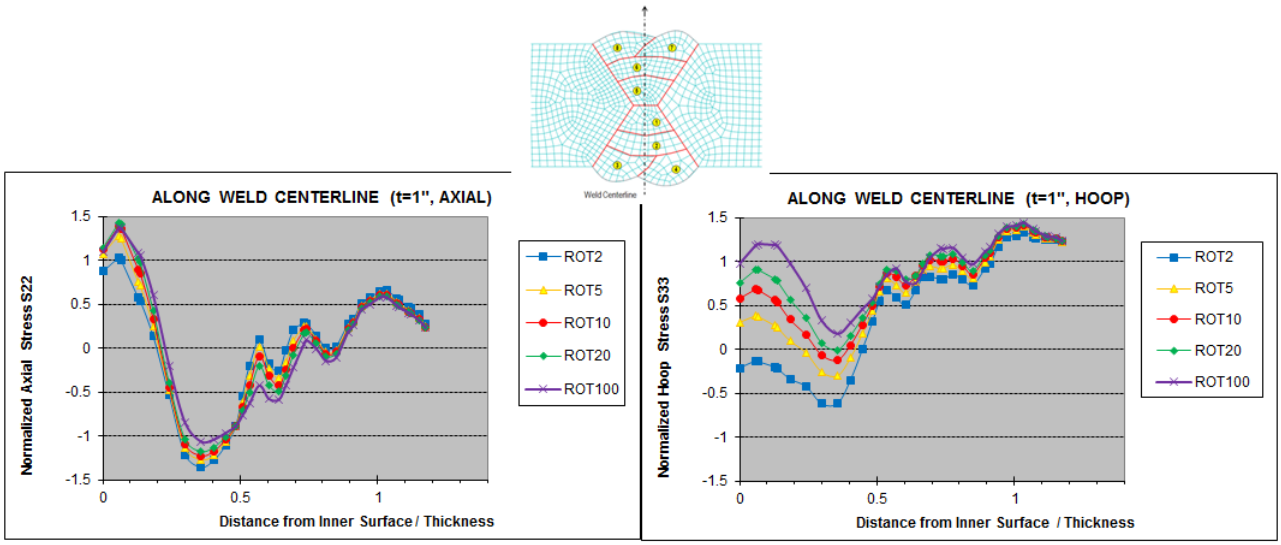

Figure 4-31 Through-thickness residual stress line plots along WCL for DV girth welds with t=1": r/t ratio effects

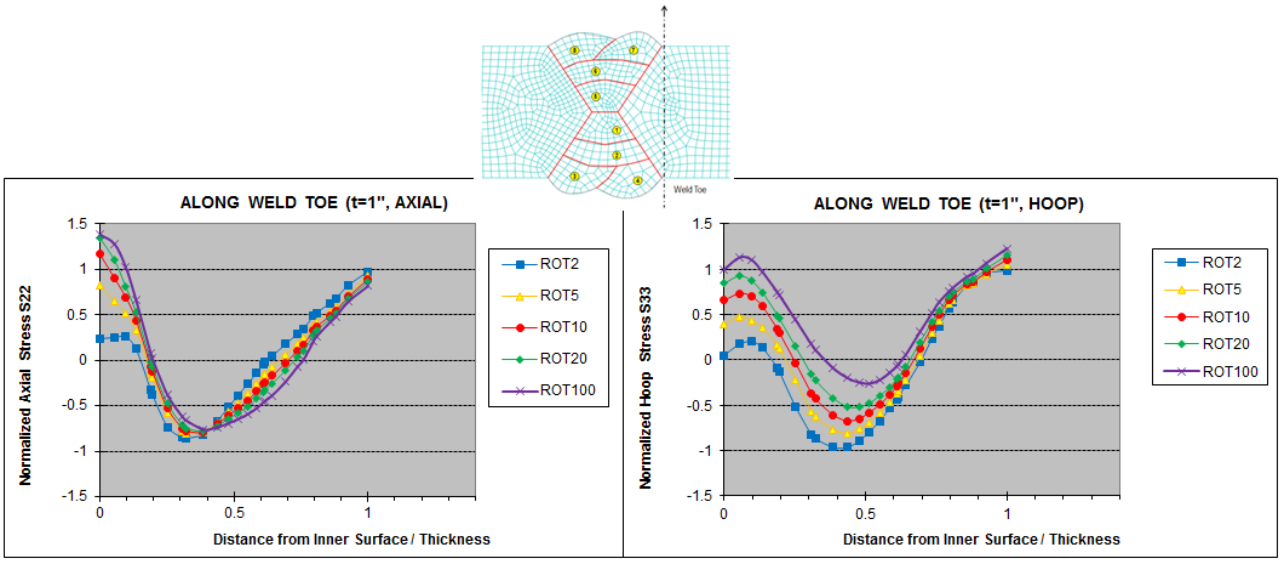

Figure 4-32 Through-thickness residual stress line plots along WT for DV girth welds with t=1": r/t ratio effects

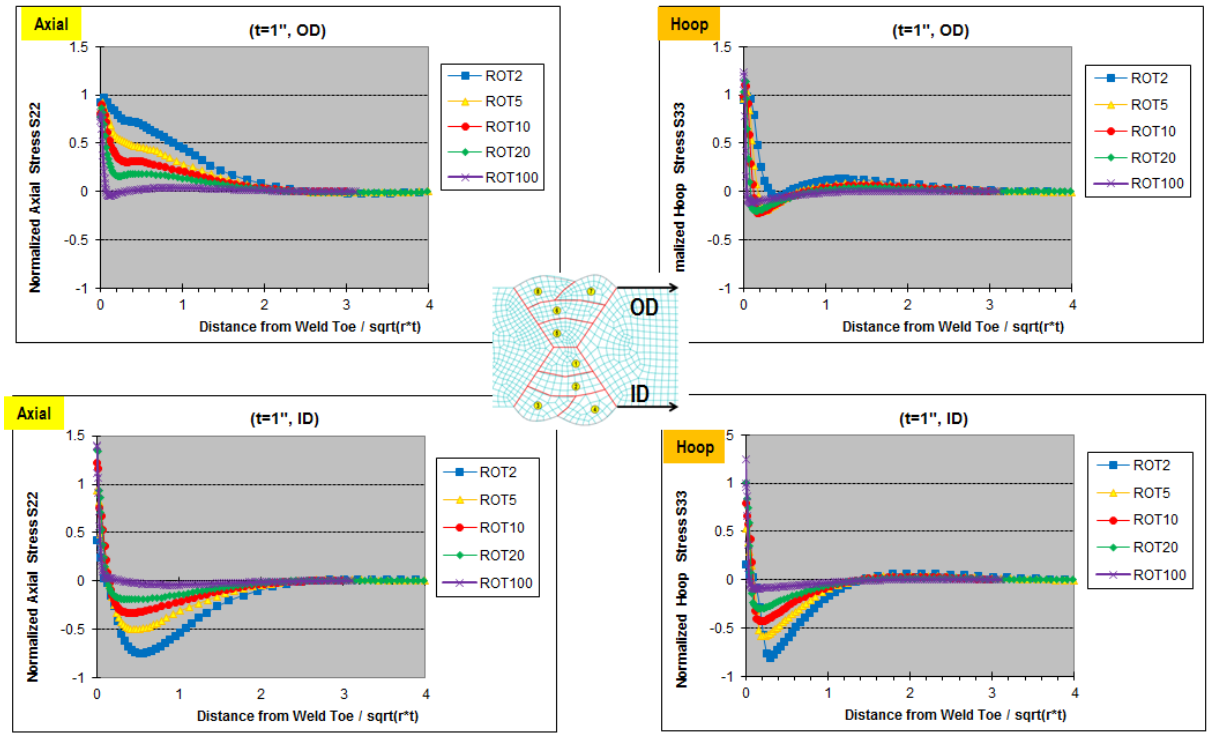

Figure 4-33 Surface residual stress line plots along ID and OD for DV girth welds with t=1": r/t ratio effects

Distortion plots for 1" thickness Double-V girth welds are shown in Figure 4-34 with the same deformation factor of 10 as those plotted in Figure 4-21 for Single-V welds. The corresponding detailed radial displacement line plots along ID are present in Figure 4-35. As we can see, radial displacement increases with increasing r/t ratio due to a reduced radial restraint. Radial displacements for Double-V girth welds are smaller than the ones for Single-V welds shown in Figure 4-22. This is mainly because the symmetrical welding sequence of Double-V girth welds, which provides a balance of distortion during inner and outer groove weld deposition.

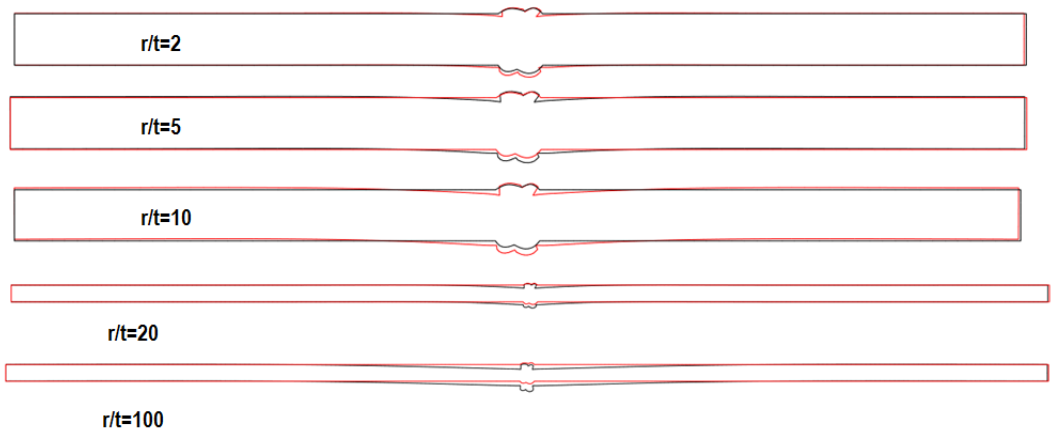

Figure 4-34 Distortion for DV girth welds with t=1": r/t ratio effects

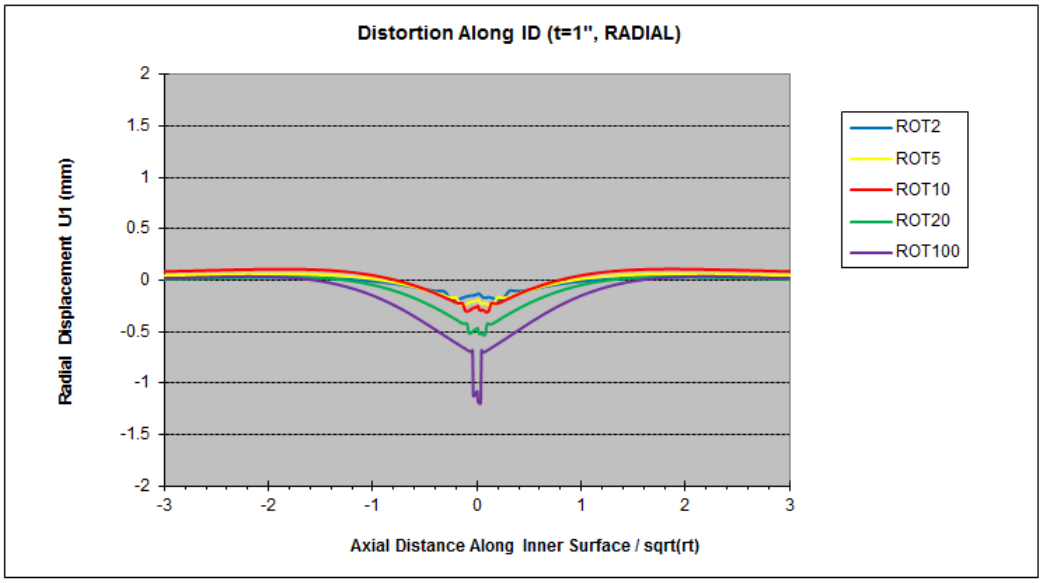

Figure 4-35 Distortion line plots along ID for DV girth welds with t=1": r/t ratio Figure

Figure 4-36, Figure 4-37 and Figure 4-38 show residual stress contour plots for Double-V girth welds of 2" thickness, 4" thickness and 10" thickness, respectively. The scale is the same as before. Similar trends discussed above are obtained compared with the results of 1" thickness Double-V girth welds.

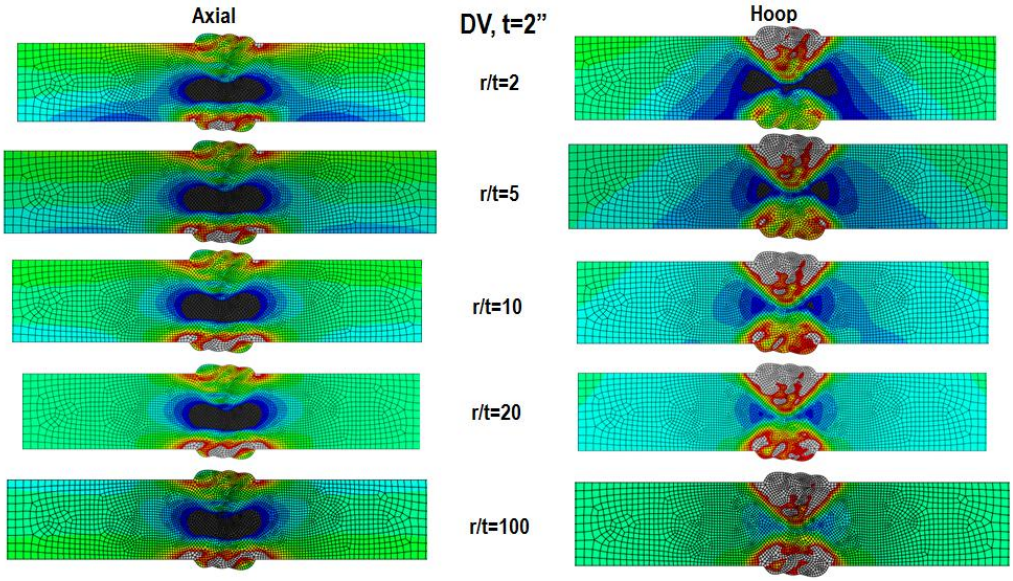

Figure 4-36 Residual stress contour plots for DV girth welds with t=2": r/t ratio effects

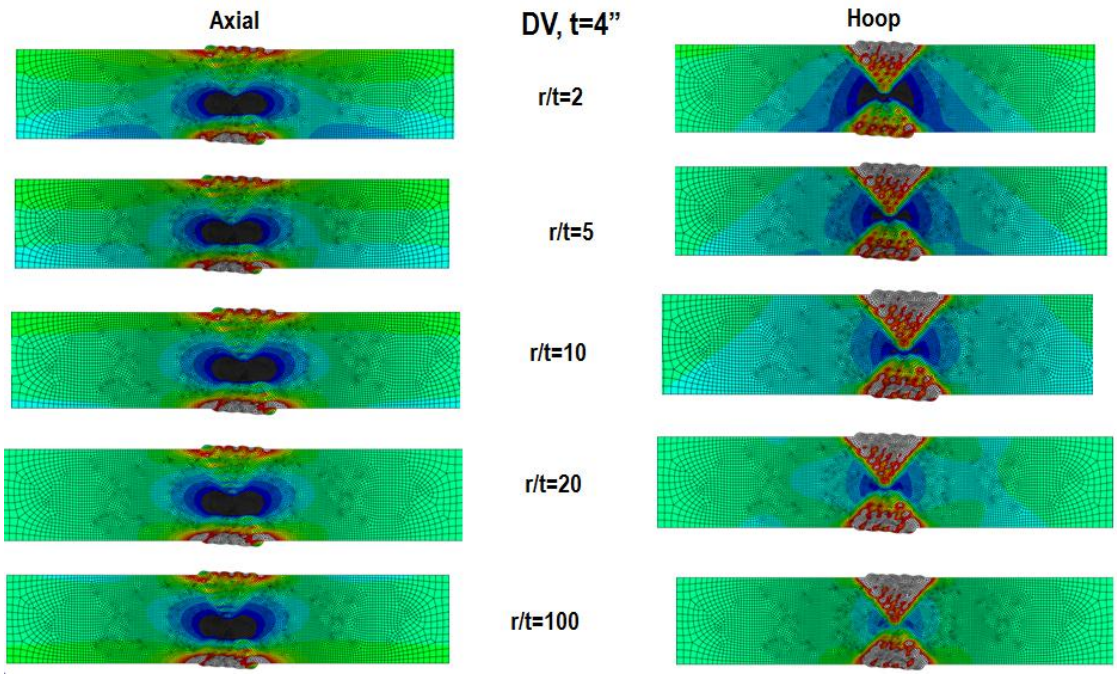

Figure 4-37 Residual stress contour plots for DV girth welds with t=4”: r/t ratio effects

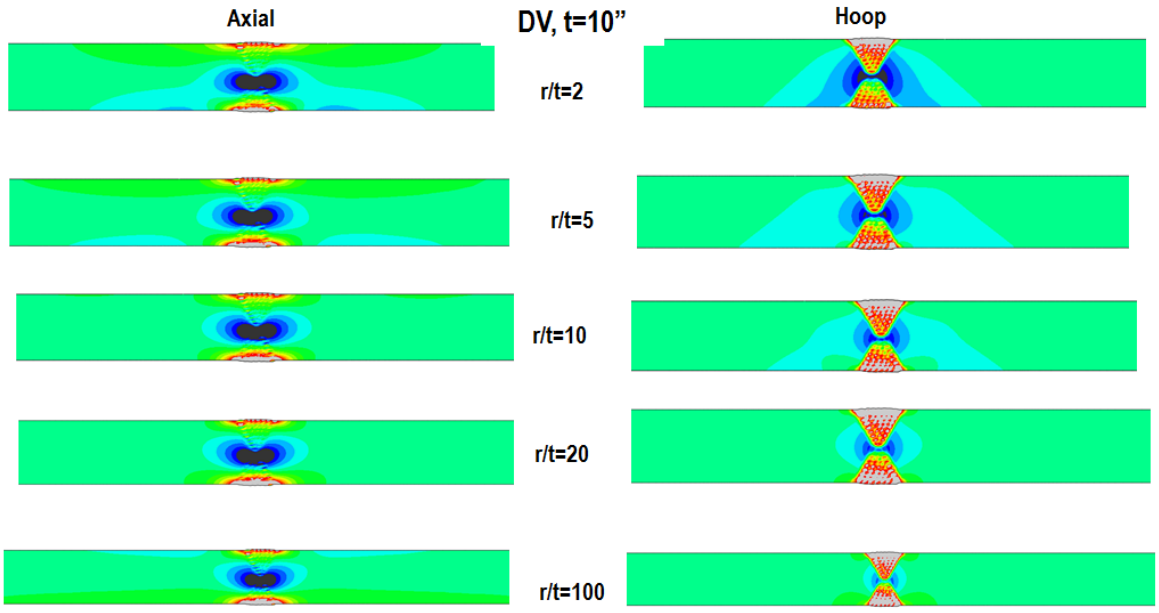

Figure 4-38 Residual stress contour plots for DV girth welds with t=10”: r/t ratio effects

In order to quantitatively evaluate the transition behavior in residual stress distribution types seen above, all through-thickness residual stress distributions obtained in this section are decomposed according to Eq. (3.1). Residual stress results, normalized by the yield strength at weld centerline location (WCL) as a function of r/t ratio, are shown in Figure 4-39 for Single-V welds, in Figure 4-40 for Narrow Groove welds, and in Figure 4-41 for Double-V welds, respectively. Results at weld toe position (WT) are shown in Figure 4-42 for Single-V welds, in Figure 4-43 for Narrow Groove welds, and in Figure 4-44 for Double-V welds, respectively. The overall results clearly indicate the following trends:

1. The decomposed bending parts of axial (dark blue) and hoop (red) residual stresses decrease monotonically with increasing r/t ratio, implying a reduced radial restraint as r/t ratio increases.

2. The decomposed membrane part of hoop (purple) residual stresses show a clear dependence on r/t ratio, monotonically increasing with increasing r/t ratio.

3. The two observations above with regard to r/t ratio effects can be applied to cases for all joint preparations (SV, DV, and NG), all thicknesses (1”~10”), and interested locations (WCL and WT) investigated in this section.

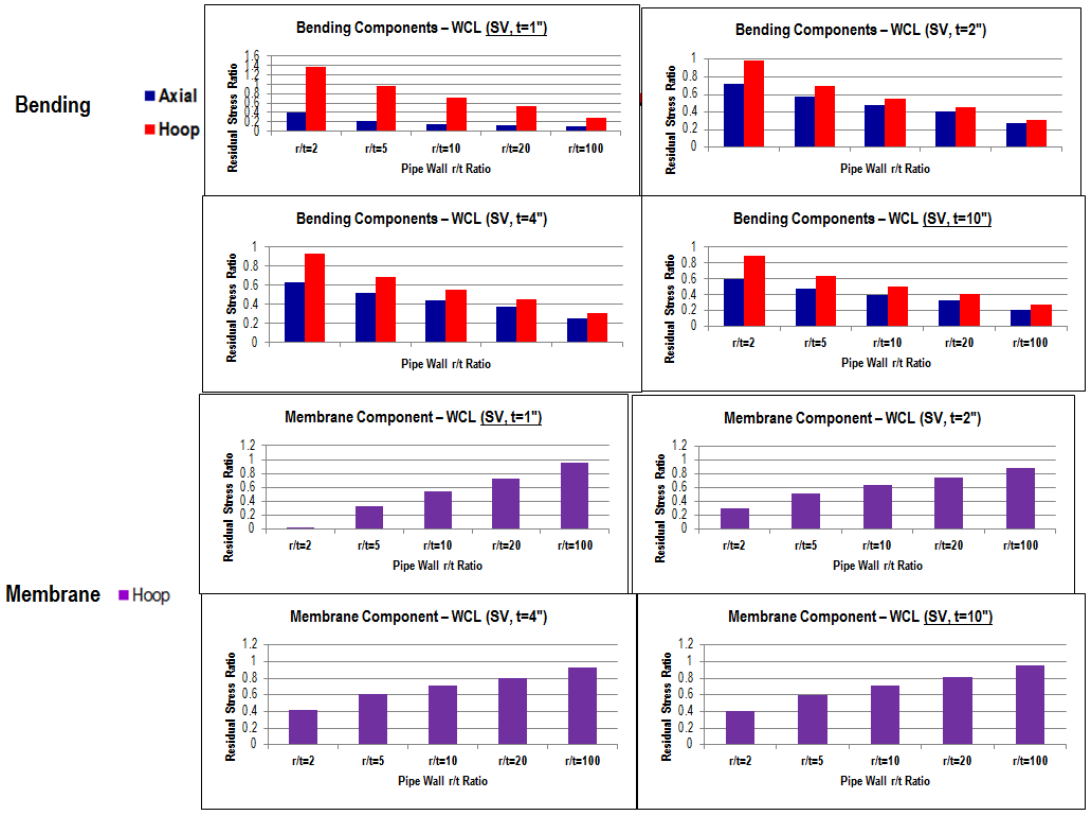

Figure 4-39 Decomposed residual stress components at WCL as a function of r/t ratio for SV girth welds: axial and hoop bending components, and hoop membrane component

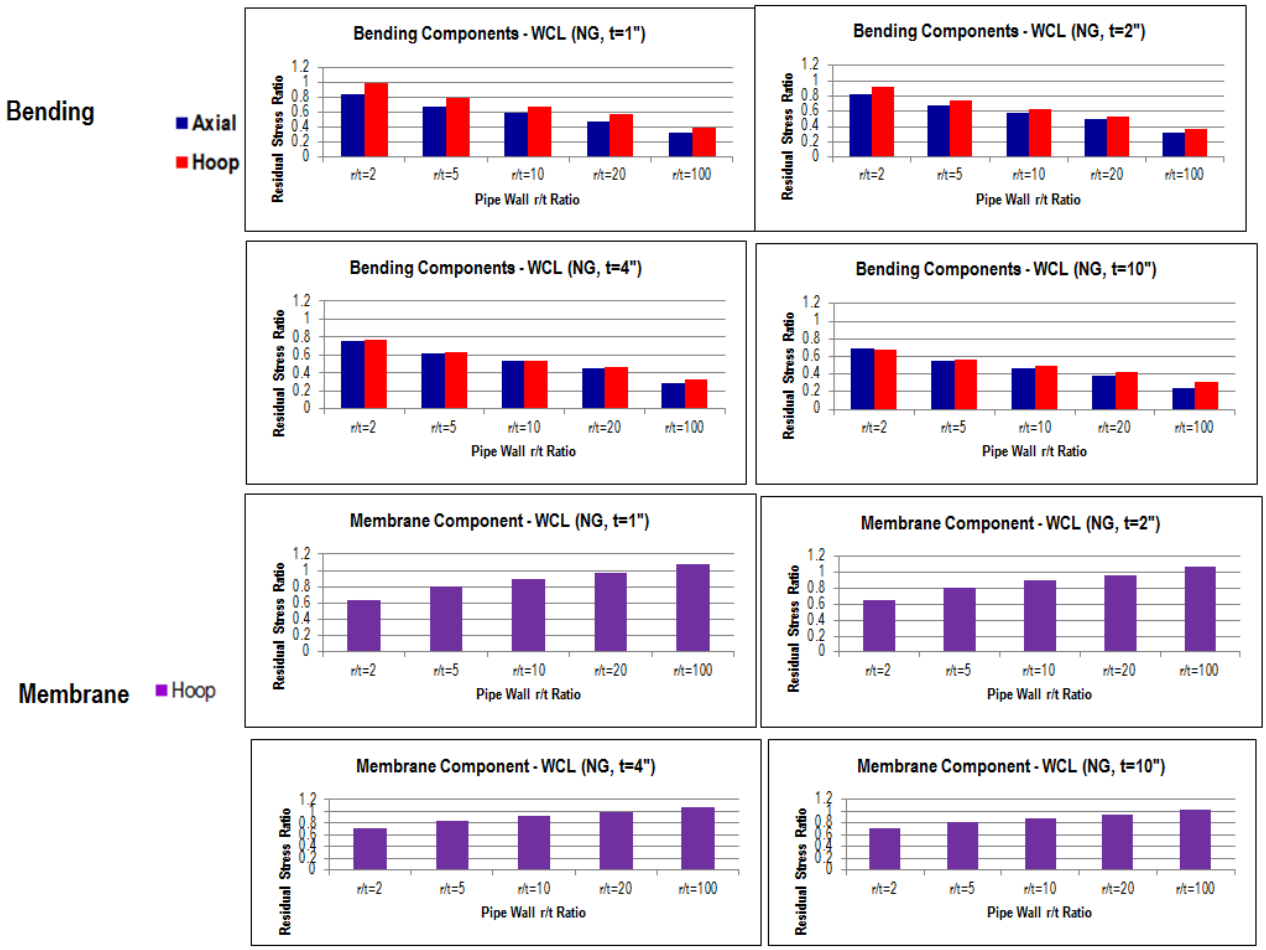

Figure 4-40 Decomposed residual stress components at WCL as a function of r/t ratio for ND girth welds: axial and hoop bending components, and hoop membrane component

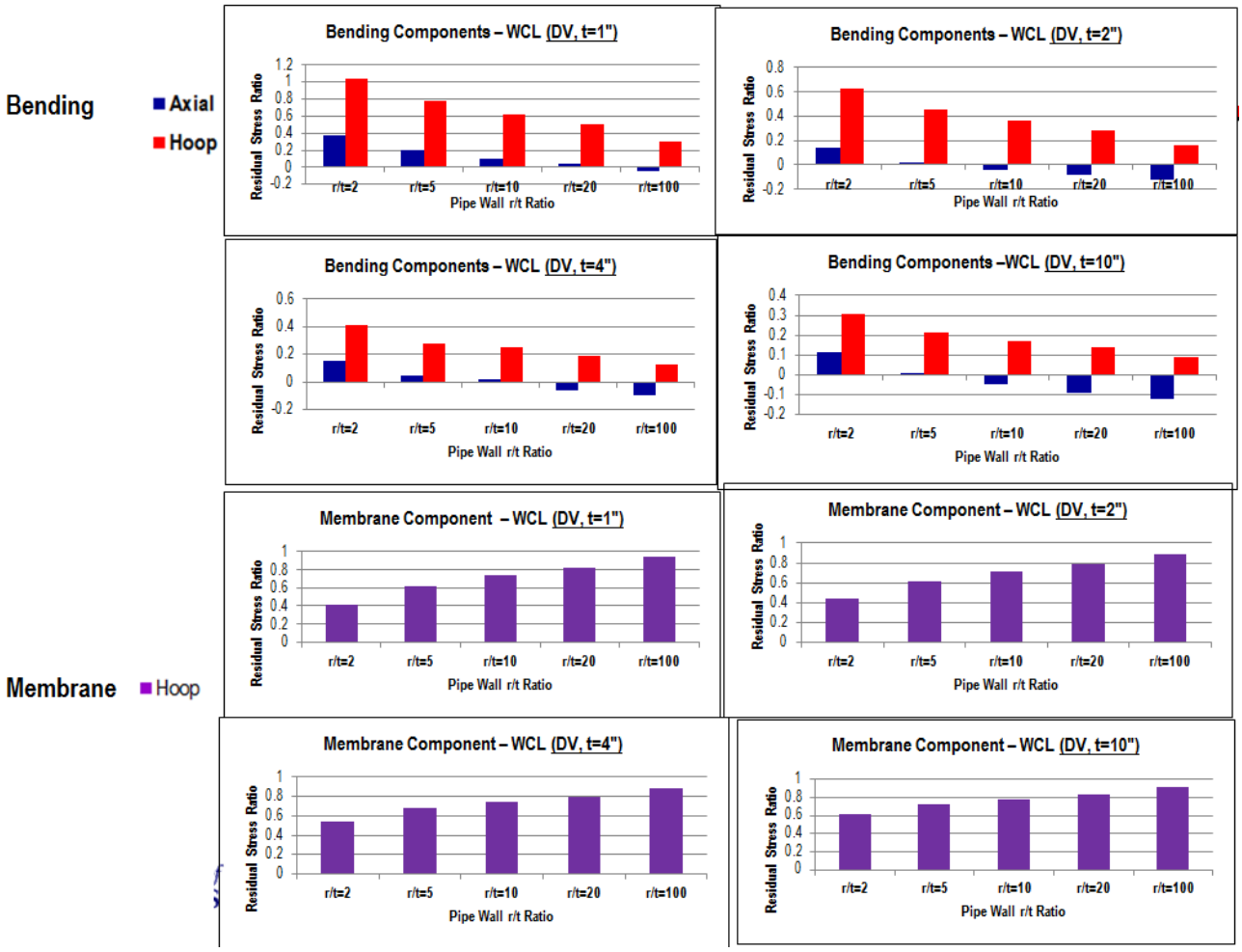

Figure 4-41 Decomposed residual stress components at WCL as a function of r/t ratio for DV girth welds: axial and hoop bending components, and hoop membrane component

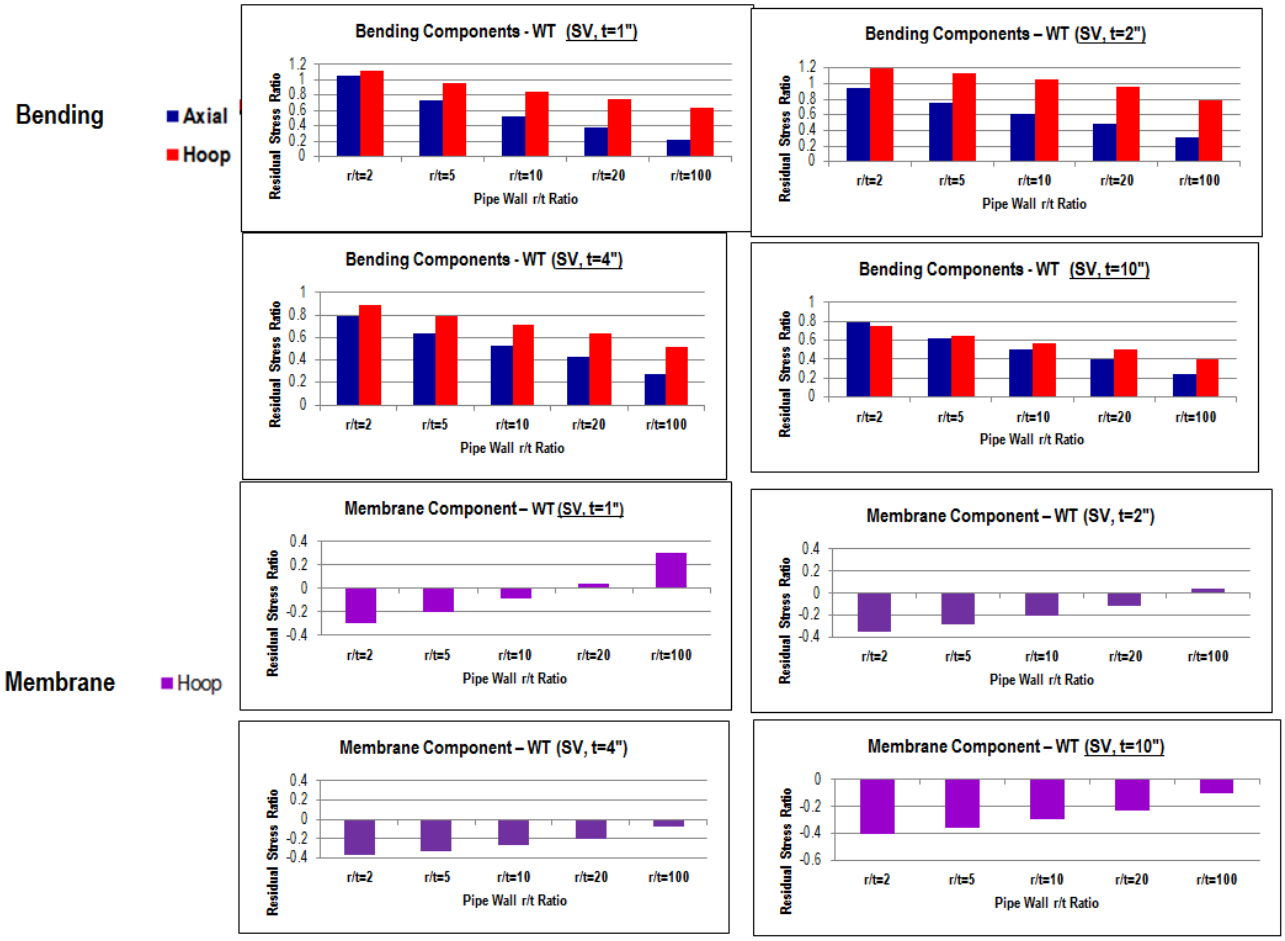

Figure 4-42 Decomposed residual stress components at WT as a function of r/t ratio for SV girth welds: axial and hoop bending components, and hoop membrane component

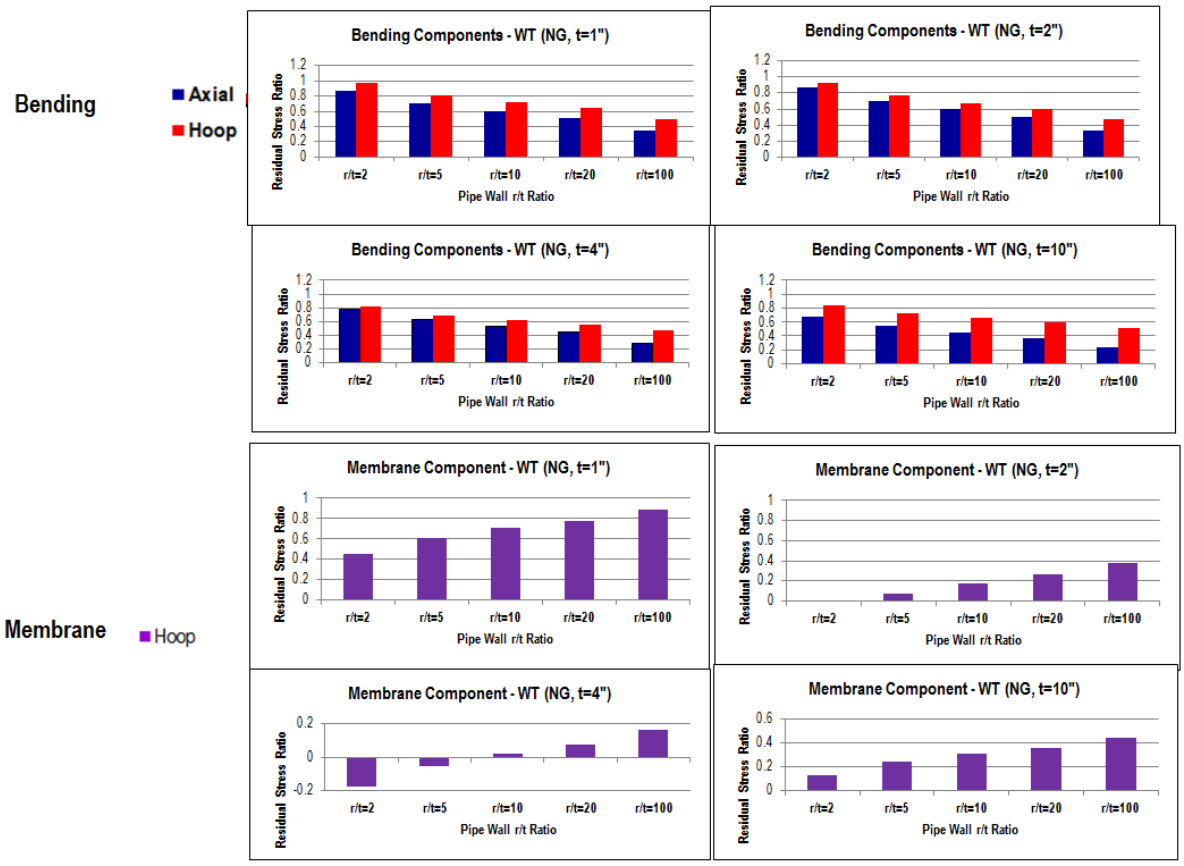

Figure 4-43 Decomposed residual stress components at WT as a function of r/t ratio for NG girth welds: axial and hoop bending components, and hoop membrane component

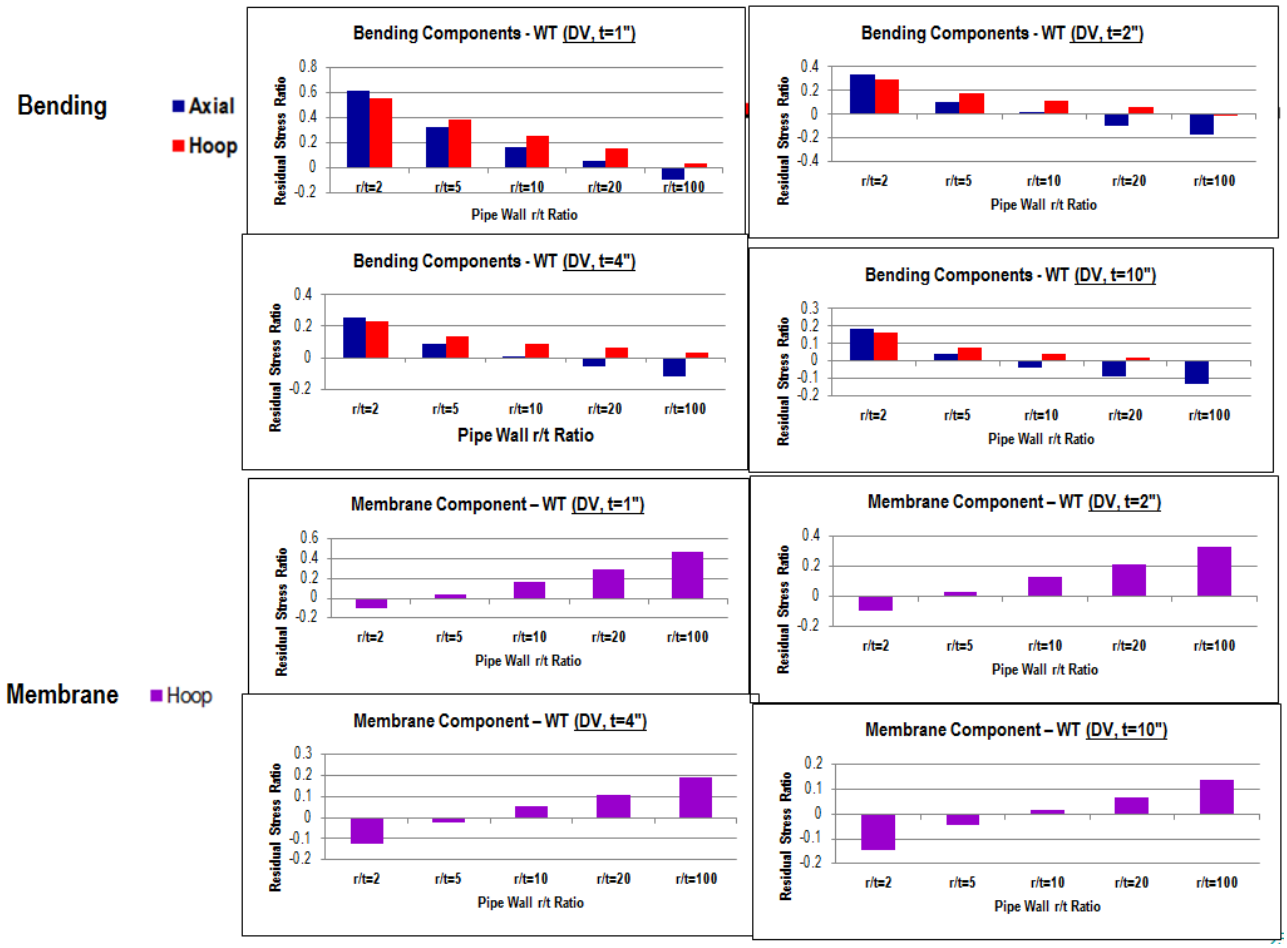

Figure 4-44 Decomposed residual stress components at WT as a function of r/t ratio for DV girth welds: axial and hoop bending components, and hoop membrane component

4.3 Thickness effects

Besides all of the cases summarized in Table 4-2 in the previous section (r/t ratio effect), some of thin wall welds (e.g., t=1/4", t=1/2") documented in the Phase I report [13] are also re-analyzed in order to capture the characteristics of thickness effects. As such, a full range of thicknesses varying from ¼" to 10" with joint preparation of Single-V, Double-V and Narrow Groove are investigated in this section.

Using the same results summarized for r/t ratio effects in the previous section, Figure 4-45 exhibits some distinct characteristic types of through-thickness residual stress distributions at certain range of r/t and t values. Stress scale is the same as in the previous section, which is from -350MPa to 558MPa. It is clearly shown that the transition from one residual stress distribution type to another is dominated by both r/t and t. A similar trend was first found in the Phase I report [13] where a smaller range of r/t and t for girth welds was studied with thickness less than 2". For small thickness (e.g., t=1/4") and small r/t (e.g., 2), axial residual stress distributions can

be characterized as a through-wall global bending type with OD under compression and ID under tension. As thickness t increases while keeping r/t constant, the global bending type of axial residual stress distributions are transitioned to a local bending type with OD under tension and ID under compression. As either thickness t and/or r/t increases, the local bending type is gradually transitioned to a through-wall self-equilibrating type (e.g., at t=10" and r/t =100).

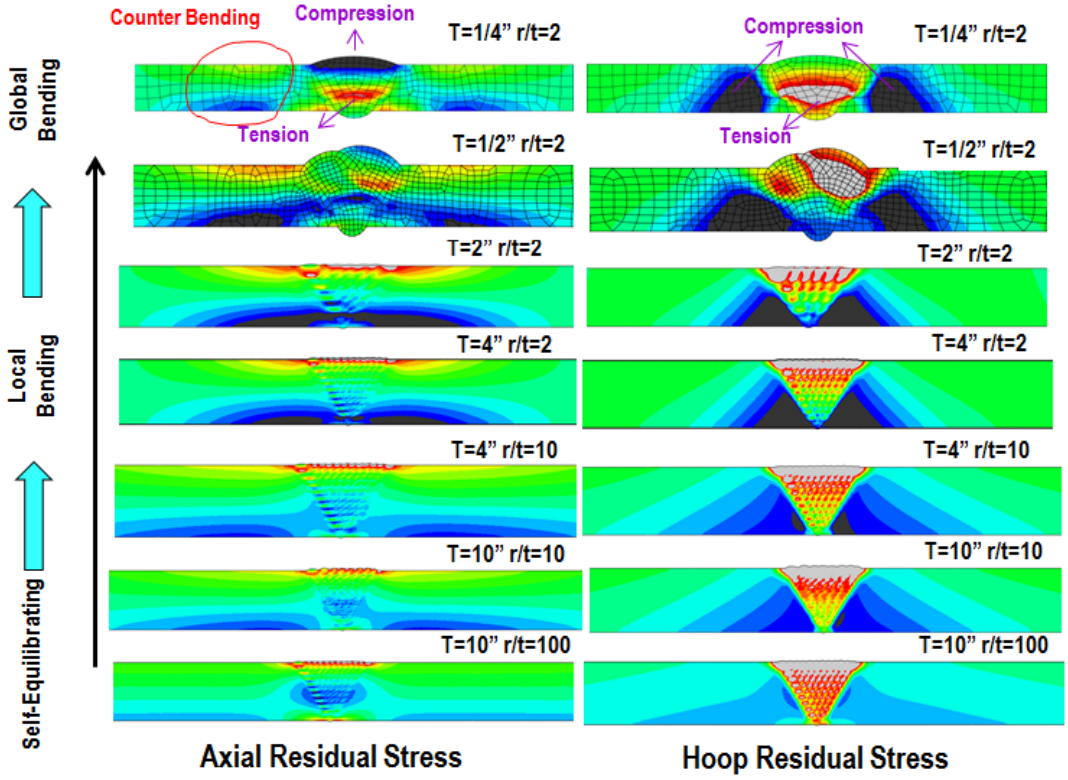

Figure 4-45 Axial and hoop residual stress distributions for SV girth welds: transition from through-thickness self-equilibrating to local bending as a function of r/t and t

To separately evaluate thickness effects contributed to the transition behavior in through-thickness residual stress distribution types, all decomposed residual stress according to Eq. (3.1) obtained in the previous section are re-arranged as a function of thickness. Figure 4-46, Figure 4-47, and Figure 4-48 show some of the representative decomposed residual stress results, normalized by the material yield strength along weld centerline (WCL), for Single-V welds, Narrow Groove welds, and Double-V welds, respectively. Although the trends are not as clear as the ones observed for r/t ratio effects, some characteristics can still be observed as summarized below:

Single-V: For r/t ratio of 2 and 10, axial and hoop bending components initially increase from thickness of ¼" to about 1", and then does not change in any significant manner up to thickness of 10". The increasing part is primary due to the global bending transiting to the local bending which has totally opposite through-thickness bending behavior as shown in Figure 4-45. As

thickness increases while keeping r/t ratio constant, local bending type is maintained. While with a large r/t ratio (e.g, r/t=100), even though self-equilibrating type of through-thickness residual stress is presented at the thick section, such bending behavior still stands only with a smaller value. There is no clear trend for hoop membrane component as a function of thickness. At a large r/t ratio (e.g., r/t=100), hoop membrane component for each thickness remains the same due to highly tensile stress within the weld area (see the corresponding contour plots in Figure 4-17, Figure 4-23, Figure 4-24, and Figure 4-25). The reason for a small value of 1" thickness hoop membrane component at r/t=2 is that the net hoop stress is almost zero and resultant shrinkage force is small (see Figure 4-17).

Narrow Groove: Due to the identical local bending type distribution for r/t =2 and 10 (see the corresponding contour plots in Figure 4-26, Figure 4-27, Figure 4-28, and Figure 4-29), axial and hoop bending components remain roughly the same for each thickness with a given r/t ratio. For r/t=100, such trend still stands but the value is smaller. Hoop membrane component also remains the same for each thickness with a given r/t ratio.

Double-V: Axial bending component is negligible owing to the self-equilibrating type of through-thickness axial residual stress distribution (see Figure 4-30, Figure 4-36, Figure 4-37 and Figure 4-38). Hoop bending components slightly decreases with increasing thickness, and hoop membrane component remains roughly unchanged.

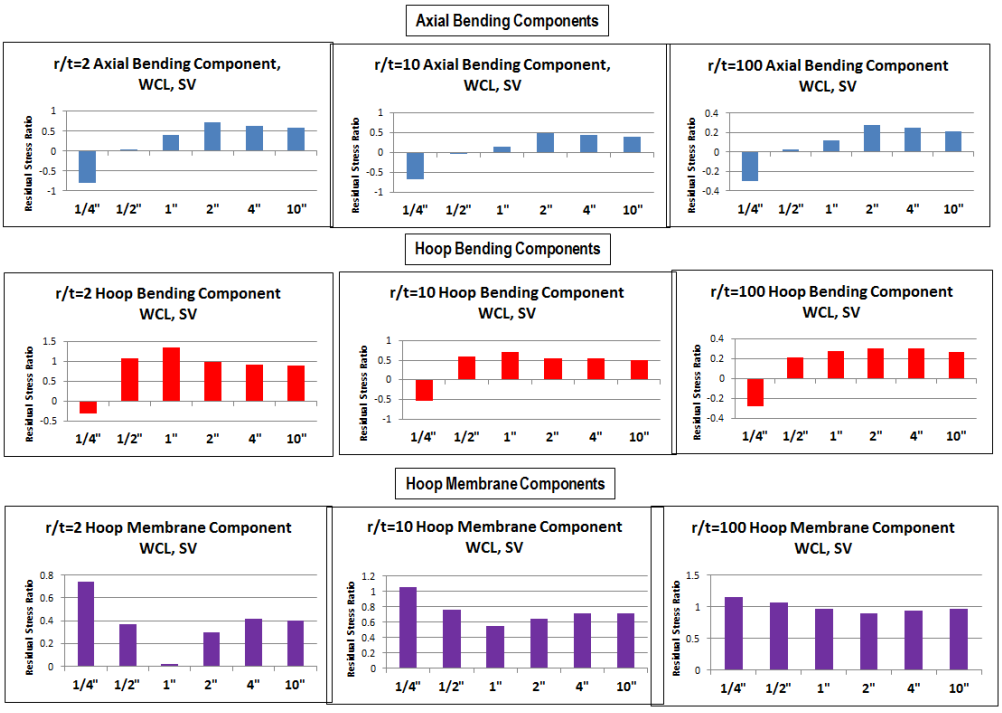

Figure 4-46 Decomposed residual stress components at WCL as a function of thickness for SV girth welds: axial bending components, hoop bending components, and hoop membrane components

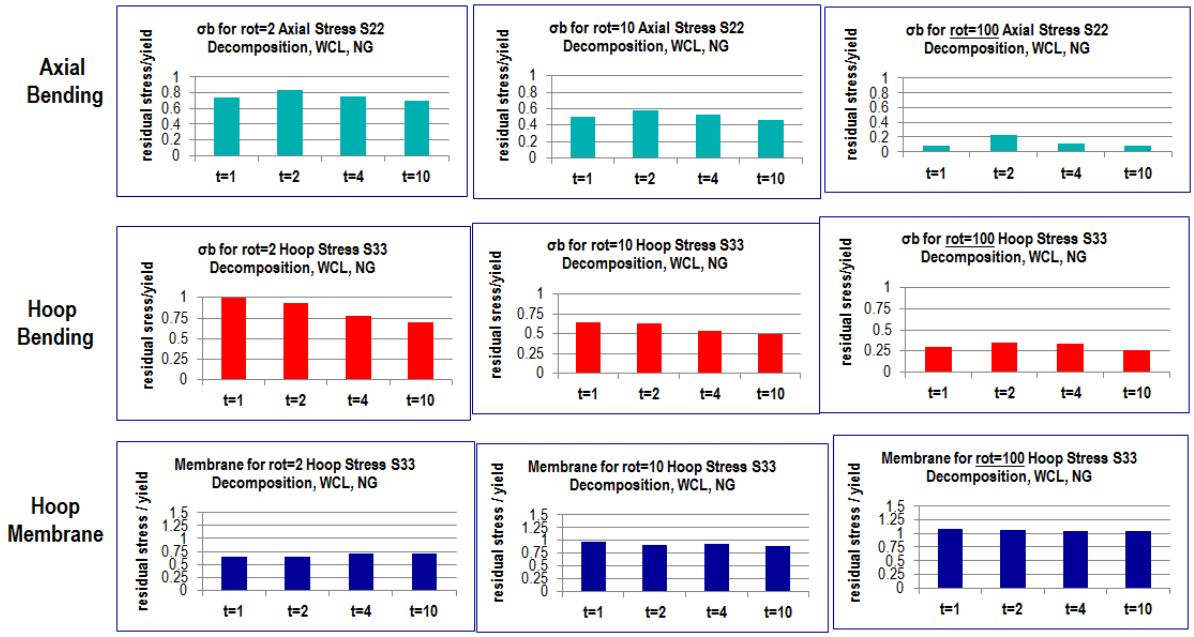

Figure 4-47 Decomposed residual stress components at WCL as a function of thickness for NG girth welds: axial bending components, hoop bending components, and hoop membrane components

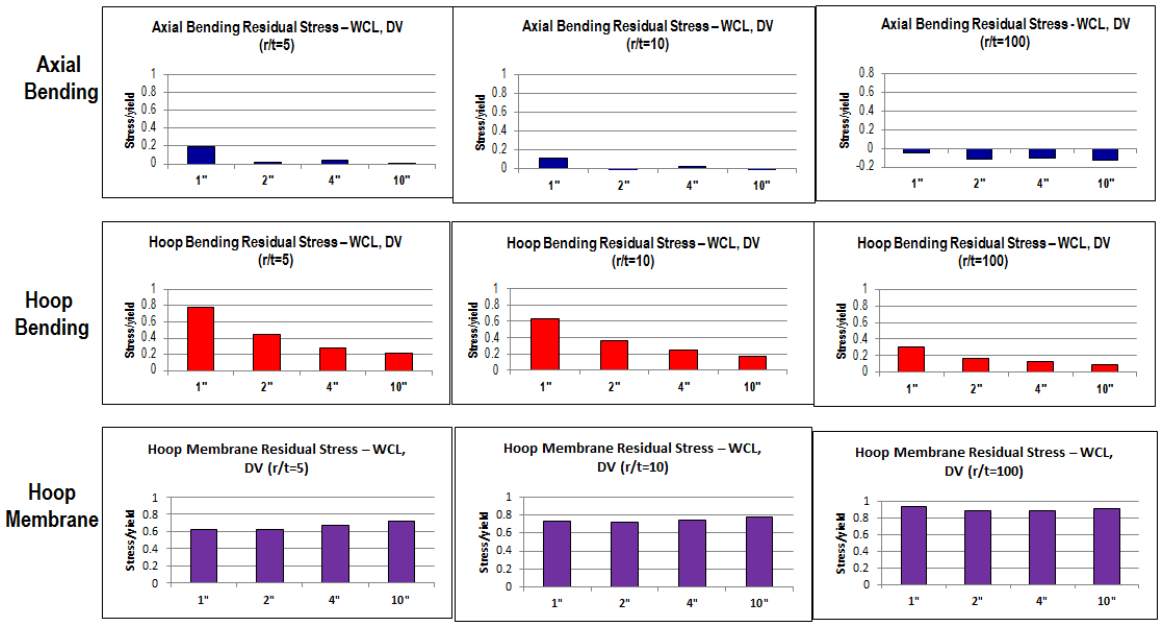

Figure 4-48 Decomposed residual stress components at WCL as a function of thickness for DV girth welds: axial bending components, hoop bending components, and hoop membrane components

Figure 4-49, Figure 4-50 and Figure 4-51 show some of the representative decomposed residual stress results, normalized by the material yield strength along weld toe (WT), for Single-V welds, Narrow Groove welds, and Double-V welds, respectively. Without the complex interactions among weld passes, some of trends can be clearly observed:

Single-V and Double-V: Axial and Hoop bending components increase from ¼" thickness to about 1", and then remain constant up to thickness of 10". The decomposed membrane part of hoop residual stress decreases as thickness increases.

Narrow Groove: The composed bending parts of axial and hoop residual stresses remain rougly the same with increasing thickness. No clear trend can be found for the hoop membrane component.

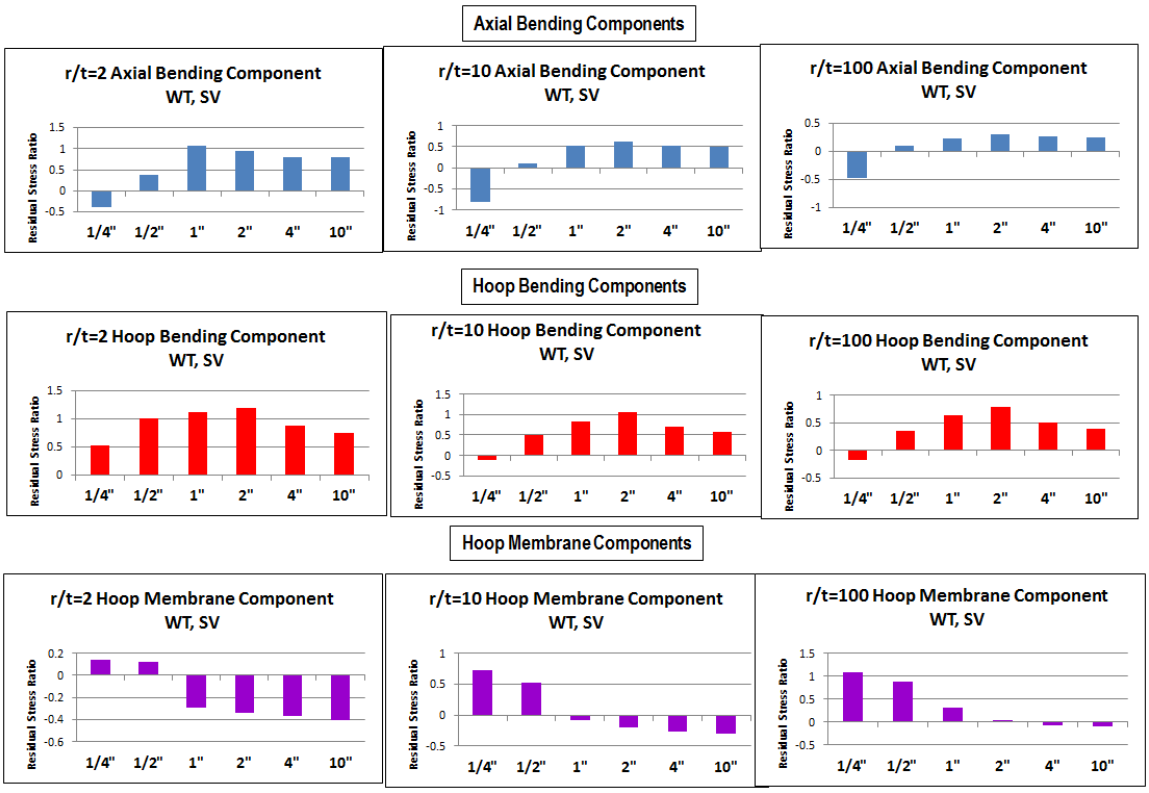

Figure 4-49 Decomposed residual stress components at WT as a function of thickness for SV girth welds: axial bending components, hoop bending components, and hoop membrane components

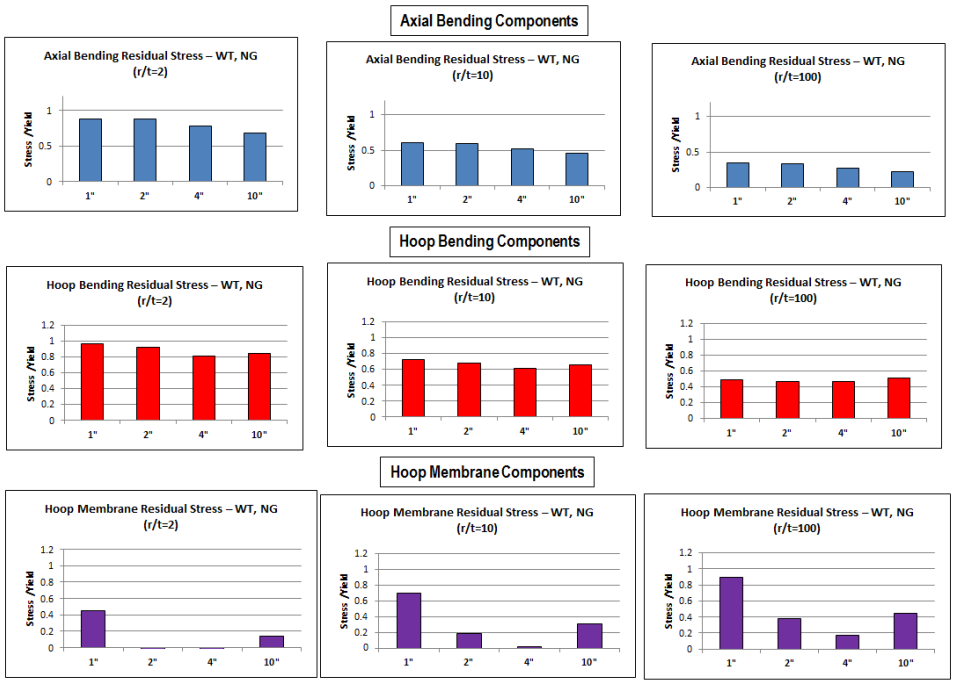

Figure 4-50 Decomposed residual stress components at WT as a function of thickness for NG girth welds: axial bending components, hoop bending components, and hoop membrane components

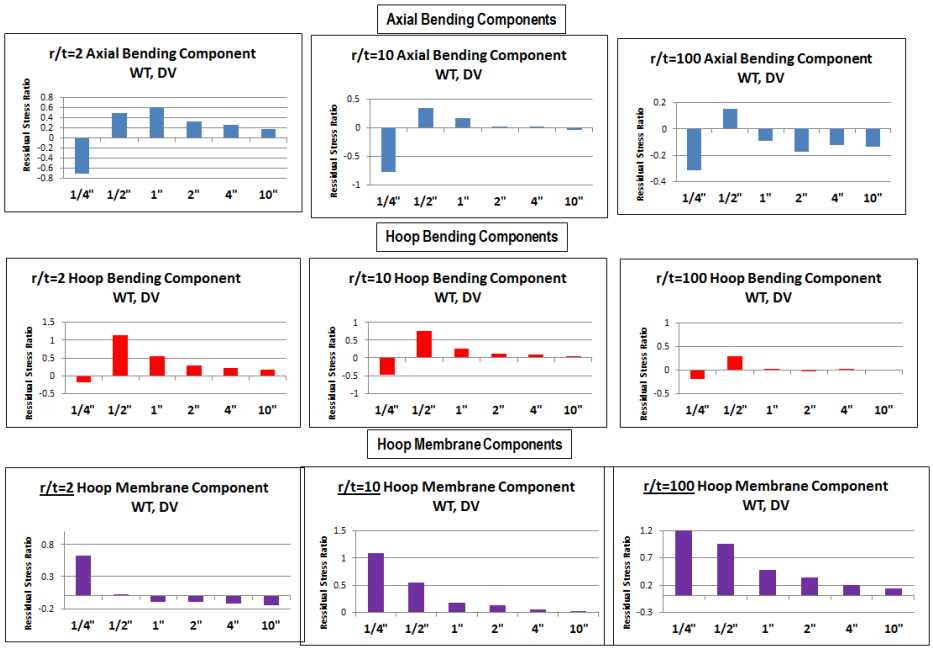

Figure 4-51 Decomposed residual stress components at WT as a function of thickness for DV girth welds: axial bending components, hoop bending components, and hoop membrane components

In summary, the observations obtained from the decomposed residual stresses for the wall thickness effects are shown in Table 4-3. From the discussion above, thickness effects are related to the characteristic types of through-thickness residual stress distribution, which has three distinct types: global bending, local bending, and self-equilibrating type. However, overall there are no clear independent effects of thickness, which requires further investigation.

Table 4-3 Observations of thickness effects

With increasing thickness (t is from ¼" to10"), decomposed residual stress components would be						
	at Weld Centerline			at Weld Toe		
	Axial bending	Hoop bending	Hoop membrane	Axial bending	Hoop bending	Hoop membrane
Single-V	Increase (1/4"-1") Constant (1"-10")	Increase (1/4"-1") Constant (1"-10")	N/A	Increase (1/4"-1") Constant (1"-10")	Increase (1/4"-1") Constant (1"-10")	decrease
Narrow Groove	constant	constant	constant	constant	constant	N/A
Double-V	Negligible	decrease	constant	Increase (1/4"-1") Constant (1"-10")	Increase (1/4"-1") Constant (1"-10")	decrease

4.4 Material effects

For all of the parametric analyses discussed in the previous sections, the material used is the ferritic steel 2.25CrMo-V. It is of interest to investigate some other common materials used in the pressure vessel community, e.g., stainless steel, INCO600, etc.

4.4.1 Material properties

Recognizing the differences in material properties between low alloy and high alloy steels, it may be useful to shed some light on the differences and similarities in the residual stress distribution for these two kinds of alloys. Although the welding procedure and process parameters may be different in welding these two different materials in practice, for the sake of comparison purpose, it is assumed in this discussion that the welding parameters used are the same for welding the same girth weld configuration.

Some representative material properties and interpretations are summarized in Table 4-4 for 2.25 CrMo-V, 1.25CrMo, SS304, and INCO600. The material properties listed here is for room temperature. As we can see, the differences in conductivity result in different thermal diffusivity.

Low alloy steel has almost three times larger diffusivity than those of high alloy materials. Another important parameter is ΔT_p (Eq. 3.28) which is the temperature at which material yields. It is related to yield strength, Young's modulus, and thermal expansion coefficient. ΔT_p is a parameter contributing to the plastic zone size estimation. Figure 4-52shows the plastic zone size measured from weld toe for each material. Since SS304 and INCO600 share almost the identical ΔT_p, only SS3034 is considered in this comparison. As can be seen, the plastic zone size decreases with increasing ΔT_p. It is due to the higher ΔT_p, the higher temperature is needed to yield the material and generate plastic strain. The analytical relationship between ΔT_p and plastic zone size will be elaborated in the later section.

Table 4-4 Comparison of important properties and their interpretations

At Room Temperature	2.25CrMo-V	1.25CrMo	SS304	INCO600
Density [g/cm³]	7.84	7.84	7.86	7.8
Conductivity [W/m/°C]	36.5	42.6	15.4	14.8
Specific Heat [J/g/°C]	0.448	0.514	0.476	0.486
Thermal Expansion [1E-6/mm/°C]	13.8	11.6	15.5	12.3
Thermal Diffusivity [mm²/s]	**10.39**	**10.57**	**4.12**	**3.9**
Young's Modulus [Gpa]	220.448	212.7	199.3	213.2
Yield Strength [Mpa]	**558**	**342**	**310.6**	**272**
ΔTp [°C]	**183.4**	**138.6**	**100.54**	**103.7**

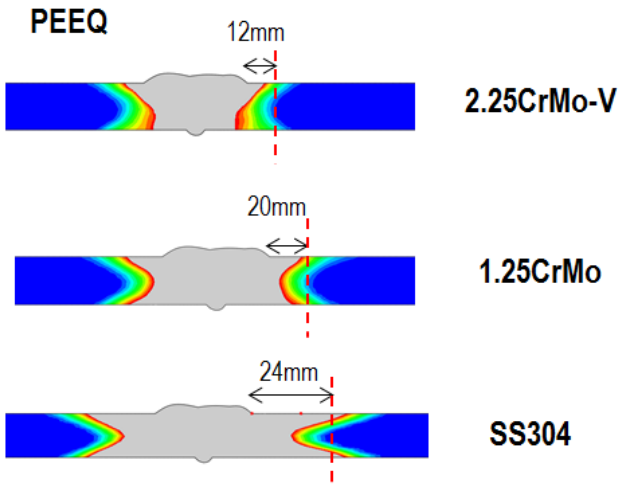

Figure 4-52 As-welded plastic zone size comparison

4.4.2 Residual Stress Distribution

Figure 4-53 exhibits contour plots of axial and hoop residual stresses for the four materials summarized in Table 3-4. Contour scale is from the negative value of material yield to the

positive one. It can be seen that the overall residual stress distributions are almost the same, except for some local variations. Through-thickness axial residual stress distribution is in the middle of transition from local bending to global bending. Detailed line plots along weld centerline and weld toe are shown in Figure 4-54 and Figure 4-55, respectively, for 2.25CrMo-V and INCO600. The residual stress magnitude is normalized by the yield strength of the corresponding material, and the horizontal axis is the normalized distance by thickness. It is seen from the plots that there are no significant differences in the overall distributions between these two materials.

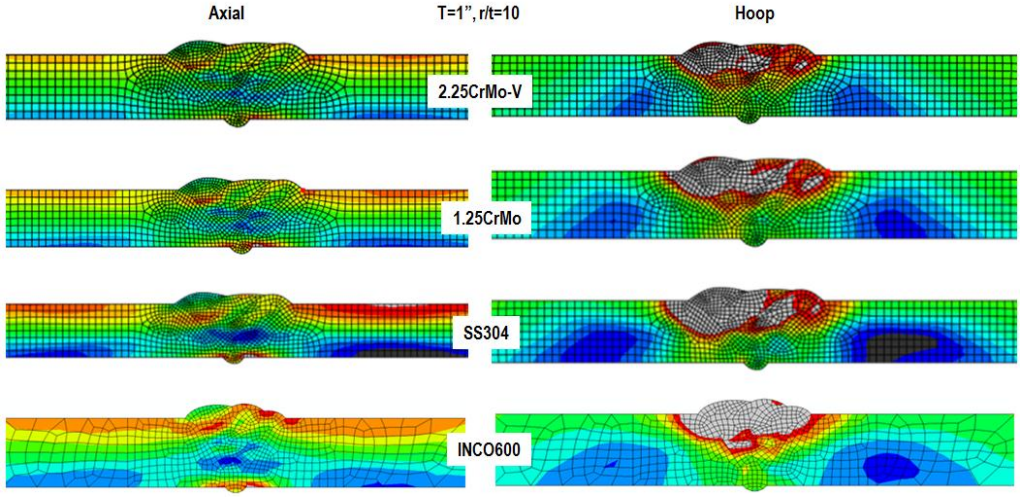

Figure 4-53 Comparison of contour plots for t=1", r/t=10 SV girth welds: 2.25CrMo-V, 1.25CrMo, SS304, and INCO600.

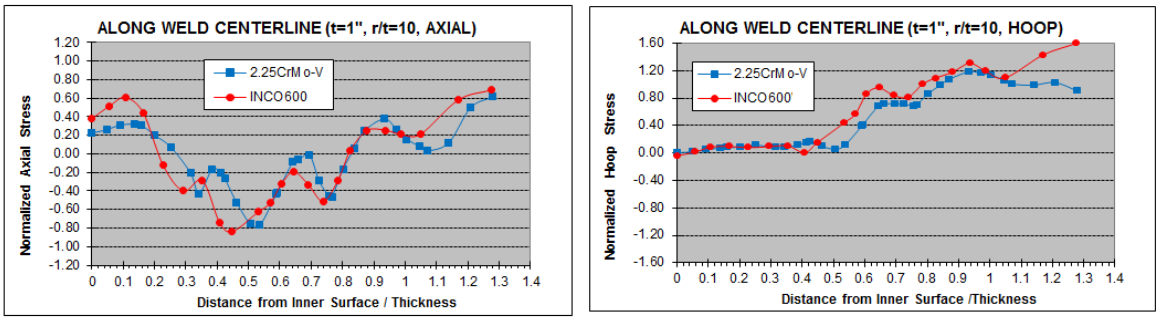

Figure 4-54 Residual stress distribution line plots along weld centerline for t=1", r/t=10 girth welds: 2.25CrMo-V, INCO600

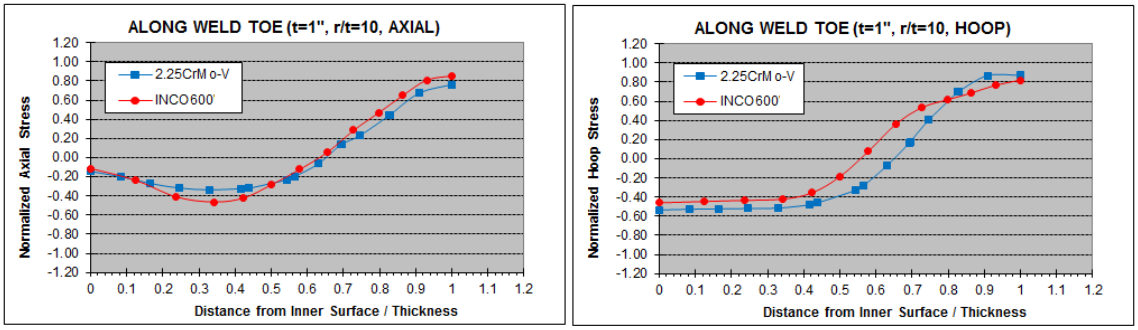

Figure 4-55 Residual stress distribution line plots along weld toe for t=1", r/t=10 girth welds: 2.25CrMo-V, INCO600

4.5 Heat Input Effects

As discussed in the Phase I report [13], actual welding parameters based heat input such as linear heat input with a unit of J/mm should be rephrased in the form of characteristic heat input per unit area (e.g., J/mm^2) or per unit volume (J/mm^3), depending upon its demonstrated ability to correlate a large number of residual stress distributions under different heat input conditions.

In the Phase II investigation, it is found that a parameter $\hat{Q}$ (referred to as characteristic heat input), as defined below, is effective in correlating a large number of residual stress distributions.

$$\hat{Q} = \frac{Q'}{A_{pass}} \cdot t_n \qquad \textbf{(4.2)}$$

where Q' stands for linear heat input having a dimension of J/mm discussed in the previous chapter, A_{pass} is the average pass area and t_n represents weld pass layer thickness. Q' can be calculated by Eq. (2.1) if actual welding parameters are known, or by Eq. (3.23) with η'= 1.35 based on FE model or macrograph of cross section. $\hat{Q}$ has a dimension of J/mm^2. Here, $\hat{Q}$ can be interpreted as a heat put per unit weld layer cross-section area.

Figure 4-56 shows the detailed parameters needed for calculating $\hat{Q}$ using Eq. (3.20) and (3.21), and the decomposed residual stress components, normalized by the material yield strength at weld toe location for Single-V girth welds, with respect to characteristics linear heat input $\hat{Q}$. Please note that the parameters exhibited in Figure 4-56(a) are obtained by carefully examining the 2D weld profiles shown in Figure 4-2. The results in (b)-(d) demonstrate that $\hat{Q}$ can well distinguish the pipe geometry effect (r/t and t) for Single-V welds. The results for Double-V girth welds are summarized in Figure 4-57 in the same manner as a function of $\hat{Q}$. It can be seen that the proposed parameter $\hat{Q}$ is effective in correlating a large number of residual stress distributions related to r/t ratio and thickness effects.

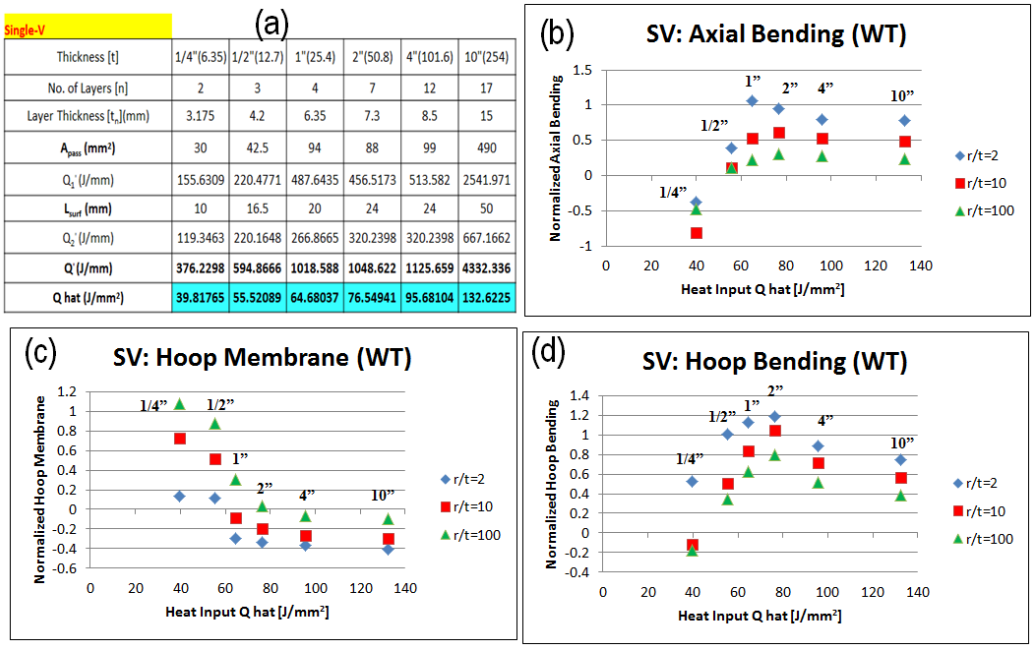

Figure 4-56 Decomposed residual stress components at WT as a function of characteristics heat input $\hat{Q}$ for SV girth welds: (a) detailed parameters for $\hat{Q}$ calculation, (b) axial bending component, (c) hoop membrane component and (d) hoop bending component

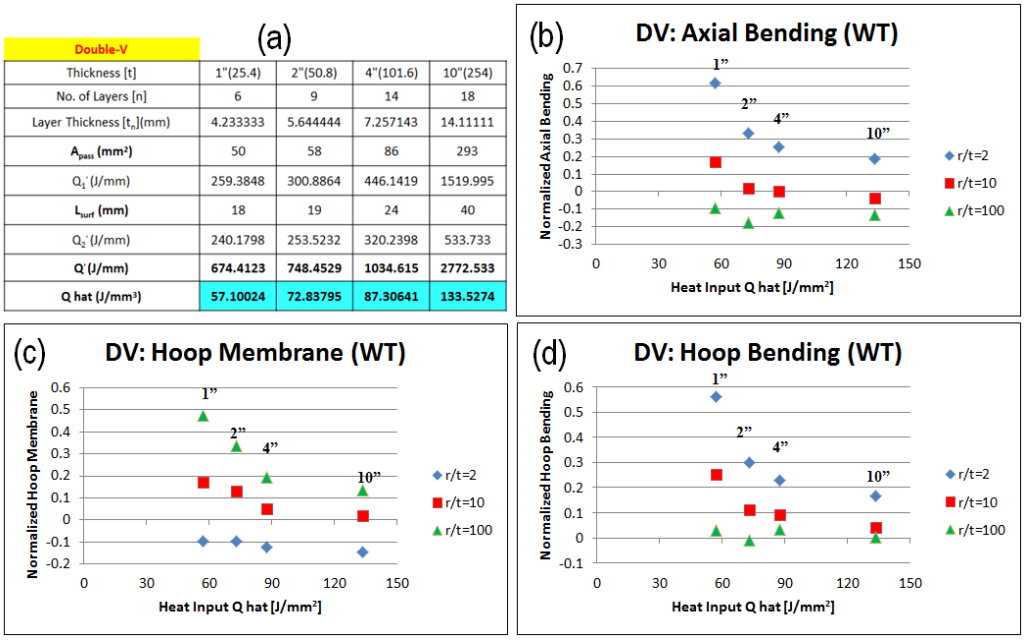

Figure 4-57 Decomposed residual stress components at WT as a function of characteristics heat input $\hat{Q}$ for DV girth welds: (a) detailed parameters for $\hat{Q}$ calculation, (b) axial bending component, (c) hoop membrane component and (d) hoop bending component

With the demonstrated ability of distinguishing the effects of r/t ratio and thickness for residual stress distribution of pipe girth welds, $\hat{Q}$ is then used for lumped pass effects. Figure 4-58 shows detailed parameters needed for calculating $\hat{Q}$ using Eq. (3.23) and (4.2), and decomposed residual stress components, normalized by the material yield strength at weld centerline location for 1" thickness Narrow Groove girth welds, with respect to characteristics linear heat input $\hat{Q}$. The results for thickness of 2", 4", and 10" Narrow Groove welds are summarized in the same manner in Figure 4-59, Figure 4-60, and Figure 4-61, respectively. The overall results clearly indicate that characteristic linear heat input $\hat{Q}$ can differentiate lumped pass effects. It is interesting to note that decomposed residual stress components remain constant when heat input is small. This suggests that there exists a maximum characteristic linear heat input below which the decomposed residual stress components no longer changes in any significant manner. This means that if t_n (=t/n) is decreased below a certain value residual stress components would remain roughly the same (since $\hat{Q} = t_n [Q_1'(A_{pass}) + Q_2'(A_{pass})] / A_{pass}$). This is consistent with the finding in lumped pass effects.

(a)

Narrow Groove 1", r/t=10						
No. of Layers [n]	20	10	8	6	4	2
Layer Thickness [t_n](mm)	1.27	2.54	3.175	4.233333	6.35	12.7
A_{pass} (mm²)	4.1	8.3	10.3	13.78	20.67	41.34
Q_1' (J/mm)	21.26956	43.05788	53.43328	71.48646	107.2297	214.4594
L_{surf} (mm)	4.5	5.7	6.4	7.4	9.5	14
Q_2' (J/mm)	60.04496	76.05695	85.39727	98.7406	126.7616	186.8065
Q' (J/mm)	**109.7746**	**160.805**	**187.4212**	**229.8065**	**315.8882**	**541.709**
Q hat (J/mm²)	**34.00335**	**49.21021**	**57.77305**	**70.59852**	**97.04355**	**166.4176**

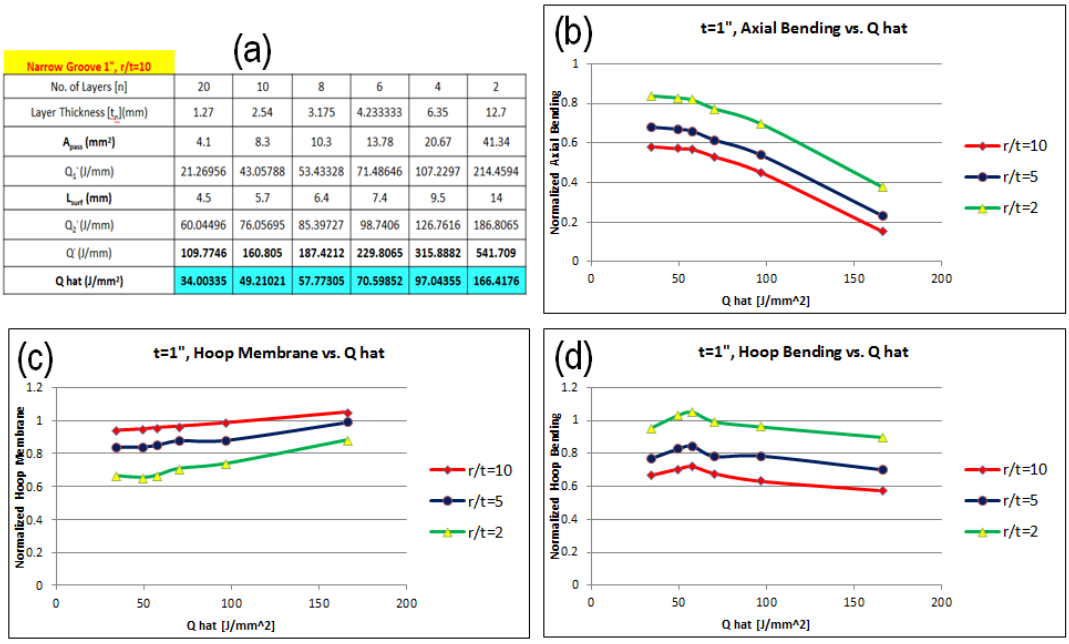

Figure 4-58 Decomposed residual stress components at WCL as a function of characteristics heat input $\hat{Q}$ for NG, t=1" girth welds: (a) detailed parameters for $\hat{Q}$ calculation, (b) axial bending component, (c) hoop membrane component and (d) hoop bending component

(a)

Narrow Groove 2",r/t=10						
No. of Layers [n]	20	10	8	6	4	2
Layer Thickness [t_{cc}](mm)	2.543	5.086	6.3575	8.476667	12.715	25.43
A_{pass} (mm²)	21	42	52.5	70	105	210
Q_1' (J/mm)	108.9416	217.8833	272.3541	363.1388	544.7081	1089.416
L_{surf} (mm)	10.5	13	14.5	16.5	20.5	29.5
Q_2' (J/mm)	140.1049	173.4632	193.4782	220.1648	273.5381	393.6281
Q' (J/mm)	**336.2128**	**528.3177**	**628.8736**	**787.4599**	**1104.632**	**2002.11**
Q hat (J/mm²)	**40.71377**	**63.97676**	**76.15359**	**95.35764**	**133.7657**	**242.446**

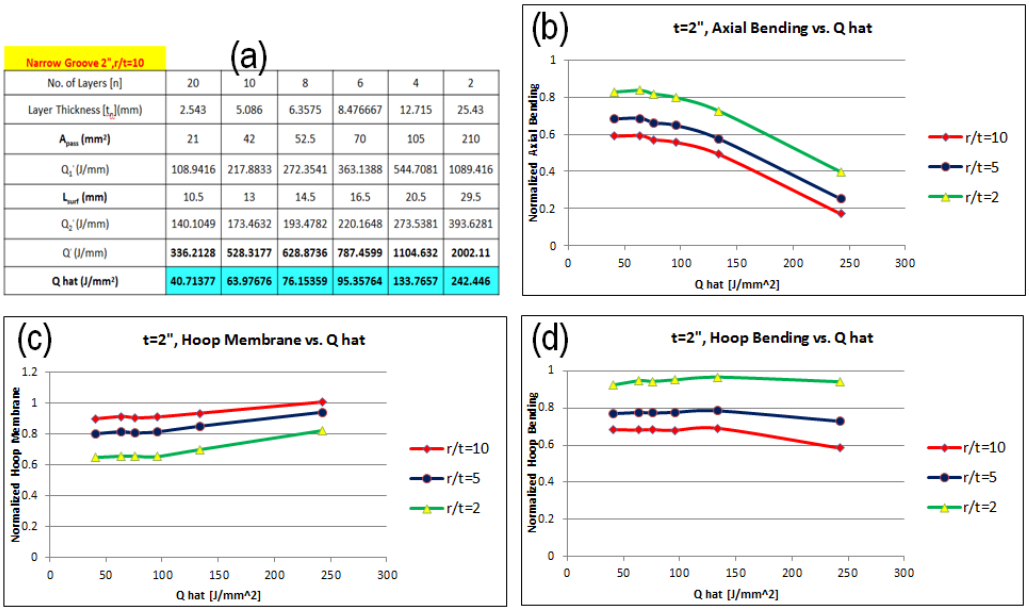

Figure 4-59 Decomposed residual stress components at WT as a function of characteristics heat input $\hat{Q}$ for NG, t=2" girth welds: (a) detailed parameters for $\hat{Q}$ calculation, (b) axial bending component, (c) hoop membrane component and (d) hoop bending component

(a)

Narrow Groove 4",r/t=10					
No. of Layers [n]	52	26	13	7	4
Layer Thickness [t_{cc}](mm)	1.953846	3.907692	7.815385	14.51429	25.4
A_{pass} (mm²)	23	45	90	180	300
Q_1' (J/mm)	119.317	233.4463	466.8927	933.7854	1556.309
L_{surf} (mm)	13	15	19	25	32
Q_2' (J/mm)	173.4632	200.1499	253.5232	333.5831	426.9864
Q' (J/mm)	**395.2533**	**585.3549**	**972.5614**	**1710.947**	**2677.449**
Q hat (J/mm²)	**33.5767**	**50.83082**	**84.4549**	**137.9621**	**226.6907**

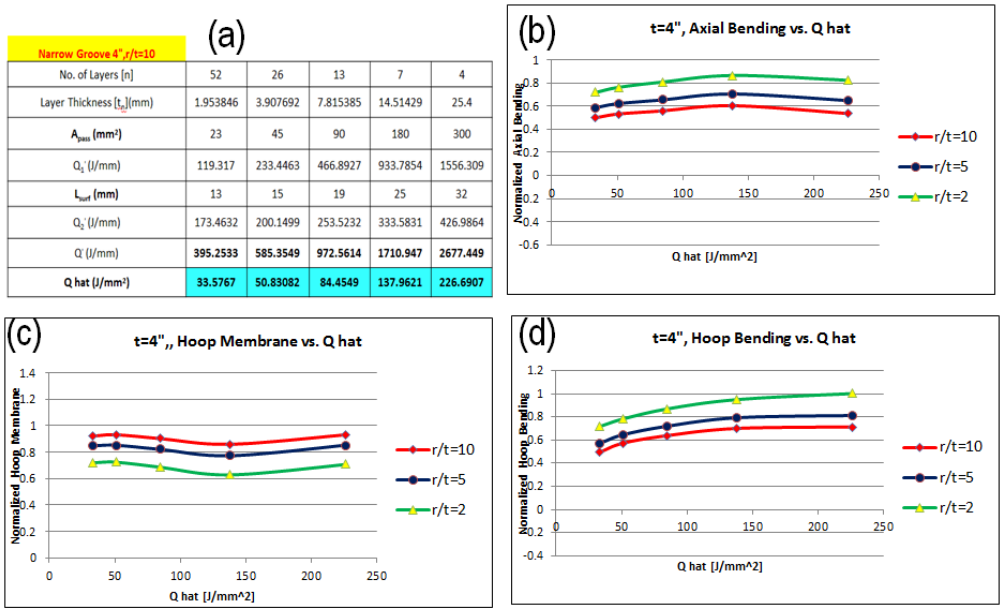

Figure 4-60 Decomposed residual stress components at WT as a function of characteristics heat input $\hat{Q}$ for NG, t=4" girth welds: (a) detailed parameters for $\hat{Q}$ calculation, (b) axial bending component, (c) hoop membrane component and (d) hoop bending component

(a)

Narrow Groove 10",r/t=10					
No. of Layers [n]	25	18	10	5	2
Layer Thickness [tn](mm)	10.16	14.11111	25.4	50.8	127
A_{pass} (mm²)	184	250	460	920	2300
Q_1' (J/mm)	954.5362	1296.924	2386.34	4772.681	11931.7
L_{surf} (mm)	28	33	45	65	130
Q2' (J/mm)	373.6131	440.3297	600.4496	867.3161	1734.632
Q' (J/mm)	**1793.001**	**2345.293**	**4032.167**	**7613.996**	**18449.55**
Q hat (J/mm²)	**99.00486**	**132.3787**	**222.6457**	**420.425**	**1018.736**

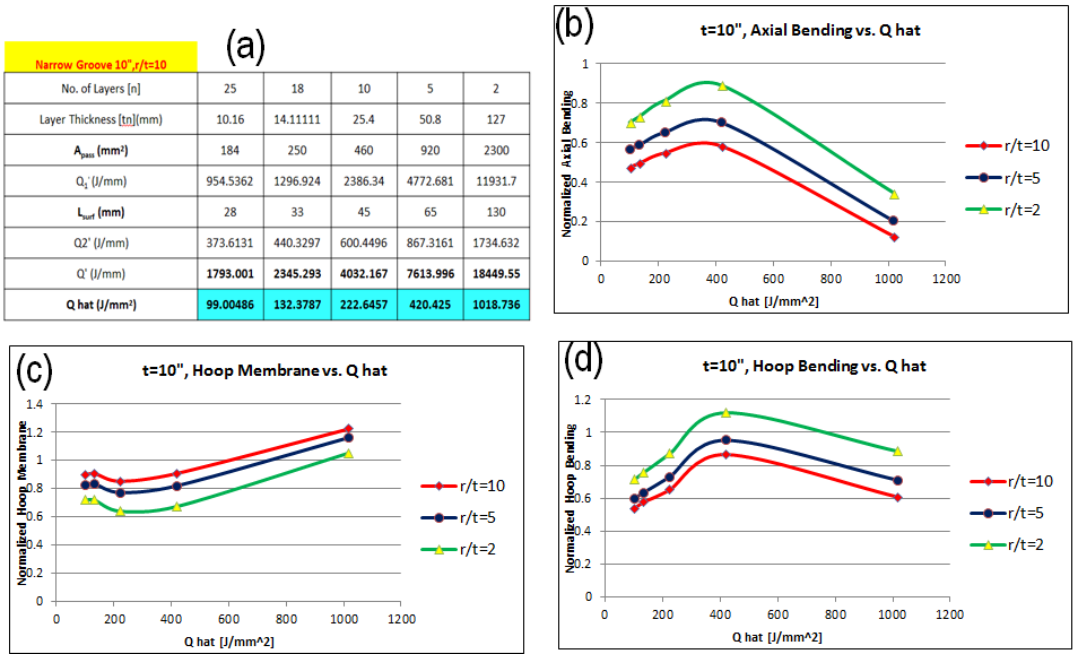

Figure 4-61 Decomposed residual stress components at WT as a function of characteristics heat input $\hat{Q}$ for NG, t=10" girth welds: (a) detailed parameters for $\hat{Q}$ calculation, (b) axial bending component, (c) hoop membrane component and (d) hoop bending component

4.6 Full-field generalizations (membrane, bending and self-equilibrating)

As demonstrated in the previous sections, high surface residual stresses can be present at quite a distance away from the weld area, which may have significant impact on fracture mechanics based structural integrity assessment. Consequently, it is of practical importance to have a full-filed residual stress distribution and understand its corresponding characteristics based on residual stress decomposition technique. So far, the discussion on residual stress characteristics observed in terms of through-thickness membrane and bending are limited to the weld locations, e.g., at weld centerline and weld toe locations. There is a need to establish these membrane and bending components away from weld locations until they become negligible.

In doing so, some through-thickness locations within and away from a weld (e.g., red dotted lines in Figure 4-62) are selected for performing residual stress decomposition according to Eq. (4.1). The number of selected locations should be large enough in order to accurately obtain a full-filed residual stress distribution. The representative through-thickness residual stress distribution (e.g., location of highest bending, stress transition) needs to be well captured. Once membrane and bending components at each location are obtained, stresses along OD are plotted as membrane plus bending components and compared with FE outer surface residual stress output. The stresses on ID are plotted as membrane plus opposite sign of OD bending against FE inner surface residual distribution. By definition (Eq. (4.1)), the difference between each pair is a surface value of the corresponding self-equilibrating part. The cases studied using above procedure are summarized in Table 4-5. The total number of cases for this study is 42.

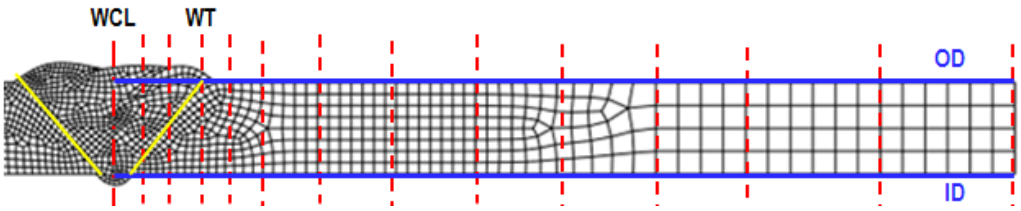

Figure 4-62 Representative through-thickness locations within and away from a Single-V weld selected for performing stress decomposition

Table 4-5 Analysis matrix for full-field generalizations

Single-V Double-V Narrow Groove		Wall Thickness			
		t=1”	t=2”	t=4”	t=10”
r/t	r/t=2	X	X	X	X
	r/t=5	X			
	r/t=10	X	X	X	X
	r/t=20	X			
	r/t=100	X	X	X	X

4.6.1 Results for membrane and bending components of through-thickness residual stress in pipe axial direction

Figure 4-63 shows the through-thickness axial (perpendicular) and hoop (parallel) residual stress components, normalized by the material yield strength, in comparison with the surface residual stress obtained from FEA for Single-V girth weld of 1” thickness and r/t ratio of 2. The horizontal axis is measured from weld centerline and normalized by $\sqrt{rt}$. Blue squares denote the surface residual stress values directly extracted from FEA, while yellow triangles represent the membrane component at each through-thickness location, red round for bending component, and purple diamond for membrane plus bending (bending on ID is with opposite sign of the one on OD). Axial membrane component is negligible due to free end condition in axial direction, as shown in Figure 4-63(a) and (c). It can be seen that after a certain distance from weld, the results of membrane plus bending perfectly match surface residual stress obtained directly from FEA in all plots. This indicates that self-equilibrating part is only existed within a certain range from weld. Beyond this range, the self-equilibrating part is vanished. Along this line of thinking, the followings questions need to be answered:

1. How to estimate residual stress profiles of membrane and bending components along pipe axial direction at each through-thickness location

2. How to determine the location where the self-equilibrating part is vanished

3. How to estimate residual stress profile of self-equilibrating part within the weld

If the answers to these 3 questions are known, a full-field residual stress distribution can then be obtained. These answers will be explored in later sections.

For other thickness and r/t ratio cases listed in Table 3-4 for the Single-V weld, similar observations can be obtained. The results are summarized in the same manner from Figure 4-63 to Figure 4-76. For completeness, the results for Narrow Groove and Double-V welds are summarized from Figure 4-77 to Figure 4-88 and Figure 4-89 to Figure 4-100, respectively.

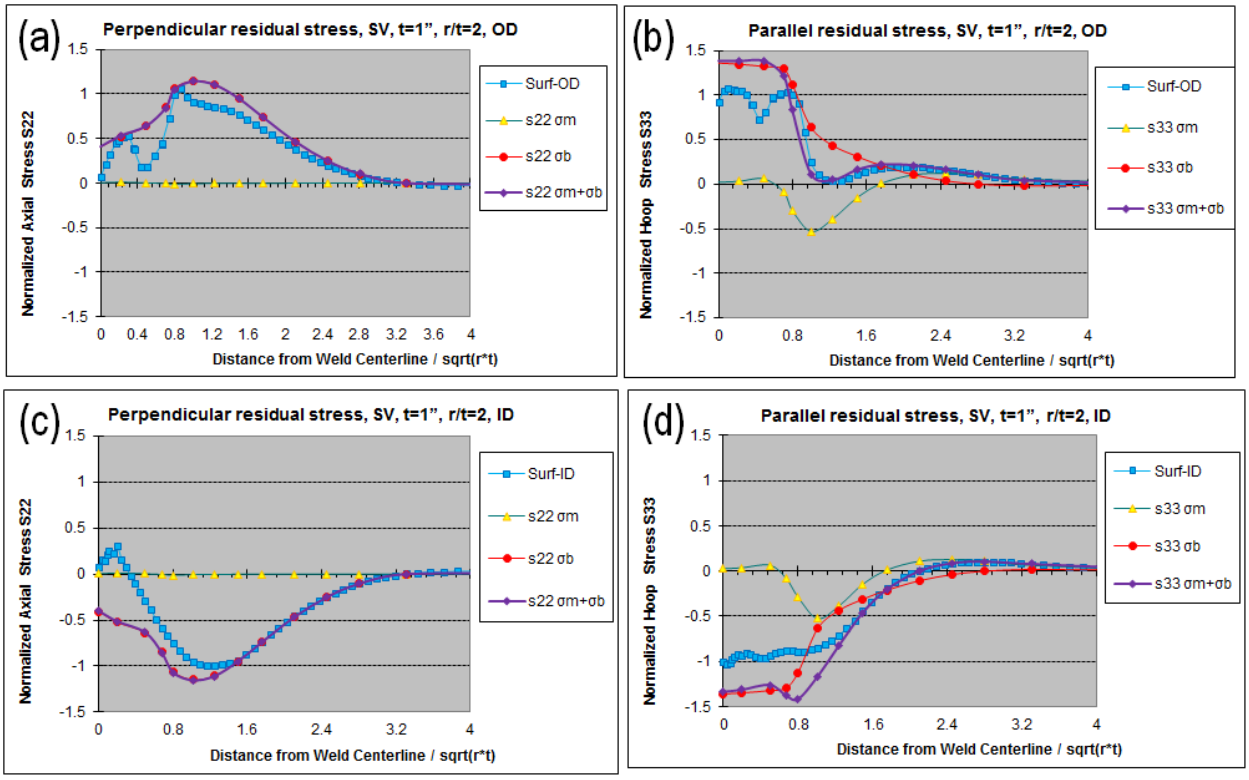

Figure 4-63 SV with t=1", r/t=2 through-thickness axial and hoop residual stress components along OD and ID

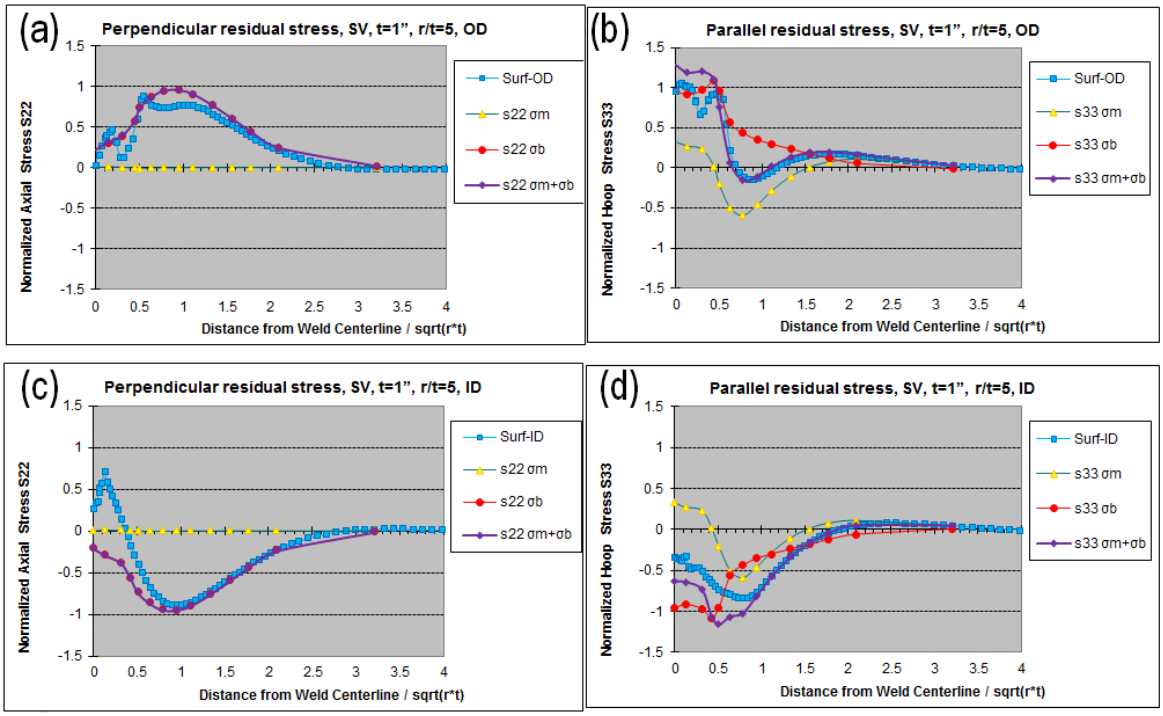

Figure 4-64 SV with t=1", r/t=5 through-thickness axial and hoop residual stress components along OD and ID

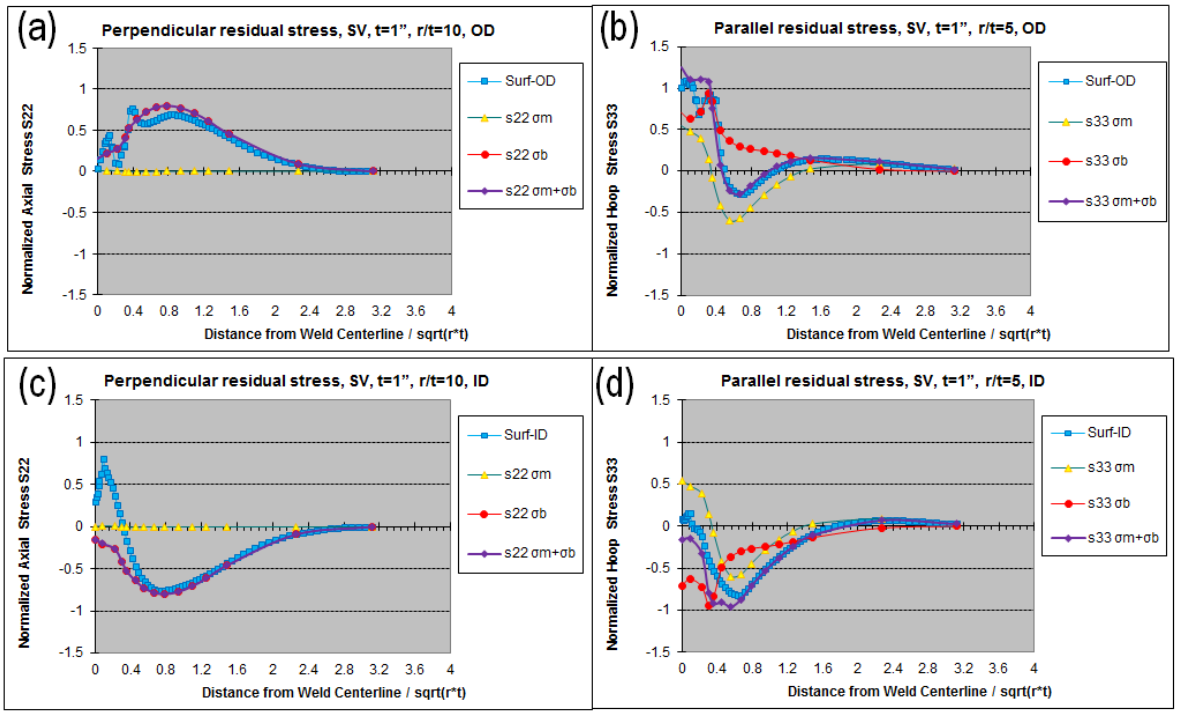

Figure 4-65 SV with t=1", r/t=10 through-thickness axial and hoop residual stress components along OD and ID

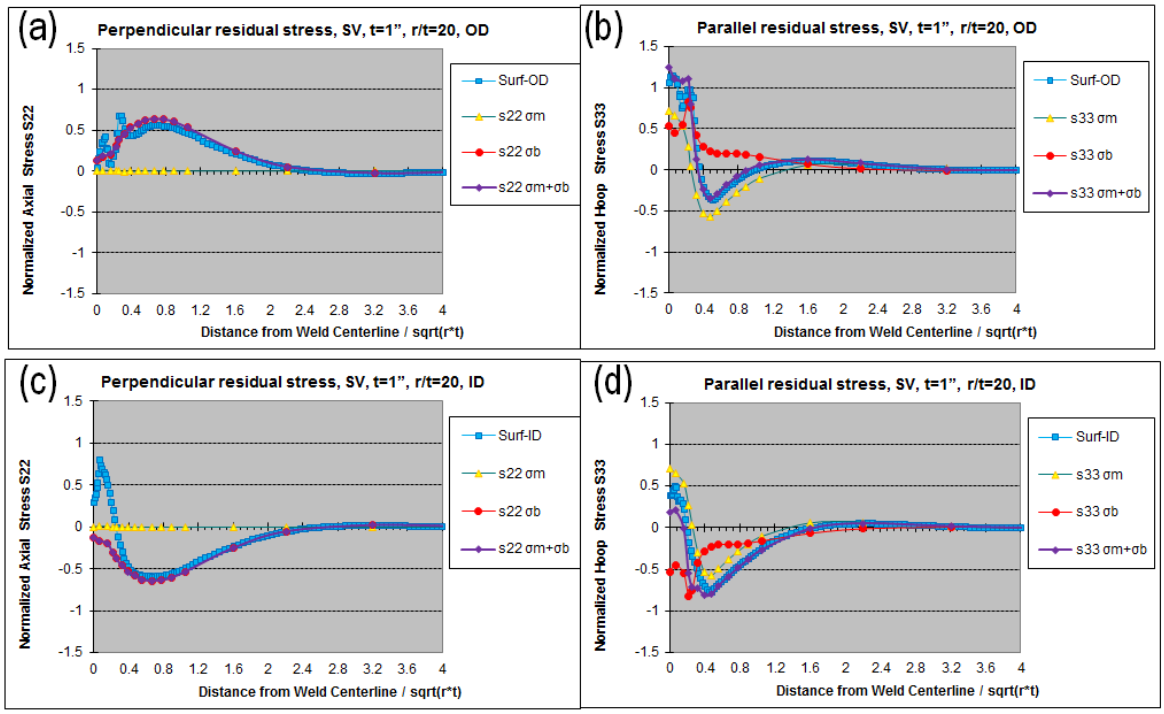

Figure 4-66 SV with t=1", r/t=20 through-thickness axial and hoop residual stress components along OD and ID

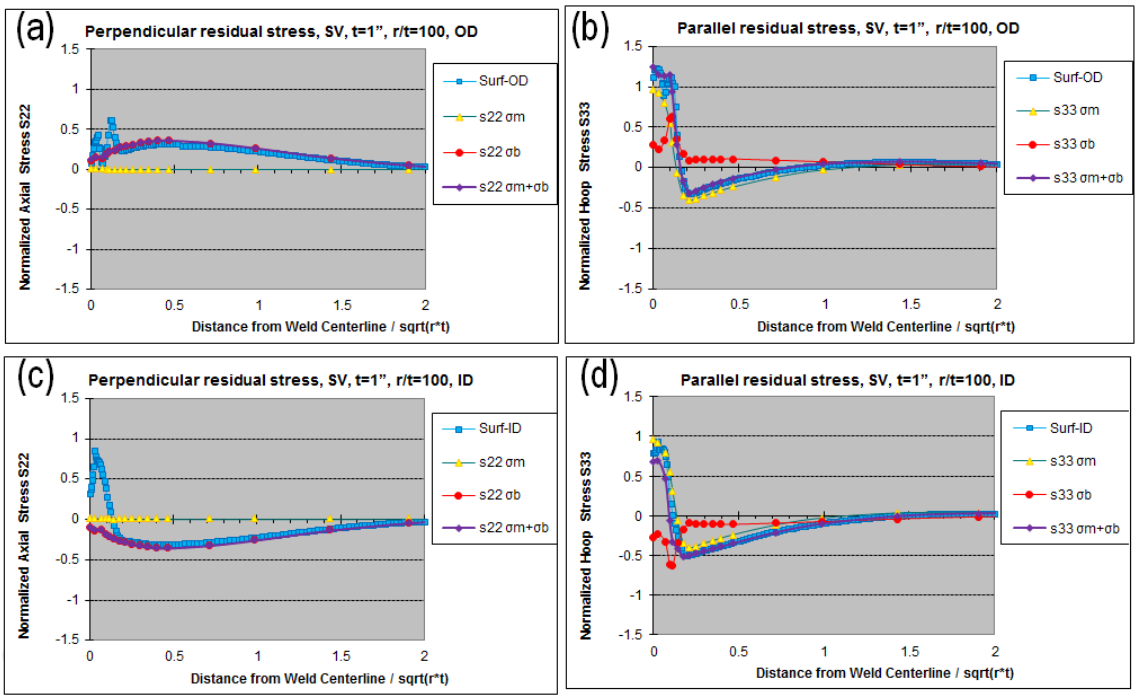

Figure 4-67 SV with t=1", r/t=100 through-thickness axial and hoop residual stress components along OD and ID

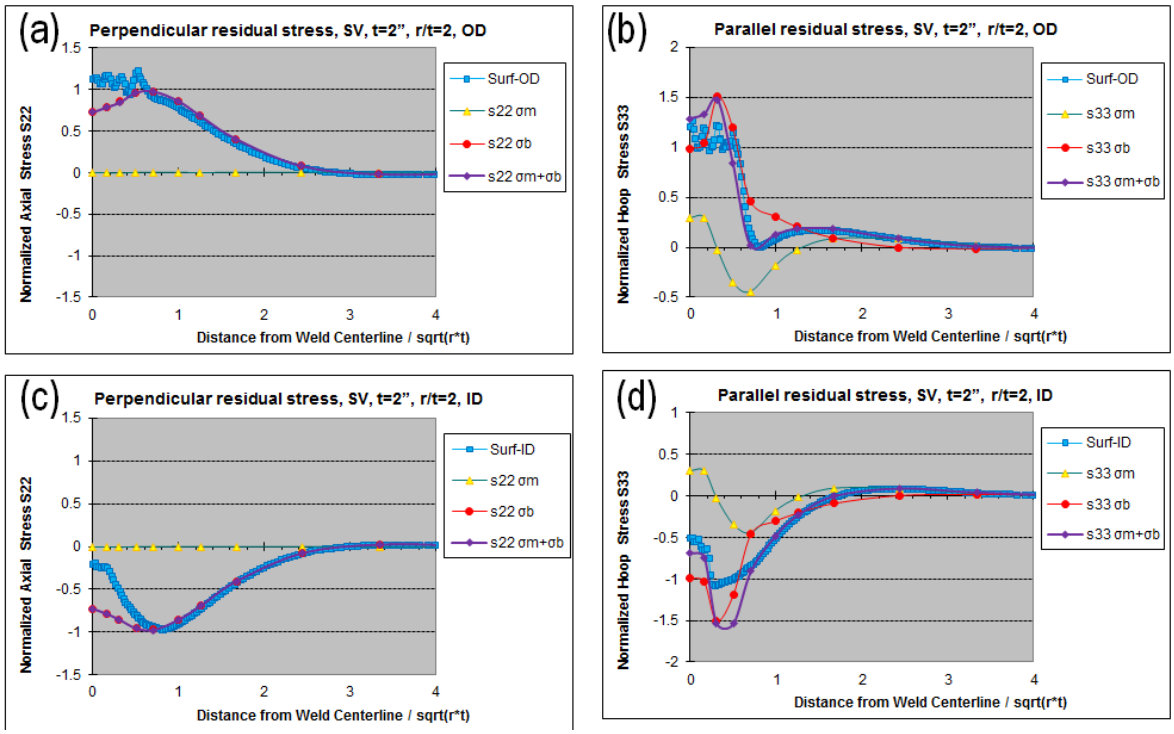

Figure 4-68 SV with t=2", r/t=2 through-thickness axial and hoop residual stress components along OD and ID

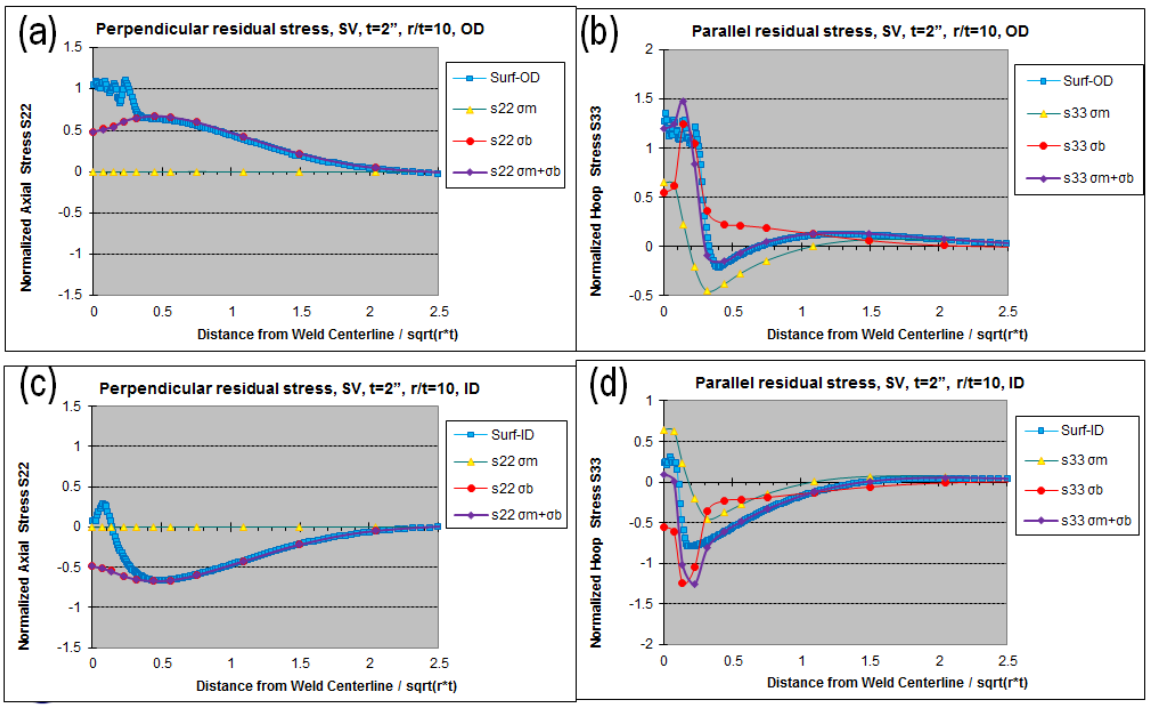

Figure 4-69: SV with t=2", r/t=10 through-thickness axial and hoop residual stress components along OD and ID

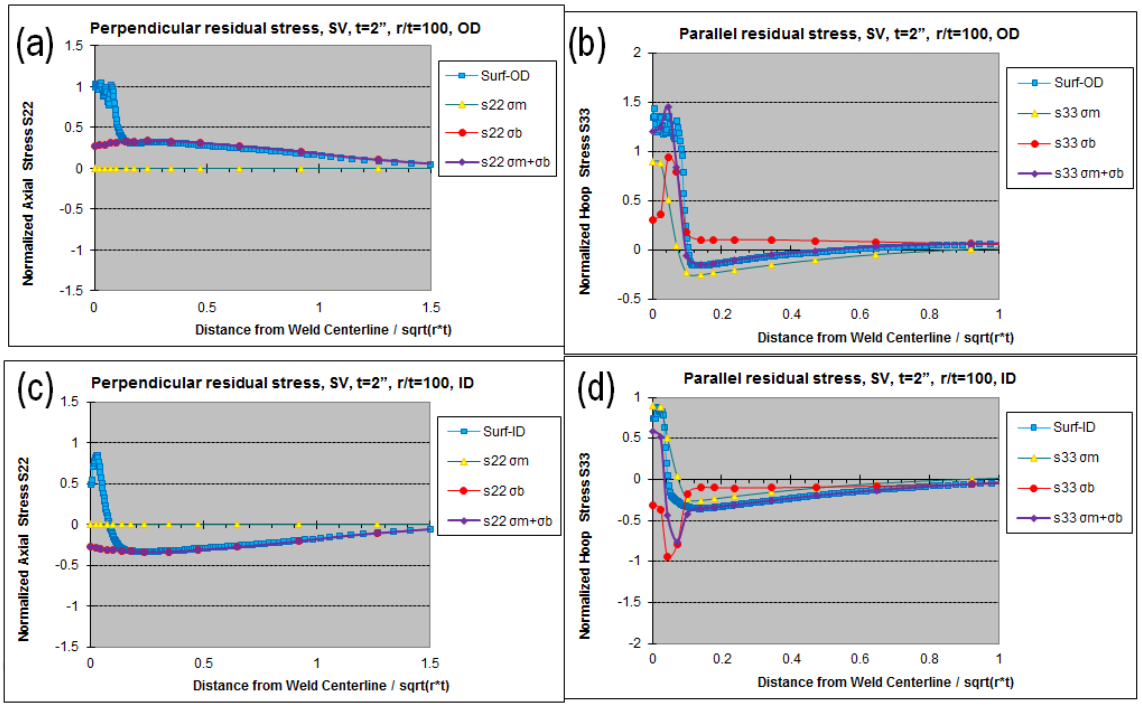

Figure 4-70 SV with t=2", r/t=100 through-thickness axial and hoop residual stress components along OD and ID

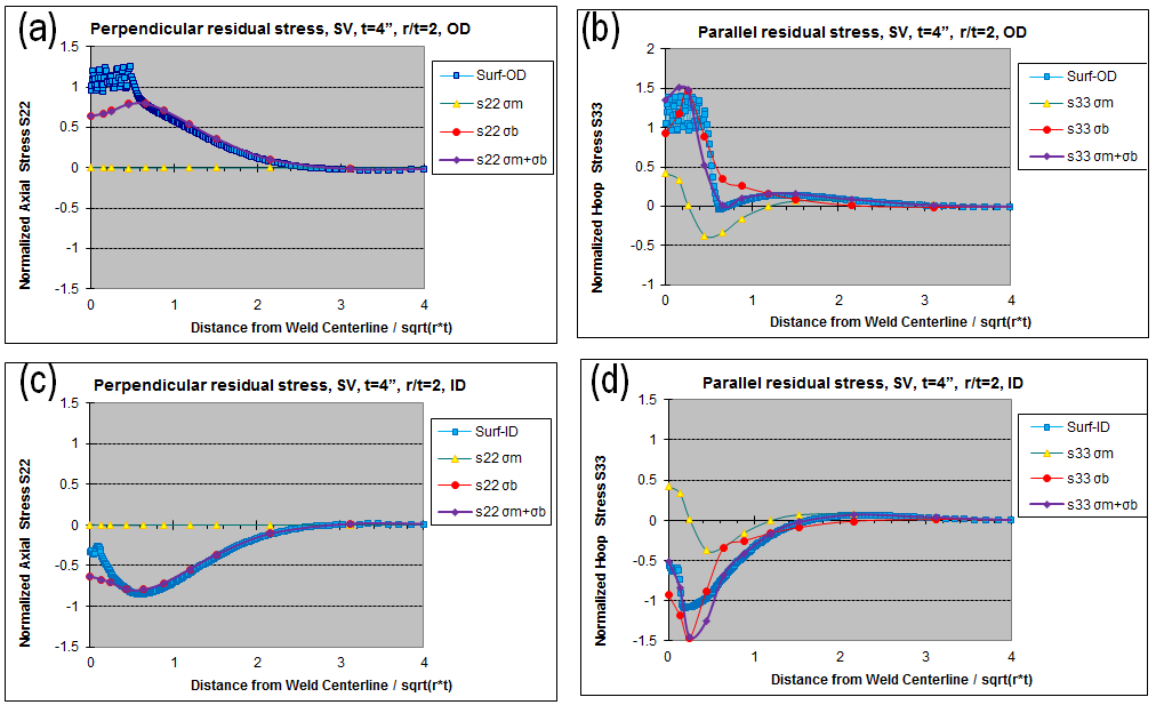

Figure 4-71 SV with t=4", r/t=2 through-thickness axial and hoop residual stress components along OD and ID

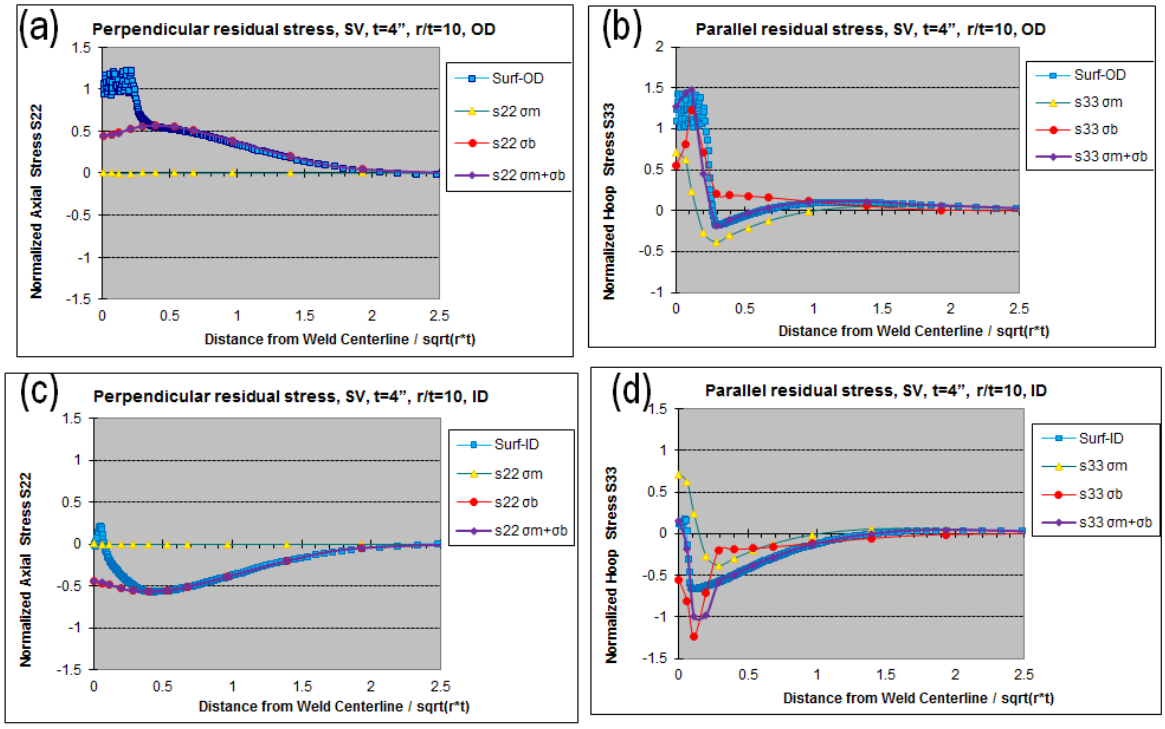

Figure 4-72 SV with t=4", r/t=10 through-thickness axial and hoop residual stress components along OD and ID

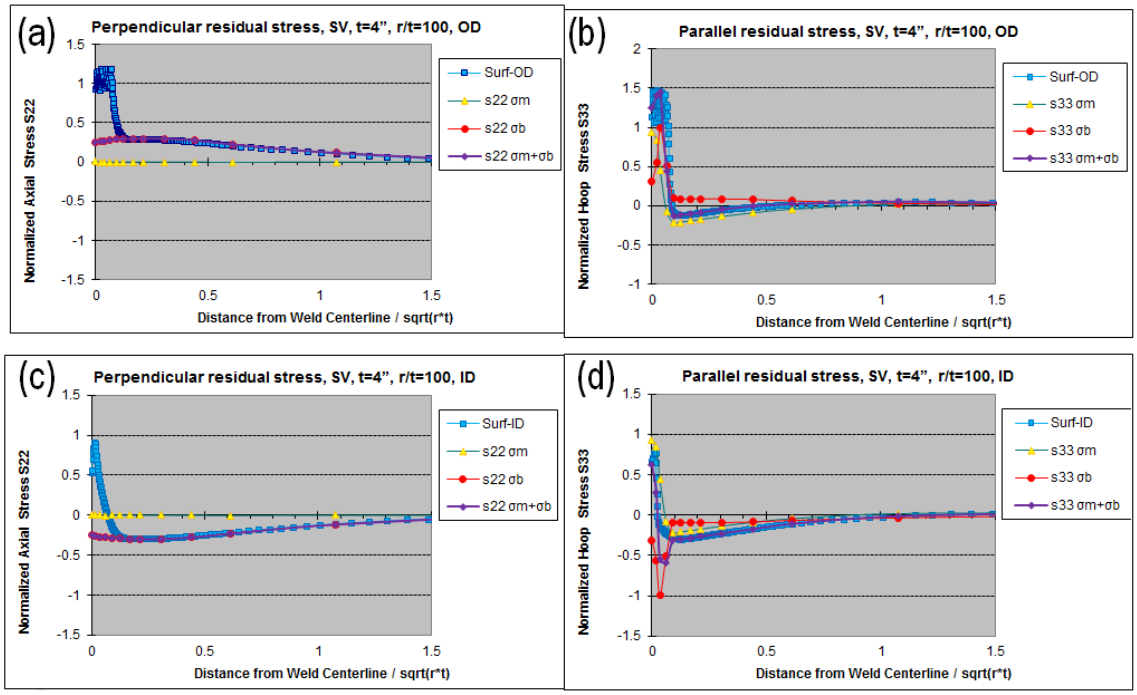

Figure 4-73 SV with t=4", r/t=100 through-thickness axial and hoop residual stress components along OD and ID

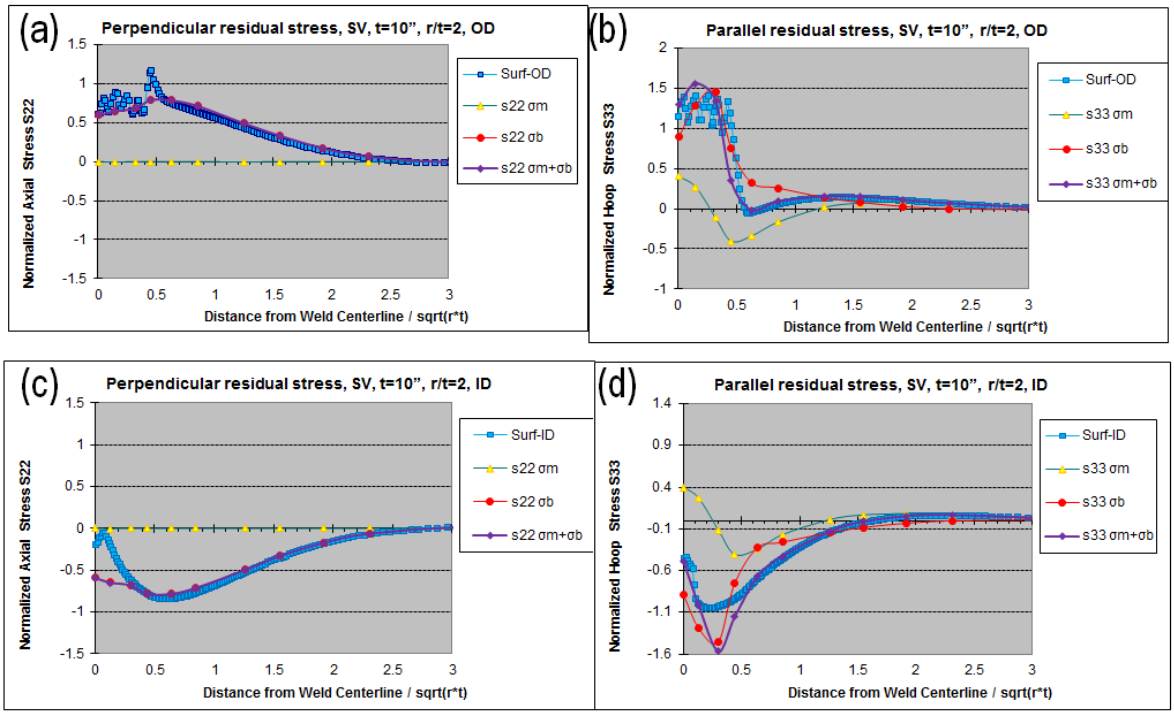

Figure 4-74 SV with t=10", r/t=2 through-thickness axial and hoop residual stress components along OD and ID

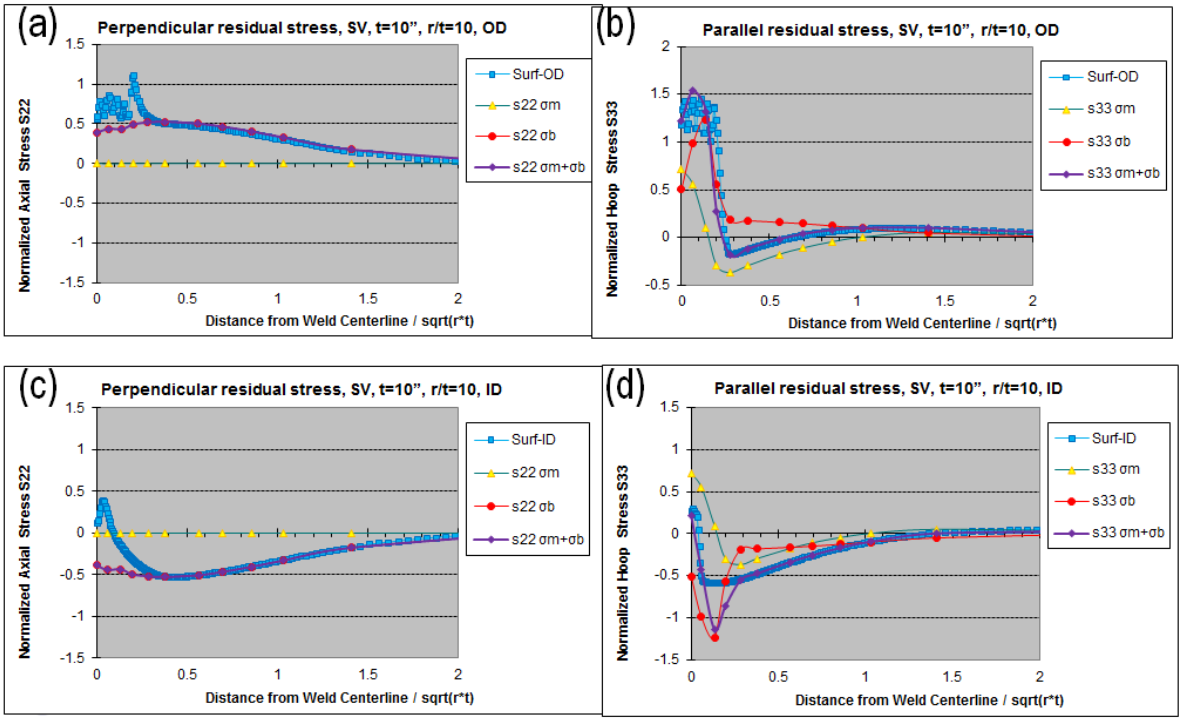

Figure 4-75 SV with t=10", r/t=10 through-thickness axial and hoop residual stress components along OD and ID

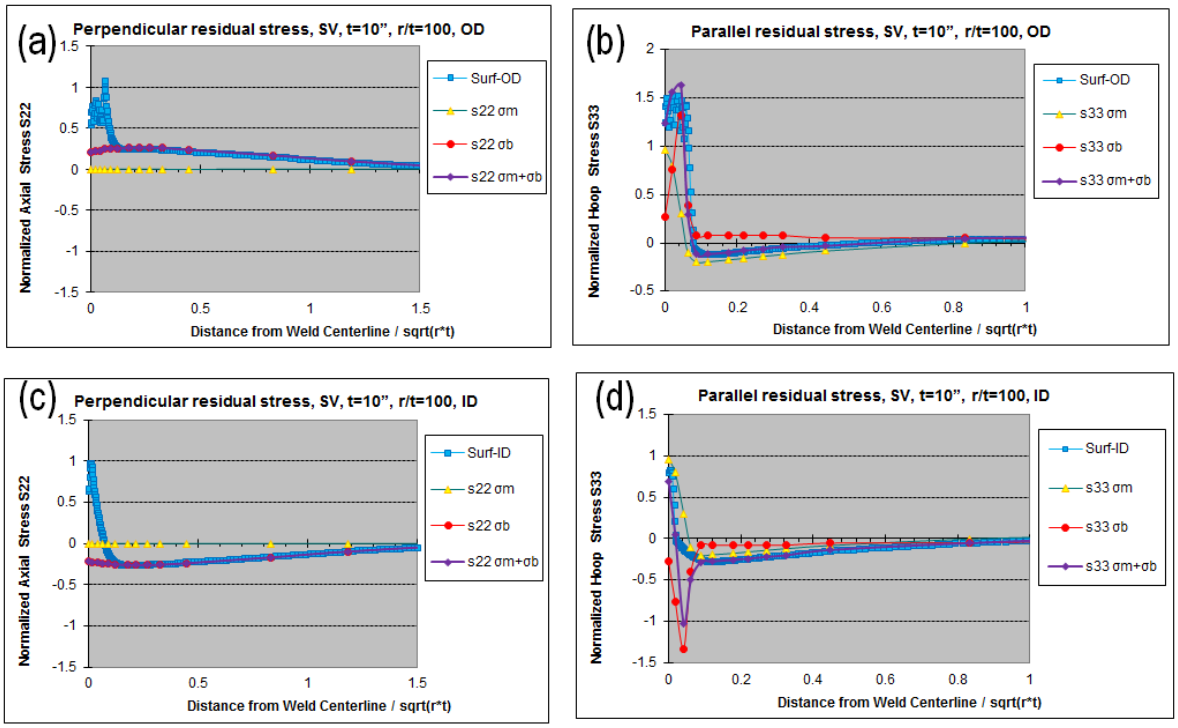

Figure 4-76 SV with t=10", r/t=100 through-thickness axial and hoop residual stress components along OD and ID

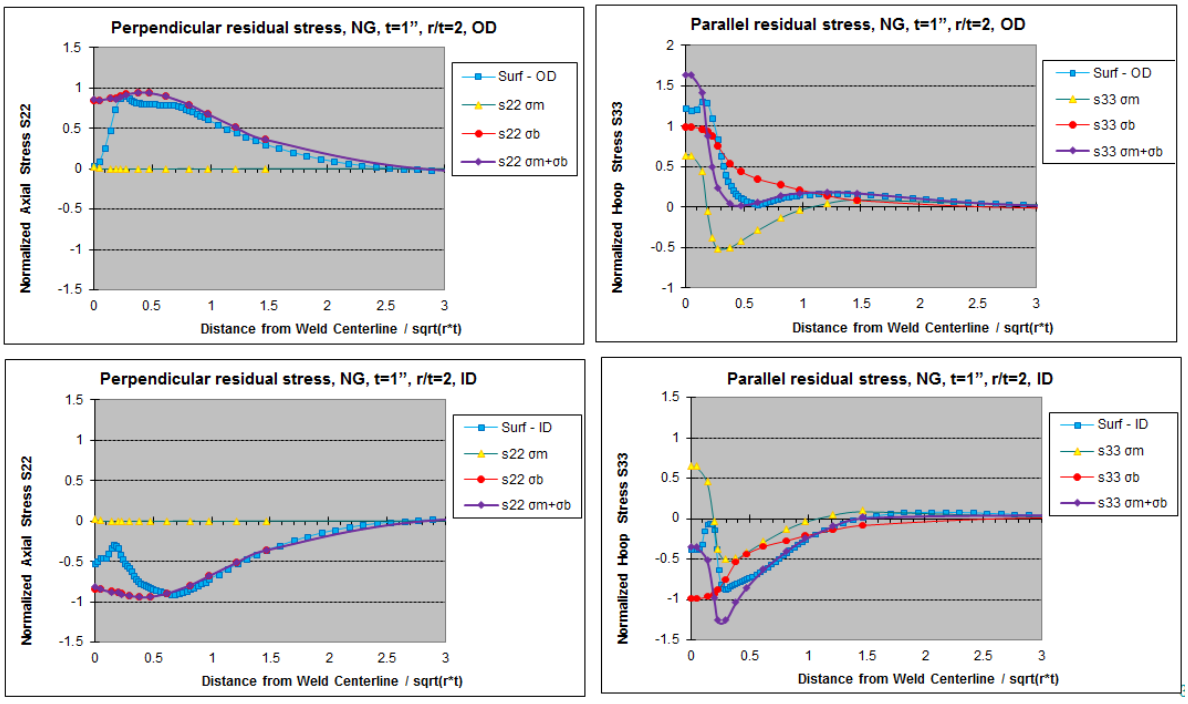

Figure 4-77 NG with t=1", r/t=2 through-thickness axial and hoop residual stress components along OD and ID

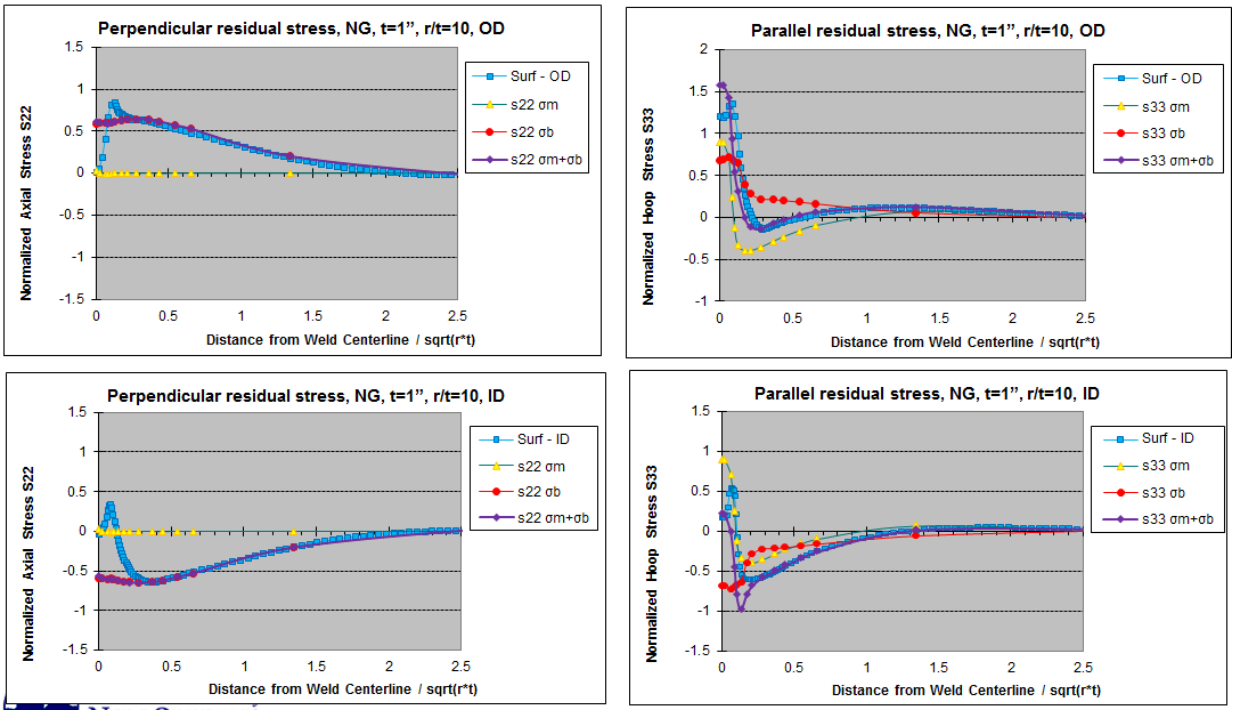

Figure 4-78 NG with t=1", r/t=10 through-thickness axial and hoop residual stress components along OD and ID

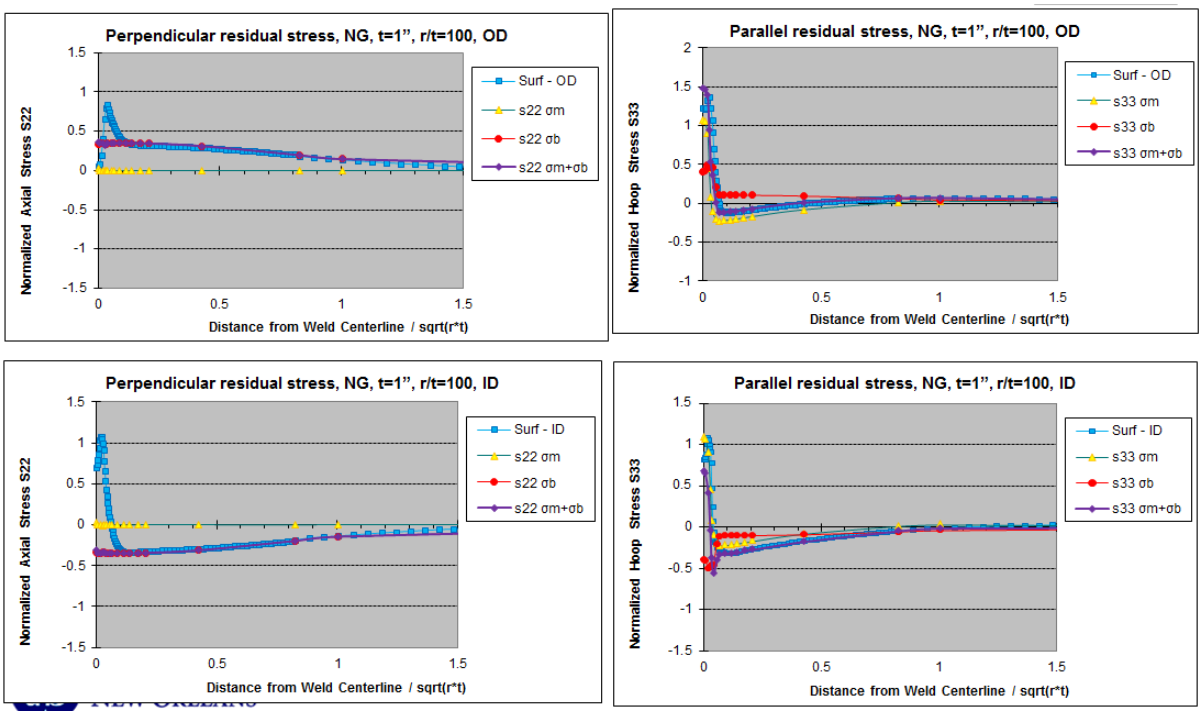

Figure 4-79 NG with t=1", r/t=100 through-thickness axial and hoop residual stress components along OD and ID

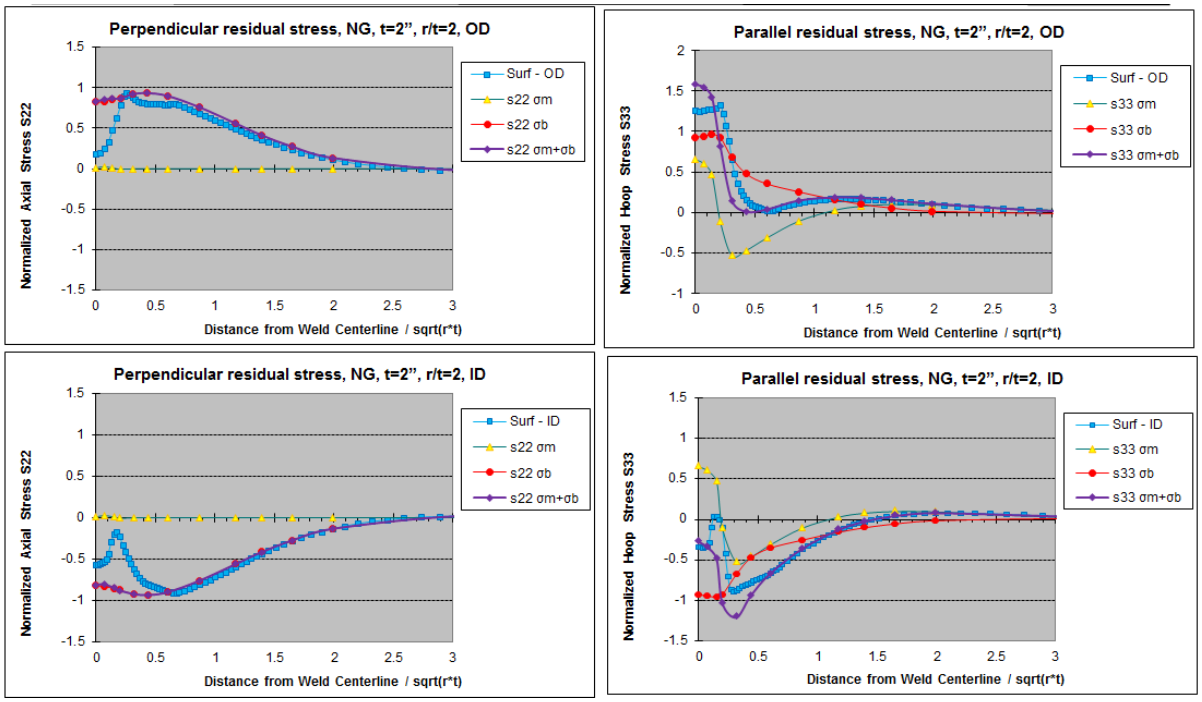

Figure 4-80 NG with t=2", r/t=2 through-thickness axial and hoop residual stress components along OD and ID

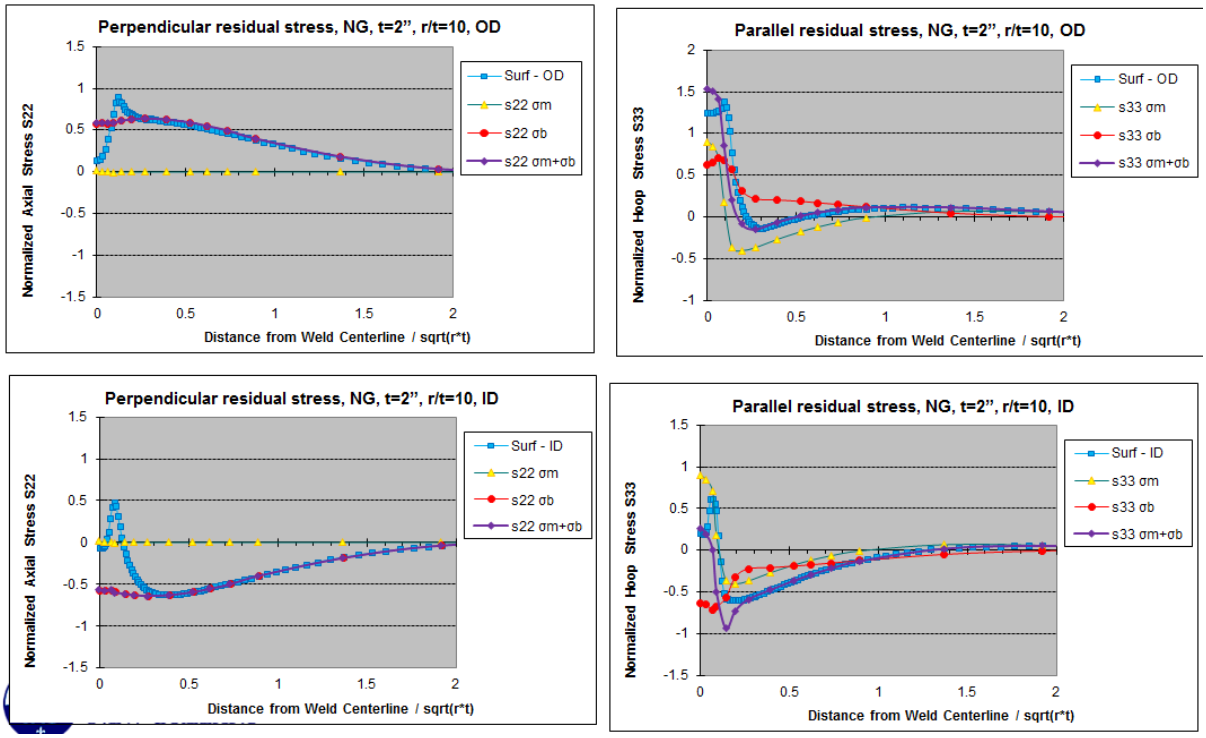

Figure 4-81 NG with t=2", r/t=10 through-thickness axial and hoop residual stress components along OD and ID

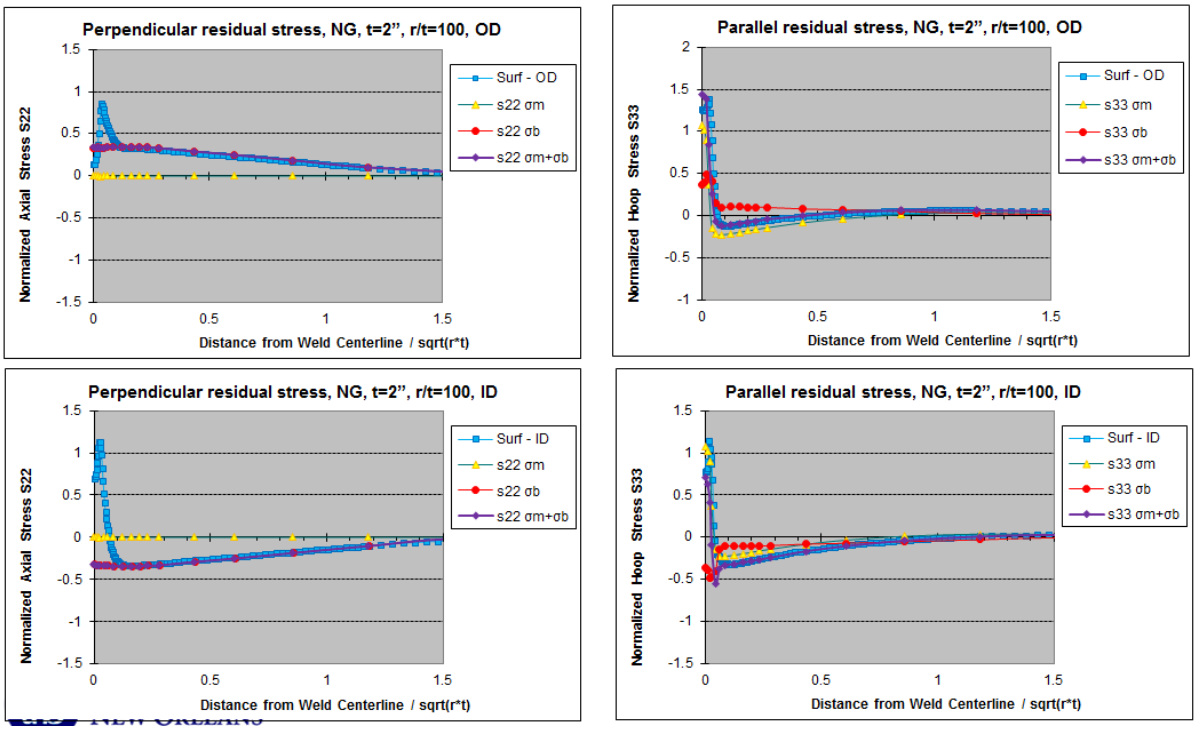

Figure 4-82 NG with t=2", r/t=100 through-thickness axial and hoop residual stress components along OD and ID

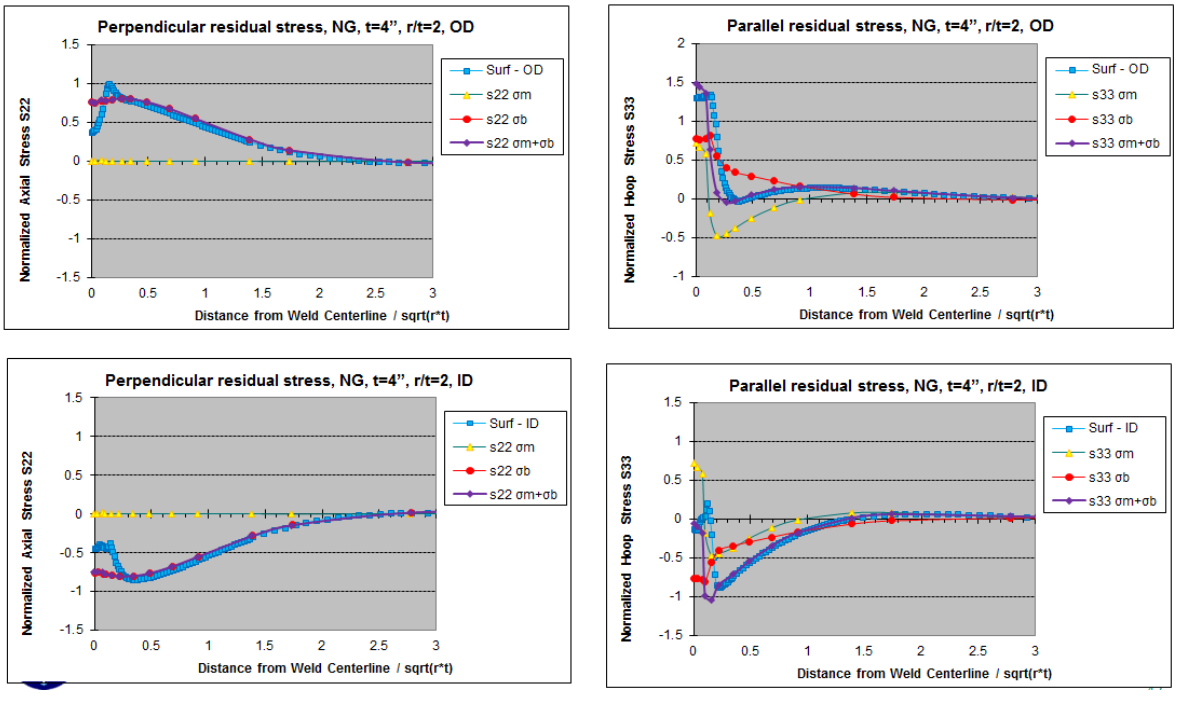

Figure 4-83 NG with t=4", r/t=2 through-thickness axial and hoop residual stress components along OD and ID

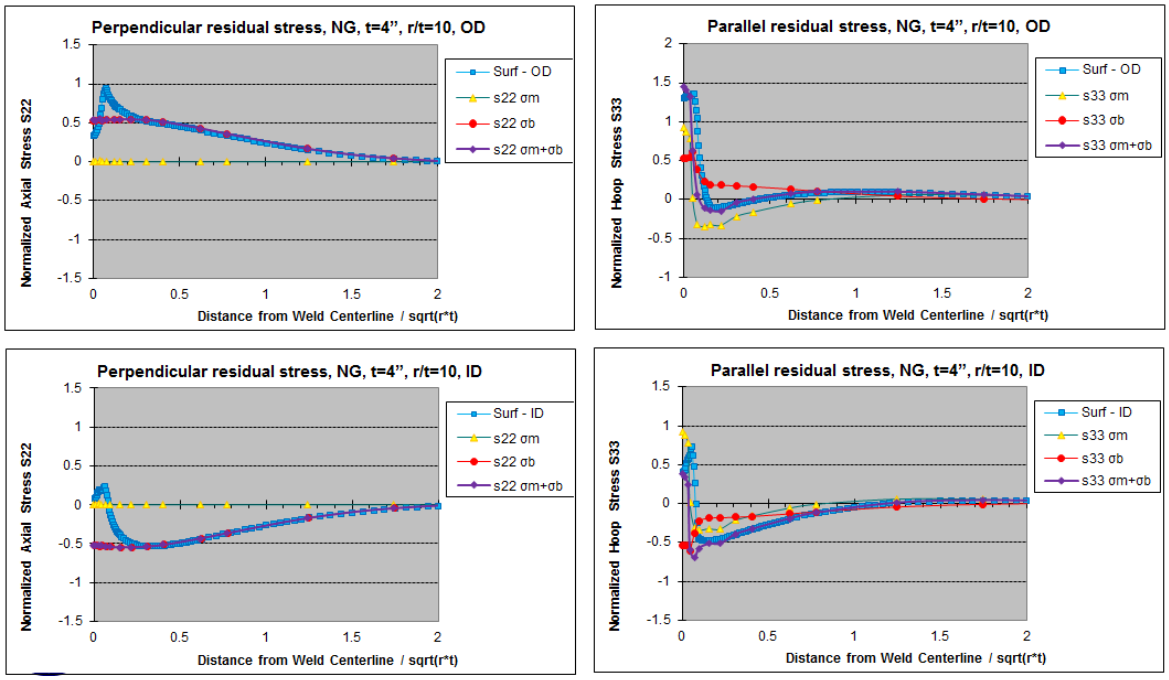

Figure 4-84 NG with t=4", r/t=10 through-thickness axial and hoop residual stress components along OD and ID

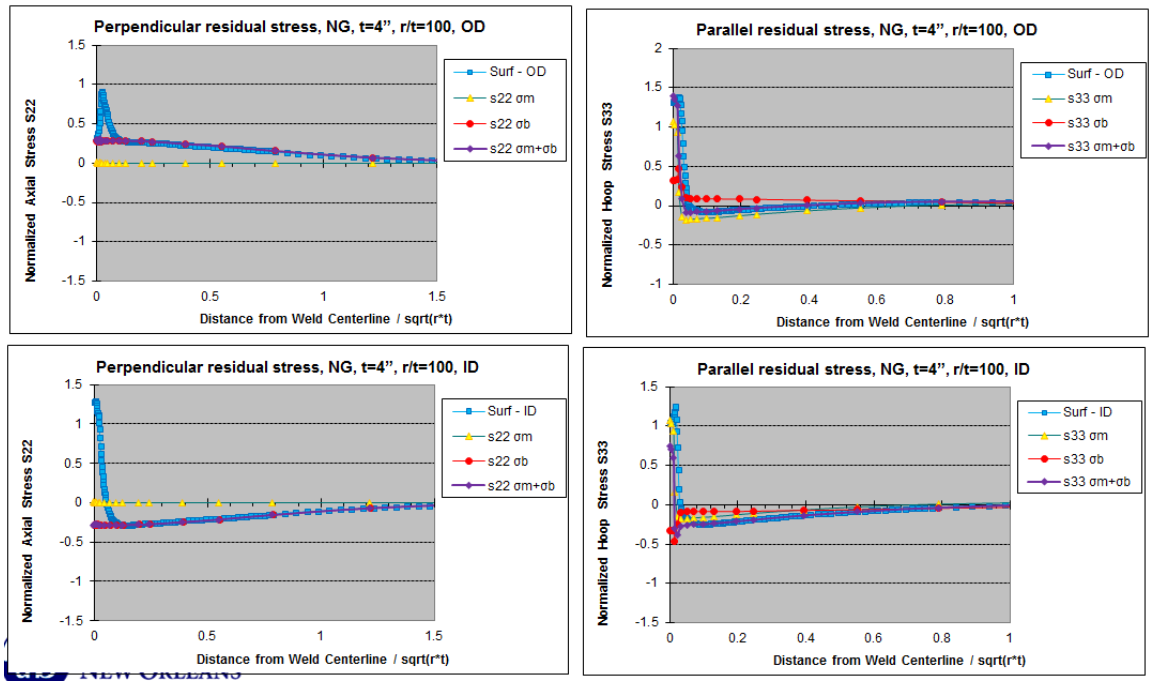

Figure 4-85 NG with t=4", r/t=100 through-thickness axial and hoop residual stress components along OD and ID

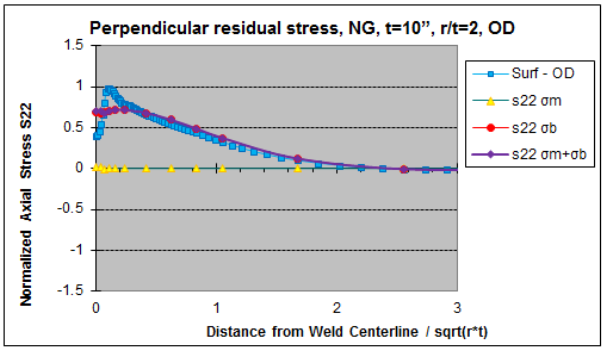

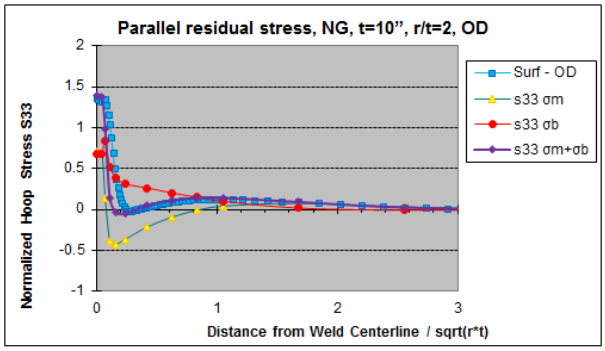

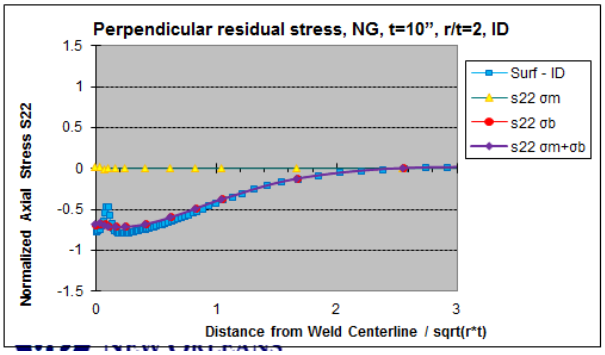

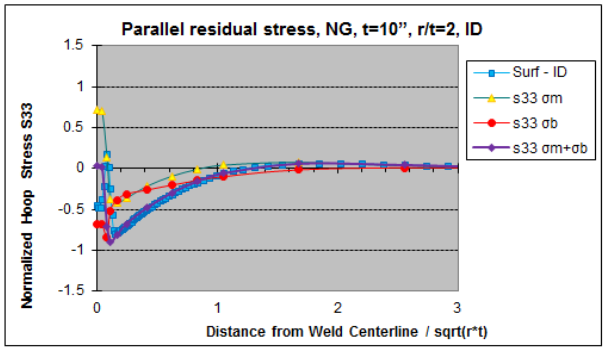

Figure 4-86 NG with t=10", r/t=2 through-thickness axial and hoop residual stress components along OD and ID

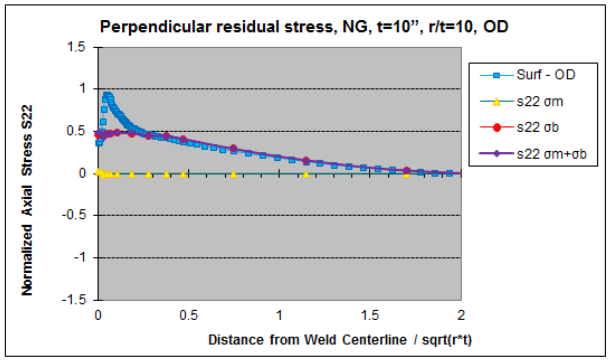

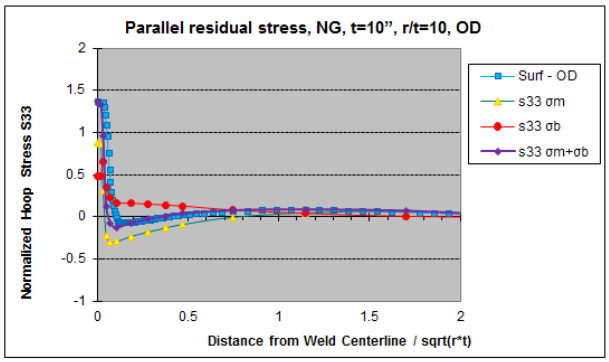

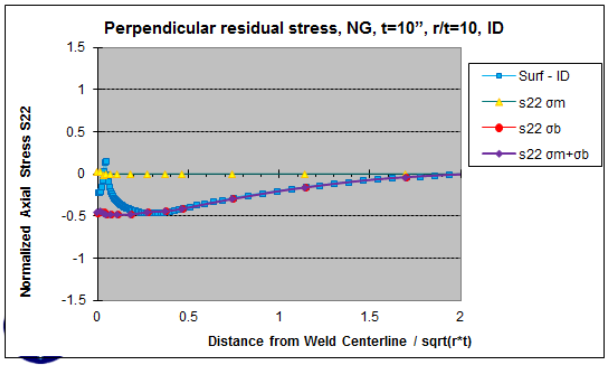

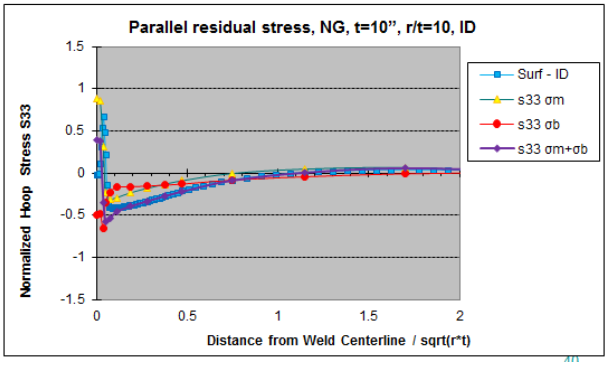

Figure 4-87 NG with t=10", r/t=10 through-thickness axial and hoop residual stress components along OD and ID

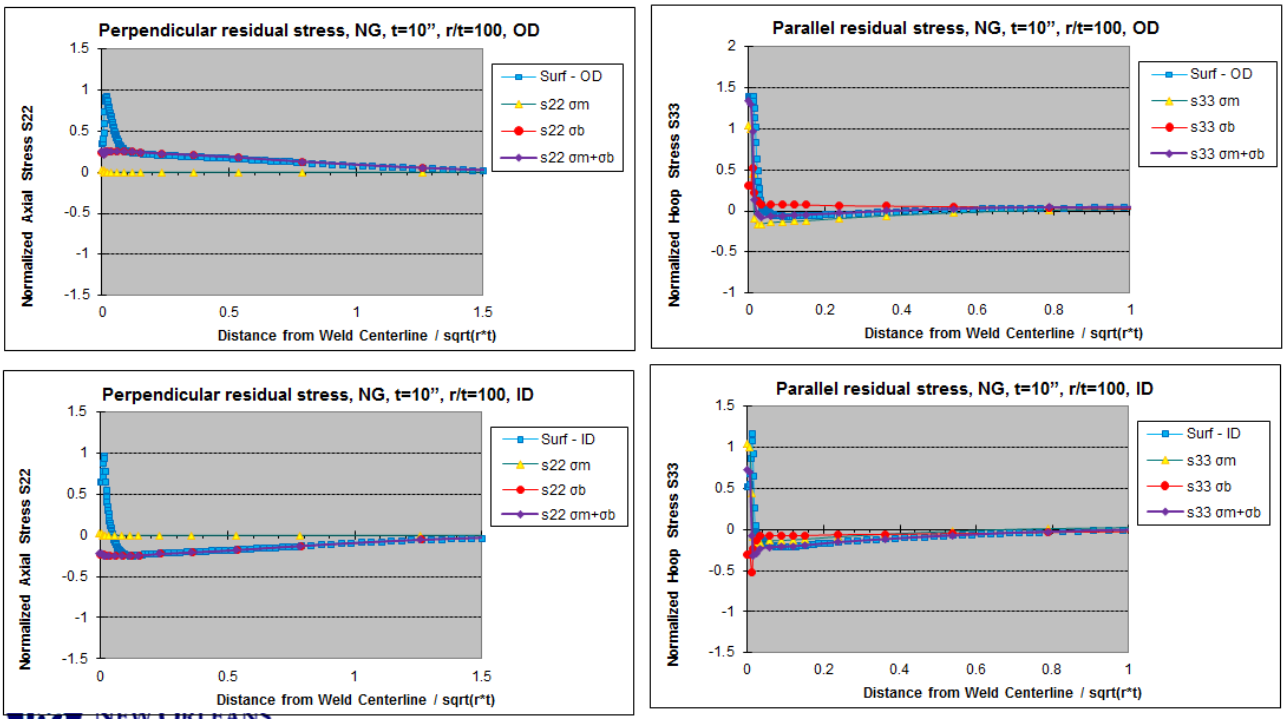

Figure 4-88 NG with t=10", r/t=100 through-thickness axial and hoop residual stress components along OD and ID

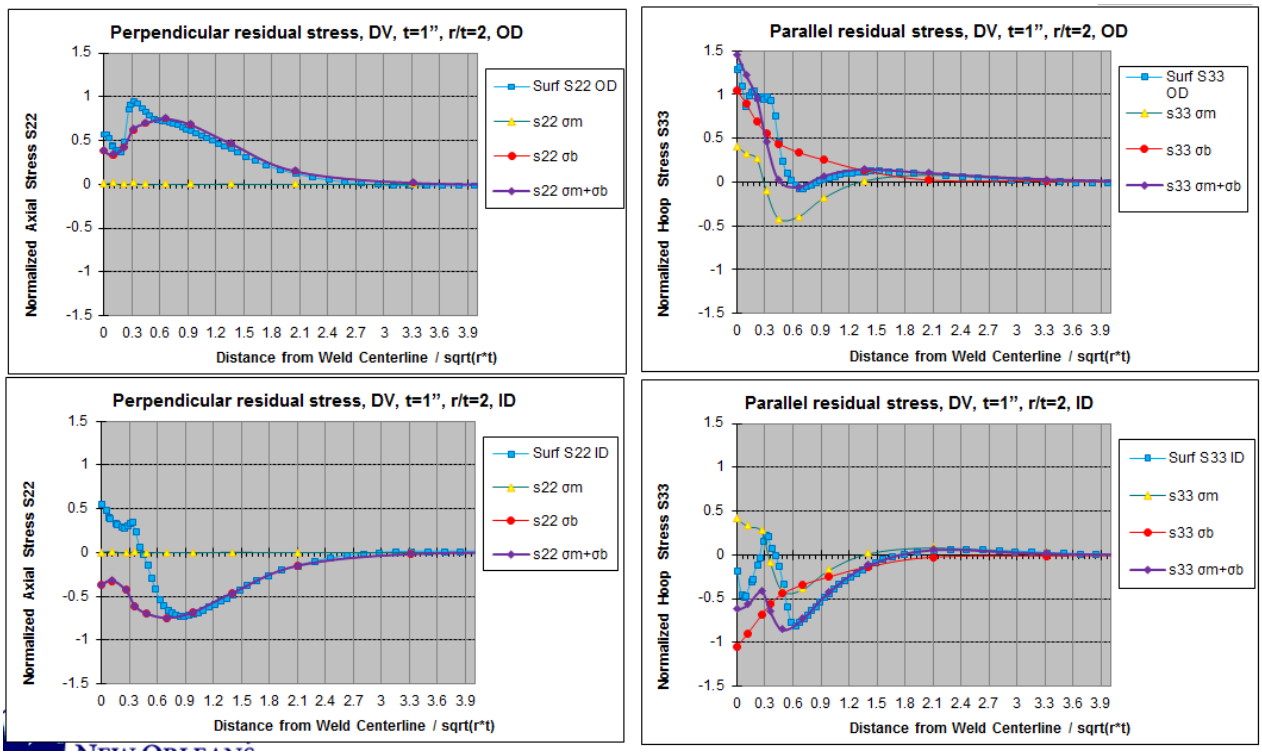

Figure 4-89 DV with t=1", r/t=2 through-thickness axial and hoop residual stress components along OD and ID

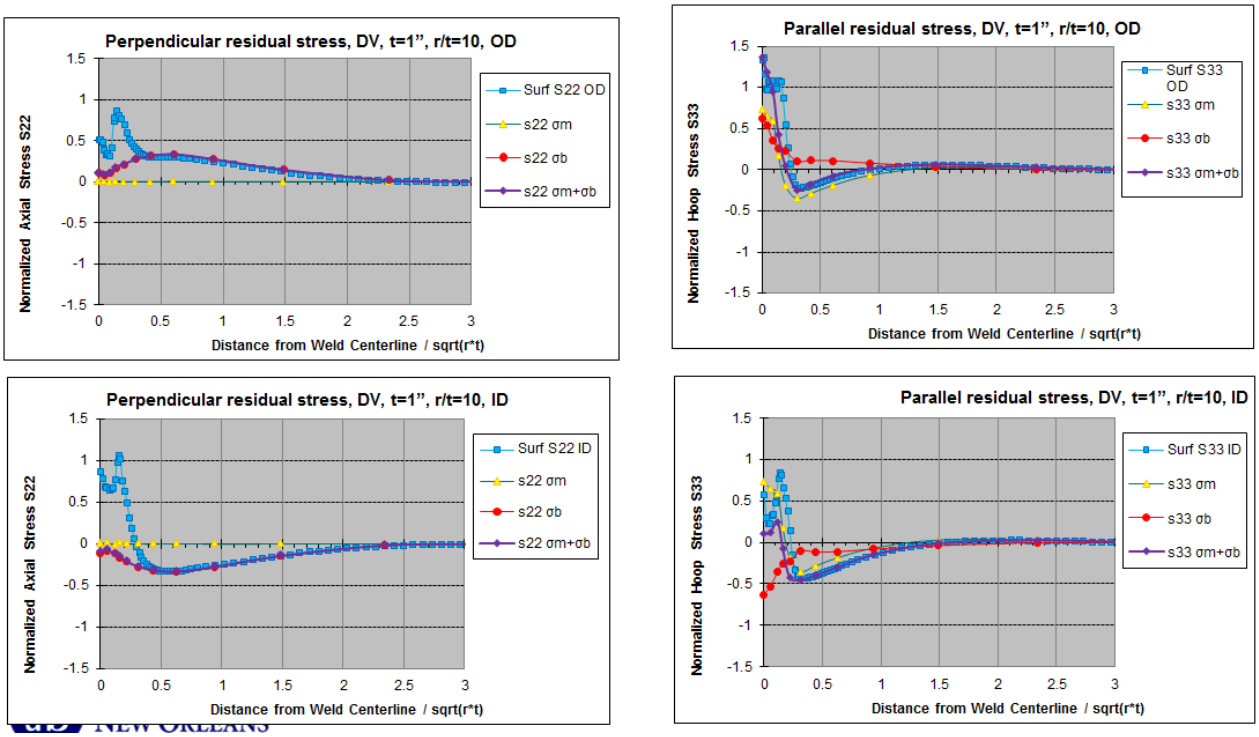

Figure 4-90 DV with t=1", r/t=10 through-thickness axial and hoop residual stress components along OD and ID

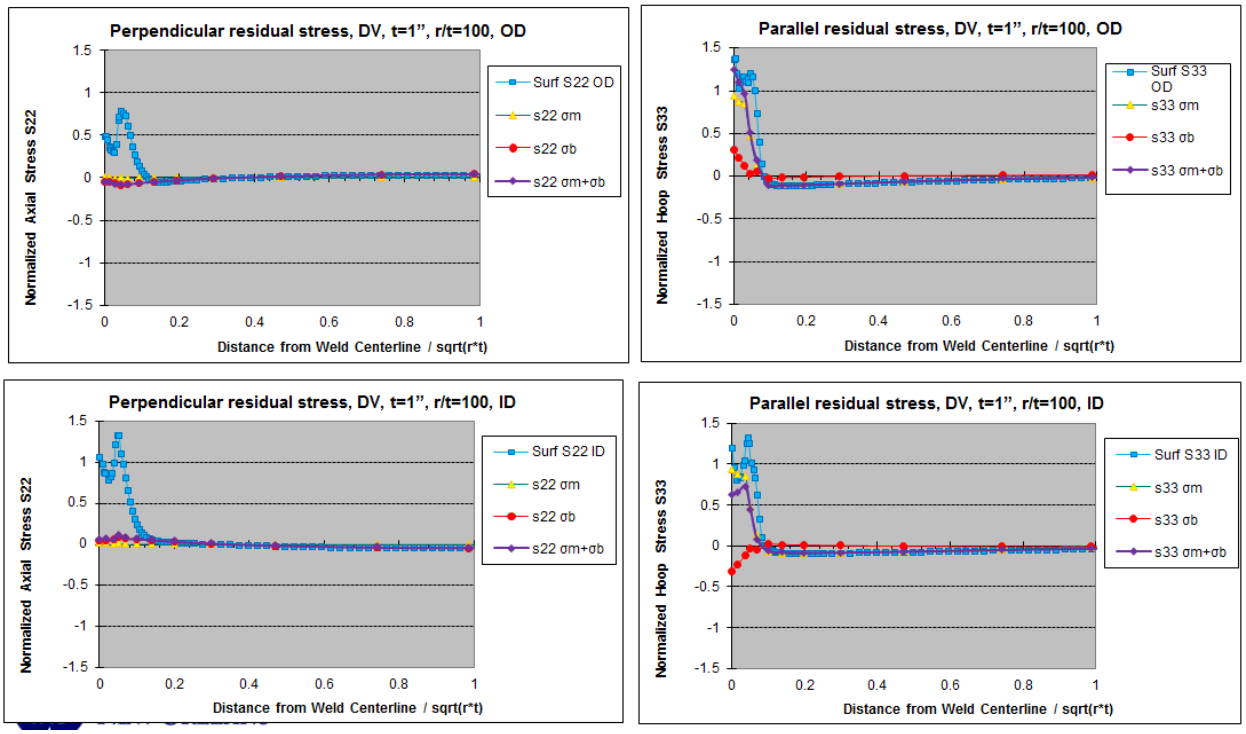

Figure 4-91 DV with t=1", r/t=100 through-thickness axial and hoop residual stress components along OD and ID

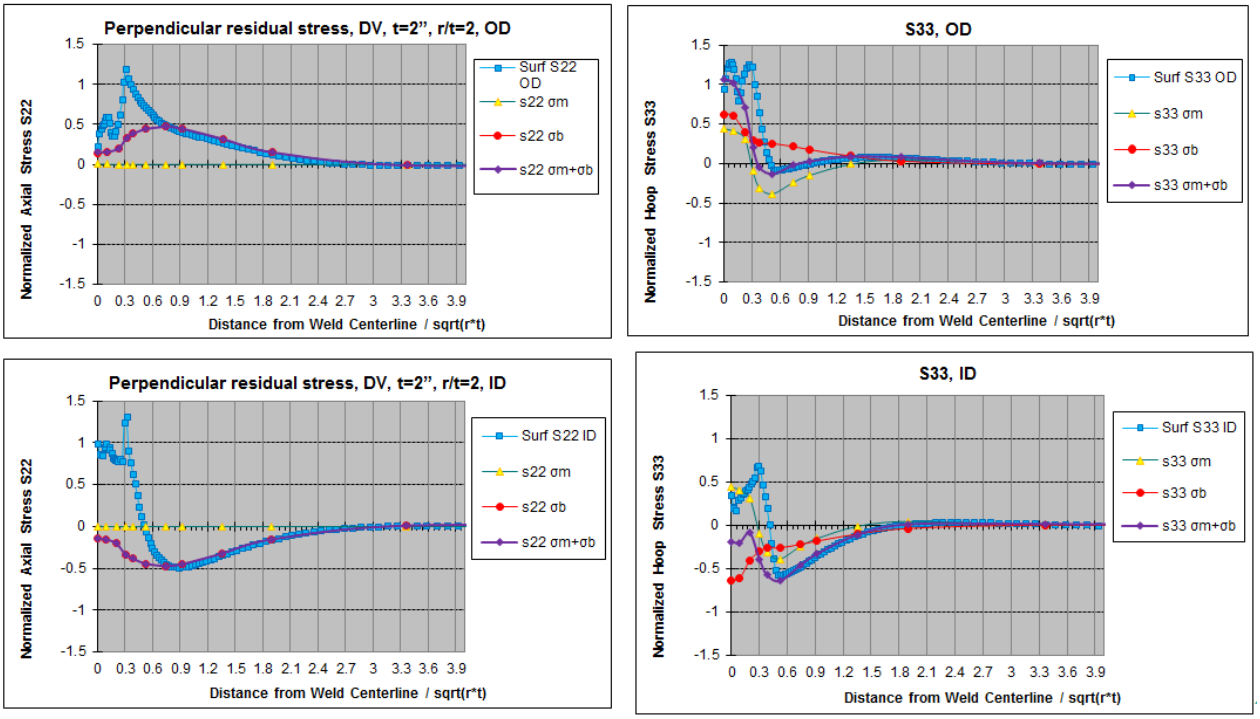

Figure 4-92 DV with t=2", r/t=2 through-thickness axial and hoop residual stress components along OD and ID

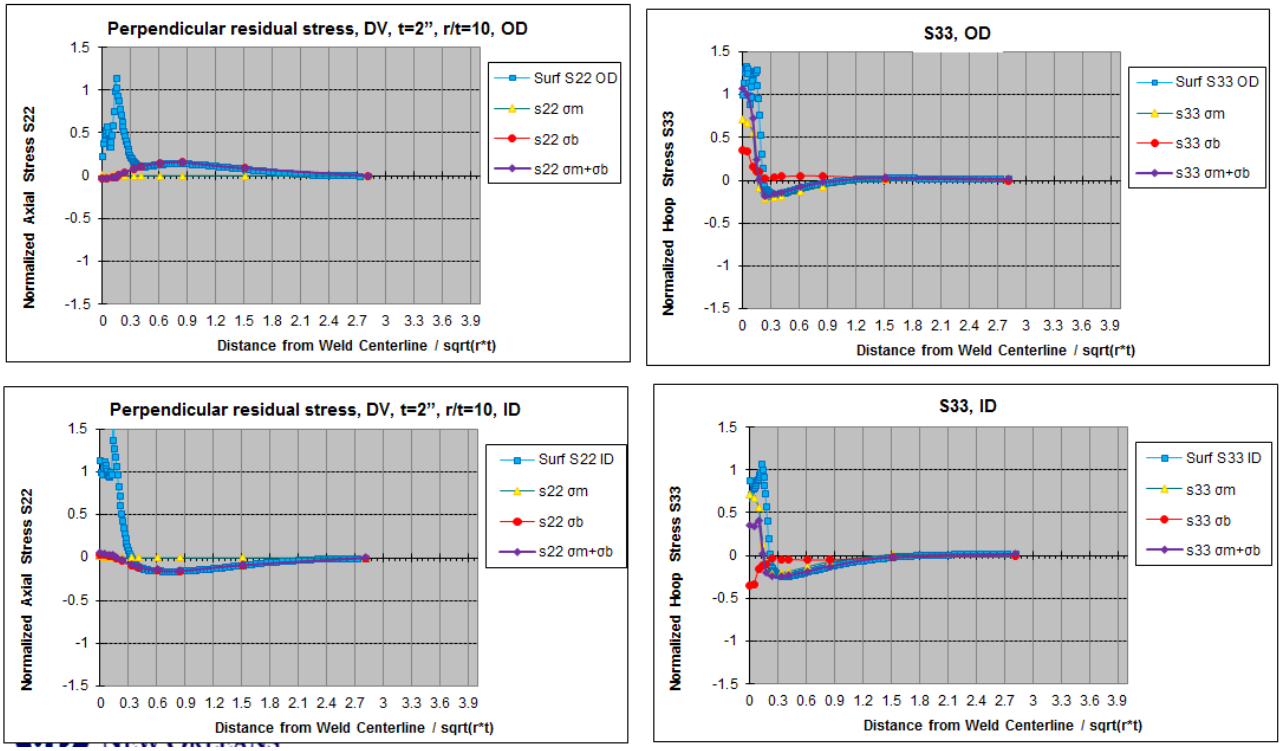

Figure 4-93 DV with t=2", r/t=10 through-thickness axial and hoop residual stress components along OD and ID

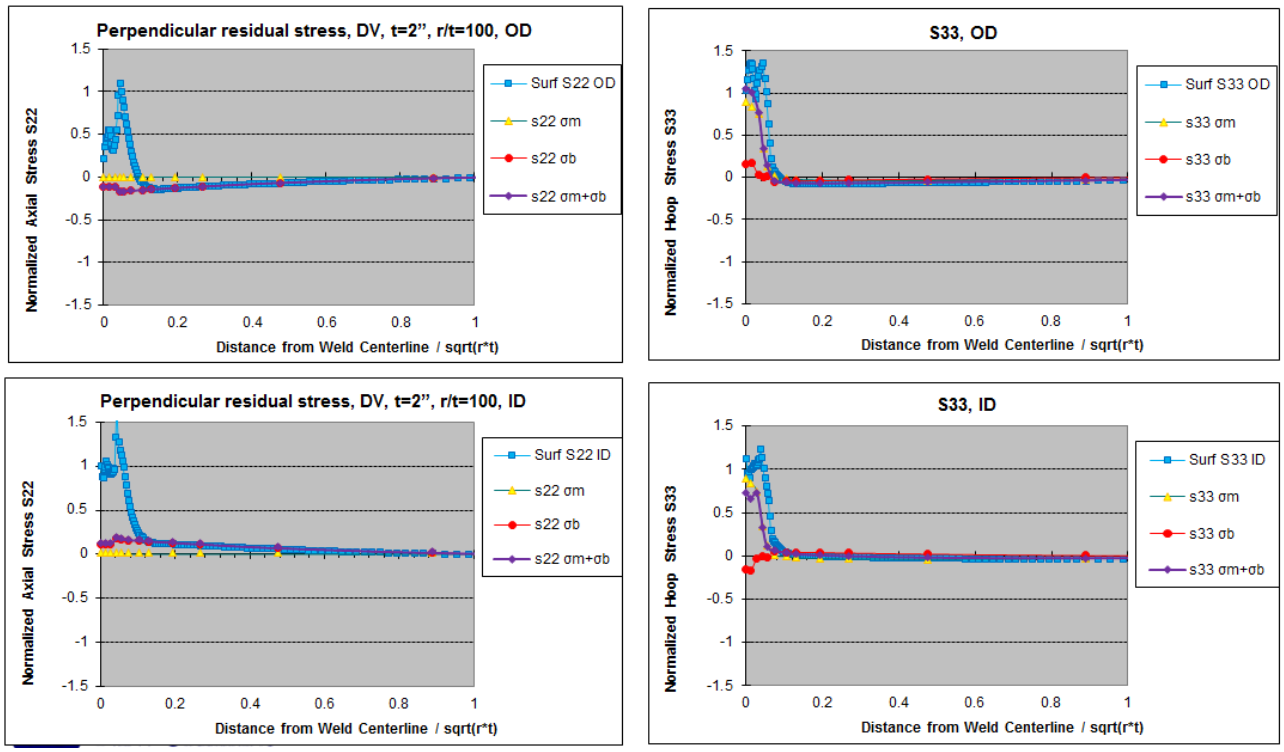

Figure 4-94 DV with t=2", r/t=100 through-thickness axial and hoop residual stress components along OD and ID

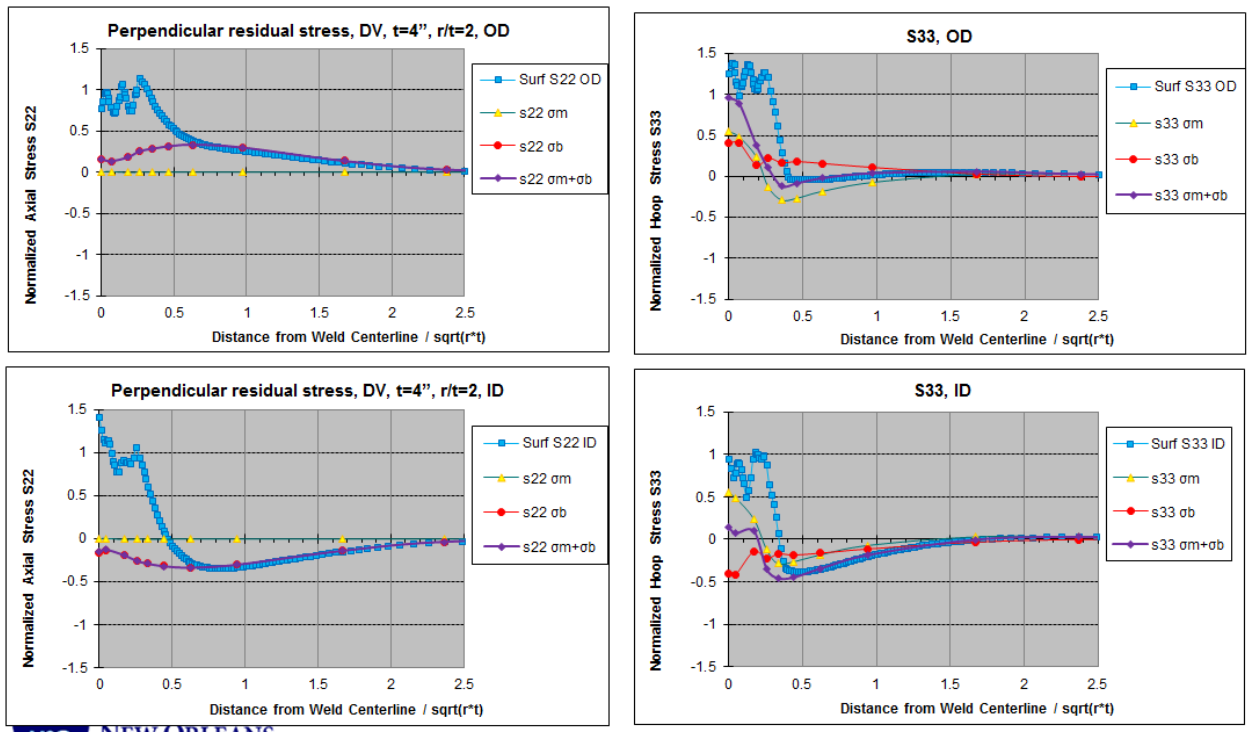

Figure 4-95 DV with t=4", r/t=2 through-thickness axial and hoop residual stress components along OD and ID

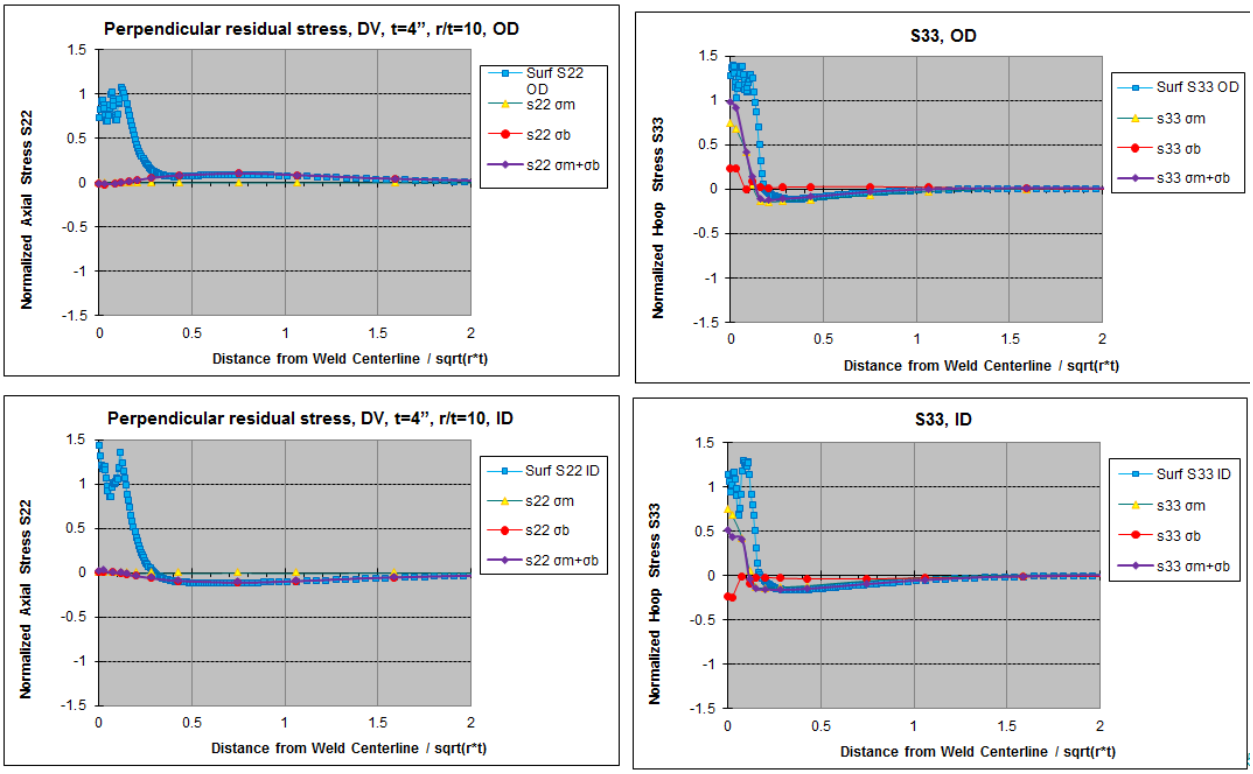

Figure 4-96 DV with t=4", r/t=10 through-thickness axial and hoop residual stress components along OD and ID

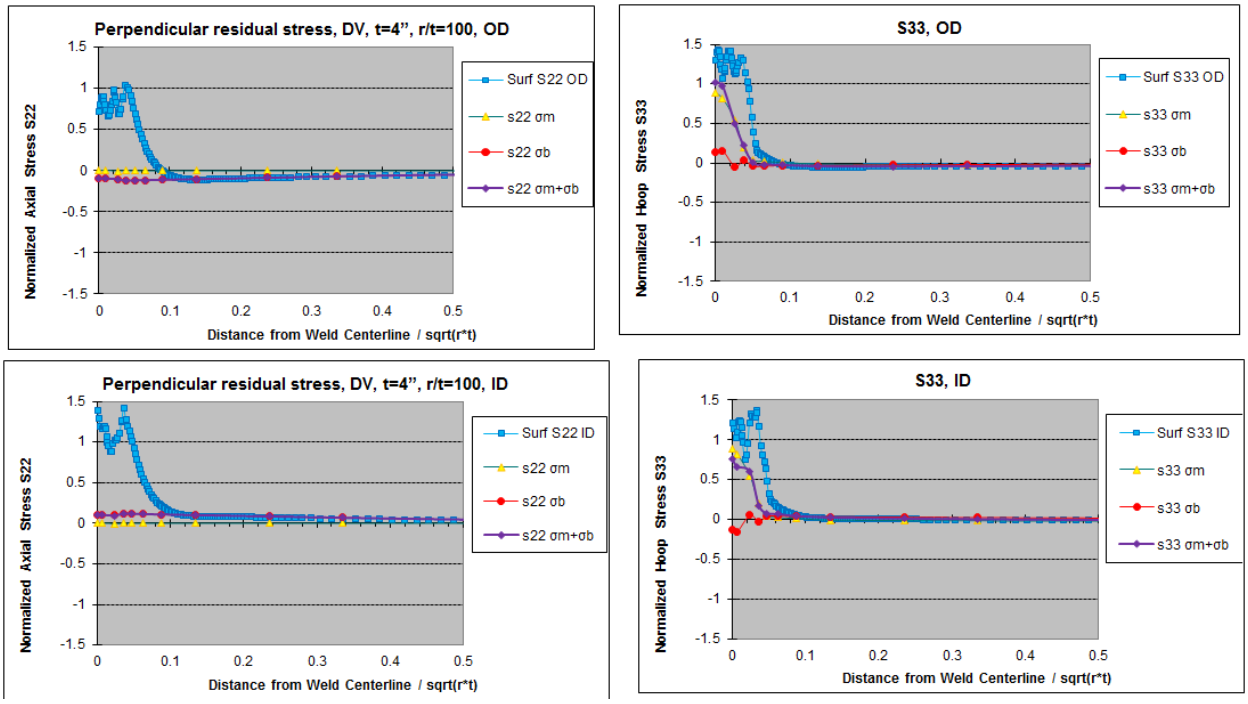

Figure 4-97 DV with t=4", r/t=100 through-thickness axial and hoop residual stress components along OD and ID

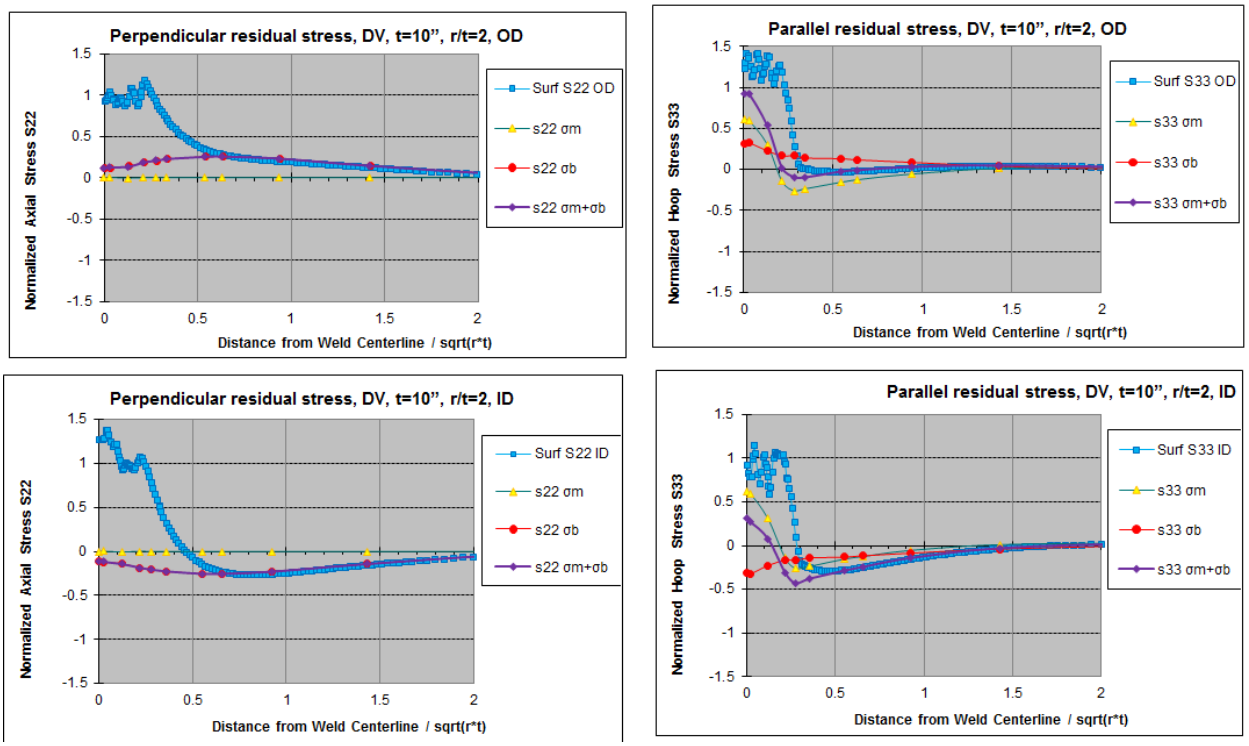

Figure 4-98 DV with t=10", r/t=2 through-thickness axial and hoop residual stress components along OD and ID

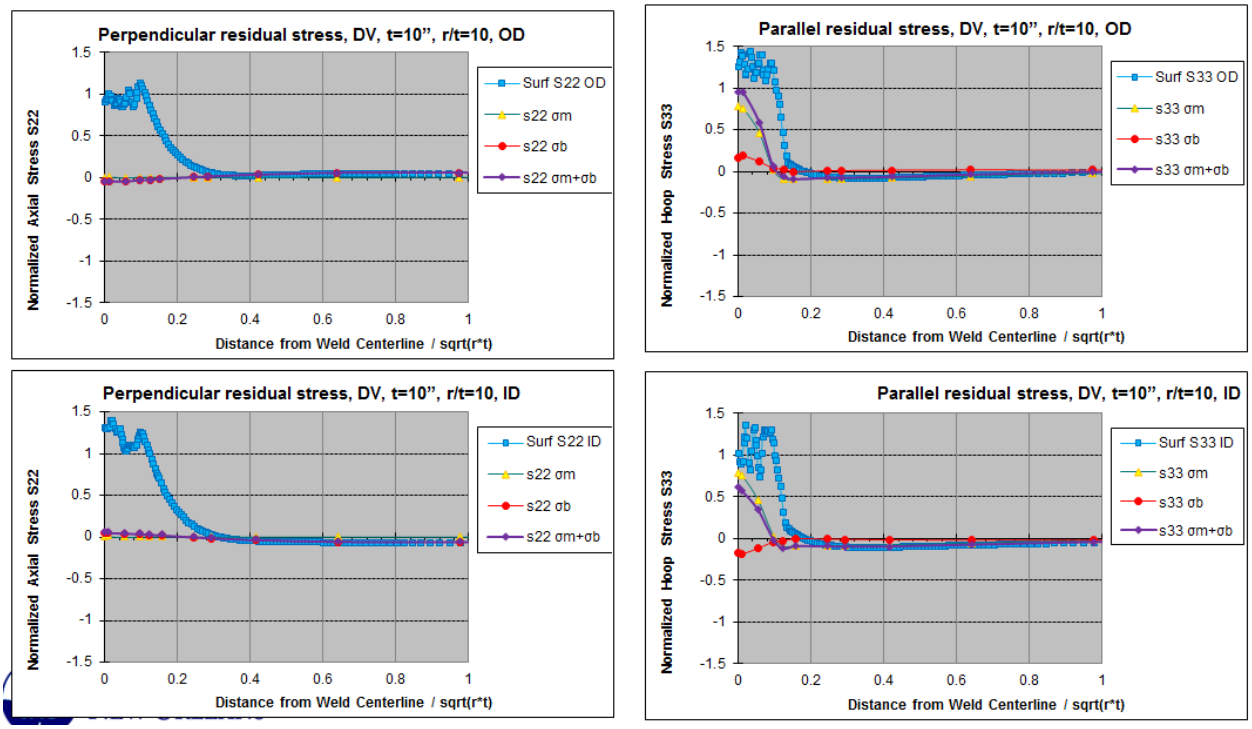

Figure 4-99 DV with t=10", r/t=100 through-thickness axial and hoop residual stress components along OD and ID

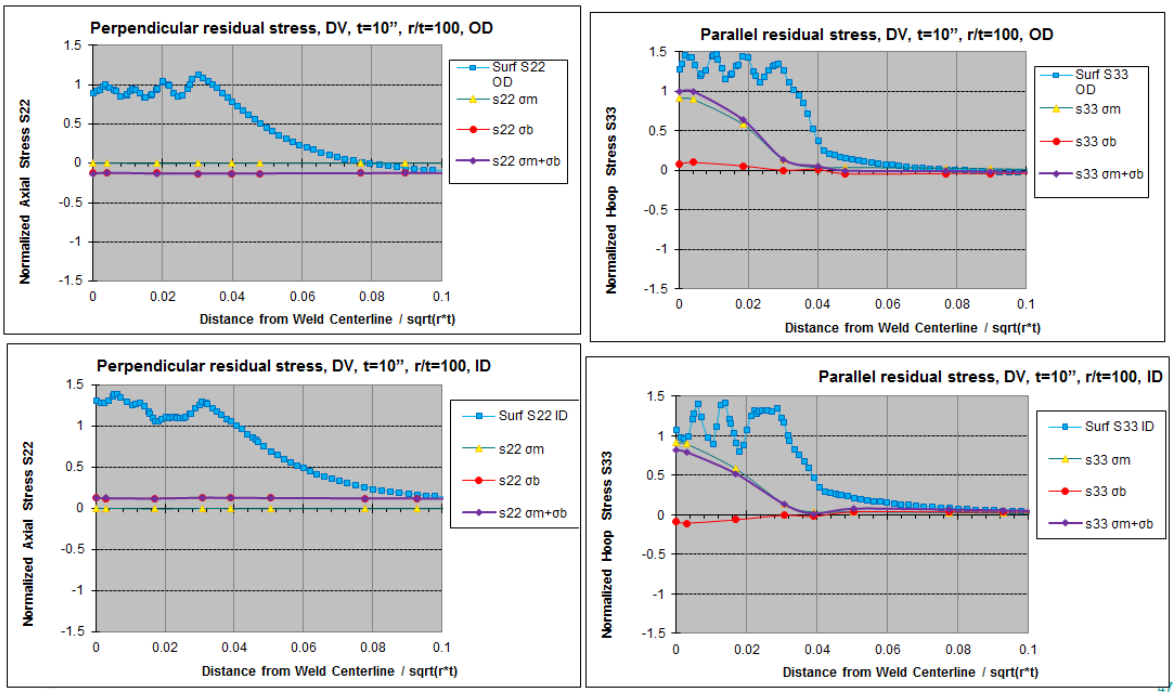

Figure 4-100 DV with t=10", r/t=100 through-thickness axial and hoop residual stress components along OD and ID

4.6.2 Results for self-equilibrating part of through-thickness residual stress at weld centerline

In order to establish an estimation scheme for the self-equilibrating stress component, it needs to understand its distribution pattern first. Figure 4-101 shows the perpendicular (axial) and parallel (hoop) residual stresses along weld centerline for Single-V of 1" thickness and r/t ratio of 10. Black line indicates the original residual stress directly obtained from FEA in the earlier parametric analyses, while red line indicates the corresponding self-equilibrating part, blue line for bending part and green line for membrane part. The horizontal axis is measured from ID and normalized by thickness. By definition, the self-equilibrating component must meet the stress equilibrium conditions along the cross section, i.e., the summation of force is zero and bending moment is zero. Also, sine-wave stress oscillation is exhibited for the self-equilibrating component. This is mainly due to the interaction between weld passes. It is observed that the wave number is corresponding to the number of weld layers.

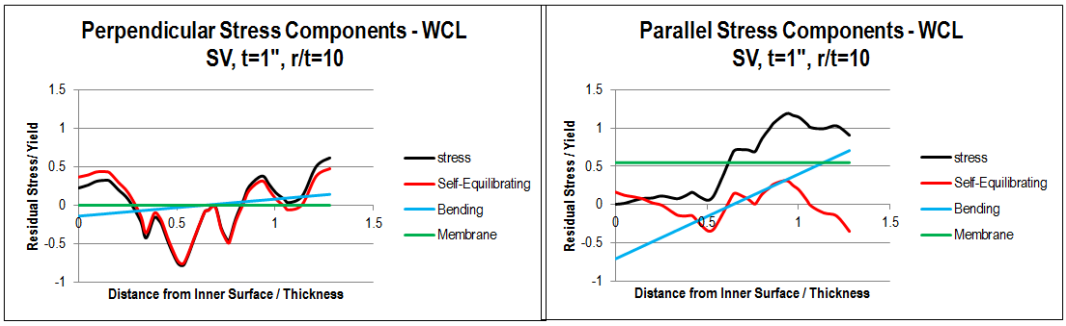

Figure 4-101 Weld centerline decomposed perpendicular and parallel residual stress components for SV with t=1", r/t=10

The results for other Single-V girth welds with varying thickness from 1" to 10" and r/t ratio from 2 to 100 are summarized in the same manner from Figure 4-102 to Figure 4-112. The results for Narrow Groove welds are shown from Figure 4-113 to Figure 4-124, and Double-V results are shown from Figure 4-125 to Figure 4-136.

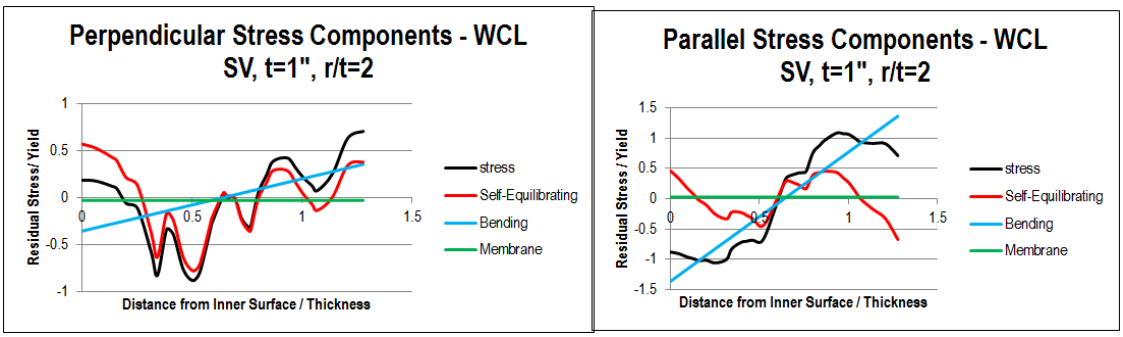

Figure 4-102 Weld centerline decomposed perpendicular and parallel residual stress components for SV with t=1", r/t=2

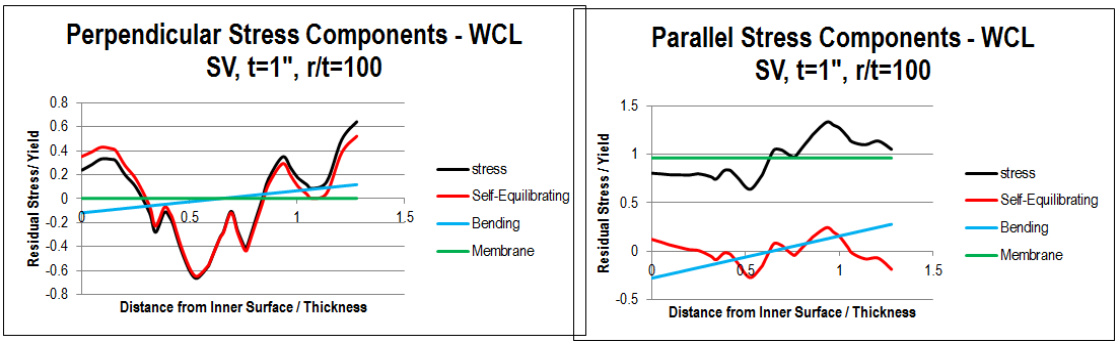

Figure 4-103 Weld centerline decomposed perpendicular and parallel residual stress components for SV with t=1", r/t=100

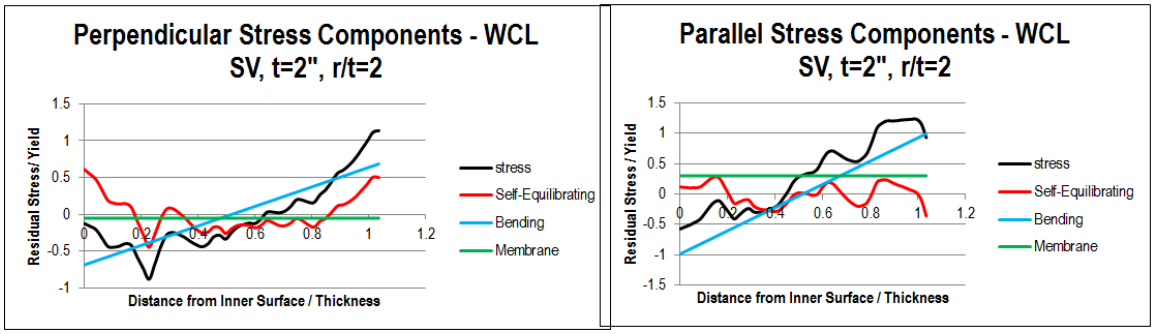

Figure 4-104 Weld centerline decomposed perpendicular and parallel residual stress components for SV with t=2", r/t=2

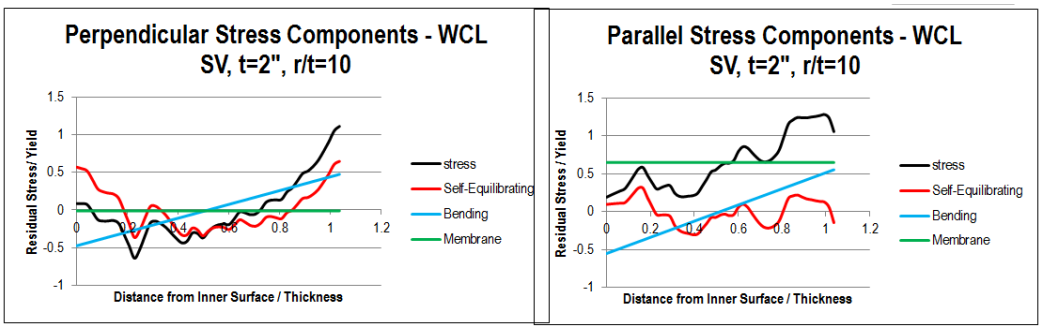

Figure 4-105 Weld centerline decomposed perpendicular and parallel residual stress components for SV with t=2", r/t=10

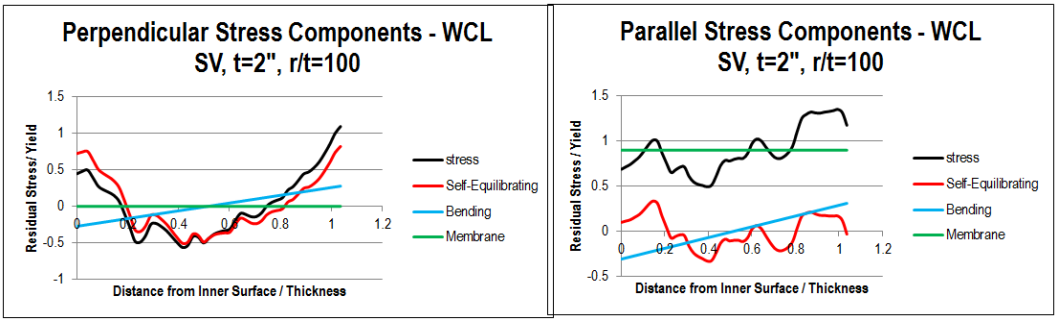

Figure 4-106 Weld centerline decomposed perpendicular and parallel residual stress components for SV with t=2", r/t=100

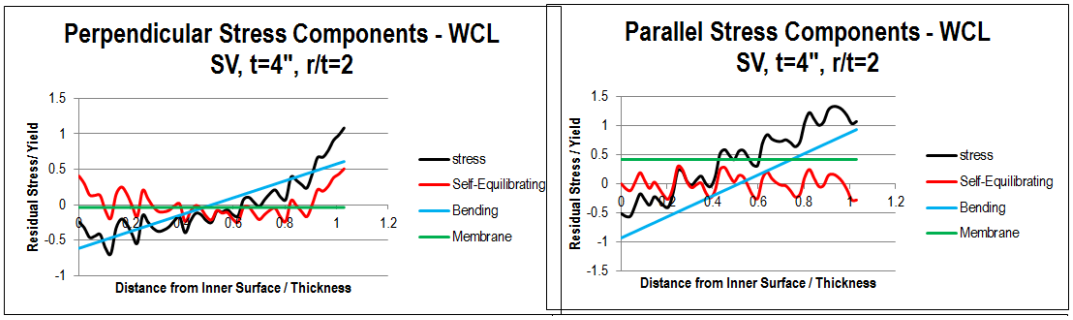

Figure 4-107 Weld centerline decomposed perpendicular and parallel residual stress components for SV with t=4", r/t=2

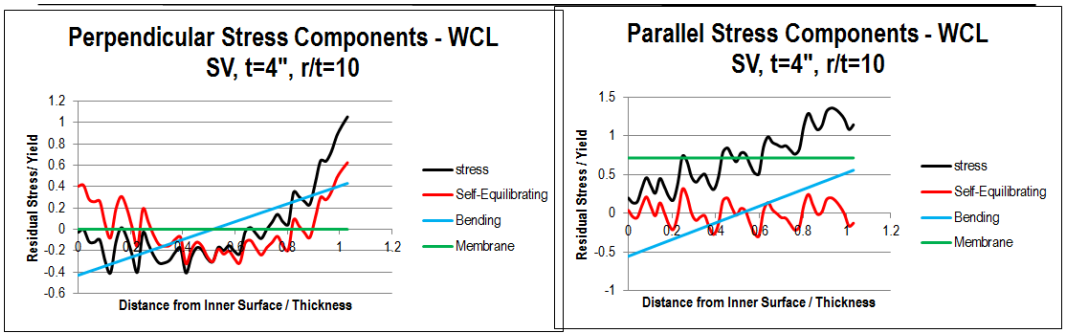

Figure 4-108 Weld centerline decomposed perpendicular and parallel residual stress components for SV with t=4", r/t=10

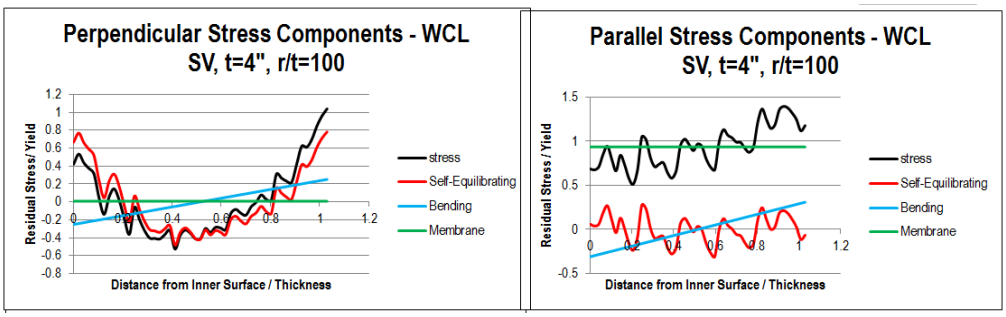

Figure 4-109 Weld centerline decomposed perpendicular and parallel residual stress components for SV with t=4", r/t=100

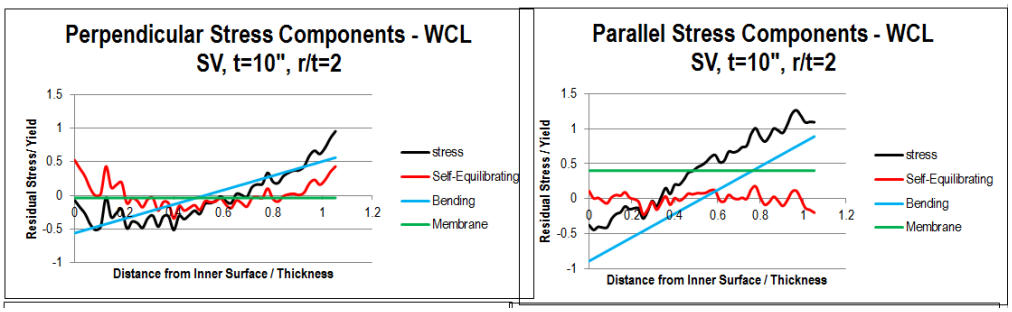

Figure 4-110 Weld centerline decomposed perpendicular and parallel residual stress components for SV with t=10", r/t=2

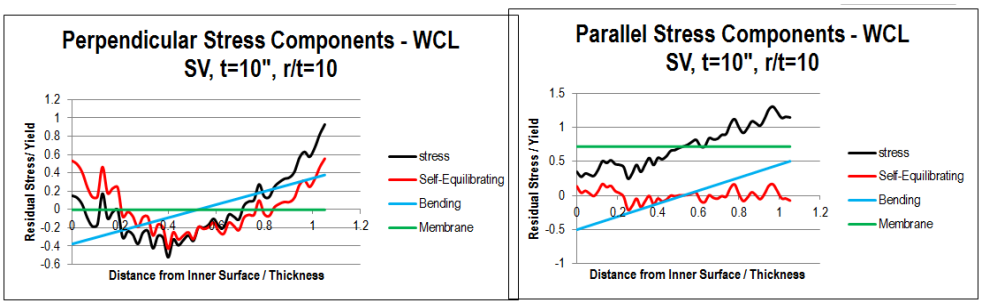

Figure 4-111 Weld centerline decomposed perpendicular and parallel residual stress components for SV with t=10", r/t=10

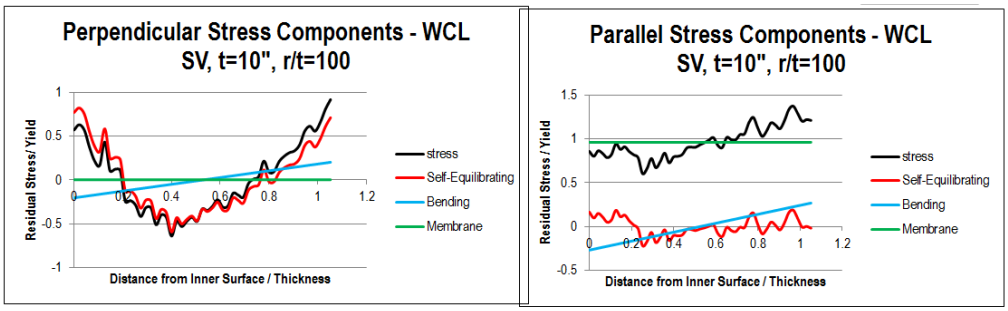

Figure 4-112 Weld centerline decomposed perpendicular and parallel residual stress components for SV with t=10", r/t=100

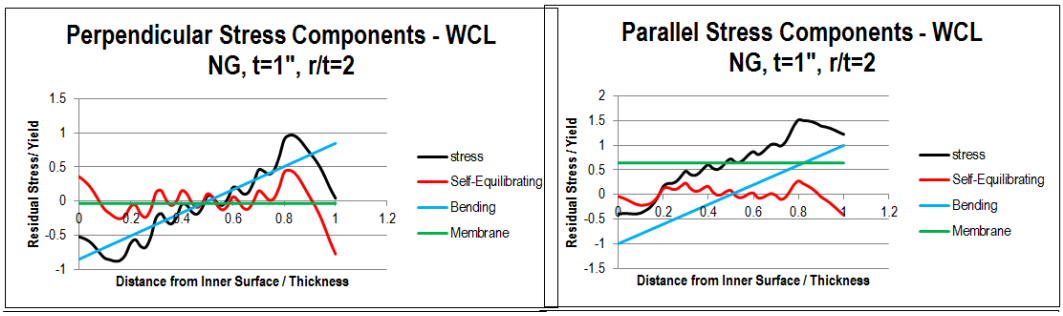

Figure 4-113 Weld centerline decomposed perpendicular and parallel residual stress components for NG with t=1", r/t=2

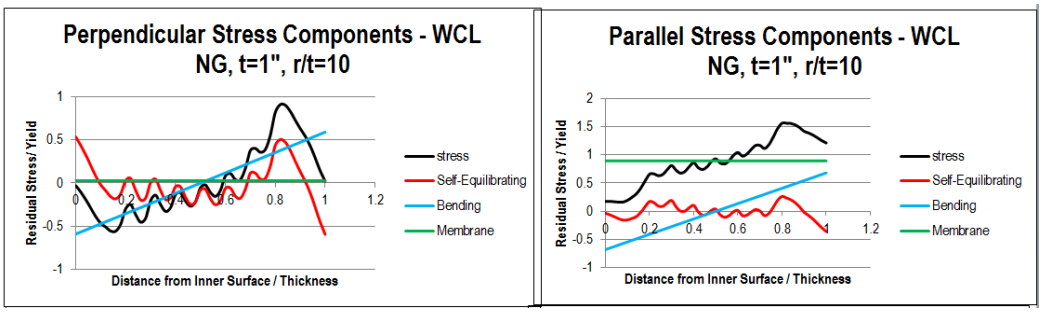

Figure 4-114 Weld centerline decomposed perpendicular and parallel residual stress components for NG with t=1", r/t=10

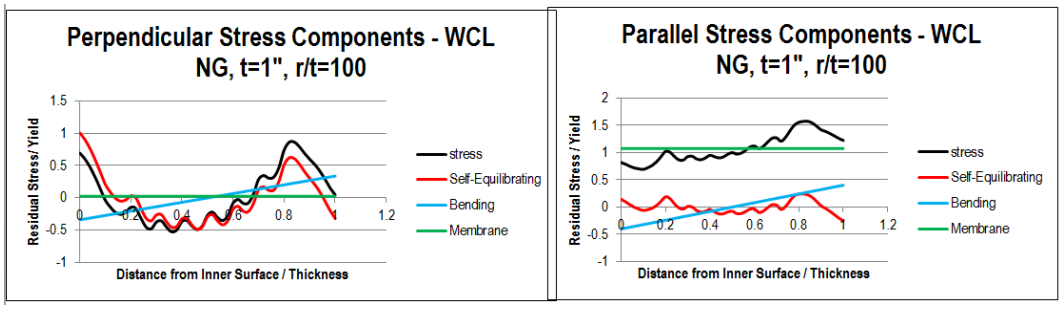

Figure 4-115 Weld centerline decomposed perpendicular and parallel residual stress components for NG with t=1", r/t=100

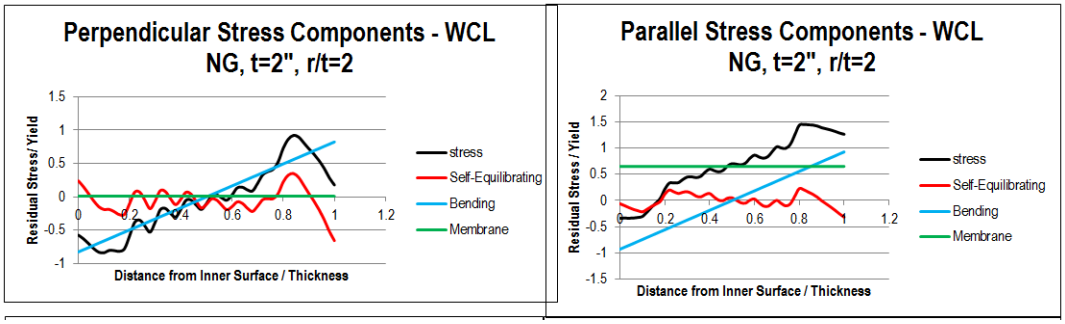

Figure 4-116 Weld centerline decomposed perpendicular and parallel residual stress components for NG with t=2", r/t=2

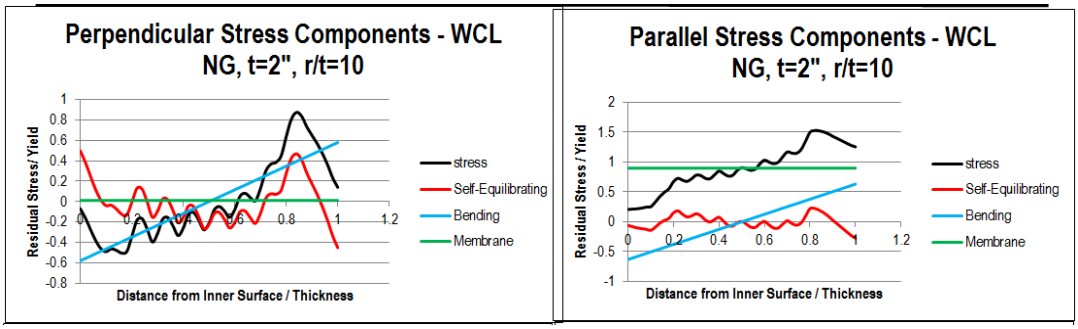

Figure 4-117 Weld centerline decomposed perpendicular and parallel residual stress components for NG with t=2", r/t=10

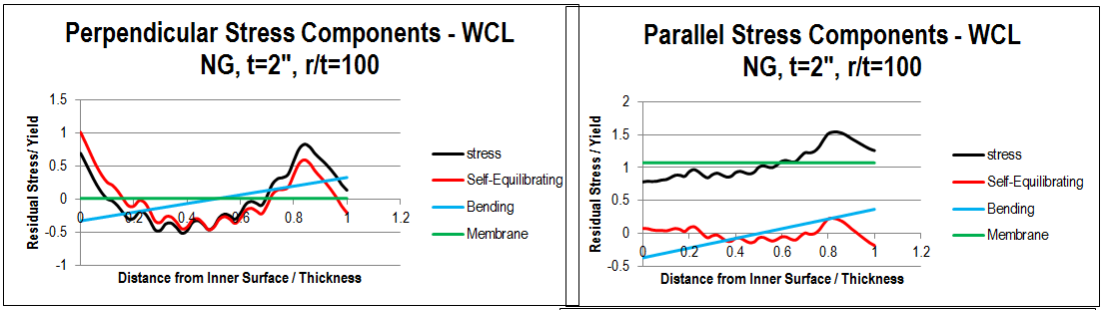

Figure 4-118 Weld centerline decomposed perpendicular and parallel residual stress components for NG with t=2", r/t=100

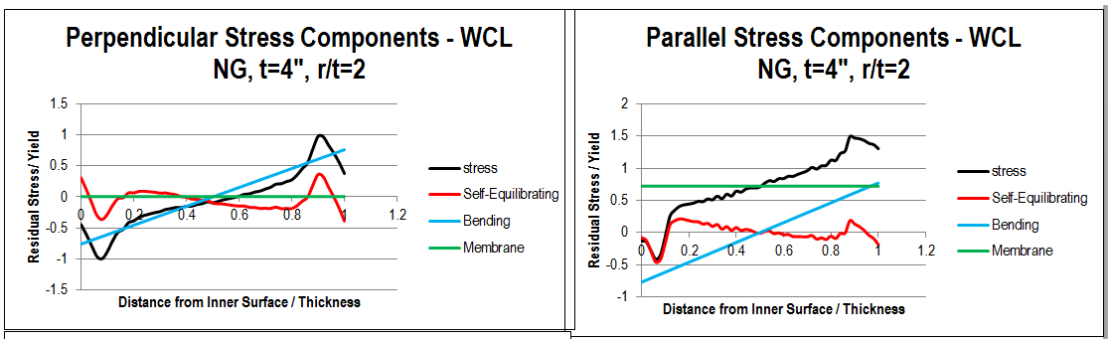

Figure 4-119 Weld centerline decomposed perpendicular and parallel residual stress components for NG with t=4", r/t=2

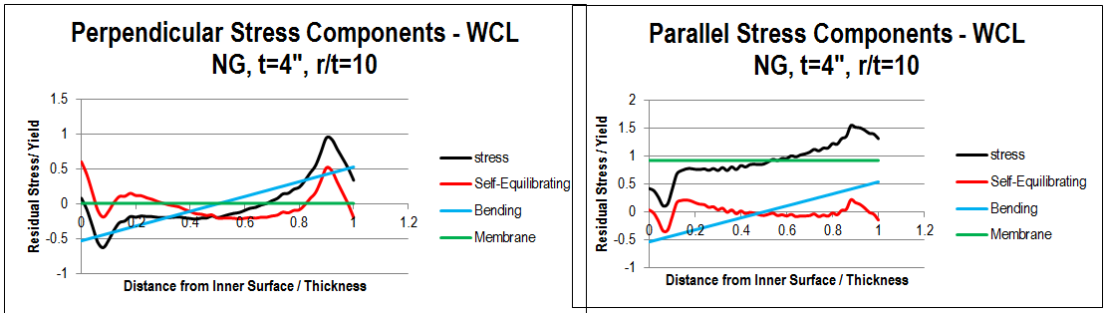

Figure 4-120 Weld centerline decomposed perpendicular and parallel residual stress components for NG with t=4", r/t=10

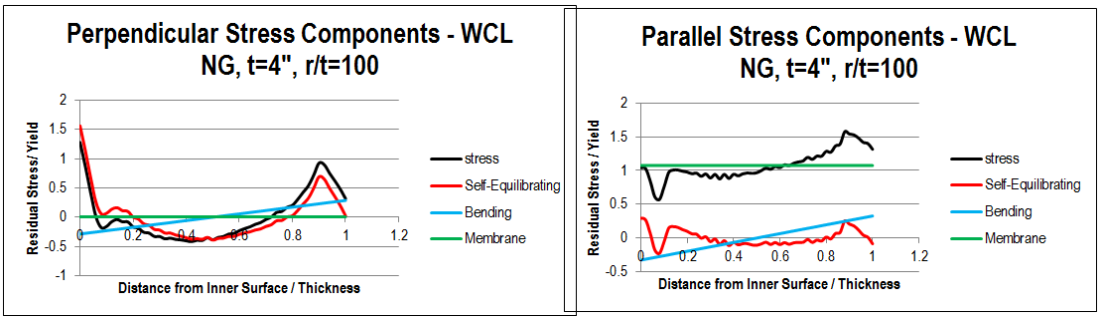

Figure 4-121 Weld centerline decomposed perpendicular and parallel residual stress components for NG with t=4", r/t=100

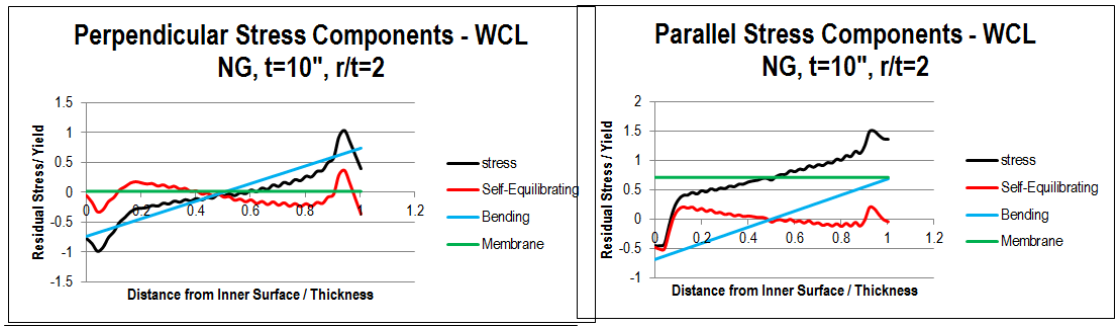

Figure 4-122 Weld centerline decomposed perpendicular and parallel residual stress components for NG with t=10", r/t=2

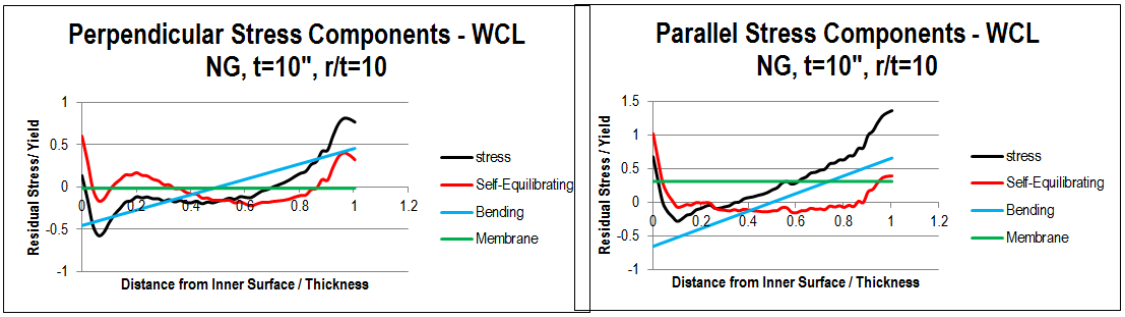

Figure 4-123 Weld centerline decomposed perpendicular and parallel residual stress components for NG with t=10", r/t=10

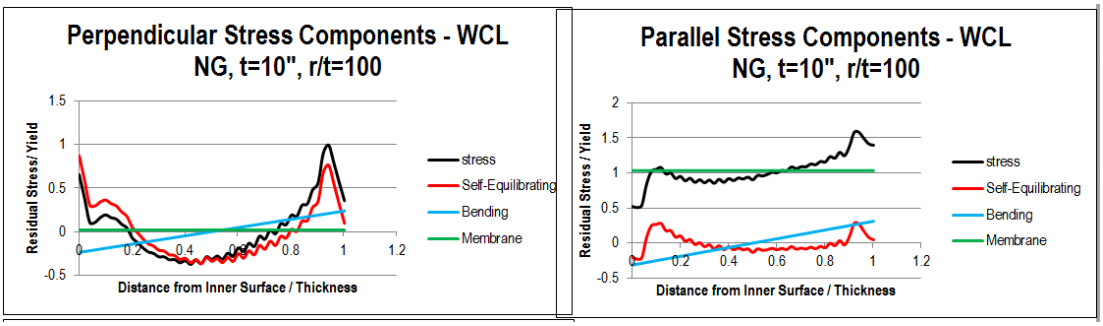

Figure 4-124 Weld centerline decomposed perpendicular and parallel residual stress components for NG with t=10", r/t=100

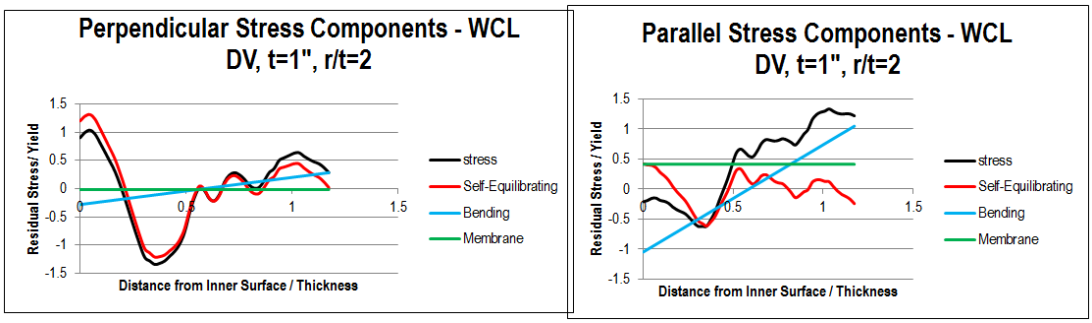

Figure 4-125 Weld centerline decomposed perpendicular and parallel residual stress components for DV with t=1", r/t=2

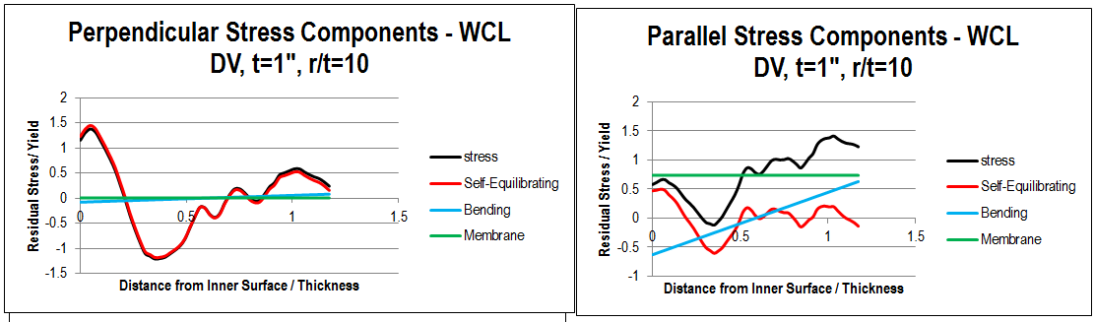

Figure 4-126 Weld centerline decomposed perpendicular and parallel residual stress components for DV with t=1", r/t=10

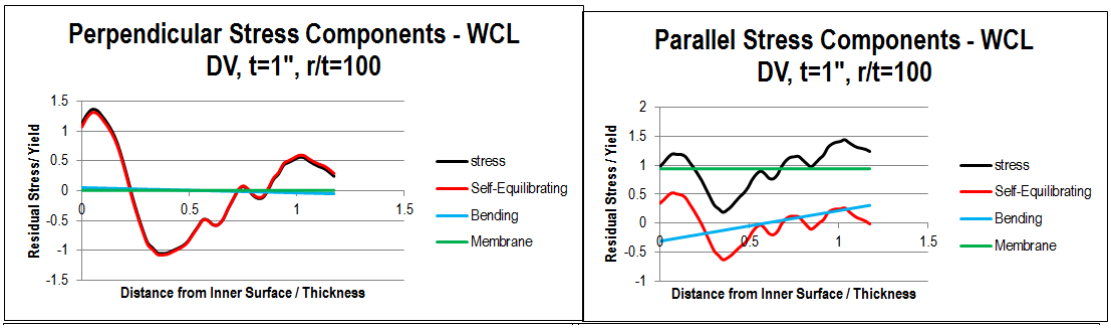

Figure 4-127 Weld centerline decomposed perpendicular and parallel residual stress components for DV with t=1", r/t=100

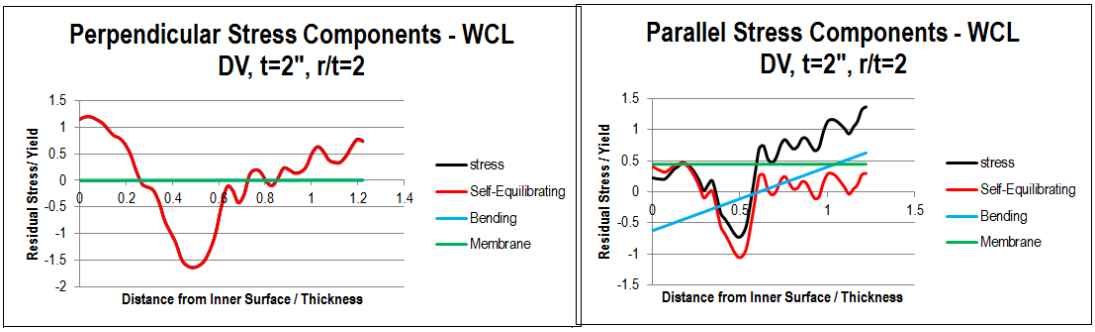

Figure 4-128 Weld centerline decomposed perpendicular and parallel residual stress components for DV with t=2", r/t=2

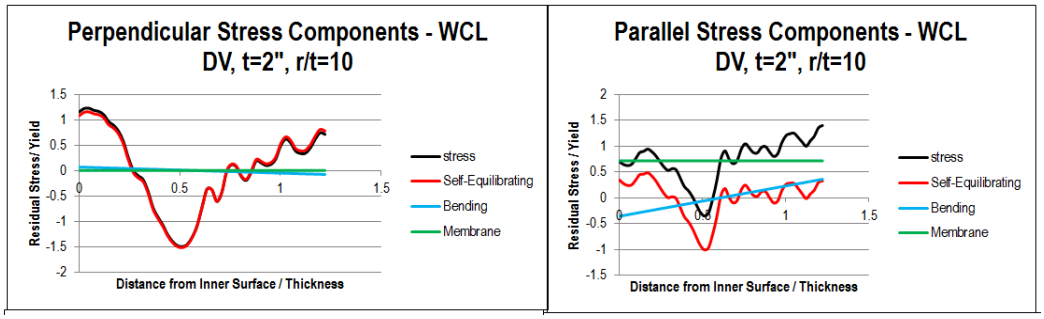

Figure 4-129 Weld centerline decomposed perpendicular and parallel residual stress components for DV with t=2", r/t=10

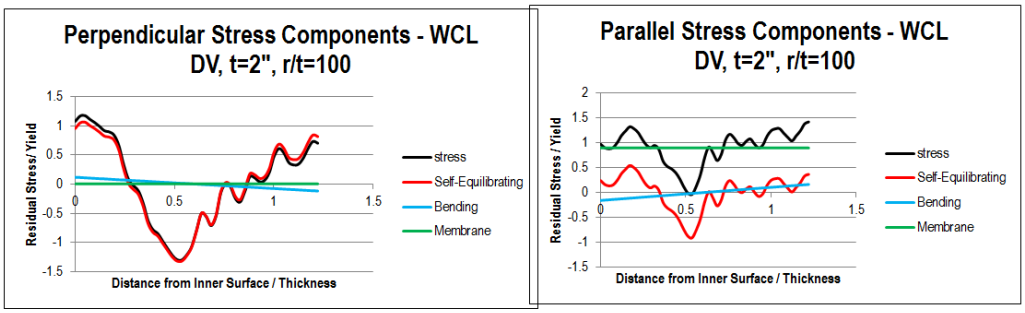

Figure 4-130 Weld centerline decomposed perpendicular and parallel residual stress components for DV with t=2", r/t=100

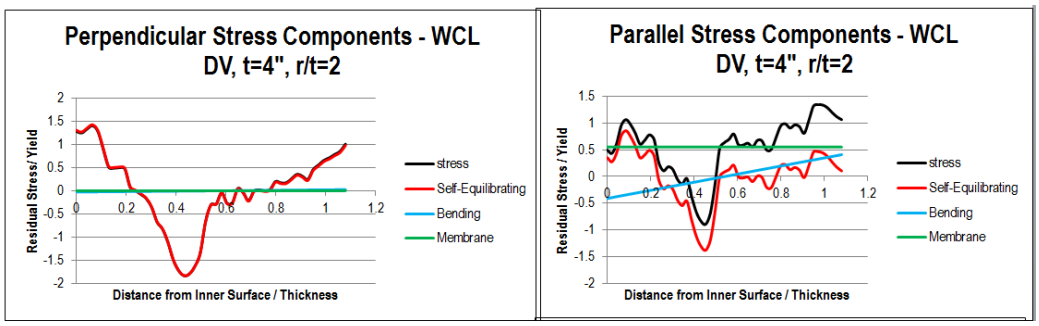

Figure 4-131 Weld centerline decomposed perpendicular and parallel residual stress components for DV with t=4", r/t=2

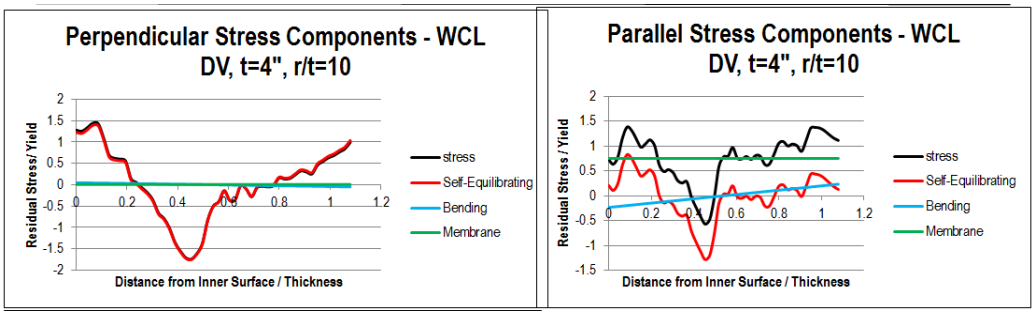

Figure 4-132 Weld centerline decomposed perpendicular and parallel residual stress components for DV with t=4", r/t=10

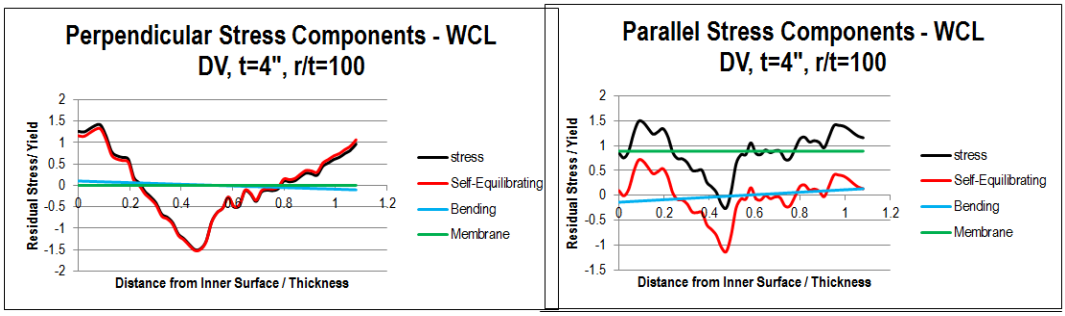

Figure 4-133 Weld centerline decomposed perpendicular and parallel residual stress components for DV with t=4", r/t=100

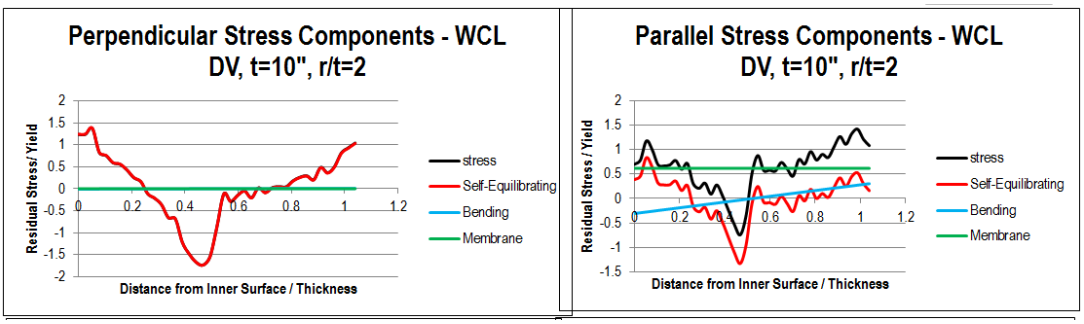

Figure 4-134 Weld centerline decomposed perpendicular and parallel residual stress components for DV with t=10", r/t=2

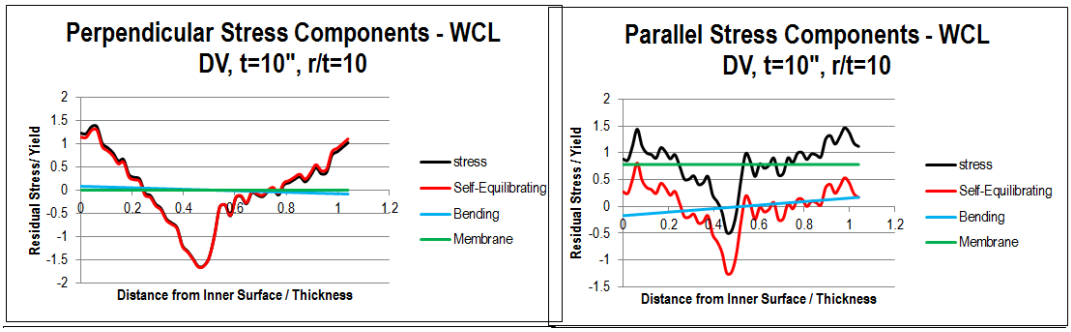

Figure 4-135 Weld centerline decomposed perpendicular and parallel residual stress components for DV with t=10", r/t=10

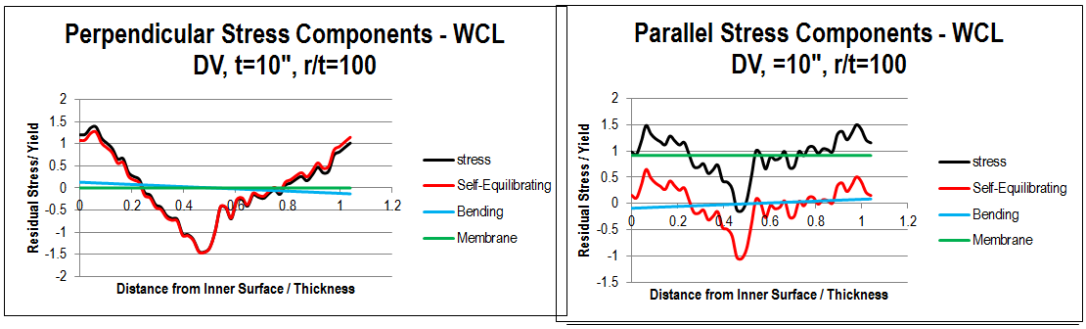

Figure 4-136 Weld centerline decomposed perpendicular and parallel residual stress components for DV with t=10", r/t=100

4.7 A shell-theory based full-field residual stress estimation scheme

As discussed above, it is of interest to estimate the profiles of membrane and bending stress components along pipe axial direction at each through-thickness location in order to obtain the

full-field residual stress distribution. To accomplish this, the classical shell theory [138] is adopted here to seek a mechanics-based approach. The known through-thickness residual stress distribution described in the previous sections can be used to provide additional information to this approach.

4.7.1 A two-part shell model and shrinkage force definition

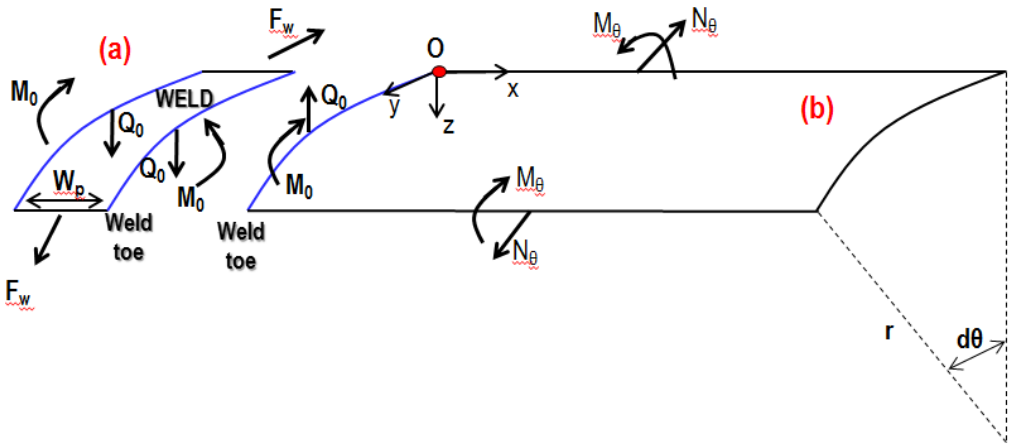

Figure 4-137 A two-part shell assembly model: (a) a shell section representing a girth weld of an equivalent width of W_p and (b) shell section representing pipe or vessel section away from the weld

From a mechanics point of view, a pipe girth weld can be viewed as a cylindrical shell subject to a circumferential shrinkage force. Figure 4-137 shows a slice of two-part shell assembly model representing a pipe girth weld. The small part (a) with width W_p represents the weld area. The large part (b) represents the pipe or vessel section away from the weld. At the interface between these two parts, there is an out-of-plane ring shear force Q_0 and ring moment M_0. These ring shear force and moment are due to reactions to the weld shrinkage force along the pipe hoop direction, F_w. For a given ring shear force Q_0 and ring moment M_0 acting at x=0, the radial displacement and axial line moments for the shell section on the right hand side can be described as [138]:

$$w(x) = -\frac{1}{2\beta^3 D}\left[\beta M_0 e^{-\beta x}(\cos\beta x - \sin\beta x) + Q_0 e^{-\beta x}\cos\beta x\right] \quad \textbf{(4.3)}$$

$$M_x(x) = M_0 e^{-\beta x}(\cos\beta x + \sin\beta x) + \frac{1}{\beta} Q_0 e^{-\beta x}\sin\beta x \quad \textbf{(4.4)}$$

where, β and D are defined as:

$$\beta = \frac{\sqrt[4]{3(1-\upsilon^2)}}{\sqrt{rt}}, \quad D = \frac{Et^3}{12(1-\upsilon^2)} \tag{4.5}$$

in which r is the mean radius of the pipe and t is the thickness. Once $M_x(x)$ and $w(x)$ are known, line moment $M_\theta(x)$ and line force $N_\theta(x)$ in the hoop direction in Figure 4-137(b) can be obtained as follows:

$$M_\theta(x) = \upsilon M_x(x) \tag{4.6}$$

$$N_\theta(x) = \frac{Etw(x)}{r} \tag{4.7}$$

In Eqs. (4.3) and (4.4), line moment M_0 can be approximated by the through-wall axial bending residual stresses at weld toe location, which can be obtained from the FE parametric analyses discussed in the previous sections and is referred to as $\sigma^0_{x,b}$ here:

$$M_0 = \frac{t^2}{6}\sigma^0_{x,b} \tag{4.8}$$

Q_0 can be derived from the welding shrinkage force F_w acting along the circumferential direction. The shrinkage force F_w can be approximated by the product of plastic zone width w_p (induced by welding) and the averaged hoop residual stress within the plastic zone encompassing the weld. Then, with the free body diagram shown in Figure 4-137(a), the radial line force Q_0 can be written as:

$$Q_0 = -\frac{F_w}{2r} = -\frac{\sigma^{ave}_{\theta,m} \cdot w_p \cdot t}{2r} = -\frac{\sigma^{ave}_{\theta,m} \cdot A_p}{2r} \tag{4.9}$$

where A_p is the plastic zone size which is typically larger than the area defined by the weld fusion zone profile, as shown by the shaded areas in Figure 4-138. The averaged hoop residual stress $\sigma^{ave}_{\theta,m}$ can be approximated by the membrane part of the hoop residual stress at weld centerline, which is already available from the parametric analyses discussed in the previous sections.

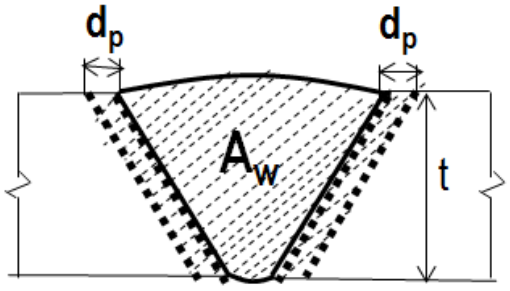

Figure 4-138 Welding-induced plastic zone area

One more parameter, i.e., w_p or A_p, however, remains to be determined before Eq. (4.9) can be used in solving Eqs. (4.3) and (4.4). Obviously, FE modeling can be used to determine w_p, which is only applicable for a case by case calculation. Given that the purpose of this study is to develop a simple engineering scheme for estimating through-thickness residual stress profile for fitness for service assessment, a simple plastic zone estimation method is proposed based on a 1D transient heat transfer and thermoplaticity theory. This method is elaborated next.

4.7.2 Simple plastic zone size estimation and validation

The extent of plastic zone beyond the weld fusion boundary, designated as d_p in Figure 4-138, can be simply modeled as a transient heat transfer problem with a molten weld deposit of size r_w without considering heat loss shown in Figure 4-139. As discussed before, the plastic zone size is related to ΔT_p which is the minimum temperature difference required to induce plastic strain in material. Once the temperature history $T(x, \lambda)$ is known, the plastic zone size d_p can be determined by checking the temperature over the entire domain where the condition shown in Figure 4-139 is satisfied. This condition will be further elaborated in a later section.

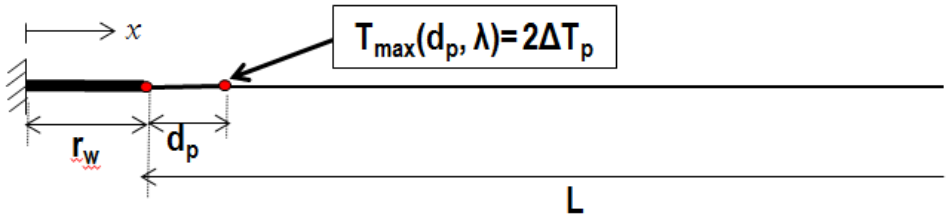

Figure 4-139 1D transient heat transfer model with weld deposition size r_w and plastic zone width d_p measured from fusion boundary

4.7.2.1 Analytical expression for 1D transient heat transfer problem and its validation

The governing equation for the 1D heat transfer model shown in is Figure 4-139 is given as:

$$\frac{\partial^2 T}{\partial x^2} = \frac{1}{\alpha}\frac{\partial T}{\partial \lambda} \tag{4.10}$$

Without considering heat loss, e.g. convection or radiation effect, the thermal boundary conditions are described as:

$$\frac{\partial T(0,\lambda)}{\partial x} = 0$$
$$\frac{\partial T(r_w + L,\lambda)}{\partial x} = 0 \quad \textbf{(4.11)}$$

and the initial conditions are:

$$T(x,0) = \begin{cases} T_m & (0 \le x \le r_w) \\ T_i(x,\lambda_w) & (r_w \le x \le L) \end{cases} \quad \textbf{(4.12)}$$

Note that in above equations, λ represents time, x distance, T temperature and L model length. The model length is set to be large enough to have no impact on the final solution. $\lambda_w = 1/v$ represents a dwell time and can be calculated using the welding travel speed v and material's thermal diffusivity α. In FE analysis, λ_w is also referred as holding time. $T_i(x,\lambda_w)$ in Eq. (4.12) is the initial temperature distribution in the domain at the positions starting from r_w. This initial temperature distribution can be determined by a point source with temperature T_m conducting in a finite length model as shown in Figure 4-140.

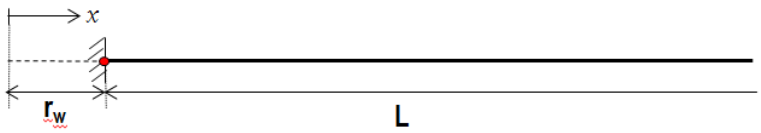

Figure 4-140 1D transient heat transfer model: a point heat source with temperature T_m

Note that in Figure 4-140, location of heat source is not set at the zero but at $x = r_w$ in order to obtain the corresponding solution of $T_i(x,\lambda_w)$ in Eq. (4.12). The governing equation of this model is the same as Eq. (4.10) but with different boundary conditions due to the prescribed heat source temperature T_m:

$$T_i(r_w,\lambda) = T_m$$
$$\frac{\partial T_i(r_w + L,\lambda)}{\partial x} = 0 \quad \textbf{(4.13)}$$

and initial condition:

$$T_i(x,0) = T_0 \quad \textbf{(4.14)}$$

where T_0 represents ambient temperature, e.g., room temperature. The solution of $T_i(x,\lambda_w)$ can be solved in as:

$$T_i(x,\lambda_w)=\sum_{n=0}^{\infty}\left\{\frac{4(T_0-T_m)}{(2n+1)\pi}e^{-\alpha\left(\frac{(2n+1)\pi}{2L}\right)^2\lambda_w}\sin\left[\frac{(2n+1)\pi}{2L}(x-r_w)\right]\right\}+T_m \qquad (r_w\le x\le L) \tag{4.15}$$

Once initial temperature $T_i(x,\lambda_w)$ in Eq. (4.12) is available, the solution of temperature distribution for 1D model shown in Figure 4-139 can then be expressed in a closed from as follows:

$$T(x,\lambda)=\sum_{j=1}^{\infty}C_j\exp\left(-\alpha b_j^2\lambda_w\right)\cos(b_j x)+C_0 \tag{4.16}$$

where, the coefficients C_j , b_j and C_0 are given as:

$$\begin{aligned}
&(a_i=b_j)\Rightarrow C_j=\frac{2}{L+r_w}\sum_{i=0}^{\infty}D_i\frac{\cos(b_j r_w)}{a_i^2-b_j^2}\\
&(a_i\neq b_j)\Rightarrow C_j=\frac{2}{L+r_w}\left(\frac{\cos(b_j r_w)}{2b_j}+\frac{L}{2}\sin(b_j r_w)\right)\\
&C_0=T_m+\frac{1}{L+r_w}\sum_{i=0}^{\infty}\frac{D_i}{a_i}\\
&b_j=\frac{j\pi}{L+r_w}\\
&a_i=\frac{2i+1}{2L}\pi\\
&D_i=\frac{2(T_0-T_m)}{a_i L}\exp\left(-\alpha a_i\lambda_w\right),
\end{aligned} \tag{4.17}$$

The analytical solution obtained from Eqs. (4.16-4.17) is validated by using 1D heat transfer FE model. The FE model is shown in Figure 4-141. The element size is 0.083mm which is small enough to ensure accurate temperature distribution. The deposit weld size of r_w is 5mm as shown in red in Figure 4-141 with the initial temperature T_m=1500 ℃. The length *L* (in blue) is 295mm with the initial temperature T_0=23 ℃. Only a small portion of *L* is shown in Figure 4-141 because of space limitation. λ_w is set as 0.5s and is applied to r_w. After that, heat conduction occurs for enough long time until the entire model reaches to constant temperature. For consistency, heat loss is not considered in the model. For simplicity, 2.25CrMo-V room temperature thermal properties are used here, which are available in Figure 4-3.

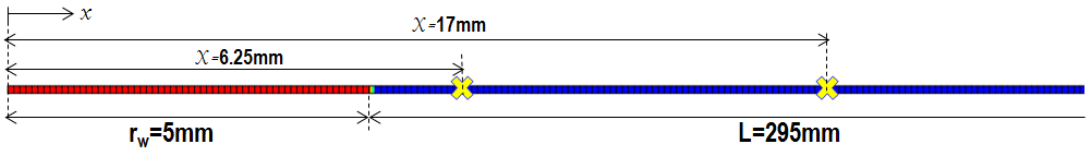

Figure 4-141 1D heat transfer finite element model with r_w of 5mm and L of 300mm

The temperature histories at two points in the model are examined in detail. As shown in Figure 4-141, one point is at 1.25mm away from the weld edge at *x*=6.25mm and the other point is at *x*=17mm.
Figure 4-143 and
Figure 4-143 show a comparison of temperature histories obtained from the analytical solution and FE model at these two positions, respectively. The results are plotted after 0.5s of λ_w time at each position. The values of i and j in Eqs. (4.16-4.17) are set as 100, large enough to obtain accurate result from analytical solution. It can be seen from the plots that the results obtained from the analytical solution and FEA are in good agreement.

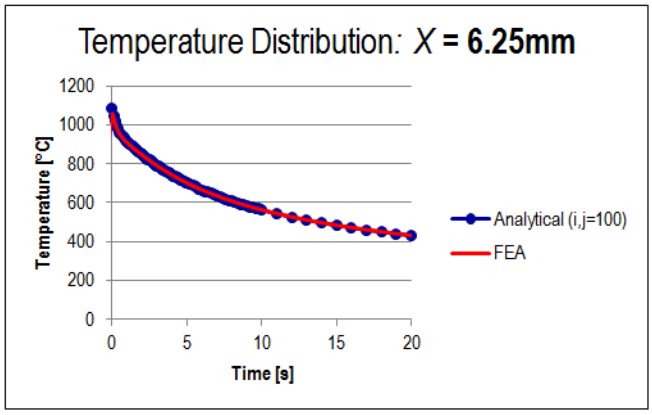

Figure 4-142 Analytical solution versus FE result at locations of *x*=6.25mm

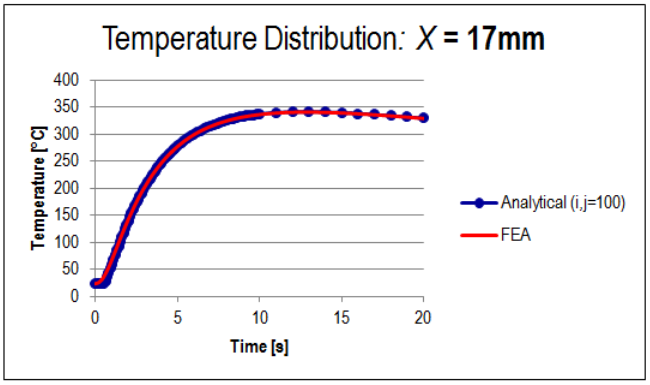

Figure 4-143 Analytical solution versus FE result at locations of *x*=17mm

4.7.2.2 Approximate solution for estimating plastic zone size and its validation

With the knowledge of temperature history T(x, λ), plastic zone size parameter d_p can be determined by checking the maximum temperature experienced at each position in the domain. The condition for determining d_p is $T_{max}=2\Delta T_p$ as shown in Figure 4-139, as discussed in 3.2.3 1-D bar model illustration. ΔT_p can be determined using a simple 1D bar model. Consider a bar under a fully restraint condition with elastic perfectly plastic material and isotropic hardening. The bar is heated to a certain temperature ΔT_p when plastic strain starts to occur. ΔT_p can be expressed as:

$$\Delta T_P = \frac{S_Y}{E \times CTE} \tag{4.18}$$

where S_Y is the yield strength of material of interest, E Young's modulus and CTE coefficient of thermal expansion. In order to generate plastic strain after cooling down to room temperature, the heating temperature should be greater than $2\Delta T_p$. So an upper bound estimate of d_p in Figure 4-139 can be written as:

$$T_{\max}(d_p, \lambda) = 2\Delta T_p \tag{4.19}$$

However, it is difficult to derive an explicit expression of d_p directly from the analytical solution Eqs. (4.16-4.17) because the maximum temperature history at each position T_{max} (x, λ) needs to be explicitly derived first. Therefore, we approach this from another angle. Based on the discussion so far, it has been found that d_p is dependent on temperature difference (T_m- T_0), weld size r_w, time λ_w, thermal diffusivity α from Eqs. (4.16-4.17), and maximum temperature boundary $2\Delta T_p$ from Eq. (4.19). These governing parameters are explored individually with respect to plastic zone size d_p, as shown in Figure 4-144. It is clearly observed that d_p increases monotonically with the increase of (T_m- T_0), r_w, square root of λ_w and α, and decreases with the increase of $2\Delta T_p$. Using a linear regression analysis technique, this leads to the following approximate solution for d_p:

$$d_p = \frac{r_w + 2\sqrt{\alpha \lambda_W / \pi}}{2\Delta T_P - T_0} \times \frac{T_m - T_0}{2} - r_w \tag{4.20}$$

Then, the resulting plastic zone area in Figure 4-138 can be estimated as:

$$A_p = A_w + 2d_p t \tag{4.21}$$

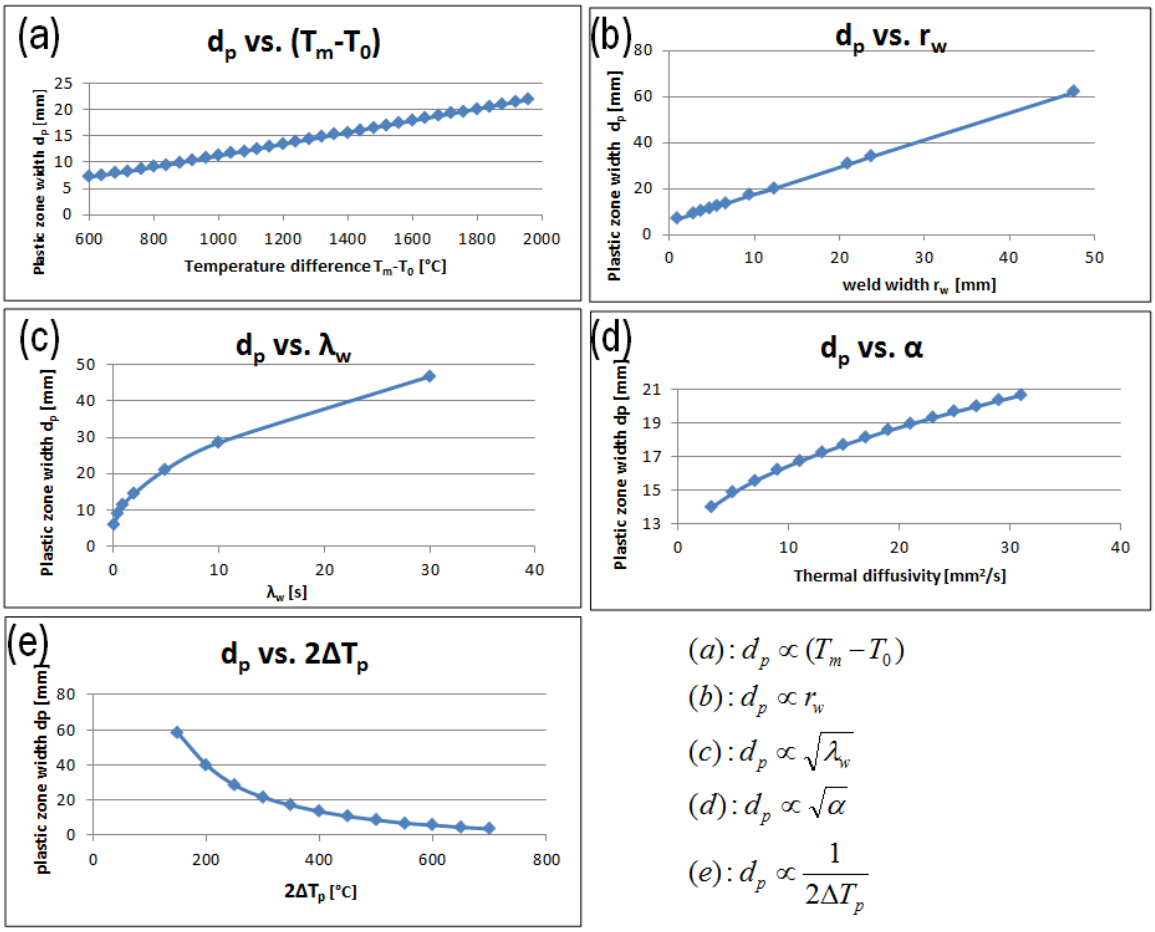

Figure 4-144 Relationships between d_p and each governing parameter: (a) d_p versus (T_m-T_0), (b) d_p versus r_w (c) d_p versus λ_w, (d) d_p versus α, and (e) d_p versus $2\Delta T_p$

Validation of the above plastic zone size estimation scheme is conducted by using FEA for various girth weld configurations discussed before. Table 4-6 summarizes a comparison of the d_p results obtained from the estimation scheme of Eq. (4.20) and FEA analyses. Please note that r_w in the table is the radius of the averaged pass area A_{pass}. Overall, a good agreement is achieved, except for the case of Single V with a thickness of 10". As to be illustrated later, this discrepancy does not significantly affect the shell theory based residual stress distribution estimation. Additional girth weld results obtained by Eq. (4.20) and FEA in Figure 4-52 are summarized in Table 4-7. A good agreement is also observed.

Table 4-6 d_p comparison between Eq. (4.20) and FEA results: girth welds

dp Comparison Between Estimation and FEA [mm]					
	Thickness	A_{pass}	r_w	d_p (estimation)	d_p (FEA Girth Weld r/t=10)
Single V	0.25"	28	3	8.95	10
	1"	94	5.47	12	18
	10"	490	12.5	19.8	45
Double V	2"	58	4.29	10.46	13
Narrow Groove	4"	92	5.41	11.73	18

Table 4-7 d_p comparison between Eq. (4.20) and FEA results: girth welds

Single V, t=1", r/t=10 [*mm*]		
Estimation		**FEA (Fig. 3.71)**
Thickness	1"	
Pass Area	94	
r_w	**5.47**	
d_p *2.25CrMo-V*	**12**	**12**
d_p *1.25CrMo*	**20.4**	**20**
d_p *SS304*	**24**	**24**

Another validation is performed on a T-fillet weld joint using gerneralized plane strain conditions. Detailed model geomety is shown in Figure 4-145. The weld area is 12.5mm^2 which corresponds r_w of 2*mm*, and thickness is 6.35*mm*. Four materials (ship hull steel, aluminum 6061, titanium Ti-CP, and titanium alloy Ti-6-4) are used in the analysis with different holding time λ_w. Parameters used in Eq. (4.20) are also summarized in Table 4-8. Again, a good agreement is observed between the estimations from Eq. (4.20) and FEA results.

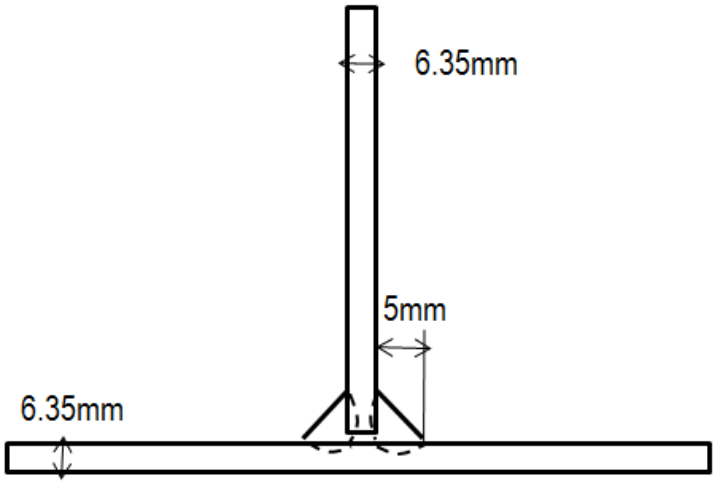

Figure 4-145 T-joint fillet weld geometry

Table 4-8 d_p comparison between Eq. (4.20) and FEA results: T-joint fillet weld

dp Comparison Between Estimation and FEA						
	T_m [°C]	$2\Delta T_p$ [°C]	α [mm/s]	λ_w [s]	d_p from estimation [mm]	d_p From FEA [mm]
Steel	1500	282	10.57	0.35	9.88	11.5
Aluminum	615	338	59.6	0.1	2.41	2.25
Ti-CP	1676	779	8.95	0.45	2.66	2.1
Ti-6-4	1649	1614	2.57	1.0	0	0

4.7.2.3 Explanation of the approximate solution for plastic zone size estimation

It is surprised to see that the expression of Eq. (4.20) for plastic zone size d_p can be expressed in such a concise form, rather than a complex formulation derived from the analytical solution Eqs. (4.16-4.17). However, with further analysis, the simple form of Eq. (4.20) can be explained by linear heat input calculation from the perspective of conservation of energy. With the validated two parts linear heat inputs using Eqs. (3.21-3.24) as described in Chapter 3, the corresponding thermal energy inputs for 1D model in Figure 4-139 can be re-written by using the parameters for determining d_p as follows:

$$Q_{in-1}' = \rho \cdot C_p \cdot (T_m - T_0) \cdot r_w \quad \textbf{(4.22)}$$

$$Q_{in-2}' = 2k \cdot (T_m - T_0) \cdot \sqrt{\frac{\lambda_w}{\pi\alpha}} \tag{4.23}$$

The resulting total thermal energy input can be written as, with $\alpha = k/\rho/C_p$:

$$\begin{aligned} Q_{in}' &= Q_{in-1}' + Q_{in-2}' = \rho \cdot C_p \cdot (T_m - T_0) \cdot r_w + 2k \cdot (T_m - T_0) \cdot \sqrt{\frac{\lambda_w}{\pi\alpha}} \\ &= \rho C_p \cdot (T_m - T_0) \cdot \left(r_w + 2\sqrt{\frac{\alpha\lambda_w}{\pi}} \right) \end{aligned} \tag{4.24}$$

Thermal energy reserved at any time for this 1D model can be described as:

$$Q_{rev}' = \rho C_p \cdot \int_0^{r_w+L} (T(x) - T_0)\, dx \tag{4.25}$$

At a given point x^*, the temperature history for this point can be denoted as $T(x^*, \lambda)$. Assuming at $\lambda=\lambda^*$, maximum temperature $T(x^*, \lambda^*)$ is reached by $T(x^*, \lambda)$ which satisfies the condition:

$$\left. \frac{\partial T(x^*, \lambda)}{\partial t} \right|_{\lambda = \lambda^*} = 0 \tag{4.26}$$

According to the governing equation Eq. (4.10), Eq. (4.26) can be re-written as:

$$\left. \frac{\partial^2 T(x, \lambda^*)}{\partial x^2} \right|_{x = x^*} = 0 \tag{4.27}$$

which means at time λ^*, temperature distribution $T(x, \lambda^*)$ satisfies the above condition when the maximum temperature $T(x^*, \lambda^*)$ is reached for the location of $x=x^*$. Also, Eq. (4.27) suggests that at the maximum temperature $T(x^*, \lambda^*)$ the tangent line $\partial T(x, \lambda^*)/\partial x$ is identical in the neighborhood of $x=x^*$. This makes a part of reserved energy, calculated by Eq. (4.25) where $T(x) = T(x, \lambda^*)$, centrosymmetric with respect to the point $(x^*, T(x^*, \lambda^*))$. In this regard, reserved thermal energy can be simplified to a certain level.

Figure 4-146 illustrates how an original reserved thermal energy is transformed to a simplified form. Figure 4-146(a) is the original reserved energy for a certain temperature distribution $T(x, \lambda^*)$ which is marked as a blue curve. The shaded area is represented by Eq. (4.25). At the inflection point of $(x^*, T(x^*, \lambda^*))$, based on the condition in Eq. (4.27), the upper dotted area shifts to the lower right area outside of $T(x, \lambda^*)$ as shown in (b). By switching a small part on the lower right corner, the area under the curve $T(x, \lambda^*)$ in (a) can be transformed to a rectangle in (c).

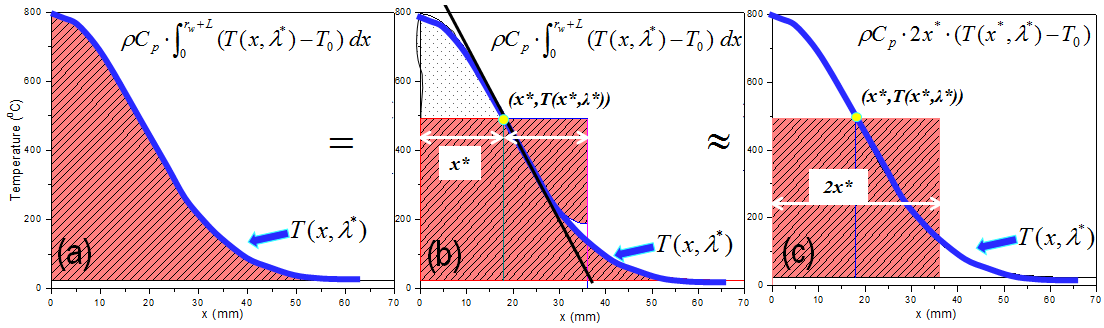

Figure 4-146 Reserved thermal energy: (a) original reserved thermal energy, (b) transition and (c) approximate reserved thermal energy

Please note x^*= r_w+ d_p, and T(x^*, λ^*)=2ΔT_p. Eq. (4.25) then becomes as below:

$$Q_{rev}' \approx \rho C_p \cdot 2(r_w + d_p) \cdot (2\Delta T_p - T_0) \quad \textbf{(4.28)}$$

By the law of energy conservation, thermal energy input (Eq. (4.24)) is equal to the energy reserved (Eq. (4.28)) for any model without considering energy loss, which results in:

$$Q_{in}' = Q_{rev}' \Rightarrow \rho C_p \cdot (T_m - T_0) \cdot \left(r_w + 2\sqrt{\frac{\alpha \lambda_w}{\pi}} \right) = \rho C_p \cdot 2(r_w + d_p) \cdot (2\Delta T_p - T_0) \quad \textbf{(4.29)}$$

The expression Eq. (4.20) of plastic zone size d_p can then be obtained by re-arranging Eq. (4.29).

4.7.3 Shell-theory based estimations versus FE results for selected cases

With plastic zone area estimated from Eq. (4.21), M_0 and Q_0 can now be calculated from Eqs. (4.8) and (4.9), respectively. Eq. (4.4) can then be used to calculate the resulting axial residual stress as a function of distance from the plastic zone boundary, representing a through-thickness bending component in Eq. (4.1):

$$\sigma_{x,b} = \frac{6M_x(x)}{t^2} \quad \textbf{(4.30)}$$

where x is, strictly speaking, measured from the plastic zone boundary. For convenience, it is shown next that x can be assumed to be originated from weld toe without introducing any noticeable error.

The corresponding hoop residual stresses in the form of through-thickness membrane and bending components, by inserting M_θ (x) and N_θ (x) from Eqs. (4.6-4.7) can now be simply expressed as:

$$\sigma_{\theta,b} = \frac{6M_\theta(x)}{t^2}$$
$$\sigma_{\theta,m} = \frac{N_\theta(x)}{t} \quad \textbf{(4.31)}$$

Again, x is measured from the plastic zone boundary. However, due to the nature of elastic Hooks' law used by the elastic shell solution given by Eq. (4.31), Eqs. (4.6-4.7) introduce a stress discontinuity at the plastic zone boundary. This difficulty can be overcome by introducing a linear distribution from weld toe position to the plastic zone boundary. Eq. (4.31) then becomes as below:

$$\sigma_{\theta,b} = \left(-\frac{h_b}{d_p}\xi + h_b \right) + \frac{6M_\theta(x)}{t^2}, \quad 0 \le \xi \le d_p$$
$$h_b = \sigma^0_{\theta,b} - \left[\frac{6M_\theta(x)}{t^2} \right]_{x=0} \quad \textbf{(4.32)}$$

$$\sigma_{\theta,m} = \left(-\frac{h_m}{d_p}\xi + h_m \right) + \frac{N_\theta(x)}{t}, \quad 0 \le \xi \le d_p$$
$$h_m = \sigma^0_{\theta,m} - \left[\frac{N_\theta(x)}{t} \right]_{x=0} \quad \textbf{(4.33)}$$

where $\sigma^0_{\theta,m}$ and $\sigma^0_{\theta,b}$ are the hoop membrane and bending components calculated from FEA and h_b and h_m are the differences in hoop bending and hoop membrane stresses between the estimated values and FEA results. ζ is the distance of the linear part, which is measured from zero to d_p.

The cases investigated using the simple estimation scheme are summarized in Table 4-4. Some of the thin wall cases (e.g., t=1/4", t=1/2") documented in [13] are also re-analyzed for completeness of thickness range. As such, the cases studied cover all of the joint preparations (SV, DV, NG), material types (low alloy, high alloy), r/t ratio ranging from 2 to 100, pipe/vessel wall thickness ranging from ¼" to 10". The simple estimation scheme is first used to develop profiles of membrane and bending components along pipe axial direction for a girth weld with a thickness of ¼" (single V preparation). Figure 4-147 and Figure 4-148show the results for the two cases with r/t ratio of 10 and 100, respectively. The results of residual stress components are presented in terms of normalized residual stresses by material yield strengths and compared with full-field finite element modeling results (available in Section 4.6). And the results of radial deflection are plotted by the actual displacement in *mm*. The horizontal axis is measured from weld toe and normalized by $\sqrt{rt}$. The results calculated based on the estimation scheme are plotted in blue and FEA results in red. It can be seen that the two sets of results are in good agreement from weld toe position to a distance where all residual stresses vanish. The same trend can also be seen in Figure 4-149 for the case of wall thickness of 1" and r/t ratio of 10, and in

Figure 4-150, Figure 4-151, and Figure 4-152 for the cases of wall thickness of 2", r/t ratio of 2, 10, and 100, respectively.

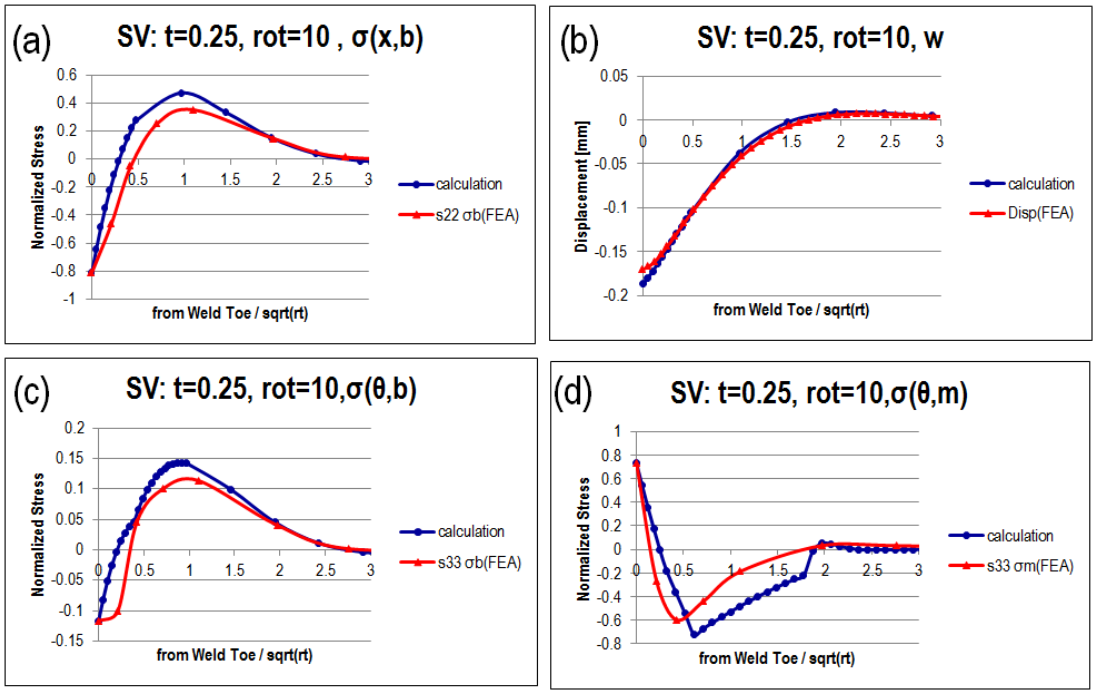

Figure 4-147 Simple estimation scheme based calculated results versus FE results for SV 1/4" thickness and r/t of 10: (a) axial bending residual stresses; (b) radial deflection (c) hoop bending residual stresses and (d) hoop membrane residual stresses

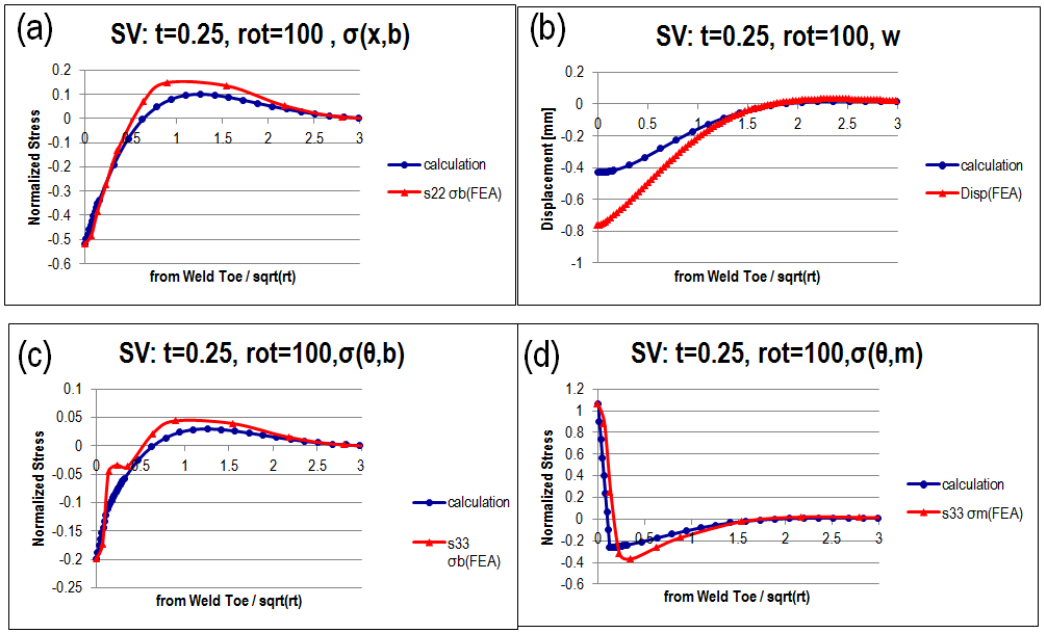

Figure 4-148 Simple estimation scheme based calculated results versus FE results for SV 1/4" thickness and r/t of 100: (a) axial bending residual stresses; (b) radial deflection (c) hoop bending residual stresses and (d) hoop membrane residual stresses

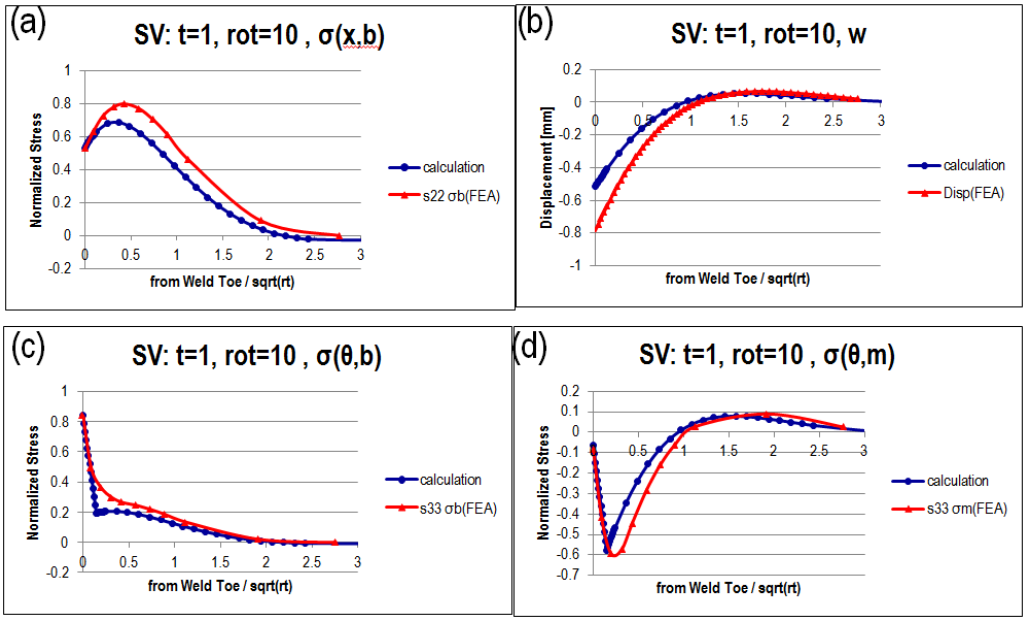

Figure 4-149 Simple estimation scheme based calculated results versus FE results for SV 1" thickness and r/t of 10: (a) axial bending residual stresses; (b) radial deflection (c) hoop bending residual stresses and (d) hoop membrane residual stresses

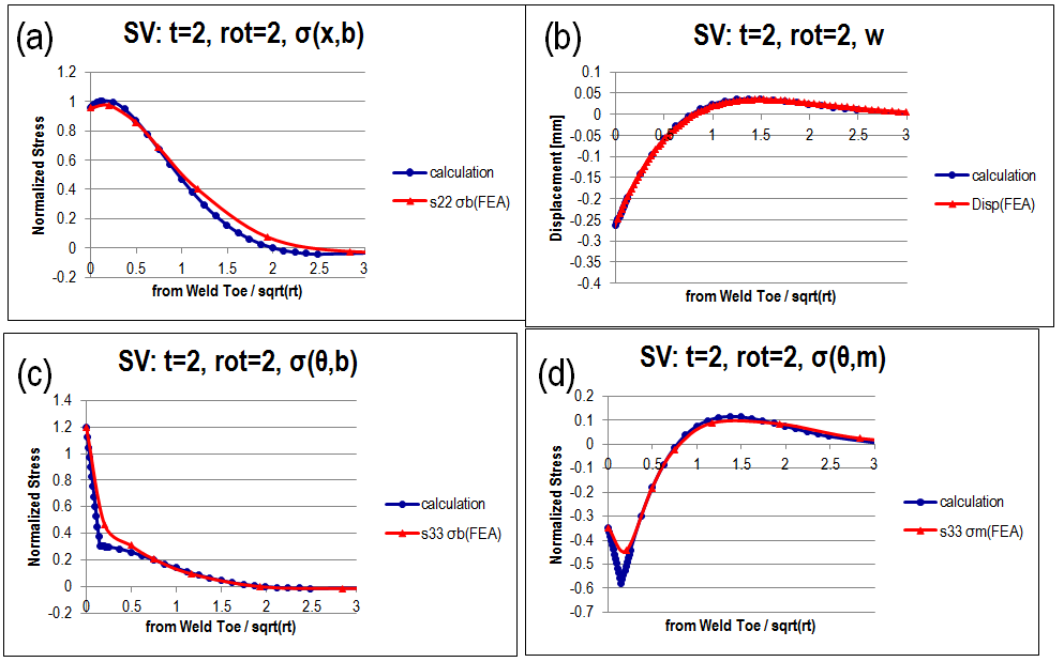

Figure 4-150 Simple estimation scheme based calculated results versus FE results for SV, 2" thickness and r/t of 2: (a) axial bending residual stresses; (b) radial deflection (c) hoop bending residual stresses and (d) hoop membrane residual stresses

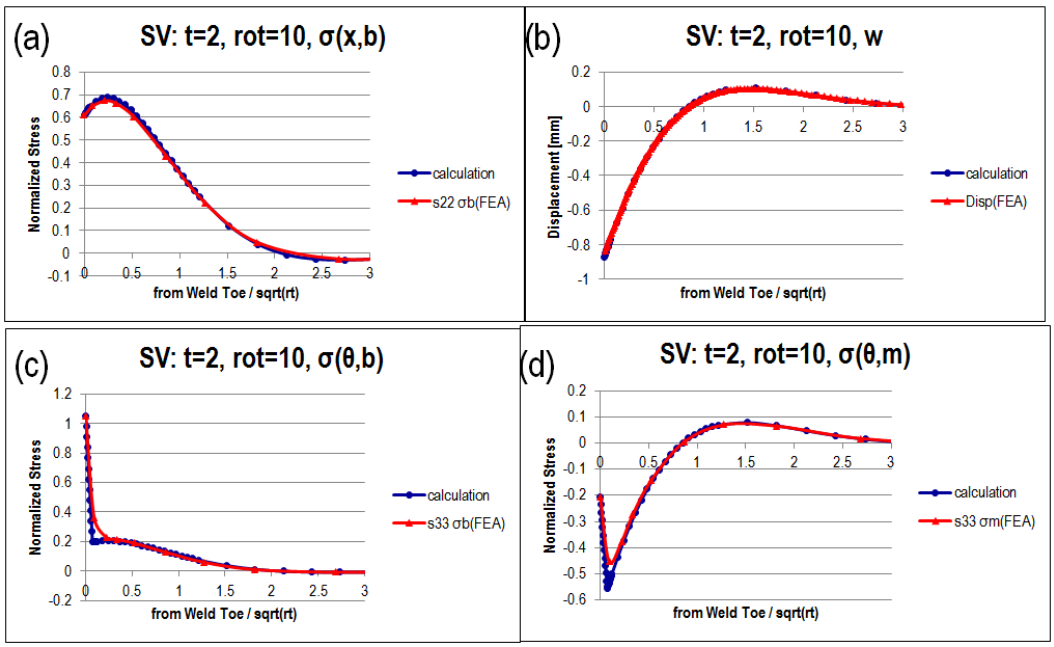

Figure 4-151 Simple estimation scheme based calculated results versus FE results for SV, 2" thickness and r/t of 10: (a) axial bending residual stresses; (b) radial deflection (c) hoop bending residual stresses and (d) hoop membrane residual stresses

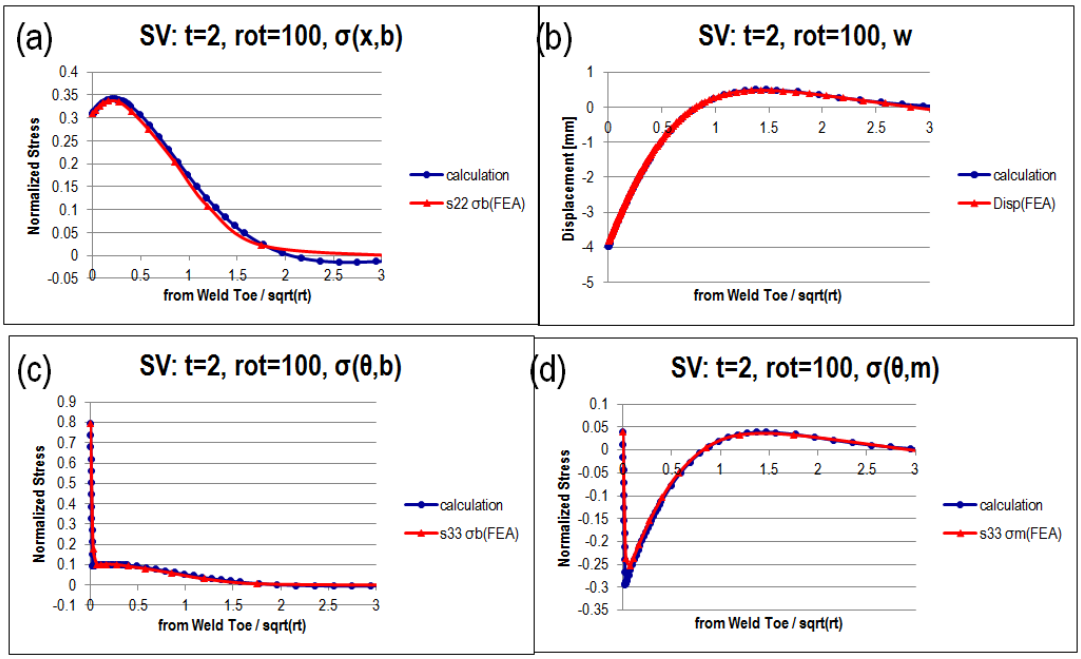

Figure 4-152 Simple estimation scheme based calculated results versus FE results for SV, 2" thickness and r/t of 100: (a) axial bending residual stresses; (b) radial deflection (c) hoop bending residual stresses and (d) hoop membrane residual stresses

As for thick wall section, two cases of 10" thick single V joint preparation are presented in Figure 4-153 and Figure 4-154. One is with r/t ratio of 10, and the other one is 100. An excellent agreement between shell based simple estimations and FEA results are observed, although there is a noticeable difference in the estimated plastic zone width d_p as shown in Table 4-5. These cases demonstrate that shell theory based simple estimation scheme is also applicable for thick section girth weld.

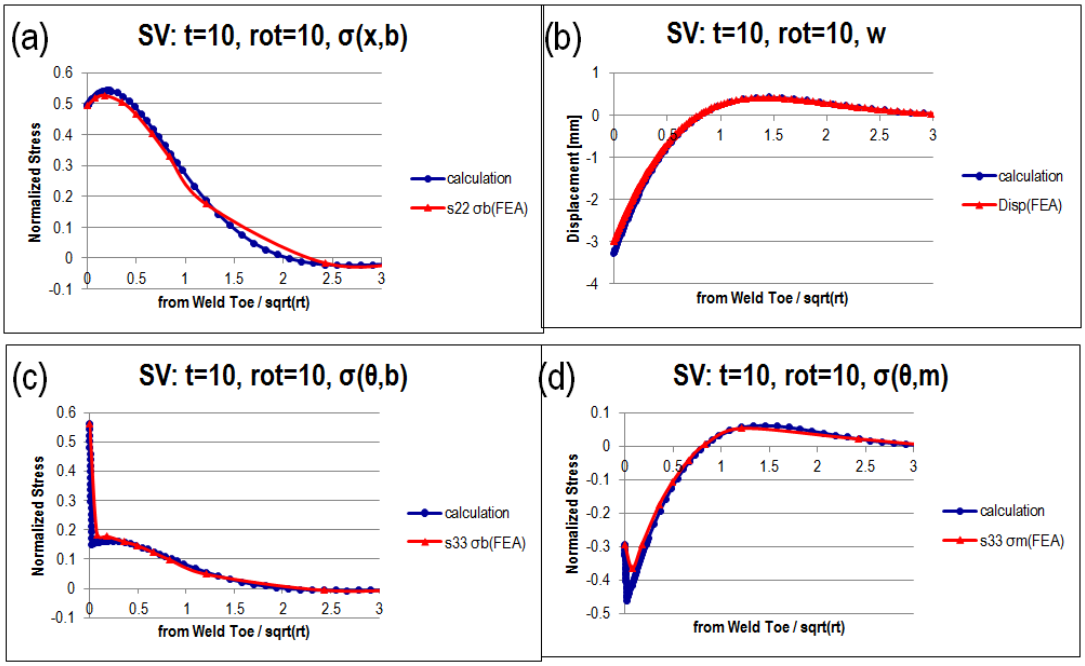

Figure 4-153 Simple estimation scheme based calculated results versus FE results for SV 10" thickness and r/t of 10: (a) axial bending residual stresses; (b) radial deflection (c) hoop bending residual stresses and (d) hoop membrane residual stresses

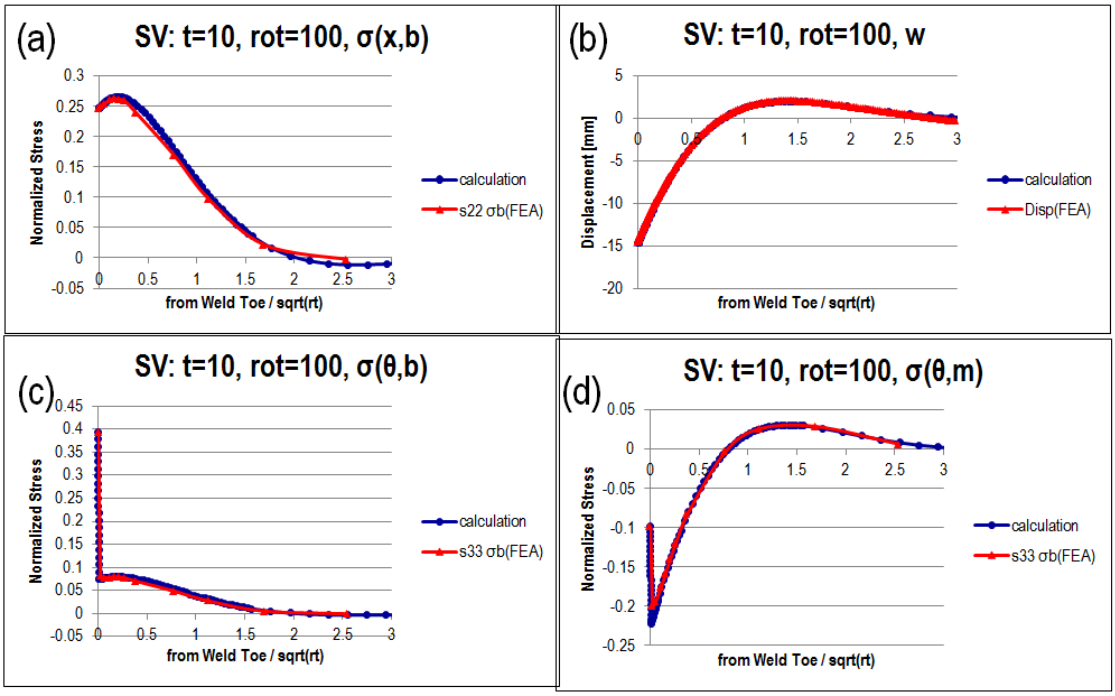

Figure 4-154 Simple estimation scheme based calculated results versus FE results for SV 10" thickness and r/t of 100: (a) axial bending residual stresses; (b) radial deflection (c) hoop bending residual stresses and (d) hoop membrane residual stresses

The cases studied for Narrow Groove girth welds are presented in Figure 4-155, Figure 4-156 and Figure 4-157 for 1" thickness, r/t ratio of 2, 10, and 100, respectively. Figure 4-158, Figure 4-159, and Figure 4-160 are for the cases of 10" thickness, r/t ratio of 2, 10, and 100, respectively. Double-V girth welds results are summarized in the same manner for 1" and 10" thickness, r/t ratio of 2, 10, and 100 in Figure 4-161, Figure 4-162 to Figure 4-163. A good agreement is observed in all of cases analyzed between the simple estimation scheme based calculation and finite element results.

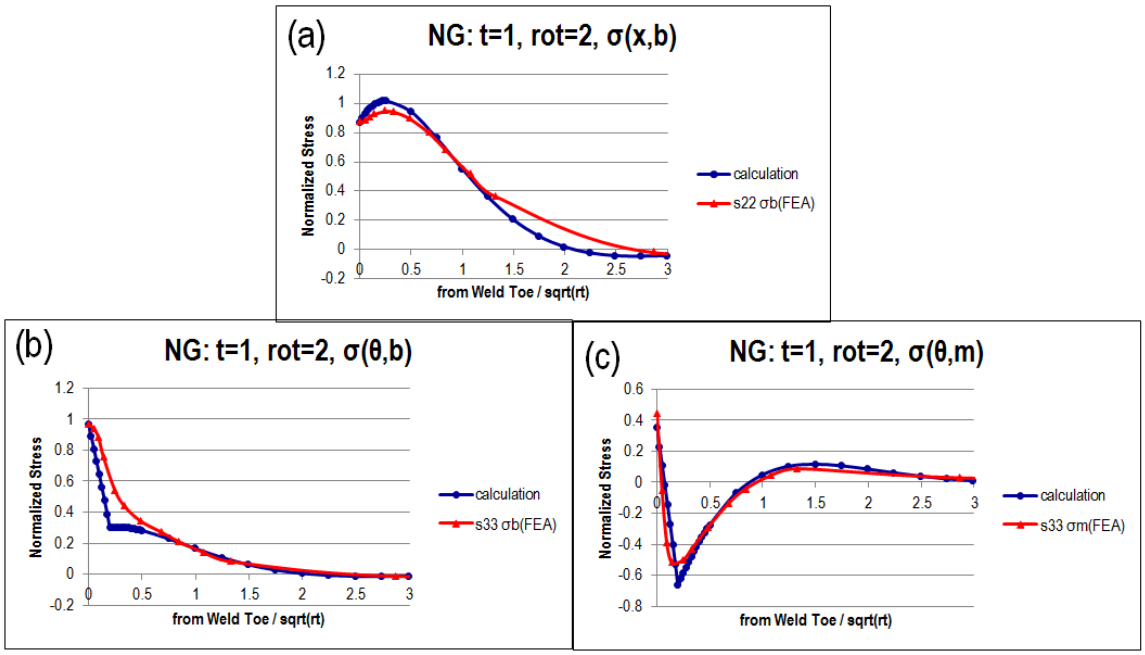

Figure 4-155 Simple estimation scheme based calculated results versus FE results for NG 1" thickness and r/t of 2: (a) axial bending residual stresses, (b) hoop bending residual stresses and (c) hoop membrane residual stresses

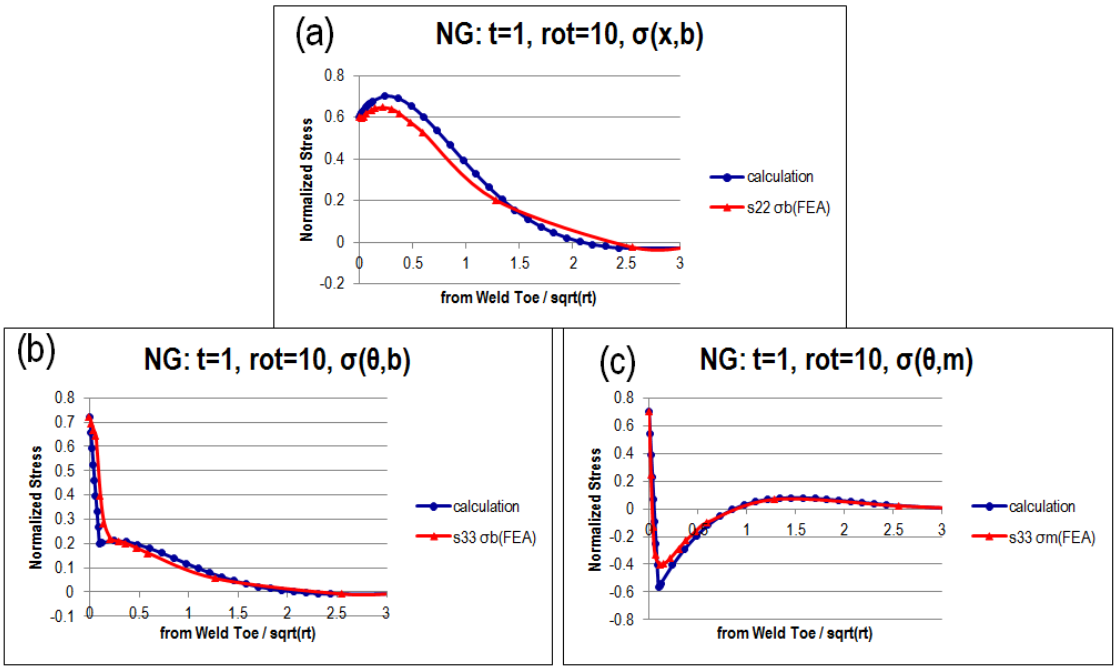

Figure 4-156 Simple estimation scheme based calculated results versus FE results for NG 1" thickness and r/t of 10: (a) axial bending residual stresses, (b) hoop bending residual stresses and (c) hoop membrane residual stresses

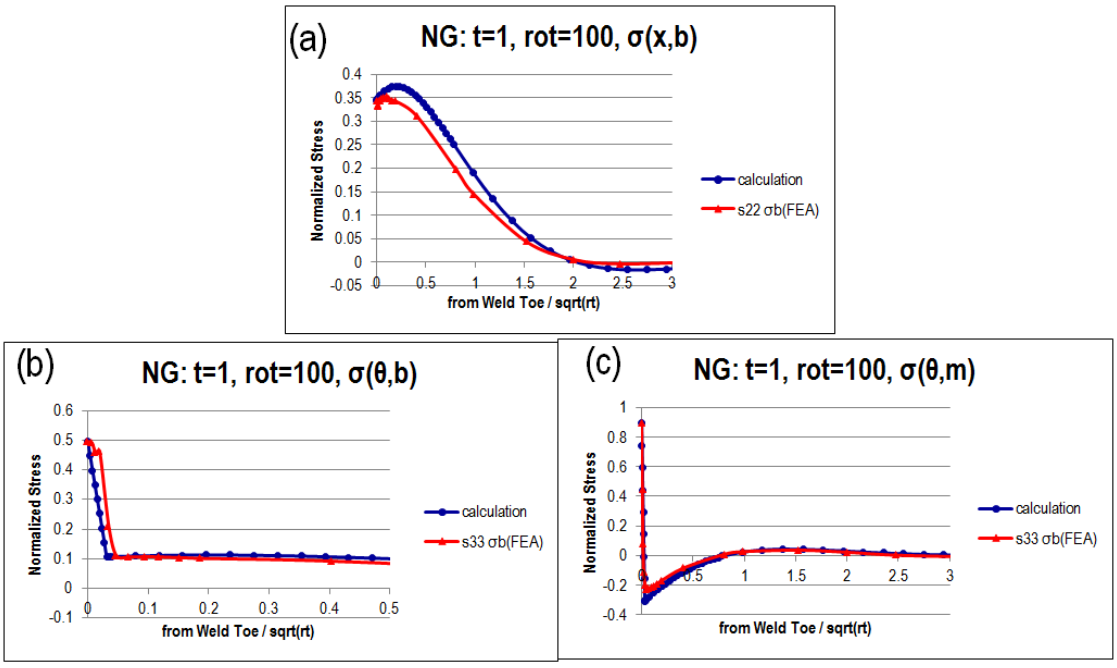

Figure 4-157 Simple estimation scheme based calculated results versus FE results for NG 1" thickness and r/t of 100: (a) axial bending residual stresses, (b) hoop bending residual stresses and (c) hoop membrane residual stresses

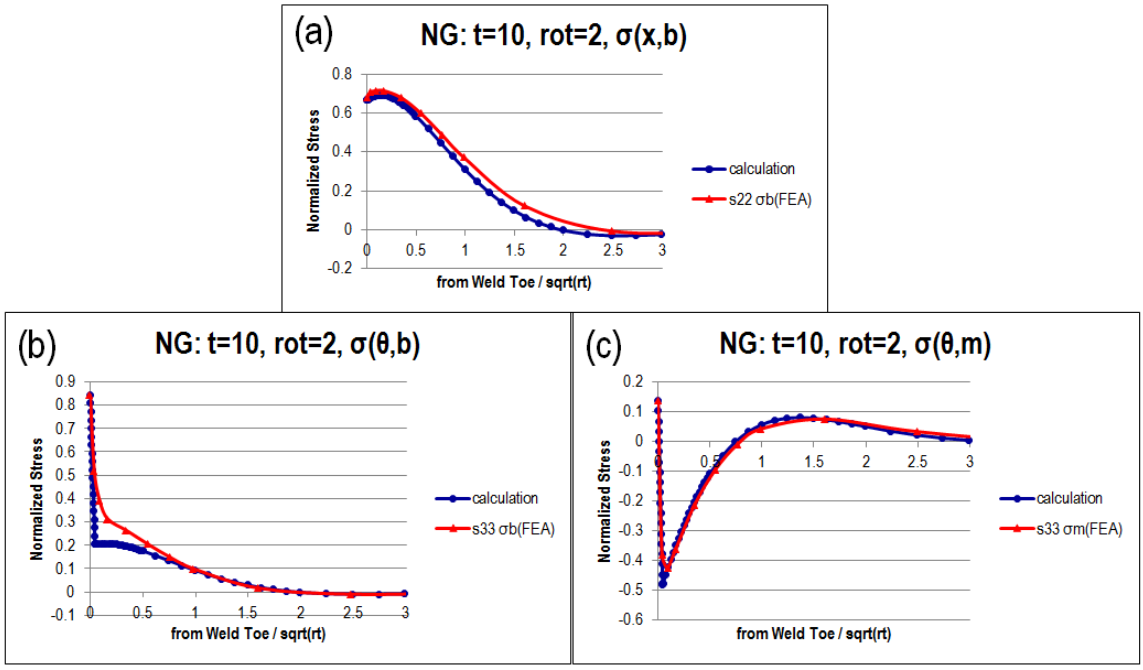

Figure 4-158 Simple estimation scheme based calculated results versus FE results for NG 10" thickness and r/t of 2: (a) axial bending residual stresses, (b) hoop bending residual stresses and (c) hoop membrane residual stresses

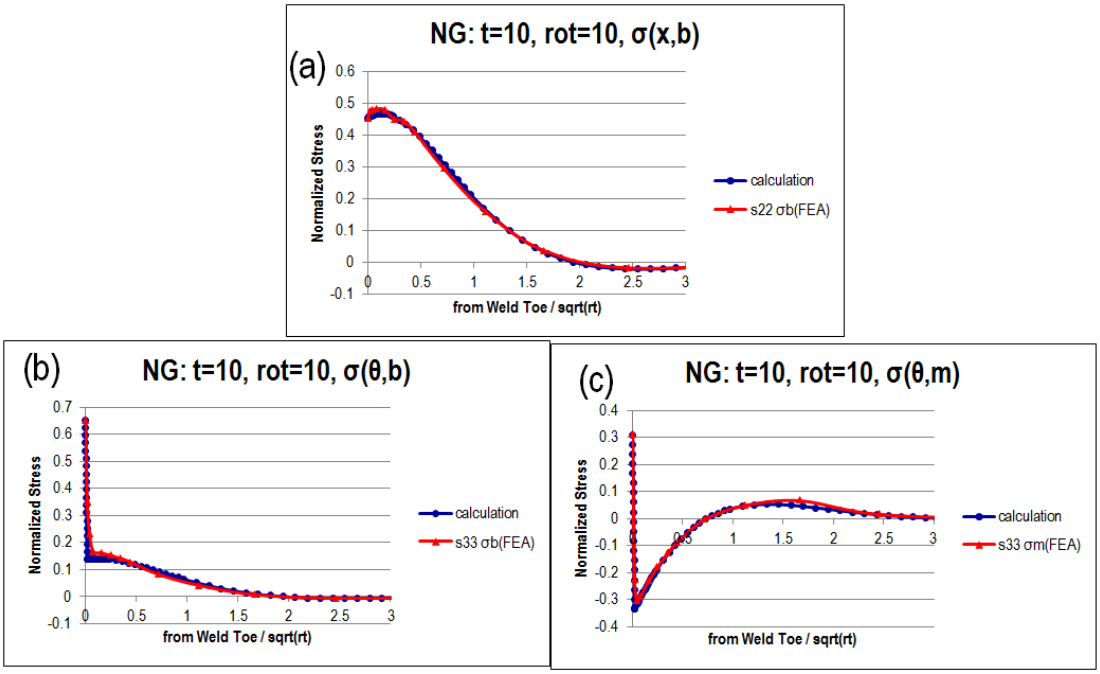

Figure 4-159 Simple estimation scheme based calculated results versus FE results for NG 10" thickness and r/t of 10: (a) axial bending residual stresses, (b) hoop bending residual stresses and (c) hoop membrane residual stresses

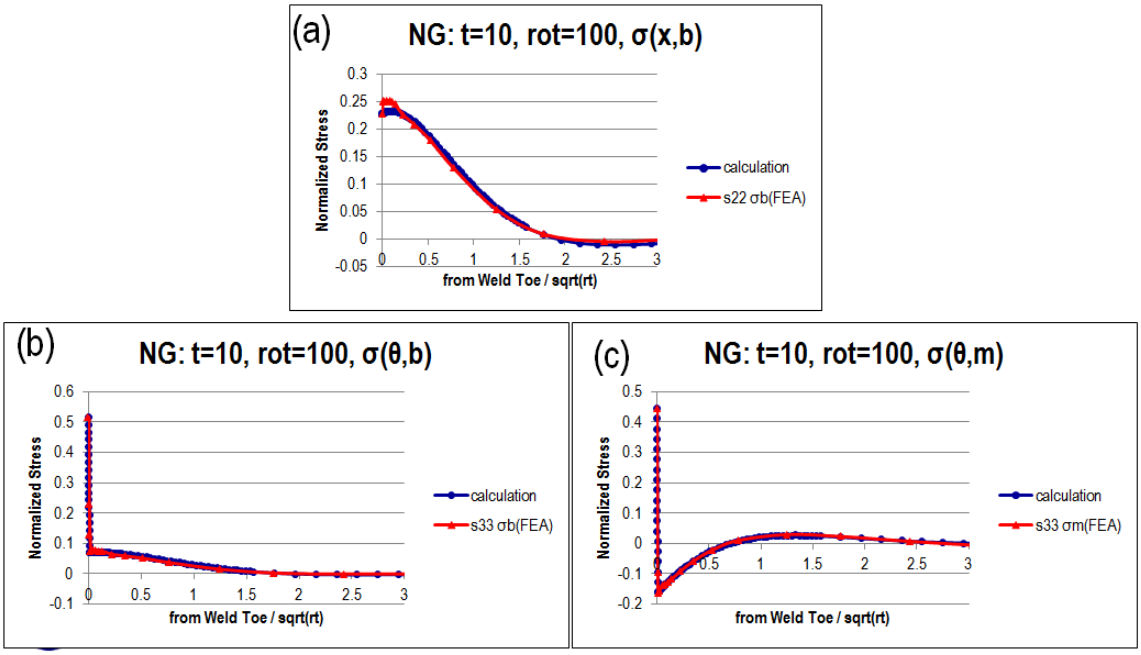

Figure 4-160 Simple estimation scheme based calculated results versus FE results for NG 10" thickness and r/t of 100: (a) axial bending residual stresses, (b) hoop bending residual stresses and (c) hoop membrane residual stresses

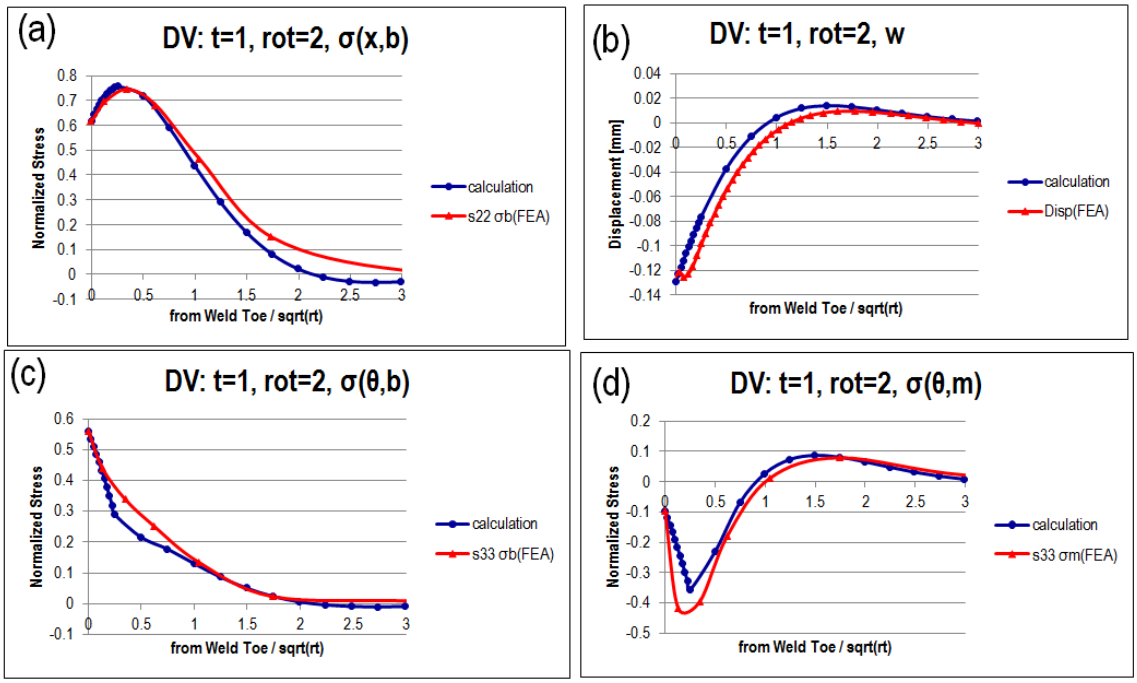

Figure 4-161 Simple estimation scheme based calculated results versus FE results for DV 1" thickness and r/t of 2: (a) axial bending residual stresses; (b) radial deflection (c) hoop bending residual stresses and (d) hoop membrane residual stresses

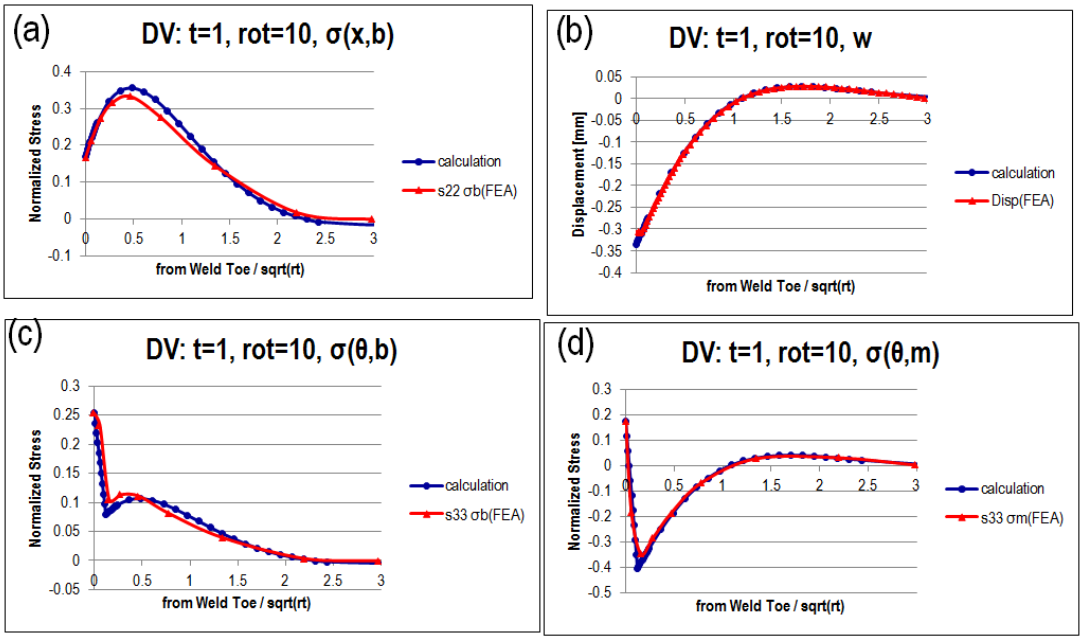

Figure 4-162 Simple estimation scheme based calculated results versus FE results for DV 1" thickness and r/t of 10: (a) axial bending residual stresses; (b) radial deflection (c) hoop bending residual stresses and (d) hoop membrane residual stresses

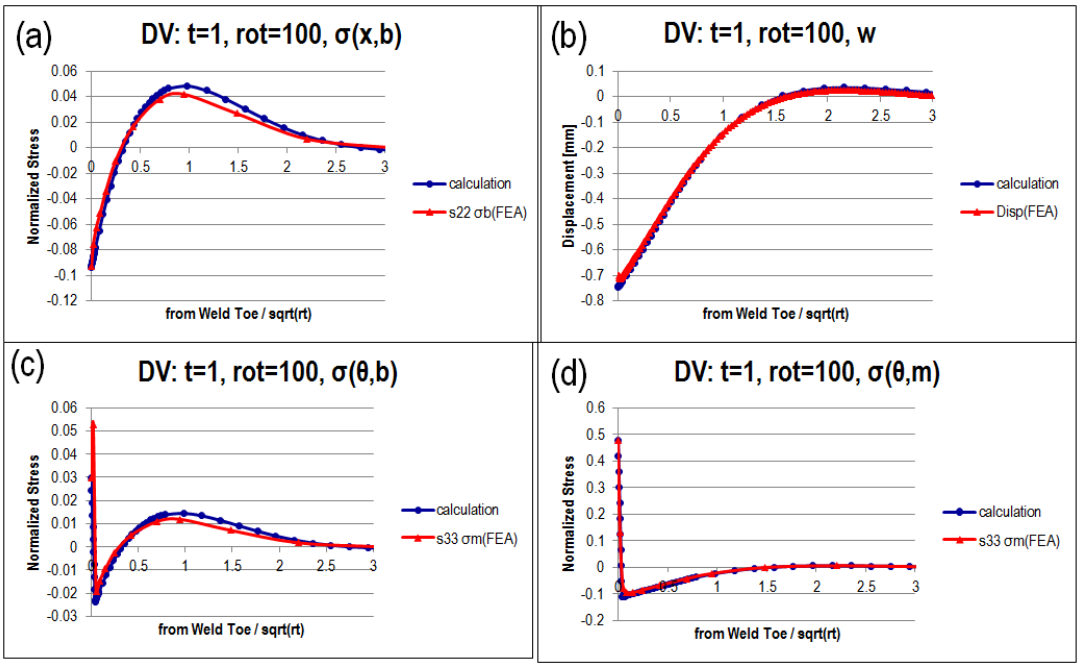

Figure 4-163 Simple estimation scheme based calculated results versus FE results for DV 1" thickness and r/t of 100: (a) axial bending residual stresses; (b) radial deflection (c) hoop bending residual stresses and (d) hoop membrane residual stresses

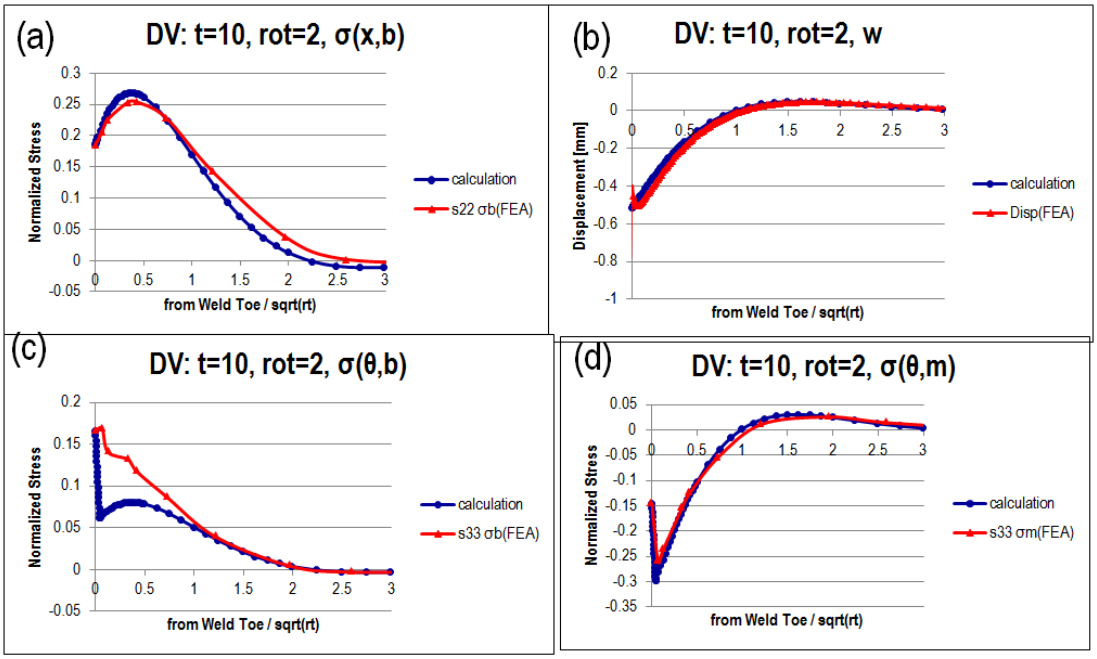

Figure 4-164 Simple estimation scheme based calculated results versus FE results for DV 10" thickness and r/t of 2: (a) axial bending residual stresses; (b) radial deflection (c) hoop bending residual stresses and (d) hoop membrane residual stresses

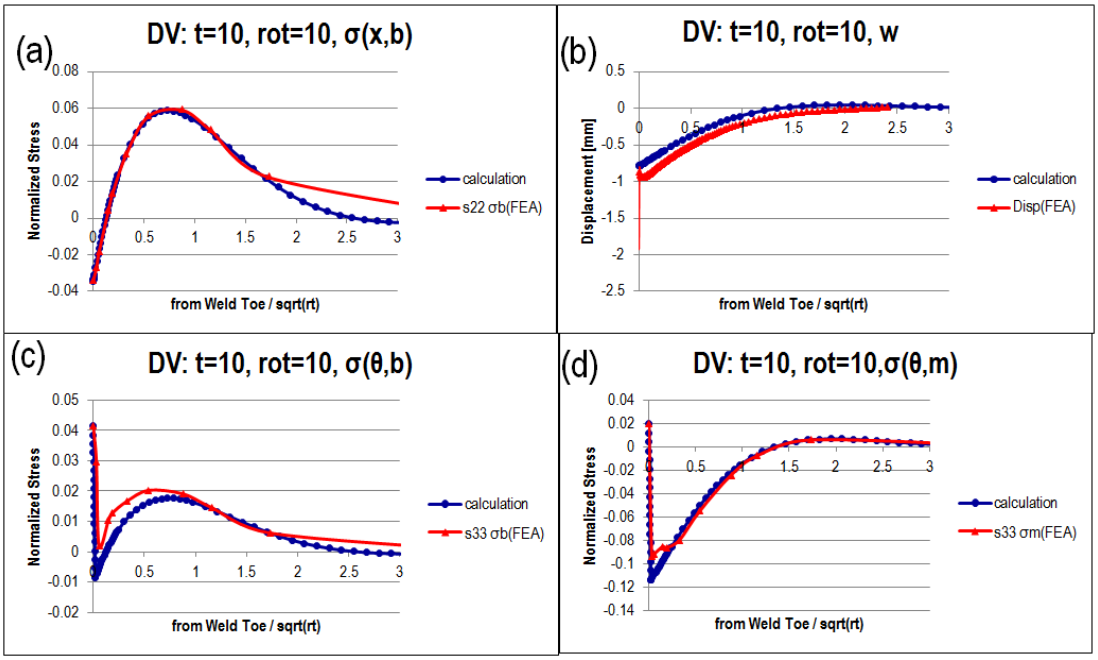

Figure 4-165 Simple estimation scheme based calculated results versus FE results for DV 10" thickness and r/t of 10: (a) axial bending residual stresses; (b) radial deflection (c) hoop bending residual stresses and (d) hoop membrane residual stresses

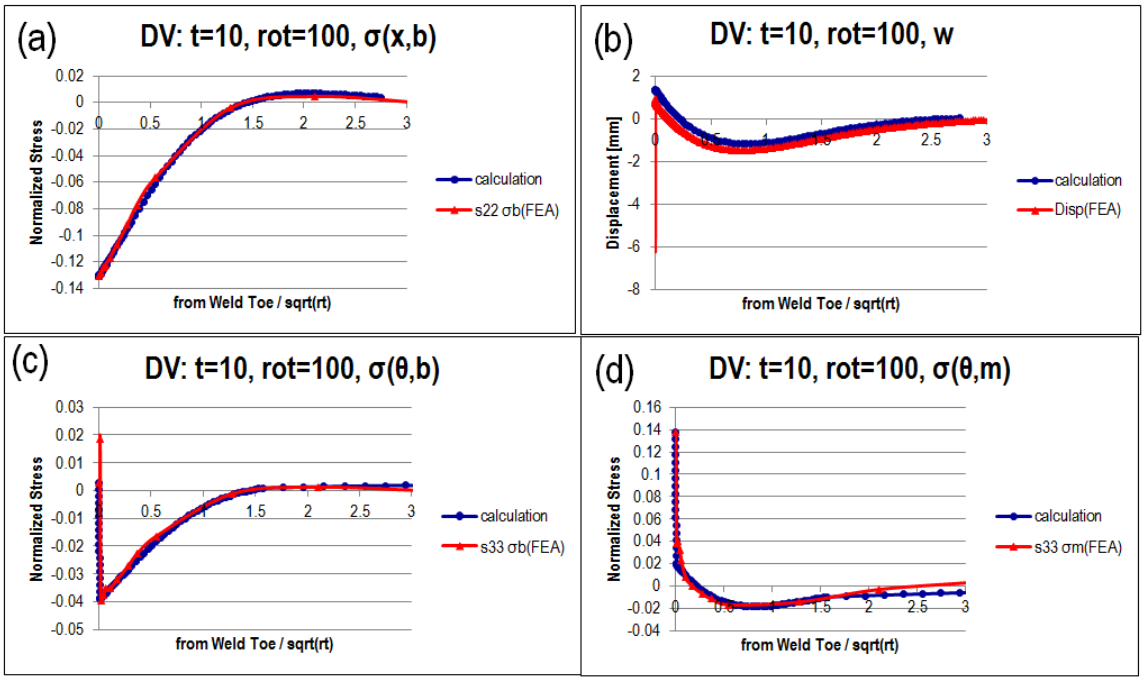

Figure 4-166 Simple estimation scheme based calculation results versus FE results for DV 10" thickness and r/t of 100: (a) axial bending residual stresses; (b) radial deflection (c) hoop bending residual stresses and (d) hoop membrane residual stresses

Welding heat input effects on residual stresses are represented as a characteristic heat input density parameter given by Eq. (4.2). It directly impacts the plastic zone size as described in Eq. (4.20). Consider a baseline case with thickness of 1" and r/t ratio of 10 in single V joint preparation as shown in Figure 4-149. If linear heat input is increased by a factor, the characteristic heat input density is also increased by the same factor according to Eq. (4.2).

Now consider a case with heat input four times larger than the baseline case as shown in Figure 4-167. Compared with the baseline case, the through-thickness bending components become smaller in magnitude (Figure 4-149). This can be attributed to smaller temperature gradients. Another case with heat input of eight times larger is also analyzed and the result is shown Figure 4-168. It can be seen that the simple estimation scheme can correctly capture the heat input effect.

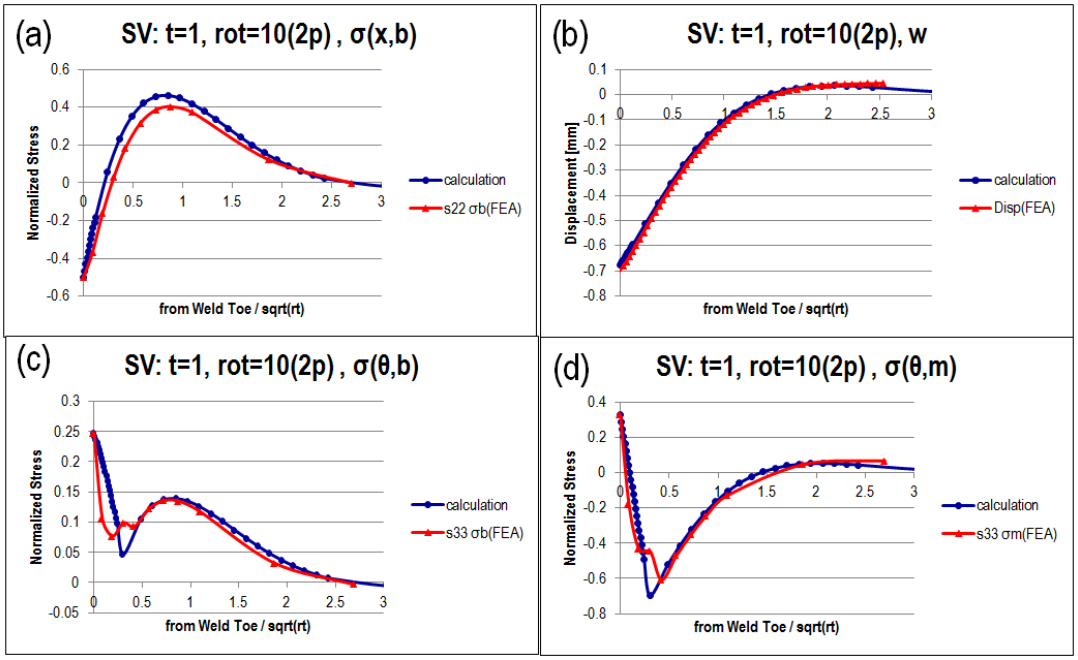

Figure 4-167 Simple estimation scheme based calculation results versus FE results for high welding heat input (four times larger than the case shown in Figure 4-149) – SV 1" thickness and r/t of 10: (a) axial bending residual stresses, (b) radial deflection (c) hoop bending residual stresses and (d) hoop membrane residual stresses

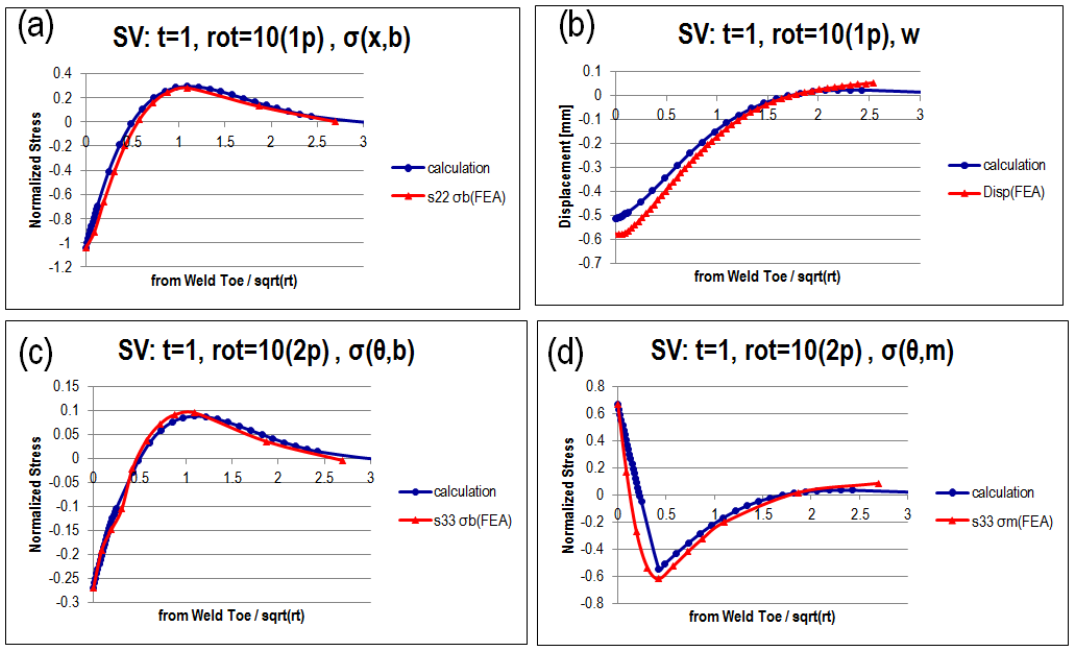

Figure 4-168 Simple estimation scheme based calculation results versus FE results for high welding heat input (eight times larger than the case shown in Figure 4-149) – SV 1" thickness and r/t of 10: (a) axial bending residual stresses, (b) radial deflection (c) hoop bending residual stresses and (d) hoop membrane residual stresses

The simple estimation scheme can also capture the material effect through two parameters: characteristic heat input density (Eq. 4.2) and plastic zone size (Eq. 4.20). If a different base material is used, its effects should be captured by the yield strength of the material and thermomechanical properties in Eq. (4.20) in plastic zone size estimation.

The material for all the cases shown above is 2.25CrMo-V. Consider another low alloy material, 1.25CrMo. Figure 4-169 and Figure 4-170summarize the results obtained by the simple estimation scheme and FEA. A good agreement is shown in these two figures. For high alloy material, stainless steel 304 is considered. The results are shown in Figure 4-171 and Figure 4-172 for Single-V with r/t ratio of 10, thickness of 1" and 2", respectively. Again, a good agreement is clearly observed for high alloy steels.

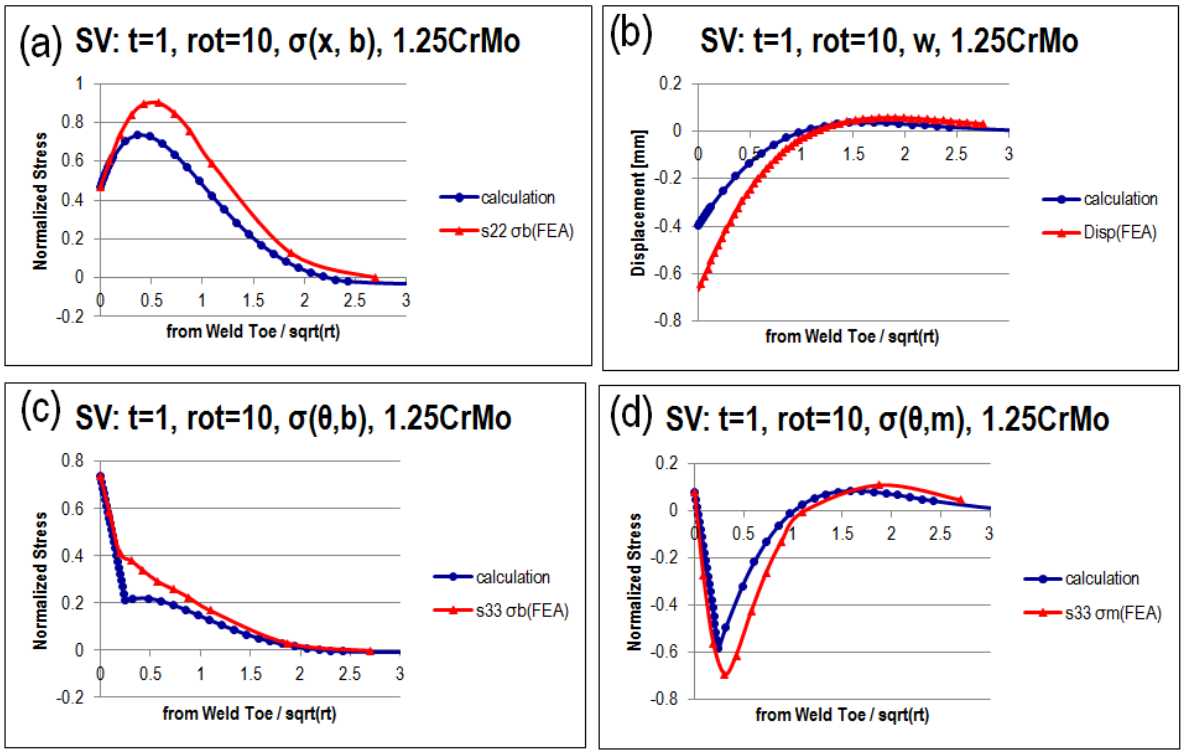

Figure 4-169 Simple estimation scheme based calculation results versus FE results for 1.25CrMo (base case with 2.25CrMo-V shown in Figure 4-149) – SV 1" thickness and r/t of 10: (a) axial bending residual stresses, (b) radial deflection (c) hoop bending residual stresses and (d) hoop membrane residual stresses

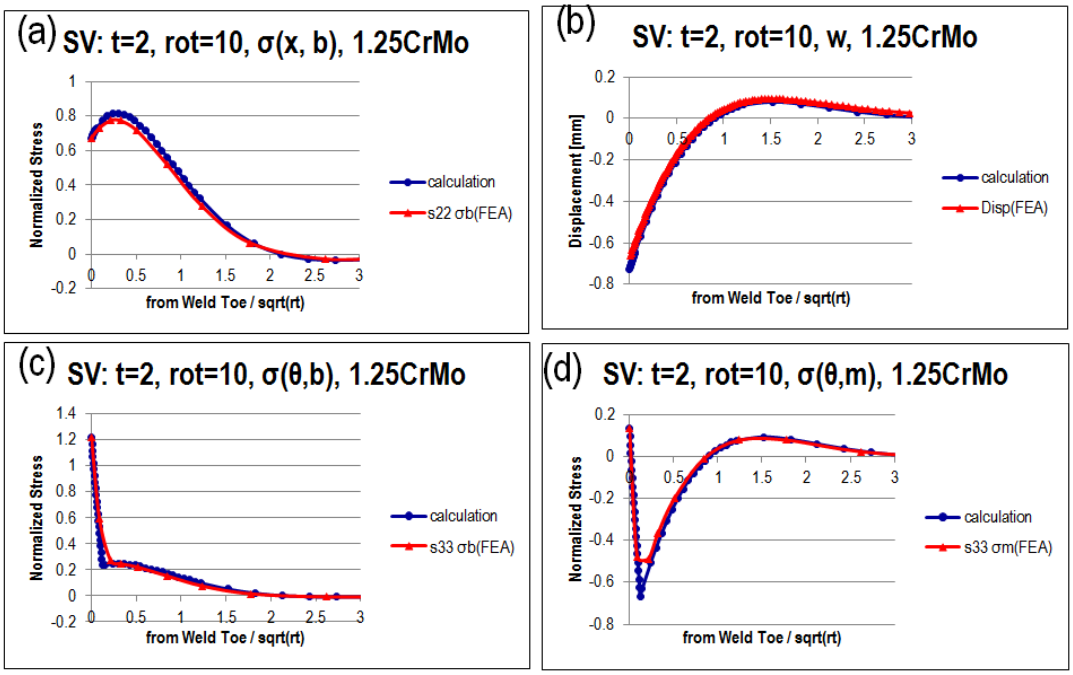

Figure 4-170 Simple estimation scheme based calculation results versus FE results for 1.25CrMo (base case with 2.25CrMo-V shown in Figure 4-151) – SV 2" thickness and r/t of 10: (a) axial bending residual stresses, (b) radial deflection (c) hoop bending residual stresses and (d) hoop membrane residual stresses

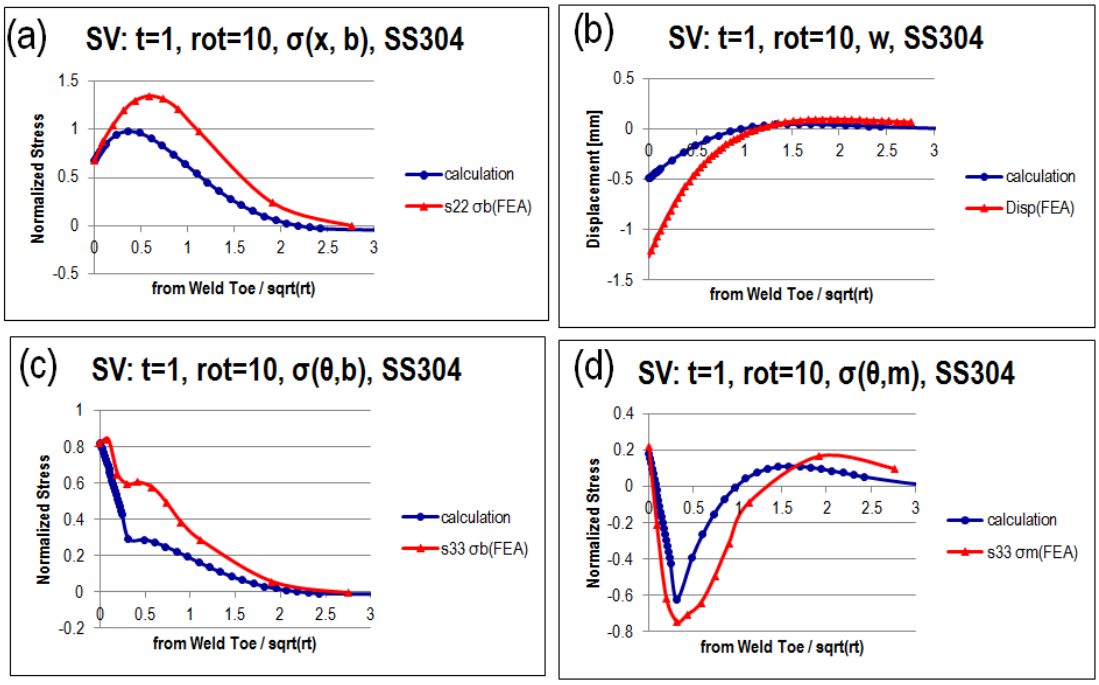

Figure 4-171 Simple estimation scheme based calculation results versus FE results for SS304 (base case with 2.25CrMo-V shown in Figure 4-149) – SV 1" thickness and r/t of 10:

(a) axial bending residual stresses, (b) radial deflection (c) hoop bending residual stresses and (d) hoop membrane residual stresses

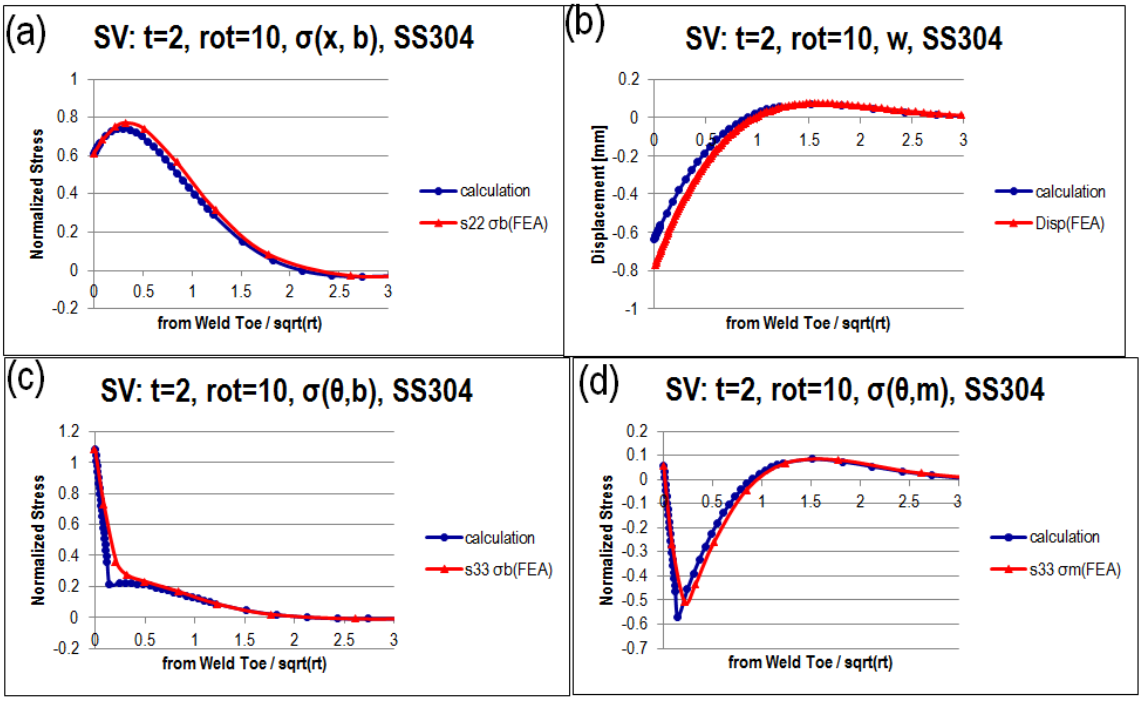

Figure 4-172 Simple estimation scheme based calculation results versus FE results for SS304 (base case with 2.25CrMo-V shown in Figure 4-151) – SV 2" thickness and r/t of 10: (a) axial bending residual stresses, (b) radial deflection (c) hoop bending residual stresses and (d) hoop membrane residual stresses

4.8 Formulation for self-equilibrating component and validation

With the estimation formula established for the profiles of membrane and bending components along pipe axial direction as described in the previous section, there are two remaining tasks proposed in Section 4.6 in order to complete the entire estimation scheme: one is to determine the axial location away from weld where self-equilibrating component vanishes, and another is to come up with an analytical estimation formula for the self-equilibrating stress component within the weld area.

4.8.1 Estimation for self-equilibrating component vanishing location

From a mechanics point of view, the root cause of self-equilibrating component is primarily due to the plasticity introduced during welding. Along this line of thinking, plastic zone size d_p calculated using Eq. (4.20) can serve as a parameter indicating the location where self-equilibrating part is almost reduced to zero in the axial direction. Table 4-9 summaries d_p and the location where self-equilibrating part is vanished. Values in the last column are obtained by carefully examining the plots of through-thickness residual stress component distributions from

FEA in the axial direction, as discussed in Section 4.6. Please note that the distance in the table is measured from weld toe position. From the comparison, it can be seen that plastic zone size d_p can serve as an effective parameter to indicate the position at which self-equilibrating part vanishes, even though d_p is smaller for cases of thickness of 10".

Table 4-9 dp versus the location where self-equilibrating part vanishes measured from weld toe

	Thickness	r/t	d_p (estimation)	Where SE vanishes (FEA)
Single V	1"	2	12	10
		10		18
		100		20
	10"	2	19.8	40
		10		50
		100		55
Double V	2"	2	10.46	12
		10		13
		100		18
Narrow Groove	4"	2	11.73	13
		10		19
		100		20

4.8.2 Functional form for self-equilibrating component at weld centerline and validation

As for the estimation of self-equilibrating part within the weld area, a simple cubic polynomial functional form is proposed at weld centerline location:

$$f(\xi) = a + b\xi + c\xi^2 + d\xi^3 \tag{4.34}$$

where ζ (= x/t) is the normalized distance by thickness. It is assumed that surface values (inner and outer surfaces) for the self-equilibrating part of residuals tress distribution are known (from FEA). Along with another two conditions (summation of stress is zero, and summation of bending moment is zero) based on the definition of self-equilibrium component, the parameters in Eq. (4.34) can be obtained as follows:

$$\begin{aligned} a &= S_-^{s.e.} \\ b &= 3S_+^{s.e.} - 9S_-^{s.e.} \\ c &= -12S_+^{s.e.} + 18S_-^{s.e.} \\ d &= 10(S_+^{s.e.} - S_-^{s.e.}) \end{aligned} \tag{4.35}$$

Where $S_+^{s.e.}$ is the self-equilibrating part surface value where bending is positive (tension), and $S_-^{s.e.}$ is the surface value where bending is negative (compression). For instance, in Figure 4-101 bending part shows OD in tension and ID in compression. Correspondingly, $S_+^{s.e.}$ is for OD and $S_-^{s.e.}$ for ID. By carefully examining a large number of parametric analysis results obtained so far, $S_+^{s.e.}$ and $S_-^{s.e.}$ can be estimated as follows:

$$\begin{aligned} S_+^{s.e.} &= K - \sigma_m - \sigma_b \\ S_-^{s.e.} &= 1.2 S_+^{s.e.} \end{aligned} \quad \textbf{(4.36)}$$

where *K* is residual stress factor. *K*=1.2 is for residual stress perpendicular to the weld, and *K*=1.2 for residual stress parallel to the weld.

As shown in Figure 4-9, the number of weld layers can significantly change the distribution pattern of self-equilibrating part. Also as illustrated in Section 4.6, stress oscillates as a sine wave and the wave number is related to the number of weld layers. In order to capture these characteristics of stress distribution for self-equilibrating part, additional sine term is added to the cubic polynomial functional form. Eq. (4.34) then becomes:

$$f(\xi) = a + b\xi + c\xi^2 + d\xi^3 + p\sin[n\pi(2\xi - 1)] \quad \textbf{(4.37)}$$

Where *a*, *b*, *c*, and *d* can be obtained by Eq. (4.35), *n* is the number of weld layers, *p* is an empirical factor defined as:

$$p = \frac{S_-^{s.e.} + S_+^{s.e.}}{n} \quad \textbf{(4.38)}$$

The sine term doesn't satisfy one condition listed above, i.e, the summation of stress bending moment is not equal to zero:

$$\int_0^1 p\sin[n\pi(2\xi - 1)] \cdot \xi d\xi = -\frac{p}{2n\pi}\cos(n\pi) = -\frac{S_-^{s.e.} + S_+^{s.e.}}{2\pi n^2}\cos(n\pi) \quad \textbf{(4.39)}$$

Apparently, the value of Eq. (4.39) is very small if the number of weld layers *n* is large. As to be illustrated later, this value does not significantly affect the overall estimation of self-equilibrating component.

The above mentioned self-equilibrating component estimation scheme are validated against the FE results documented in Section 4.6. Eq. (4.37) is first used to estimate the stress distribution of self-equilibrating component at weld centerline for the 1" thickness and r/t ratio of 10 Single-V weld. This is because this weld profile has the minimum number of layers among all other ones as shown in Figure 4-2. According to Eq. (4.39), if the summation of bending moment is sufficiently small for this case, other cases do not need to be further examined for this term. The results are shown in Figure 4-173 for this case. The results obtained from the estimation scheme

are plotted in blue and the actual self-equilibrating part extracted from FEA in red. Due to the existence of sine term in the estimation formula, there are multiple waves in the estimation curves similar to the FEA ones. Eq. (4.29) gives a value of -0.023 (-2.3%) for perpendicular stress and -0.005 (-0.5%) for parallel stress. These values are very small and negligible for the final results. Surface (ID and OD) values obtained from the estimation scheme are slightly higher. This provides a conservative estimate for fracture mechanics based structural integrity assessment. Overall, these two curves show a similar trend in patterns.

The results for other cases are shown from Figure 4-174 to Figure 4-184 for Single-V, Narrow Groove and Double-V girth welds with varying thickness from 1" to 10". A good agreement is also observed from these cases investigated.

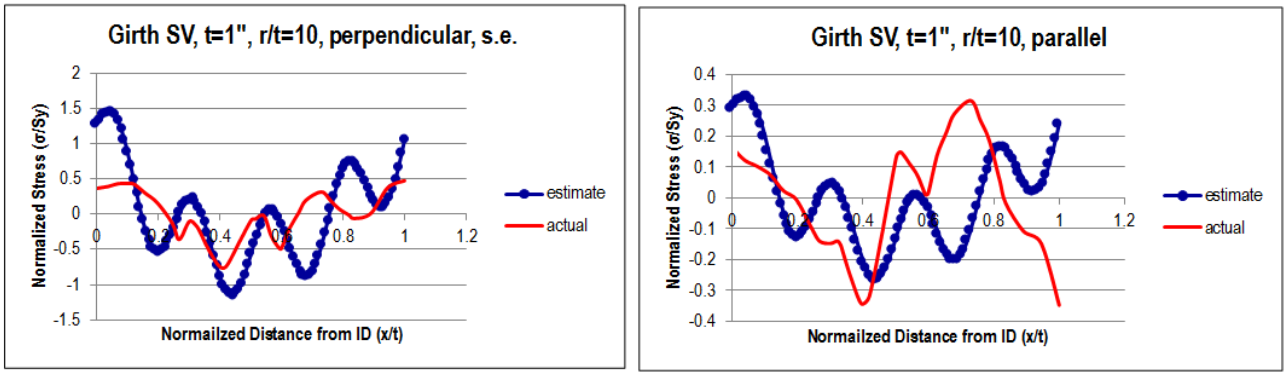

Figure 4-173 Estimation versus FE results for SV, t=1", r/t=10: self-equilibrating components of perpendicular and parallel residual stresses at WCL

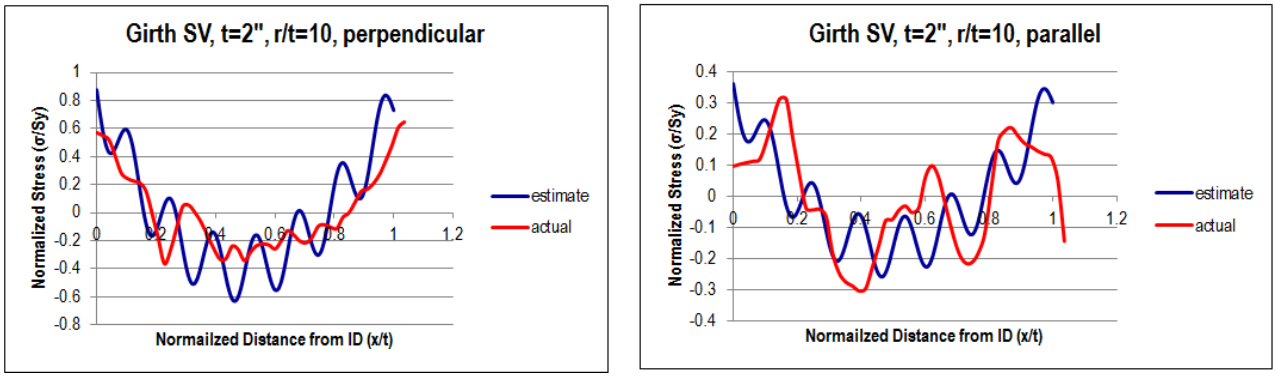

Figure 4-174 Estimation versus FE results for SV, t=2", r/t=10: self-equilibrating components of perpendicular and parallel residual stresses at WCL

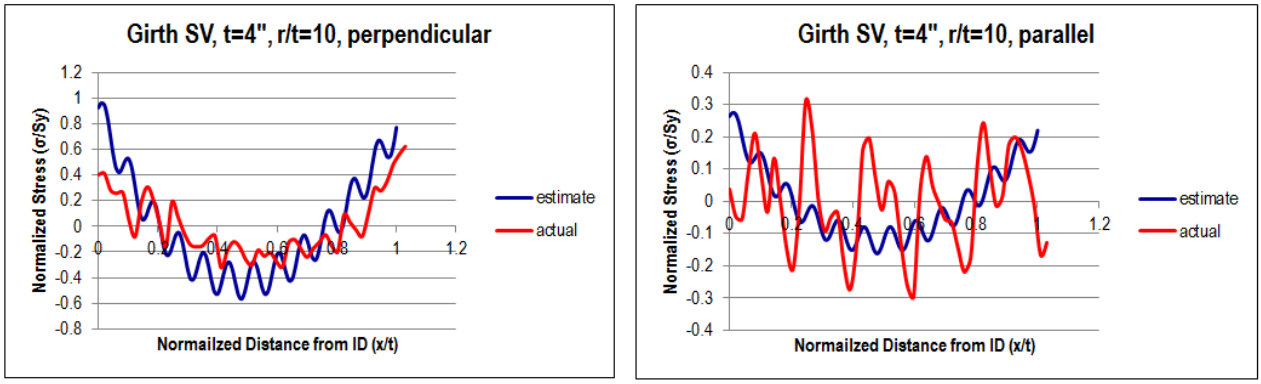

Figure 4-175 Estimation versus FE results for SV, t=4", r/t=10: self-equilibrating components of perpendicular and parallel residual stresses at WCL

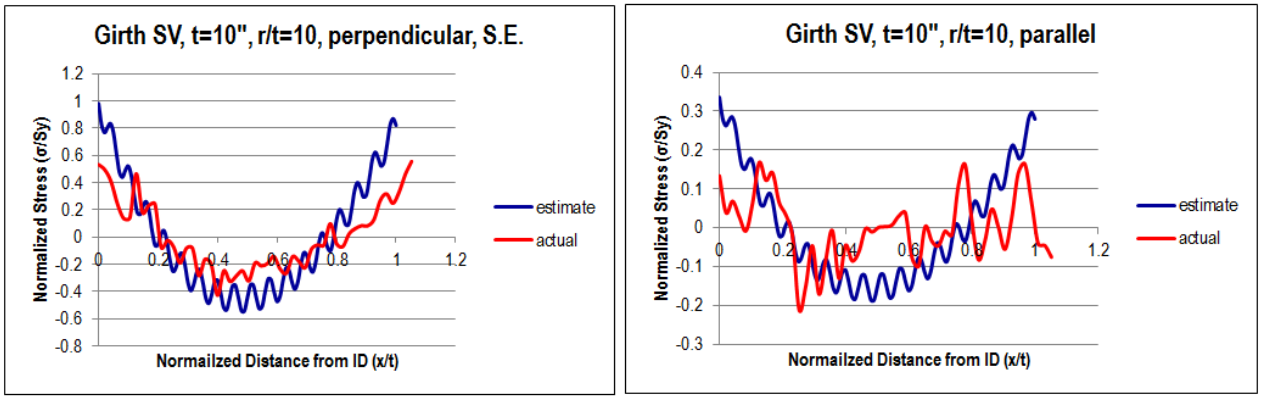

Figure 4-176 Estimation versus FE results for SV, t=10", r/t=10: self-equilibrating components of perpendicular and parallel residual stresses at WCL

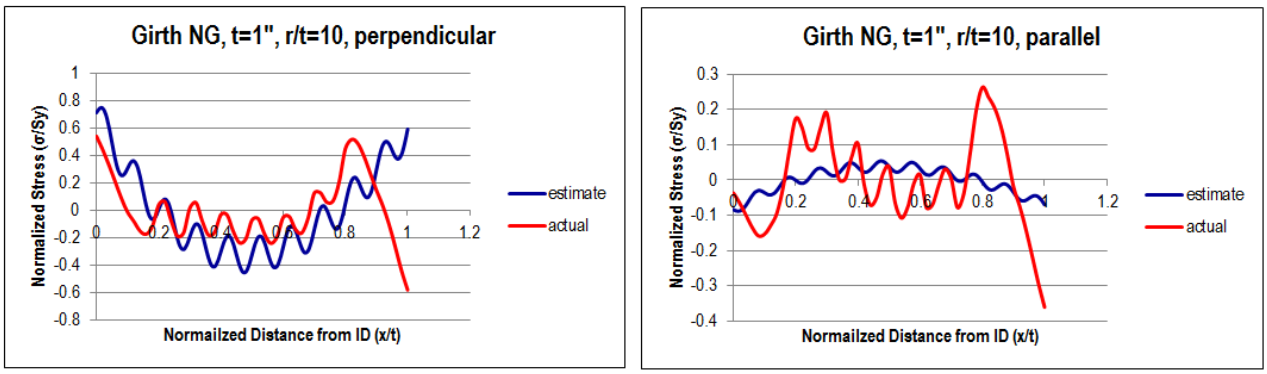

Figure 4-177 Estimation versus FE results for NG, t=1", r/t=10: self-equilibrating components of perpendicular and parallel residual stresses at WCL

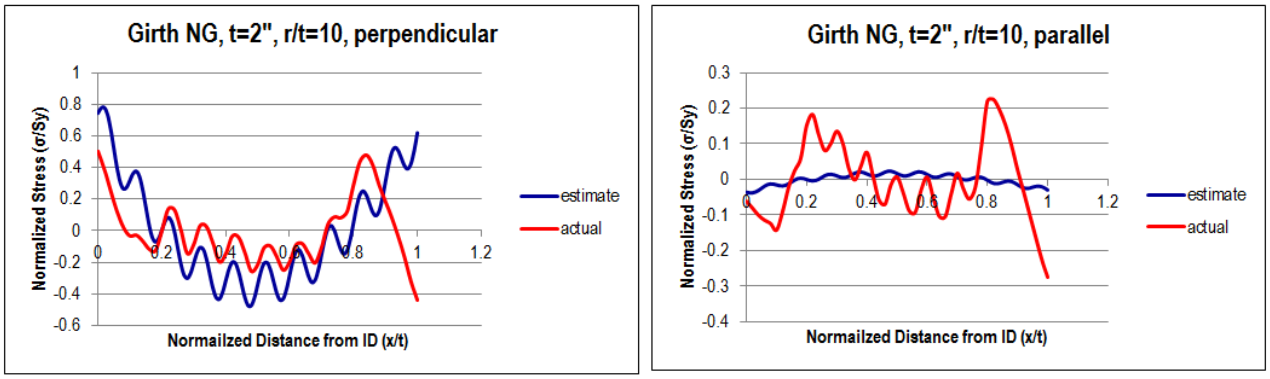

Figure 4-178 Estimation versus FE results for NG, t=2", r/t=10: self-equilibrating components of perpendicular and parallel residual stresses at WCL

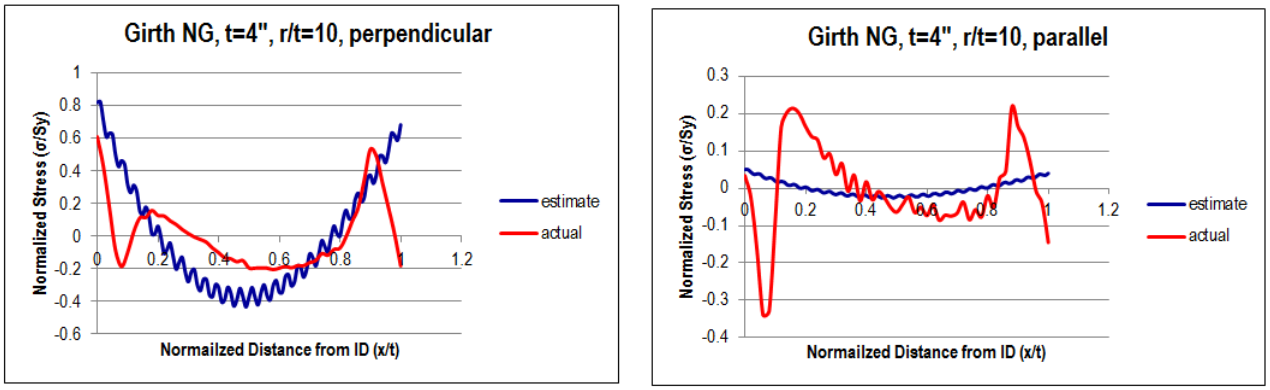

Figure 4-179 Estimation versus FE results for NG, t=4", r/t=10: self-equilibrating components of perpendicular and parallel residual stresses at WCL

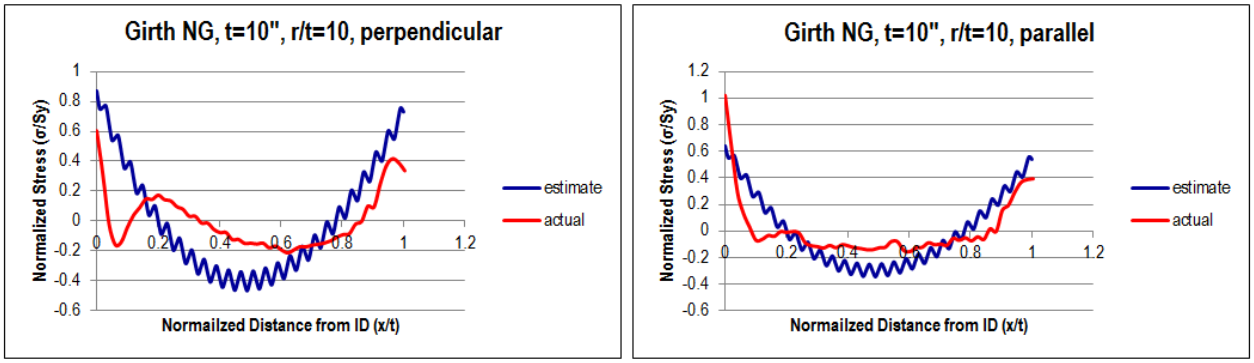

Figure 4-180 Estimation versus FE results for NG, t=10", r/t=10: self-equilibrating components of perpendicular and parallel residual stresses at WCL

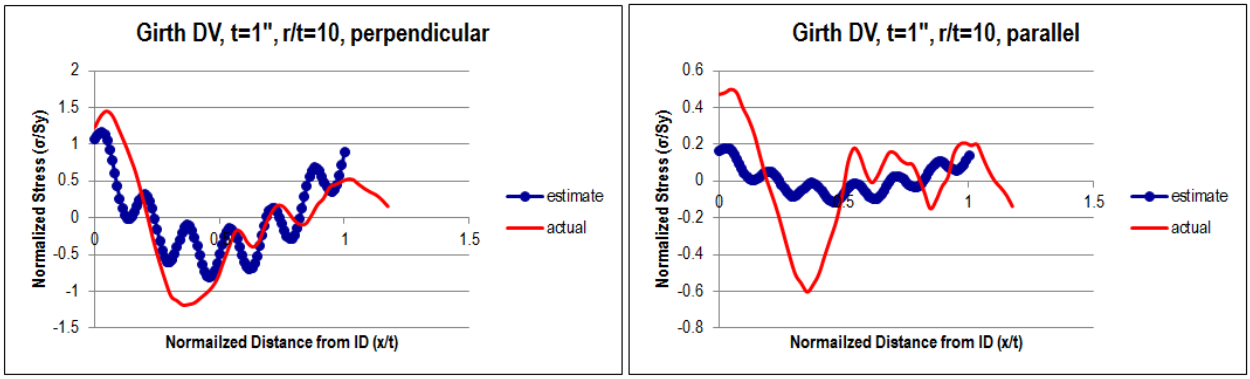

Figure 4-181 Estimation versus FE results for DV, t=1", r/t=10: self-equilibrating components of perpendicular and parallel residual stresses at WCL

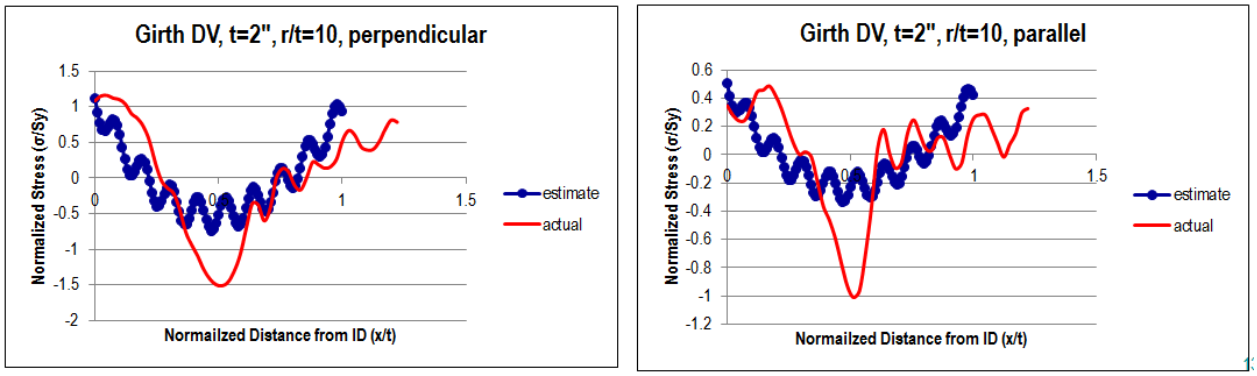

Figure 4-182 Estimation versus FE results for DV, t=2", r/t=10: self-equilibrating components of perpendicular and parallel residual stresses at WCL

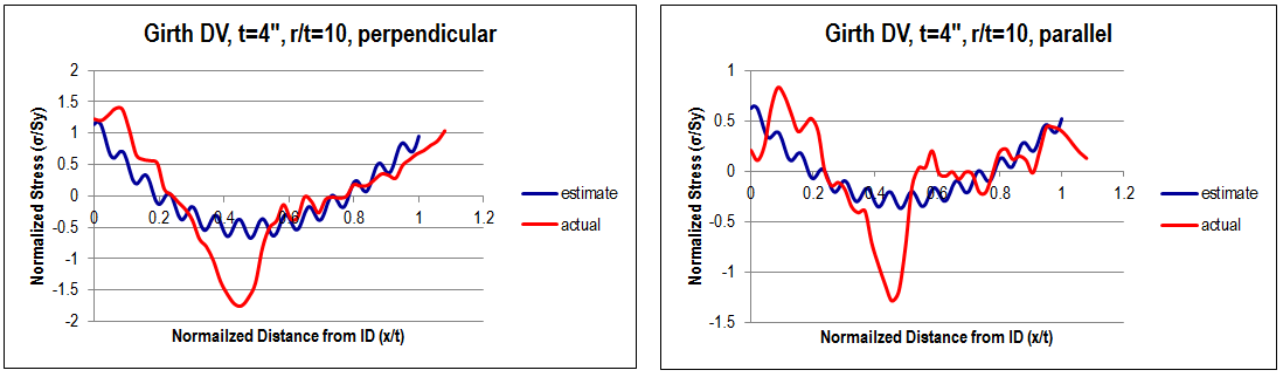

Figure 4-183 Estimation versus FE results for DV, t=4", r/t=10: self-equilibrating components of perpendicular and parallel residual stresses at WCL

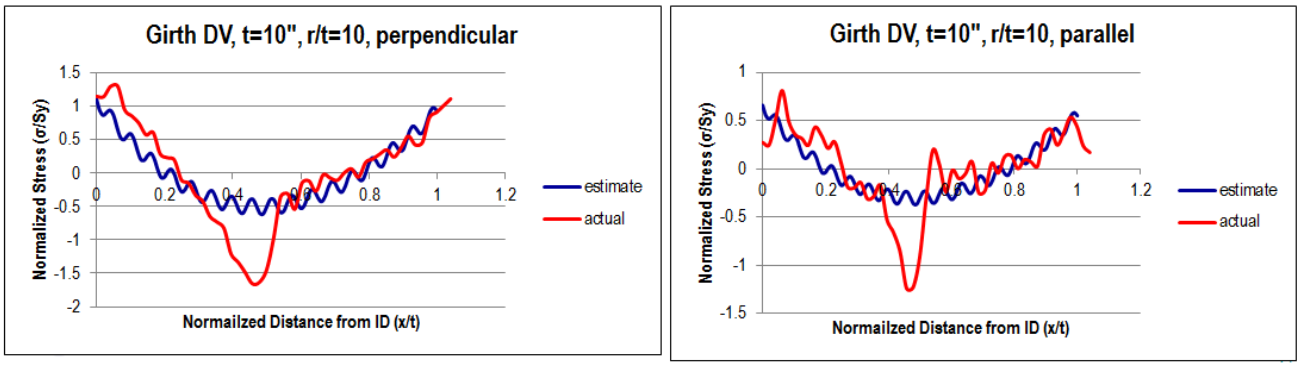

Figure 4-184 Estimation versus FE results for DV, t=10", r/t=10: self-equilibrating components of perpendicular and parallel residual stresses at WCL

4.8.3 Total through-thickness residual stress distribution at weld centerline

With the establishment of stress profile estimation for self-equilibrating part, the total residual stress distribution can be expressed as follows, based on Eq. (4.1):

$$\sigma(\xi) = \sigma_m + \sigma_b(2\xi - 1) + a + b\xi + c\xi^2 + d\xi^3 + p\sin[n\pi(2\xi - 1)] \qquad \textbf{(4.40)}$$

Where ζ (= *x/t*) is the normalized distance by thickness, *a*, *b*, *c*, and *d* can be obtained by Eq. (4.35), *p* is estimated by Eq. (4.38), *n* is the number of weld layers. The decomposed membrane σ_m and bending σ_b can be found in the earlier parametric analyses. Figure 4-185 shows the results for the thickness of 1"and r/t ratio of 10 Single-V girth weld case. Again, results estimated by Eq. (4.40) is in blue and FEA in red. In general, a good agreement is achieved between two sets of results. Other cases of 4" thickness and r/t ratio of 10 for Single-V, Narrow Groove, and Double-V girth welds are presented in Figure 4-186, Figure 4-187, and Figure 4-188, respectively. All results show a very good agreement for the overall distribution.

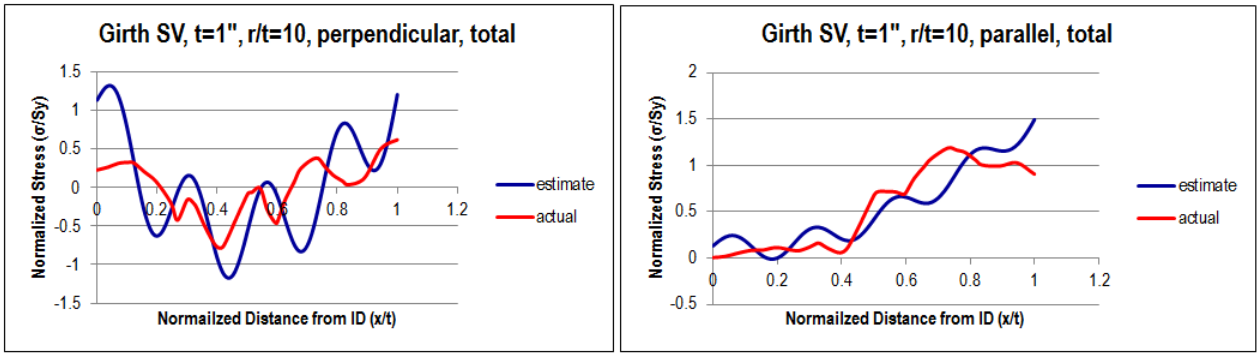

Figure 4-185 Estimation versus FE results for SV, t=1", r/t=10: perpendicular and parallel residual stresses at WCL

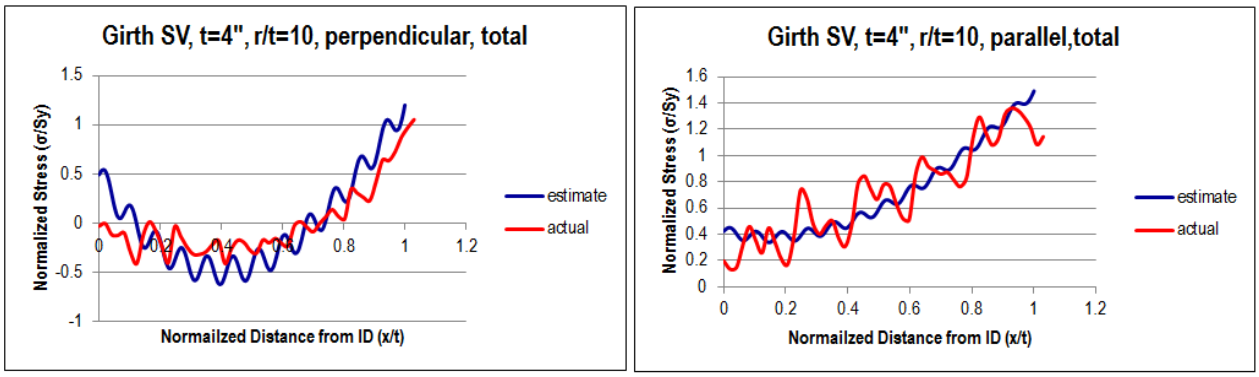

Figure 4-186 Estimation versus FE results for SV, t=4", r/t=10: perpendicular and parallel residual stresses at WCL

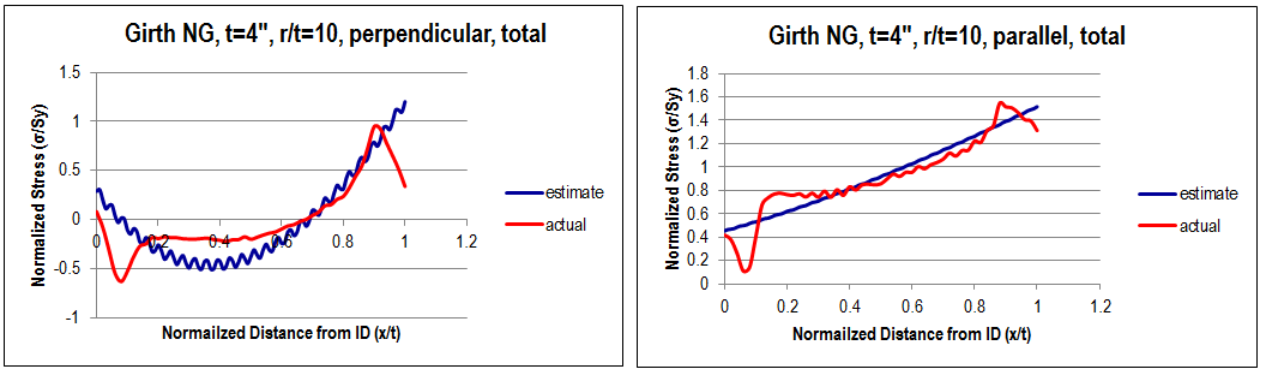

Figure 4-187 Estimation versus FE results for NG, t=4", r/t=10: perpendicular and parallel residual stresses at WCL

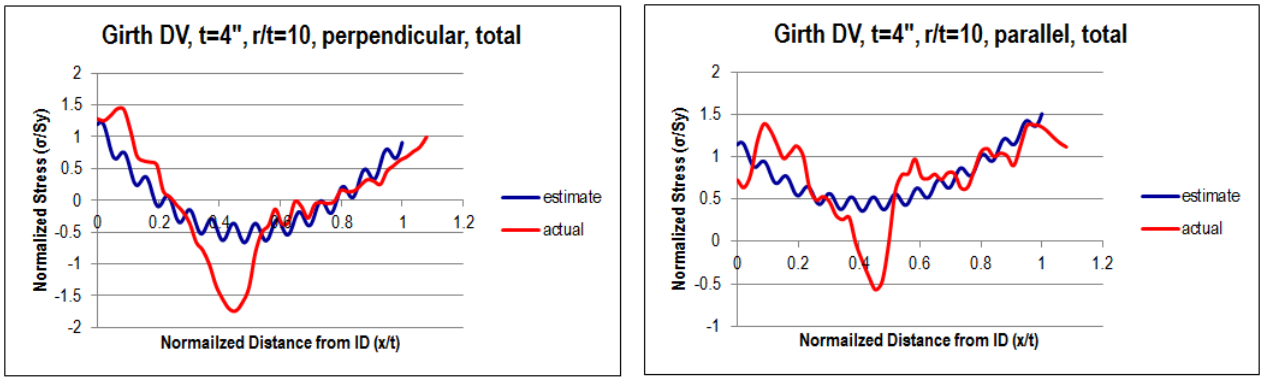

Figure 4-188 Estimation versus FE results for DV, t=4", r/t=10: perpendicular and parallel residual stresses at WCL

5. SEAM WELDS

In this section, characteristics of residual stresses in pipe seam welds are investigated in detail. Similar to girth welds, seam welds are subject to bending type of restraints which can be considered as a unique condition to contribute through-thickness residual stress distributions. Important residual stress features and their governing parameters are identified through a large number of parametric analyses by varying pipe geometries. Stress decomposition technique as described in Section 3.4.1 (Eq. 3.29 or 4.1) is also used to categorize the contributions of different stress components and to facilitate the characterization process.

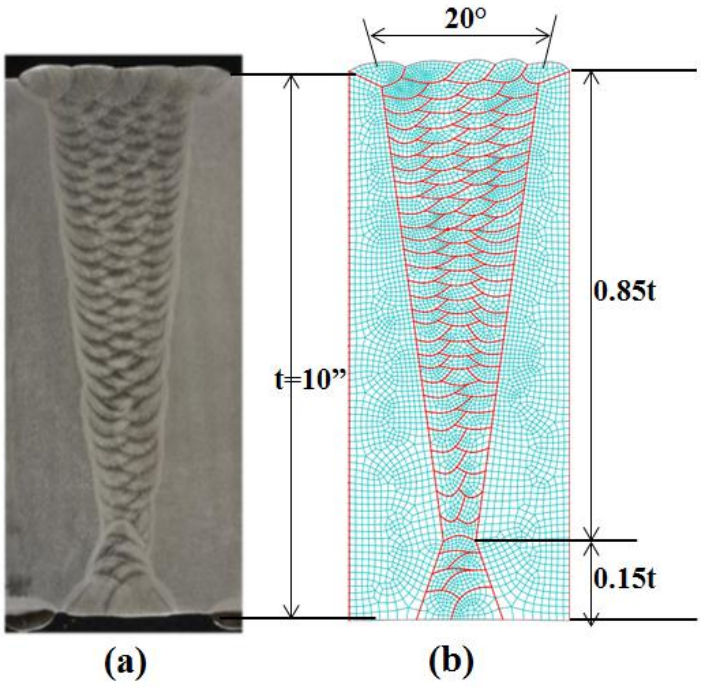

Figure 5-1 Seam weld joint preparation: (a) macrograph of weld cross section, and (b) corresponding FE weld profile with configuration

As mentioned at the beginning of this report, residuals tress distributions in thick (>50mm) welded components are of interest in this investigate. A macrograph of 10” thick weld cross section was provided by Dr. Martin Prager, as shown in Figure 5-1(a). The corresponding FE weld profile is presented in Figure 5-1(b) with the detailed configuration and meshing information. By scaling this 10” thick model, FE weld profiles are obtained for other thicknesses (e.g., 2” and 4”), as shown in Figure 5-2. Welding sequence is also shown in Figure 5-2. Back gouging is welded first from inner surface and then followed by other passes from outer surface. Discussion about this welding sequence and joint preparation will be presented in a later section. The element type of generalized plane strain is used in this investigation. The material used for most cases is 2.25 CrMo-V steel. The temperature-dependent material properties for this material are summarized in Chapter 3 and Figure 4.3. For clarity, Figure 5-3 shows the definition of seam weld and stress components used throughout this investigation.

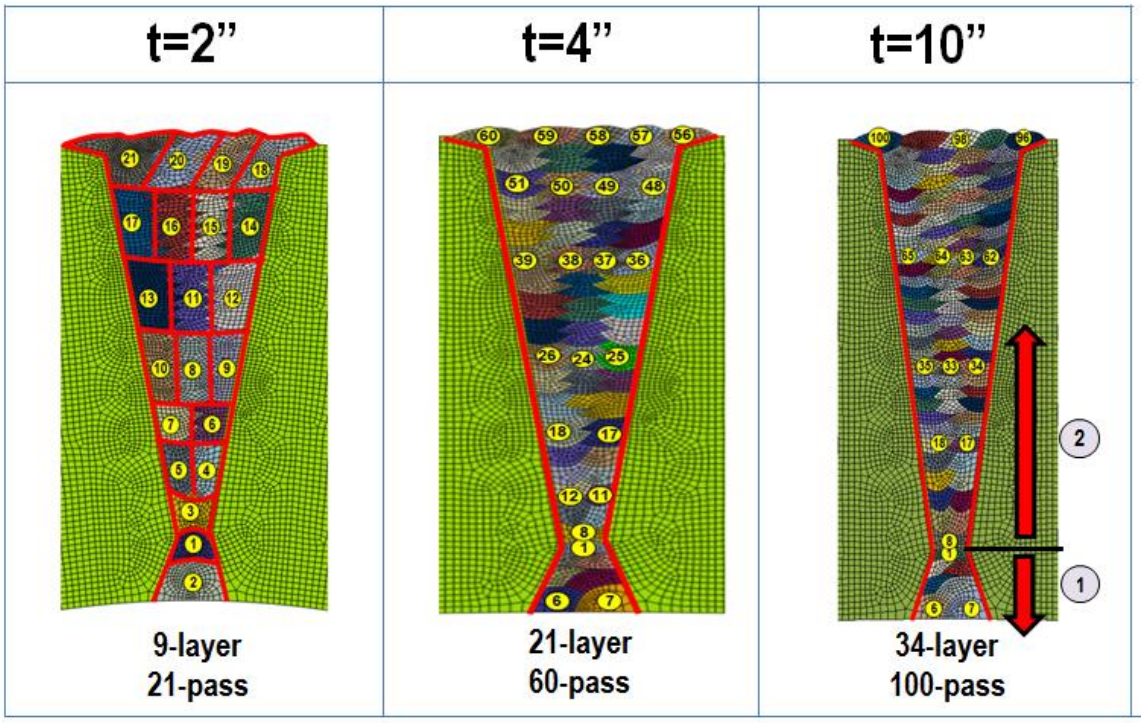

Figure 5-2 Detailed weld profiles for different wall thicknesses: t=2”, t=4” and t=10” and welding sequence

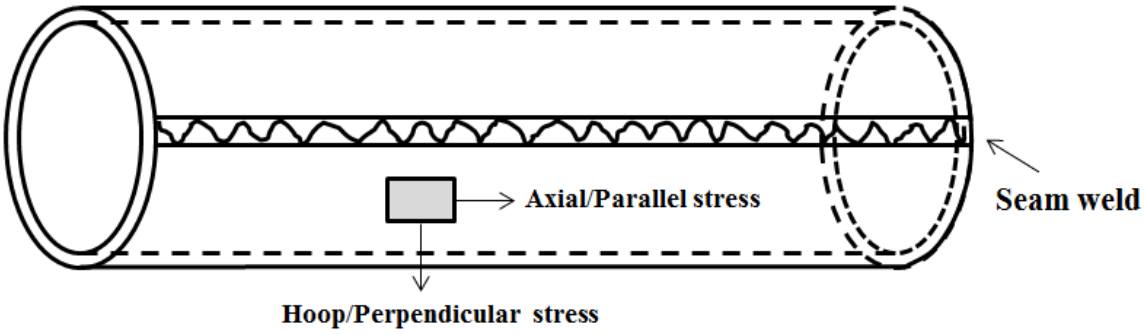

Figure 5-3 Identification of seam weld and stresses

5.1 Lumped pass effects

As discussed in the previous section for girth welds, there exist a minimum number of layers beyond which the decomposed residual stress components do not change significantly (see Figure 4-16). For seam welds in a thick pipe, it is necessary to exam whether a similar lumped pass effect stands too.

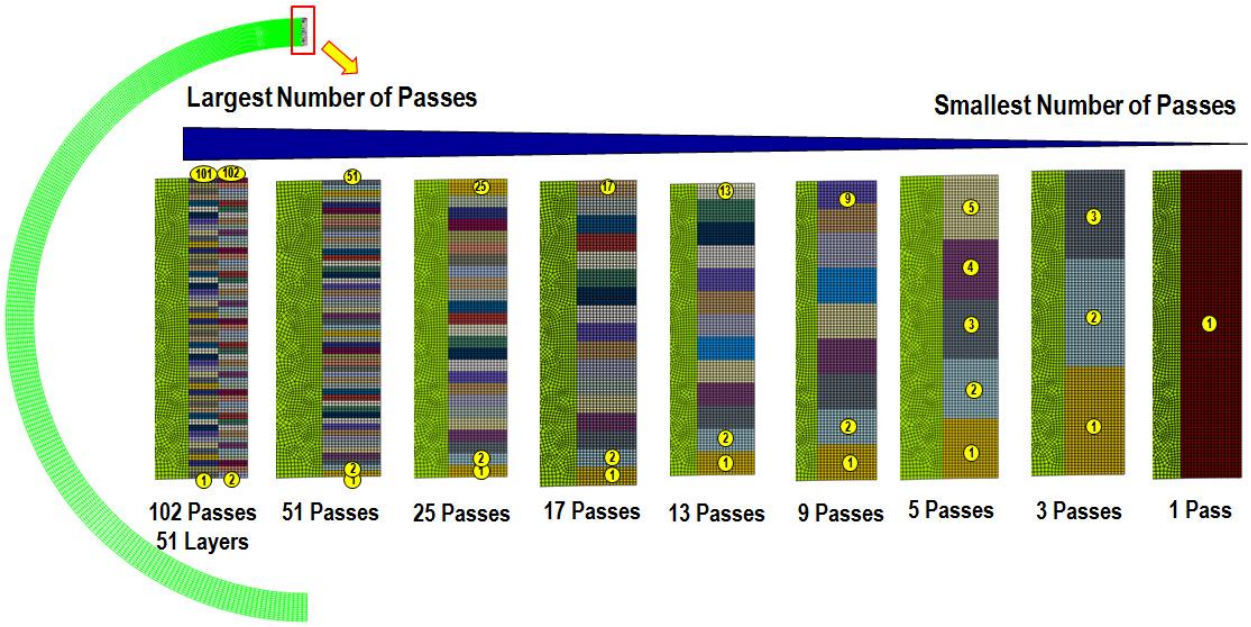

Figure 5-4 Nine lumped models with pass number from 102 to 1 for a thickness of 10" and r/t ratio of 10 seam weld: detailed pass size and welding sequence

For generalization purposes, an idealized weld profile is used for investigating the lumped pass effects as shown in Figure 5-4. The idealized profile has the same size for each pass in order to reduce any additional localized residual stress effect. Figure 5-4 represents a symmetrical FE cross section model for a thickness of 10" and r/t ratio of 10 seam weld. The weld pass size and welding sequence for each lumped model are identified. The weld pass number decreases from 102 to 1 from outer to inner surface in the first model. It is interesting to note that the first two lumped models share the same number of layers (51 layers) but with different pass numbers. So another intention in this investigation is to exam if residual stress distribution is dramatically changed between these first two models or roughly maintained the same because of the same number of layers.

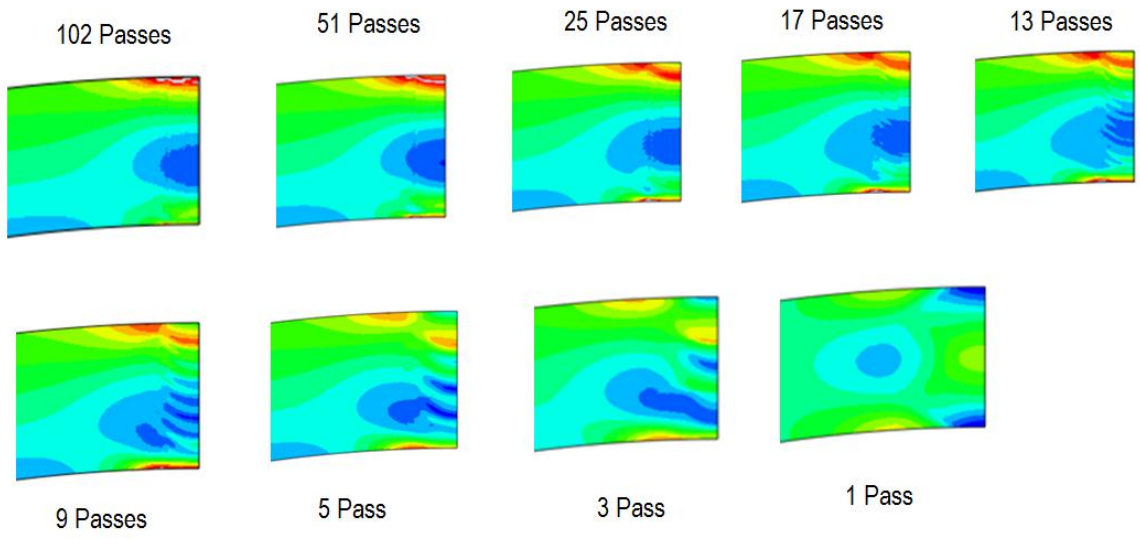

Figure 5-5 Contour plots of perpendicular stress for nine lumped model with pass number from 102 to 1 for a thickness of 10" and r/t ratio of 10 seam weld

Perpendicular residual stress contour plots for nine lumped models are shown in Figure 5-5. It can be seen that though-thickness residual stress distributions are almost identical for the first six models (pass number is no smaller than 9), all of which show a self-equilibrating type of distribution with tension on both ID and OD and compression in the mid thickness. When the number of passes is smaller than 5, residual stress distribution starts to change significantly. This is especially true for the 1 pass model where the through-thickness residual stress distribution is similar to a laser beam weld with compression in both ID and OD and tension in the mid section.

The corresponding perpendicular residual stress line plots along weld centerline are shown in Figure 5-6(a) and parallel stress line plots in Figure 5-6(b). For completeness, perpendicular and parallel residual stress distributions for weld toe location are also shown in Figure 5-7(a) and Figure 5-7(b), respectively, which have almost identical distributions as at weld centerline due to the idealized weld profile. From these results, similar trends can be observed for the lump pass effect. Higher degree of stress oscillation is present through the thickness when the number of passes is decreased. These results suggest that the minimum number of layers is about 9 for the 10" seam weld.

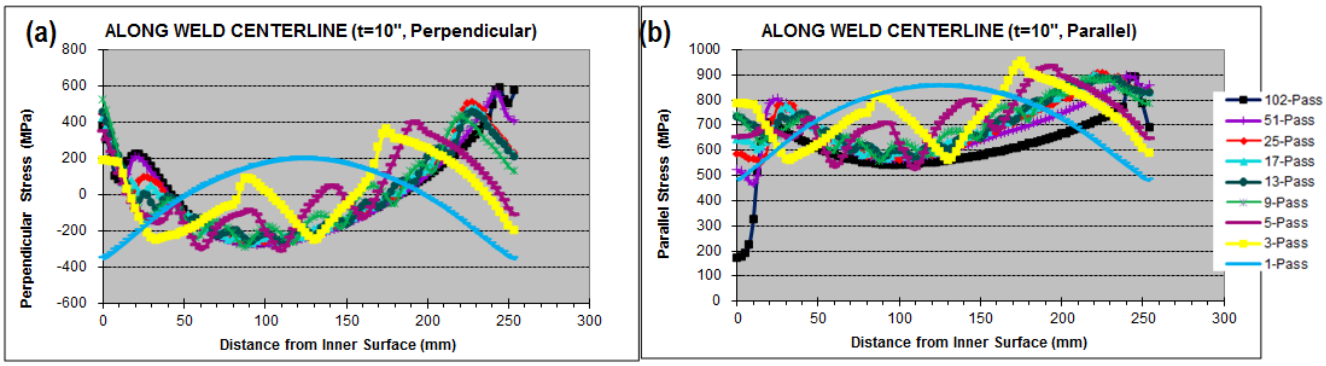

Figure 5-6 Residual stress distribution along weld centerline (WCL) for nine lumped model with pass number from 102 to 1 for a thickness of 10" and r/t ratio of 10 seam weld – (a) perpendicular residual stress, and (b) parallel residual stress

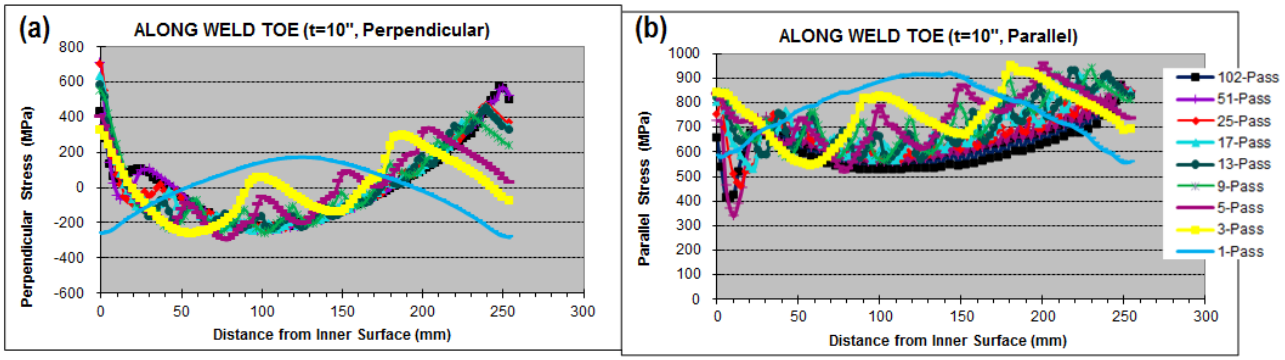

Figure 5-7 Residual stress distribution along weld toe (WT) for nine lumped model with pass number from 102 to 1 for a thickness of 10" and r/t ratio of 10 seam weld – (a) perpendicular residual stress, and (b) parallel residual stress

In order to clearly demonstrate the transition behavior in though-thickness residual stress distributions, the stress decomposition technique described in Section 2.4.4 is adopted here. Figure 5-8 and Figure 5-9 show results of residual stress components as a function of number of passes at weld centerline and weld toe locations, respectively. Perpendicular membrane stress component is negligible (less than 10*MPa*). It is obvious from these plots that there exists a minimum number of layers, about 5-9 (smaller than 12 found in girth welds), beyond which the bending components of perpendicular and parallel residual stresses roughly maintain the same. Membrane component of parallel stress does not change significantly with decreasing pass number. Also, residual stress components are almost identical for the first two models (102-pass with 51-layer, and 51-pass with 51-layer). This indicates that weld pass layer, as discusses in Section 3 for girth welds, is a better parameter for characterizing though-thickness residual stress distribution as shown in Figure 5-8, Figure 5-9. This is consistent with the findings from the girth weld analyses in Section 3.

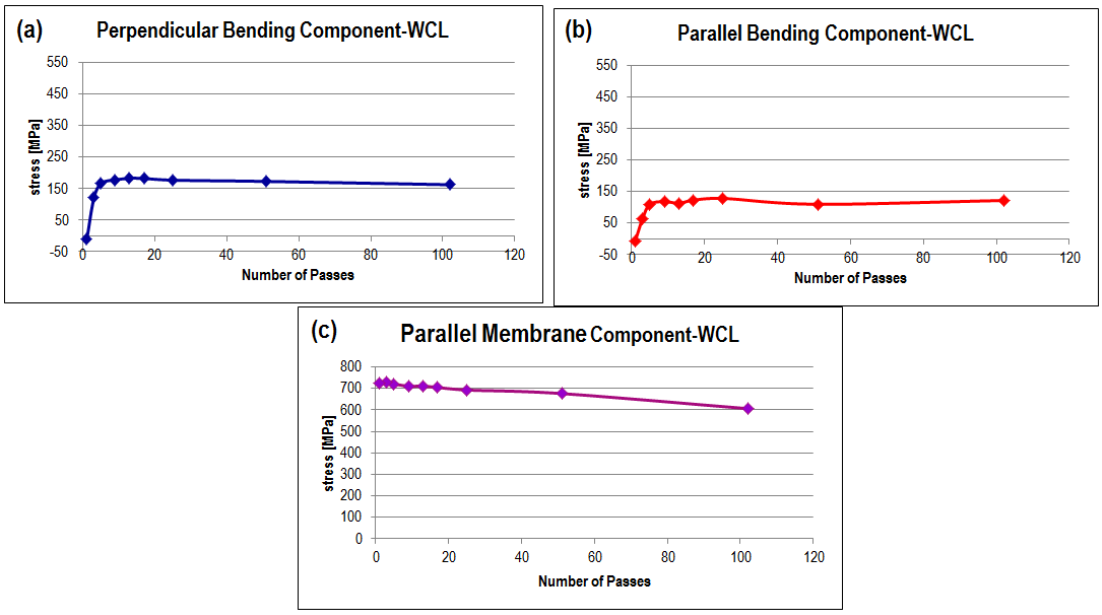

Figure 5-8 Decomposed residual stress components at WCL vs. Number of passes for a thickness of 10" and r/t ratio of 10 seam weld – (a) perpendicular bending component, (b) parallel bending component, and (c) parallel membrane component

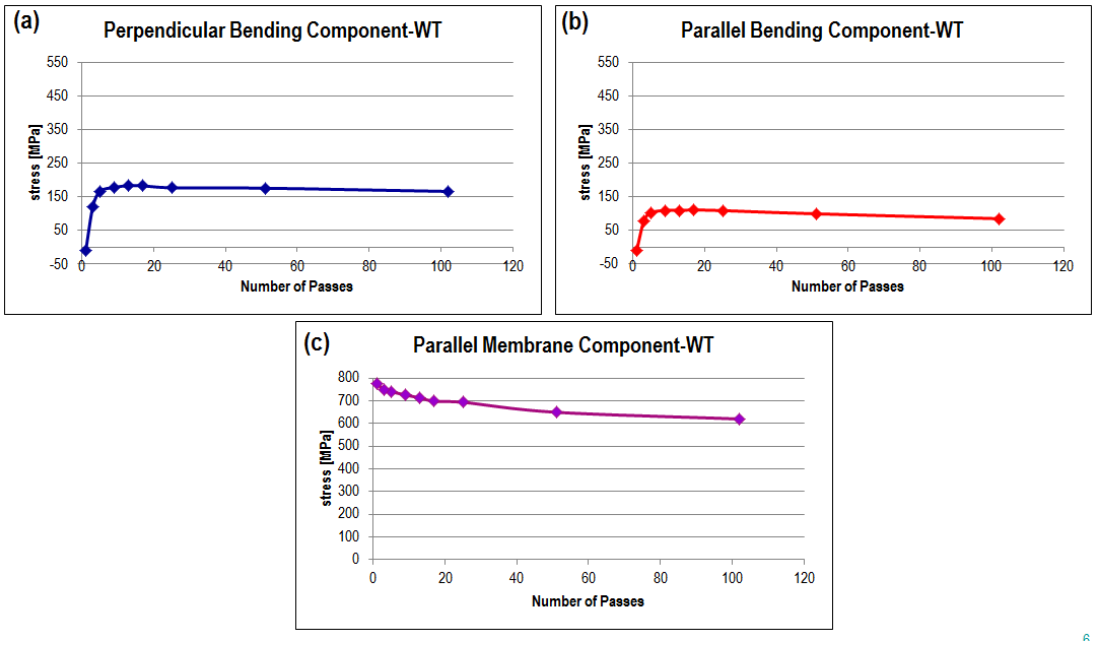

Figure 5-9 Decomposed residual stress components at WT vs. Number of passes for a thickness of 10" and r/t ratio of 10 seam weld – (a) perpendicular bending component, (b) parallel bending component, and (c) parallel membrane component

5.2 r/t ratio effects

In this section, a series of parametric analyses are performed to investigate r/t ratio effect for seam weld. The pipe wall thickness is greater than 1" and the r/t ratio varies from 2 to 10. As discussed in Phase I report [13], if r/t ratio is >10 a butt joint in flat plate can be assumed for residual stress estimation of seam weld. This is primary due to the insignificant effect of curvature on residual stress distribution and magnitude. The parametric analysis matrix for this section is given by Table 5-1 and the corresponding weld profiles are presented in Figure 5-2. The FE models are generated based on the cross section macrograph exhibited in Figure 5-1(a) and the minimum number of layers required for each thickness shown in Figure 4-16.

Table 5-1Analysis matric for r/t ratio effects

	t=2"	t=4"	t=10"
Layer#	9	21	34
Pass#	21	60	100
r/t=2	X	X	X
r/t=5	X	X	X
r/t=10	X	X	X

Let's discuss the 2" thick cases first (first column in Table 4-1). The contour plots of residual stress distribution are shown in Figure 5-10. The top row in Figure 5-10 is for stress perpendicular to the weld and the bottom row for stress parallel to the weld. The scale for these contour plots is the same as for girth welds, which is from -350MPa to 558 MPa (2.25CrMo-V yield strength). It can be seen that at r/t =2 the through-thickness perpendicular residual stress within the weld shows a strong local bending type distribution, with tension on OD and compression near ID. As r/t ratio increases (e.g., r/t $\geq$ 5), a more self-equilibrating type of perpendicular residual stress distribution is developed within the weld, with tension on both of OD and ID and compression in the mid thickness. Parallel residual stress shows highly tensile within the weld for all cases of 2" thickness due to the severe restraint condition (against weld shrinkage) in this direction. Magnitude of two compressive stress zones along ID on each side the weld area for both perpendicular and parallel residual stresses is decreased with increasing r/t ratio, implying a reduced restraint as r/t increases.

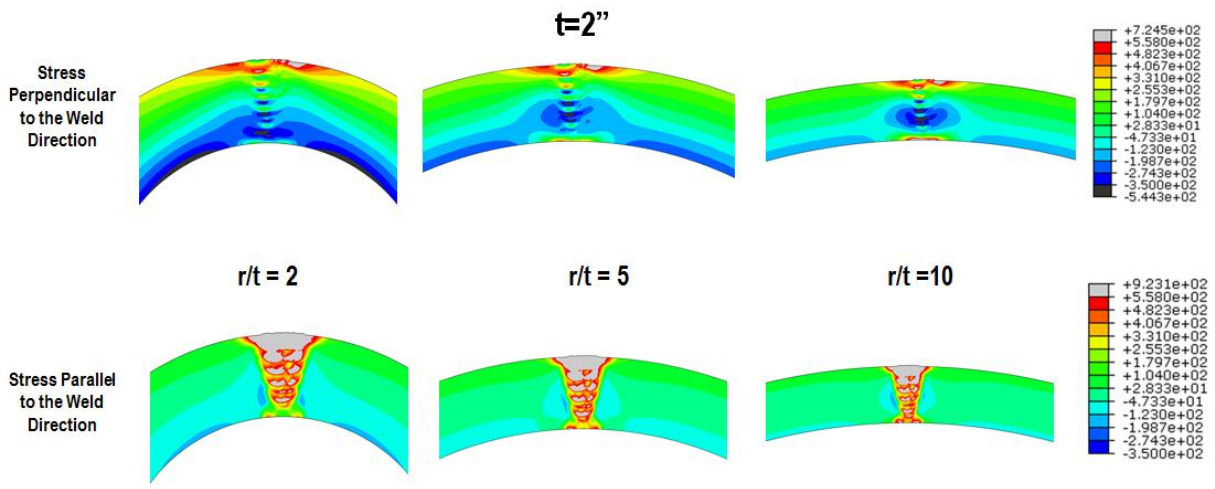

Figure 5-10 Residual stress contour plots for 2” thickness seam welds: r/t ratio effects

Detailed through-thickness residual stress line plots at both weld centerline (WCL) and weld toe (WT) locations are shown in Figure 5-11and Figure 5-12, respectively. Plots for perpendicular stress are on the left hand side and parallel stress on the right hand side. Similar to what observed in girth welds, lines of residual stress distribution at weld toe are much smoother than the ones at weld centerline, due to the less complex local interactions among the weld passes. Overall, the results indicate the stress near ID (0*mm* – 10*mm* from ID) increase with increasing r/t ratio for all cases. This results in a transition of though-thickness residual stress distribution type from local bending to self-equilibrating. This is consistent with the findings from the contour plots in Figure 5-10.

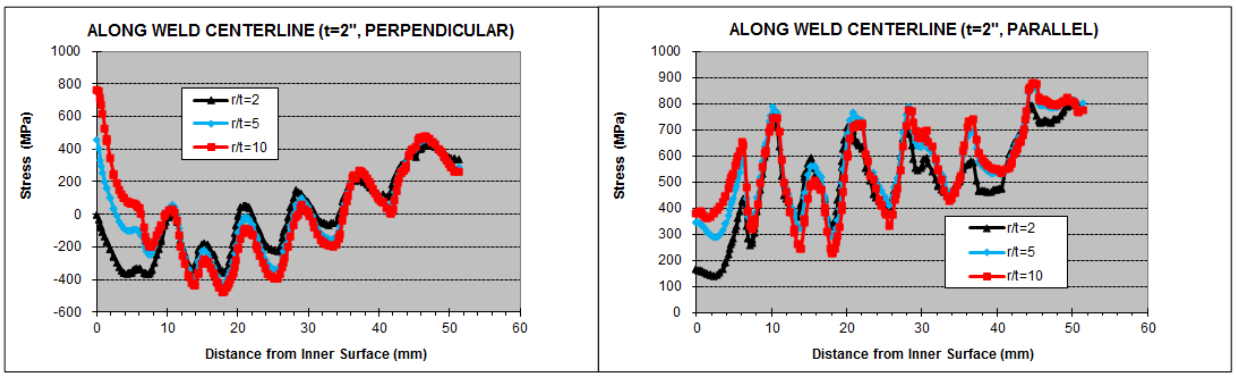

Figure 5-11 Through-thickness residual stress line plots along WCL for 2” thickness seam welds: r/t ratio effects

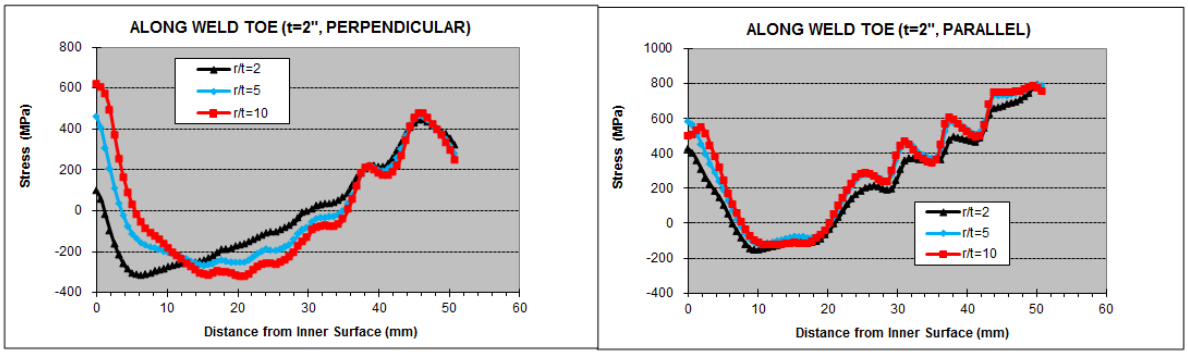

Figure 5-12 Through-thickness residual stress line plots along WT for 2" thickness seam welds: r/t ratio effects

In order to obtain a full-field residual stress profile, perpendicular and parallel residual stress distributions are plotted along pipe outer surface (OD) and inner surface (ID), as shown in Figure 5-13. The top two plots are for stress along OD and bottom two for stress along ID. The horizontal axis is measured from weld toe position and converted to angle position. It can be observed that, as r/t increases, the magnitude of tension zone on OD and compression zone on ID (at about 12 °~30 °) is reduced and the curves move towards the weld. The residual stress is negligible after 120 °.

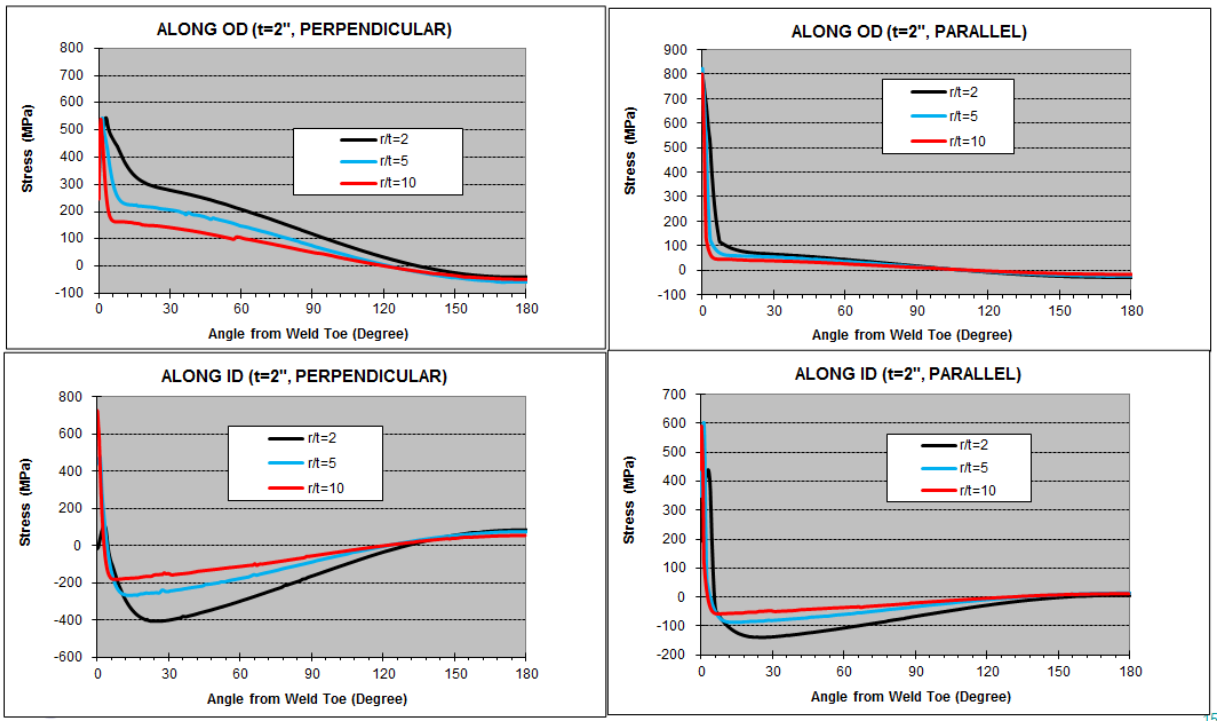

Figure 5-13 Surface residual stress line plots along OD and ID for 2" thickness seam welds: r/t ratio effects

Figure 5-14 and Figure 5-15 show the contour plots for thickness of 4” and 10” seam welds, respectively. Similar trends are observed as discussed for 2” thickness cases above. The exception is the case of 10” thickness with r/t ratio of 2 where a small area of tensile perpendicular stress already exists on ID of the weld.

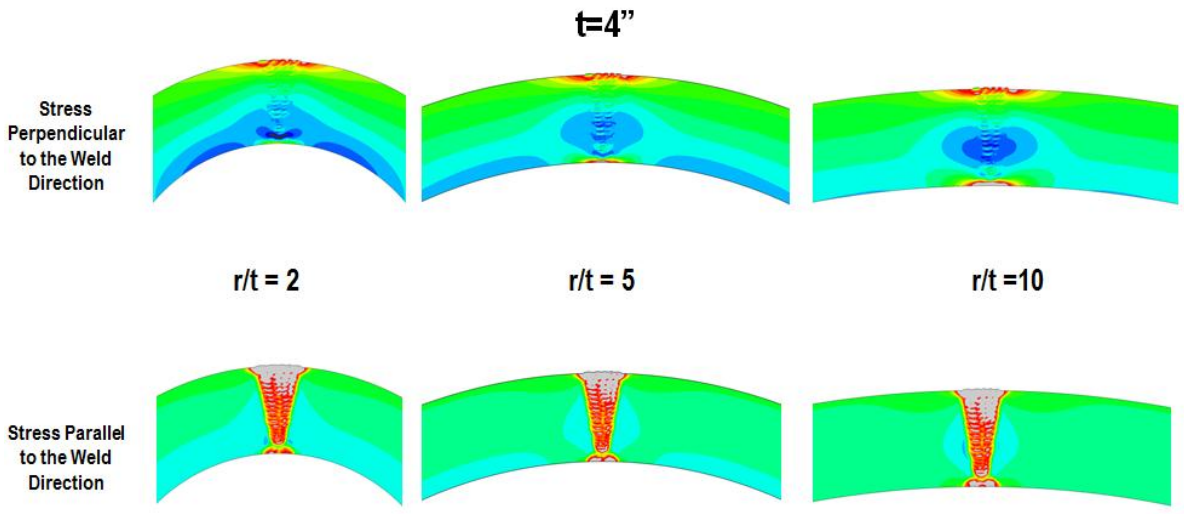

Figure 5-14 Residual stress contour plots for 4” thickness seam welds: r/t ratio effects

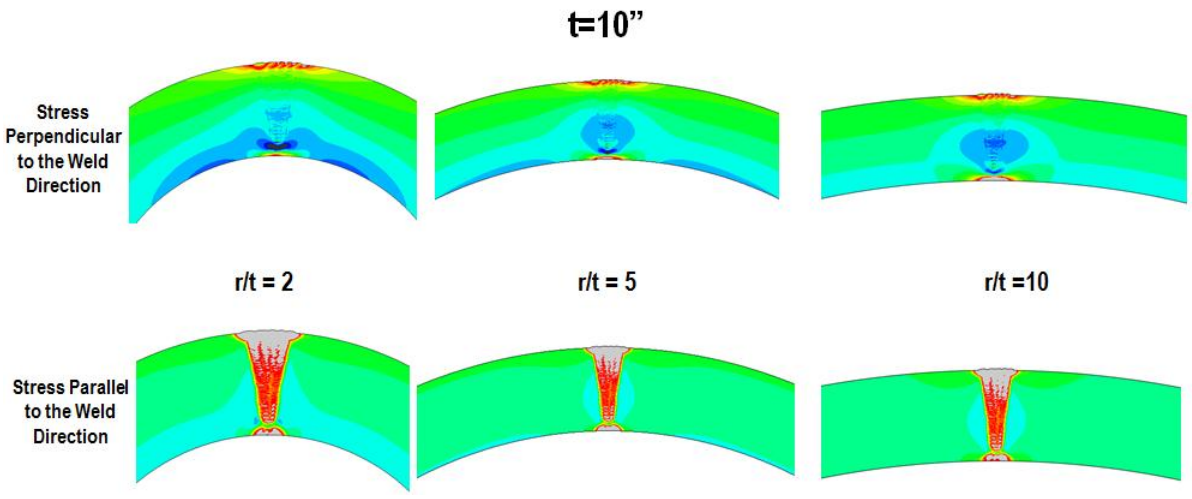

Figure 5-15 Residual stress contour plots for 10” thickness seam welds: r/t ratio effects

The residual stresses of seam welds are also decomposed according to Section 2.4.4. The decomposed residual stress components with respect to r/t ratio for thickness of 2”, 4” and 10” are shown in Figure 5-16, Figure 5-17, and Figure 5-18, respectively. The results at weld

centerline are shown on the left hand side and the results at weld toe on the right hand side. Overall, the following trends can be observed:

1. The decomposed bending components of parallel (blue) and perpendicular (red) stresses show a clear dependence on r/t ratio, monotonically decreasing with increasing r/t ratio. This implies a reduced restraint as r/t ratio increases.

2. The decomposed membrane components of parallel (purple) and perpendicular (green) stresses increase slightly with increasing r/t ratio.

3. The above two observations on r/t ratio effect can be applied to the cases with thicknesses from 2" to 10" at any interested locations (WCL and WT) investigated in this section.

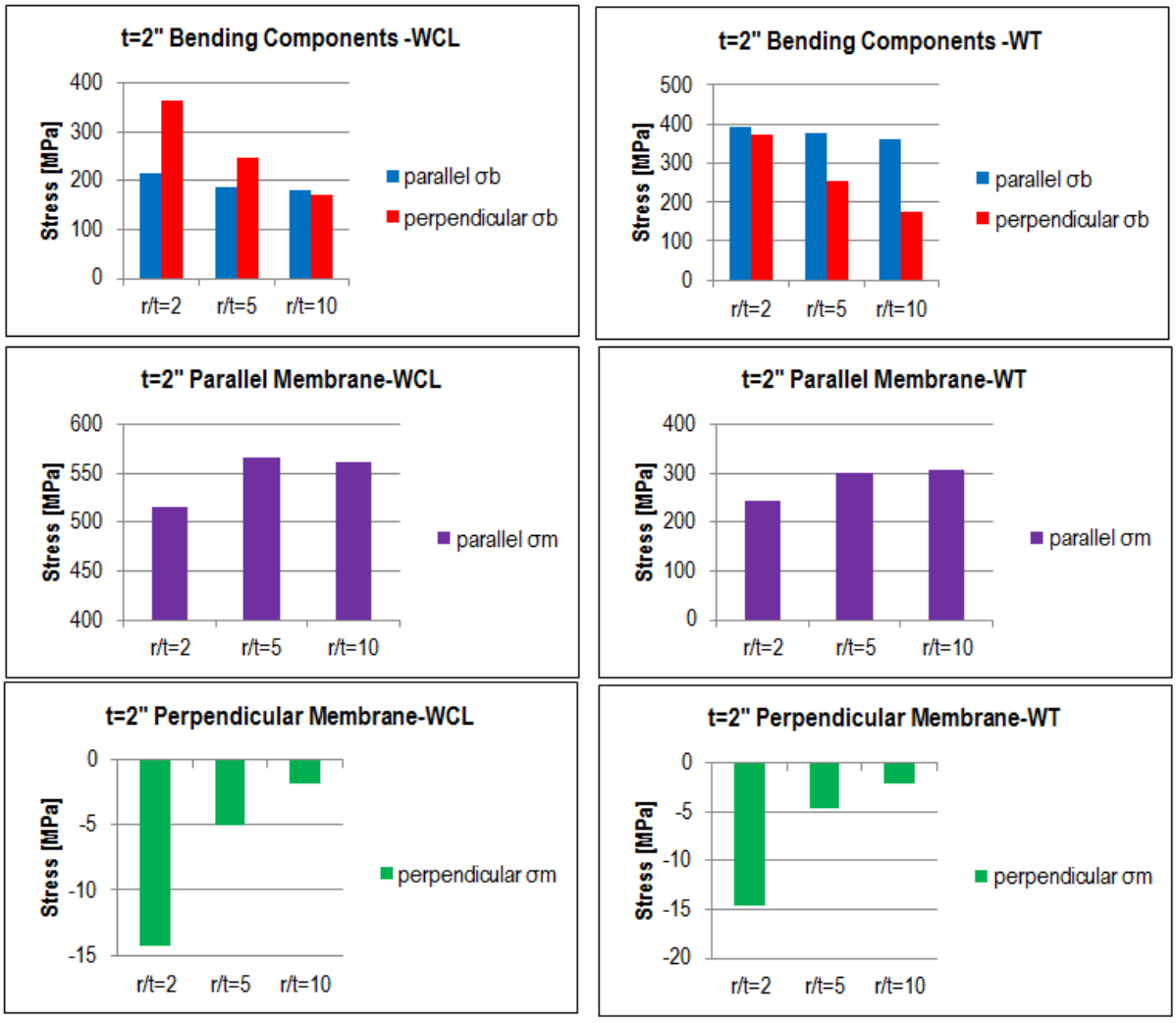

Figure 5-16 Decomposed residuals stress components at WCL and WT as a function of r/t ratio for 2" thickness seam welds

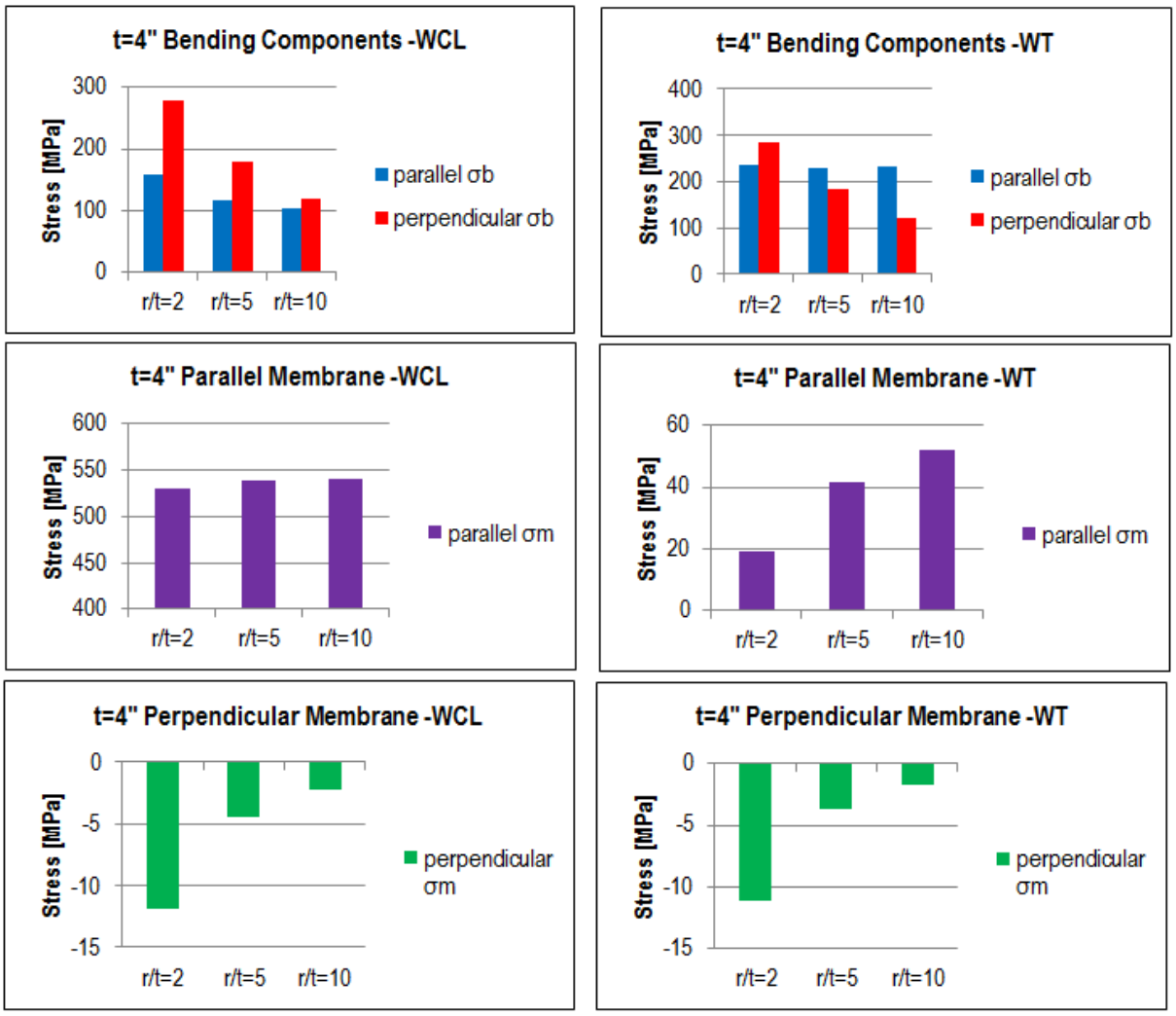

Figure 5-17 Decomposed residuals stress components at WCL and WT as a function of r/t ratio for 4" thickness seam welds

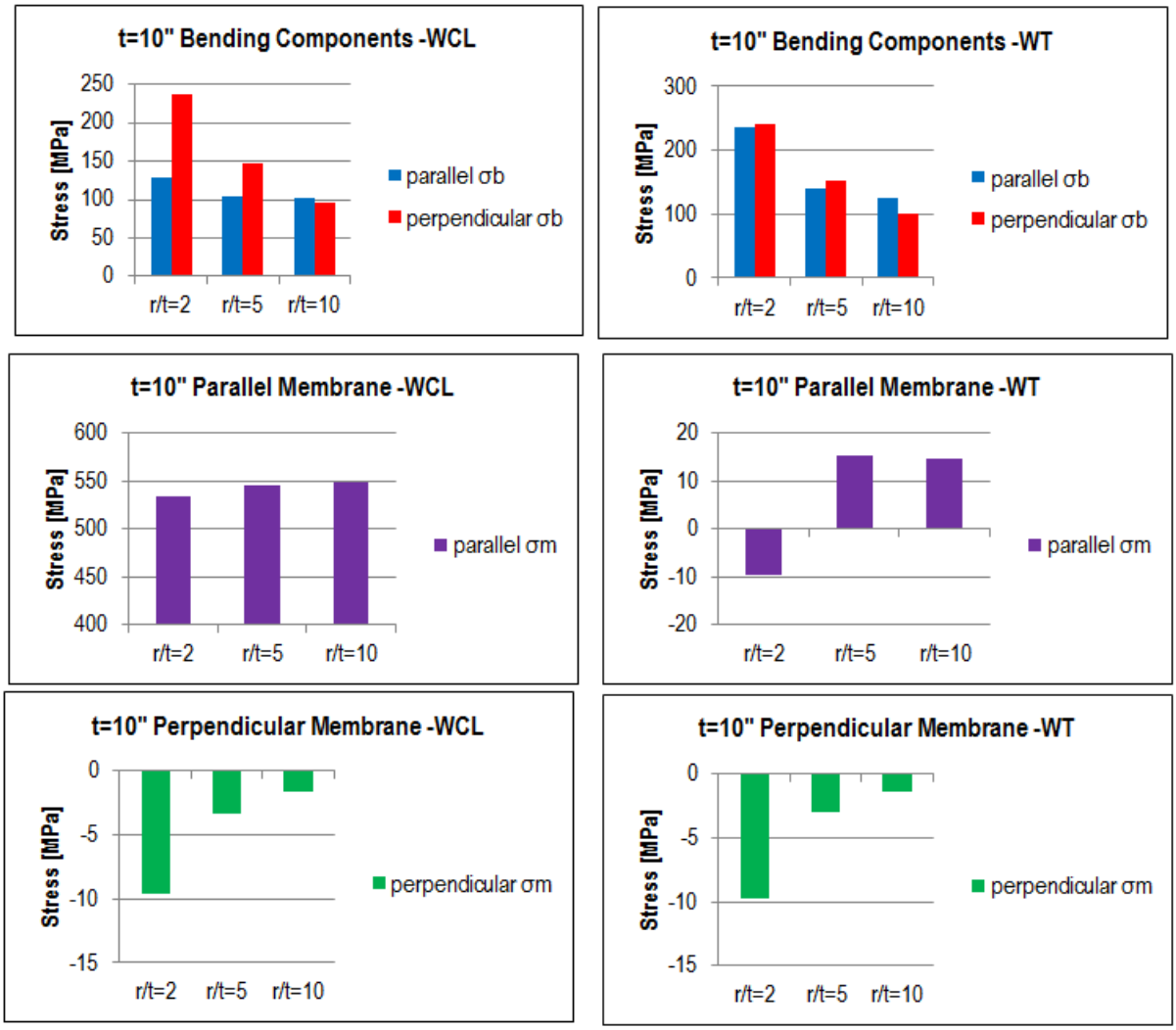

Figure 5-18 Decomposed residuals stress components at WCL and WT as a function of r/t ratio for 10" thickness seam welds

5.3 Thickness effects

Figure 5-19 shows some distinct characteristic types of through-thickness perpendicular residual stress distributions with certain range of r/t and t values. The stress scale is the same as before, i.e., from -350MPa to 558MPa. From this figure, it can be clearly observed that residual stress distribution is transitioned from one distribution type to another. The transition is dominated by r/t and t. For small thickness (e.g., t=2") and small r/t (e.g., r/t=2), perpendicular residual stress distribution can be characterized as a through-wall local bending type with OD under tension and ID under compression. As either thickness t or r/t increases, the local bending type is gradually transitioned to a through-wall self-equilibrating type (e.g., at t=10" with r/t =2, or at t=2" with r/t=10).

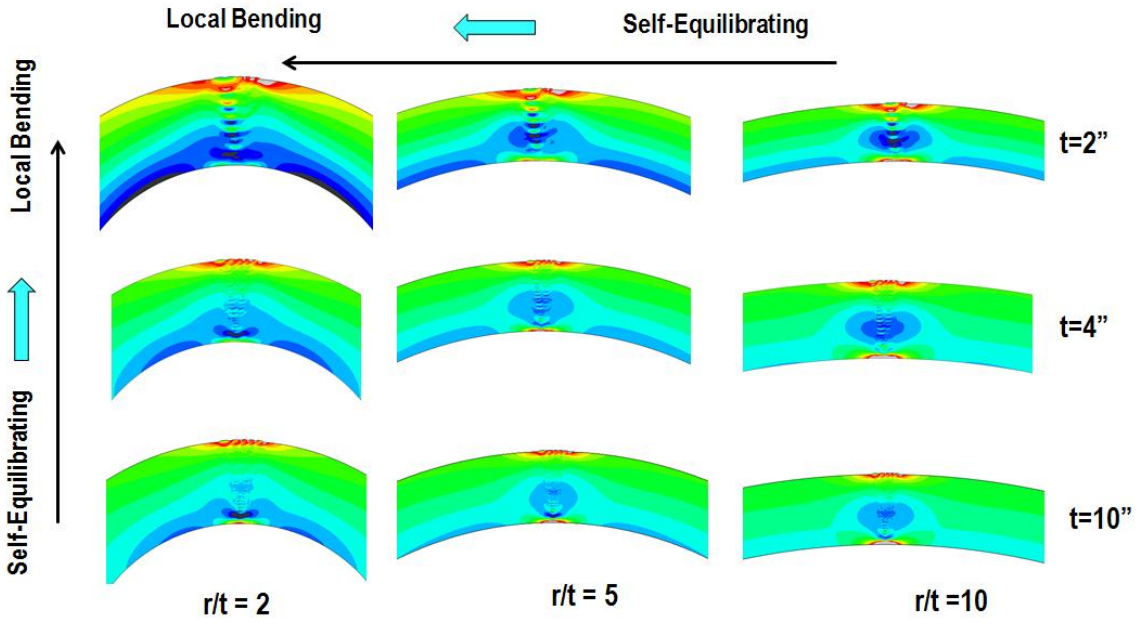

Figure 5-19 Perpendicular residual stress contour plots for seam welds as a function of r/t and t

Again, the decomposed residual stress components are investigated for the trend of thickness effect. The decomposed stress results in the previous section are re-arranged as a function of thickness. Figure 5-20, Figure 5-21, and Figure 5-22 shows the results with respect to thickness for r/t ratio of 2, 5, and 10, respectively. The decomposed residual stress components at weld centerline (WCL) location are shown on the left hand side and the ones at weld toe (WT) on the right hand side. The trends observed from these results are summarized below:

1) At weld centerline, the decomposed bending parts of perpendicular and parallel residual stress decrease monotonically with increasing thickness, expect for the case of perpendicular bending component for r/t=10 with thickness of 2”. The decomposed membrane component of perpendicular residual stress increases with the increase of thickness, and the membrane part of parallel residual stress maintains almost the same for all thickness.

2) At weld toe, the bending components have the same trend as those at weld centerline. The bending stress decreases as thickness increases. Perpendicular membrane component increases slightly with the increase of thickness. Parallel membrane component remains relatively unchanged for all thickness.

A summary of thickness effects discussed above is given by Table 5-2.

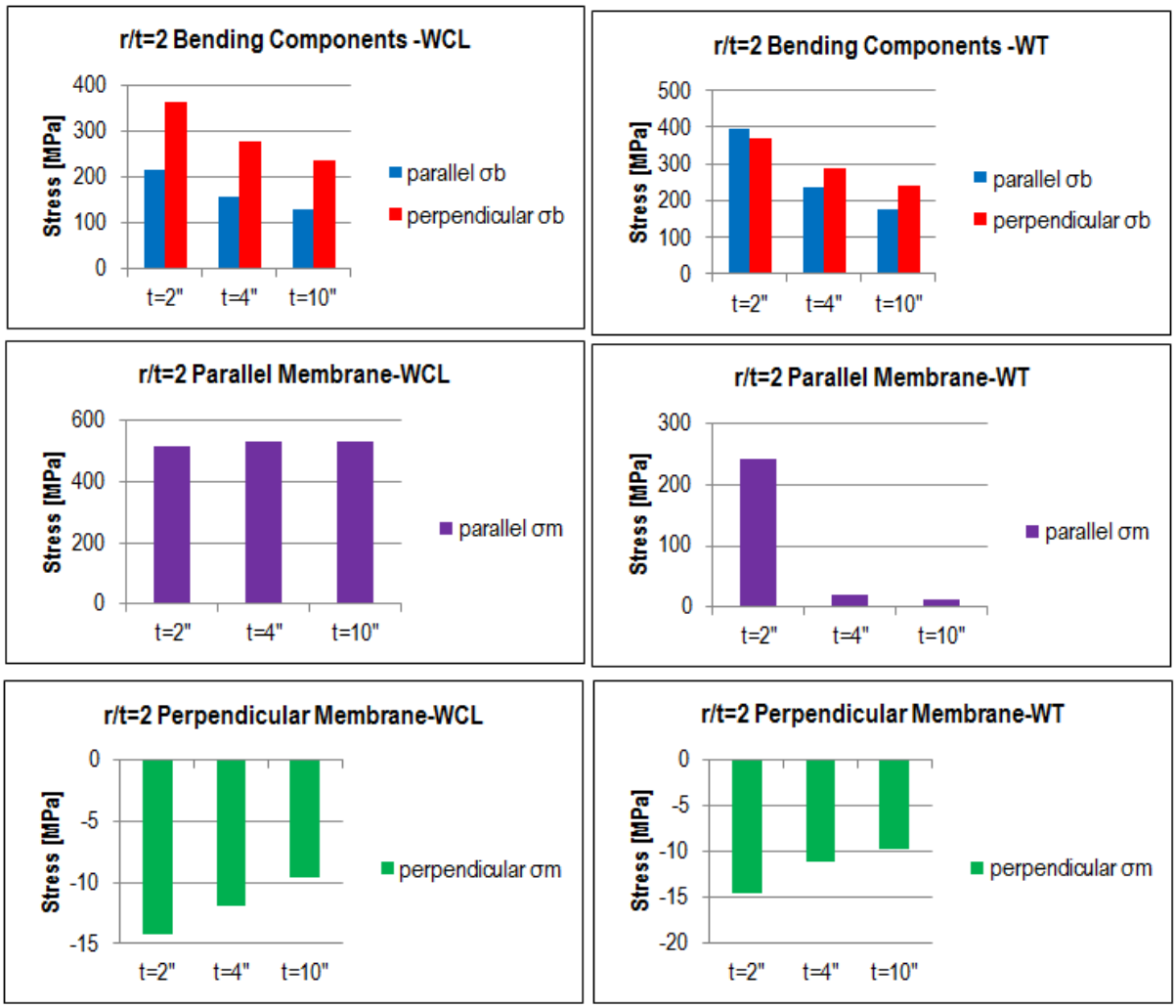

Figure 5-20 Decomposed residuals stress components at WCL and WT as a function of thickness for r/t ratio of 2 seam welds

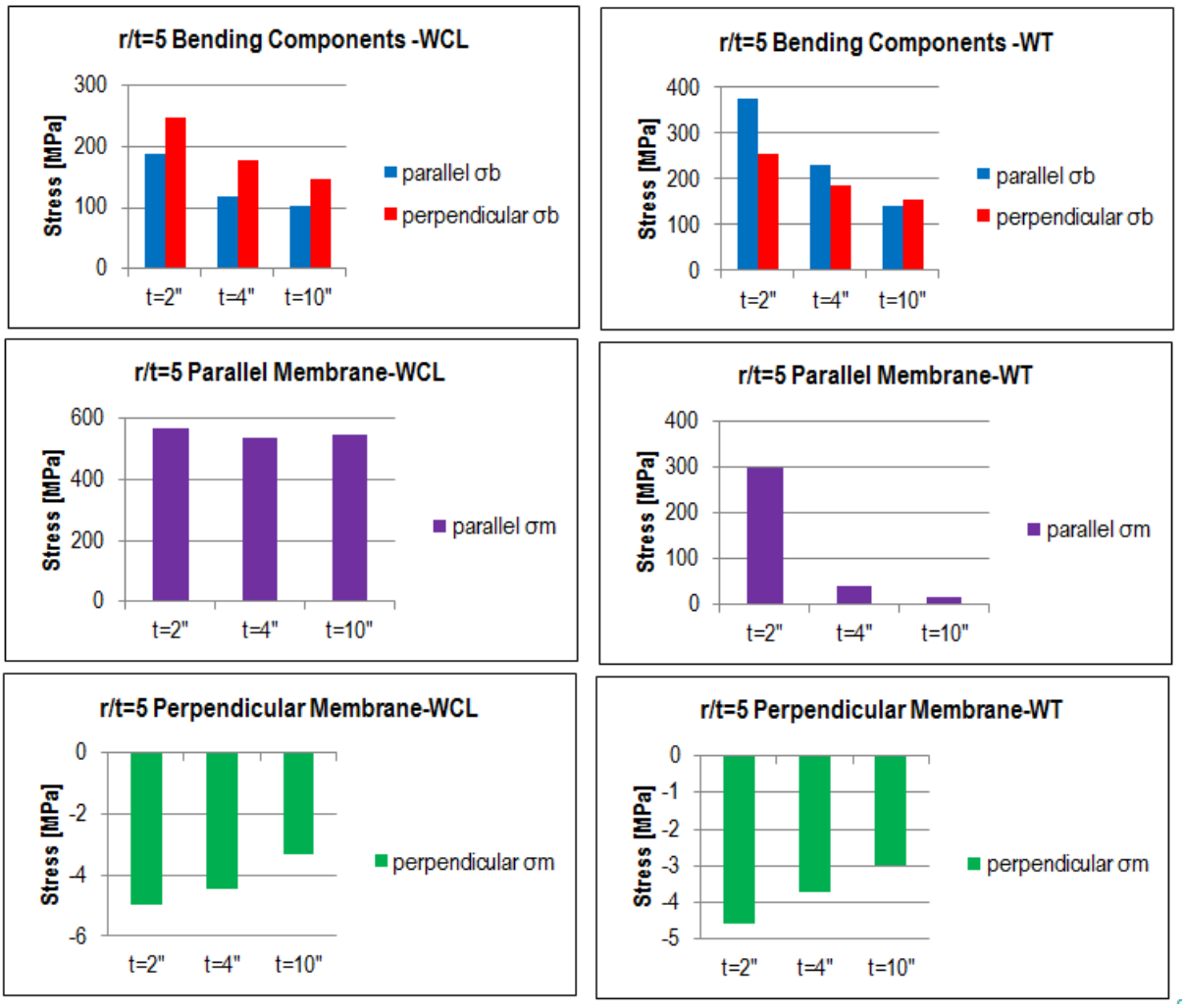

Figure 5-21 Decomposed residuals stress components at WCL and WT as a function of thickness for r/t ratio of 5 seam welds

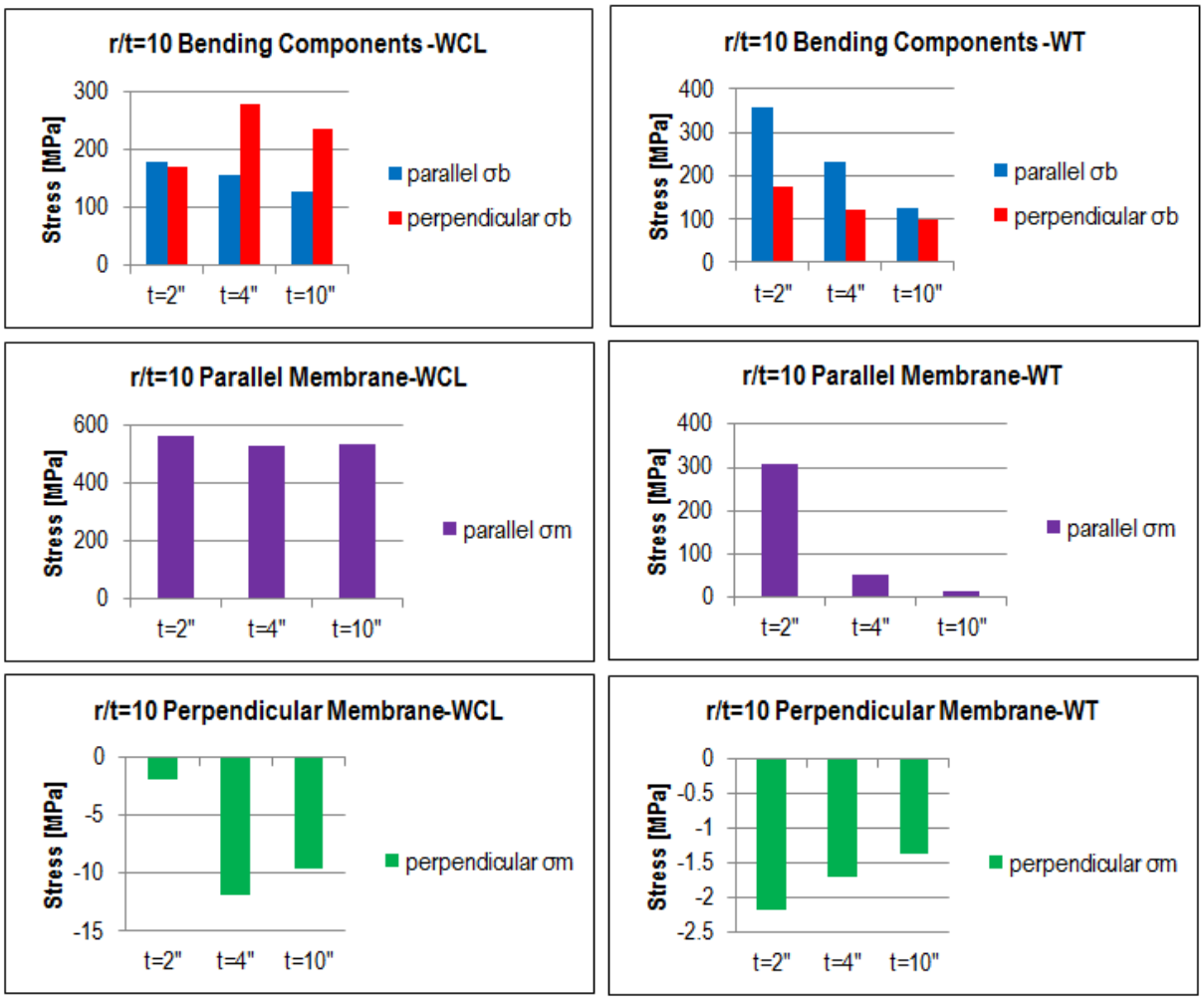

Figure 5-22 Decomposed residuals stress components at WCL and WT as a function of thickness for r/t ratio of 10 seam welds

Table 5-2 Observations of thickness effect

With increasing thickness (t is from 2" to 10"), decomposed residual stress components would be						
	at Weld Centerline (WCL)			at Weld Toe (WT)		
	Bending Parallel & Perpendicular	**Membrane** Perpendicular	**Membrane** Perpendicular	**Bending** Parallel & Perpendicular	**Membrane** Perpendicular	**Membrane** Perpendicular
Seam welds	Decrease	Increase	Constant	Decrease	Increase	Decrease

5.4 Full-field generalizations (membrane, bending and self-equilibrating)

Full-field residual stress distributions are essential for fracture mechanics based structural integrity assessments. With the help of residual stress decomposition technique, in this section distributions of membrane and bending components are established along pipe circumference from weld toe location. Similar to girth welds, through-thickness locations (highlighted as red lines) are selected for performing stress decomposition, as shown in Figure 5-23. The angle θ is measured from weld toe position to the half of the pipe circumference. The analysis procedure is the same as described for girth welds. Once membrane and bending components are obtained at each location, stresses on OD are plotted as membrane plus bending and then compared with FE distributions on outer surface. The stresses on ID are plotted as membrane plus opposite sign of OD bending stress. By definition (Eq. 3.29 or 4.1), the difference between each pair is a surface value of the corresponding self-equilibrating component. The cases studied are summarized in Table 5-3. Compared with Table 4-1, one additional group is added (t=2" with 100-pass) as highlighted in purple in order to capture some lumped pass effects.

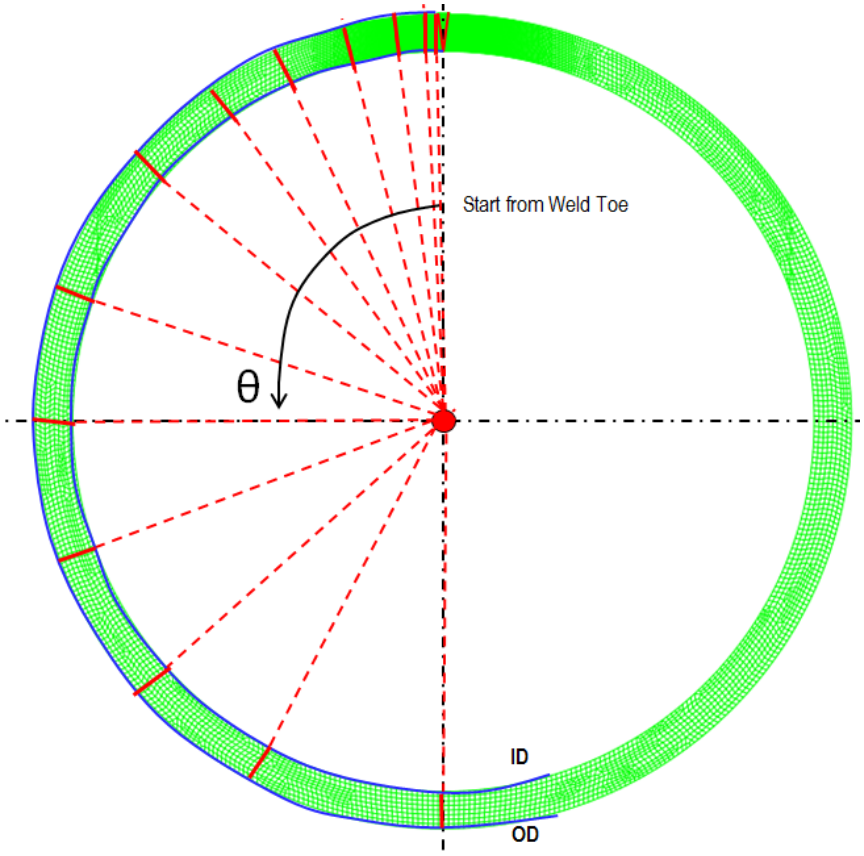

Figure 5-23 Representative through-thickness locations started from weld toe for performing stress decomposition

Table 5-3 Analysis matrix for full-field generalizations

	t=2”	t=2”	t=4”	t=10”
Layer#	9	34	21	34
Pass#	21	100	60	100
r/t=2	X	X	X	X
r/t=5	X	X	X	X
r/t=10	X	X	X	X

5.4.1 Results for membrane and bending components of through-thickness residual stress along pipe circumference

Figure 5-24 shows the comparison of through-thickness perpendicular and parallel residual stress components with the surface residual stress obtained from FEA for the 1” thick seam weld with 21-pass and r/t ratio of 2. The horizontal axis is the angle θ. Plots are marked in the same manner as girth welds with blue diamond indicating the surface residual stress directly from FEA, yellow triangle membrane for component at each though-thickness location, red round for the bending component, black square for the membrane plus actual bending (bending on ID is with opposite sign of the one on OD). The results for other cases are summarized from Figure 5-25 to Figure 5-35.

The perpendicular membrane components are small. Similar to what observed in girth welds, after a certain distance from weld, now known as plastic zone width d_p, the results of membrane plus bending stress match the surface residual stress obtained directly from FEA in all plots. This indicates that self-equilibrating part is only significant within d_p. Similar to girth welds, the following questions need to be answered:

1. How to estimate residual stress profiles of membrane and bending components along pipe circumference at each through-thickness location

2. How to estimate residual stress profile for the self-equilibrating part within the weld

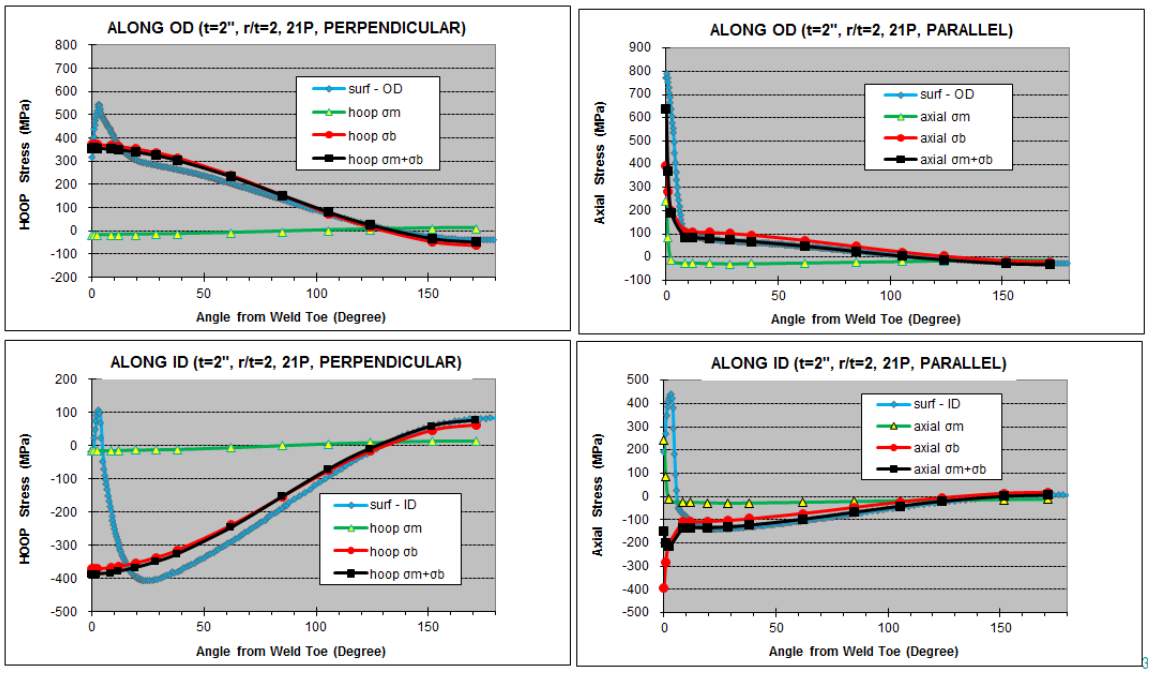

Figure 5-24 t=2", r/t=2, 21-pass, through-thickness perpendicular and parallel residual stress components along OD and ID

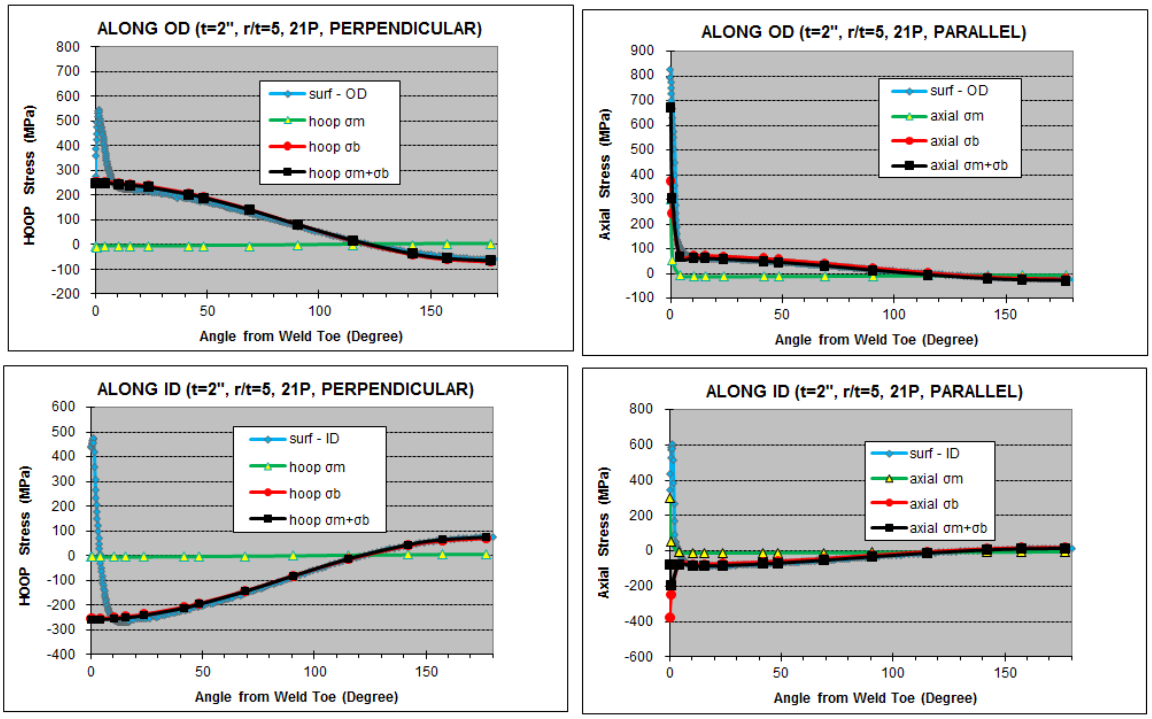

Figure 5-25 t=2", r/t=5, 21-pass, through-thickness perpendicular and parallel residual stress components along OD and ID

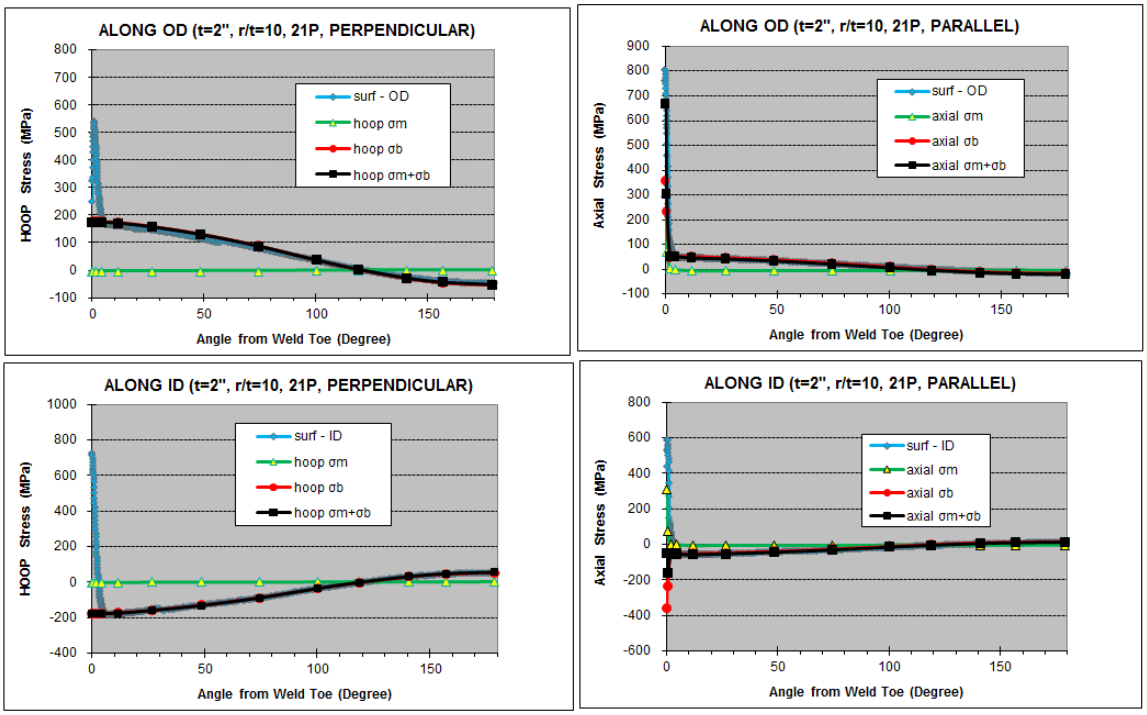

Figure 5-26 t=2", r/t=10, 21-pass, through-thickness perpendicular and parallel residual stress components along OD and ID

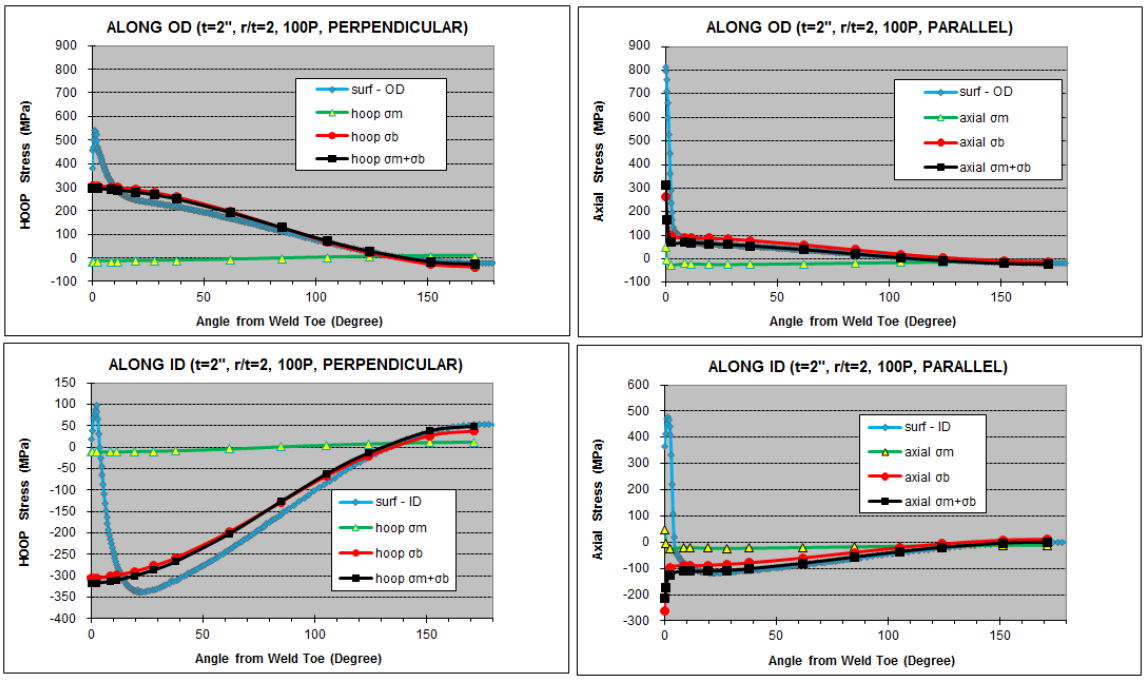

Figure 5-27 t=2", r/t=2, 100-pass, through-thickness perpendicular and parallel residual stress components along OD and ID

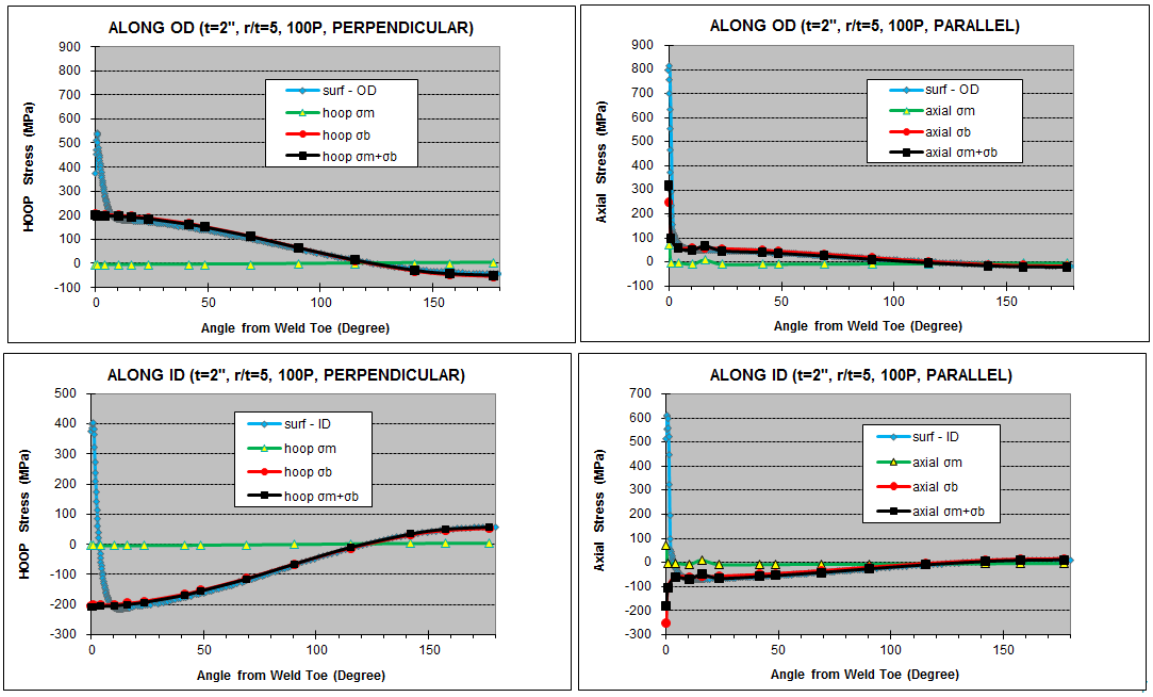

Figure 5-28 t=2", r/t=5, 100-pass, through-thickness perpendicular and parallel residual stress components along OD and ID

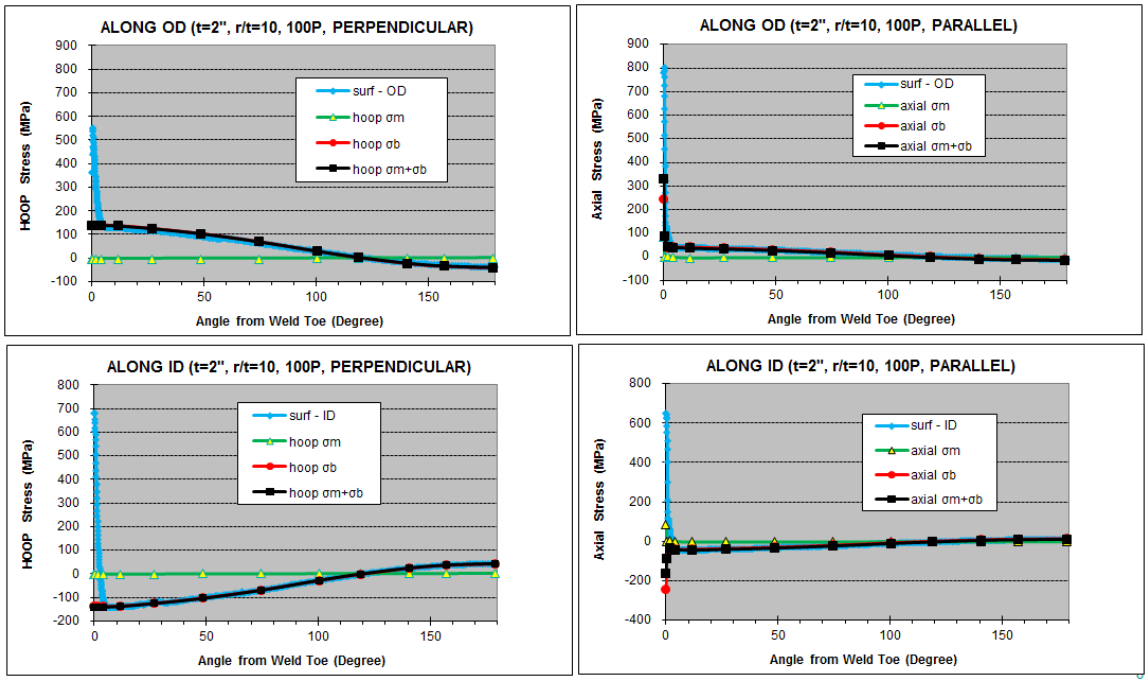

Figure 5-29 t=2", r/t=10, 100-pass, through-thickness perpendicular and parallel residual stress components along OD and ID

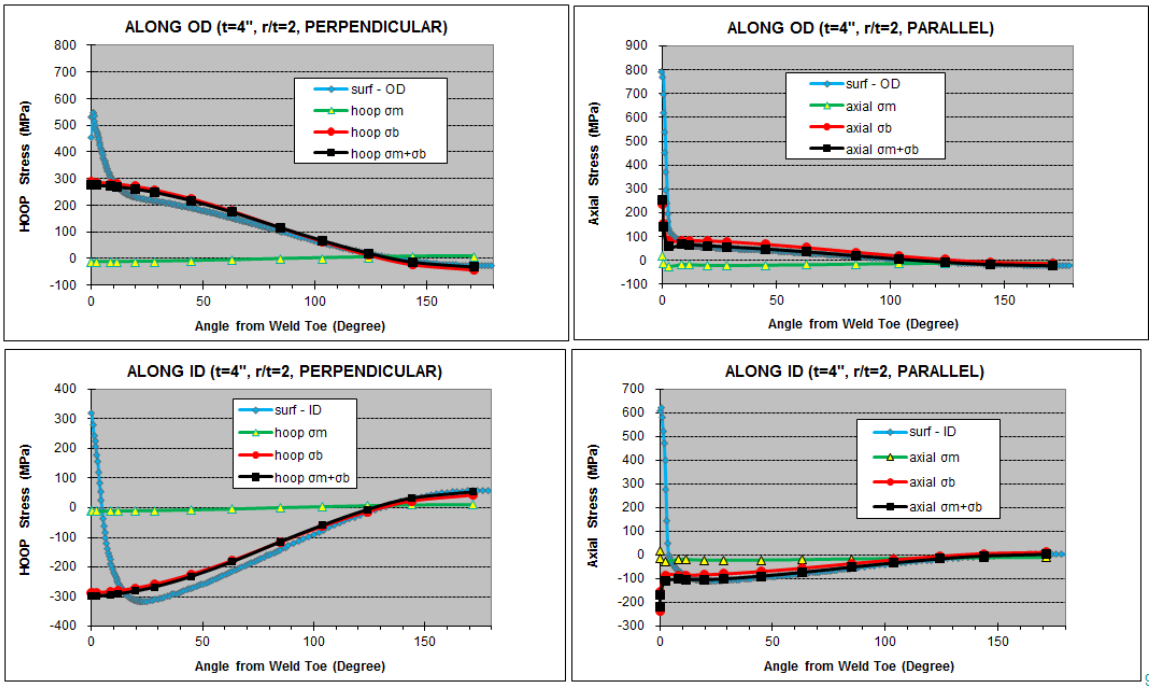

Figure 5-30 t=4", r/t=2 through-thickness perpendicular and parallel residual stress components along OD and ID

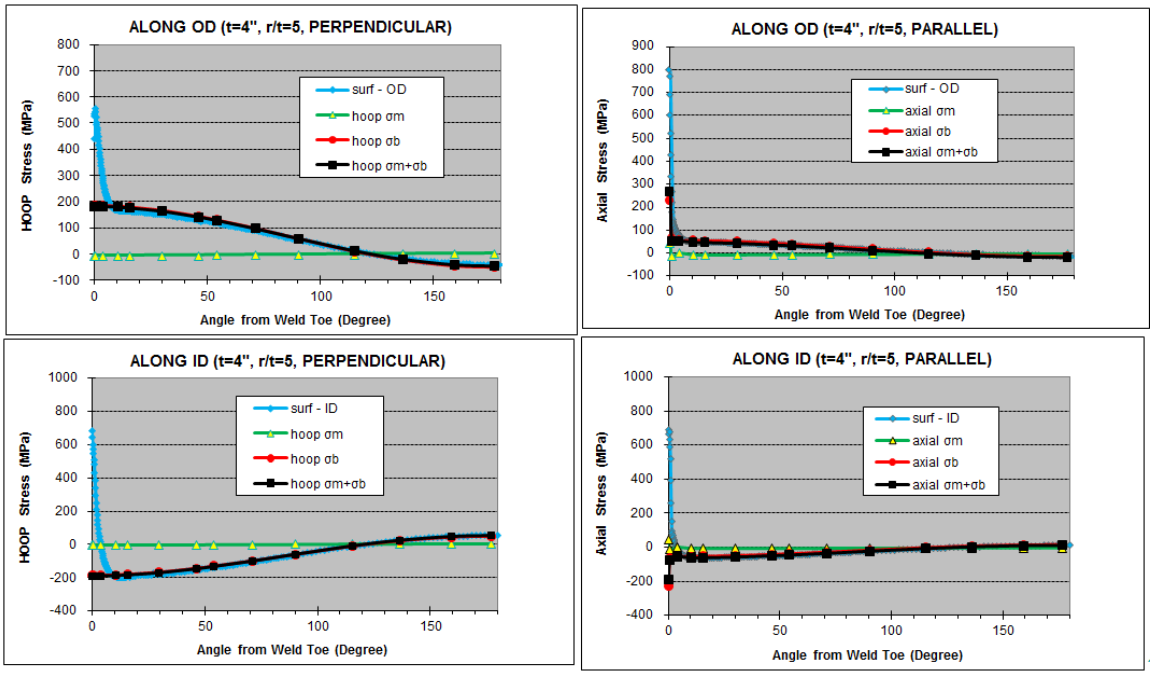

Figure 5-31 t=4", r/t=5 through-thickness perpendicular and parallel residual stress components along OD and ID

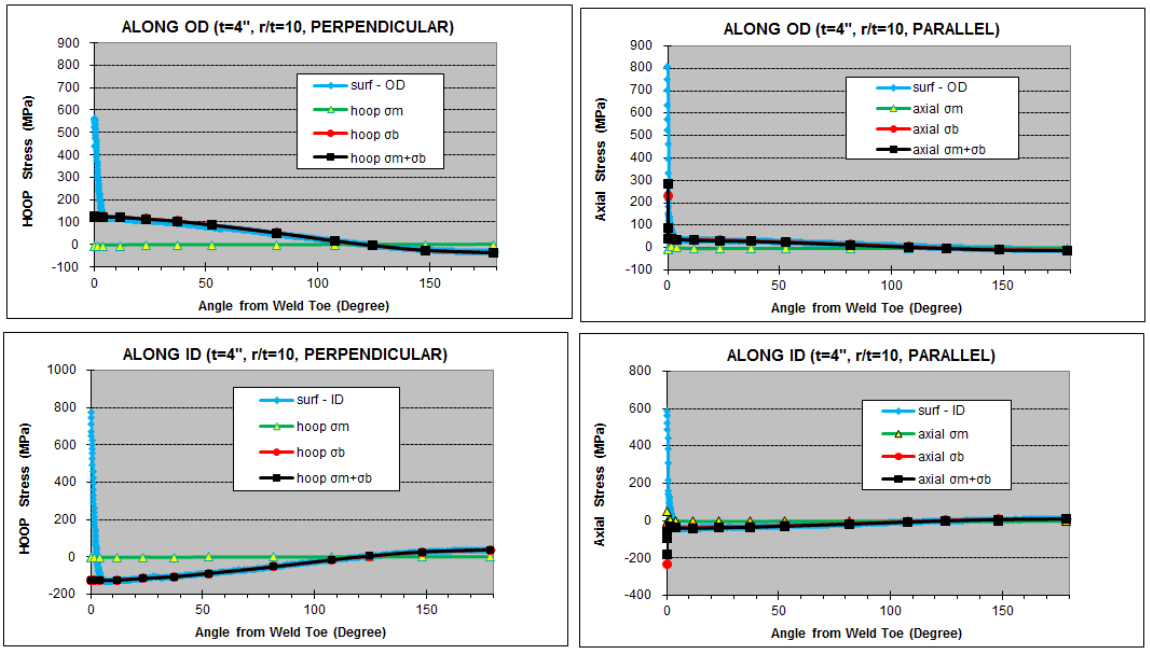

Figure 5-32 t=4", r/t=10 through-thickness perpendicular and parallel residual stress components along OD and ID

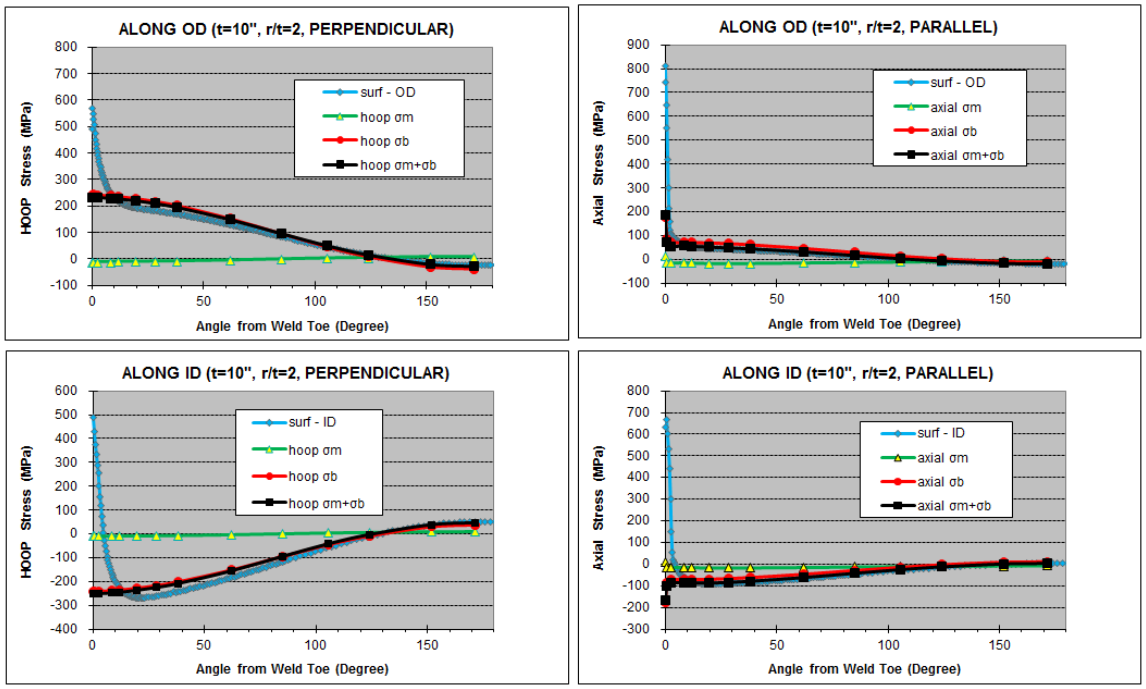

Figure 5-33 t=10", r/t=2 through-thickness perpendicular and parallel residual stress components along OD and ID

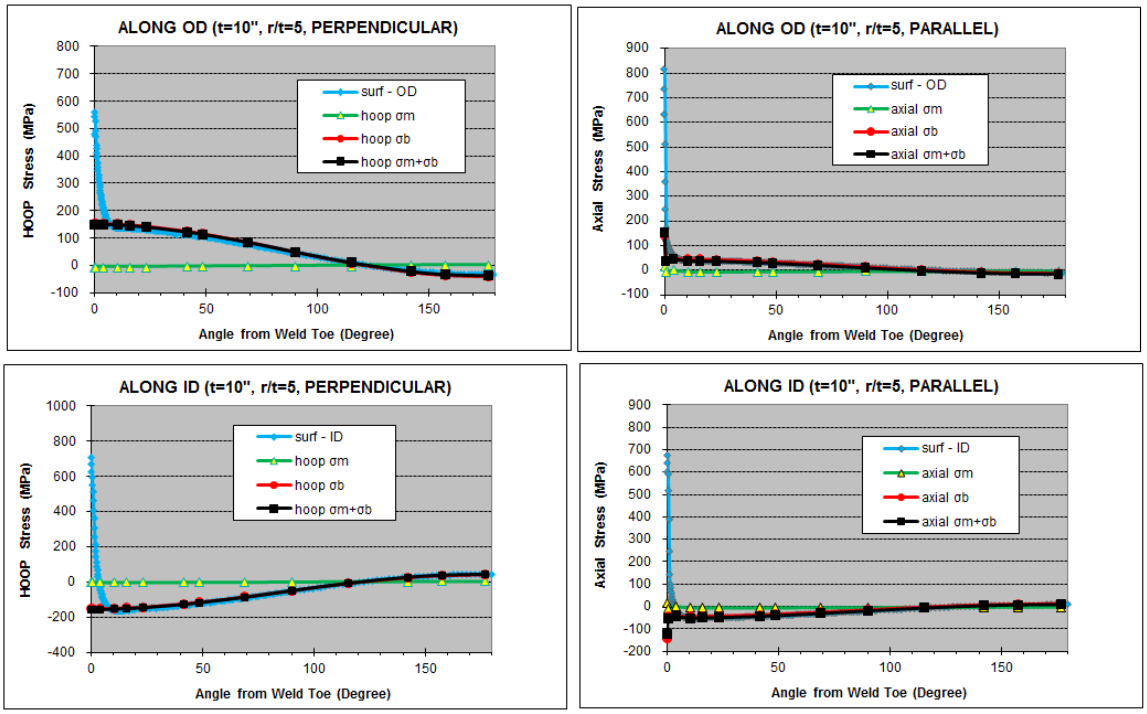

Figure 5-34 t=10", r/t=5 through-thickness perpendicular and parallel residual stress components along OD and ID

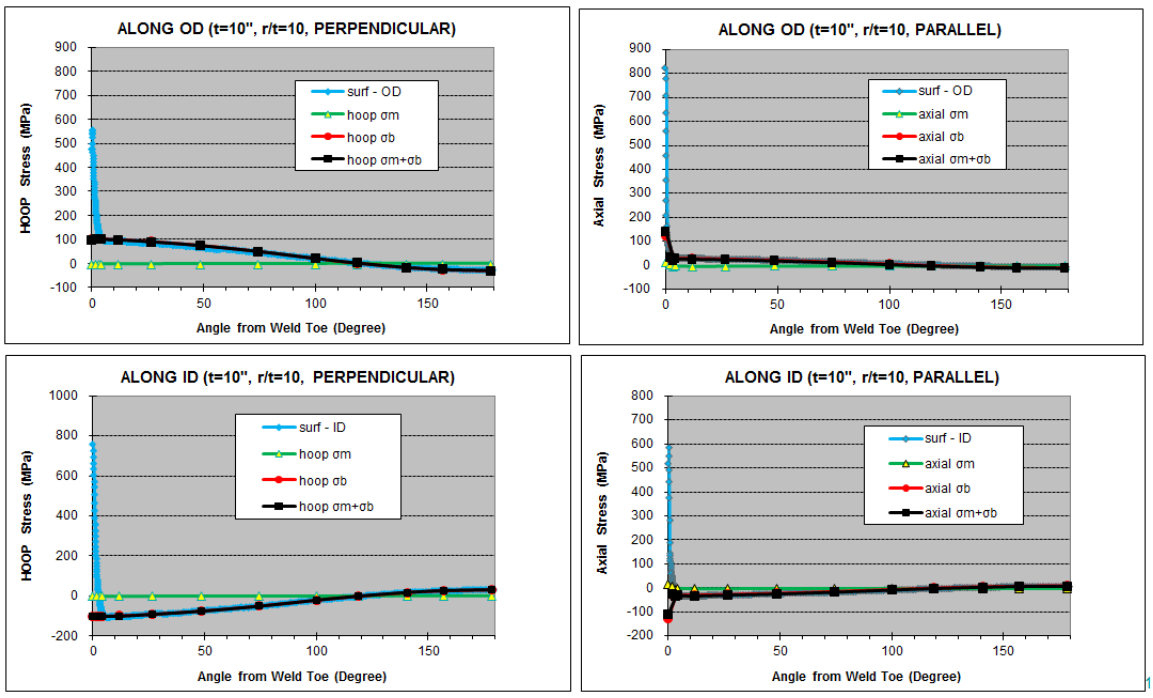

Figure 5-35 t=10", r/t=10 through-thickness perpendicular and parallel residual stress components along OD and ID

5.4.2 Results for self-equilibrating part of through-thickness residual stress at weld centerline

Figure 5-36 to Figure 5-47 exhibit the stress components at weld centerline for cases listed in Table 4-3. Black line indicates the original residual stress directly from FEA, red line for the corresponding self-equilibrating part, blue line for bending part and green line for membrane part. The horizontal axis is measured from ID and normalized by thickness. Sine wave stress oscillations are exhibited in the self-equilibrating part due to the interaction between weld passes. The wave number is corresponding to the number of weld layers. By comparing Figure 5-36 and Figure 5-39, it can be seen that stress oscillation is more significant for 21-pass case than 100-pass case. This is consistent with the findings in lumped pass effects.

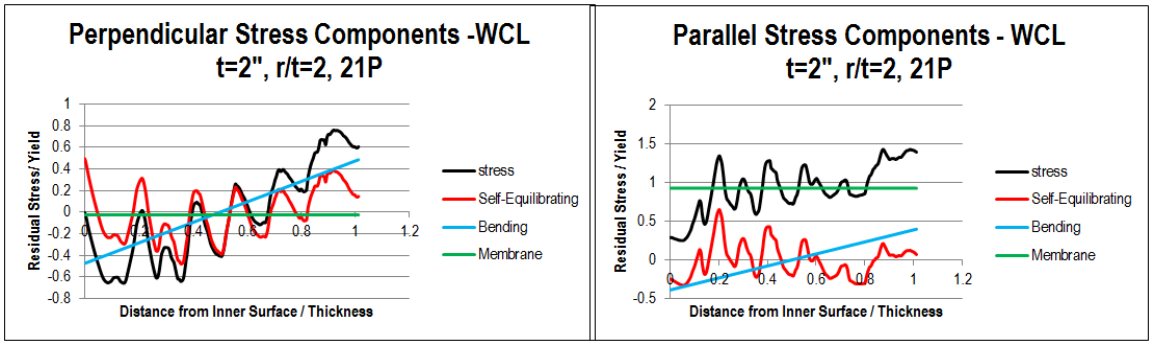

Figure 5-36 Weld centerline decomposed perpendicular and parallel residual stress components for t=2", r/t=2, 21-pass

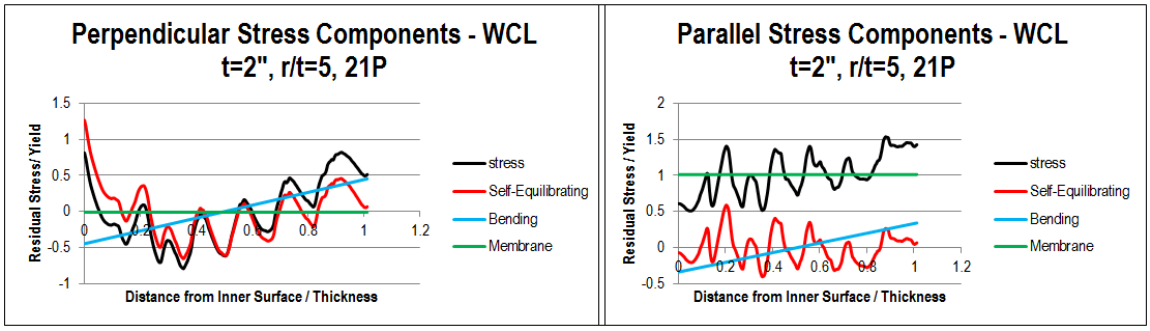

Figure 5-37 Weld centerline decomposed perpendicular and parallel residual stress components for t=2", r/t=5, 21-pass

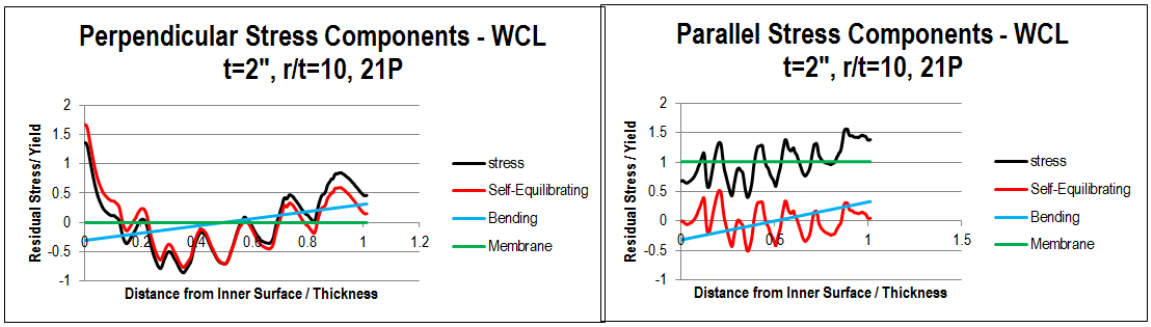

Figure 5-38 Weld centerline decomposed perpendicular and parallel residual stress components for t=2", r/t=10, 21-pass

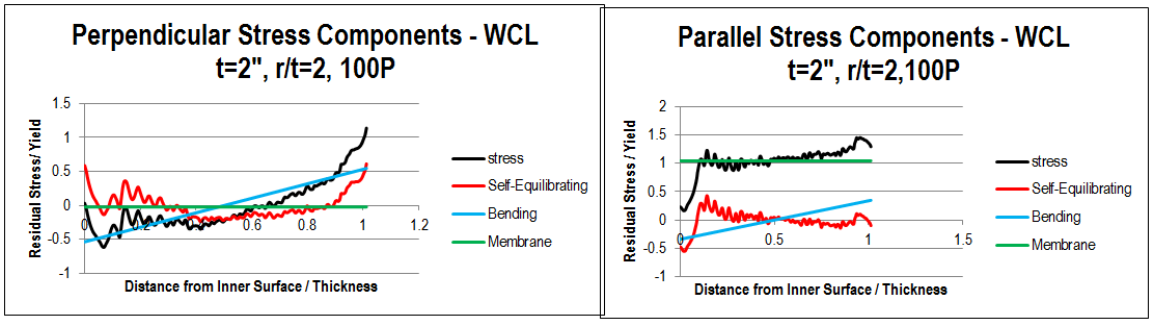

Figure 5-39 Weld centerline decomposed perpendicular and parallel residual stress components for t=2", r/t=2, 100-pass

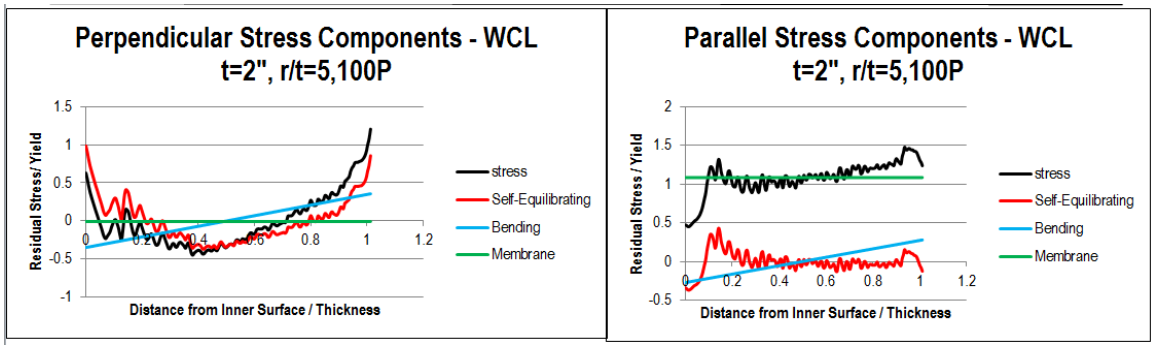

Figure 5-40 Weld centerline decomposed perpendicular and parallel residual stress components for t=2", r/t=5, 100-pass

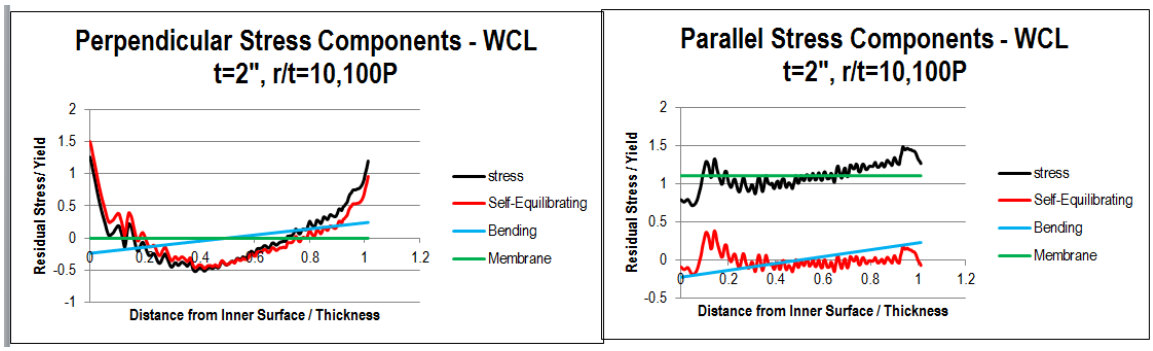

Figure 5-41 Weld centerline decomposed perpendicular and parallel residual stress components for t=2", r/t=10, 100-pass

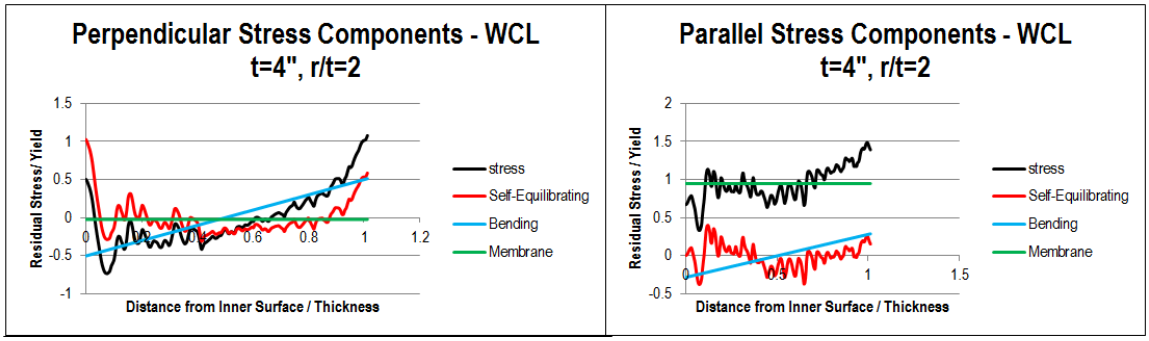

Figure 5-42 Weld centerline decomposed perpendicular and parallel residual stress components for t=4", r/t=2

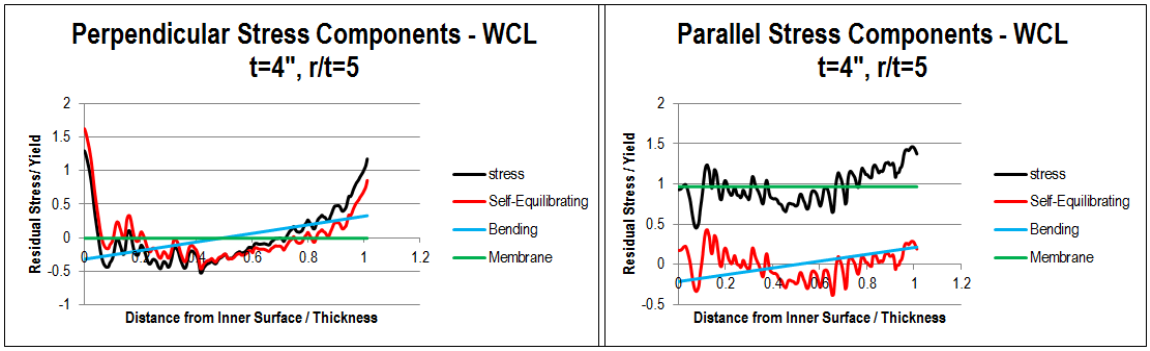

Figure 5-43 Weld centerline decomposed perpendicular and parallel residual stress components for t=4", r/t=5

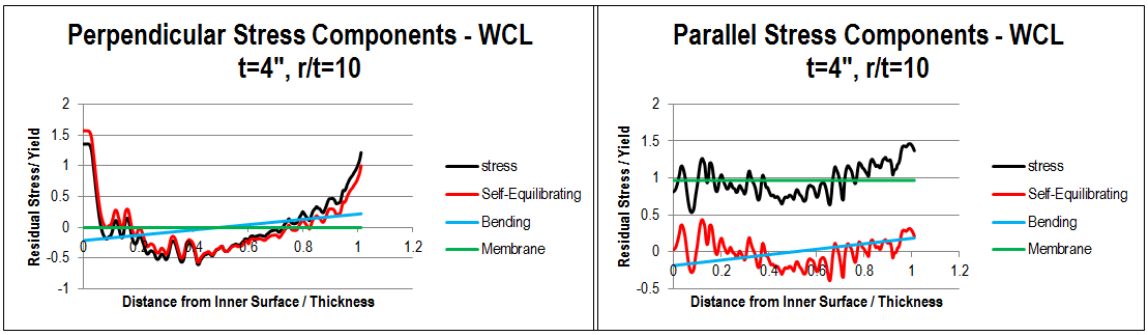

Figure 5-44 Weld centerline decomposed perpendicular and parallel residual stress components for t=4", r/t=10

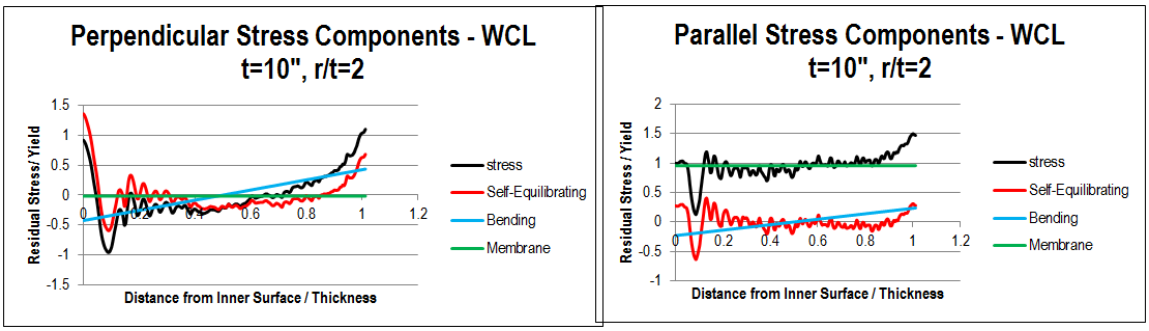

Figure 5-45 Weld centerline decomposed perpendicular and parallel residual stress components for t=10", r/t=2

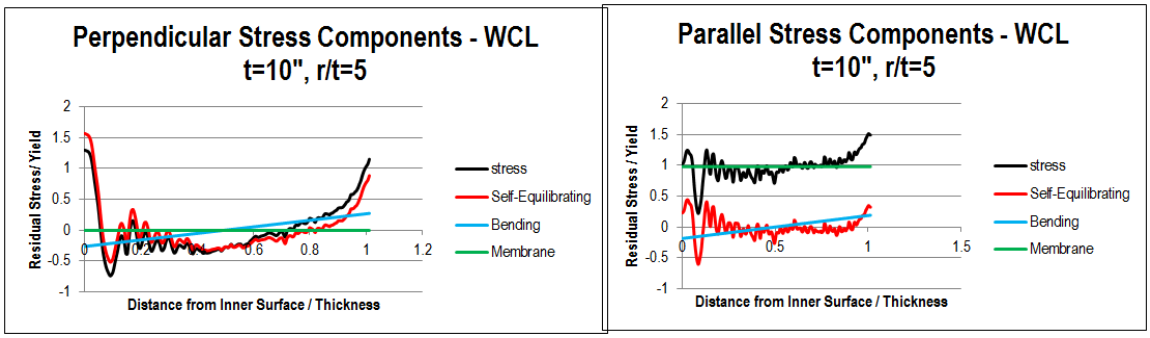

Figure 5-46 Weld centerline decomposed perpendicular and parallel residual stress components for t=10", r/t=5

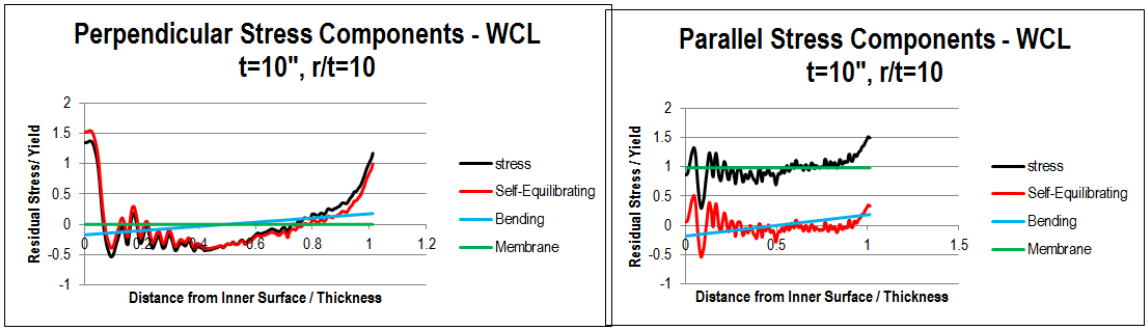

Figure 5-47 Weld centerline decomposed perpendicular and parallel residual stress components for t=10", r/t=10

5.5 A curved bar based full-field residual stress estimation scheme

The objective in this section is to seek a mechanics based approach to estimate membrane and bending components along pipe circumference. It should make use of the through-thickness residual stress distributions at selected cross sections described in the previous section. To accomplish this, a curved bar based theory is adopted here.

5.5.1 Model definition and curved bar based estimations (membrane and bending) versus FE results

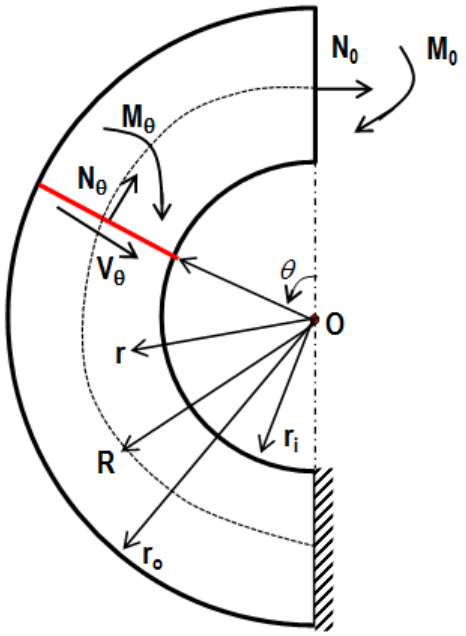

Figure 5-48 Curved bar model definition with N_0 and M_0 at weld toe

Let's consider a curved bar model shown in Figure 5-48. The model represents one half of seam weld at the top end (θ=0). For a given normal force N_0 and moment M_0 at θ=0 (weld toe

location), the normal force and moment at any location along circle circumference can be described as:

$$N_{h,\theta} = N_0 \cdot \cos\theta \quad \textbf{(5.1)}$$

$$M_{h,\theta} = M_0 + N_0 \cdot R(1-\cos\theta) \quad \textbf{(5.2)}$$

where R is mean radius of the pipe. N_0 and M_0 are due to pipe reactions to weld shrinkage force in the direction parallel to the weld. As a result, N_0 can be approximated by the through-thickness perpendicular (hoop) membrane residual stress at weld toe location, which can obtained from parametric analyses in the previous sections, referred to as $\sigma^0_{\theta,m}$. M_0 can be related to perpendicular (hoop) bending component at weld toe location, denoted as $\sigma^0_{\theta,b}$.

$$N_0 = \sigma^0_{\theta,m} \cdot t \quad \textbf{(5.3)}$$

$$M_0 = \sigma^0_{\theta,b} \cdot \frac{t^2}{6} \quad \textbf{(5.4)}$$

With N_0 and M_0 known, Eqs. (5.1-5.2) can be used to calculate through-thickness hoop (perpendicular) residual stress membrane and bending components as a function of angle θ starting from weld toe:

$$\sigma_{\theta,m}(\theta) = \frac{N_{h,\theta}}{t} \quad \textbf{(5.5)}$$

$$\sigma_{\theta,b}(\theta) = \frac{6}{t^2} M_{h,\theta} \quad \textbf{(5.6)}$$

The parallel (axial) residual stress under the plane strain condition is:

$$\sigma_{axial} = \nu \cdot (\sigma_{hoop} + \sigma_{radial}) \quad \textbf{(5.7)}$$

The hoop (perpendicular) residual stress has already been discussed in the previous sections. However, radial residual stress needs to be examined before Eq. (5.5) can be used. Figure 5-49shows two path locations where residual stress distributions are investigated under Eq. (5.5). Path-1 is very close to the weld toe and Path-2 is far away from the weld toe.

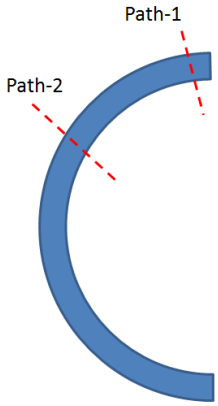

Figure 5-49 Two path selected for examining axial (parallel) residual stress under plain strain condition for t=4", r/t=10

Radial and hoop residual stress distributions along Path-1 and Path-2 are shown in Figure 5-50 and Figure 5-51, respectively. It can be seen that hoop stress exhibits a pure bending type distribution and radial stress is almost a flat line near zero. Because the radia stress is so small, it can be ignored in Eq. (5.5). Figure 5-52 and Figure 5-53 show the axial residual stress calculated using Eq. (5.5) with and without radial stress along Path-1 and Path-2, respectively. It is confirmed that ignoring radial stress does not affect the calculation result for axial stress.

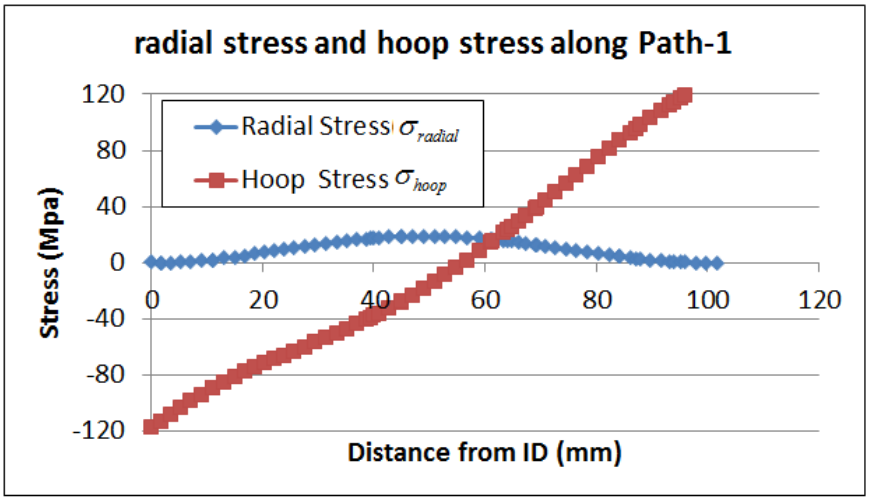

Figure 5-50 Radial and hoop residual stress distributions along Path-1

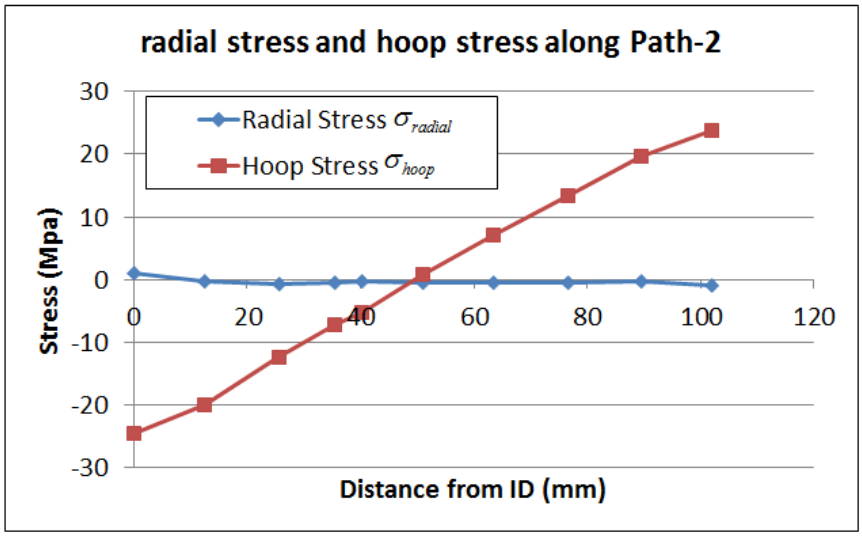

Figure 5-51 Radial and hoop residual stress distributions along Path-2

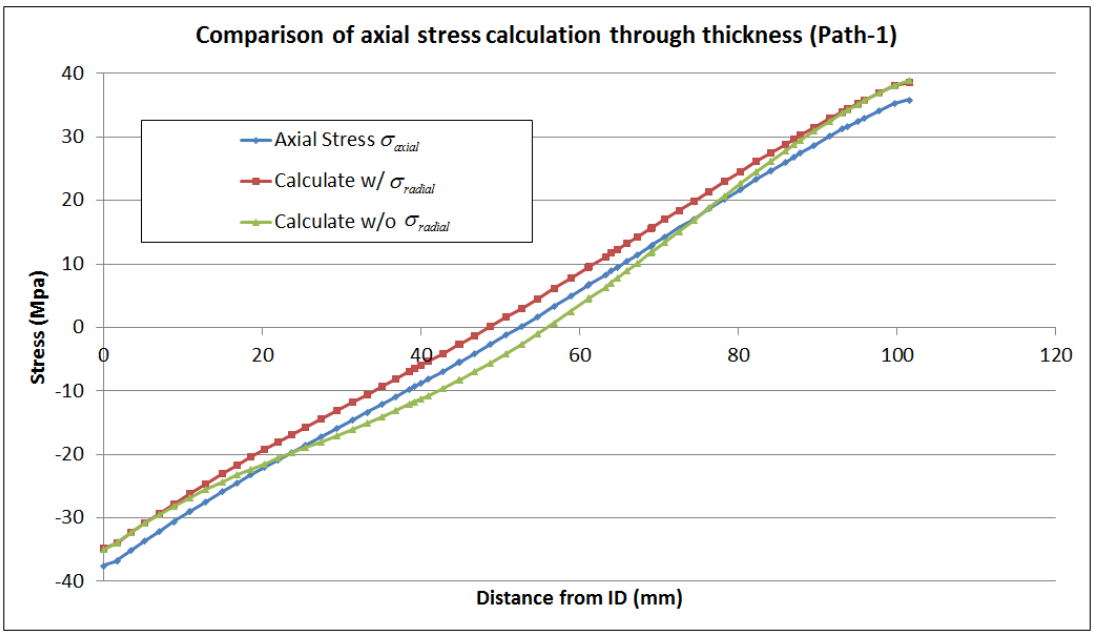

Figure 5-52 Axial residual stress calculation with and without radial stress for Path-1

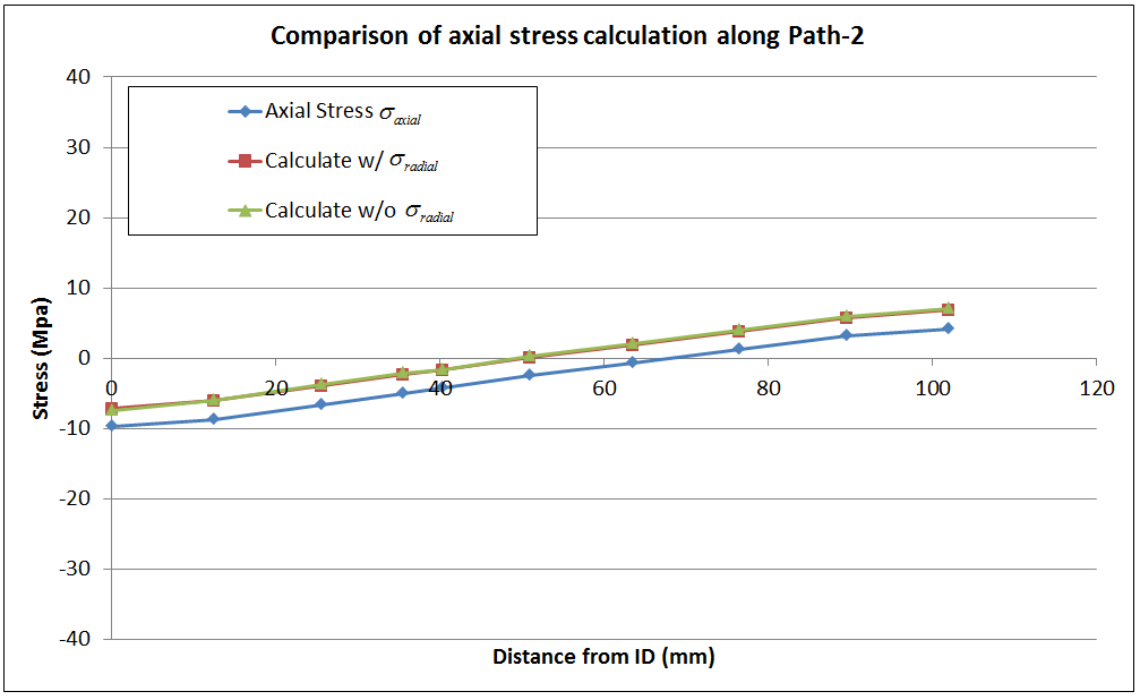

Figure 5-53 Axial residual stress calculation with and without radial stress for Path-2

The bending moment in the axial (parallel) direction can be written as:

$$M_{a,\theta} = \nu M_{h,\theta} \tag{5.8}$$

Similar to girth welds, by introducing a linear distribution from weld toe position to the plastic zone boundary, axial (parallel) residual stress bending component can be described as:

$$\sigma_{a,b}(\theta) = (-\frac{Rh}{d_p}\xi + h) + \frac{6}{t^2}M_{a,\theta}, 0 \le \xi \le \frac{d_p}{r}$$
$$h = \sigma_{a,b}^0 - \frac{6}{t^2}M_{a,\theta}\Big|_{x=0} \tag{5.9}$$

where $\sigma_{a,b}^0$ is the axial (parallel) residual stress bending component at weld toe calculated from FEA. ζ is the angle measured from zero to d_p/R. The axial stress membrane component is negligible in this part.

Figure 5-54 to Figure 5-65 show the results for cases listed in Table 5-3. Estimations obtained from the above equations are in red and FE results in blue. Overall, an excellent agreement is observed between estimations and FE results. The plastic zone width d_p discussed in Section 3 is served as an effective parameter to correlate axial residual stress components for seam welds.

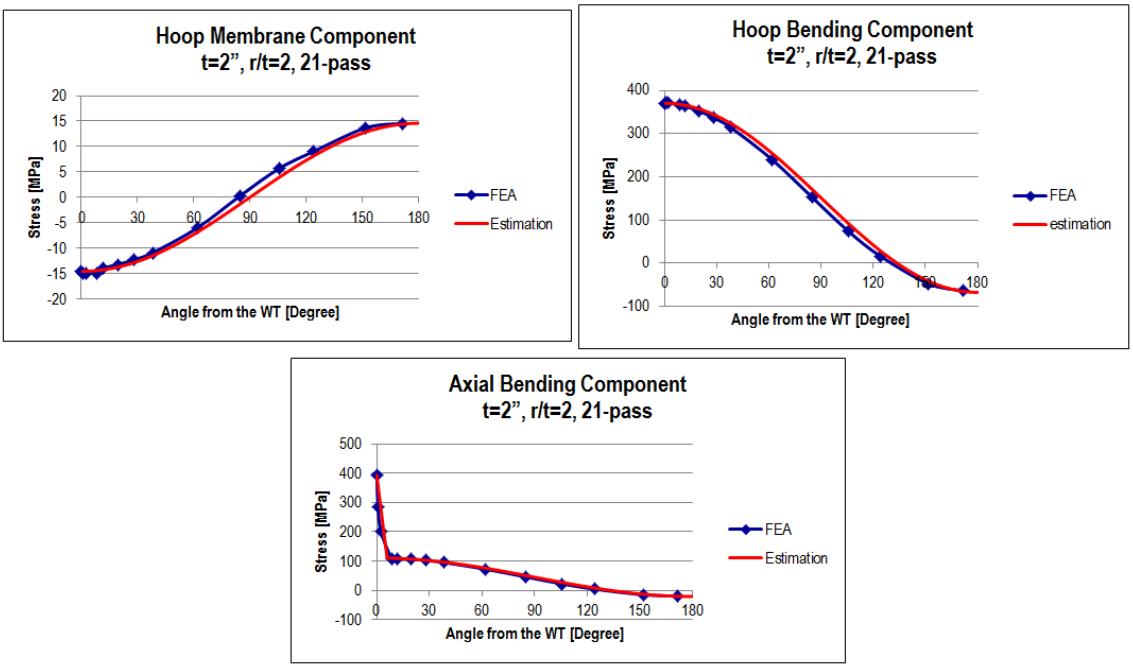

Figure 5-54 membrane and bending estimation versus FE results for t=2", r/t=2, 21-pass

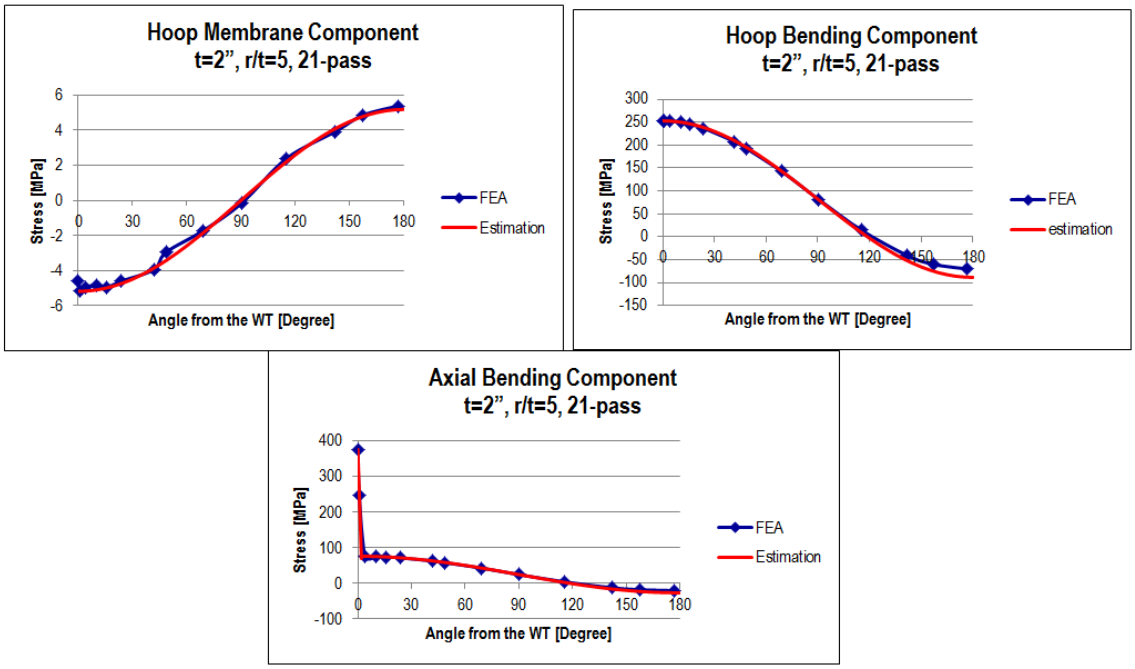

Figure 5-55 membrane and bending estimation versus FE results for t=2", r/t=5, 21-pass

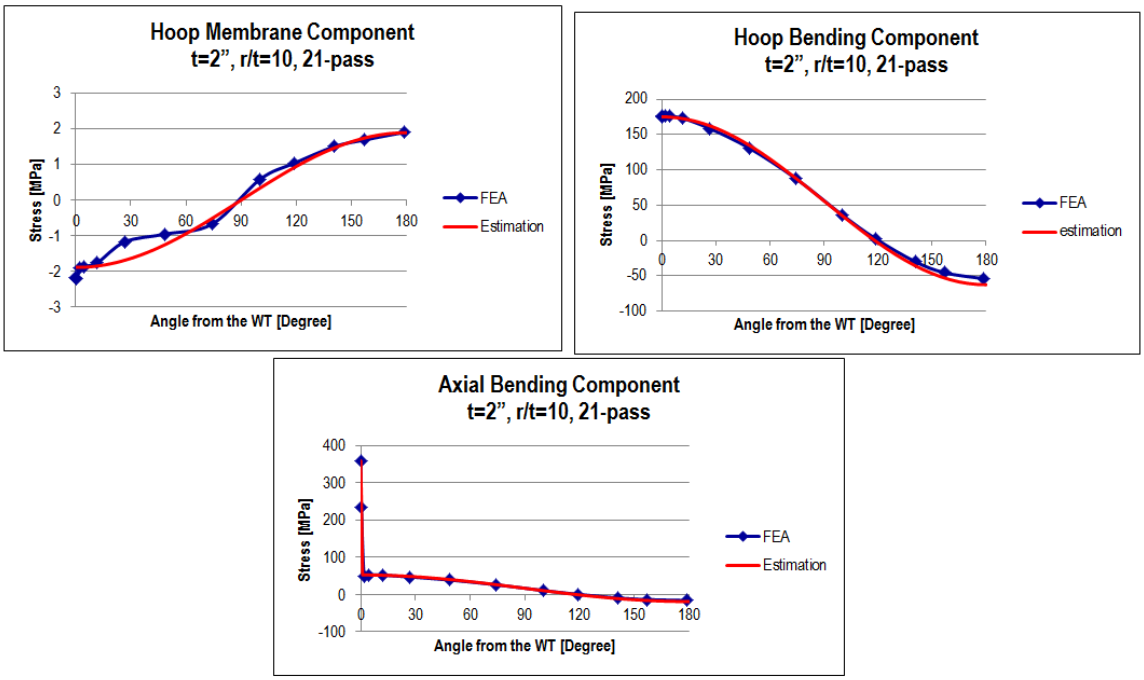

Figure 5-56 membrane and bending estimation versus FE results for t=2", r/t=10, 21-pass

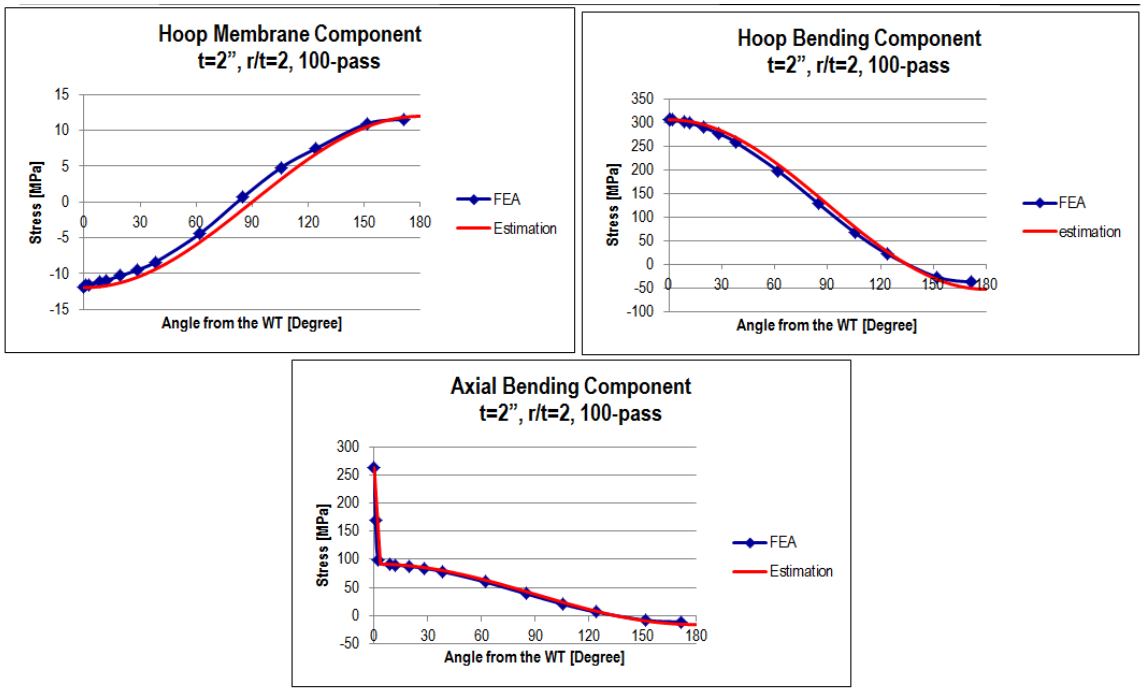

Figure 5-57 membrane and bending estimation versus FE results for t=2", r/t=2, 100-pass

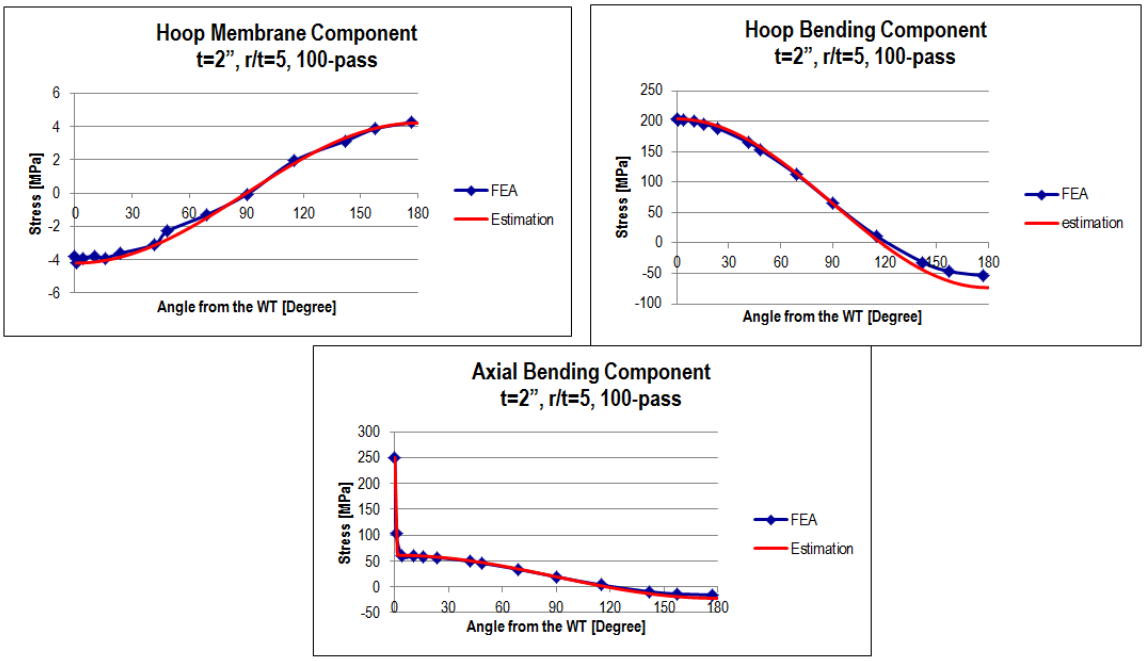

Figure 5-58 membrane and bending estimation versus FE results for t=2", r/t=5, 100-pass

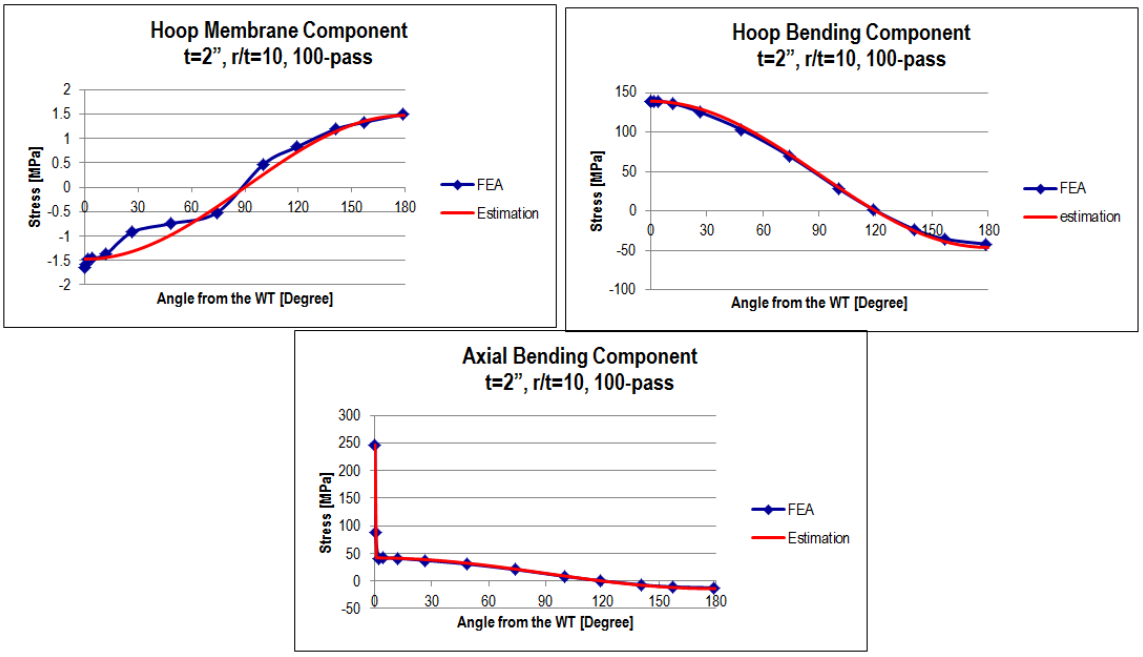

Figure 5-59 membrane and bending estimation versus FE results for t=2", r/t=10, 100-pass

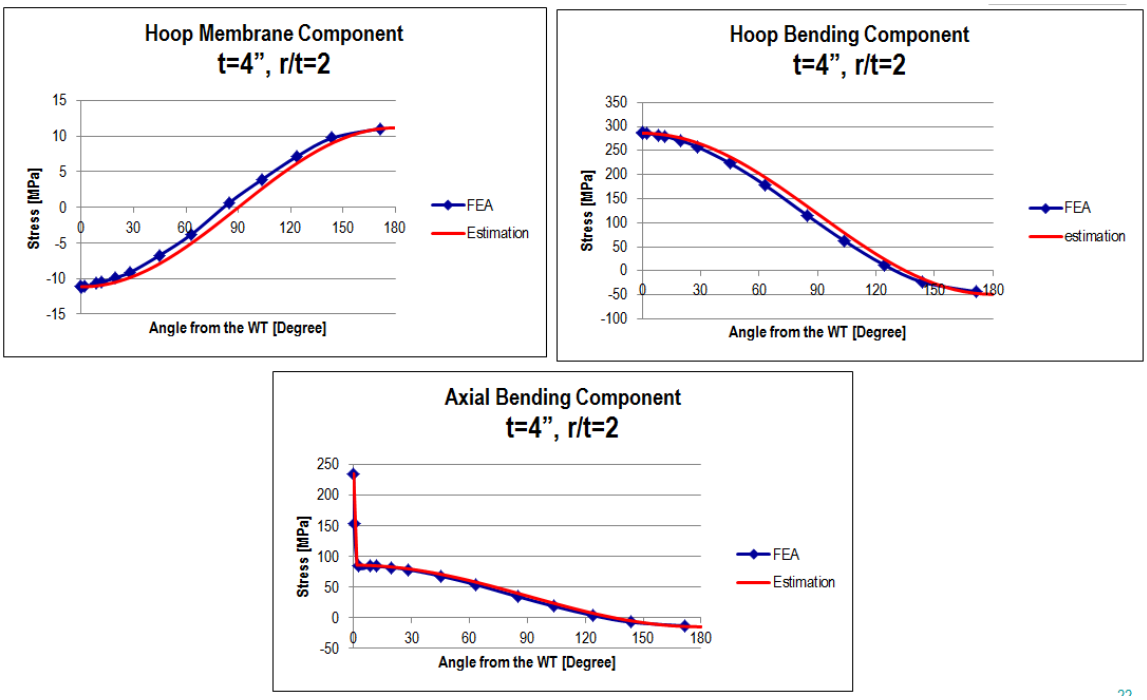

Figure 5-60 membrane and bending estimation versus FE results for t=4", r/t=2

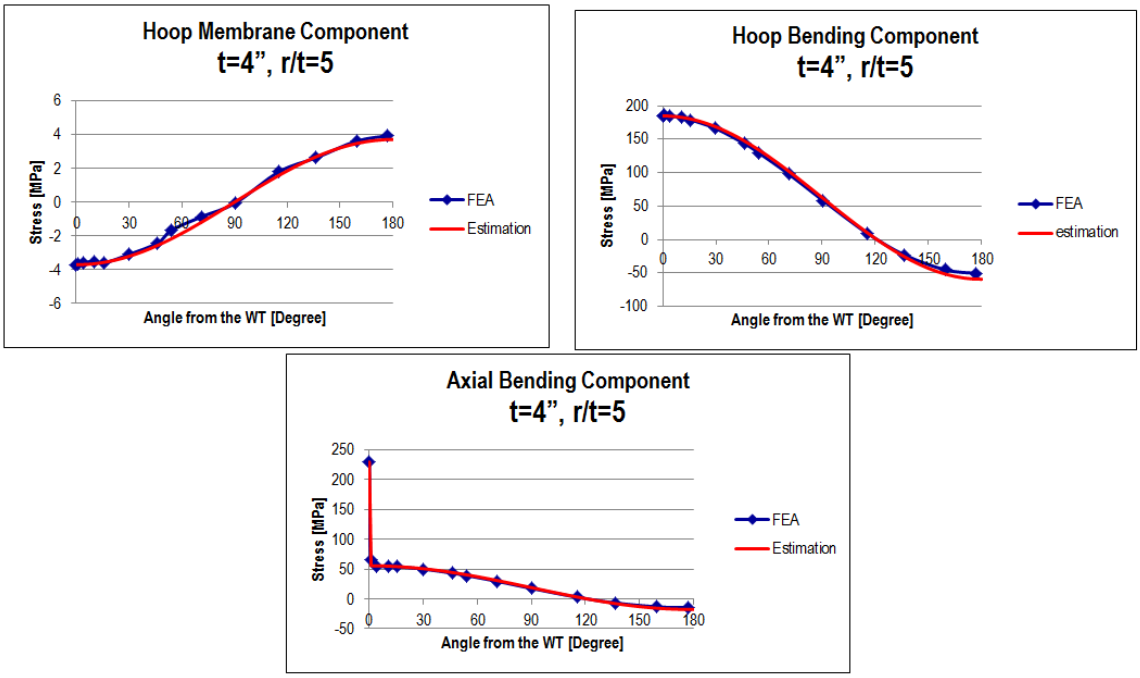

Figure 5-61 membrane and bending estimation versus FE results for t=4", r/t=5

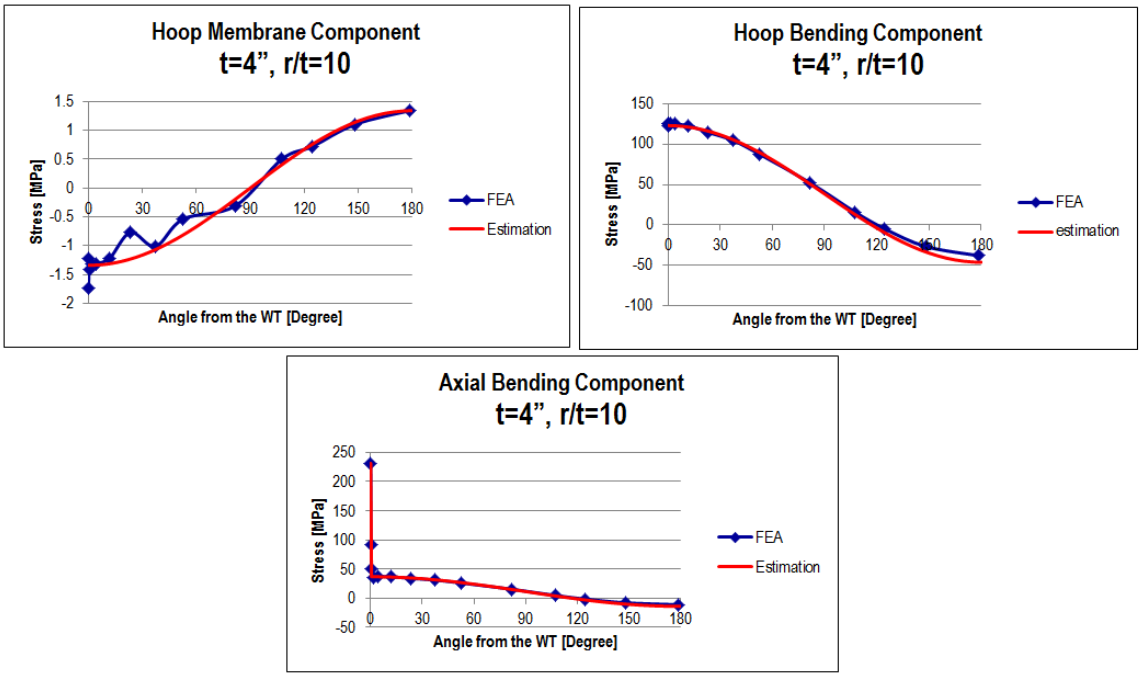

Figure 5-62 membrane and bending estimation versus FE results for t=4", r/t=10

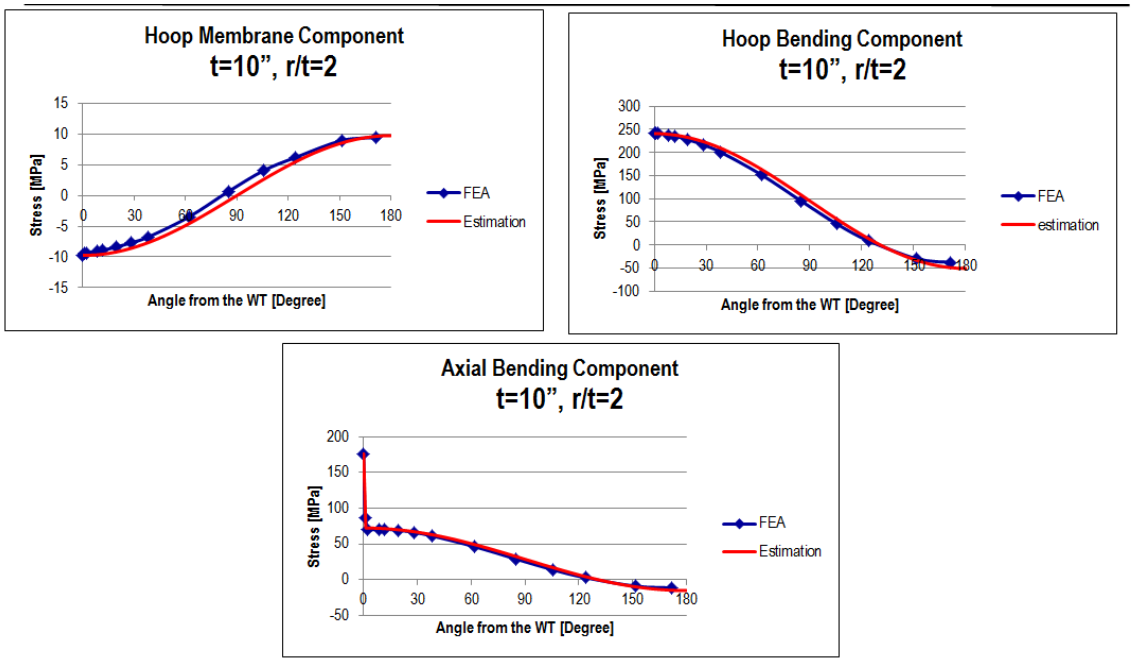

Figure 5-63 membrane and bending estimation versus FE results for t=10", r/t=2

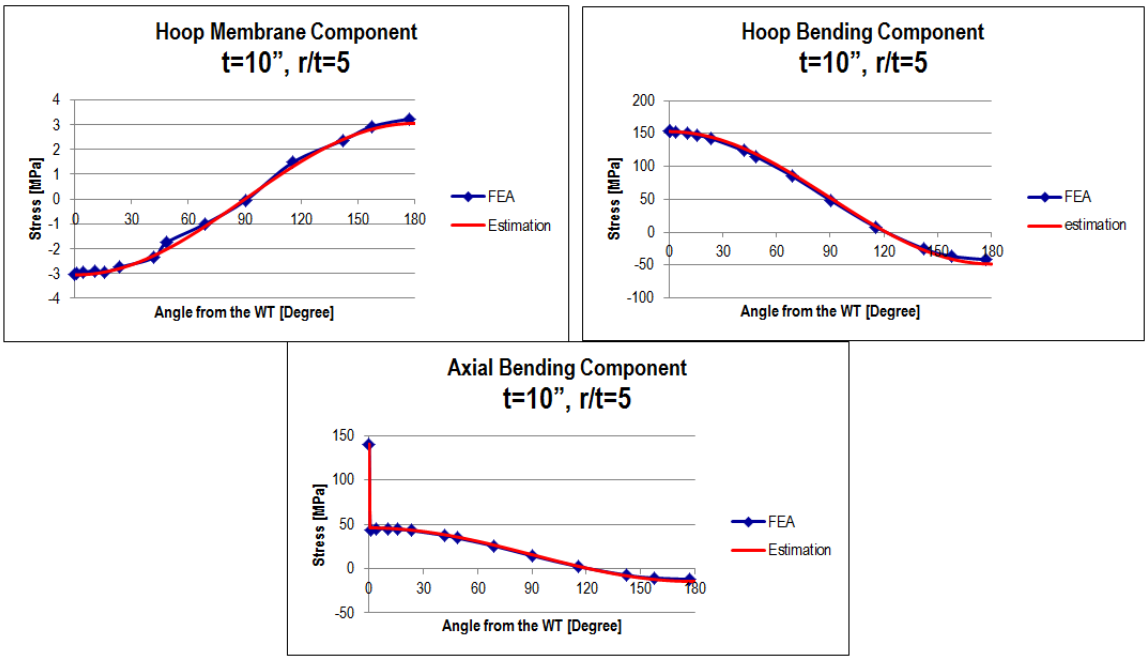

Figure 5-64 membrane and bending estimation versus FE results for t=10", r/t=5

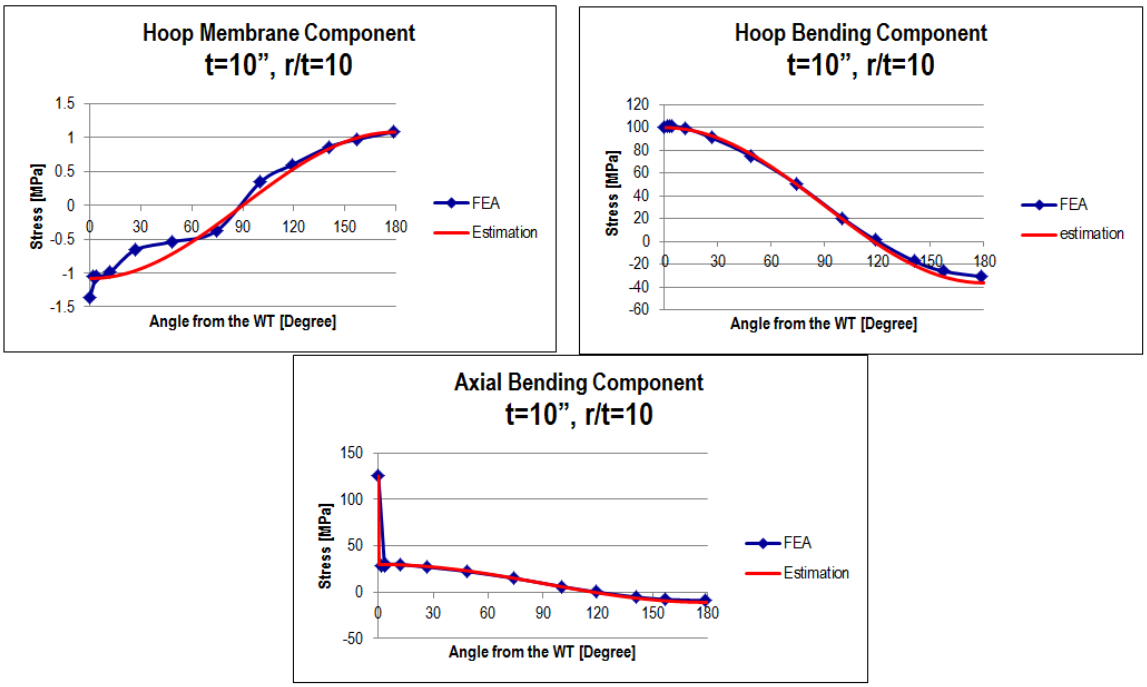

Figure 5-65 membrane and bending estimation versus FE results for t=10", r/t=10

5.5.2 Curved bar based estimations (hoop, radial, and shear stresses) versus FE results for selected cases

As documented in [139-142], through-thickness hoop, radial and shear stresses for a curved bar model (Figure 5-48) can be described as:

$$\sigma_{hoop} = \frac{N_\theta}{A} + \frac{M_\theta (A - rA_m)}{Ar(RA_m - A)}$$

$$\sigma_{radial} = \frac{1}{r}\left(\frac{A'}{A} N_\theta + \frac{AA'_m - A' A_m}{A(RA_m - A)} M_\theta \right) \quad \textbf{(5.10)}$$

$$\sigma_{shear} = \frac{V_\theta (R - e) Q}{Ae(R - y)^2}$$

where r is the distance from the pipe center, as shown in Figure 5-48. N_θ, M_θ shown in Figure 5-48 are given by Eq. (5.1) and Eq. (5.2), respectively, and they have been discussed in the previous section. V_θ is the shear force and can be expressed as:

$$V_\theta = N_0 \cdot \sin\theta \quad \textbf{(5.11)}$$

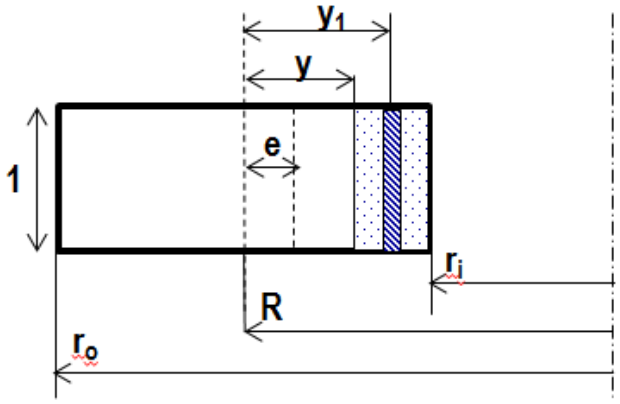

Figure 5-66 Unit cross section diagram for shear stress calculation

The term Q in the shear stress formula of Eq. (5.10) can be expressed as:

$$Q = \int_y^{(r_o - r_i)/2} y_1 dA \quad \textbf{(5.12)}$$

where y and y_1 are shown in Figure 5-66, and A is the area of a unit cross section. The other parameters in Eq. (5.10) are given as blow:

$$A = r_o - r_i, \quad A' = r - r_i, \quad A_m = \ln\frac{r_o}{r_i}$$

$$A'_m = \ln\frac{r}{r_i}, \quad R = \frac{r_o + r_i}{2}, \quad R_n = \frac{A}{A_m} \qquad \textbf{(5.13)}$$

$$e = R - R_n$$

A comparison of the results obtained from Eq. (5.10) and FE outputs are shown in Figure 5-67 to Figure 5-72 for various thickness, r/t ratio, pass number, and location θ. The estimations calculated from Eq. (5.10) are in red and FE results in blue. Generally, an excellent agreement is observed. It needs to be noted that the strength of material approach used by Eq. (5.10) is only applicable outside of the plastic zone.

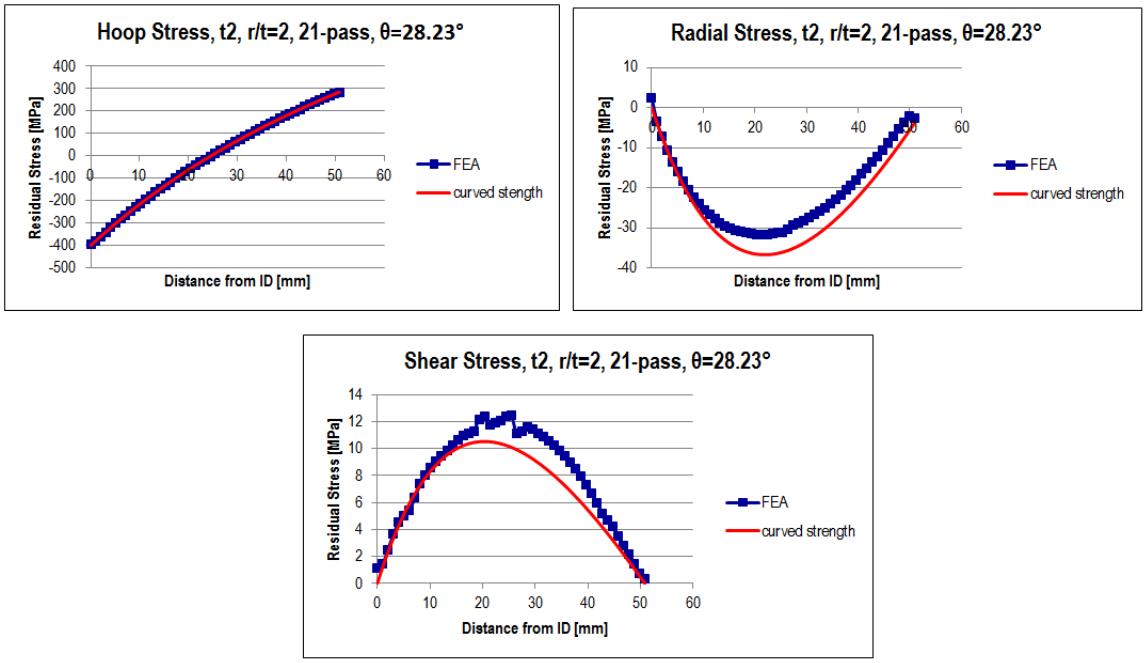

Figure 5-67 hoop, radial and shear residual stresses estimation versus FE results for t=2", r/t=2, 21-pass at θ=28.23 °

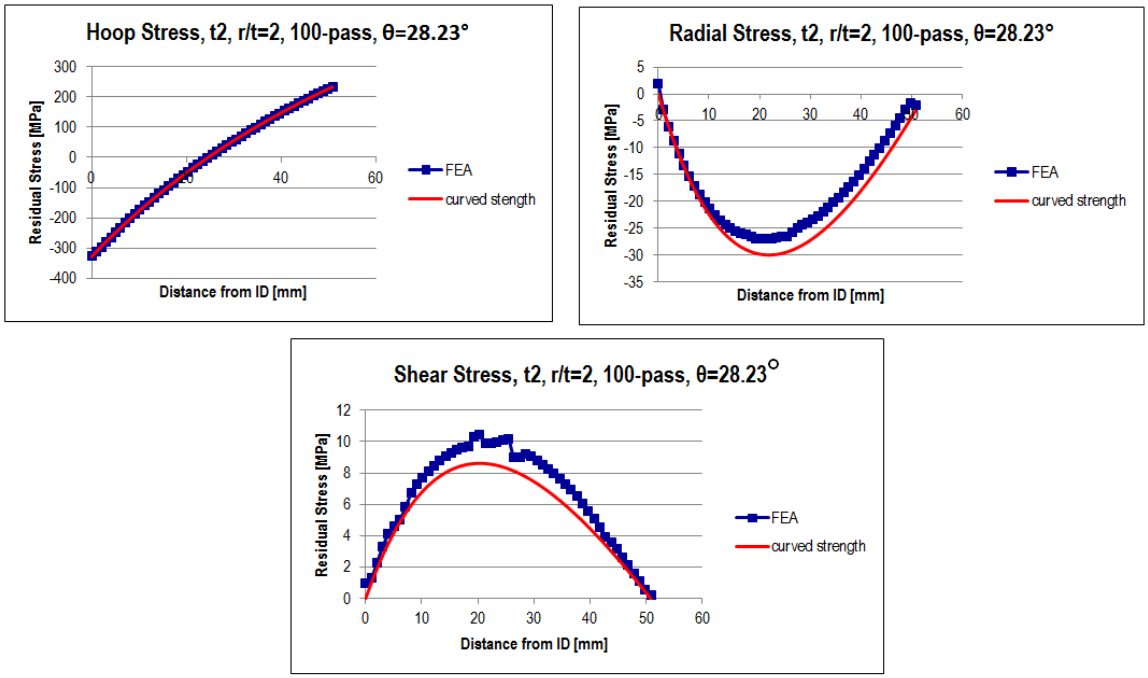

Figure 5-68 hoop, radial and shear residual stresses estimation versus FE results for t=2", r/t=2, 100-pass at θ=28.23 °

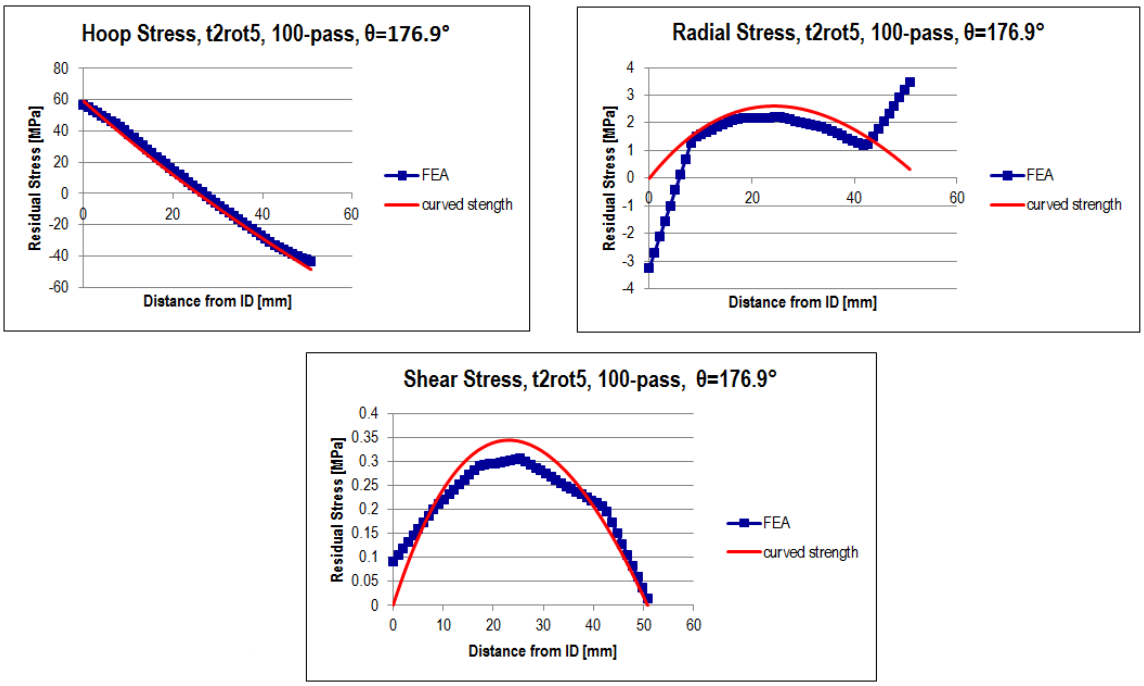

Figure 5-69 hoop, radial and shear residual stresses estimation versus FE results for t=12", r/t=5, 100-pass at θ=176.9 °

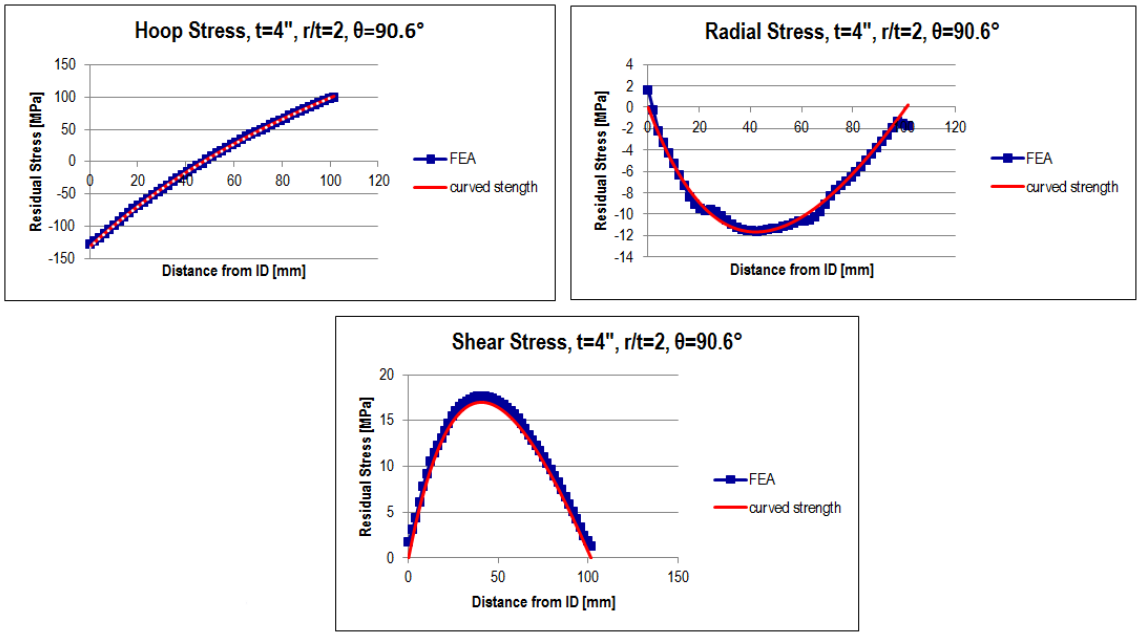

Figure 5-70 hoop, radial and shear residual stresses estimation versus FE results for t=4", r/t=2 at θ=90.6 °

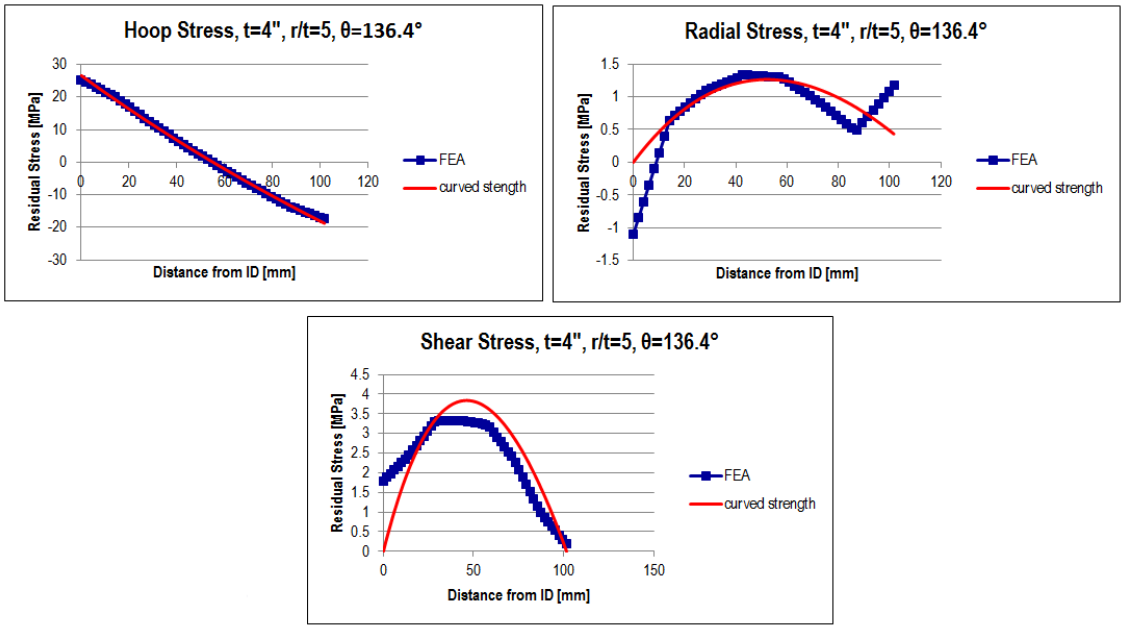

Figure 5-71 hoop, radial and shear residual stresses estimation versus FE results for t=4", r/t=5 at θ=136.4 °

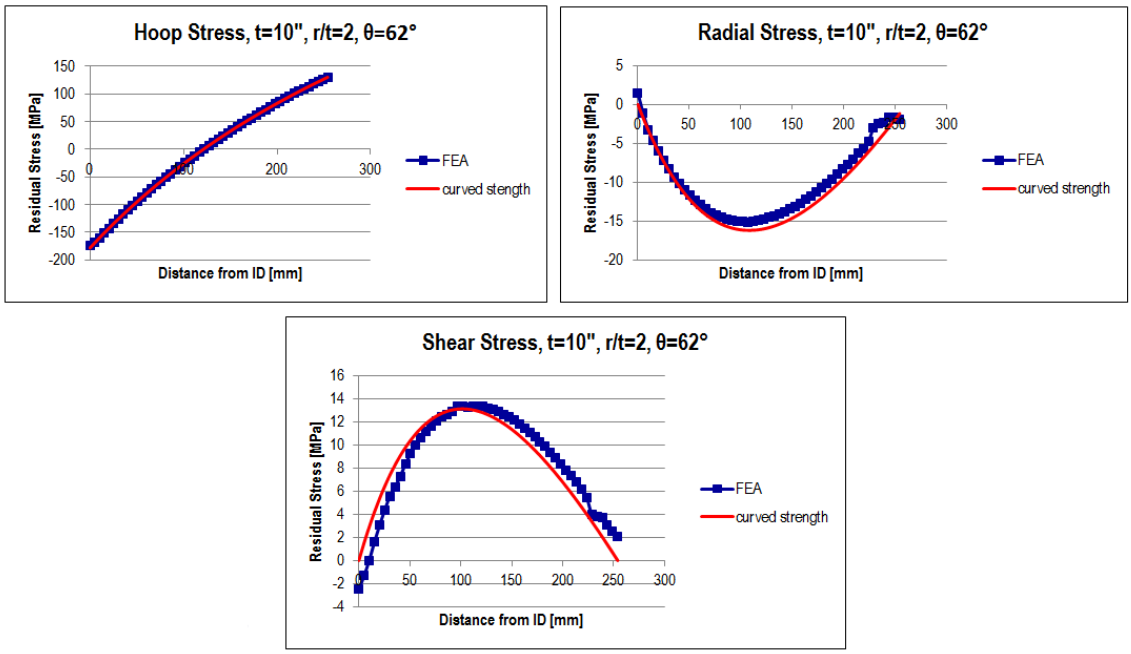

Figure 5-72 hoop, radial and shear residual stresses estimation versus FE results for t=10", r/t=2 at θ=62 °

5.6 Formulation of self-equilibrating component and validation

5.6.1 Self-equilibrating component at weld centerline and validation

In this section, Eq. (4.37) is still used for estimating the self-equilibrating component of perpendicular and parallel residual stresses at weld centerline (WCL) for seam welds. A comparison of the estimated results with FEA output is shown in Figure 5-73 to Figure 5-76. The estimations calculated by Eq. (4.37) are in blue and FE results in red. Again, a good agreement is observed for the overall distribution.

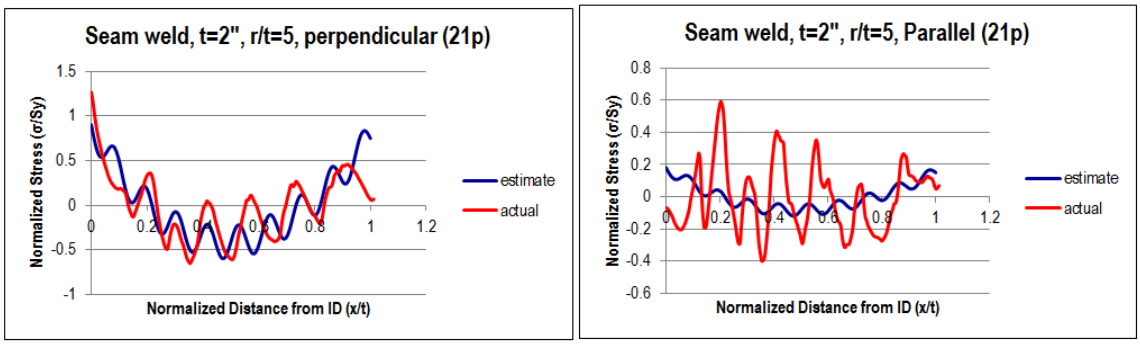

Figure 5-73 Estimation versus FE results for t=2", r/t=5, 21-pass: self-equilibrating components of perpendicular and parallel residual stresses at WCL

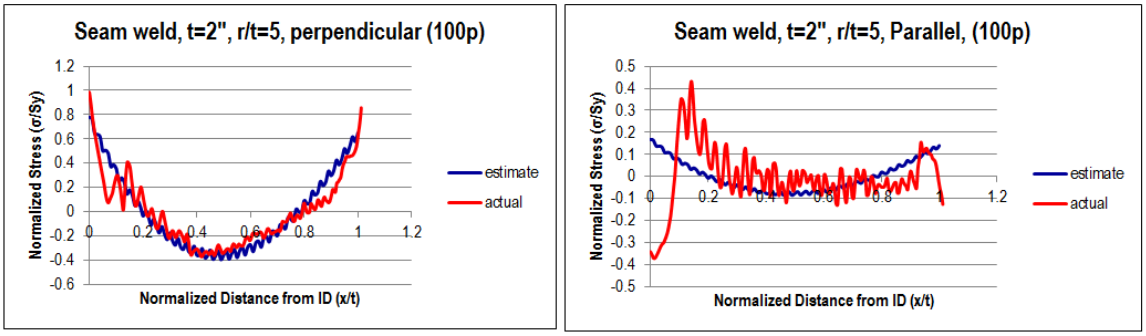

Figure 5-74 Estimation versus FE results for t=2", r/t=5, 100-pass: self-equilibrating components of perpendicular and parallel residual stresses at WCL

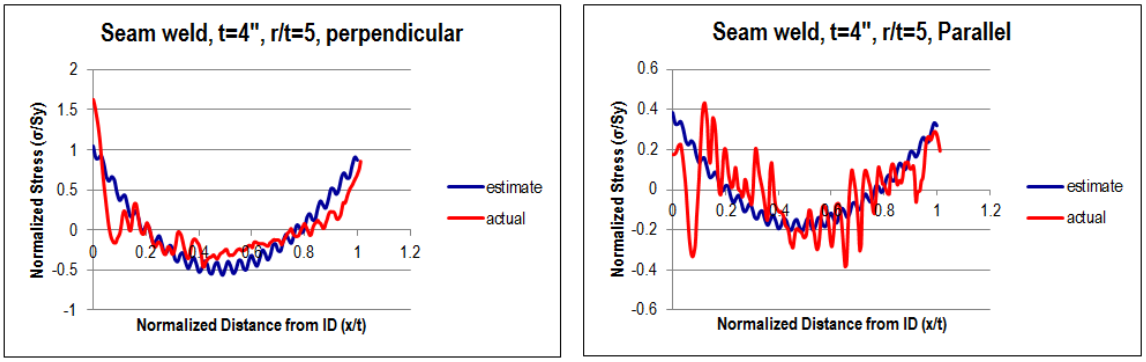

Figure 5-75 Estimation versus FE results for t=4", r/t=5: self-equilibrating components of perpendicular and parallel residual stresses at WCL

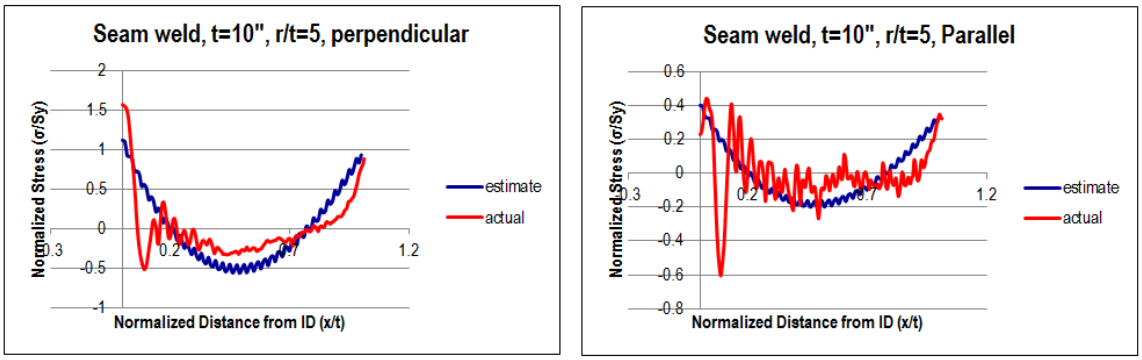

Figure 5-76 Estimation versus FE results for t=10", r/t=5: self-equilibrating components of perpendicular and parallel residual stresses at WCL

5.6.2 Total through-thickness residual stress distribution at weld centerline

Similar to girth welds, the total through-thickness residual stress distributions for perpendicular and parallel stresses can be estimated using Eq. (4.40). The results are shown in Figure 5-77 to Figure 5-80 at weld centerline (WCL). Again, a good agreement between the estimations obtained from Eq. (4.40) and FE results is achieved.

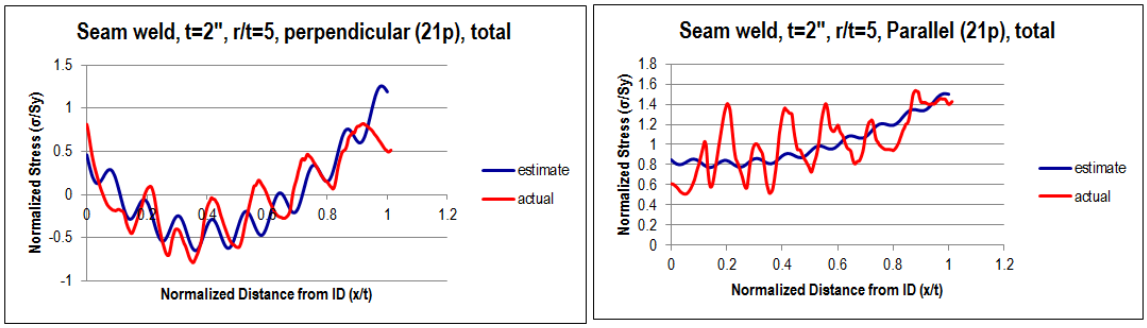

Figure 5-77 Estimation versus FE results for t=2", r/t=5, 21-pass: perpendicular and parallel residual stresses at WCL

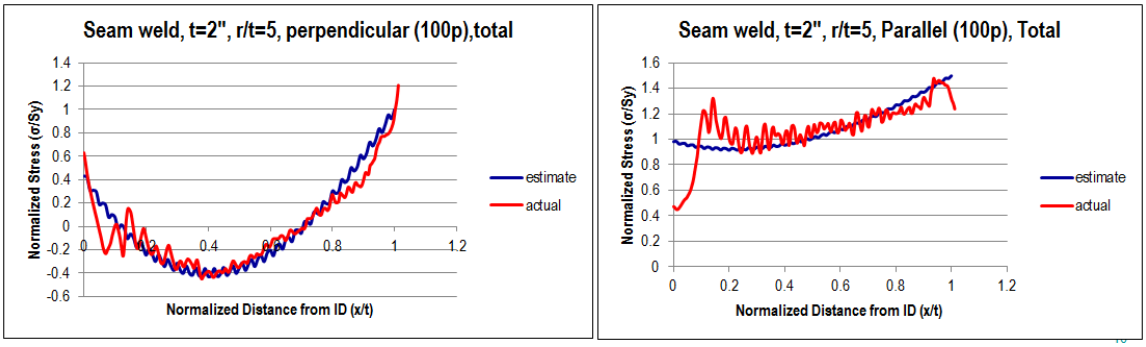

Figure 5-78 Estimation versus FE results for t=2", r/t=5, 100-pass: perpendicular and parallel residual stresses at WCL

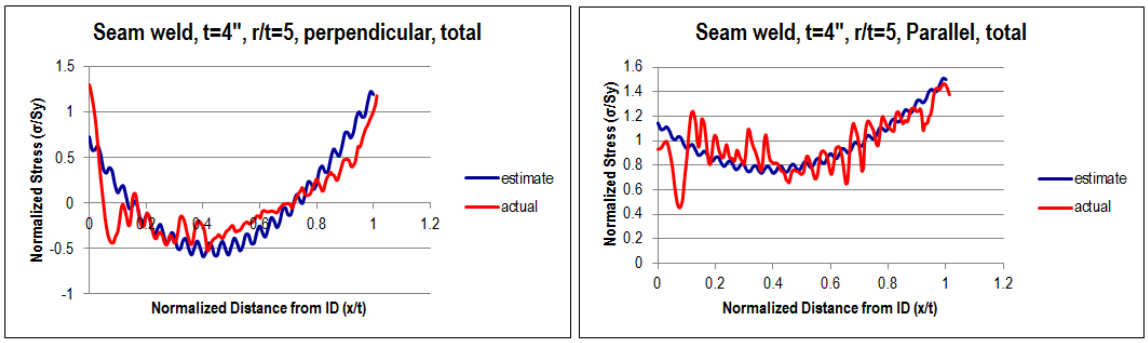

Figure 5-79 Estimation versus FE results for t=4”, r/t=5: perpendicular and parallel residual stresses at WCL

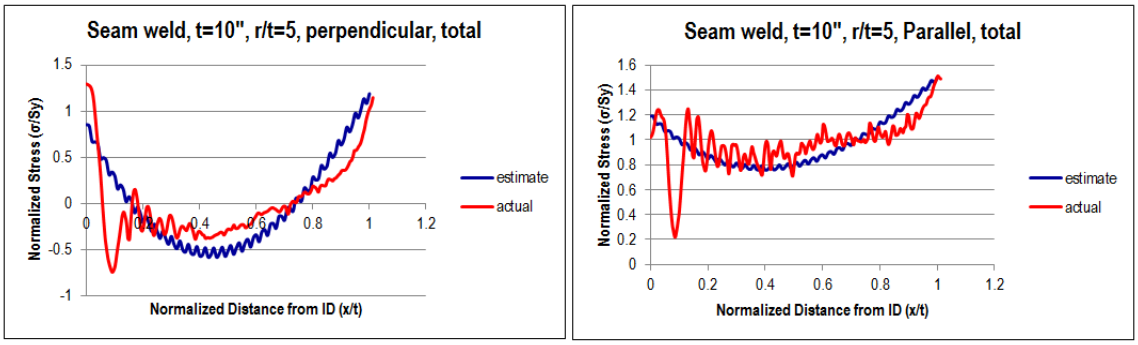

Figure 5-80 Estimation versus FE results for t=10”, r/t=5: perpendicular and parallel residual stresses at WCL

6. CONCLUSIONS

In this research, an effective and consistent mechanics based scheme describing full field residual stress distributions has been established. The main advantage of this scheme is its versatility, it can be applied to any typical pipe and vessel welds, additionally is valid not only at the limited weld locations (e.g., weld centerline and weld toe) as it currently supported by the FFS assessment procedures, but also at any distance from the weld toe up to a position at which residual stresses die out. A large number of parametric residual stress analysis cases have presented in terms of important residual stress features identified in the form of through-thickness membrane and bending based decomposition. With the controlling parameters, full-field residual stress distribution estimation schemes are derived based upon the classical shell theory for pipe girth welds and the curved bar theory for pipe seam welds.

The following is a summary of this research:

- A welding heating input characterization procedure has been developed and validated to relate prescribed temperature thermal modeling procedure to conventional linear input definition.

- Validations of the finite element procedure used in this research are carried out against measured residual stress data. The validation results show a good agreement between the finite element predications and measured data. This modeling procedure is not only valid for typical steel pipe and vessel fusion welds, but also valid for titanium alloy including friction stir welds.

- A series of parametric finite element analyses are conducted on a large number of pipe girth and seam weld cases. These cases include different weld joint preparations (Single-V, double-V, narrow groove), pipe thickness (1/4” to 10”), r/t ratio (2 to 100), materials (low alloy, high alloy) and different heat inputs. After a comprehensive review and analysis of the finite element results obtained, three controlling parameters are identified to have significant impact on residual stress profiles: characteristic heat input intensity; vessel and pipe radius over the thickness ratio (r/t).

- An analytical formula is proposed for the estimation of plastic zone size. The simple formula is validated against finite element results for a variety of weld cases.

- Estimation schemes for providing full-field residual stress profiles for pipe girths are established. The methods are derived based on the classical shell theory for pipe girth girths and the curved bar theory for seam welds with three controlling parameters identified in the parametric study. A good agreement is achieved between the proposed analytical method and full-blown finite element solution on all of the cases analyzed. This demonstrates that the proposed method is consistent and accurate, and it can be used for residual stress estimation for fitness-for-service assessment.

- In a similar manner, a curve bar theory based residual stress estimation scheme has also developed for longitudinal seam welds. A good agreement is achieved between the proposed analytical method and full-blown finite element solution for all of the cases analyzed.

- An effective estimation scheme is established for self-equilibrating component of through-thickness residual stress. A good agreement is achieved between the proposed scheme and finite element results.

REFERENCES

1 Huang, T.D., Conrardy, C., Dong, P., Keene, P., Kvidahl, L., and DeCan, L., 2007, "Engineering and Production Technology for Lightweight Ship Structures, Part II: Distortion Mitigation Technique and Implementation", *Journal of Ship Production*, 23(**2**), pp. 82-93

2 Dong, P., 2008, NAME 6098 Finite Element Analysis of Marine Structures, School of Naval Architecture and Marine Engineering, University of New Orleans

3 Dong, P., 2007, "On the Mechanics of Residual Stresses in Girth Welds", *Journal of Pressure Vessel Technology*, **129**, pp. 345-354.

4 Bouchard, P.J., 2007, "Validated Residual Stress Profiles for Fracture Assessments of Stainless Steel Pipe Girth Welds", *International Journal of Pressure Vessels and Piping*, **84**, pp. 195-222.

5 American Petroleum Institute, 2007, API Recommended Practice 579, Second Edition

6 British Standards Institution, 2005, BS 7910:2005, Guide to Methods for Assessing the Acceptability of Flaws in Metallic Structures

7 British Energy Generation Ltd, 2006, Procedure R6 Revision 4, Assessment of the integrity of structures containing defects

8 SINTAP: 1999, Structural Integrity Assessment Procedures for European Industry, Brite-EuRam Project Final Report

9 FITNET 2006, European Fitness-for-service Network

10 Dong, P., 2008, "Length Scale of Secondary Stresses in Fracture and Fatigue", *International Journal of Pressure Vessels and Piping*, **85**, pp. 128-143.

11 Dong, P., and Brust, F.W., 2000, "Welding Residual Stress and Effects on Fracture in Pressure Vessel and Piping Components: A Millennium Review and Beyond", *Journal of Pressure Vessel Technology*, **22**, pp. 329-338

12 Dong, P., and Hong, J.K., 2003, "Recommendations on Residual Stresses Estimate for Fitness-for-Service Assessment", WRC Bulletin, No. 476, Welding Research Council, New York

13 Dong, P., Cao, Z., and Hong, J.K., 2005, "Final PVRC Residual Stress and Local PWHT JIP Report on Investigation of Weld Residual Stresses and Local Post Weld Heat Treatment", Phase I

14 Dong, P., 2005, "Residual Stresses and Distortions in Welded Structures: A Perspective for Engineering Applications", *Science and Technology of Welding and Joining*, **10**(4), pp. 389-298.

15 Dong, P., Zhang, J., Li, M.V., 1998, "Computational Modeling of Weld Residual Stresses

16 and Distortions – An Integrated Framework and Industrial Applications", *ASME PVP, Fatigue, Fracture, and Residual Stress*, pp. 311-335

17 Dong, P., Cao, Z., Hong, J.K., Zhang, J., Brust, F., Bel, W., and McDonald, E.J., 2000, "Recent Progress in Analysis of Welding Residual Stresses", WRC Bulletin, No. 455, Welding Research Council, New York

18 Dong, P., 2001, "Residual Stress Analysis of a Multi-Pass Girth Weld: 3-D Special Shell Versus Axisymmetric Models*", Journal of Pressure Vessel Technology*, **123**, pp. 207-213

19 Dong, P., and Hong, J.K., 2002, "Consistent Treatment of Weld Residual Stresses in Fracture Assessment", *Proceedings of ASME PVP2002*, Van Couver, Canada

20 Dong, P., Hong, J.K., 2002, " Analysis of IIW X/XV RSDP Phase I Round-Robin Residual Stress Resutls", IIW-X/XIII/XV-RSDP-71-02/X-1515-02
21 Dong, P., and Hong, J.K., 2007, "On the Residual Stresses Profiles in New API 579/ASME FFS-1 Appendix E", *Welding in the World*, **51**(5), pp. 119-127
22 Zhang, J., and Dong, P., 2000, "Residual Stresses in Welded Moment Frames and Implications for Structural Performance, *ASCE Journal of Structural Engineering*, March, pp. 306-315
23 Song, S., Dong, P., Zhang, J., 2012, "A Full-Field Residual Stress Profiles Estimation Scheme for Pipe Girth Welds", *Proc. The ASME 2012 Pressure Vessel and Piping Division Conference, Toronto, Ontario, Canada*, PVP2012-78560, 12 pages
24 Leggatt, R.H., 2008, "Residual Stress in Welded Structures", *International Journal of Pressure Vessels and Piping*, **85**, pp. 144-151.
25 Lindgren, L.E., 2001, "Finite Element Modeling and Simulation of Welding Part I: Increased Complexity", *Journal of Thermal Stresses*, **24**, pp. 141-192.
26 Lindgren, L.E., 2001, "Finite Element Modeling and Simulation of Welding Part II: Improved Material Modeling", *Journal of Thermal Stresses*, **24**, pp. 195-231.
27 Lindgren, L.E., 2001, "Finite Element Modeling and Simulation of Welding Part III: Efficiency and Integration", *Journal of Thermal Stresses*, **24**, pp. 305-334.
28 Mackerle, J., 1996, "Finite Element Analysis and Simulation of Welding: a Bibliography (1976-1996)", *Modelling and Simulation in Materials Science and Engineering*, **4**, pp. 501-533.
29 Mackerle, J., 2002, "Finite Element Analysis and Simulation of Welding: a Bibliography (1996-2001)", *Modelling and Simulation in Materials Science and Engineering*, **10**, pp. 295-318.
30 Goldak, J.A. and Akhlaghi, M., 2005, "Computational Welding Mechanics", ISBN-10:0-387-23287-7, Spinger Science+Business Media, Inc.
31 Boulton, N.S. and Lance Martin, H.E., 1936, "Residual Stresses in Arc-Welded Plates", *Proceedings – Institution of Mechanical Engineers*, **133**, pp. 295-347
32 Rodgers, E. and Fetcher, J. R., 1938, "The determination of internal stresses from the temperature history of a butt-welded plate," *Welding Research Supplement*, pp. 4-7.
33 Rosenthal, D. and Zabrs, J., 1940, "Temperature distribution and shrinkage stresses in arc welding", *Welding Research Supplement*, **19**(9), pp. 323-331
34 Tall, L., 1964, "Residual Stresses in Welded Plates – A Theoretical Study", *Welding Research Supplement*, **43**, pp. 10-23.
35 Masubuchi, K., Simmons, F.B. and Monroe, R.E., 1968, "Analysis of Thermal Stresses and Metal Movement During Welding", Battelle Memorial Institute, NASA-TM-X-61300, N68-37857
36 Vaidyanathan, S., Todaro, A.F., and Finnie, I., 1973, "Residual Stresses Due to Circumferential Welds", *ASME Journal of Engineering Materials and Technology*, **95**, pp. 233-237
37 Vaidyanathan, S., Weiss, H., and Finnie, I., 1973, "A Further Study of Residual Stresses in Circumferential Welds", *ASME Journal of Engineering Materials and Technology*, **95**(4), pp. 238-242
38 Umemoto, T. and Tanaka, S., 1984, "A Simplified Approach to Calculate Weld Residual Stresses in a Pipe*", IHI Engineering Review*, **7**, pp. 177-183.

39 Umemoto, T. and Furuya, S., 1989, "A Simplified Approach to Assess Weld Residual Stress Distribution Through Pipe Wall", *Nuclear Engineering and Design*, **111** (1), pp. 159-171.
40 Ueda, Y. and Yamakawa, T., 1971, "Analysis of Thermal Elastic-Plastic Stress and Strain during Welding by Finite Element Method", *Transactions of the Japan Welding Society*, **2**(2), pp. 90-100
41 Hibbitt, H.D. and Marcal, P.V., 1972, "A Numerical Thermo-Mechanical Model for the Welding and Subsequent Loading of a Fabricated Structure", *Office of Naval Research (ONR) under Contract No. N00014-67-A-0191-0006*, 65 pages
42 Nickell, R.E. and H.D. Hibbitt, 1975, "Thermal and Mechanical Analysis of Welded Structures", *Nuclear Engineering and Design*, **32**, pp. 110-120
43 Friedman, E. 1975, "Thermomechanical Analysis of the Welding Process Using the Finite Element Method", *Journal of Pressure Vessel Technology*, **97**(3), pp. 206-213.
44 Rybicki, E.F., Schmueser, D.W., Stonesifer, R.W., Groom, J.J., Mishler, H.W., 1978, "A Finite-Element Model for Residual Stresses and Deflections in Girth-Butt Welded Pipes", *Journal of Pressure Vessel Technology*, **100**, pp. 256-261
45 Rybicki, E.F. and Stonesifer, R.W., 1979, "Computation of Residual Stresses due to Multipass Welds in Piping Systems", *Journal of Pressure Vessel Technology*, **101**, pp. 149-154
46 Brust, F.W., Kanninen, M.F., 1981, "Effects of Weld Parameters on Residual Stresses in BWR Piping Systems", EPRI Final Report, NP-1743
47 Brust, F.W., Stonesifer, R.B., 1981, "Analysis of Residual Stresses in Girth Welded Type 304-Stainless Pipes", ASME J. Mater. Energy Sys., **3**(3), 56-62
48 Brust, F.W. and Rybicki, E.F., 1981, "A Computational Model of Backlay Welding for Controlling Residual Stresses in Welded Pipes", *Journal of Pressure Vessel Technology*, **103**, pp. 226-232
49 Rybicki, E.F. and McGuire, P.A., 1981, "A Computational Model for Improving Weld Residual Stresses in Small Diameter Pipes by Induction Heating", *Journal of Pressure Vessel Technology*, **103**, pp. 294-299
50 Rybicki, E.F. and McGuire, P.A., 1982, "The Effects of Induction Heating Conditions on Controlling Residual Stresses in Welded Pipes", *Journal of Engineering Materials and Technology*, **104**, pp. 267-272
51 Wilkening, W.W. and Snow, J.L., 1993, "Analysis of Welding-Induced Residual Stresses with the ADINA System", *Computers and Structures*, **47**, pp. 767-786.
52 Rybicki, E.F., McGuire, P.A., Merrick, E.A., Wert, J., 1982, "The Effects of Pipe Thickness on Residual Stress due to Girth Welds", *Journal of Pressure Vessel Technology*, **104**(3), pp. 204-209
53 Brickstad, B., and Josefson, B.L., 1998, "A parametric Study of Residual Stresses in Multi-Pass Butt-Welded Stainless Steel Pipes", *International Journal of Pressure Vessels and Piping*, **75** (1), pp. 11-25.
54 Brust, F.W., Dong, P., Zhang, J., 1997, "A Constitute for Welding Process Simulation Using Finite Element Methods", *Advances in Computational Engineering Science, Proceedings of ICES Conference*, pp. 51-56.
55 Jonsson, M. and Josefen, B.L., 1988, "Experimentally Determined Transient and Residual Stresses in a Butt-Welded Pipe", *Journal of Strain Analysis*, **23**(1), pp. 25-31

56 Jonsson, M., Josefen, B.L., Nasstrom, M., 1989, "Experimentally Determined Deformations and Stresses in Narrow Gap and Single-U Multi-Pass Butt Welded Pipes", *ASME Journal of Offshore Mechanics and Arctic Engineering*, **115**(2), pp. 116-122
57 Yaghi, A.H., Hyde, T.H., Becker, A.A., Sun, W., Williams, J.A., 2006, "Residual Stress Simulation in Thin and Thick-Walled Stainless Steel Pipe Welds Including Pipe Diameter Effects", *International Journal of Pressure Vessel and Piping*, **83**, pp. 864-874.
58 Lindgren, L.E. and Jonsson, M., 1988, "Deformations and Stresses in Welding of Shell Structures", *International Journal for Numerical Models in Engineering*, **25**, pp. 635-655
59 Karlsson, R.I. and Josefen, B.L, 1990, "Three-Dimensional Finite Element Analysis of Temperatures and Stresses in a Single-Pass Butt-Welded Pipe", *Journal of Pressure Vessel Technology*, **112**, pp. 76-84
60 Li, M., 1995, "An experimental and finite element analysis of temperature and stress fields in girth welded 304L stainless steel pipes", Doctoral Dissertation in Materials Science and Engineering, Oregon Graduate Institute of Science and Technology, 271 pages
61 Zhang, J., Dong, P., Brust, F.W.,1997, "A 3D Composite Shell Element Model for Residual Stress Analysis of Multi-Pass Welds", *Trans., 14th International Conference on Structural Mechanics in Reactor Technology*, SMiRT 14, Lyon, France, **1**, pp. 439-445
62 Maekawa, A., Takahashi, S., Serizawa, H. and Murakawa, H., 2011, "Fast Computational Residual Stress Analysis for Welded Pipe Joint Based on Iterative Substructure Method", *Proc. The ASME 2011 Pressure Vessel and Piping Division Conference, Baltimore, MD,US,* PVP2011-57237, 10 pages
63 Maekawa, A., Kawahara, A., Serizawa, H. and Murakawa, H., 2012, "Prediction of Weld Residual Stress in a PWR Pressurizer Surge Nozzle: A Proposed Fast Computational 3D Analysis Method and influence of Its Heat Source Model", *Proc. The ASME 2012 Pressure Vessel and Piping Division Conference, Toronto, Ontario, Canada*, PVP2012-78032, 12 pages
64 1993, "Non-Destructive Measurement And Analysis Of Residual Stress In And Around Welds - A State-Of-The-Art Survey", WRC Bulletin, No. 383, Welding Research Council, New York
65 Kandil, F.A., Lord, J.D., Fry, A.T., Grant, P.V., 2001, "A Review of Residual Stress Measurement Methods – A Guide to Technique Selection", National Physical Laborary, UK, ISSN 1473-2734
66 Withers, P.J. and Bhadeshia, H.K.D.H., 2000, "Residual Stress Part 1 – Measurement Techniques", *Materials Science and Technology*, **17**, pp. 355-365
67 Withers, P.J., 2007, "Residual Stress and Its Role in Failure", *Reports on Progress in Physics*, **70**, 2211-2264
68 Withers, P.J., Turski, M., Edwards, L., Bouchard, P.J., Buttle, D.J., 2008, "Recent Advances in Residual Stress Measurement", *International Journal of Pressure Vessel and Piping*, **85**, pp. 118-127
69 Paradowska, A.M., Price, J.W.H., Finlayson, T.R., 2008, "Efficient Use of Available Techniques to Measure Residual Stresses in Welded Components", *International Workshop on Thermal Forming and Welding Distortion*, Bremen, 12 pages
70 Kingston, E., Smith, D.J., Watson, C., 2007, "Measurement of Residual Stress in Tube Penetration Welds for Ferritic Steel Hemispherical Pressure Vessel Heads", *Trans., SMiRT 19*, Toronto, 8 pages

71 Mathar, J., 1934, “Determination of Initial Stresses by Measuring the Deformation Around Drilled Holes”, *Trans. ASME,* **56**(4), pp. 249-254
72 Obert, L., Merrill, R., Morgan, R.H., 1962, “Borehole Deformation Gauge for Determining the Stresses in Mine Rock”, Report USBM RI 5978
73 Crouch, S.L. and Fairhurst, C., 1966, “A four-component borehole deformation gauge for the determination of in situ stresses in rock masses”, *Int. J Rock Mech Min Sci*, **4**, pp. 209-217
74 Leggatt, R.H., Smith, D.J., Smith, S.D., Faure, F., 1996, “Development and Experimental Validation of the Deep Hole Method for Residual Stress Measurement”, *Journal of Strain Analysis for Engineering Design*, **31**, 177-186
75 Smith, D.J., Bouchard, P.J., George, D., 2000, “Measurement and Prediction of Residual Stressed in Thick-Section Steel Welds”, *Journal of Strain Analysis for Engineering Design*, **35**(4), 287-305
76 George, D. and Smith, D.J., 2005, “Through-Thickness Measurement of Residual Stresses in Stainless Steel Cylinder Containing Shallow and Deep Weld Repairs”, *International Journal of Pressure Vessel and Piping*, **82**, pp. 279-287
77 Kingston, E.J., Stefanesch, D., Mahmoudi, A.H., Truman, C.E., Smith, D.J., 2006, “Novel Applications of the Deep-Hole Drilling Technique for Measuring Through-Thickness Residual Stress Distributions”, *J. ASTM int.*, **3**(4), 12 pages
78 Goudar, D.M., Truman, C.E., Smith, D.J., 2011, “Evaluating Uncertainty in Residual Stress Measured Using the Deep-Hole Drilling Technique”, *Strain*, **47**, 62-74
79 Hosseinzadeh, F., Mahmoudi, A.H., Truman, C.E., Smith, D.J., 2011, “Application of Deep Hole Drilling to the Measurement and Analysis of Residual Stresses in Steel Shrink-Fitted Assemblies”, *Strain*, **47**(Suppl. 2), 412-426
80 Schajer, G.S., 2010, “Hole-Drilling Residual Stress Measurement at 75: Origins, Advances, Opportunities”, *Experimental Mechanics*, **50**, 245-253
81 Schajer, G.S., 2010, “Advances in Hole-Drilling Residual Stress Measurements”, *Experimental Mechanics*, **50**, 159-168
82 Withers, P.J., Preuss, M., Steuwer, A., Pang, J.W.L., 2007, “Methods for Obtaining the Strain Free lattice Parameter When Using Diffraction to Determine Residual Stress”, *Journal of Applied Crystallography*, **40**(5), pp. 891-904
83 Webster, P.J., Wang, X.D., Mills, G., 1996, “Through Thickness Strain Scanning Using Synchrotron Radiation”, Mat. Sci. Forum, 228, pp. 227-232
84 Reimers, W., Broda, M., Brusch., G., Dantz, D., Liss, K.D., Pyzalla, A., Schmackers, T., Tschentscher, T., 1998, “Evaluation of Residual Stresses in the Bulk of Materials by High Energy Synchrotron Diffraction”, *Journal of Nondestructive Evaluation*, **17**(3), pp. 129-140
85 Paradowska, A.M., Price, J.W.H., Finlayson, T.R., Lienert, U., Ibrahim, R., 2010, “Comparison of Neutron and Synchrotron Diffraction Measurements of Residual Stress in Bead-on-Plate Weldments” *Journal of Pressure Vessel Technology*, **132**, 8 pages
86 Allen, A., Andreani, C., Hutchings, M.T., Windsor, C.G., 1981, “ Measurement of Internal Stress Within Bulk Matrials using Neutron Diffraction”, *NDT International*, **14**(5), pp. 249-254
87 Lorentzen, T., 1988, “Nondestructive Evaluation of Residual Stresses by Neutron Diffraction”, *NDT International*, **21**(6), pp. 385-388

88 ISO/TTA 3:2001 Polycrystalline materials – Determination of Residual Stress by Neutron Diffraction
89 Withers. P.J. and Webster, P.J, 2001, "Neutron and Synchrotron X-Ray Strain Scanning", *Strain*, **37**(1), pp. 19-33
90 Owen, R.A., Preston, R.V., Withers, P.J., Shercliff, H.R., Webster, P.J., 2003, "Neutron and Synchrotron Measurements of Residual Strain in TIG Welded Aluminum Alloy 2024", *Materials Science and Engineering: A*, **346**, pp. 159-167
91 Paradowska, A.M., Price, J.W.H., Ibrahim, R., Finlayson, T.R., 2005, "A Neutron Diffraction Study of Residual Stress Due to Welding", *Journal of Materials Processing Technology*, **164-165**, pp. 1099-1105
92 Paradowska, A.M., Price, J.W.H., Ibrahim, R., Finlayson, T.R., Blevins, R., Ripley, M., 2006, "Residual Stress Measurements by Neutron Diffraction in Multi-Bead Welding", *Physica B*, **385-386**, pp. 890-893
93 Paradowska, A.M., Finlayson, T.R., Price, J.W.H., Ibrahim, R., Steuwer, A., Ripley, M., 2006, "Investigation of Reference Samples for Residual Strain Measurements in a Welded Specimen by Neutron and Synchrotron X-Ray Diffraction", *Physica B*, **385-386**, pp. 904-907
94 Price, J.W.H., Paradowska, A.M., Joshi, S., Finlayson, T.R., 2006, "Residual Stress Measurements by Neutron Diffraction and Theoretical Estimation in a Single Weld Bead" *International Journal of Pressure Vessel and Piping*, **83**, pp. 381-387
95 Paradowska, A.M., Price, J.W.H., Finlayson, T.R., Lienert, U., Walls, P., Ibrahim, R., 2009, "Residual Stress Distribution in Steel Butt Welds Measured Using Neutron and Synchrotron Diffraction" *J. Phys.: Condens. Matter*, **21**, pp. 124213 (8 pages)
96 Paradowska, A.M., Price, J.W.H., Finlayson, T.R., Rogge, R.B., Donaberger, R.L., Ibrahim, R., 2010, "Comparison of Neutron Diffraction Measurements of Residual Stress of Steel Butt Welds with Current Fitness-for-Purpose Assessments" *Journal of Pressure Vessel Technology*, **132**(5), 8 pages
97 Paradowska, A.M., Suder, W., Williams, S., 2010, "Neutron Diffraction Residual Stress Measurements in Key-Hole Laser Formed Weldments", *Journal of Physics: Conference Series*, **251**, 5 pages
98 Zhang, J., Song, S., Dong, P., 2011, "Important Residual Stress Features in Reactor Nozzle Dissimilar Metal Welds", *Proc. The ASME 2011 Pressure Vessel and Piping Division Conference, Baltimore, MD,US,* PVP2011-57824, 9 pages
99 Zhang, J., Dong, P., Song, S., 2011, "Stress Relaxation Behavior in PWHT of Welded Components", *Proc. The ASME 2011 Pressure Vessel and Piping Division Conference, Baltimore, MD,US,* PVP2011-57826, 8 pages
100 Broussard, J., Crooker, P., 2011, "NRC/EPRI Residual Stress Validation Program Phase I – Experimental Specimen Modeling and Measurement", *Proc. The ASME 2011 Pressure Vessel and Piping Division Conference, Baltimore, MD,US,* PVP2011-57677, 8 pages
101 Kerr, M., Rudland, D.L., Prime, M.B., Swenson, H., Buechler, M.A., Clausen, B., 2011, "Characterization of a Plate Specimen from Phase I of the NRC/EPRI Weld Residual Stress Program", *Proc. The ASME 2011 Pressure Vessel and Piping Division Conference, Baltimore, MD,US,* PVP2011-57687, 9 pages
102 Rathbun, H.J., Fredette, L.F., Scott, P.M., Csontos, A.A., Rudland, D.L., 2011, "NRC Welding Residual Stress Validation Program International Round Robin Program and

Finding", *Proc. The ASME 2011 Pressure Vessel and Piping Division Conference, Baltimore, MD,US,* PVP2011-57642, 7 pages
103 Kerr, M. and Rathbun, H.J., 2012, "Summary of Finite Element (FE) Sensitivity Studies Conducted in Support of the NRC/EPRI Welding Residual Stress Program", *Proc. The ASME 2012 Pressure Vessel and Piping Division Conference, Toronto, Ontario, Canada*, PVP2012-78883, 11 pages
104 Goldak, J.A., Tchernov, S., Zhou, J., Downey, D., 2012, "A Sensitivity Analysis of NRC Welding Residual Stress Validation Program International Round Robin Program", *Proc. The ASME 2012 Pressure Vessel and Piping Division Conference, Toronto, Ontario, Canada*, PVP2012-78657, 10 pages
105 Ku, F.H., Tang, S.S., 2012, "Investigative Study of 2-D vs. 3-D Weld Residual Stress Analysis of the NRC Phase II Mockup", *Proc. The ASME 2012 Pressure Vessel and Piping Division Conference, Toronto, Ontario, Canada*, PVP2012-78760, 7 pages
106 Fredette, L.F., Broussard, J.E., Kerr, M., Rathbun, H.J., 2011, "NRC/EPRI Welding Residual Stress Validation Program – Phase III Details and Findings", *Proc. The ASME 2011 Pressure Vessel and Piping Division Conference, Baltimore, MD,US,* PVP2011-57645, 9 pages
107 Youtsos, A.G., 2003, "Research and Standardization Activities on Neutron Methods at HFR-Petten", Physics Section, International Atomic Energy Agency, IAEA-TECDOC-1457, pp. 33-49
108 Pratihar, S., Turski, M., Edwards, L.E., Bouchard, P.J., 2009, "Neutron Diffraction Residual Stress Measurements in a 316L Stainless Steel Bead-on-Plate Weld Specimen" *Int. J. Pres. Ves. & Piping*, **86**(1), pp. 13-19
109 Ficquet, X., Smith, D.J., Truman, C.E., Kingston, E.J., and Dennis, R.J., 2009, "Measurement and prediction of residual stress in a bead-on-plate weld benchmark specimen", *Int. J. Pres. Ves. & Piping*, **86**(1), pp. 20-30.
110 Bouchard, P.J., 2009, "The NeT Bead-on-Plate Benchmark for Weld Residual Stress Simulation", *Int. J. Pres. Ves. & Piping*, **86**(1), pp. 31-42.
111 Wimpory, R.C., Ohms, C., Hoffman, M., Schneider, R., Youtsos, A.G., 2009, "Statistical Analysis of Residual Stress Determination Using Neutron Diffraction", *Int. J. Pres. Ves. & Piping*, **86**(1), pp. 48-62
112 Ohms, C., Wimpory, R.C., Katsareas, D.E., Youtsos, A.G., 2009, " NET TG1: Residual Stress Assessment by Neutron Diffraction and Finite Element Modeling on a Single Weld on a Steel Plate", *Int. J. Pres. Ves. & Piping*, **86**(1), pp. 63-72
113 Bate, S.K., Charles, R., Warren, A., 2009, "Finite Element Analysis of a Single Bead-on-Plate Specimen Using SYSWELD", *Int. J. Pres. Ves. & Piping*, **86**(1), pp. 73-78
114 Smith, M.C. and Smith, A.C., 2009, "NeT Bead-on-Plate Round Robin: Comparison of Residual Stress Predictions and Measurement", *Int. J. Pres. Ves. & Piping*, **86**(1), pp. 79-95
115 Smith, M.C. and Smith, A.C., 2009, "NeT Bead-on-Plate Round Robin: Comparison of Transient Thermal Predictions and Measurement", *Int. J. Pres. Ves. & Piping*, **86**(1), pp. 96-109
116 Shan, X., Davies, C.M., Wangsdan, T., O'Dowd, N.P., Nikbin, K.M., 2009, "Thermo-Mechanical Modeling of a Single-Bead-on-Plate Weld Using the Finite Element Method", *Int. J. Pres. Ves. & Piping*, **86**(1), pp. 110-121

117 Turski, M., Edwards, L.E., 2009, "Residual Stress Measurements of a 316L Stainless Steel Bead-on-Plate Specimen Utilizing the Contour Method", *Int. J. Pres. Ves. & Piping*, **86**(1), pp. 126-131
118 Muransky, O., Smith, M.C., Bendeich, P.J., Holden, T.M., Luzin, V., Martins, R.V., and Edwards, L., 2012, "Comprehensive numerical analysis of a three-pass bead-in-slot weld and its critical validation using neutron and synchrotron diffraction residual stress measurements", *Int. J. Solids & Structures*, **49**, pp. 1045-1062.
119 Smith, M.C., Muransky, O., Austin, C., Bendeich, P.J., and Edwards, L., 2012, "Optimized Modeling of Weld Metal Constitutive Behavior in the NET TG4 International Weld Simulation and Measurement Benchmark", *Proc. The ASME 2012 Pressure Vessel and Piping Division Conference, Toronto, Ontario, Canada*, PVP2012-78405, 13 pages
120 Joosten, M.M. and Gallegillo, M.S., 2012, "A Study of the Effect of Hardening Model in the Prediction of Welding Residual Stress", *Proc. The ASME 2012 Pressure Vessel and Piping Division Conference, Toronto, Ontario, Canada*, PVP2012-78055, 10 pages
121 Hamelin, C.J., Muransky, O., Bendeich, P.J., and Edwards, L., 2012, "Predicting Post-Weld Residual Stresses in Ferritic Steel Weldments", *Proc. The ASME 2012 Pressure Vessel and Piping Division Conference, Toronto, Ontario, Canada*, PVP2012-78073, 9 pages
122 VORSAC (Variation Of Residual Stress in Aged Components), European Commission Framework Programme On Nuclear Fission Safety, TWI Ref: 8829/14/01
123 Zang, W., Gunnars, J., Dong, P., Hong, J.K., 2009, "Improvement and Validation of Weld Residual Stress Modeling Procedure", Swedish Radiation Safety Authority, SSM. Report number: 2009:15, ISSN: 2000-0456
124 ABAQUS, 2010, User's Manual, Version 6.9
125 Green, A.E., and Naghdi, P.M., 1965, "A General Theoty of an Elastic-Plastic Continuum", Arch. Rational Mech. Anal., 18(**4**), 251-351
126 Rosenthal, D., "The theory of moving sources of heat and its application to metal treatments", *Transactions of the ASME*, **43**(11), 1946, pp. 849-866
127 Azar, A.S. As., S.K., and Akselsen, O.M., "Determination of welding heat source parameters from actual bead shape", *Computational Materials Science*, **54**, 2012, pp. 176-182
128 Wahab, M.A. and Painter, M.J., "Numerical models of gas metal arc welds using experimentally determined weld pool shapes as the representation of the welding heat source", *Int. J. Pres. Ves. & Piping*, **73**, 1997, pp. 153-159
129 Cho, J.R., Conlon, K.T., and Reed, R.C., "Residual Stresses in an Electron Beam Weld of Ti-834: Characterization and Numerical Modeling", *Metallurgical and Materials Transactions*, **34A**, 2003, pp. 2935-2946
130 Yaghi, A.H., Hyde, T.H., Becker, A.A., Sun, W., "Numerical Simulation of P91 Pipe Welding Including the Effects of Solid State Phase Transformation on Residual Stress", *Proc. Inst. Mech. Eng., Part L*, **221**, 2007, pp. 213-224
131 Leblond, J. B., Mottet, G., and Devaux, J. C., 1986, "A theoretical and Numerical Approach to the Plastic Behaviour of Steels During Phase Transformations", J. Mech. Phys. Solids, 34, (**4**), 395–409
132 Clerge, M., Boucher, C., Pillot, S., Bourges, P., "Numerical simulation of CrMo steels thick welds intermediate post weld heat treatments", *2005 ASME Pressure Vessels and Piping (PVP) Conference*, PVP2005-71626, 8 pages

133 Yaghi, A.H., Hyde, T.H., Becker, A.A., Sun, W., Hilson, G., Simandjuntak, S., Flewitt, P.E.J., Pavier, M.J., Smith, D.J., " A Comparison Between Measured and Modeled Residual Stresses in a Circumferentially Butt-Welded P91 Steel Pipe", *Journal of Pressure Vessel Technology*, **132**, 2010, 10 pages
134 Paddea, S., Francis, J.A., Paradowska, A.M., Bouchard, P.J., Shibli, I.A., 2012 "Residual Stress Distribution in a P91 Steel-Pipe Girth Weld Before and After Post Weld Heat Treatment", *Materials Science and Engineering A*, **534**, 663-672
135 Lohwasser, D. and Chen, Z., 2012, "Friction Stir Welding – From Basis to Applications", CRC Press, ISBN 978-1-84569-450-0
136 Yaghi, A.H., Hyde, T.H., Becker, A.A., Sun, W., Williams, J.A., "Residual Stress Simulation in Thin and Thick-Walled Stainless Steel Pipe Welds Including Pipe Diameter Effects", *International Journal of Pressure Vessel and Piping*, **83**, 2006, pp. 864-874
137 Brickstad, B., Josefson, B.L., "A parametric Study of Residual Stresses in Multi-Pass Butt-Welded Stainless Steel Pipes", *International Journal of Pressure Vessels and Piping*, **75** (1), 1998, pp. 11-25
138 Timoshenko, S., 1959, "Theory of Plates and Shells", 2nd Edition, McGraw-Hill, Inc., ISBN 0-07-085820-9
139 Boresi, A.P., and Sidebottom, O.M., "Advanced Mechanics of Materials", Fourth Edition, ISBN 0-471-88392-1, 1985
140 Cook, R.D. "Circumferential Stresses in Curved Beams", *ASME J. Appl. Mech*., Vol. 59, No. 1, 1992, pp. 224-225
141 Young, W.C., and Cook, R.D. "Radial Stress Formula for Curved Beams", ASME J. Vibrat. Acoust. Stress Reliab. Des., Vol. 111, No. 4, 1989, pp. 491-492
142 Wang, T.S. " Shear Stresses in Curved Beams", Mach. Des., Vol. 39, No. 28, 1967, pp. 175-178

VITA

Shaopin Song was born on February 14, 1984 in Dalian, China. He obtained his Bachelor of Science degree from Dalian University of Technology in July 2007. Then he joined the graduate program in the School of Naval Architecture and Marine Engineering at the University of New Orleans in August 2007 and received his M.S. degree in May 2009. He continued his Ph.D. study under the supervision of Dr. Pingsha Dong focusing upon advanced residual stress modeling and analysis of welded structures. He received his Ph.D. degree in December 2012.